GENERATION AND PROPAGATION OF ROGUE WAVES IN OPTICAL FIBERS AND CHIRAL MEDIA

Thesis

Submitted and defended publicly in fulfillment of the requirements for the degree of

Doctor of Philosophy in Physics

Speciality: **Mechanics, Materials and Structures**

By

TEMGOUA DJOUATSA Diane Estelle

Registration number: **11W1325**

Master of Science in Physics, Option: **Mechanics and Materials**

Under the Codirection of

TCHOULA TCHOKONTE Moise Bertin

Associate Professor,
University of the Western Cape

KOFANE Timoleon Crepin

Professor,
University of Yaoundé I

Year 2020

Dedication

This work is dedicated to:

- My late mother **NGUETSA Elisabeth**.

- My brother **Serge Alexis**, his wife **Marie** and their kids **Joseph**, **Eli**, and **Lyne**.

- My dear sister **Gaëls Elisée**.

- My dear brothers **Jean brice**, and **Gide Brunel**.

Acknowledgments

She sincerely thank her friends **Dr. Thomas Frank DJOMATCHOUA**, **Dr. Igor Simplice MOKEM**, **Dr. André-Marie FOPOSSI**, **Dr. Duplex Steve MBIEDA**, **Dr. Thierry Landry Michel DJOMO**, **Mlle Carine FEUZING**, **Mr. Fernand NAHA**, **Mr. Carlos Lawrence GNINZANLONG**, **Mr. Fabrice Maxime KEPNANG** and **Mr. Martin FOKOU** for sharing their insights and scientific enthusiasm. Her gratefulness is also intended for the current and former members of laboratory of Mechanics, Materials and Structures for their help and friendship.

The author is deeply grateful to **Ms. Cécil**, **Ms. Vanessa Coralie**, **Mr. Jean Jules**, **Dr. Esther White**, **Dr. Chioma**, **Dr. Dorcas**, and **Dr. Theresa** for all their support and kind attention in Cameroon and South Africa.

The author acknowledges the support and encouragement from her parents. She is especially grateful to her late mother **Elisabeth NGUETSA**, who did not spare her energy when struggling for her education. She also thanks the families **FEUDJI**, **TEMGOUA**, **TONFACK** and **NANFACK** for their great support.

FUNDING

Contents

VII

List of Figures

X

XVIII

List of abbreviations

RWs: *Rogue waves*

NOAA: *National Oceanic and Atmospheric Administration*

USGS: *United States Geological Survey*

NLS: *Nonlinear Schrödinger*

DT: *Darboux transformation*

mDT: *modified Darboux transformation*

SPM: *Self-phase modulation*

GVD: *Group-velocity dispersion*

PS: *Peregrine soliton*

KM solitons: *Kuznetsov-Ma soliton*

ABs: *Akhmediev breathers*

CNLS: *Coupled nonlinear Schrödinger*

TOD: *Third-order dispersion*

CW: *Continuous-wave*

PCFs: *Photonic crystal fibers*

PBG: *Photonic band gaps*

HC-PBG fibers: *Hollow-core photonic bandgap fibers*

SC-PBG fibers: *Solid-core photonic bandgap fibers*

SC-PBG-1:   *first SC-PBG-1*

SC-PBG-2:   *first SC-PBG-2*

SEM: *Scanning electron microscopy*

TIR: *Total internal reflections*

BBO: *Beta-Barium Borate*

sCMOS: *Scientific CMOS*

TM: *time-microscope (TM)*

ZDW: *zero-dispersion wavelengths*

XPM: *Cross-phase modulation*

MI: *Modulational instability*

NLSE: *Nonlinear Schrödinger equation*

BEC: *Bose-Einstein condensate*

SS: *Self-steepening*

SFS: *Self-frequency shift*

SRS: *Stimulated Raman scattering*

SBS: *Stimulated Brillouin scattering*

FOPAs: *fibre optical parametric amplifiers*

FWM: *Four-wave mixing*

TWM: *Two-wave mixing*

LCP: *Left-circularly polarized*

RCP: *Right-circularly polarized*

CD: *Circular dichrosim*

SC: *supercontinuum*

SCG: *Supercontinuum generation*

SFB: *Soliton on finite background*

ASE: *Amplified Spontaneous Emission*

WDM: *Wavelength-division multiplexing*

NA: *Numerical aperture*

DDE method: *Difference-differential equation method*

DDT: *Darboux dressing transformation*

FFTs: *Fast Fourier transforms*

SHG - CD: *Second-harmonic generation - circular dichroism*

SHG - ORD: *Second-harmonic generation - optical rotatory dispersion*

SWH: *Significant wave height*

SVEA: *Slowly varying envelope approximation*

PDF: *Probability distribution function*

RK4:   *fourth-order Runge-Kutta*

OFN: *Optical-Fiber Nanowire*

PDEs: *Partial differential equations*

ODEs: *Ordinary differential equation*

AKNS method: *Ablowitz-Kaup-Newell-Segur method*

SOM: *Squared-operator iteration methods*

Newton-CG methods: *Newton conjugate-gradient methods*

Résumé

Cette thèse décrit la génération, la propagation et les structures des ondes extrêmes optiques dans les milieux Kerr et chiraux. Le comportement dynamique du phénomène d'onde extrême est étudié à travers des modèles scalaires et vectoriels de Schrödinger non linéaire. Ensuite, les transformations de similitude et de Darboux sont utilisées pour construire les solutions rationnelles reliées aux ondes extrêmes optiques. Les propriétés linéaires et non linéaires des prototypes d'ondes extrêmes sont mises en exergue à travers des méthodes analytiques et numériques. Puis, l'influence et la controllabilité des effets linéaires et non linéaires sur leur propagation sont soulignées.

Cette étude commence avec une équation inhomogène non paraxiale de Schrödinger non linéaire à coeficients de dispersion, de non-linéarité et de non paraxialité variables, qui gouvernent la propagation non linéaire des ondes dans un système optique inhomogène. Les propriétés des ondes extrêmes sont analysées à l'aide des fonctions polynomiales et elliptiques Jacobiennes. Par la suite, se fait la derivation scalaire et vectorielle des équations de Schrödinger non linéaires avec polarisation non linéaire droite et gauche. Les propriétés des ondes extrêmes optiques chirales sont analysées à partir des résultats analytiques, montrant l'influence de l'activité optique sur les ondes extrêmes. L'ensemble des équations scalaires et vectorielles de Schrödinger non linéaires non paraxiales à coefficients constants et variables sont derivées pour améliorer la description de la propagation des ondes extrêmes dans les milieux optiques chiraux. La condition d'instabilité modulationnelle du background revèle l'existence des vecteurs d'ondes extrêmes et le nombre de branches stables et instables. De plus, l'influence de non paraxialité, de l'activité optique et de la vitesse de groupe linéaire sont également mises en evidence sous les regimes defocalisant et focalisant de l'équation vectorielle non paraxiale de schrödinger non linéaire à coefficients constants et variables. À travers un schema algorithmique de grande applicabilité sur les méthodes de propagation des ondes non paraxiales, l'effet le plus influent et la controlabilité simultanée des effets combinés sont revelés.

Mots clés: *Ondes extrêmes optiques, milieux Kerr et chiraux, non paraxialité, transformation de similitude, transformation de Darboux modifiée, activité optique.*

Abstract

This thesis describes the generation, the propagation and structures of optical rogue waves in Kerr and chiral media. The dynamical behavior of rogue wave phenomenon is studied through scalar and vectorial nonlinear Schrödinger (NLS) models. Then, the similarity and Darboux transformations are used to construct the first-and second-order rational solutions related to optical rogue waves. The linear and nonlinear properties of rogue wave prototypes are investigated through analytical and numerical methods. Then, the influence and controllability of linear and nonlinear effects on rogue wave propagation are underlined.

The study starts with an inhomogeneous nonparaxial NLS equation with varying dispersion, nonlinearity and nonparaxiality coefficients which governs the nonlinear wave propagation in an inhomogeneous optical fiber system. Optical rogue wave properties are analyzed through polynomial and Jacobian elliptic functions. Then follow the derivation of scalar and vectorial NLS equations with right-and left-hand nonlinear polarization. The features of chiral optical rogue waves are analyzed from analytical results, showing the influence of optical activity on rogue waves. Then, both scalar and vector nonparaxial NLS equations with constant and modulated coefficients are derived to improve the description of rogue wave propagation in optical chiral media. The condition of modulation instability of the background reveals the existence of vector rogue waves and the number of stable and unstable branches. Moreover, the influence of nonparaxiality, optical activity and walk-off effect are also evidence under the defocusing and focusing regimes of the vector nonparaxial NLS equations with constant and modulated coefficients. Through an algorithm scheme of wider applicability on nonparaxial beam propagation methods, the most influential effect and the simultaneous controllability of combined effects are underlined.

Keywords: *Optical rogue waves, Kerr and chiral media, nonparaxiality, similarity transformation, modified Darboux transformation, optical activity.*

General Introduction

Intercontinental exchanges have an undeniable importance and are of special interest in the development of a country and people well-being. These exchanges have been done for centuries by different modes of transportation as airways, waterways and roadways. Among these exchanges, maritime transport is a paramount vital for international trading and is a well-known way of heavy exchanges, especially for petroleum product transportation which are more often done on farther distances in which it is the most economic mode if not, the only possible way. Maritime transport also called waterborne transport, has been achieved widely for many decades as one of easier transportation of persons and goods [1]. As any transportation mode has advantages and disadvantages, maritime transport has known several maritime disasters and risks due to giant waves in the deep sea. Before 1826, those giant waves were called white wall by mariners and their appearances were a maritime myth until the first photographic cash by the ship commandant "ESSO languedoc" in 1980. On 1 January 1995, those giant waves were measured precisely and scientifically at the Draupner oil plateform in the north sea [2, 3]. The measurement of the wave was 25.6 m whereas the significant wave height (SWH) of the water was 10.8 m. Since that day was born the English name rogue waves or freak waves. In order to reduce the travel risk for mariners, rogue waves have been studied extensively in the ocean and are also called monster waves, killer waves, giant waves, extreme waves, or abnormal waves [4, 5, 6, 7, 8, 9, 10]. The study of this strange and disastrous phenomenon was a very big challenge because of their rarity and spontaneous appearance in the ocean. Rogue wave events were sometimes observed after many months and even years and it was neither easier for scientist to observe the rogue wave appearance because of their short lifetime and nor safer because of their potential destructive nature. After many studies, researchers like J.M. Soto-Crespo, Ph. Grelu and Nail Akhmediev [11] have shown through experiences that it will be easier and safer to study rogue wave phenomenon in laboratory rather than in ocean.

As pointed out by many scientists, rogue waves are nonlinear single oceanic waves of extremely large amplitude, much higher than the average waves and are localized both in space and time [11, 12, 13]. They appear from nowhere and disappear without a trace and their reappearance without major shape changes gives rise to a novel appellation of rogue waves, namely rogons [14]. Because of their more complicated way to be studied in oceans, researchers extended this strange phenomenon in optical fibers for better understanding and the cause

of their enormous growth became a subject of scientific research. Thus, the nature of rogue wave has been discussed in hydrodynamics [15, 16, 17, 18] and initiated in nonlinear optics, by the pioneering measurement of Solli *et al.* [19]. Through the analysis of the supercontinuum generation in optical fibers, and later in a photonic crystal fiber [20]. Their occurrences have been later observed in optical cavities [21], optical wave guides [22], Bose-Einstein condensates [23, 24, 25, 26], capillary waves [27], superfluids [317], laser-plasma interactions [29, 30], in the atmosphere [31, 32], econophysics [33] and even in finance [34, 35].

Rogue wave phenomena can be described in both physical and mathematical aspects. In its physical aspect, three main features have been set to qualify a rogue wave phenomenon. First, the wave events should be twice more higher than the wave amplitude of the SWH with extremely large amplitude. Secondly, they should appear and disappear unpredictably. This qualifier is equivalent to their unexpectedly reappearance and disappearance. Lastly, rogue wave events should arise more frequently and their probability distribution function (PDF) should display an L-shaped distribution of amplitude [19, 16, 36, 37, 38]. In its mathematical aspect, rogue wave is an exact rational solution obtained from the integrable scalar nonlinear Schrödinger (NLS) equation with finite background, called Peregrine soliton [39]. The Peregrine soliton (PS) is the mathematical rogue wave prototype in self-focusing regime due to its localization in both space and time, hence, it denomination usual rogue wave. In the same aspect, others rogue wave solutions with finite backgrounds called unusual rogue waves were obtained from the focusing stardard NLS equation. On the one hand, one denotes the Kuznetsov-Ma (KM) solitons [40] which have the peculiarity of being localized in temporal dimension with periodicity along the propagation direction and on the other hand, the Akhmediev breathers (ABs) [41] which have the peculiarity of being localized along the propagation direction with periodicity in temporal dimension [42].

The concept of rogue waves which refers to rogons has been applied to pulses emerging from optical fibers and both numerical simulations and experiments have shown that the probability of their generations increases with the increase of the initial noise level responsible for the modulation instability (MI) [43, 44, 45, 46, 47, 48, 49, 50, 51]. It is worth noting that the MI leads to their generation evolves two distinct directions with opposite sense. On the one hand, it deals with the undesirable effects like the non-return-to-zero code in optical communication, the drastic enhancement of MI gain in the WDM (wavelength-division multiplexing) systems which sets the limitation of the bandwidth window of the communication system, MI lasers and the new frequency generations of ultra short pulses in optical systems. On the other hand, a suitable manipulation of MI has also found important applications in optical amplification of weak signal, dispersion management, optical switching and the production of ultra short pulses. Although their multiple observations in many other fields, the origins and the predictability of rogons remain uncertainty as well as the kind of MI that leads to rogue wave generation. In fact, in optical communication systems, many works have been done with the objective of

reducing the disastrous effects caused by MI [52, 53, 54]. Important progress has been done very recently by Baronio *et al.* [55] who showed that the MI is a necessary but not a sufficient condition for the existence of rogue waves. Through their results, they confirmed that rogue waves can exist if and only if the MI gain band also contains the zero-frequency perturbation as a limiting case known as baseband MI.

The standard NLS equation is known as the universal model to describe rogue wave phenomenon in oceans [56, 57, 58], optical fibers [15, 59] and in many physical systems [60, 61, 62]. In particular, rogue wave solutions emerging from optical fibers have been found analytically for many types of generalized NLS models such as NLS models with constant coefficients [39, 63] and NLS models with varying coefficients [14, 64, 65]. After many years, scientists recognized that, describing complex systems with the standard NLS equation is to oversimplify the nonlinear phenomena that can occur in those systems. They found in practice that, the standard NLS equation is not adequate for the description of some realistic problems like the transmission of ultrashort pulses of the order of subpicosecond and femtosecond frequencies in highly dispersive optical fibers. As consequence, this problem pushes the researchers to turn out to higher-order NLS equations [66, 67, 68]. Therefore, the NLS equation has been extended to take into account the third-order dispersion (TOD) [69, 70, 71, 72] and nonlinear effects such as self-phase modulation (SPM) [72, 73], cross-phase modulation (XPM) [24, 72], self-steepening (SS) [68], self-frequency shift (SFS) [67, 71], and four-wave mixing (FWM) [24, 71, 72]. Thus, many works have been carried out based on higher-order NLS equations with constant coefficients and with varying coefficients. Moreover, it was pointed out that the vector NLS equations describe rogue waves with higher accuracy than the scalar models [74, 75, 76]. Under this assumption, the existence of vector rogue waves in the defocusing regime was a crucial progress in the explanation of rogue wave in multicomponent systems [55].

Several nonlinear phenomena [77, 78, 79, 80] have been studied in optical fibers with the objective to solve the problem of controllability of spontaneous waves. Therefore, controllability of spontaneous waves has been performed in both theoretical and experimental approaches to investigate the interesting phenomena of rogue waves in optical fibers. Much attention has been focused on understanding of rogue wave propagation in optical fibers filled with chiral materials, with the objectives to control the chiral level and protect organic chiral materials from damage, during the processing temperature of silica [81, 82, 83, 84, 85, 86]. Despite this evident progress, the problem of controllability in the presence of higher-order terms remain unknown. It has been found that, the shape, the amplitude, the existence and even the propagation of rogue waves in Kerr and chiral media can be strongly affected by nonlinear effects which can be generated from the addition of higher-order terms. One of these effects is the nonparaxiality which arises in the miniaturization of devices involving multiplexed beams [62, 87, 315]. According to the controllability of rogue waves, the problem now is what waves, which are localized in both space and time and depict a unique event that appears from nowhere and disappears

without a trace, can exist in the presence of the GVD and Kerr nonlinearity in the nonparaxial approximation. In addition, under the assumption of high intensity and beam narrowness, what will be the adequate model, which can be used efficiently to describe simultaneous effects of the nonparaxiality [60], optical activity [74, 89, 90] and walk-off [91] on rogue waves propagating in optical fibers, filled with chiral materials. In view of great scientific importance of chiral molecules in life-science and pharmaceutical industries [92], what will be the impact of chiral materials like chiral optical fibers in optics and optical communication.

In this thesis, one mainly focuses on the generation and propagation of rogue waves in optical Kerr and chiral media. The study is based on improved scalar and vector NLS models derived under the Born-Fedorov formalism, based on the predicted Maxwell's equations for isotropic chiral media. The novelty in the study is the use of models which satisfy both, the breakdown of the paraxial approximation as well as the requirements of time-reversal symmetry and reciprocity through the Drude-Born-Federov formalism [82, 84, 85], which is an improvement in the description of spontaneous waves in chiral media. Analytical methods such as the similarity reduction, modified Darboux transformation (mDT) [63, 93, 94] and dressing-Darboux transformation (DDT) [75, 95, 96, 97, 98, 99] methods are of especial interest to investigate rational solutions that lead to rogue wave generation in optical fibers. Numerical methods such as the fourth-order Runge-Kutta method and pseudo-spectral technique [61] are used to compute efficiently and accurately the dynamic behavior of optical rogue wave solutions. These solutions are of great importance in the sense that they reveal the properties and features of the interesting phenomenon of rogue wave, on the one hand, and the possible control of chiral level, control on the existence of left or right-handed and control of energy transfer from one component to another in chiral optical fibers, on the other hand. In addition they reveal the contrast of optical activity and the interplay of chiral materials which is a scientific improvement of great importance for technological industries.

In chapter 1, the historical context of rogue waves in oceanography and from hydrodynamics to optics, as well as the technological evolution of information transportation in different types of optical fibers and wave guides is given. Experimental generation of rogue waves in optical fibers is described and the characteristic properties of the equipment are underlined. The concordance between the analytical, numerical and experimental rogue wave generation methods is presented. Significant advances of rogue wave origins and predictability, description and controllability are summarized. Then, the important progress of scientific works and their potential applications are elucidated.

In chapter 2, the integrability method called similarity transformation or symmetry reduction method is developed for non integrable models. The modulation instability phenomenon is studied to determine the stable and unstable branches and by the way the existence and non existence of rogue wave components in chiral media. Then, the Lax pair, the mDT and DDT analytical methods are presented as the key to construct the prototypes of rogue wave solutions.

Fourth-order Runge-Kutta method, difference-differential equation method and fast Fourier transforms (FFTs) are also presented as efficient numerical methods to generate usual and unusual rogue waves.

Chapter 3, presents the results of the thesis.

Firstly, the similarity transformation and the mDT are used to investigate the analytical nonparaxial rogue wave solutions. Then, a particular attention is focused on the effect of nonparaxiality, and then, on the propagation of rogue waves, to solve the problem of their controllability in the nonparaxial approximation, with particular selection of parameters of the original equation.

Secondly, starting from the Born-Fedorov equations, the derivation of the two-dimensional NLS equation in chiral optical fibers is presented. The symmetry reduction and the mDT are used to generate the analytical chiral optical rogue wave solutions in the presence and in the absence of management. Then, the influence of optical activity on the propagation of optical rogue waves is presented, showing their possible control in chiral media. The exact solutions of the chiral couple nonlinear Schrödinger (CNLS) equations with coupled space-dependence coupling field are constructed. Then, the physical properties of vector rogue waves with mixed polarization in chiral optical fiber are given.

Thirdly, one finds under the boundedness condition, the nonparaxial chiral optical rogue waves with modulated coefficients via the mDT method. An investigation on the dynamical behavior and features of nonparaxial chiral optical rogue waves is made through their specific control parameters. Then, the influence of nonparaxiality, optical activity and walk-off on the vector nonparaxial chiral NLS equations with constant coefficients is analyzed. In addition, the influence of combined effects through the vector nonparaxial chiral NLS equations with modulated coefficients is revealed .

Lastly, the model is introduced and the integrability constraints are presented. Then, the first-and second-order rogue wave solutions, investigated analytically by the mDT and numerically by one pseudo-spectral method names, difference-differential equation method is presented. Moreover, the contrast of optical activity through the rogue wave profiles is shown and the interplay of chiral materials is elucidated.

The thesis ends with a general conclusion where are summarized the mainly outcomes. Some prospects are given for further investigations on the progress of optical rogue wave field.

Chapter 1

Rogue wave historical context: From hydrodynamics to optics

1.1 Introduction

The rogue wave (RW) phenomenon was a maritime myth which had been nourished longtime ago by sailor folklore of monster or killer waves. After the first photographic cash in 1980, it was scientifically confirmed by live accounts of maritime disasters involving tankers and liners as well as anomalous water elevation recordings on offshore platforms, such as the henceforth notorious New Year's wave at the Draupner platform in the North Sea, recorded on January 1st, 1995 [7]. The field of Rogue waves (RWs) is one of the most active multidisciplinary areas of research [42]. The concept of RW has been studied extensively in oceanography, hydrodynamics, optics and photonics, plasma physics, and Bose-Einstein condensation [16, 100]. Scientists from a wide range of disciplines acknowledge that this general rogue wave concept can describe in a relevant way extreme wave events of different origins, from the killer waves in the ocean [7, 58, 101, 102] to the extreme pulses in optics [17, 103], and even the financial crises in economy [34]. As their understanding may be essential for reducing the travel risk on high seas, the RW concept introduced a unifying idea that can be applied to a variety of extreme phenomena in different fields. Among this filed, optical RW field occupies a special place because of its wide potential applications, which have significantly enriched the original concept. Optical RW was initiated in nonlinear optics, by Solli *et al.* [19] in 2007, and later in a photonic crystal fiber [20], effectively announcing the birth of optical RW field. This found of RWs as high amplitude pulses in supercontinuum generation is not the only type of RWs in optics. They can also be found in the output of laser radiation [11, 36, 104, 105, 106] and in other types of optical cavities [107, 108, 109, 110]. They can be influenced by Brillouin scattering [111] or by the Raman effect [112]. Indeed, there is a multiplicity of RW forms [17, 103, 113, 114, 115], and this can make them

difficult to be classified. The models describing these physical systems are most often based on the nonlinear Schrödinger (NLS) equation and its variants [63]. Gradually, the RW has been found in many other systems such as the Hirota equation [116], Davey-Stewartson equation [117], Boussinesq equation [118], Sasa-Satsuma equation [119], Fokas-Lenells equation [120], the Manakov system [121], coupled Hirota equations [122, 123], NLS-Maxwell-Bloch system [124] and Yajima-Oikawa system [125]. The first-order rational solution of the NLS equation was constructed by the British mathematician Howell Peregrine in 1982. This first-order RW solution, called Peregrine soliton is endowed with localization in both space and time (1+1) dimensions [39]. Although this solution is usually termed as "Peregrine soliton", is not a soliton in the ordinary sense, since its profile never stays stationary. Its high peak amplitude as well as its asymptotic connection with a constant background, which supports the idea that this extreme wave comes from nowhere and disappears without a trace [12], has made the Peregrine soliton a central prototype of rogue wave manifestations, even though the notion of statistical distributions, which is meant to confront the experimental appearance of rogue waves among chaotic wave fields. Until now, the Peregrine soliton known as usual RW, has continued to play a pivotal role for modelling RWs in scalar NLS systems, as well as a gauge to assess other RW solutions proposed for systems other than the NLS equation [42]. Analytically, it can be viewed as the limiting case of Kuzenetsov-Ma [40] and Akhmediev breathers [41]. These RW prototypes are RW solutions with finite backgrounds called unusual RWs. These three exact solutions provide controllable initial excitation conditions for the realization of rogue waves [126]. Of the current physical systems of interest, nonlinear optical fibers represent the mature experimental platform for observing optical rogue waves [15, 40, 57, 127, 128, 129]. Therefore, Dudley et al. [15] realized experimentally in 2009, the Akhmediev breathers. Then, in 2010, Kibler et al. [127] confirmed the existence of Peregrine rogue wave by using the frequency-resolved optical gating technique. Later, in more detailed experimental observations, Hammani *et al.* [128] revealed the spectral evolution of the growth and attenuation of Akhmediev breathers. Moreover, the Kuznetsov-Ma soliton was also confirmed experimentally in [40].

In this chapter, the historical context of rogue waves in oceanography and from hydrodynamics to optics, as well as the technological evolution of optical communication in different types of optical fibers and wave guides is revealed. Experimental generation of rogue waves in optical fibers is described and the characteristic properties of the equipment are underlined. The concordance between the analytical, numerical and experimental rogue wave generation methods is presented. Significant advances of rogue wave origins and predictability, description and controllability are summarized. Finally, the important progress of scientific works and their potential applications are elucidated.

1.2   Rogue wave historical context in oceanography

Rogue waves (RWs), known as the oceanic phenomena responsible for the maritime disasters, have been thought to appear from nowhere and disappear without a trace [12, 21, 101]. It has been proved that rogue wave is localized in both space and time with crest height two times larger, sometimes, more than three times larger, than the significant wave height of its surroundings [7, 130]. RWs also called freak waves are waves of giant amplitude that occur more frequently than expected from the normal law [4, 113].

1.2.1   Rogue wave etymology

Freak, rogue, or giant waves correspond to large amplitude waves surprisingly appearing on the sea surface ("wave from nowhere"). Ocean RWs are rare events with extreme magnitude which can pose a serious threat to large ships in the ocean. Such waves can be accompanied by deep troughs (holes), which occur before and/or after the largest crest. As pointed out by Lawton [131], the freak waves have been part of marine folklore for centuries. Seafarers speak of "walls of water", or of "holes in the sea", or of several successive high waves ("three sisters"), which appear without warning in otherwise benign conditions. Observations gathered by the oil and shipping industries suggest there really is something out a true monster of the deep that devours ships and sailors without mercy or warning. There are several definitions for such surprising huge waves. Very often the term "extreme waves" is used to specify the tail of some typical statistical distribution of wave heights (generally a Rayleigh distribution), meanwhile the term "freak waves" describes the large amplitude waves occurring more often than would be expected from the background probability distribution. Sometimes, the definition of the freak waves includes that such waves are too high, too asymmetric and too steep. More popular now is the amplitude criterion of freak waves: its height should exceed the significant wave height in 2 to 2.2 times. Many investigations have been done to understand the physics behind the spontaneous appearance of freak wave and its relation with environmental conditions such as the wind, atmospheric pressure, bathymetry and current field [5].

1.2.2   Rogue wave events in oceanography

In 2001, a large collection of freak wave observations from ships was given in the New Scientist Magazine [131]. It was shown that twenty-two super-carriers were lost due to collisions with rogue waves from 1969 to 1994 in the Pacific and Atlantic, causing 525 fatalities, see Fig. 1.

At the very least, twelve events of the ship collisions with freak waves were recorded after 1952 in the Indian Ocean, near the Agulhas Current, coast off South Africa [132]. As illustration, the rogue wave event that occurred in shallow water on the 4th of November 2000
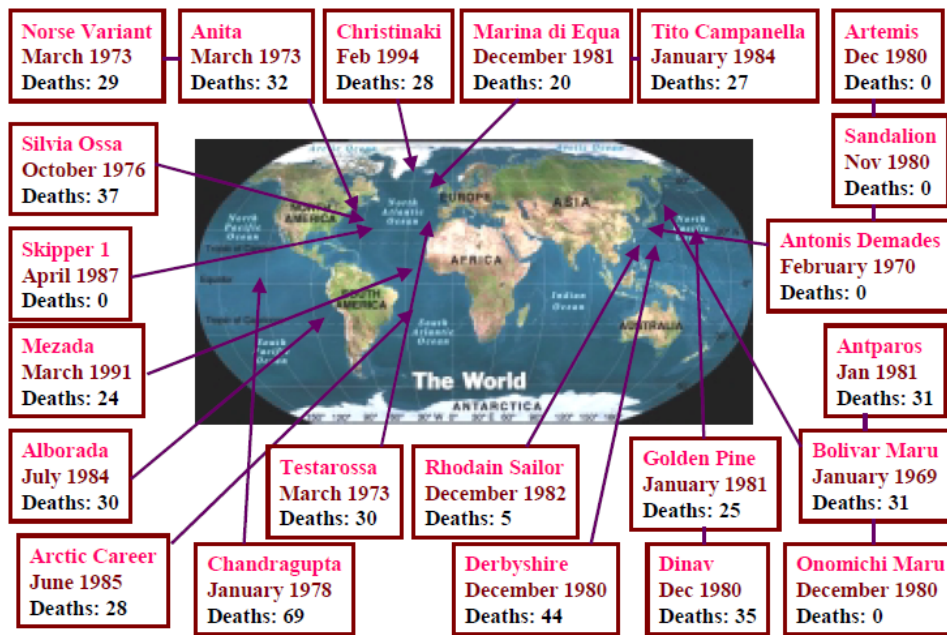
Figure 1: Statistics of super-carrier collision with rogue waves for 1968-1994 [5].

with the NOAA vessel is reported in the above description reproduced from Graham [133]. "*At 11:30 a.m. last Saturday morning (November 4, 2000), the 56-foot research vessel R/V Ballena capsized in a rogue wave south of Point Arguello, California. The Channel Islands National Marine Sanctuary's research vessel was engaged in a routine side-scan sonar survey for the U. S. Geological Survey of the seafloor along the 30-foot-depth contour approximately 1/4 nautical mile from the shore. The crew of the R/V Ballena, all of whom survived, consisted of the captain, NOAA Corps officer LCdr. Mark Pickett, USGS research scientist Dr. Guy Cochrane, and USGS research assistant, Mike Boyle. According to National Oceanic and Atmospheric Administration spokesman Matthew Stout, the weather was good, with clear skies and glassy swells. The forecasted swell was 7 feet and the actual swell appeared to be 5-7 feet. At approximately 11:30 a.m., Pickett and Boyle said they observed a 15-foot swell begin to break 100 feet from the vessel. The wave crested and broke above the vessel, caught the Ballena broadside, and quickly overturned her. All crewmembers were able to escape the overturned vessel and deploy the vessel's liferaft. The crew attempted to paddle to the shore, but realized the possibility of navigating the raft safely to shore was unlikely due to strong near-shore currents. The crew abandoned the liferaft approximately 150 feet from shore and attempted to swim to safety. After reaching shore, Pickett swam back out first to assist Boyle to safety and again to assist Cochrane safely to shore. The crew climbed the rocky cliffs along the shore. The R/V Ballena is a total loss.*"

Some photos of rogue waves are presented on Fig. 2. The description of the conditions when one of the photos (left upper) was taken is given below [135]. "*A substantial gale was moving across Long Island, sending a very long swell down our way, meeting the Gulf Stream. We*

Figure 2: Various photos of Rogue waves [134].

saw several rogue waves during the late morning on the horizon, but thought they were whales jumping. It was actually a nice day with light breezes and no significant sea. Only the very long swell, of about 15 feet high and probably 600 to 1000 feet long. This one hit us at the change of the watch at about noon. The photographer was an engineer, and this was the last photo on his roll of film. We were on the wing of the bridge, with a height of eye of 56 feet, and this wave broke over our heads. This shot was taken as we were diving down off the face of the second of a set of three waves, so the ship just kept falling into the trough, which just kept opening up under us. It bent the foremast (shown) back about 20 degrees, tore the foreword firefighting station (also shown) off the deck (rails, monitor, platform and all) and threw it against the face of the house. It also bent all the catwalks back severely. Later that night, about 19:30, another wave hit the after house, hitting the stack and sending solid water down into the engine room through the forced draft blower intakes." These description is an evidence that rogue waves are unusually large amplitude waves that appear from nowhere in the open sea.

1.2.3   Main features of rogue wave phenomenon

Evidence that extreme waves can occur in nature is provided, among others, by the Draupner and Andrea events, which have been extensively studied over the last decade [58, 102, 136, 137, 138, 139]. Tayfun analysi's on oceanic measurements has shown that large waves (measured as a function of time at a given point) result from the constructive interference (focusing) of elementary waves with random amplitudes and phases enhanced by second-order non-resonant

10

or bound nonlinearities [140]. Moreover, it has been proved that the surface statistics follow the Tayfun[141] distribution[141] in accordance with the observations [140, 142, 143, 144]. This result has been confirmed by a recent data quality control and statistical analysis of single-point measurements from fixed sensors mounted on offshore platforms, the majority of which were recorded in the North Sea [145]. The analysis of an ensemble of 122 million individual waves revealed 3649 rogue events, concluding that rogue waves observed at a point in time are merely rare events induced by dispersive focusing. Thus, a wave whose crest height exceeds the rogue threshold [102] $1.25H_s$ occurs on average once every $N_r \sim 10^4$ waves with N_r referred to as the return period of a rogue wave and H_s is the significant wave height. Some even more recent measurements off the west coast of Ireland [146] revealed similar statistics with 13 rogue events out of an ensemble of 750873 individual waves and $N_r \sim 6 \times 10^4$. Further, Fedele *et al.* [147] have considered the famous Draupner and Andrea rogue waves and the less well-known Killard rogue wave [146]. Among these events, the Andrea rogue wave was measured by Conoco on 9 November 2007 with a system of four Teledyne Optech lasers mounted in a square array on the Ekofisk platform in the North Sea in a water depth $d = 74m$ [137, 138]. The metocean conditions of the Andrea wave were similar to those of the Draupner wave measured by Statoil at a nearby platform ($d = 70m$) on 1 January 1995 with a downward-looking laser-based wave sensor [148]. The Killard wave was measured by ESB International on 28 January 2014 by a Waverider buoy off the west coast of Ireland in a water depth $d = 39m$. The wave parameters of the three sea states in which the rogue wave had occurred are summarized in Table 1. Through the Methods section, Fedele *et al.* have shown that the actual crest-to-trough (wave) heights H and crest heights h meet the classical criteria [102] $\frac{H}{H_s} > 2$ and $\frac{h}{H_s} > 1.25$ to qualify the Andrea, Draupner and Killard extreme events as rogue waves. See Table 1

To summarize, three main features are used to qualify an event as rogue wave. First, the wave events should be at the very least, twice more higher than the wave amplitude of the significant wave height (SWH) with extremely large amplitude. Secondly, they should appear and disappear unpredictably. This qualifier is also in agreement with their unexpectedly reappearance and disappearance. Lastly, rogue wave events should arise more frequently and their probability distribution function (PDF) should display an L-shaped distribution of amplitude [19, 36, 37].

1.3 Extension of rogue wave phenomenon in optical fiber

Scientific interest in the rogue wave phenomenon was to a great extend supported by the fact that severe sea waves exceeded scientist expectations. Hence the builders and customers of ships and offshore constructions are unable to adequately estimate the safety and risks [149].

	Andrea	Draupner	Killard
Significant wave height H_s [m]	10.0	11.2	11.4
Dominant wave period T_p [s]	14.3	15.0	17.2
Mean zero-crossing wave period T_0 [s]	11.6	12.1	14.0
Mean wavelength L_0 [m]	209	219	268
Depth d [m], $k_0 d$	74, 2.23	70, 2.01	58, 1.36
Spectral bandwidth ν	0.35	0.36	0.37
Angular spreading σ_θ	0.37	0.39	0.34
Parameter $R = \sigma_\theta^2 / 2\nu^2$ [240]	0.56	0.59	0.42
Benjamin Feir Index BFI in deep water[8]	0.24	0.23	0.18
Depth factor α_S[40]	0.31	0.36	0.04
Tayfun NB skewness $\lambda_{3,NB}$[41]	0.159	0.165	0.145
Mean skewness λ_3 from HOS simulations	0.141	0.146	0.142
Maximum NB dynamic excess kurtosis $\lambda_{40,max}^d$[29]	$2.3 \cdot 10^{-3}$	$2.1 \cdot 10^{-3}$	$2.7 \cdot 10^{-4}$
Janssen NB bound excess kurtosis $\lambda_{40,NB}^b$[45]	0.065	0.074	0.076
Mean excess kurtosis λ_{40} from HOS simulations	0.041	0.032	-0.011
Janssen NB setdown ST_{NB}/H_s[45], predicted HOS setdown	0.12, 0.08	0.1, 0.11	0.1, 0.07
Maximum crest height h/H_s: observed, numerical	1.63, 1.71	1.55, 1.54	1.44, 1.57
Maximum crest-to-trough (wave) height H/H_s: observed, numerical	2.30, 2.51	2.10, 2.23	2.00, 2.28
Maximum trough-to-crest (wave) height H/H_s: observed, numerical	2.49, 2.67	2.15, 2.09	2.32, 2.29

Table 1: Wave parameters and various statistics of the simulated sea states labelled Andrea, Draupner and Killard. The Killard rogue wave occurred on a water depth of $39m$, however the hincast input spectrum could only be computed at an averaged water depth of $58m$. Statistical parameters are from an ensemble of 50 HOS simulations of sea states. We refer to the Methods section for the definitions of the wave parameters. Note that two wave heights are given for each wave: the zero-downcrossing value (crest to trough) and the zero-upcrossing value (trough to crest). [147].

1.3.1 Challenge of rogue wave study in deep water

Prediction is a central goal and a yet-unresolved challenge in the investigation of oceanic RWs. In the ocean, RW phenomena are still mysterious events. Although decades of research have shed a lot of light on several aspects of RW generation [5], their predictability remain uncertainty as well as the kind of MI that leads to rogue wave generation. One of the most challenge on RW study was to find reasonable physical principles that can be formulated in mathematical terms which can generate useful predictions on what can happen, based on observations and parameters. As to date, important progress has been done and mathematical solutions are in accordance with the observations [149]. For instance, in oceanography, there is a predictability time scale associated with rogue wave events. It has been shown that larger rogue waves have a shorter horizon of predictability. Therefore, RW events are less predictable in rougher seas due to nonlinearities. In spite of advances of RW study in oceanography, the direct effect of wind on rogue wave dynamics is also of great importance in their occurrence probability. But, until now, only simple models have been used to consider wind input on RW

generation [149]. Confronted with the short lifetime, rarety appearance and the potential destructive nature of RWs in the ocean, as well as their exact prediction, scientists decided to focus their attention on other physical systems to explain the RW behavior.

1.3.2 Easier and safer way of rogue wave study

Many physical systems exhibit behavior associated with the emergence of high amplitude events that occur with low probability but with dramatic impact. After the pioneering measurement of Solli *et al.* [19] through the analysis of the supercontinuum generation in optical fibers and later in a photonic crystal fiber (PCF) [20], an analogy between optical instability and oceanic RWs was suggested. These pioneering results made possible the first quantitative analysis of the fluctuation at the spectral edge of a broadband supercontinuum and have shown how large amplitude structures can emerge from optical systems. In optics, Rws have been identified through the probability theory that associates RW events with extreme value of probability distributions and on the approach, based on their amplitude comparatively to the SWH in oceanography. Instead of considering the field amplitude as in the deep sea, the intensity is of special interest in optics and can takes many forms such as the intensity time series, the level of two dimensional camera image and the space-time intensity evolution of the optical field [36]. Moreover, it was found that RW content of a turbulent wave field, represented by extreme deviations from the average wave amplitude [150, 151]. Most importantly, the RW appearance probability depends on initial conditions [151] which can generate chaotic wave field due to MI [17]. Briefly, optical fibers are favorable tabletop laboratories to investigate both coherent and incoherent nonlinear waves and integrable turbulence [47, 51, 151, 152, 153, 154].

1.3.3 Raisons of rogue wave extension in optical fiber

The term RW originates from oceanography, is a mysterious and severely destructive wave [5, 17, 155]. So far, the characteristic of oceanic RW has been found in different physical contexts and optical RW, firstly discovered by Solli *et al.* in the PCF, is deemed to be an optical analogue of oceanic RW because of two reasons [19]. Firstly, the highly skewed L-shaped probability soliton intensity distribution with long tail can be regarded as a specified feature of RW, which predicts the occurrence of high amplitude event with a low probability [156, 157]. Secondly, modulation instability (MI) can make optical RW generated when considering the initial noise perturbation, which is also a dramatic nonlinear effect related to the generation of oceanic RW [49, 58]. Later, optical RW has also been found in many other optical systems, such as mode-locked laser [11] and fiber Raman amplifiers [158]. Therefore, in the process of supercontinuum (SC) generation occurring in optical fibers [70], the appearance of Rw seems to be spontaneous, which is a sudden and rare event [16, 150, 159].

1.4 Rogue wave generation in optics

1.4.1 Origins and predictability of rogue waves in optical fiber

"Optical rogue waves" term, coined by Solli *et al.* [19] is based on striking phenomenological and physical similarities between the extreme events in optical system and oceanic RWs. Nonlinear mechanisms such as the nonlinear focusing due to the MI [4, 160, 161, 162, 163], as well as the nonlinear spectral instability [10], and anomalous wind excitation [21], have been suggested to explain oceanic RWs. In reality, Oceanic RWs appear to follow the "L-shape" statistics in which most waves have small amplitudes but, extreme striking waves can occur with non-negligible probability [164, 165]. RWs appear like "walls of water" and required extreme sensitivity to initial conditions for their generation. So far, the same highly sensitivity to initial conditions have been observed in Supercontinuum generation in optics. Moreover, the self-frequency shift which occur in water wave propagation is also observed in nonlinear fiber. Hence, the analogy between hydrodynamics and optics [166] on the one hand. On the other hand, the analogy between oceanic RW dynamics and pulse propagation in optics, is based on the central role of NLS equation. As shown by A. R. Osbone, the NLS equation describes the evolution of light pulse envelope, modulating an electric field in optics, and the evolution of a group envelope, modulating the surface waves, in deep water. See Fig. 3
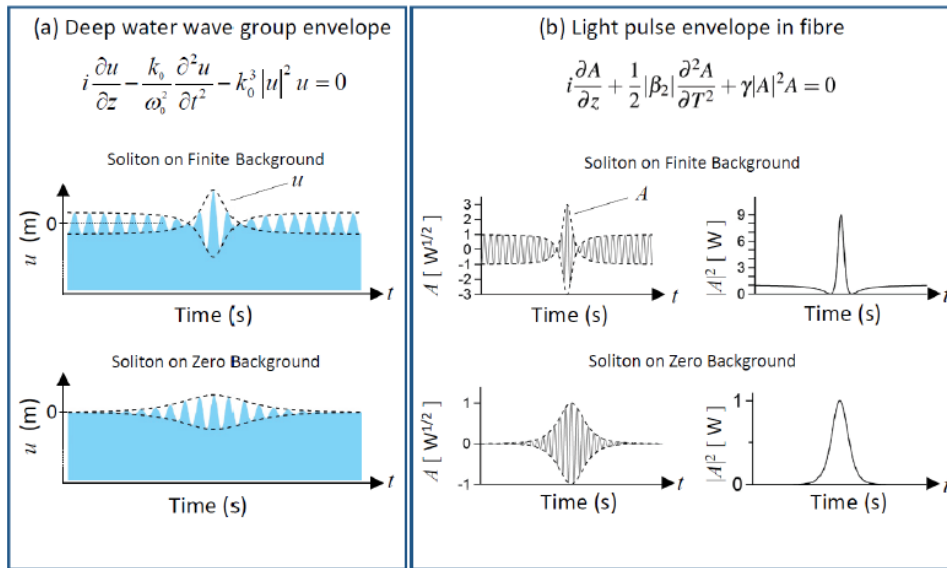
Figure 3: The NLSE describes evolution in a frame of reference moving at the group velocity of: (a) wave group envelopes u on deep water; (b) light pulse envelopes A in optical fibre with anomalous GVD. The figures illustrate solitons on finite background (top) and solitons on zero background (bottom). For the ocean wave case, there is always deep water underneath $u(z,t)$. For the water wave NLSE, k_0 is the wavenumber m^{-1}, ω_0 is the carrier frequency $\left[rad\,s^{-1}\right]$; for the fibre NLSE, $\beta_2 < 0$ is the GVD $\left[ps^2\,m^{-1}\right]$, γ is the nonlinear coefficient in $\left[w^{-1}\,m^{-1}\right]$. A water wave NLSE with time and space interchanged is also encountered but in this case the coefficients need to be adapted [58].

Yet, it has been shown that this clear analogy based on standard NLS equation becomes uncertain with extended NLS models. This rigorous standard of analogy between oceanic and optical RWs is influenced by higher-order effects of extended NLS equation.

1.4.2 Experimental generation of rogue wave in optical fibers

As confirmed by Solli *et al.* [19] and very recently by Suret *et al.* [167], the critical challenge in observing optical rogue waves is the lack of real-time instruments that can capture a large number of very short random events in a single shot. To solve this problem, Solli and co-workers have used a real-time detection technique in which the group-velocity dispersion (GVD) is used to stretch the waves temporally so that many thousands of random ultrashort events will be captured in real time. By using that technique, they find significant fraction of extreme waves among the large number of events, thus allowing the first observation of optical RWs. In their experiments, they used a supercontinuum radiation, which is generated by sending seed picosecond pulses at 1,064nm through a length of highly nonlinear microstructured optical fiber with matched zero-dispersion wavelength. Then, the output is red-pass filtered at 1,450nm and stretched for many thousands of events to be captured with high resolution in a single-shot measurement. So doing, they found that the vast majority of events were so weak and concentrated in a small number of bins. However, the most extreme ones were thirty to forty times the average intensities, displaying a clear L-shape profile. These characteristics are the main features of RW events. The setup and the histograms of the experiment is presented in Fig. 4.

From the standard NLS equation was found the RW prototypes of finite background such as the Peregrine solitons (PS), the Kuznetsov-Ma (KM) soliton and the Akhmediev breathers (ABs). These RW prototypes have been generated from coherent and deterministic means, non-stochastic initial conditions in optical fibers. Later, there have been observed in experiments from femtosecond to picosecond range. Therefore, an adequate method for the precise observation of their propagation was a very big challenge. However, the methodology of intensity autocorrelation and frequency-resolved optical gating have been used in experiments by Kibler *et al.* to observe the dynamics of PS in 2010 [127] and KM soliton, in 2012 [40]. The ABs observation in picosecond range was made possible by Frisquet and co-workers [168] in 2013. In spite of these observations in optical fibers, the methods used were restricted to obey to the periodic wave propagation and not to the non-periodic random waves. As consequence, many experiments were devoted in single-mode fiber to provide single short observations of RW structures. As results, direct observation of spatial structures of intensity profile was made possible with camera [37, 38, 169] and the single shot observation of RWs was evidence, but, not provided through the spectral filtering [19, 170, 171] and statistical measurement techniques [151], in fast time scales of fluctuations involving picosecond range. So far, the evidence of the single shot observation via the statistical measurement, was performed with photodetectors [105]. In spite
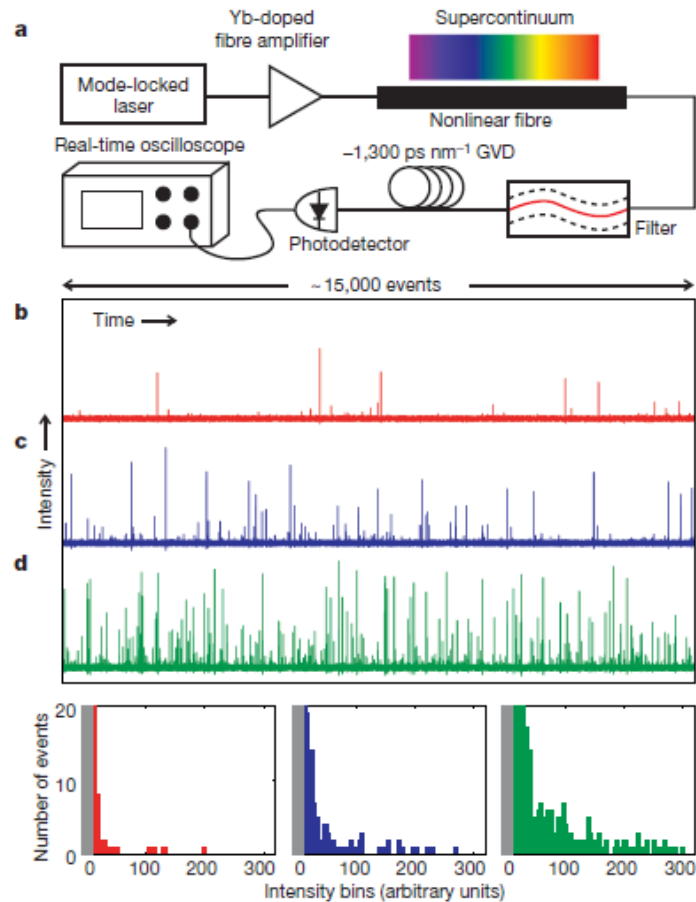
Figure 4: Experimental observation of optical rogue waves. (a), Schematic of experimental apparatus. (b-d), Single-shot time traces containing roughly $15,000$ pulses each and associated histograms (bottom of figure: left, (b); middle, (c); right, (d) for average power levels $0.8\mu W$ (red), $3.2\mu W$ (blue) and $12.8\mu W$ (green), respectively. The grey shaded area in each histogram demarcates the noise floor of the measurement process. In each measurement, the vast majority of events ($> 99.9\%$ for the lowest power) are buried in this low intensity range, and the rogue events reach intensities of at least $30 - 40$ times the average value. These distributions are very different from those encountered in most stochastic processes [19].

of these evidence progress in optic experiments, the real-time and single short observation in picosecond time scale of RW structures, generated from the nonlinear propagation of random waves, remain so far unknown. Nevertheless, the direct single shot recordings of optical RWs was first evidence with time lens by B. H. Kolner and M. Nazarathy [172], then by Bennett and Kolner [173] with time microscope (TM) and finally by Foster and co-workers with the ultrafast optical oscilloscope [174]. Very recently, P. Suret *et al.* [167] have performed the observation of the fast dynamics of integrable turbulence related to optical RWs with temporal resolution of $250 fs$ of TM. So doing, they observed a frequent emergence of subpicosecond structures with peak powers much higher than the average of optical random waves. Therefore, their result was in accordance with the well-known principle of generation of integrable turbulence via initial

conditions in the form of random waves and Gaussian statistics. As it is well-known that heavy tail deviations issue from Gaussian statistics occur in integrable turbulence, they are responsible of usual RW generation in optical fibers. An overview of experimental observation of fast dynamics and ultrafast observation of RWs with a TM is displayed respectively in [Figs. 5 and 6]
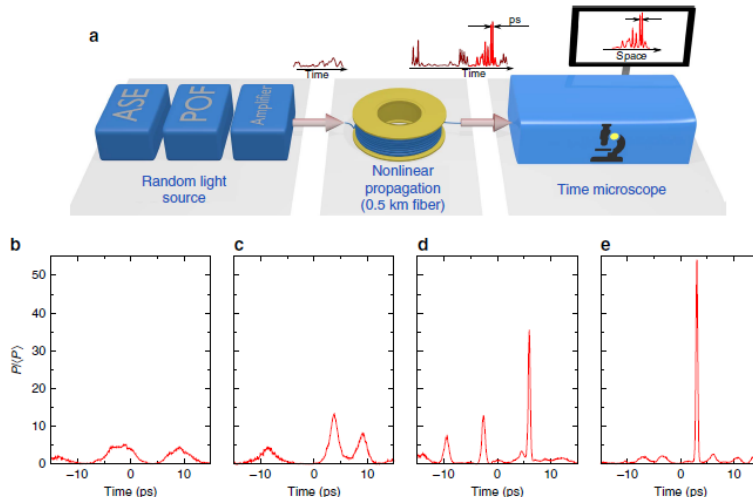
Figure 5: Overview of experiments. (a) Global strategy for the experimental observation of the fast dynamics. Incoherent light from a $1560nm$ Amplified Spontaneous Emission (ASE) source is filtered by using a Programmable Optical Filter (POF) and amplified before experiencing nonlinear propagation in a polarization maintaining fibre. Single-shot measurement of random light is achieved by using a specially designed time-microscope (TM). The TM, which maps the temporal evolution onto the spatial coordinate of a sCMOS camera (Scientific CMOS), has a temporal resolution of $250fs$ (see Fig. 7 and Methods for details). (b-e) Typical single-shot recordings of the fast dynamics of optical power (normalized by its mean value). Initial spectral width $\Delta\nu = 0.1THz$. (b) Initial condition. (c-e) Structures observed at the output of the fibre for mean powers $\langle P \rangle = 0.5W$ (c), $\langle P \rangle = 2.6W$(d), $\langle P \rangle = 4W$ (e) [167].

Despite of some similarity between the optical RW observed in experiments and oceanic RW observed in the sea, the optic ones could not be observed in deep water because of the breaking phenomenon. Therefore, the nature of extreme events emerging in the context of random waves, on the one hand, and in the context of MI, on the other hand, remains an open question.

1.5 Nonlinear propagation of a pulse of light in a fiber

The propagation of light in an optical fiber can be described in two main ways. One denotes, on the one hand, the geometrical or ray optics approach which can be appropriated to describe some properties of the fiber, if the diameter of the core where the light propagates, is big enough compared to the wavelength of the light. On the other hand, as in many cases, it is necessary to use the electromagnetic theory to describe the set of electromagnetic waves propagating in the fiber, called the modes of the fiber [175].
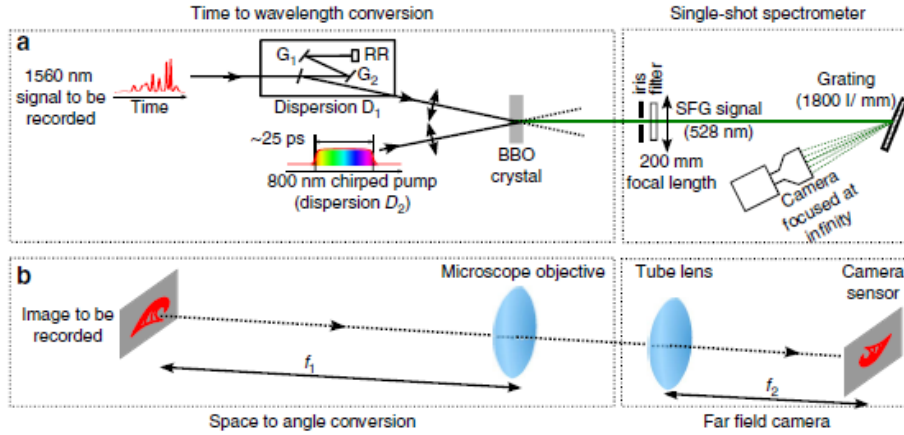
Figure 6: TM realized for the ultrafast observation of optical rogue waves. (a) Experimental setup. A key element is the time lens, which is composed of the Beta Barium Borate (BBO) crystal, pumped by the stretched $800nm$ pulse. (b) Spatial analog of the TM. The dispersion D_1 (provided by the grating compressor) is analogue to the diffraction between the initial image and the lens with focal length f1. The time lens is the analog of the (f_1) lens. The singleshot spectrometer is formally analogue to the far-field camera. G_1 and G_2 are 600 lines mm^{-1} gratings, RR is a roof retroreflector. Note that the BBO crystal is placed at the focal plane of the $200mm$ collimating lens. Transport optics are not represented [167].

1.5.1   Wave propagation equation

Like any other electromagnetic phenomenon, the propagation of a pulse of light in a fiber is governed by Maxwell's equations. In the International System of Units, Maxwell's equations yield [176]

$$\nabla \cdot D = \rho_f,$$

$$\nabla \cdot B = 0,$$

$$\nabla \times E = -\frac{\partial B}{\partial t},$$

$$\nabla \times H = J + \frac{\partial D}{\partial t},$$

(1.1)

where E and H are electric and magnetic field vectors, respectively, and D and B are corresponding electric and magnetic flux densities. The current density vector J and the charge density ρ_f represent the sources for the electromagnetic field. In the absence of free charges in a medium such as optical fibers, $J = 0$ and $\rho_f = 0$.

The flux densities D and B arise in response to the electric and magnetic fields E and H propagate inside a Kerr medium and are related to the constitutive relations

$$D = \varepsilon_0 E + P,$$
$$B = \mu_0 H + M,$$

(1.2)

18

where ε_0 is the vacuum permittivity, μ_0 is the vacuum permeability, and P and M are the induced electric and magnetic polarizations. In a nonmagnetic medium such as optical fibers, $M = 0$. Maxwell's equations can be used to obtain the wave equation that describes light propagation in optical fibers. The substitution of Eq. (1.2) into Eqs. (1.1), gives

$$\nabla \times \nabla \times E = -\frac{1}{c^2}\frac{\partial^2 E}{\partial t^2} - \mu_0\frac{\partial^2 P}{\partial t^2}, \tag{1.3}$$

where c is the speed of light in vacuum with $\mu_0\varepsilon_0 = 1/c^2$ and P the polarization.

It is well-known in the literature that the response of any dielectric to light becomes nonlinear for intense electromagnetic fields, and optical fibers are no exception. The origin of nonlinear response is related to an anharmonic motion of bound electrons under the influence of an applied field. As consequence, the total polarization P induced by electric dipoles is nonlinear in the electric field E, and satisfies the relation

$$P(r,t) = \varepsilon_0\left(\chi^{(1)}E(r,t) + \chi^{(2)}E(r,t) + \chi^{(3)}E(r,t) + \cdots\right), \tag{1.4}$$

where the linear susceptibility $\chi^{(1)}$ is responsible for the linear effects included through the refractive index n and the attenuation coefficient α. The second-order susceptibility $\chi^{(2)}$, is responsible for nonlinear effects such as the second-harmonic generation (SHG) and sum-frequency generation [177]. However, $\chi^{(2)}$ vanishes in optical fibers made of silica glasses ($SiO2$) which lack an inversion symmetry at the molecular level. The third-order susceptibility $\chi^{(3)}$, as regards, is the lowest-order nonlinear effects in optical fibers, responsible for the third-harmonic generation (THG), four-wave mixing (FWM), and nonlinear refraction [177]. Therefore, Eq. (1.4) can be written as

$$P(r,t) = P_L(r,t) + P_{NL}(r,t), \tag{1.5}$$

where

$$P_L(r,t) = \varepsilon_0 \int_{-\infty}^{t} \chi^{(1)}(t-t') \cdot E(r,t')\,dt',$$

$$
\begin{aligned}
&P_{NL}(r,t) = \varepsilon_0 \int_{-\infty}^{t} dt_1 \int_{-\infty}^{t} dt_2 \int_{-\infty}^{t} dt_3 \\
&\times \chi^{(3)}(t-t_1, t-t_2, t-t_3) \vdots E(r,t_1)E(r,t_2)E(r,t_3).
\end{aligned}
$$

$$(1.6)$$

Therefore, Eq. (1.3) takes the form

$$\nabla^2 E - \frac{1}{c^2}\frac{\partial^2 E}{\partial t^2} = \mu_0\frac{\partial^2 P_L}{\partial t^2} + \mu_0\frac{\partial^2 P_{NL}}{\partial t^2}. \tag{1.7}$$

Let start with the resolution of Eq. (1.7) with $P_{NL} = 0$. It is useful to write E in the frequency domain as

$$\nabla \times \nabla \times \tilde{E}(r,\omega) = \varepsilon(\omega)\frac{\omega^2}{c^2}\tilde{E}(r,\omega), \tag{1.8}$$

where $\tilde{E}(r, \omega)$ is the Fourier transform of $E(r, t)$ defined as

$$\tilde{E}(r, \omega) = \int\limits_{-\infty}^{+\infty} E(r, t) \exp(i\omega t) dt, \qquad (1.9)$$

and the frequency-dependent dielectric constant stands for

$$\varepsilon(\omega) = 1 + \chi^{(1)}(\omega), \qquad (1.10)$$

where $\chi^{(1)}(\omega)$ is the Fourier transform of $\chi^{(1)}(t)$. As $\chi^{(1)}(\omega)$ is in general complex, so is $\varepsilon(\omega)$ which can be written in a real and imaginary parts, related to the refractive index $n(\omega)$ and the absorption coefficient $\alpha(\omega)$ as follows

$$\varepsilon = (n + i\alpha c/2\omega)^2, \qquad (1.11)$$

where n and α take the forms

$$n(\omega) = 1 + \frac{1}{2}\text{Re}\left[\chi^{(1)}(\omega)\right], \quad \alpha(\omega) = \frac{\omega}{nc}\text{Im}\left[\chi^{(1)}(\omega)\right], \qquad (1.12)$$

where Re and Im stand for the real and imaginary parts, respectively. Due to low optical losses in fibers (i.e. $\varepsilon(\omega) \approx n^2$) on the one hand, and to the independence in spatial coordinates of n in both core and cladding of step-index fibers (i.e $(\nabla \cdot E) = 0$) on the other hand, Eq. (1.8) takes the form of the Helmholtz equation

$$\nabla^2 \tilde{E} + n^2(\omega)\frac{\omega^2}{c^2}\tilde{E} = 0. \qquad (1.13)$$

As the wave propagation equation has been derived in the linear approximation ($P_{NL} = 0$), let consider the case where $P_{NL} \neq 0$ to find the nonlinear propagation equation.

1.5.2 Nonlinear Pulse propagation equation

The study of nonlinear effects in optical fibers involves the use of short pulses with widths ranging from approximately $10ns$ to $10fs$. When such optical pulses propagate inside a fiber, both dispersive and nonlinear effects influence their shapes and spectra. In this case, $P_{NL} \neq 0$ and the equation that describes light propagation in optical fibers takes the form

$$\nabla^2 E - \frac{1}{c^2}\frac{\partial^2 E}{\partial t^2} = \mu_0 \frac{\partial^2 P_L}{\partial t^2} + \mu_0 \frac{\partial^2 P_{NL}}{\partial t^2}. \qquad (1.14)$$

To derive the basic equation that governs propagation of optical pulses in nonlinear dispersive fibers, some assumptions are necessary [68].

First assumption: The P_{NL} should be treated as a small perturbation to P_L.

Second assumption: The optical field is assumed to maintain its polarization along the fiber length so that a scalar approach is valid.

Third assumption: The optical field is assumed to be quasi-monochromatic, i.e., the pulse spectrum, centered at ω_0, is assumed to have a spectral width $\Delta\omega$ such that $\Delta\omega/\omega_0 << 1$.

In the paraxial approximation (i.e. slowly varying envelope approximation), it is useful to separate the rapidly varying part of the electric field and polarization components by writing them in the form

$$E(r,t) = \tfrac{1}{2}\hat{x}\left[E(r,t)\exp(-i\omega_0 t) + c.c.\right],$$

$$P_L(r,t) = \tfrac{1}{2}\hat{x}\left[P_L(r,t)\exp(-i\omega_0 t) + c.c.\right], \tag{1.15}$$

$$P_{NL}(r,t) = \tfrac{1}{2}\hat{x}\left[P_{NL}(r,t)\exp(-i\omega_0 t) + c.c.\right],$$

where $\hat{x}$ is the polarization unit vector, and $E(r,t)$ is a slowly varying function of time (relative to the optical period). Therefore, the nonlinear polarization P_{NL} can be reduced to

$$P_{NL}(r,t) \approx \varepsilon_0 \varepsilon_{NL} E(r,t), \tag{1.16}$$

where the nonlinear contribution to the dielectric constant is

$$\varepsilon_{NL} = \frac{3}{4}\chi^{(3)}_{xxxx}|E(r,t)|^2. \tag{1.17}$$

To obtain the wave equation for the slowly varying amplitude $E(r,t)$, it is more convenient to work in the Fourier domain. So doing, $E(r,t)$ defined as

$$\tilde{E}(r,\omega-\omega_0) = \int\limits_{-\infty}^{+\infty} E(r,t)\exp\left[i(\omega-\omega_0)t\right]dt, \tag{1.18}$$

is found to satisfy the Helmholtz equation below

$$\nabla^2 \tilde{E} + \varepsilon(\omega)k_0^2 \tilde{E} = 0, \tag{1.19}$$

with

$$\varepsilon(\omega) = 1 + \tilde{\chi}^{(1)}_{xx}(\omega) + \varepsilon_{NL}, \quad k_0 = \frac{\omega}{c}. \tag{1.20}$$

Therefore, the refractive index $\tilde{n}$ and the absorption coefficient $\tilde{\alpha}$ become

$$\tilde{n} = n + n_2|E|^2, \quad \tilde{\alpha} = \alpha + \alpha_2|E|^2, \tag{1.21}$$

For $\varepsilon = (\tilde{n} + i\tilde{\alpha}/2k_0)^2$, the nonlinear-index coefficient n_2 and the two-photon absorption coefficient α_2 yield

$$n_2 = \frac{3}{8n}\mathrm{Re}\left(\tilde{\chi}^{(3)}_{xxxx}\right), \quad \alpha_2 = \frac{3\omega_0}{4nc}\mathrm{Im}\left(\tilde{\chi}^{(3)}_{xxxx}\right). \tag{1.22}$$

One should keep in might that α_2 is relatively small in silica fibers, and is often ignored.

1.5.3 Nonlinear Schrödinger equation

Equation (1.19) can be solved by using the method of separation of variables [68]. Let assume that the solution has the form

$$\tilde{E}\left(r, \omega - \omega_0\right) = F\left(x, y\right) \tilde{A}\left(z, \omega - \omega_0\right) \exp\left(i\beta_0 z\right), \tag{1.23}$$

where $\tilde{A}\left(z, \omega\right)$ is a slowly varying function of z and β_0, the wave number.

Equation (1.19) leads to the following two equations in the case of nonparaxiality

$$\frac{\partial^2 F}{\partial x^2} + \frac{\partial^2 F}{\partial y^2} + \left[\varepsilon(\omega)k_0^2 - \tilde{\beta}^2\right] F = 0,$$

$$\frac{\partial^2 \tilde{A}}{\partial z^2} + 2i\beta_0 \frac{\partial \tilde{A}}{\partial z} + \left(\tilde{\beta}^2 - \beta_0^2\right) \tilde{A} = 0. \tag{1.24}$$

In the case of paraxial approximation, one neglects the second derivative $\frac{\partial^2 \tilde{A}}{\partial z^2}$ since $\tilde{A}\left(z, \omega\right)$ is assumed to be a slowly varying function of z. It follows that

$$\frac{\partial^2 F}{\partial x^2} + \frac{\partial^2 F}{\partial y^2} + \left[\varepsilon(\omega)k_0^2 - \tilde{\beta}^2\right] F = 0,$$

$$2i\beta_0 \frac{\partial \tilde{A}}{\partial z} + \left(\tilde{\beta}^2 - \beta_0^2\right) \tilde{A} = 0, \tag{1.25}$$

where $F(x, y)$ is the modal distribution and $\beta(\omega)$ the corresponding wave number. In a single-mode fiber, $F(x, y)$ refers to the modal distribution of the fundamental fiber mode.

Let consider the above approximation of the dielectric constant $\varepsilon(\omega)$

$$\varepsilon = (n + \Delta n)^2 \approx n^2 + 2n\Delta n, \tag{1.26}$$

where the small perturbation Δn takes the form

$$\Delta n = n_2 |E|^2 + \frac{i\tilde{\alpha}}{2k_0}. \tag{1.27}$$

The first-order perturbation theory [10] has been used to determine the wave number $\tilde{\beta}$

$$\tilde{\beta}\left(\omega\right) = \beta\left(\omega\right) + \Delta\beta\left(\omega\right), \tag{1.28}$$

where

$$\Delta\beta\left(\omega\right) = \frac{\omega^2 n\left(\omega\right)}{c^2 \beta^2\left(\omega\right)} \frac{\int\limits_{-\infty}^{+\infty} \Delta n\left(\omega\right) |F\left(x, y\right)|^2 dx dy}{\int\limits_{-\infty}^{+\infty} |F\left(x, y\right)|^2 dx dy}. \tag{1.29}$$

It follows that the electric field $E(r, t)$ can be written as

$$\tilde{E}\left(r, \omega\right) = \frac{1}{2}\tilde{x}\left\{F\left(x, y\right) A\left(z, t\right) \exp\left[i\left(\beta_0 z - \omega_0 t\right)\right] + c.c\right\}, \tag{1.30}$$

where $A(z,t)$ is the slowly varying pulse envelope. Its Fourier transform satisfies $\tilde{A}(z, \omega - \omega_0)$ Eq. (1.25) as follows

$$\frac{\partial \tilde{A}}{\partial z} = i\left[\beta\left(\omega\right) + \Delta\beta\left(\omega\right) - \beta_0\right]\tilde{A}. \tag{1.31}$$

During the propagation in the fiber, each spectral component acquires a phase shift whose magnitude is both frequency and intensity dependent. To obtain the propagation equation for $A(z,t)$, let take the inverse Fourier transform of Eq. (1.31). It is helpful to expand $\beta\left(\omega\right)$ and $\Delta\beta\left(\omega\right)$ in a Taylor series around the carrier frequency ω_0 as

$$\beta\left(\omega\right) = \beta_0 + \left(\omega - \omega_0\right)\beta_1 + \tfrac{1}{2}(\omega - \omega_0)^2\beta_2 + \tfrac{1}{6}(\omega - \omega_0)^3\beta_3 + \cdots,$$

$$\Delta\beta\left(\omega\right) = \Delta\beta_0 + \left(\omega - \omega_0\right)\Delta\beta_1 + \tfrac{1}{2}(\omega - \omega_0)^2\Delta\beta_2 + \cdots, \tag{1.32}$$

where, $\beta_0 \equiv \beta\left(\omega_0\right)$ and $\Delta\beta \approx \Delta\beta_0$, with

$$\beta_m = \left(\frac{d^m\beta}{d\omega^m}\right)_{\omega=\omega_0}, \quad (m = 1, 2, ...). \tag{1.33}$$

In Eqs. (1.32), the cubic and higher-order terms are negligible if the spectral width of the pulse satisfies the condition $\Delta\omega << \omega_0$. Considering the inverse Fourier transform

$$A\left(z, t\right) = \frac{1}{2\pi}\int\limits_{-\infty}^{+\infty}\tilde{A}\left(z, \omega - \omega_0\right)\exp\left[-i\left(\omega - \omega_0\right)t\right]d\omega, \tag{1.34}$$

the resulting equation for $A(z,t)$ becomes

$$\frac{\partial A}{\partial z} + \beta_1\frac{\partial A}{\partial t} + \frac{i\beta_2}{2}\frac{\partial^2 A}{\partial t^2} = i\Delta\beta_0 A, \tag{1.35}$$

where $\Delta\beta_0$ includes the effects of fiber loss and nonlinearity. Using $\beta\left(\omega\right) \approx n\left(\omega\right)\omega/c$ and assuming that the variation of $F(x,y)$ over the pulse bandwidth is small, Eq. (1.35) takes the form

$$\frac{\partial A}{\partial z} + \beta_1\frac{\partial A}{\partial t} + \frac{i\beta_2}{2}\frac{\partial^2 A}{\partial t^2} + \frac{\alpha}{2}A = i\gamma\left(\omega_0\right)\left|A\right|^2 A. \tag{1.36}$$

where the nonlinear parameter γ is defined as

$$\gamma\left(\omega_0\right) = \frac{n_2\left(\omega_0\right)\omega_0}{cA_{eff}}, \tag{1.37}$$

where the parameter A_{eff} is known as the effective mode area and is defined as

$$A_{eff} = \frac{\left(\int\limits_{-\infty}^{+\infty}\left|F\left(x,y\right)\right|^2 dxdy\right)^2}{\int\limits_{-\infty}^{+\infty}\left|F\left(x,y\right)\right|^4 dxdy}. \tag{1.38}$$

Equation (1.36) describes the propagation of picosecond optical pulse in single-mode fibers and is related to the NLS equation under certain conditions [68]. Equation (1.36) governs some

nonlinear effects such as the fiber losses through the parameter α, the chromatic dispersion through the terms β_1 and β_2 and the SPM nonlinearity through the coefficient γ . The pulse envelope moves at the group velocity $v_g \equiv 1/\beta_1$, while the effects of group-velocity dispersion (GVD) are governed by β_2. The GVD parameter β_2 can be positive or negative depending on whether the wavelength λ is below or above the zero-dispersion wavelength λ_D of the fiber. In the anomalous-dispersion regime, $(\lambda > \lambda_D)$, β_2 is negative, and positive in the focusing regime. The term proportional to β_1 is canceled when transforming to a reference frame moving with the pulse at the group velocity, by applying the change of variable $T = t - z/v_g \equiv t - \beta_1 z$.

$$i\frac{\partial A}{\partial z} + i\frac{\alpha}{2}A - \frac{\beta_2}{2}\frac{\partial^2 A}{\partial T^2} + \gamma|A|^2 A = 0. \tag{1.39}$$

If the absorption is neglected ($\alpha = 0$), the usual form of the NLSE stands

$$i\frac{\partial A}{\partial z} - \frac{\beta_2}{2}\frac{\partial^2 A}{\partial T^2} + \gamma|A|^2 A = 0. \tag{1.40}$$

Equation (1.40) is the standard NLS equation.

1.6 Nonlinear effects in optical fibers

1.6.1 Attenuation

From the beginning, telecommunication systems based on optical fiber were constructed in the assumption of linear transmission. Nevertheless, optical transmissions with high debit and far distances newly constructed are connected to powerful amplifier of emission which induce very high ejected powers in optical fiber. This ejection is responsible to the generation and amplification of parasite effects or interference such as linear and nonlinear effects. However, optical nonlinearity can significantly degrade the information capacity and limit the channel power in high-speed and long-range optical communications. Nonlinear fiber optics has been widely investigated in standard fiber systems [178]. In the literature, scientist denote two types of dispersion mechanisms in the fiber. The intramodal dispersion which is due to the dispersive properties of the optical fiber material, hence the denomination, material dispersion, on the one hand. Then, the intermodal dispersion, due to the guidance effects of the optical fiber, hence the denomination, waveguide dispersion, on the other hand.

In the context of intramodal dispersion, one denote the attenuation which is a linear effect, frequently observes in single mode fiber. Attenuation effect is the reduction of signal strength or light power over the length of the light-carrying medium [179]. This fiber attenuation is a function of wavelength, measured in decibels per kilometer and can be classified in two main types. The intrinsic losses, such as the infrared (IR) absorption by Si-O coupling [180], observe at higher wavelengths around $1.4\mu m$ to $1.6\mu m$ and the ultraviolet (UV) absorption due to electron transitions, observe at lower wavelengths near to $0.8\mu m$ with a loss of $0.3dB/km$. As illustration, Fig. 7 exhibits the spectral attenuation of a silica optical fiber.
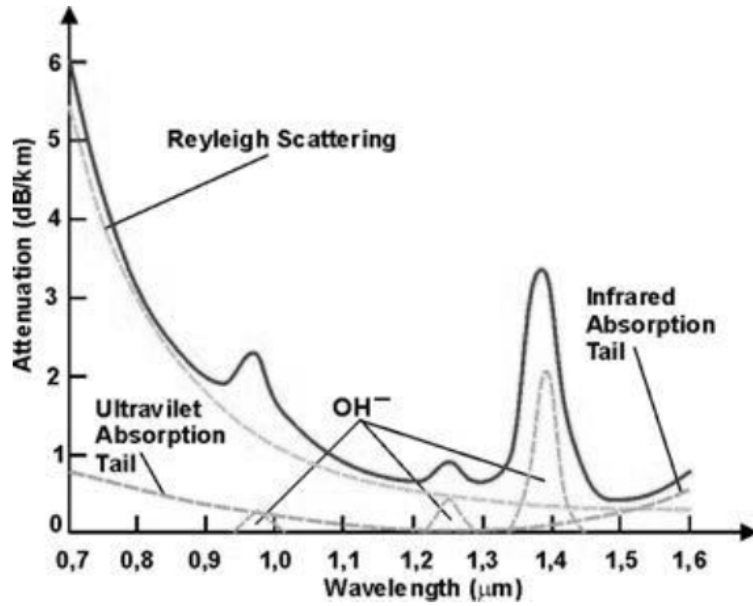
Figure 7: Spectral attenuation of a silica optical fiber [179].

Moreover, attenuation can be caused by other factors, such as the diffusion phenomenon names, Rayleigh scattering effect, originates from microscopic irregularities in the glass structure and absorption due to the lattice vibration which can be describes as the conversion process of electromagnetic wave energy into other forms. The Rayleigh scattering effect is inversely proportional to λ^4 and can be expressed as [181]

$$\alpha_R \left[dB/km \right] = 1.7 \left(\frac{0.85}{\lambda \left[\mu m \right]} \right). \tag{1.41}$$

The Rayleigh effect produces high losses of $0.6 dB/km$ in the ultraviolet region when the wavelength is around $0.8 \mu m$ to $1 \mu m$. The above Fig.8 describes the Rayleigh scattering effect.
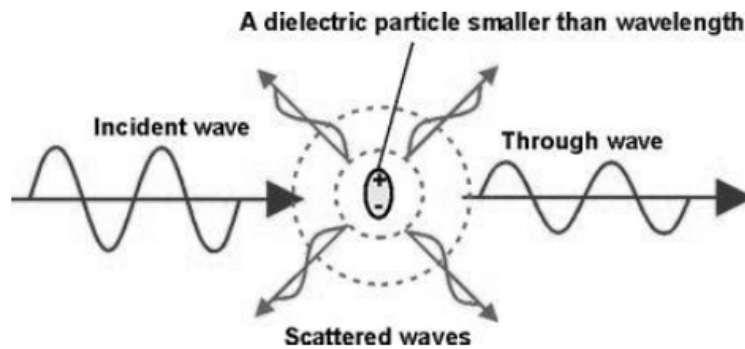
Figure 8: Illustration of Rayleigh scattering effect [179].

Another factor of attenuation is light absorbtion within the fiber core and inner cladding by

residual species such as OH ions. Such ions removal are of special interest in fiber fabrication because this extraction reduces the optical loss thus, the attenuation in the fiber. Figure 9 shows the spectral attenuation of different material fibers. One denotes another form of attenuation
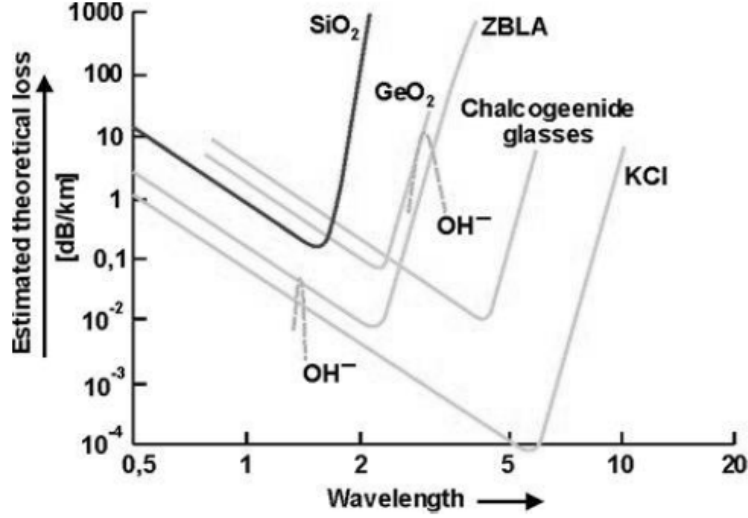
Figure 9: Spectral attenuation of different material fibers [179].

due to local distortions of the fiber geometry, and nonlinear scattering occurring when installing fibers.

1.6.2 Chromatic dispersion

The NLSE (1.40) shows that group-velocity dispersion (GVD, β_2) and nonlinearity (γ) are two phenomena playing a major role in the propagation of a pulse of light in a fiber. The GVD, known as chromatic dispersion, is a linear effect which occurs in optical fiber systems, particularly on single-mode wavelength-division multiplexing (WDM) systems. This effect is due to the fact that an optical source contains different wavelength components that travel at different speeds. An illustration of the chromatic dispersion in optical-fiber nanowire (OFN) is presented in Fig. 10. The dispersion, function of the optical frequency, is commonly expanded in Taylor series with dispersion coefficients β_n. The Taylor coefficient β_2 (ps^2/km) is related to the engineering unit of the GVD, measured in $(ps/(nm.km))$ and expressed as follows [183]

$$D = \frac{2\pi c}{\lambda^2} \frac{d^2\beta}{d\omega^2}. \tag{1.42}$$

Let us detail independently, the GVD effect on the pulse propagation in solid core fibers [184] through the NLS equation bellow

$$i\frac{\partial E\left(z,t\right)}{\partial z} - \frac{\beta_2}{2}\frac{\partial^2 E\left(z,t\right)}{\partial t^2} + \gamma |E\left(z,t\right)|^2 E\left(z,t\right) = 0. \tag{1.43}$$

26
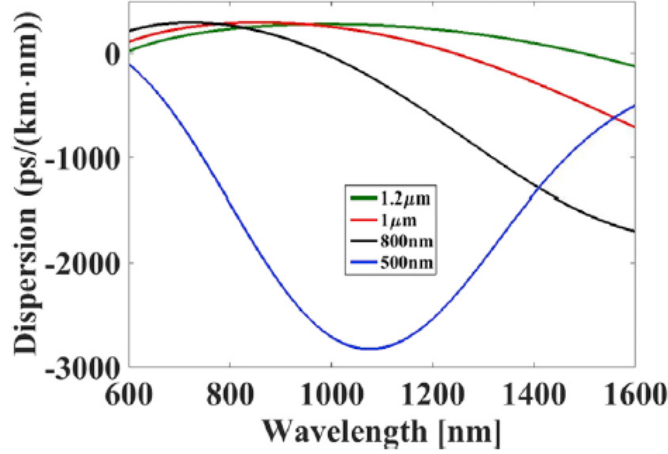
Figure 10: Dependence of the GVD on the wavelength for four different OFN diameters [182].

To study the effect of GVD alone, let set γ to zero in Eq. (1.43). Then, it follows

$$\frac{\partial E\left(z,t\right)}{\partial z} = -\frac{i\beta_2}{2}\frac{\partial^2 E\left(z,t\right)}{\partial t^2}. \tag{1.44}$$

Using the gaussian pulse, Eq. (1.44) is solved in the Fourier domain and the result yields

$$E\left(z,t\right) = E_1(z)\exp\left(-\frac{t^2}{T_{eff}^2(z)}\right)\exp\left(-i\phi_D\left(z,t\right)\right), \tag{1.45}$$

where

$$E_1(z) = \frac{E_0}{T_{eff}}, \ \ T_{eff} = \tau\left[1+(z/L_D)^2\right]^{1/2}, \ \ L_D = \tau^2/\left|\beta_2\right|,$$

$$\phi_D\left(z,t\right) = \frac{-t^2\beta_2 z}{\tau^4+\beta_2^2 z^2} + \frac{1}{2}\tan^{-1}\left(\frac{\beta_2 z}{\tau^2}\right), \tag{1.46}$$

One remarks that the pulse remains Gaussian but its duration T_{eff} increases during the propagation along z. The instantaneous frequency variation (or chirp) is deduced from the time derivative of the temporal phase $\phi_D\left(z,t\right)$ and takes the form

$$\delta\omega\left(z,t\right) = \frac{2\beta_2 z}{\tau^4 + \beta_2^2 z^2}t. \tag{1.47}$$

It can be seen that the chirp is a linear time dependence. This means that the GVD induces a linear chirp on the pulse during its propagation. If β_2 is positive (normal dispersion), at $t < 0$ (i.e. on the leading part of the pulse), then, $\delta\omega < 0$. In the case where $t > 0$ (i.e. on the trailing part of the pulse), $\delta\omega > 0$. In other words, this means that, the red travels faster than the blue (like in the majority of the classical materials). On the contrary, if β_2 is negative (anomalous dispersion), the blue travels faster than the red. Therefore, $T_{eff}(z)$ depends on β_2^2. So, in both cases, an initially Fourier-transform-limited the pulse broadens during the propagation [184].

In the case of photonic crystal fibers (PCFs) [184], the GVD can be positive or negative depending on the wavelength. There can be one or several wavelengths for which the GVD is

27

zero, namely, the zero-dispersion wavelengths (ZDW). The dispersion curves for two different PCFs are shown in Fig. 11. As features of PCFs, one denotes one anomalous dispersion range, two normal dispersion ranges and two ZDW. In addition, the spectrum is not $z-$dependent, it stays identical throughout the propagation. As consequence, the only effect of GVD is the temporal broadening occurring because, the frequencies present in the pulse, travel at different velocities in the fiber.
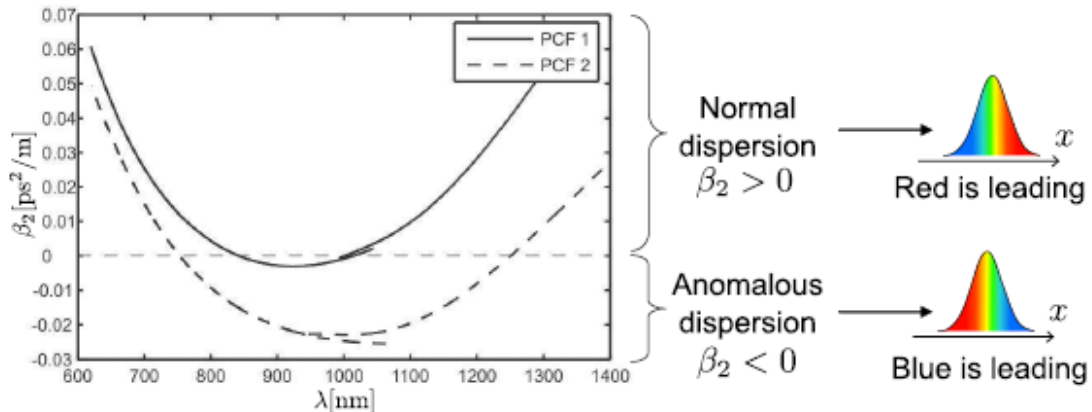
Figure 11: Example of group-velocity dispersion for two solid-core PCFs and interpretation for the propagation of the frequencies in the pulse [184]. Graph: Courtesy of Esben R. Andresen.

The GVD plays an undeniable role in all fiber nonlinear applications, especially in SC generation [185], which has a very broad frequency spectrum and numerous applications in pulse compression, parametric amplifiers, SC-based WDM telecom sources, and so on. Among linear effects which occur in optical fiber systems, scientist denote the mode polarization dispersion. It can be due to unpredictable and uncontrollable variation of the birefringence and polarization or to the non homogeneity of the index, an imperfection of the fiber.

1.6.3   Nonlinear effects

A. Self-phase modulation

In the optical Kerr effect, the nonlinear phase shift or self-phase modulation (SPM) induced by an intense high-power pump beam, is used to change the transmission of a weak probe through a nonlinear medium. This effect can be used to make an optical shutter with picosecond response times. For a very intense optical pulse, the fibre refractive index increases as the intensity of the light increases. Named after a 19th century, the nonlinear effect γ, was discovered by Scotsman John Kerr in 1875 and has come to be known as the Kerr optical effect or the Kerr nonlinearity. The higher-order dispersion terms do not affect the spectrum. As discussed in chromatic dispersion subsection, this is easily seen from the fact that the dispersion amounts to

multiplication of $e^{i\phi(\omega)}$ onto $\tilde{E}(\omega)$. The exponential cancels out upon taking the squared norm $\left|\tilde{E}(\omega)\right|^2$ to arrive at the spectrum. Figure 12 exhibited the features of GVD and SPM.
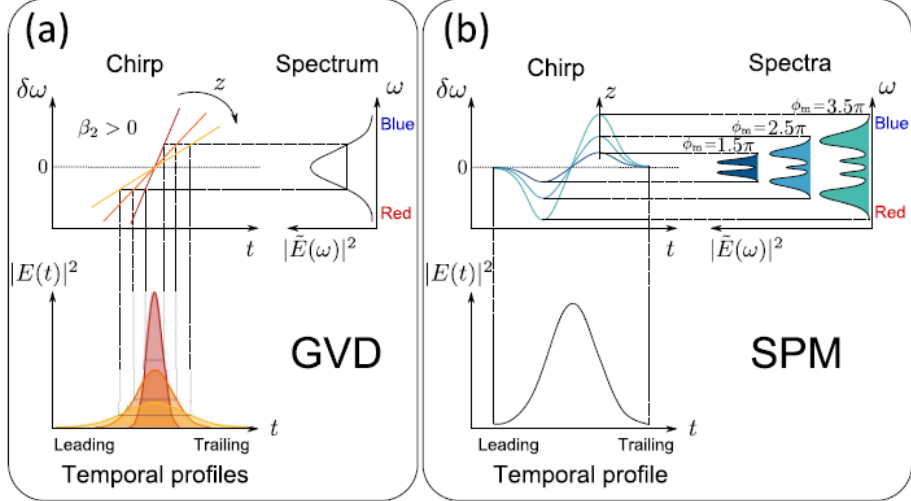
Figure 12: Separate effects of (a) GVD and (b) SPM on an unchirped Gaussian pulse propagating in a fiber along direction z. (a) The spectrum stays unchanged, but the pulse temporally broadens when it propagates. The GVD-induced chirp is linear. The scheme was drawn for $\beta_2 > 0$, so the chirp is positive and the red wavelengths go faster than the blue ones. If $\beta_2 < 0$, the pulse broadens in the same way, but the chirp is negative and the blue goes faster than the red. (b) The temporal profile stays unchanged, but SPM generates new frequencies, and the spectrum broadens. The chirp has the shape of the derivative of a Gaussian and its amplitude increases when the pulse propagates. Because of this shape, one frequency can be traveling with two different phases, which can cause constructive or destructive interference, hence the oscillating pattern of the spectrum. The three examples of spectra drawn on the scheme correspond to three values of the maximum nonlinear phase (1.5π, 2.5π and 3.5π). As the spectrum broadens, the Fourier-transform-limited duration of the pulse decreases, but the actual duration of the pulse stays unchanged because of the chirp [184].

The nonlinearities in the fiber cause a change of refractive index in the medium that is proportional to $|E|^2$. This phenomenon is called "optical Kerr effect", because of its similarities to the Kerr electro-optic effect, where an electric field is applied to a medium and changes its refractive index in a quadratic way.

As already defined in the previous section, the nonlinear coefficient can be written as

$$\gamma = \frac{n_2 \omega_0}{c A_{eff}}, \tag{1.48}$$

where n_2 is the nonlinear refractive index such as $\Delta n = n_2 |E|^2$. To study the effect of SPM alone, β_2 is set to zero in the NLS equation (1.43). Thus, Eq. (1.43) becomes

$$\frac{\partial E(z,t)}{\partial z} = i\gamma |E(z,t)|^2 E(z,t). \tag{1.49}$$

When solved in the time domain, Eq. (1.49) gives the result bellow

$$E(z,t) = E(0,t) \exp(\phi_{NL} t), \tag{1.50}$$

29

where

$$\phi_{NL} = \gamma|E(0,t)|^2 z, \quad E(0,t) = E_0 \exp\left(\frac{-t^2}{(2\tau^2)}\right). \tag{1.51}$$

The temporal phase ϕ_{NL} that is imposed on the pulse is intensity dependent and reaches its maximum at $t = 0$ and its shape follows the Gaussian profile of the pulse in the time-domain.

The nonlinear length L_{NL} can be defined such as $\phi_{NL}(t) = z/L_{NL}$, with $L_{NL} = 1/\gamma P_0$. Then, the derivative of the phase gives the instantaneous frequency

$$\delta\omega(z,t) = \frac{2\gamma P_0 z}{\tau^2} t e^{-t^2/\tau^2}. \tag{1.52}$$

Eq. (1.52) describes the nonlinearity effect, called, self-phase modulation (SPM) [184]. The change of refractive index induced by the intense optical electric field perturbs the propagation of the pulse. In silica fibers, the nonlinear index $n_2 > 0$. So, $\delta\omega < 0$ for $t < 0$ at the leading edge (i.e., the right side of the pulse) and $\delta\omega > 0$ for $t > 0$ at the trailing edge. As in the case of GVD for normal dispersion, the red part of the spectrum goes overall faster than the blue part. However, the dependence is far from being linear as it has the shape of the derivative of a Gaussian. Thus, new frequencies are continuously created during the propagation of the pulse. The resulting spectrum for unchirped Gaussian pulse experiencing SPM consists of several peaks that appear because each frequency can be generated with two different phases, causing interferences. An estimation of the broadening can be made with Eq. (1.52). As observed in Fig. 12(b), the spectral width can roughly be estimated by $\delta\omega_{\max}$ in the chirp graph or by calculating the time derivative of Eq. (1.52) and setting it to zero. So doing, it yields

$$\delta\omega_{\max} = \sqrt{2}e^{-1/2\frac{\gamma P_0 z}{T_0}}. \tag{1.53}$$

One can notice that $|E(z,t)|^2 = |E(0,t)|^2$ is not z-dependent. Therefore, the pulse does not get broader or narrower when it propagates. However, as the spectrum broadens, the Fourier-transform-limited duration of the pulse decreases, and one would recover the shorter pulse by compensating the chirp induced by SPM.

The above analytical results can only be apply to Gaussian pulses. However, the qualitative conclusions stand for any pulse shape. Any temporal pulse shape will remain unchanged under the action of SPM alone. Indeed, the SPM amounts to multiplication of $e^{i\gamma t}$ onto $E(z,t)$ and this factor disappears upon taking the squared norm of $E(z,t)$. Figure 12(b) revealed the features of SPM. If the input pulse is initially chirped, the resulting spectrum can be drastically changed. In particular, under some conditions, a negatively chirped pulse experiencing SPM in a fiber can result in spectral compression [186].

In summary, the GVD and SPM act on the pulse propagating in optical fibers and their effects cannot be separated. The interplay between the GVD and SPM, can be revealed through the parameter N which yields

$$N^2 = \frac{L_D}{L_{NL}} = \frac{\gamma P_0 T_0^2}{|\beta_2|}. \tag{1.54}$$

If $N >> 1$, the dispersion length is much longer than the nonlinear length, so SPM dominates. On the contrary, if $N << 1$, GVD dominates. If $N = 1$ and $\beta_2 > 0$, some temporal broadening appears, and the spectral broadening is reduced compared to the SPM-only case (see Fig. 12(b)). Throughout Fig. 12(b), it can be seen that the SPM generate new red frequencies at the leading edge, and new blue frequencies created at the trailing edge. Thus, because of the positive dispersion, the leading red components travel faster than he already delayed blue components, which results in an extra temporal broadening. That helps thinking that the chirp created by GVD lowers the amplitude of the one created by SPM. Therefore, the resulting maximum nonlinear phase is reduced and the spectrum broadening is slowed down [184]. If $N = 1$ and $\beta_2 < 0$, the opposite situation may occurs. The red components created at the leading edge are going slower and the blues components created at the trailing edge act against the temporal broadening of the pulse. Furthermore, the negative chirp induced by GVD acts against the spectral broadening caused by SPM. In this case, the combined effects of GVD and SPM generate the "soliton" or a "chirp-free pulse" (i.e. solitary wave, solution of a nonlinear equation) which can propagate in the fiber without changing its shape and velocity.

B. Third-order dispersion

When optical pulses propagate relatively far from the zero-dispersion wavelength of an optical fiber, the TOD effects on pulses are small and can be treated perturbatively. It is well-known that the dispersion-induced pulse broadening is due to the lowest-order of GVD term proportional to β_2 in Eq. (1.32). Although the contribution of this term dominates in most cases of practical interest, it is sometimes necessary to include the third-order dispersion (TOD) governed by β_3. For example, if the pulse wavelength nearly coincides with the zero-dispersion wavelength λ_D and $\beta_2 \approx 0$, the β_3 term provides the dominant contribution to the GVD effects [189]. For ultrashort pulses (with width $T_0 < 1\text{ps}$), it is necessary to include the β_3 term even when $\beta_2 \neq 0$ because the expansion parameter $\Delta\omega/\omega_0$ is no longer small enough to justify the truncation of the expansion in Eq. (1.32) after the β_2 term.

To discuss the effect of TOD on optical fibers, one may choose the model below [187]

$$iu_Z + \frac{1}{2}u_{\tau\tau} + |u|^2 u = i\delta_3 u_{\tau\tau\tau}, \tag{1.55}$$

where δ_3 is the third-order dispersion coefficient with

$$\tau = T/T_0, \;\; Z = z/L_D, \;\; u = \sqrt{\gamma L_D}U, \;\; L_D = T_0^2/|\beta_2|. \tag{1.56}$$

For the initial condition with unit amplitude $u(0,\tau) = \sec h\,\tau$, the simulation of Eq. (1.55) with $\delta_3 = 0.1$ is displayed in Fig. 13. It is seen that the third-order dispersion causes a position shift to the soliton. More significantly, a high-frequency continuous-wave (CW) tail approximately at $1/2\delta_3$ (frequency peak) appears on the trailing edge (right side) of the soliton (see Fig. 13(b)). Then, the emission of this CW tail drains energy from the soliton and causes it to decay. Figure
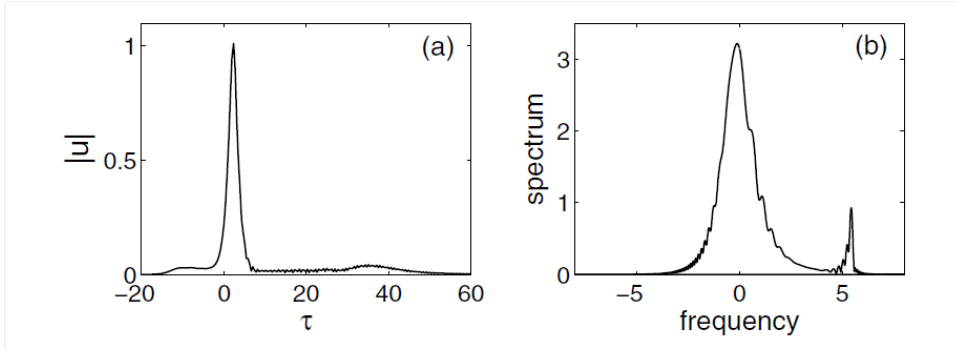
Figure 13: Amplitude and spectrum of an NLS soliton under third-order dispersion effect at $z = 15$ with the initial condition, $u(0, \tau) = \sec h \, \tau$, and TOD coefficient $\delta_3 = 0.1$. [187].

13 exhibits the amplitude and spectrum of the solution at $z = 15$. Regarding the high-frequency CW tail emitted at the trailing edge of the soliton, it originates from a resonance between the soliton and the continuous spectrum of the system. This happens because the energy is fed into the resonant frequency mode $\omega_c = 1/2\delta_3$ and thus, a CW tail with this frequency appears. Moreover, this phenomenon is due to the fact that the amplitude of the CW tail turns out to be exponentially small in δ_3.

To summarize, the main effect of TOD is to shift the soliton peak linearly with distance z. Whether the pulse is delayed or advanced depends on the sign of β_2. When β_3 is positive, the TOD slows down the soliton, and the soliton peak is delayed by an amount that increases linearly with distance. This TOD-induced delay is negligible in most fibers for picosecond pulses. If we use a typical value of $\beta_3 = 0.1ps^3/km$, the temporal shift is only $0.1ps$ for $T_0 = 10ps$ even after a distance of $100km$. However, the shift becomes relatively large for femtosecond pulses. For example, when $T_0 = 100fs$, the shift becomes $1ps$ after $1km$.

C. Self-steepening

Now let consider the NLS equation under the self-steepening (SS) effect [187]

$$iu_Z + \frac{1}{2}u_{\tau\tau} + |u|^2 u = -is\big(|u|^2 u\big)_\tau, \tag{1.57}$$

with the same nondimensional variables (1.56). In the absence of the second-order dispersion term $u_{\tau\tau}$, the self-steepening term on the right-hand side of Eq. (1.57) causes an optical pulse to become asymmetric and steepen up at the trailing edge (i.e., the right side of the pulse) [188]. The second-order dispersion reduces this SS considerably. To illustrate the SS effect, let take as initial condition, a sech pulse with unit amplitude, $u(0, \tau) = \sec h \, \tau$, and the SS coefficient, $s = 0.2$. The evolution of the pulse under the SS effect is numerically determined and displayed in Fig. 14.
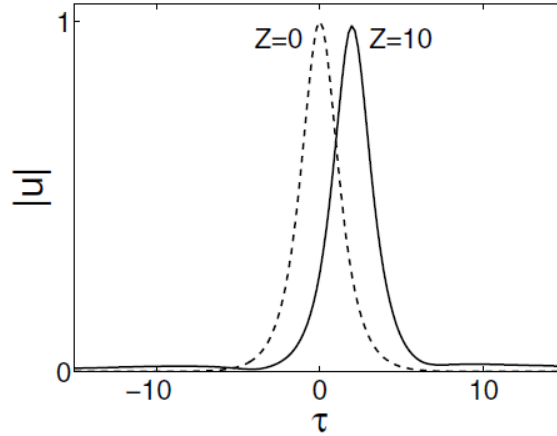
Figure 14: Evolution of an NLS soliton under self-steepening effect with the initial condition, $u(0, \tau) = \sec h \tau$ and SS coefficient, s $= 0.2$ [187].

It is seen that the main effect of the self-steepening term is a position shift of the soliton. This position shift linearly increases with distance. The most important feature of SS is that it can produce spectral and temporal shifts of the soliton even when the SS coefficient is nil [188]. In the literature, it is well-known that the NLS equation with the self-steepening in the form (1.57), is integrable for arbitrary values of the SS coefficient.

D. Self-frequency shift

The NLSE with higher-order effects can be written as [190]

$$\frac{\partial E}{\partial z} + \frac{i}{2}\beta_2 \frac{\partial^2 E}{\partial t^2} - i\gamma |E|^2 E = \sum_{p=2}^{\infty} -\frac{(i)^{p-1}}{p!}\frac{\partial^p E}{\partial t^p} - \frac{\gamma}{\omega_0}\frac{\partial}{\partial t}\left(|E|^2 E\right) - i\gamma T_R E \frac{\partial |E|^2}{\partial t}, \qquad (1.58)$$

where the parameter T_R is related to the full Raman response function of the medium $R(t)$, that takes into account the electronic (instantaneous) and vibrational (delayed) Raman response

$$T_R = \int_{-\infty}^{+\infty} tR(t)dt. \qquad (1.59)$$

The intrapulse Raman scattering known as the self-frequency shift (SFS) is the most important higher-order effect that influences pulses in optical fibers. The SFS takes it origins from the delayed Raman response of the medium. When the pulse is very short (typically $\approx$ 100 fs), its spectrum is broad enough to generate an effect similar to stimulated Raman scattering that can occur between the blue and the red components, mediated by the vibration modes of silica. More specifically, the red part of the spectrum experiences a Raman gain, while the blue part experiences a Raman loss. This effect can be considered as an energy transfer between the blue

and the red part of the spectrum [184]. Therefore, the soliton continuously redshifts along its propagation in the fiber as shown in Fig. 15. This phenomenon is called soliton SFS [191].
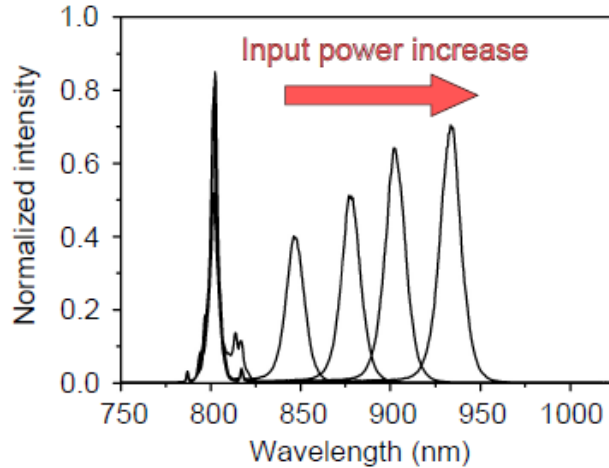
Figure 15: Example of increasing soliton redshift with increasing input power. The peak at 800 nm is the residue from the pump laser [184].

An estimation of the variation of the central frequency of the soliton yields

$$\Delta\omega_R \propto -\frac{|\beta_2|\, z}{T_0^2}, \tag{1.60}$$

where P_0 is the peak power of the pulse and T_0, its duration. As consequence, the redshift increases proportionally with the distance traveled in the fiber (i.e., the longer is the fiber, the higher is the final redshift at the output). In addition, when more power is injected into the fiber, the duration of the pulse decreases by the means of this relation $\gamma P_0 T_0^2/|\beta_2| = 1$. The redshift is proportional to T_0^{-4} and any small decrease of the duration of the pulse translates to an enhancement of the redshift. Thus, the wavelength of the soliton can be tuned by changing the input power, while the duration of the pulse remains almost constant.

To summarize, it is important to note that femtosecond higher-order pulses are not stables because of the combined effects of higher-order dispersion, SS and SFS, which leads to the breakup of these pulses into optical fibers. This phenomenon is known as the soliton decay (see Fig. 15).

E. Cross-phase modulation

Only a single electromagnetic wave is assumed to propagate inside a single mode fibers. When two or more optical fields, having different wavelengths propagate simultaneously inside a fiber, they interact with each other through the fiber nonlinearity. The XPM can be described by the

following model

$$\frac{\partial u_1}{\partial \xi} - \frac{d_1}{2} \frac{\partial^2 u_1}{\partial \tau^2} + \left(|u_1|^2 + \sigma |u_2|^2\right) u_1 = 0,$$

$$\frac{\partial u_2}{\partial \xi} + \frac{d_1}{2} \frac{\partial^2 u_2}{\partial \tau^2} + \left(|u_2|^2 + \sigma |u_1|^2\right) u_2 = 0,$$

(1.61)

where $d_j = |\beta_{2j}/\beta_{20}|$. The parameter β_{20} is the reference value used to define the dispersion length, and u_1 is assumed to propagate in the normal-dispersion region. The parameter σ has a value of 2 when all waves are linearly polarized but becomes <1 for orthogonally polarized waves. In general, such an interaction can generate new waves under appropriate conditions through a variety of nonlinear phenomena such as stimulated Raman scattering (SRS) or stimulated Brillouin scattering (SBS), harmonic generation, and FWM. The Kerr nonlinearity can also couple two optical fields through cross-phase modulation (XPM) without inducing any energy transfer between them. In practice, XPM always accompanies SPM when two or more optical fields are launched simultaneously into an optical fiber. From a physical perspective, XPM occurs because the effective refractive index seen by an optical beam in a nonlinear medium, depends not only on the intensity of that beam, but also on the intensity of other copropagating beams [192].
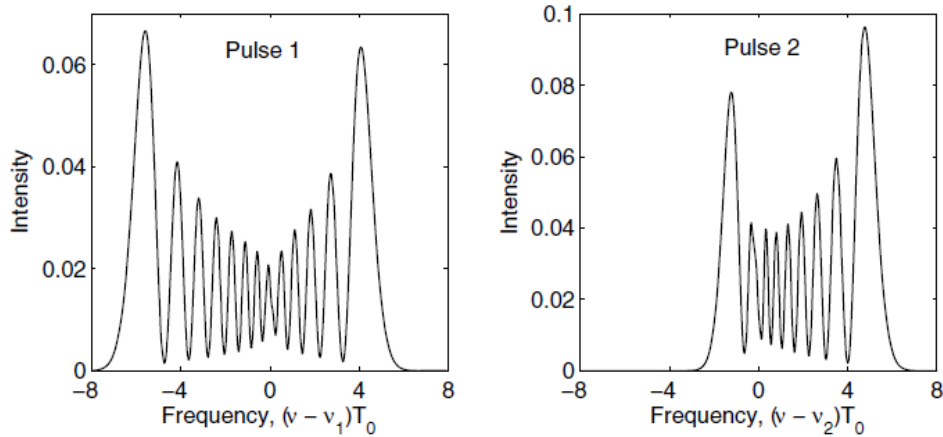
Figure 16: Spectra of two pulses exhibiting XPM-induced asymmetric spectral broadening. The parameters are $\gamma_1 P_1 L = 40$, $P_2/P_1 = 0.5$, $\gamma_2/\gamma_1 = 1.2$, $\tau_d = 0$, and $L/L_W = 5$ [188].

Application of XPM

The nonlinear phenomenon of XPM can be both beneficial and harmful. Its most direct impact is related to multichannel lightwave systems whose performance is invariably limited by the XPM interaction among neighboring channels. Such systems are also affected by the so-called intrachannel XPM, resulting from overlapping of neighboring pulses belonging to the same channel [193]. This section is devoted to the beneficial applications of XPM such as pulse compression and optical switching.

XPM-Induced Pulse Compression

It is well-known that the SPM-induced chirp can be used to compress optical pulses [190]. Because XPM also imposes a frequency chirp on an optical pulse, it can be used for pulse compression as well [194]. An obvious advantage of XPM-induced pulse compression is that, in contrast to the SPM technique requiring the input pulse to be intense and energetic, XPM can compress weak input pulses because the frequency chirp is produced by a copropagating intense pump pulse. However, the XPM-induced chirp is affected by the walk-off effects and depends critically on the initial relative pump-probe delay. As result, the practical use of XPM-induced pulse compression requires a careful control of the pump-pulse parameters such as its width, peak power, wavelength, and initial delay relative to the probe pulse.
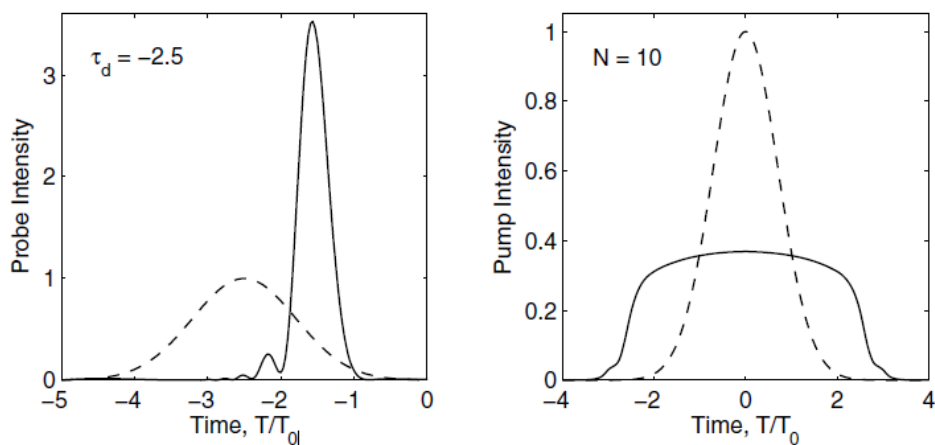
Figure 17: Pulse shapes for the pump and probe at a distance $z/L_D = 0.2$. The dashed curves show for comparison input pulse shapes at $z = 0$. XPM-induced pulse compression is realized using pump pulses of peak power such that $N = 10$ [188].

XPM-Induced Optical Switching

The XPM-induced phaseshift can also be used for optical switching [190]. Several interferometric schemes have been used to take advantage of XPM for ultrafast optical switching [195]. The physics behind XPM-induced switching can be understood by considering a generic interferometer designed such that a weak signal pulse, divided equally between its two arms, experiences identical phase shifts in each arm and is transmitted through constructive interference. If a pump pulse at a different wavelength is injected into one of the arms of the interferometer, it would change the signal phase through XPM in that arm. If the XPM-induced phase shift is large enough (close to π), the signal pulse will not be transmitted because of the destructive interference occurring at the output. Thus, an intense pump pulse can switch the signal pulse through the XPM-induced phase shift.

F. Four-wave mixing

Optical fibers play an important role in the stimulated scattering processes [188]. Their actions

can be active or passive depending on nonlinear processes in the system. They play an active role in the sense that the process depends on molecular vibrations or density variations of silica. In the parametric processes, except for mediating interaction among optical waves, optical fibers play a passive role in the sense that, they involve modulation of a medium parameter, such as the refractive index, and require phase-matching before they can build up along the fiber. Among these, FWM plays the dominant role. Although FWM can be harmful for WDM systems that must be designed to reduce its impact, it is also useful for a variety of applications.

The origin of Four-wave mixing (FWM) lies in the nonlinear response of bound electrons of a material to an electromagnetic field. In the literature, it is well-known that the polarization induced in optical fiber media contains terms, whose magnitude is governed by the nonlinear susceptibilities [188]. The resulting nonlinear effects can be classified as second- or third-order parametric processes, depending on the level of susceptibility (second-order susceptibility $\chi^{(2)}$, or third-order susceptibility $\chi^{(3)}$), responsible of their generation. Generally, the second-order susceptibility $\chi^{(2)}$ vanishes in isotropic medium (in the dipole approximation) and as consequence, the second-order processes such as second-harmonic generation should not occur in silica fibers. But, in practice, they do occur with a relatively low conversion efficiency, due to the quadrupole and magnetic-dipole effects.

As an example of FWM, Fig. 18 exhibited the spectra at the fiber output as the pump peak intensity is increased above the FWM threshold occurring near $500 \text{ MW}/cm^2$. Only the pump line is observed below threshold (see Fig. 18 (a)). Three pairs of Stokes and anti-Stokes lines with frequency shifts in the range $1 - 8$ THz are observed just above threshold (see Fig. 18 (b)). All of these lines have nearly the same amplitude, indicating that the stimulated Raman scattering (SRS) does not play a significant role at this pump power. As pump power is slightly increased, the Stokes lines become much more intense than the anti-Stokes lines as a result of Raman amplification (see Fig. 18 (c)). With a further increase in pump power, the Stokes line closest to the Raman-gain peak becomes as intense as the pump line itself whereas the anti-Stokes lines are nearly depleted (see Fig. 18 (d)).

As applications, the FWM in optical fibers can be both harmful and beneficial depending on the application [188]. One the one hand, The FWM can induce crosstalk in WDM communication systems and limit the performance of such systems. The FWM-induced crosstalk can be avoided in practice through dispersion management, a technique in which the dispersion of each fiber section is made large enough that the FWM process is not phase matched throughout the link length [188]. One the other hand, the FWM is useful for a variety of applications. The fibre optical parametric amplifiers (FOPAs) can be employed for signal amplification, phase conjugation, and wavelength conversion. In addition to these, FWM can be useful for applications such as optical sampling, channel demultiplexing, pulse generation, and high-speed optical switching [188]. It can also be used for reducing quantum noise through squeezing, and for generating photon pairs that are quantum-correlated.
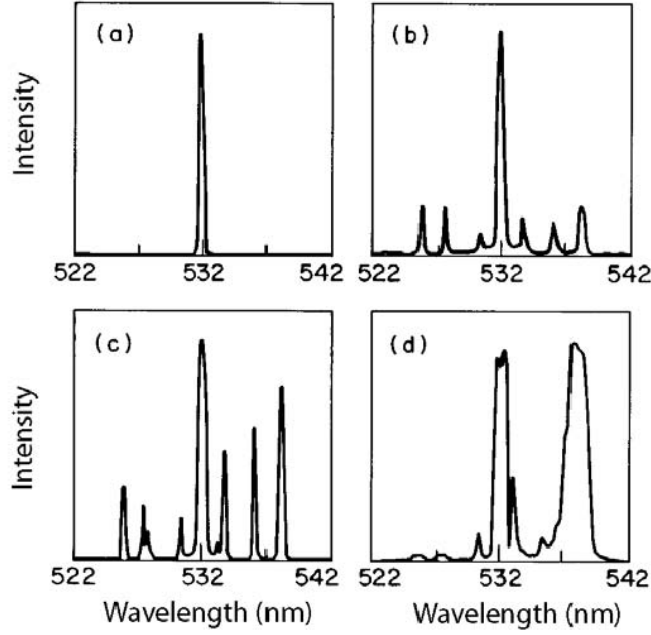
Figure 18: Spectra of 25−ps pump pulses at fiber output. The peak intensity is increased progressively beyond the FWM threshold (≈ 500 MW/cm^2) in going from (a) to (d) [188].

1.7   Scientific progress of optical rogue wave field

1.7.1   Concordance of different methods on rogue waves generation

Let consider the dimensionless NLS equation below

$$i\frac{\partial \psi}{\partial \xi} + \frac{1}{2}\frac{\partial^2 \psi}{\partial \tau^2} + |\psi|^2 \psi = 0, \tag{1.62}$$

where $\psi(\xi, \tau)$ is a function of ξ (propagation distance) and τ (co-moving time). Equation (1.62) can be used to describe the dynamics of pulses in optical fiber as represented in Fig. 3 with the timescale $T_0 = (|\beta_2| L_{NL})^{1/2}$ and nonlinear length $L_{NL} = (\gamma P_0)^{-1}$, where P_0 is the optical background power in Watt. The dimensional field $A(z, T)[W1/2]$ takes the form $A = \sqrt{P_0}\psi$. The dimensional time $T[s]$ gives $T = \tau T_0$ and the dimensional distance $z[m]$ yields $z = \xi L_{NL}$. The particular solution that describes MI growth and decay can be written as [41, 196]

$$\psi(\xi, \tau) = e^{i\xi}\left[1 + \frac{2(1-2a)\cosh(\beta\xi) + ib\sinh(\beta\xi)}{\sqrt{2a}\cos(\omega\tau) - \cosh(\beta\xi)}\right], \tag{1.63}$$

where the solution's properties are determined by the positive parameter a such as $a \neq 1/2$ through arguments $b = [8a(-2a)]^{1/2}$ and $\omega = 2(1-2a)^{1/2}$. Over the range $0 < a < 1/2$ the solution (1.63) gives the Akhmediev breather (AB) prototype where one observes the evolution from the trivial plane wave ($a = 0$) to a train of localized pulses with temporal period $\Delta\tau = \pi/(1-2a)^{1/2}$ [41]. The AB solution provides MI analytic framework, with the real parameter

ω corresponding to the modulation frequency, and the real parameter b giving the parametric gain coefficient [197]. The MI instability growth rate is maximal at $a = 1/4$, but increasing a actually leads to stronger localization in both dimensions until the limit $a \to 1/2$ which gives the Peregrine Soliton (PS) [39]

$$\psi\left(\xi, \tau\right) = \left[1 - \frac{4\left(1 + 2i\xi\right)}{\left(1 + 4\tau^2 + 4\xi^2\right)}\right] e^{i\xi}, \tag{1.64}$$

which corresponds to a single pulse with localization in both space (ξ) and time (τ). Then, when $a > 1/2$, the parameters ω and b become imaginary, and the solution exhibits localization in the temporal dimension τ with periodicity along the propagation direction ξ. Hence the Kuznetsov-Ma (KM) soliton [199, 198] which is shown in Fig. 19(a) for $a = 0.7$.
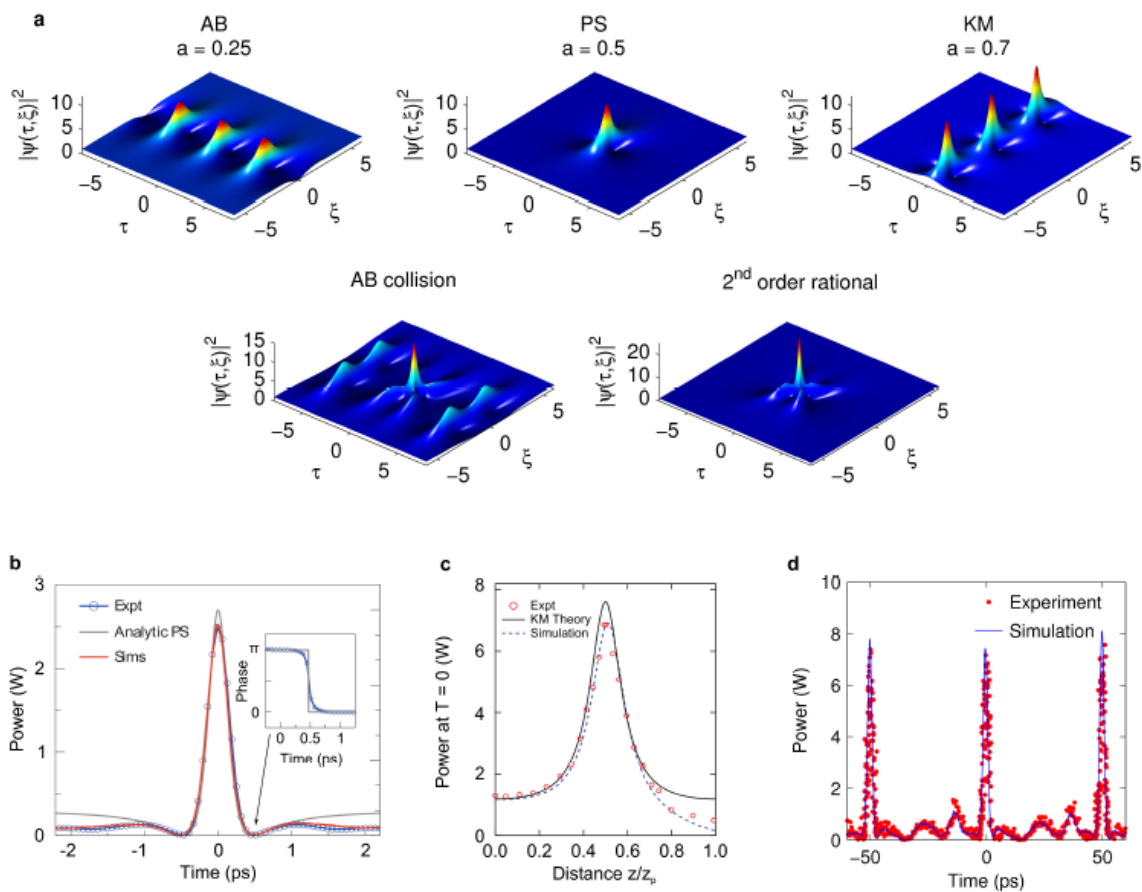
Figure 19: Soliton on finite background (SFB) solutions of the NLSE. (a), Analytical SFB solutions of Eq. (1.63) for varying parameter a. From left to right: an Akhmediev breather (AB); Peregrine soliton (PS); Kuznetsov-Ma (KM) soliton [40]. An example of an AB collision and the second-order rational soliton (or second-order PS) are also shown. (b)-(d), Experimental results. (b) shows temporal PS properties asymptotically approached for $a = 0.42$ [127], (c) shows KM dynamics along the propagation direction for $a = 1$ [40] with experiments, simulations and theory compared in each case. Here $z_p = 5.3km$ corresponds to one period of the KM cycle. (d) compares experiments and simulations of a second-order solution consisting of the collision of two ABs ($a = 0.14$ and $a' = 0.34$) [168].

The analytical results above have been used to design experiments with controlled initial conditions to excite particular SFB dynamics in optical fiber. The use of optical fibers provides an especially convenient experimental platform as the dispersion and nonlinearity parameters can be conveniently matched to available optical sources to yield a propagation regime where the NLSE is a valid model for the dynamics. Experiments typically inject a multi-frequency field into a nonlinear fiber, similar to the method developed for coherent pulse train generation in telecommunications [200, 201].

1.7.2   Improvement on the description and controllability of rogue wave propagation in optical fiber

Nonlinearities within photonic crystal fibers (i.e., a form of light-matter interaction) cause intense incoming light pulses to break up into trains of short pulses, called solitons. These solitons exhibit particle-like behavior, and their shape tends to be preserved during propagation. When the solitons are sufficiently short (typically less than 1ps), a cascade of high-order linear and nonlinear phenomena results in the generation of a broad optical spectrum, known as SC. During this process, rare events can occur in unpredictable manners. For instance, an unusually high wave can appear at the fiber output such as optical RW, analogue to oceanic RWs. Several numerical and experimental studies have been conducted to characterize and control optical rogue waves and rogue solitons. The main theoretical explanation derived from these investigations is that these phenomena correspond to exact solutions of the universal mathematical model, the NLS equation. The solutions of these models are of special interest in the fundamental theory, with several applications in many fields of science. After many studies, Scientists found in practice that the standard NLS equation is poetical to some realistic problems like the transmission of ultrashort pulses of the order of subpicosecond and femtosecond frequencies in highly dispersive optical fibers. Therefore, the NLS equation has been extended to take into account the thrid-order dispersion (TOD) and self-steepening (SS) nonlinearity. Thus, the integrable Hirota equation has been derived, even extended to take into account others nonlinear effects . One of these effects is the nonparaxiality which arises in the miniaturization of devices involving multiplexed beams. Moreover, chiral effects have attracted more attention in many fields of science.

A. Chirality in optics: optical activity.

The term chirality [95] is a well-known concept of great interest in chemistry, biology, pharmacology and optical fields [357]. In the context of chemistry, chirality refers to molecules that lack mirror symmetry. One of the most universally known example is the human hands. In fact, no matter how the two hands are oriented, it is impossible for the both hands to be coincide through translations and rotations. In the context of optics, chirality refers to optical activity which is the ability to rotate plane polarized light. The observe rotation of this plane polarized light can be directed to the right-hand, that is a clockwise rotation, called dextrorotatory

or to the left-hand, that is a counter clockwise rotation, called levorotatory. As consequence, enantiomers or optical isomers are designated in the literature as right-and left-handed [203]. Therefore, chirality can be defined as fundamental property of molecules and materials that leads to optical activity effects [204]. Some examples of chiral and achiral materials are depicted in Fig. 20
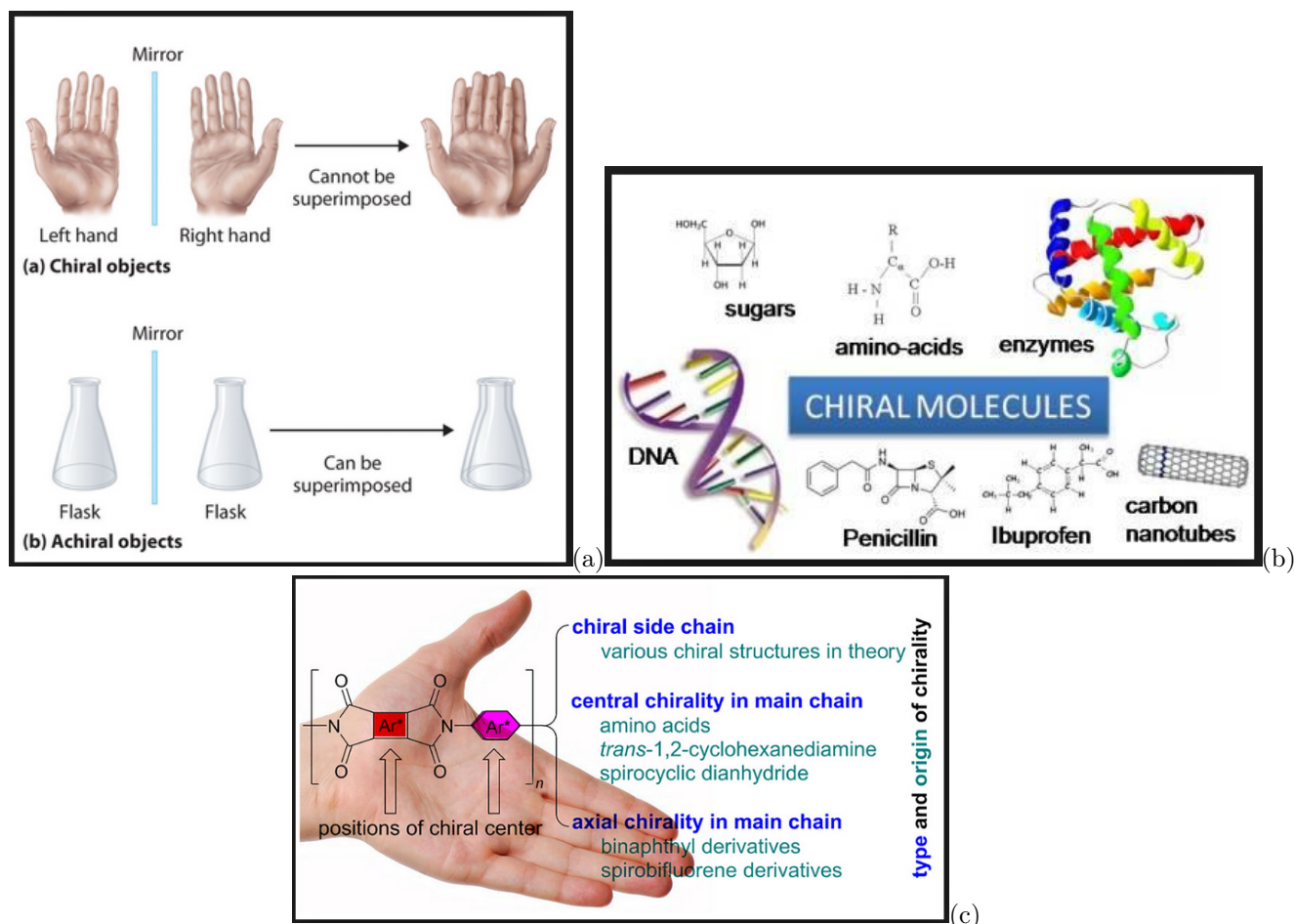
Figure 20: (a) Chiral and achiral objects. (b) Types of chiral molecules. (c) Type and origin of chirality.

Among chiral materials, chiral optical fibers are materials of crucial importance. They give rise to optical activity effects such as optical rotation and circular dichroism which are optical characterization techniques of molecules [357]. In fact, these effects are used to investigate the structures of molecules and to elucidate the secondary structure of biomolecules. Optical activity has attracted and inspired great effort in the developing of active photonic chiral metamaterials [205]. These materials are designated to deliver an unusual electromagnetic response, in spite of the fact that, optical activity is a linear effect.

To summarize, optical activity effects have been found in both linear and nonlinear optics. In nonlinear optical fields, others characterization techniques like the second-harmonic generation -

circular dichroism (SHG - CD) and the second-harmonic generation - optical rotatory dispersion (SHG - ORD) were undertaken by T. Verbiest *et al.* [206]. Later, A. Bruyere *et al.* [207] have studied the formation of chiral supramolecular aggregates at an air-water interface with the SHG technique. Futhermore, Huttunen *et al.* [208] have shown that the third-harmonic generation - circular dichroism (THG - CD) effects could occur in biological materials. Briefly, many works have been done in chiral metamaterials [209], nanomaterials [210, 211] and in photonic crystals [212].

1.7.3 Optical fiber devices, characteristic and applications

Optical fibers are cylindrical dielectric waveguides in which light can propagate at optical frequencies along its main axis [184]. Since the beginning of 20th century, one denotes an improvement and several scientific progress in the understanding, design, fabrication and applications of optical fibers. One can mention in telecommunication domain, a higher production level of optical fibers which are used throughout the world to transmit information (i.e., for communication). More specifically, optical fibers have several applications in life-science and industry fields. So far, one can mention, on the one hand, the sensing, medical imaging, power transmission, illumination and decoration in the industry area. On the other hand, one can mention the spectroscopy, optical imaging, fabrication of lasers and optical amplifiers. Concerning the improvement on fiber design, one denotes the step-index fibers, made with cylindrical core of high refractive index n_1 where the light propagates, surrounded by a cladding of low refractive index n_2 that traps the light through total internal reflection. Most of them are made of fused silica SiO_2 and the refractive index difference can be slightly modified by chemical doping. The Snell's law of refraction (i.e., a total reflection of light at an interface between two materials of refractive index n_1 and n_2 (with n1 > n2), for incident angles $\alpha > \alpha_{min} = \sin^{-1}(n_2/n_1)$) defines the angles of which the light is transmitted through the fiber after multiple reflections (see Fig. 21).

There is a cone of light at the input of the fiber for which the incident angles on the interface core/cladding are higher than $\alpha_{\max}$, and for which the light is transmitted. Outside of this cone, the light escapes through refraction in the cladding. This cone of light defines the numerical aperture (NA) of the optical fiber. By applying the Snell's law to the end of the fiber, the NA yields [184]

$$NA = n\sin\left(\frac{\pi}{2} - \alpha_{\min}\right) = \sqrt{(n_1^2 - n_2^2)}, \qquad (1.65)$$

where n is the refractive index of the outside medium. Through Fig. 21, one can assume that any ray entering the fiber within the cone defined by NA can be transmitted.

It is well-known that, when interference effects are taken into account, it becomes clear that only a discrete set of rays are allowed to propagate in the fiber. Therefore, one can observe different modes of propagation summarize in Fig. 22
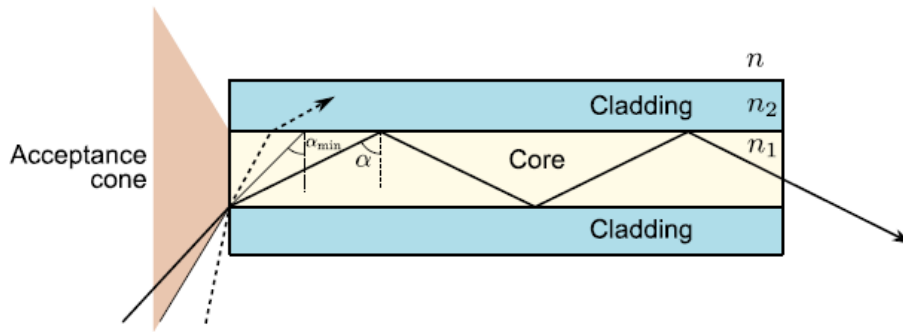
Figure 21: Light transmission in a step-index fiber based on multiple total internal reflections at the interface between the core (refractive index n_1) and the cladding (refractive index n_2). The acceptance cone is defined by the minimum incidence angle α_{min} allowing the total internal reflections. The rays entering the fiber from outside this cone will experience power loss due to refraction, and all their energy will be dissipated in the cladding after few reflections [175]1.

In Fig. 22 (a), each ray corresponds to one mode but, the downside is that multimode step-index fiber undergo the intermodal dispersion. Therefore, there will be a delay between the exit time of two modes, as the rays follow different optical paths. Figure 22 (b), exhibits the graded-index fiber where the rays are continuously deflected instead of propagating along straight lines between two reflections. Moreover, the refractive index continuously decreases from the central axis to the cladding and the intermodal dispersion induced by the fiber is decreased because the difference between the optical paths of small and large incident angles is minimized. The NA of graded-index fiber, is maximum at the center and decreases as a function of the radial distance, when the rays enter closer to the cladding. As consequence, graded-index fibers are less mode fibers and less transmitted light compared to a step-index fibers (see 22 (a) and (c)).

Photonic crystal fibers (PCFs).

As scientific progress, the micro-structured fibers, called photonic crystal fibers (PCFs) have been developed in 1990s by the group of Philip St. J. Russell [213]. The core of PCF is made of a periodic arrangement of microscopic air holes running along the whole length of the fiber made with silica. Their idea was to trap the light in a hollow core by preventing its propagation in the cladding by the means of a 2-D photonic crystal. Photonic crystals are periodically organized nanostructures that creates "stop-bands", or photonic band gaps (PBG), preventing the propagation of light in one, two or three dimensions. It is well to mention that, the trapping of the light and its propagation in the core does not always come from the PBG effect but, depends on the design of the fiber, particularly, on the structure of the core. To summarize, fiber properties depends on the composition of the fiber. Thus, wide diversity of PCFs has been fabricated by doping the silica and are used in fiber-optical parametric oscillators and amplifiers [214, 215], artificial black holes [216] or intense SC generation [217, 218] for fluorescence microscopy [219], optical metrology [220] and optical coherence tomography [221]. An example, of solid-core PCF is designed in Fig. 23.
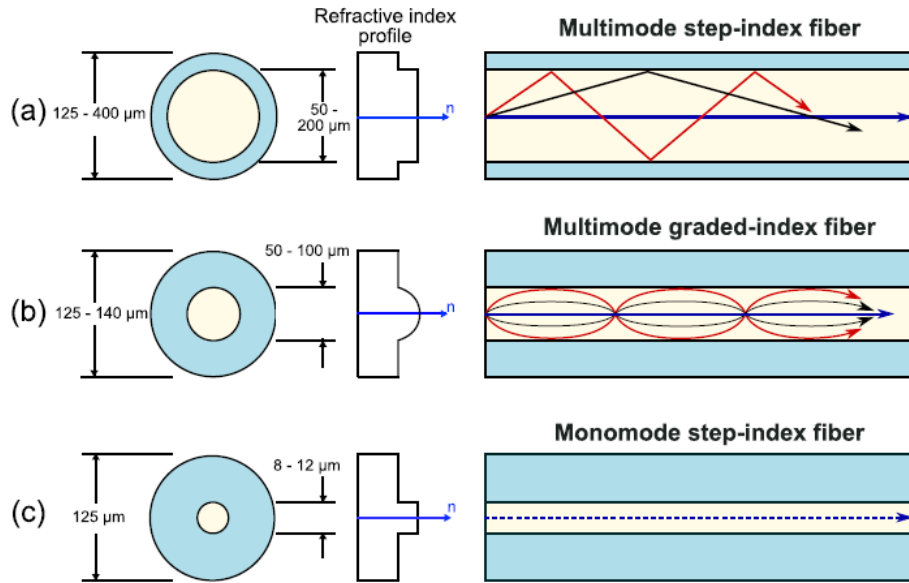
Figure 22: Typical dimensions, refractive index profiles, and rays paths in (a) multimode step-index fiber, (b) multimode graded-index fiber and (c) monomode step-index fiber [213].

Figure 23 depicts the simplest kind of PCFs which has a hexagonal pattern of air holes, with one hole missing in the center (core) made of silica, where the light propagates. The parameters d and Λ are the diameter of the hole and the hole-to-hole distance (pitch). The mechanism of guidance is conceptually similar to the total internal reflections (TIR) in classical fibers, but an advantage of PCFs is the possibility to tailor some of their properties by changing d and/or Λ. For instance, the dispersion of a fiber can be modified by changing the design. This is a big advantage compared to classical fibers where the value of dispersion cannot be changed too far away from the dispersion of the bulk material [184]. Another remarkable feature of PCFs is their ability to exhibit single-mode behavior for a wide range of wavelengths [222]. Moreover, one advantage of PCFs over classical fibers, is their small core where the strong confinement of the light can lead to increased intensity, which is useful for studying and using nonlinear effects. However, as the modal filtering depends only on the d/Λ ratio, it is possible to design fibers with large cores, by scaling the whole structure. This is the principle of large-mode area fibers, that are useful if one wants to avoid the nonlinear effects caused by the presence of high powers in silica.

Photonic band-gap (PBG) fibers.

Among micro-structured fibers, one denotes the Photonic band-gap (PBG) fibers whose core refractive index is higher than the cladding refractive index. In practice, the total internal reflection (TIR) guiding dominates, in spite of occurrence of the PBG. In the opposite case where the core refractive index is lower that the cladding refractive index, the TIR cannot operate. Then, the guidance relies only on the PBG effect [223].

44
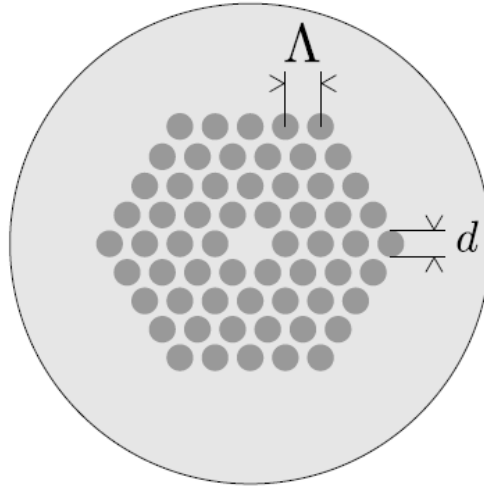
Figure 23: Scheme of a solid-core PCF. The light gray area is silica and the darker inclusions are air holes. d is the diameter of a hole, and Λ is the pitch [184].

Hollow-core photonic bandgap (HC-PBG).

Another technological improvements, is the fabrication of Hollow-core photonic bandgap (HC-PBG) fibers where the light propagates in an air core [224, 225, 226]. Their key parameter is the ratio d/Λ, which corresponds here, to the air filling fraction of the photonic cladding. The width of PBG increases for increasing ratio d/Λ. The broad transmission bands is obtained when the ratio $(d/\Lambda) > 0.9$. The broadest bands could be achieved for $(d/\Lambda) = 1$, but the fabrication of a such fiber is not feasible. As the light propagates in air rather than in silica, HC-PBG fibers have been used for the transmission of high-energy pulses. The transmission losses of such fibers are theoretically lower than those of conventional all-silica fibers, because the intrinsic transmission of air is much higher than the one of silica. But in practice, HC-PBG are still suffer from losses due to surface roughness (1.2 dB/km at 1600 nm) whereas Silica fibers have gone through several technological improvements and have come close to the limit of Rayleigh scattering, with transmission losses as low as 0.15 dB/km. Roberts *et al.* have shown that the design of HC-PBG could be optimized to reach transmission losses of 0.1 dB/km [227].

Kagomé fibers.

An interesting type of hollow-core fiber, namely, Kagomé fiber, was made without photonic band gaps. Its photonic cladding is based on a kagomé lattice of silica [228, 229], whose pattern looks like a Star of David and where the light propagates in an air core surrounded by an air / silica microstructure (photonic cladding). Its guiding properties are not fully understood, but they have a very wide bandwidth of transmission, which can be used in several applications. One of the main drawback of Kagomé fibers, is their higher losses which are important compare to other HC-PBG fibers.

Solid-core photonic bandgap (SC-PBG) fibers.

In SC-PBG fibers, the core is made of low-index silica, while the photonic cladding is made of an array of high-index silica. As illustration, Luan and co-workers demonstrated the first SC-PBG fiber with a core made of LLF1 glass and a photonic cladding made of inclusions of SF6 glass [230]. So far, the possibility to dope silica with diverse rare-earth ions allows to design a wide range of fibers with different properties. The use of SC-PBG fibers is promising in fiber lasers [231, 232] and fiber amplifiers [233] as well as in the investigation and control of nonlinear effects such as SC generation and soliton propagation [234].

A great scientific progress, such as the design and fabrication of the first SC-PBG-1 (SC-PBG-1) and second SC-PBG (SC-PBG-2) were made at IRCICA laboratory in Lille (France). These two types of SC-PBG have been used in optics and an illustration is revealed in Fig. 24 and Fig. 25.
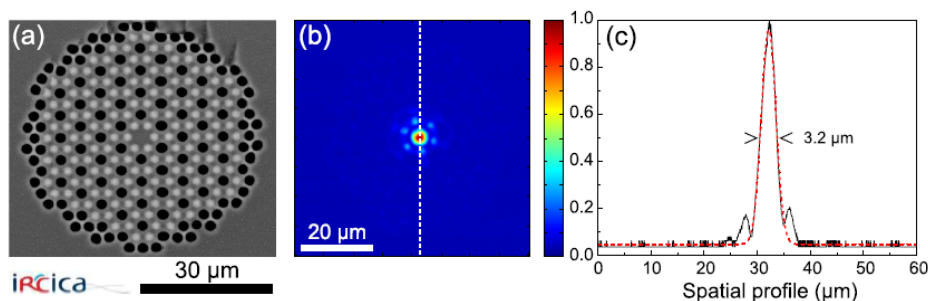
Figure 24: (a) Scanning electron microscopy (SEM) image of the core and photonic cladding of the SC-PBG-1 fiber. The dark gray area is the silica, the light gray dots are the Ge-doped rods and the black dots are the air holes. Courtesy of A. Kudlinski. (b) Image of the fundamental mode on a CMOS camera. (c) Spatial profile along the dotted white line in (b). Dotted red line: Gaussian fit [184].

Figure 24(a) shows the scanning electron microscopy (SEM) image of the cross-section of the fiber. The structure is based on silica, with a doubly periodic network of air holes and germanium doped silica rods. The Ge-doped silica rods (light gray regions) have a diameter of $2.19\mu m$ and are separated by a pitch of $3.09\mu m$. Their refractive index profile is parabolic with a maximum refractive index difference of 32×10^{-3} relative to the pure silica background (dark gray region). Air holes (black regions) of $2.33\mu m$ diameter were added periodically to the cladding. Figure 24(b) exhibits the image obtained on the CMOS camera after coupling to the fundamental mode. Its spatial profile is observed along the dotted white line. Figure 24(c) depicts the fit of the spatial profile by a Gaussian function of width $3.2\mu m$.

In Fig. 25(a), the Ge-doped silica rods (with a diameter of $1.51\mu m$), are separated by a pitch of $2.40\mu m$ and, the air holes with a diameter of $1.47\mu m$. Figure . 25(b) compares the $|\beta_2|/\gamma$ ratio of this fiber (red line), obtained by finite element calculations, with the typical values for standard PCFs (gray area).
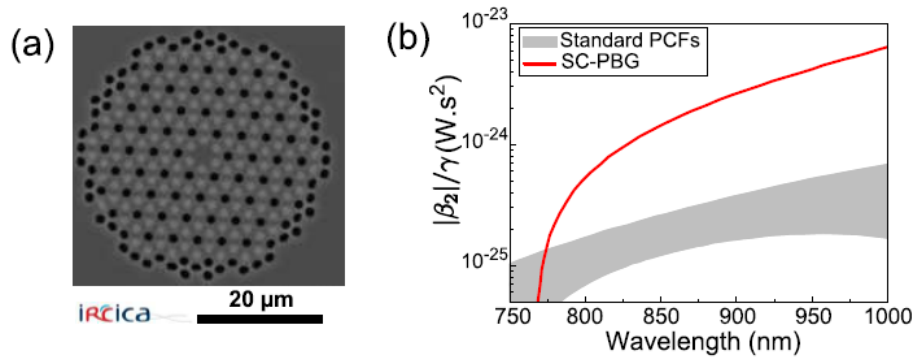
Figure 25: (a) SEM image of the cross-section of the core and photonic cladding of the SC-PBG. The dark gray area is the silica, the light gray dots are the Ge-doped rods and the black dots are the air holes. Courtesy of A. Kudlinski. (b) Calculated $|\beta_2|/\gamma$ ratio for standard PCFs and SC-PBG-2. [184].

1.8 Brief description of experimental realizations of rogue wave in extended fields of science

More often, the experimental systems offer the possibilities of handling the parameters that are responsible for the generation of extreme waves. Rogue waves in laboratory experiments are easier to investigate than rogue waves in ocean. At the same time, the collection of many events becomes possible in relatively short time intervals, depending on the typical response time of the system considered. As consequence, considerable efforts have been done to study the rogue wave phenomena in a number of different physical systems, generated from different originating mechanisms. A brief description of some experimental realizations on the transient rogue waves appearing during the inverse cascade of the wave turbulence regime in superfluid Helium [235] is developed. The linear rogue waves resulting from the inhomogeneous emission of a large number of microwave antennas [236], rogue waves occurring on the surface of a parametrically driven fluid [27] and rogue waves in plasma systems [29] are described in subsections below.

1.8.1 Rogue waves in superfluid Helium

When cooled below the critical temperature of $T_\lambda = 2.17K$, ^2He condenses to form a liquid that has remarkably different properties than a normal fluid. It is, usually, called He II to distinguish it from the He I above T_λ. He II behaves as if it were a mixture of two different fluids. A normal fluid component with viscosity and carrying all of the thermal energy of the liquid, and an inviscid superfluid component with zero entropy. The two fluids separately fill the containing vessel.

Oscillatory counterflow of the two components can occur at constant density and pressure, corresponding to a temperature-entropy wave known as second sound. Second sound has a relatively low phase velocity, approximately $20m/s$ and an extremely small attenuation coefficient

for frequencies below $1MHz$. Its velocity u_2 depends strongly on its amplitude u_{20} and can be approximated as

$$u_2 = u_{20}\left(1 + \alpha \delta T\right), \tag{1.66}$$

where u_{20} is the velocity at vanishingly small amplitude. The nonlinearity coefficient α can be made large, and either positive or negative, by adjustment of the temperature. The strength of the wave interactions is determined by α hence, can be easily controlled. These properties make He II an ideal medium for systematic studies of nonlinear interactions between waves [235, 237].

Rogue waves have been observed in an experiment involving second sound waves within a resonant cavity filled with superfluid Helium. Because of the small attenuation coefficient for the second sound, the quality factor of the cavity is very high, enabling large wave amplitudes to be achieved. Being a temperature wave, second sound can conveniently be excited with a heater and detected thermometrically. Energy is injected in the system by a thin heater sinusoidally driven by a harmonic voltage generator in the frequency range $0.1-100kHz$, while the frequency of the second sound (twice the frequency of the voltage generator) is set close to a longitudinal resonance of the cavity.

Under certain experimental conditions a direct energy cascade exists, that is, the energy injected at the driving frequency flows steadily towards higher frequencies with negligible dissipation until the viscous cut-off is reached, beyond which it is rapidly dissipated as heat. When the driving amplitude is increased or the detuning of the drive from the resonant frequency is decreased, an inverse cascade appears, which is associated with an instability against the formation of subharmonics. Rogue waves are observed during the transient evolution of the inverse cascade, that is, they accompany the subharmonic formation that characterizes the inverse cascade. A typical experimental evolution is shown in Fig. 26

Rogue waves in superfluid Helium have, so far, only been observed during the transient evolution of the second sound waves, in the wave turbulence regime and while the inverse energy cascade is evolving. Their relation with rogue waves on the ocean surface include similarities: in both cases, the phenomena under consideration are non-equilibrium in nature, the rogue waves are rare and extreme events that arise from an instability of large amplitude waves. The differences include: the second sound waves are produced directly by a periodic driving force, whereas on the ocean roughly periodic waves are created by e.g. wind of a sufficient velocity, the second sound waves are one-dimensional standing waves, within the volume of the fluid, whereas the ocean waves are on the surface and can propagate in two dimensions, rogue waves on the ocean can apparently appear under steady state conditions, whereas those in second sound have only been observed during the transient evolution of the inverse energy cascade [237].
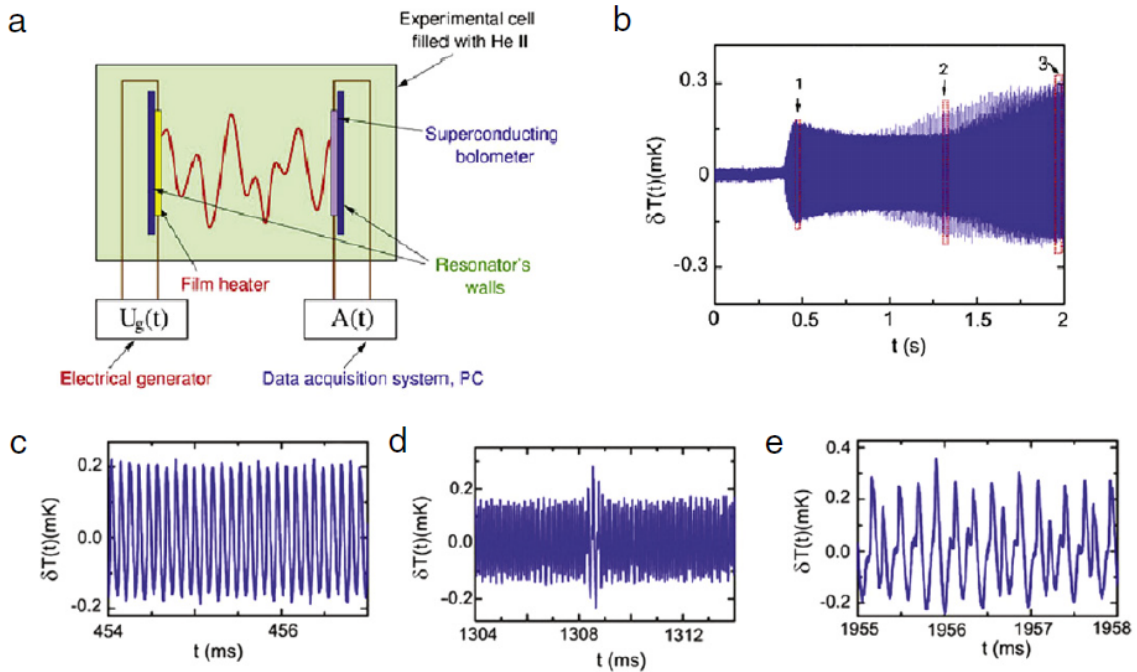
Figure 26: (a) Experimental setup for the observation of second sound waves in superfluid Helium. (b) Evolution of the second sound wave amplitude after switching on the drive at a frequency near resonance; the signals (c)-(e) are enlarged plots corresponding to the 1-3 windows indicated by the arrows. Rogue waves appear in the 2 window and typically accompany the subharmonic formation that characterizes the inverse cascade [237].

1.8.2 Rogue waves in the linear regime of microwave antennas

Rogue waves have recently been observed in a study of microwave transport [236]. The experimental setup, shown in Fig. 27, is made of randomly placed metallic cones, each mimicking an r^{-2} potential on the scale of its radius. The metallic bottom plate supports the random arrangements of scatterers. The source antenna is mounted close to one of the short sides, and varying its position enables the incoming waves to arrive from different directions. The drain antenna is mounted in the top plate (not shown) and acts as a probe. The top plate can be moved in both horizontal directions, allowing for a spatial mapping of the wave fields within the scattering arrangement.

For wavelengths smaller than or comparable to the scatterer size (frequency $f = 30 - 40$ GHz), the system shows branching structures reminiscent of electron current distributions observed in two-dimensional electron systems [236]. At wavelengths larger than the cone size (frequency $f = 7.5 - 15$ GHz), the bulk of the intensity distribution approaches a multiple-scattering correction to Rayleigh statistics, as expected in multiple-scattering media. However, the probability of finding very high intensities is greatly enhanced with respect to the predictions provided by the Rayleigh statistics.

The extreme events in the microwave system occur in space (two-dimensions) and time,
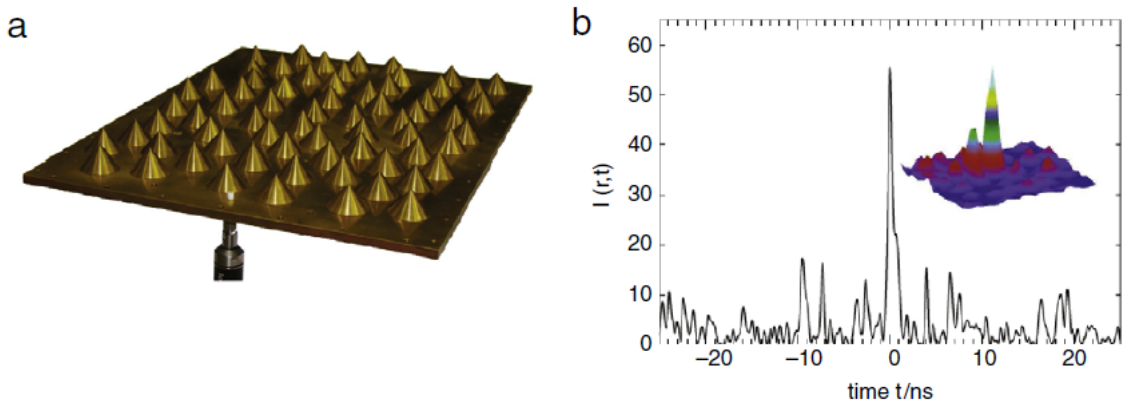
Figure 27: Experimental setup for the observation of rogue waves in a microwave system: the platform has width $260mm$ and length $360mm$; the probe antenna is fixed in a horizontally movable top plate located $20mm$ above the bottom (not shown). (b) A rogue wave event: the time evolution of wave intensity at the center of one of the hot spots is shown for the most extreme event observed; the inset shows the region surrounding the hot spot at the moment of the freak event. [236].

therefore, offering several qualitative analogies with the rogue waves on the ocean surfaces. However, the microwave system is linear, so that the origin of the extreme events cannot be searched in a modulational instability effect, as it occurs for nonlinear waves, and the description in terms of envelope solitons fails in this case. What is suggested by the authors is that the large deviations from the Rayleigh distribution is a consequence of inhomogeneities in the system and of averaging over different configurations of disorder. The randomly placed cones behaves like lens, which occasionally focus the microwaves into a hot spot. The mechanism is very similar to the focusing obtained by random currents [238]. Indeed, it is verified by fixing the probe position that the local distribution of intensities is a Rayleigh law $P_{loc}(I) = s^{-1}e^{-\frac{I}{s}}$, with the time-averaged value $s = \langle I \rangle$ depending on the chosen position. Then, the overall distribution of time-dependent intensities, collected over different positions and/or realizations of the disorder, is given by the integral of the local distributions, which yields a chi-square distribution that fits the experimental data.

This example shows how inhomogeneity can play a key role in inducing large deviations from the Gaussian wave statistics. As reported in the following section, such a key role of inhomogeneity has emerged also in optics, both in nonlinear [110] and linear experiments [239]. In particular, in the linear systems the inhomogeneity appears as an essential ingredient. Indeed, in this case the construction of the rogue wave events can be understood in terms of linear superposition of wave packets traveling with different group velocities and interfering constructively at a given space position and at a certain instant time. For this rare and positive coincidences to occur more frequently, the spectrum of the possible group velocities must be large, a condition that is enhanced if the system is largely inhomogeneous.

1.8.3 Rogue waves in capillary waves and plasmas

A. Extreme events in parametrically driven capillary waves

Parametrically excited waves occurs at the surface of vibrated fluids as a consequence of the interplay between gravity and the capillary forces that tend to maintain the surface of the liquid at its rest position. Above a critical amplitude of the forcing, an instability takes place for which small surface deformations are amplified and waves oscillating at half the forcing frequency set on the surface of the vibrated liquid [240]. Capillary waves belong to the high frequency branch of the surface waves, for which the restoring force is the surface tension. Their wavelengths are typically shorter than about $10mm$. Because of their small scale, capillary waves can be studied under well-controlled conditions in the laboratory using a variety of experimental methods.

Extreme events have been recently obtained in a system of capillary waves excited parametrically in a vertically shaken container filled with water [27]. The waves were forced by shaking the container at the frequency of 60 Hz with an acceleration in the range of $a = 0.3 - 5g$. The strength of forcing is characterized by the value of supercriticality above the threshold a_{th} of the parametric excitation, $\varepsilon = a - a_{th}$. The water surface was visualized by adding a small amount of a fluorescent dye to the water and by illuminating it with a thin green laser sheet. The motion of the fluorescent surface in the vertical cross section was then captured by a fast video camera.
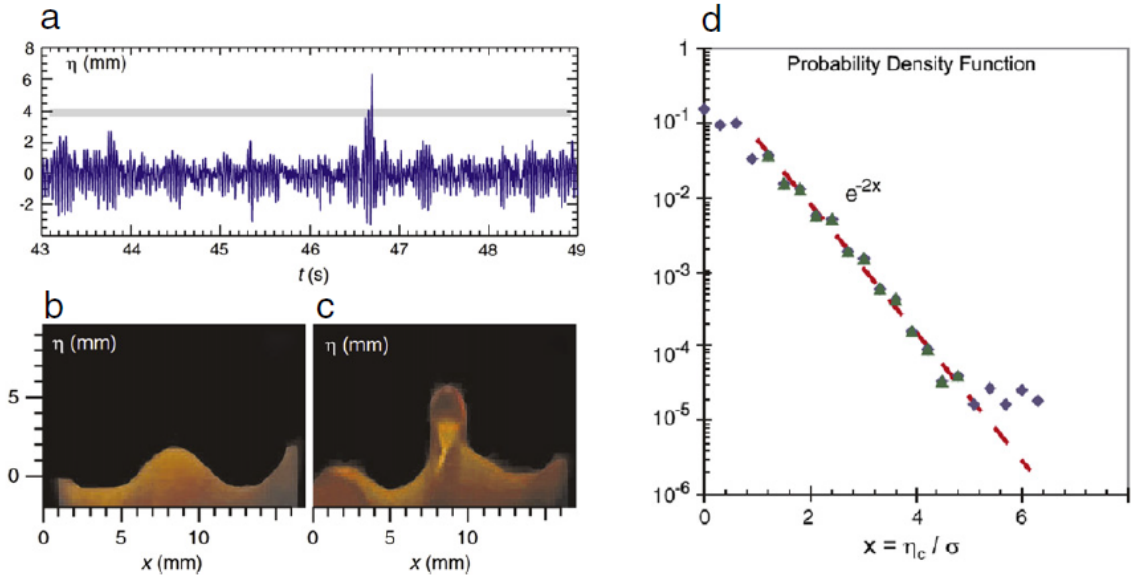
Figure 28: (a) Time trace of the surface elevation showing an extreme wave event in parametrically driven capillary waves. Instantaneous snapshots showing waveforms: (b) 4 periods before the large event, and (c) during the large wave event. (d) Probability density function of the wave crests versus the normalized crest height [27].

Fig. 28 (a) shows a time trace of the surface elevation $\eta(t)$ measured at the strongest forcing, $\varepsilon = 5$. This trace contains an extreme wave event, that is, a wave with a crest height $> 6mm$.

The peak amplitude exceeds the standard deviation of the wave background by a factor of more than five. Two instantaneous snapshots show the waveforms before the peak,(see Fig. 28 (b)), and during the large event, (see Fig. 28 (c)). Note that the rogue wave is characterized by an almost vertical wave front. Figure 28 (d) shows the probability density function (PDF) of the normalized wave crest heights $x = \eta/\sigma$, where σ is the standard deviation, recorded for $300s$, or 104 wave periods. Strongest waves, $x > 5$, have a probability which is substantially higher than expected from the e^{-2x} Gaussian trend. The system displays, therefore, a statistical behavior typical of extreme events [241]. As for the frequency spectra of the parametrically excited waves, the development of frequency sidebands is first observed when the forcing is gradually increased, thus, suggesting that the classical phenomenology of modulation instability is, here, at the origin of the rogue wave phenomenon. Indeed, at further increase of the forcing, the spectrum becomes continuously broadened and displays a triangular shape with exponential tails. Correspondingly, the PDF of the wave amplitude develops tails with crest heights in excess of 6.

The evolution of the wave amplitude in the time domain shows envelope solitons as a result of the MI, and the nonlinear broadening of the spectra seems to originate from the generation of shorter envelope solitons, in analogy to the spectral broadening of the light pulses observed in PCFs at the first stages of SC generation [218]. Then, the rogue wave generation in the parametrically excited waves probably results from a process similar to the collision of breathers as observed, for instance, in optical fibers [12]. In any case, modulation instability appears as a characteristic feature for the spectral broadening.

B. Rogue waves in plasmas

Numerical investigations have been, recently, reported for the generation of acoustic rogue waves in a dusty plasma composed of negatively charged dust grains and nonextensive electrons and ions [242]. A reductive perturbation technique has been used to obtain a NLS equation, hence, the prediction of a nonlinear evolution of modulationally unstable dust-acoustic wave packets. The authors show numerically that within the MI region a random perturbation of the amplitude grows to create the dust-acoustic rogue waves.

Experiments in a multicomponent plasma with negative ions have, recently, reported the evidence of Peregrine solitons of ion-acoustic waves [29]. It is shown that, for a critical concentration of negative ions, slowly amplitude modulated perturbations undergo self- modulation, giving rise to high amplitude localized pulses. The measured amplitude of the Peregrine soliton is 3 times the nearby carrier wave amplitude, which agrees with the theory and with the numerical solution of the NLS equation. Direct analogies for this type of soliton solutions can be established with the Peregrine solitons observed in wave tank experiments [57] and in optical fibers [127]. Finally, rogue waves, in the form of giant breathers, are numerically shown to develop in the Alfvén wave turbulence regime described by the randomly driven derivative

NLS equation in the presence of a weak dissipation [243]. The distribution of the instantaneous global maxima of the Alfvén wave intensity fluctuations is shown to be accurately fitted by power laws, which contrasts with the integrable regime (absence of dissipation and forcing) where the behavior is rather exponential. As the dissipation is reduced, rogue waves form less frequently but reach larger amplitudes. Here, the rogue wave generating mechanism appears as related to a genuine wave turbulence regime. Analogies could be drawn with the rogue waves experimentally observed in the superfluid Helium during the wave turbulence inverse cascade [235].

1.9 Conclusion

This chapter present the rogue wave historical context in oceanography then, from hydrodynamics to optics. The main features of rogue wave phenomena are elucidated as well as the process for their generation in optical fibers. Moreover, an analogy of results is shown on both theoretical, numerical and experimental realizations. In addition, the linear and nonlinear effects that can influence the rogue wave propagation in optical fibers are presented. An improvement on the description and controllability of rogue wave propagating in optical fiber are revealed. The rogue wave extension in others fields of science and their applications are given. Finally, the optical fibers are presented as high quality devices in communication and great media for wave propagation.

Chapter 2

Analytical and Numerical Methods

2.1 Introduction

Nonlinear propagation equations are widely used to describe complex phenomena in many fields of science, such as plasma physics, hydrodynamics, solid state physics and optical fibers. One of this nonlinear equation with undeniable role, is the NLS equation which was first derived in 1967 by Benney and Newell [244] in a general setting. Then, in 1968, the NLS was also derived in the study of modulational stability of deep water waves by Zakharov [245]. Later, in 1973, Hasegawa and Tappert [77] have shown that the same NLS equation governs light pulse propagation in optical fibers. The standard NLS equation is known as the universal model to describe nonlinear wave propagation as well as rogue wave phenomenon in optical fibers [15, 59]. After many studies, scientists found in practice that, the NLS equation is poetical to some realistic problems like the transmission of ultrashort pulses of the order of subpicosecond and femtosecond frequencies in highly dispersive optical fibers. Therefore, the NLS equation has been extended to higher-order NLS equations [66, 67, 68] on which the third-order dispersion (TOD) [69, 70, 71, 72] and other nonlinear effects such as self-phase modulation (SPM) [72, 73], cross-phase modulation (XPM) [24, 72], self-steepening (SS) [68], self-frequency shift (SFS) [67, 71], and four-wave mixing (FWM) [24, 71, 72] have been taken into account. Moreover, vector NLS equations has increased markedly over the past decade with the introduction of new optical fiber technology that permits the transmission of pulses through many channels in a single fiber (wavelength division multiplexing) and the production of ultrafast pulses (in terahertz range) through birefringent fibers where more than one polarization is present [246, 247]. Due to the complexity and difficulty of solving extended NLS models with higher-order effects, many analytical and numerical methods have been applied to find the exact solutions (rogue wave prototypes) and other particular solutions.

In this chapter, the description of analytical methods such as the similarity transformation, Lax pair method, mDT and DDT methods are of special interest. The investigation is based on Lax pair and DT formulations and construction hierarchy. Then, will follow the description

of the pseudospectral and difference-differential equation methods, related to the FFTs and fourth-order Runge-Kutta method. These methods are useful to study the dynamical behavior, properties and any possibilities of control of nonlinear effects on rogue wave propagation in optical Kerr and chiral fibers.

2.2   Analytical methods

The finding of rogue wave solutions of nonlinear propagation equations is of great interest. However, determining solutions of nonlinear propagation equations is a very difficult task and only in certain cases one can obtain exact solutions. Among the analytical methods, one can mentioned the DT method [248, 249], the modified DT method [63, 93], DDT method [96, 97], inverse scattering transformation [250, 251], Hirota method [252], Bilinear method [253] from which, one can obtain the exact solutions. One can also mention the Hirota bilinear method [254, 255], perturbation method [256, 257], Bäcklund transformation method [258], Lie symmetry [259, 260], $(\frac{G'}{G})$-expansion method [261, 262], F-expansion method [263, 264, 265], Jacobian-elliptic function method [266, 267], Painlevé analysis [268], Exp-function method [269, 270, 271], and the tanh function method [272, 273]. As rogue waves are related to rational solutions, particular methods such as Lax pair method, mDT and DDT method are adequate to obtain usual and unusual rogue waves.

2.3   Symmetry reduction method

In more than one space dimension, the NLS equation is not any more integrable [274]. In that case, no Lax pair and linear solution techniques are available to solve it. Moreover, the non integrability of NLS model also occurs when it has varying coefficients. Therefore, it becomes non integrable and this can strongly affect the wave propagation in Kerr and chiral media. To solve the problem of non integrability of NLS model, one can either use the symmetry reduction method using the third-order propagation vector field [275] or the envelope field in gauge form [276] to obtain some integrability conditions. The techniques do not depend on the equation under study being integrable. They consist of a systematic application of group theory to reduce the non integrable partial differential equation (PDE) to an ordinary differential equation (ODE) which is then solved whenever possible. This method is called "symmetry reduction" or "similarity transformation" and is simple, straightforward, and mathematically rigorous [274]. It goes back to Lie [278] and is described in many books [279, 280, 281, 282]. The method consists of several steps. The first is to determine the symmetry group of the considered equation. Let consider the cubic NLS equation below [274]

$$i\psi_t + \Delta\psi = a_0\psi + a_1\psi|\psi|^2 + a_2\psi|\psi|^4, \tag{2.1}$$

where $\psi = \psi(x, y, z, t)$ belong to the complex set, a_i to the real set, with $\{a_1, a_2\} \neq \{0, 0\}$ and for which the initial conditions correspond to a cylindrical geometry. More specifically, to the

impose Cauchy conditions at some time $t = t_0$ on a cylinder $\rho = \rho_0$, such as

$$\psi\left(x, y, z, t\right)|_{(t,\rho)=(t_0,\rho_0)} = f_1\left(\theta, z\right),$$

$$\left[\nabla\psi\left(x, y, z, t\right)\right]^2|_{(t,\rho)=(t_0,\rho_0)} = f_2\left(\theta, z\right), \tag{2.2}$$

$$x = \rho\cos\theta, \ y = \rho\sin\theta.$$

The quintic NLS equation (2.1) is not integrable even in $1+1$ dimensions, still less in higher dimensions. For $a_1 \neq 0$ and $a_2 \neq 0$, Eq. (2.1) belong to the extended Galilei group class [283]. If either a_1 or a_2 vanish, the symmetry group is larger, namely, the Galilei-similitude group, including dilations [283]. The second step is to classify the subgroups of the symmetry group into conjugacy classes. Both Galilei and Galilei-similitude groups have been done in the literature [283]. In this case, the interest is focus in a very specific subgroups that have orbits of codimension one, compatible with a cylindrical geometry, in the space of independent variables. The requirement that a solution should be invariant under such a subgroup reduces Eq. (2.1) to an ODE. The final step is to solve the obtained ODE. This can be done with several methods. If on the one hand, the ODE is of the Painleve type (i.e., its solutions have no moving critical points) one can reduce Eq. (2.1) to a standard form that can be solved by the mDT or DDT method as well as in terms of elementary functions, elliptic functions, or Painleve transcendent. If on the other hand, the ODE itself, still has a symmetry group, its order can be decreased by making use of that symmetry. The resolution of ODEs obtained by symmetry reduction is in general a formidable task, since the equations are nonlinear and complex. Two systematic approaches are available.

The first approach consists to find the symmetry group of the obtained ODE. If one exists, it is used to decrease the order of the equation. The second approach which was found to be more fruitful [274] is to determine whether the ODE belong to a class of integrable nonlinear ODEs, known as Painleve-type equations class. An ODE is said to have the Painleve property if none of its solutions has movable critical points (i.e., singularities) other than poles with the positions which depend on the initial conditions. Equations with the Painleve property are in general much easier to solve than other.

It should be noted that the method of symmetry reduction for a PDE involves the construction of solutions that are invariant under a subgroup of the symmetry group of the equation. When constructing the symmetry group, no mention should made of any boundary conditions. If these are added to the equation, they will cause a symmetry breaking, i.e., they will reduce the symmetry group to some subgroup (in the extreme case to the identity group, i.e., the symmetry can be completely destroyed). The symmetry reduction method has been applied in non integrable NLS models to look for exact analytical solutions and is one of adequate method to construct the rogue wave solutions when combined to the mDT [94] or DDT [98, 99] method. From this preliminary method, varying coefficients are obtained by integration of elementary functions whereas the complex field is deduced from the DT associated to the Lax pair method [277].

2.4 Lax pair method

The term Lax pairs refers to a set of two operators that, if they exist, indicate that a corresponding particular evolution equation [284]

$$F(x, t, u, ...) = 0, \tag{2.3}$$

is integrable. They represent a pair of differential operators having a characteristic whereby they yield a nonlinear evolution equation when they commute. The idea was originally published by Peter Lax in a seminal paper in 1968 [285]. A Lax pair consists of the Lax operator L which is self-adjoint (i.e. an operator that is equal to its own adjoint or, if a matrix, one that is Hermitian, i.e a matrix that is equal to its own conjugate transpose.) and may depend upon x, u_x, u_{xx},...,etc; but not explicitly upon t and the operator M that together represent a given partial differential equation such that

$$L_t = [M, L] = (ML - LM), \tag{2.4}$$

where

$$[M, L] = (ML - LM) = -(LM - ML) = -[L, M], \tag{2.5}$$

represents the commutator of the operators L and M. Operator M is required to have enough freedom in any unknown parameters or functions to enable the operator $L_t = [M, L]$ or ($L_t + [L, M] = 0$) to be chosen so that it is of degree zero, (i.e. does not contain differential operator terms and is thus a multiplicative operator). L and M can be either scalar or matrix operators. An important characteristic of operators is that they only operate on terms to their right. The process of finding of operators L and M corresponds to a given equation and is generally nontrivial. Therefore, if a clue(s) is available, inverting the process by first postulating a given L and M and then determining which partial differential equation they correspond to, can sometimes lead to good results. However, this may require the determination of many trial pairs and, ultimately, may not lead to the required solution. Because the existence of a Lax pair indicates that the corresponding evolution equation is integrable (i.e. the equation is exactly solvable, i.e. solutions obtained by linearization or direct methods). Finding Lax pairs is a way of discovering new integrable evolution equations [251, 286, 287].

In addition, if a suitable Lax pair can be found for a particular nonlinear evolutionary equation, then it is possible that they can be used to solve the associated Cauchy problem using a method such as the inverse scattering transform (IST) method derived by Gardener *et al.* [288]. Finding of rational solutions related to rogue waves with the mDT [63, 93, 94] and DDT [55, 96, 97] methods are of special interest in this thesis.

2.4.1 Lax pair analysis: Matrix form

In 1974 Ablowitz, Kaup, Newell, and Segur [289] published a matrix formalism for Lax pairs where they introduced a construction that avoids the need to consider higher-order Lax operators. This method is also referred to as the Ablowitz-Kaup- Newell-Segur (AKNS) method. In

their analysis, they introduced the following system

$$D_x \Psi = X \Psi,$$

$$D_t \Psi = T \Psi,$$

(2.6)

where X and T correspond to operators L and M, respectively, and is an auxiliary vector function. Matices X and T will, in general, both depend upon the time independent eigenvalue λ, and the size of Ψ will depend upon the order of L. Thus, if L is of order 2, then vector Ψ will has two elements and X and T will each be a 2×2 matrix. The compatibility condition for Eqs. (2.6) is

$$[D_t, D_x] \Psi = D_t(X\Psi) - D_x(T\Psi) = (D_tX)\Psi - XD_t\Psi - (D_xT)\Psi - TD_x\Psi = 0, \qquad (2.7)$$

which can be written succinctly as

$$(D_tX - D_xT + [X,T]) \Psi = 0,$$

(2.8)

where the matrix commutator is defined as

$$[X,T] := XT - TX.$$

(2.9)

Equation (2.8) is known as the matrix Lax equation. As a consequence of geometrical considerations, Eq. (2.8) is also known as the zero-curvature equation [286].

2.4.2   Lax pair of matrix ordinary differential equations (ODEs)

The Lax pair of matrix ordinary differential equations (ODEs) yields

$$\psi_x = X\psi, \ \ \psi_t = T\psi,$$

(2.10)

where ψ, X and T are $N \times N$ square matrices. $\psi = \psi(x,t,k)$ is a common solution of the two linear ODEs (2.10), while $X = X(x,t,k)$ and $T = T(x,t,k)$ depend on the coordinate x, the time t and the complex spectral parameter k according to the definitions

$$X(x,t,k) = ik\sigma + Q(x,t),$$

$$T(x,t,k) = 2ikC - \sigma W + \sigma [C, Q(x,t)],$$

(2.11)

where $[A, B]$ stands for the commutator $AB - BA$. To simplify the analysis, let consider the X and T matrices as first degree in the spectral variable k. This choice is responsible of similar role, played by the two independent variables x and t. Therefore, their interpretation as space and time can change according to the physical application. In addition, this choice leads to wave equations which are dispersionless when linearized around the vanishing solution. The dispersion terms can be easily introduced with only technical changes of the method [95], where the dispersive term of NLS type has been considered. In Eq. (2.10), σ and C are the diagonal constant matrix and an arbitrary constant block-diagonal matrix, respectively

$$\sigma = \begin{pmatrix} 1_{N^{(+)} \times N^{(+)}} & 0_{N^{(+)} \times N^{(-)}} \\ 0_{N^{(-)} \times N^{(+)}} & -1_{N^{(-)} \times N^{(-)}} \end{pmatrix},$$

(2.12)

$$C = \begin{pmatrix} C^{(+)} & 0_{N^{(+)} \times N^{(-)}} \\ 0_{N^{(-)} \times N^{(+)}} & C^{(-)} \end{pmatrix}, \tag{2.13}$$

where $C^{(+)}$ and $C^{(-)}$ are respectively $N^{(+)} \times N^{(+)}$ and $N^{(-)} \times N^{(-)}$ constant square matrices, with $N = N^{(+)} + N^{(-)}$, $N^{(+)}$ and $N^{(-)}$ being arbitrary positive integers. The potentials $Q = Q(x,t)$ and $W = W(x,t)$ are the off-diagonal and block-diagonal matrices, respectively

$$Q = \begin{pmatrix} 0_{N^{(+)} \times N^{(+)}} & S^{(+)} U^\dagger S^{(-)} \\ U & 0_{N^{(-)} \times N^{(-)}} \end{pmatrix}, \quad W = \begin{pmatrix} W^{(+)} & 0_{N^{(+)} \times N^{(-)}} \\ 0_{N^{(-)} \times N^{(+)}} & W^{(-)} \end{pmatrix}, \tag{2.14}$$

where the block $U = U(x,t)$ is a rectangular $N^{(-)} \times N^{(+)}$, while the two blocks $W^{(\pm)}$ are square $N^{(\pm)} \times N^{(\pm)}$ matrices. The superscripted dagger stand for the Hermitian conjugation. Moreover, $S^{(+)}$ and $S^{(-)}$ are $N^{(+)} \times N^{(+)}$ and $N^{(-)} \times N^{(-)}$ diagonal matrices, respectively. Their diagonal elements $s_n^{(\pm)}$, with no loss of generality, are just signs as follows

$$s^{(\pm)} = diag\left\{ s_1^{(\pm)}, ..., s_{N^{(\pm)}}^{(\pm)} \right\}, \quad s_n^{(\pm)2} = 1. \tag{2.15}$$

The compatibility of the two ODEs (2.10) entails the matrix first-order differential equations

$$U_t = U_x C^{(+)} - C^{(-)} U_x + U W^{(+)} + W^{(-)} U,$$

$$W_x^{(+)} = \left[C^{(+)}, S^{(+)} U^\dagger S^{(-)} U \right], \tag{2.16}$$

$$W_x^{(-)} = \left[C^{(-)}, U S^{(+)} U^\dagger S^{(-)} \right],$$

provided the square $N^{(\pm)} \times N^{(\pm)}$ matrices $C^{(\pm)}$ and $W^{(\pm)}$ satisfy the conditions

$$C^{(\pm)\dagger} = S^{(\pm)} C^{(\pm)} S^{(\pm)},$$

$$W^{(\pm)\dagger} = -S^{(\pm)} W^{(\pm)} S^{(\pm)}. \tag{2.17}$$

The reduced form (2.14) of the matrix $Q = Q(x,t)$ is well motivated by the fact that it captures several interesting models of multicomponent wave interactions in weakly nonlinear media [290, 291].

2.4.3 Lax pair of coupled partial differential equations (PDEs)

All systems of coupled PDEs considered can be reduced in the following matrix PDE [95]

$$Q_t = \left[C^{(0)}, Q \right] + \sigma \left[C^{(1)}, Q_x \right] - \sigma \{Q, W\} - i\gamma\sigma \left(Q_{xx} - 2Q^3 \right),$$

$$W_x = \left[C^{(1)}, Q^2 \right], \tag{2.18}$$

where the dependent variables $Q = Q(x,t)$ and $W = W(x,t)$ are $\left(N^{(+)} + N^{(-)} \right) \times \left(N^{(+)} + N^{(-)} \right)$ block matrices in the form

$$Q = \begin{pmatrix} 0_{N^{(+)} \times N^{(+)}} & Q^{(+)} \\ Q^{(-)} & 0_{N^{(-)} \times N^{(-)}} \end{pmatrix}, \quad W = \begin{pmatrix} W^{(+)} & 0_{N^{(+)} \times N^{(-)}} \\ 0_{N^{(-)} \times N^{(+)}} & W^{(-)} \end{pmatrix}, \tag{2.19}$$

Here, the diagonal entries $W^{(+)}$, $W^{(-)}$ are square matrices of dimension $N^{(+)} \times N^{(-)}$ and $N^{(-)} \times N^{(+)}$, while the two off-diagonal rectangular blocks $Q^{(+)}$ and $Q^{(-)}$ are $N^{(+)} \times N^{(-)}$ and $N^{(-)} \times N^{(+)}$ matrices, in which $N^{(+)}$ and $N^{(-)}$ are arbitrary positive integers. In self-evident notation, the constant diagonal matrix σ takes the form

$$\sigma = \begin{pmatrix} 1_{N^{(+)} \times N^{(+)}} & 0_{N^{(+)} \times N^{(-)}} \\ 0_{N^{(-)} \times N^{(+)}} & -1_{N^{(-)} \times N^{(-)}} \end{pmatrix}, \tag{2.20}$$

while the arbitrary constant block-diagonal matrices, $C^{(0)}$ and $C^{(1)}$ yield

$$C^{(j)} = \begin{pmatrix} C^{(j)(+)} & 0_{N^{(+)} \times N^{(-)}} \\ 0_{N^{(-)} \times N^{(+)}} & C^{(j)(-)} \end{pmatrix}, \quad j = 0, 1, \tag{2.21}$$

It should be noted that the block-diagonal $W = W(x, t)$ is an auxiliary dependent variable. It is well known that $[A, B]$ and $\{A, B\}$ are the commutator $AB - BA$ and anticommutator $AB + BA$. The constant coefficient γ is the real dispersion parameter, ($\gamma = \gamma*$). The coupled NLS equations obtained by reduction of Eq. (2.18), have been investigated by Calogero and Degasperis [290]. Moreover, the special case with $\gamma = 0$ has been extensively reported [291, 292], and where boomeronic and trapponic behaviours where found. It is worth noting that by setting $C^{(1)} = c\sigma$ and $W = 0$, the linear terms $[C^{(0)}, Q]$ and $\sigma[C^{(1)}, Q_x]$ can be both transformed by the obvious transformation [95]

$$Q(x, t) \rightarrow \hat{Q}(x, t) = \exp\left(-C^{(0)} t\right) Q(x - 2ct, t) \exp\left(C^{(0)} t\right). \tag{2.22}$$

Thus, the matrix evolution equation becomes

$$Q_t = -i\gamma\sigma\left(Q_{xx} - 2Q^3\right). \tag{2.23}$$

Therefore, Eq. (2.23) stands for the standard matrix version of the NLS equation [95]. However, whenever $C^{(1)}$ is a generic full block-diagonal matrix (see (2.21)), Eq. (2.18) is the most general second-order differential equation which genuinely generalizes the standard Eq. (2.23). That equation can be reformulated to coincide with the standard equations describing the resonant interaction of three waves with the remarkable consequence of boomeronic or trapponic behaviour [292, 293].

The matrix Eq. (2.18) is the compatibility condition for the Lax pair

$$\psi_x = X\psi, \quad \psi_t = T\psi, \tag{2.24}$$

where ψ, X and T are $\left(N^{(+)} + N^{(-)}\right) \times \left(N^{(+)} + N^{(-)}\right)$ square matrices. In Eq. (2.24), $\psi = \psi(x, t, k)$ is a common solution of the two linear ordinary differential matrices, while $X = X(x, t, k)$ and $T = T(x, t, k)$ depend on the coordinate x, the time t and the complex spectral parameter k according to the definitions

$$X(x, t, k) = ik\sigma + Q(x, t),$$

$$T(x, t, k) = 2\gamma k\left[ik\sigma + Q(x, t)\right] + 2ikC^{(1)} + i\gamma\sigma\left[Q^2(x, t) - Q_x(x, t)\right] - \sigma W(x, t) \qquad (2.25)$$
$$+ \sigma\left[C^{(1)}, Q(x, t)\right] + C^{(0)}.$$

To simplify the notation of the previous formula, no dimension of the matrices 0 and 1 will be specified. Hence the omission to write the matrix 1 altogether. Let consider the condition

$$Q^{(\dagger)}(x,t) = SQ(x,t)S, \qquad (2.26)$$

on the solution $Q(x,t)$ of the matrix evolution Eq. (2.18), where the dagger stands for Hermitian conjugation. The constant matrix S is a block-diagonal

$$S = \begin{pmatrix} S^{(+)} & 0 \\ 0 & S^{(-)} \end{pmatrix}, \qquad (2.27)$$

and its off-diagonal blocks are vanishing rectangular matrices while its diagonal blocks $S^{(+)}$ and $S^{(-)}$ are $N^{(+)} \times N^{(+)}$ and $N^{(-)} \times N^{(-)}$ diagonal matrices, respectively. The diagonal elements $s^{(\pm)}$, with no loss of generality, take the form

$$s^{(\pm)} = diag\left\{ s_1^{(\pm)}, ..., s_{N^{(\pm)}}^{(\pm)} \right\}, \quad s_n^{(\pm)^2} = 1. \qquad (2.28)$$

This imply that $S^2 = 1$, $S^{(+)^2} = 1$ and $S^{(-)^2} = 1$. The reduction Eq. (2.27) is well motivated by the fact that it captures several interesting models of dispersive propagation of multicomponent waves in weakly nonlinear media. Therefore, the PDEs given in Eq. (2.18) are rewritten in terms of blocks $Q^{(+)}$, $Q^{(-)}$, $W^{(+)}$ and $W^{(+)}$ (see Eq. (2.19))as

$$Q_t^{(\pm)} = C^{(0)(\pm)}Q^{(\pm)} - Q^{(\pm)}C^{(0)(\pm)} \pm \left[C^{(1)(\pm)}Q_x^{(\pm)} - Q_x^{(\pm)}C^{(1)(\mp)} \right]$$
$$\mp \left[W^{(\pm)}Q^{(\pm)} + Q^{(\pm)}W^{(\mp)} \right] + i\gamma \left[Q_{xx}^{(\pm)} - 2Q^{(\pm)}Q^{(\mp)}Q^{(\pm)} \right], \qquad (2.29)$$

$$W_x^{(\pm)} = \left[C^{(1)(\pm)}, Q^{(\pm)}Q^{(\mp)} \right],$$

where $C^{(j)(+)}$ and $C^{(j)(-)}$ are the $N^{(+)} \times N^{(+)}$ and $N^{(-)} \times N^{(-)}$ constant square matrix blocks of $C^{(j)}$ (see Eq. (2.21)). The reduction condition (2.21) is taken into account with the introduction of the dependent variable $U = U(x,t)$ through the definitions [95]

$$Q^{(-)}(x,t) = U(x,t), \quad Q^{(+)}(x,t) = S^{(+)}U^\dagger(x,t)S^{(-)}. \qquad (2.30)$$

Since the constant γ is real, the expressions of $Q^{(+)}$, and $Q^{(-)}$ in terms of the single variable $U(x,t)$ are compatible with Eqs. (2.29), which are reduced to

$$U_t = C^{(0)(-)}U - UC^{(0)(+)} - \left[C^{(1)(-)}U_x - U_x C^{(1)(+)} \right]$$
$$+ \left[W^{(-)}U + UW^{(+)} \right] + i\gamma \left[U_{xx} - 2US^{(+)}U^\dagger S^{(-)}U \right],$$

$$W_x^{(+)} = \left[C^{(1)(+)}, S^{(+)}U^\dagger S^{(-)}U \right], \qquad (2.31)$$

$$W_x^{(-)} = \left[C^{(1)(-)}, US^{(+)}U^\dagger S^{(-)} \right],$$

where U is an $N^{(-)} \times N^{(+)}$ rectangular matrix (see (2.19) and (2.30)), while the auxiliary variables $W^{(\pm)}(x,t)$ are square matrices. Then, $W^{(+)}$ and $W^{(-)}$ are $N^{(+)} \times N^{(+)}$ and $N^{(-)} \times N^{(-)}$ matrices. The matrices $W^{(\pm)}(x,t)$ satisfy the Hermitian conditions [95]

$$W^{(+)} = -S^{(+)}W^{(+)\dagger}S^{(+)}, \quad W^{(-)} = -S^{(-)}W^{(-)\dagger}S^{(-)}, \qquad (2.32)$$

hence

$$W^\dagger(x,t) = -SW(x,t)S, \qquad (2.33)$$

Similarly, the constant matrices $C^{(j)(\pm)}$ satisfy the following conditions

$$C^{(j)(\pm)} = -(-)^j S^{(\pm)} C^{(j)(\pm)\dagger} S^{(\pm)}, \quad j = 0,1. \qquad (2.34)$$

Concerning the sign of $S^{(+)}$ and $S^{(-)}$ matrices, one could set, for instance, $S_1^{(+)} = 1$ with no loss of generality. Thus, one can keep the symmetrical, notation (2.28).

2.5   Modified Darboux transformation method

The Darboux transformation (DT), originating from the work of Darboux in 1882 on the Sturm-Liouville equation, is a powerful method for constructing solutions for integrable systems [277]. This analytical method is presented in several monographs by researchers [294, 295, 296]. In the literature, various approaches have been proposed to find a DT for a given equation, for instance, the operator factorization method [297], gauge transformation method [296, 298, 299], and the loop group transformation [300]. The DT is very efficient for construction of soliton solutions and rational solutions related to rogue waves. Indeed, through iterations, one is often led to compact representations in terms of special determinants such as the Wronskian or Grammian for N-soliton solutions [277]. The aim of this section is to present the formulation of DT for the NLS equation as well as the reformulation of the N-fold generalized DT in terms of determinants. Thus, formulas for Nth-order rogue wave solutions for the NLS equation have been derived [277].

2.5.1   Darboux transformation algorithm for the standard nonlinear Schrödinger equation

The generalized DT enables to obtain, apart from the soliton solutions, rational solutions as well as multi-rogue-wave solutions [277]. Let consider the focusing NLS equation

$$iq_t + \frac{1}{2}q_{xx} + |q|^2 q = 0. \qquad (2.35)$$

Equation (2.35) is the compatibility condition of the linear spectral problems

$$\psi_x = [i\varsigma\sigma_1 + iQ]\psi,$$

$$\psi_t = \left[i\varsigma^2\sigma_1 + i\varsigma Q + \tfrac{1}{2}\sigma_1(Q_x - iQ^2)\right]\psi, \qquad (2.36)$$

where

$$\sigma_1 = \begin{pmatrix} 1 & 0 \\ 0 & -1 \end{pmatrix}, \quad Q = \begin{pmatrix} 1 & q* \\ q & 1 \end{pmatrix}. \qquad (2.37)$$

The DT in this case is defined as [295]

$$\psi[1] = T[1]\psi, \quad q[1] = q + 2(\varsigma_1^* - \varsigma_1)(P[1])_{21}, \qquad (2.38)$$

where

$$T[1] = \varsigma - \varsigma_1^* + (\varsigma_1^* - \varsigma_1) P[1], \; P[1] = \frac{\psi_1 \psi_1^\dagger}{\psi_1^\dagger \psi_1}, \tag{2.39}$$

with ψ_1, the special solution of the linear system (2.36) at $\varsigma = \zeta_1$. $(P[1])_{21}$ represents the entry of matrix $P[1]$ in the second row and first column, and a dagger denotes the matrix transpose and complex conjugation. If N distinct seed solutions $\psi_k \, (k = 1, 2, ..., N)$ are given, the basic DT may be iterated. To do the second step of transformation, one employs ψ_2 which is mapped to $\psi_2[1] = T[1]|_{\varsigma=\varsigma_2} \psi_2$.

$$\psi[2] = T[2]\psi[1], \quad q[2] = q[1] + 2(\varsigma_2^* - \varsigma_2)(P[2])_{21}, \tag{2.40}$$

where

$$T[2] = \varsigma - \varsigma_2^* + (\varsigma_2^* - \varsigma_2) P[2], \quad P[2] = \frac{\psi_2[1]\psi_2[1]^\dagger}{\psi_2[1]^\dagger \psi_2[2]}, \tag{2.41}$$

In the general case, one may have the following statements

Theorem 1 Let $\psi_1, \psi_2, \ldots, \psi_N$ be N at distinct solutions of the spectral problem (2.36) at

$\varsigma_1, \ldots, \varsigma_N$, respectively. Then, the N-fold DT for the NLS Eq. (2.35), yields

$$\psi[N] = T[N]T[N-1]\cdots T[1]\psi,$$

$$q[N] = q[0] + 2\sum_{i=1}^{N} (\varsigma_i^* - \varsigma_i)(P[i])_{21}, \tag{2.42}$$

with

$$T[i] = \varsigma - \varsigma_i^* + (\varsigma_i^* - \varsigma_i) P[i],$$

$$P[i] = \frac{\psi_i[i-1]\psi_i[i-1]^\dagger}{\psi_i[i-1]^\dagger \psi_i[i-1]},$$

$$\psi[i-1] = (T[i-1]T[i-2]\cdots T[1])|_{\varsigma=\varsigma_i}\psi_i, \tag{2.43}$$

$$q[0] = q.$$

One remarks that, the N-fold DT given by Eq. (2.42) is equivalent to the determinant representation [248]. To find the generalized DT, one supposes that $\psi_2 = \psi_1(\varsigma_1 + \delta)$ is a special solution of the system. Then, after transformation, it gives $\psi_2[1] = T_1[1]\psi_2$. Expanding ψ_2 and ς_1, we have

$$\psi_1(\varsigma_1 + \delta) = \psi_1 + \psi_1^{[1]}\delta + \psi_1^{[2]}\delta^2 + \cdots + \psi_1^{[N]}\delta^N + \cdots, \tag{2.44}$$

where

$$\psi_1^{[k]} = \frac{1}{k!}\frac{\partial^k}{\partial \varsigma^k}\psi_1(\varsigma)_{\varsigma=\varsigma_1}. \tag{2.45}$$

Through the limit process

$$\lim_{\delta \to 0} \frac{[T_1[1]|_{\varsigma=\zeta+\delta}]\psi_2}{\delta} = \lim_{\delta \to 0} \frac{[\delta + T_1[1]|_{\varsigma=\zeta_1}]\psi_2}{\delta},$$

$$\psi_1 + T_1[1]|_{\varsigma=\zeta_1}\psi_1^{[1]} \equiv \psi_1[1]. \tag{2.46}$$

Let find the solution of the linear system (2.42) with q_1 and $\varsigma = \varsigma_1$. Therefore, the next step of the DT becomes

$$T_1\left[2\right] = \varsigma - \varsigma_1^* + \left(\varsigma_1^* - \varsigma_1\right) P_1\left[2\right],$$

$$q\left[2\right] = q\left[1\right] + 2\left(\varsigma_1^* - \varsigma_1\right)\left(P_1\left[2\right]\right)_{21},$$

(2.47)

where

$$P_1\left[2\right] = \frac{\psi_1\left[1\right]\psi_1[1]^\dagger}{\psi_1[1]^\dagger\psi_1\left[1\right]},$$

(2.48)

Similarly, the limit

$$\begin{aligned}
&\lim_{\delta\to 0}\frac{\left[\delta+T_1\left[2\right]\left(\varsigma_1\right)\right]\left[\delta+T_1\left[1\right]\left(\varsigma_1\right)\right]\psi_2}{\delta^2}\\
&= \psi_1 + \left[T_1\left[1\right]\left(\varsigma_1\right)+T_1\left[2\right]\left(\varsigma_1\right)\right]\psi_1^{[1]} + T_1\left[2\right]\left(\varsigma_1\right)T_1\left[1\right]\left(\varsigma_1\right)\psi_1^{[2]}\\
&\equiv \psi_1\left[2\right],
\end{aligned}$$

(2.49)

provides us a nontrivial solution for the linear spectral problem with $q = q\left[2\right]$ and $\varsigma = \varsigma_1$. Thus, one may do the third-step iteration of the DT, which can be written as

$$T_1\left[3\right] = \varsigma - \varsigma_1^* + \left(\varsigma_1^* - \varsigma_1\right)P_1\left[3\right],\ \ P_13 = \frac{\psi_1[2]\psi_1[2]^\dagger}{\psi_1[2]^\dagger\psi_1[2]},$$

$$q\left[3\right] = q\left[2\right] + 2\left(\varsigma_1^* - \varsigma_1\right)\left(P_1\left[3\right]\right)_{21},$$

(2.50)

Continuing the above process and combining all the DT steps, the generalized DT is constructed and summarized as follows

Theorem 2 Let $\psi_1\left(\varsigma_1\right),\ \psi_2\left(\varsigma_2\right),\cdots,\psi_n\left(\varsigma_n\right)$ be n distinct solutions of the linear spectral problem (2.36), and

$$\begin{aligned}
&\psi\left(\varsigma_i+\delta\right) = \psi_i + \psi_i^{[1]}\delta + \psi_i^{[2]}\delta^2 + \cdots + \psi_i^{[m_i]}\delta^N + \cdots\\
&\left(i = 1, 2, \cdots, n\right)
\end{aligned}$$

(2.51)

be their expansions, where

$$\psi_i^{[j]} = \frac{1}{j!}\frac{\partial^j}{\partial\varsigma^j}\psi_i\left(\varsigma\right)|_{\varsigma=\varsigma_i}\ \ \left(j = 1, 2, \cdots\right).$$

(2.52)

Let define

$$T = \Gamma_n\Gamma_{n-1}\cdots\Gamma_1\Gamma_0,\ \ \Gamma_i = T_i\left[m_i\right]\cdots T_i\left[1\right]\ \left(i \geq 1\right),\ \Gamma_0 = I,$$

(2.53)

where

$$T_i\left[j\right] = \varsigma - \varsigma_i^* + \left(\varsigma_i^* - \varsigma_i\right)\left(P_ij\right),\ \ P_i\left[j\right] = \frac{\psi_i[j-1]\psi_i[j-1]^\dagger}{\psi_1[j-1]^\dagger\psi_i[j-1]},$$

$$1 \leq j \leq m_i,\ \ \psi_i\left[0\right] = \left(\Gamma_{i-1}\cdots\Gamma_1\Gamma_0\right)|_{\varsigma=\varsigma_i}\psi_i,$$

(2.54)

$$\psi_i\left[k\right] = \lim_{\delta\to 0}\frac{\left[\delta+T_i[k]_{\varsigma=\varsigma_i}\right]\cdots\left[\delta+T_i[2]_{\varsigma=\varsigma_i}\right]\left[\delta+T_i[1]_{\varsigma=\varsigma_i}\right]\Gamma_{i-1}\left(\varsigma_i+\delta\right)\cdots\Gamma_1\left(\varsigma_i+\delta\right)\Gamma_0\psi_i\left(\varsigma_i+\delta\right)}{\delta^k}.$$

$\psi_i[k]$ can be written as

$$\psi_i[k] = \psi_i + \sum_{s=1}^{k} \sum_{\substack{m_i \geq h_1^{(i)} > \ldots > h_{k_i}^{(i)} \geq 1, \\ i \geq g_1 > \ldots > g_l \geq 1, \\ if\ g_1 = i,\ then\ h_1^{(1)} \leq k}}^{\sum_{j=1}^{l} k_j + s = k} (T_{g_1}\left[h_1^{(1)}\right] \cdots T_{g_1}\left[h_{k_1}^{(1)}\right] \cdots T_{g_1}\left[h_1^{(1)}\right] \cdots T_{g_1}\left[h_{k_l}^{(l)}\right])|_{\varsigma = \varsigma_i} \psi_i^{[s]},$$

(2.55)

with $(1 \leq k < m_i)$. Then, the transformations

$$\psi[N] = T\psi, \ q[N] = q + 2 \sum_{i=1}^{n} \sum_{j=1}^{m_i} (\varsigma_i^* - \varsigma_i)(P_i[m_j])_{21} \ \left(N = n + \sum_{k=1}^{n} m_k\right),$$

(2.56)

constitute a generalized DT for the NLS equation. The solution formulas, (2.42) and (2.56)), represented in terms of summations, have of special interest. Indeed, for nonzero $\psi_k, k = 1, 2, \cdots, N$ all the denominators of $P[i]$ and $P_i[j]$ are easily seen to be nonzero in these forms. Therefore, both (2.42) and (2.56)) supply nonsingular solutions. The former could lead to N-soliton solutions, while the latter may yield rogue wave solutions.

2.5.2 Modified Darboux transformation on nonlinear Schrödinger equation

Let consider an example to illustrate the application of the above formulas to the construction of second-order rogue wave solutions [277]. To this end, we start with the seed solution $q[0] = e^{it}$. Therefore, the corresponding solution for the linear spectral problem at $\varsigma = ih$ is

$$\psi_1(f) = \begin{pmatrix} i\left(C_1 e^A - C_2 e^{-A}\right) e^{-\frac{1}{2}it} \\ \left(C_2 e^A - C_1 e^{-A}\right) e^{\frac{1}{2}it} \end{pmatrix},$$

(2.57)

where

$$C_1 = \frac{\left(h - \sqrt{h^2-1}\right)^{1/2}}{\sqrt{h^2-1}}, \quad C_2 = \frac{\left(h + \sqrt{h^2-1}\right)^{1/2}}{\sqrt{h^2-1}}, \quad A = \sqrt{h^2-1}\left(x + iht\right).$$

(2.58)

For $h = 1 + f^2$, the expansion of the vector function $\psi_1(f)$ at $f = 0$ yields

$$\psi_1(f) = \psi_1(0) + \psi_1^{[1]} f^2 + \cdots,$$

(2.59)

where

$$\psi_1(0) = \begin{pmatrix} i\left(-2t + 2ix - i\right) e^{-\frac{1}{2}it} \\ \left(2it + 2x + 1\right) e^{\frac{1}{2}it} \end{pmatrix},$$

(2.60)

$$\psi_1^{[1]} = \begin{pmatrix} \left[\frac{i}{2}x - \frac{5}{2}t + \frac{i}{4} - 2tx^2 + \frac{2i}{3}x^3 + \frac{2}{3}t^3 - 2ixt^2 - ix^2 + 2tx + it^2\right] e^{-\frac{1}{2}it} \\ \left[\frac{1}{2}x + \frac{5}{2}it - \frac{1}{4} - 2itx^2 + \frac{2}{3}x^3 - \frac{2}{3}it^3 - 2xt^2 + x^2 + 2ixt - t^2\right] e^{\frac{1}{2}it} \end{pmatrix}.$$

It can be seen that, $\psi_1(0)$ is a solution of Eqs. (2.36) at $\varsigma = i$. By means of formula (2.46), one obtain

$$\psi_1[1] = \lim_{\delta \to 0} \frac{\left[if^2 + T_1[1]\right]\psi_1(f)}{f^2} = T_1[1]\psi_1^{[1]} + i\psi_1[0],$$

(2.61)

with

$$T_1[1] = 2i\left(I - \frac{\psi_1(0)\,\psi_1(0)^\dagger}{\psi_1(0)^\dagger \psi_1(0)}\right).\tag{2.62}$$

Substituting the above data into Eqs. (2.47) yields the second-order rogue wave solution

$$q[2] = \left[1 + \frac{G_1 + itG_2}{H}\right]e^{it},\tag{2.63}$$

where

$$
\begin{aligned}
G_1 &= 36 - 288x^2 - 192x^4 - 1152t^2x^2 - 864t^2 - 960t^4,\\
G_2 &= 360 + 576x^2 - 192t^2 - 384x^4 - 768x^2t^2 - 384t^4,\\
H &= 64t^6 + 192t^4x^2 + 432t^4 + 396t^2x^4 - 288t^2x^2 + 9 + 108x^2 + 64x^6 + 48x^4,
\end{aligned}\tag{2.64}
$$

This solution was first constructed by Akhmediev *et al.* [301]. The higher-order rogue wave solutions can be constructed in a similar manner.

2.5.3 N-fold Darboux transformation for higher-order rogue waves

A general approach to construct the higher-order rogue waves has been elucidated in the literature by Matveev *et al.* [248, 277]. In generic cases, iterated DT may be given compactly by means of determinants and this is appealing mathematically. For the original DT, formulated in Eqs. (2.38) and (2.39), the result is well-known [248].

Theorem 3 Denoting $\psi_i = (\psi_i, \phi_i)^T$ $(i = 1, 2, \cdots, N)$, then the N-fold DT between fields,

(2.42), can be reformulated as

$$q[N] = q[0] - 2\frac{\Delta_2}{\Delta_1}\tag{2.65}$$

where

$$
\Delta_1 = \begin{vmatrix}
\lambda_1^{N-1}\psi_1 & \cdots & \lambda_N^{N-1}\psi_N & -\lambda_1^{*(N-1)}\phi_1^* & \cdots & -\lambda_1^{*(N-1)}\phi_N^* \\
\cdots & \cdots & \cdots & \cdots & \cdots & \cdots \\
\psi_1 & \cdots & \psi_N & -\phi_1^* & \cdots & -\phi_N^* \\
\lambda_1^{N-1}\phi_1 & \cdots & \lambda_N^{N-1}\phi_N & \lambda_1^{*(N-1)}\psi_1^* & \cdots & \lambda_N^{*(N-1)}\psi_N^* \\
\cdots & \cdots & \cdots & \cdots & \cdots & \cdots \\
\phi_1 & \cdots & \phi_N & \psi_1^* & \cdots & \psi_N^*
\end{vmatrix},
$$

$$
\Delta_2 = \begin{vmatrix}
\lambda_1^{N}\phi_1 & \cdots & \lambda_N^{N}\phi_N & \lambda_1^{*N}\psi_1^* & \cdots & \lambda_1^{*N}\psi_N^* \\
\lambda_1^{N-2}\psi_1 & \cdots & \lambda_N^{N-2}\psi_N & -\lambda_1^{*(N-2)}\phi_1^* & \cdots & -\lambda_N^{*(N-2)}\phi_N^* \\
\cdots & \cdots & \cdots & \cdots & \cdots & \cdots \\
\psi_1 & \cdots & \psi_N & -\phi_1^* & \cdots & -\phi_N^* \\
\lambda_1^{N-1}\phi_1 & \cdots & \lambda_N^{N-1}\phi_N & \lambda_1^{*(N-1)}\psi_1^* & \cdots & \lambda_N^{*(N-1)}\psi_N^* \\
\cdots & \cdots & \cdots & \cdots & \cdots & \cdots \\
\phi_1 & \cdots & \phi_N & \psi_1^* & \cdots & \psi_N^*
\end{vmatrix}.
$$

(2.66)

To find the determinant representations of the generalized DT, one may consider directly, the limit process (2.47). Then, it follows that

$$q[2] = q[1] + \lim_{\varsigma_2 \to \varsigma_1} 2(\varsigma_2^* - \varsigma_2)(P[2])_{21}. \tag{2.67}$$

Compare to the case of KdV case worked out by Matveev *et al.* [248], one may perform the limit on the determinant form, (2.65), and get the following.

Theorem 4 Assuming that N distinct solutions $\psi_i = (\psi_i, \phi_i)^T$ $(i = 1, 2, \cdots, N)$ given for the spectral problem, (2.36), at $\varsigma = \varsigma_1, \cdots, \varsigma = \varsigma_n$ and expanding as follows.

$$(\varsigma_i + \delta)^j \psi_i(\varsigma_i + \delta) = \varsigma_i^j \psi_i + \psi_i[j, 1]\delta + \psi_i[j, 2]\delta^2 + \cdots + \psi_i[j, m_i]\delta^{m_i} + \cdots,$$

$$(\varsigma_i + \delta)^j \phi_i(\varsigma_i + \delta) = \varsigma_i^j \phi_i + \phi_i[j, 1]\delta + \phi_i[j, 2]\delta^2 + \cdots + \phi_i[j, m_i]\delta^{m_i} + \cdots, \tag{2.68}$$

where

$$\psi_i[j, m] = \frac{1}{m!}\frac{\partial^m}{\partial \varsigma^m}\left[\varsigma^j \psi_i(\varsigma)\right]\big|_{\varsigma=\varsigma_i}, \quad \phi_i[j, m] = \frac{1}{m!}\frac{\partial^m}{\partial \varsigma^m}\left[\varsigma^j \phi_i(\varsigma)\right]\big|_{\varsigma=\varsigma_i}. \tag{2.69}$$

For $(j = 0, 1, \cdots N, m = 1, 2, 3, \cdots)$, one obtains

$$q[N] = q - 2\frac{D_2}{D_1}, \quad D_2 = \det\left([H_1 \cdots H_n]\right), \quad D_1 = \det\left([G_1 \cdots G_n]\right), \tag{2.70}$$

where $N = n + \sum\limits_{k=1}^{n} m_k$ and

$$G_i = \begin{bmatrix} \varsigma_i^{N-1}\psi_i & \cdots & \psi_i[N-1, m_i] & -\varsigma_i^{*(N-1)}\phi_i^* & \cdots & -\phi_i[N-1, m_i]^* \\ \cdots & \cdots & \cdots & \cdots & \cdots & \cdots \\ \psi_i & \cdots & \phi_i[N-1, m_i] & -\phi_i^* & \cdots & -\phi_i[0, m_i]^* \\ \varsigma_i^{N-1}\phi_i & \cdots & \phi_i[N-1, m_i] & \varsigma_1^{*(N-1)}\psi_i^* & \cdots & \psi_i[N-1, m_i]^* \\ \cdots & \cdots & \cdots & \cdots & \cdots & \cdots \\ \phi_i & \cdots & \phi_i[0, m_i] & \psi_i^* & \cdots & \psi_i[0, m_i]^* \end{bmatrix},$$

$$H_i = \begin{bmatrix} \varsigma_i^N\phi_i & \cdots & \phi_i[N, m_i] & \varsigma_i^{*N}\psi_i^* & \cdots & \psi_i[N, m_i]^* \\ \varsigma_i^{N-2}\psi_i & \cdots & \psi_i[N-2, m_i] & -\varsigma_i^{*(N-2)}\phi_i^* & \cdots & -\phi_i[N-2, m_i]^* \\ \cdots & \cdots & \cdots & \cdots & \cdots & \cdots \\ \psi_i & \cdots & \psi_i[0, m_i] & -\phi_i^* & \cdots & -\phi_i[0, m_i]^* \\ \varsigma_i^{N-1}\phi_i & \cdots & \phi_i[N-1, m_i] & \varsigma_i^{*(N-1)}\psi_i^* & \cdots & \psi_i[N-1, m_i]^* \\ \cdots & \cdots & \cdots & \cdots & \cdots & \cdots \\ \phi_i & \cdots & \phi_i[0, m_i] & \psi_i^* & \cdots & \psi_i[0, m_i]^* \end{bmatrix}. \tag{2.71}$$

The matrices G_i and H_i, when applied to the special seed solutions (2.70), enable to have a determinant form for higher-order rogue wave solutions. So doing, one considers

$$\psi_1 = i\left(C_1 e^A - C_2 e^{-A}\right), \quad \phi_1 = \left(C_2 e^A - C_1 e^{-A}\right), \tag{2.72}$$

where

$$C_1 = \frac{\left(1+f^2-f\sqrt{2+f^2}\right)^{1/2}}{f\sqrt{2+f^2}}, \quad C_2 = \frac{\left(1+f^2+f\sqrt{2+f^2}\right)^{1/2}}{f\sqrt{2+f^2}},$$

(2.73)

$$A = f\sqrt{2+f^2}\left[x+i\left(1+f^2\right)t+\Phi\left(f\right)\right], \Phi\left(f\right) = \sum_{i=0}^{N} s_i f^{2i}, s_i \in C.$$

The associated Taylor expansions give

$$i^j(1+f^2)^j\psi_1(f) = i^j\psi_1(0) + \psi_1[j,1]f^2 + \cdots + \psi_1[j,N]f^{2N} + \cdots,$$

$$\psi_1[j,n] = \frac{1}{(2n)!}\frac{\partial^{2n}}{\partial f^{2n}}\left[i^j(1+f^2)^j\psi_1(f)\right]|_{f=0},$$

$$i^j(1+f^2)^j\phi_1(f) = i^j\phi_1(0) + \phi_1[j,1]f^2 + \cdots + \phi_1[j,N]f^{2N} + \cdots,$$

(2.74)

$$\phi_1[j,n] = \frac{1}{(2n)!}\frac{\partial^{2n}}{\partial f^{2n}}\left[i^j(1+f^2)^j\phi_1(f)\right]|_{f=0}.$$

For $(j=0,\cdots,N, n=1,2,3,\cdots)$, it follows that the Nth-order rogue wave solution for the NLS equation (2.35) yields

$$q[N] = \left[1 - 2\frac{D_2}{D_1}\right]e^{it},$$

(2.75)

where

$$D_1 = \begin{vmatrix} i^{N-1}\psi_1 & \cdots & \psi_1[N-1,N-1] & -(-i)^{N-1}\phi_1^* & \cdots & -\phi_1[N-1,N-1]^* \\ \cdots & \cdots & \cdots & \cdots & \cdots & \cdots \\ \psi_1 & \cdots & \psi_1[0,N-1] & -\phi_1^* & \cdots & -\phi_1[0,N-1]^* \\ i^{N-1}\phi_1 & \cdots & \phi_1[N-1,N-1] & -i^{N-1}\psi_1^* & \cdots & \psi_1[N-1,N-1]^* \\ \cdots & \cdots & \cdots & \cdots & \cdots & \cdots \\ \phi_1 & \cdots & \phi_1[0,N-1] & -\psi_1^* & \cdots & -\psi_1[0,N-1]^* \end{vmatrix},$$

$$D_2 = \begin{vmatrix} i^N\phi_1 & \cdots & \phi_1[N,N-1] & (-i)^N\psi_1^* & \cdots & -\phi_1[N,N-1]^* \\ i^{N-2}\psi_1 & \cdots & \psi_1[N-2,N-1] & -(-i)^{(N-1)}\phi_1^* & \cdots & -\phi_1[N-2,N-1]^* \\ \cdots & \cdots & \cdots & \cdots & \cdots & \cdots \\ \psi_1 & \cdots & \psi_1[0,N-1] & -\phi_1^* & \cdots & -\phi_1[0,N-1]^* \\ i^{N-1}\phi_1 & \cdots & \phi_1[N-1,N-1] & -(-i)^{N-1}\psi_1^* & \cdots & \psi_1[N-1,N-1]^* \\ \cdots & \cdots & \cdots & \cdots & \cdots & \cdots \\ \phi_1 & \cdots & \phi_1[0,N-1] & \psi_1^* & \cdots & \psi_1[0,N-1]^* \end{vmatrix}.$$

(2.76)

For the case where $N = 2$, the above formula may provide the second-order rogue wave solution with two free parameters for the NLS equation [302]. It is well noted that this solution splits into three first-order rogue waves rather than two. Indeed, these results supply the high-order rogue wave solutions with more free parameters, which determine the spatial-temporal structures of the solutions. Moreover, the third-order rogue wave solution, may be worked out by setting

$N = 3$ and $\Phi(f) = (b + ic) f^2 + (e + ig) f^4$ in the above formula, whose explicit expression is omitted here.

2.6 Dressing-Darboux transformation method

Many nonlinear wave equations, with various degrees of novel mathematical features and applicative interests were found by extending and generalizing the method of the spectral transform [251, 303]. Among these integrable equations, the most notable one with great importance is the standard NLS equation. This, due to its integrability [73] and universality [304] which are related consequences of a perturbative multiscale analysis of (i.e large class) of dispersive nonlinear wave equations [305]. The key property of integrable evolution PDEs is that they express the condition that two linear differential equations (Lax pair), both for the same unknown function and whose coefficients depend also on a complex (spectral) parameter, are compatible with each other. The compatibility of the Lax pair is a local condition and it provides local properties of the associated integrable PDE, in particular local conservation laws (continuity equations) and Hamiltonian structures. The construction of solutions of integrable nonlinear PDEs is, however, a different matter. In fact, in addition to the initial value, one has to specify the domain of the space variable x together with the values which the solution (and/or its x-derivatives) takes on the domain boundary. Once the (appropriate) boundary values are fixed, then one should make use of the Lax pair to solve the Cauchy initial value problem or, more modestly, to construct special solutions [95]. Historically, the spectral technique was first applied on the KdV equation to solve the initial-value problem in the space domain with vanishing values at the boundary, $x = \pm\infty$. Later, the same spectral technique was applied by Zakharov and Shabat to a different Lax pair to solve the initial-value problem for the standard NLS equation on the entire real x-axis and for both vanishing [73] and nonvanishing [306] values at the boundary $x = \pm\infty$. Both vanishing and nonvanishing boundary values are relevant in nonlinear optics where, "bright" special solutions usually referred to the vanishing boundary values, as they are light-pulse in a dark background, on the one hand, and "dark" special solutions to nonvanishing boundary values, as they are dark-pulse in a light background, on the other hand. Thus, the DDT method yields a new (dressed) solution from a given (naked or seed) solution of the system of wave equations of interest. Therefore, the DDT may be formulated as a change of the Lax pair of linear equations via a transformation which adds one pole to the dependence of its solution on the complex spectral variable [96].

2.6.1 Dressing-Darboux transformation algorithm

Let focus our attention to the method of construction of special solutions of the general system (2.31). Let note that the reduction conditions (2.26), (2.33), (2.34), together with expressions (2.25) of the matrices $X(x, t, k)$ and $T(x, t, k)$ in the Lax pair Eq. (2.24), entail the following relations

$$X^\dagger(k*) \sum + \sum X(k) = 0, \;\; T^\dagger(k*) \sum + \sum T(k) = 0 \tag{2.77}$$

with

$$\sum = \sigma S = \begin{pmatrix} S^{(+)} & 0 \\ 0 & -S^{(-)} \end{pmatrix}, \quad \sum^{2} = 1. \tag{2.78}$$

In the notation used in (2.77), one omits writing the dependence on the variables x and t and maintains this omission in the following whenever it will cause no confusion. The property (2.77) allows to express the reduction condition induced by (2.26), (2.33), (2.34) on the solution $\psi(k)$ of the two linear equations of the Lax pair (2.24) by the following equation

$$\psi^{\dagger}(x, t, k) \sum \psi(x, t, k) = A(k, k^{*}), \tag{2.79}$$

where the matrix $A(k, k^{*})$ is constant, namely x and t independent. Therefore, it is plain that the value of $A(k, k^{*})$ depends only on the arbitrary value $\psi(x_{0}, t_{0}, k)$ that the solution ψ takes at a given point (x_{0}, t_{0}) of the (x, t) plane.

Let consider now a second pair of matrices $Q^{(0)}(x, t)$ and $W^{(0)}(x, t)$, and assume that they have the same block structure of Q and W as shown in Eq. (2.19), and satisfy the same reduction conditions given in Eqs. (2.26) and (2.33). Let $\psi^{(0)}(x, t, k)$ be a corresponding nonsingular (i.e. with nonvanishing determinant) matrix solution of Eq. (2.24)

$$\psi_{x}^{(0)} = X^{(0)}\psi^{(0)}, \quad \psi_{t}^{(0)} = T^{(0)}\psi^{(0)}, \tag{2.80}$$

with $X^{(0)}(x, t, k)$ and $T^{(0)}(x, t, k)$ having expressions (2.25) with Q and W replaced by $Q^{(0)}$ and $W^{(0)}$. Assume also that the initial condition $\psi^{(0)}(x_{0}, t_{0}, k)$ is so chosen that the constant matrix $A^{(0)}(k, k^{*})$, where of course (see (2.79))

$$A^{(0)}(k, k^{*}) = \psi^{(0)\dagger}(x, t, k^{*}) \sum \psi^{(0)}(x, t, k), \tag{2.81}$$

coincides with $A(k, k^{*})$, i.e. $A^{(0)}(k, k^{*}) = A(k, k^{*})$. Since both compatibility conditions, $\psi_{xt}^{(0)} = \psi_{tx}^{(0)}$ and $\psi_{xt} = \psi_{tx}$, are satisfied, $Q^{(0)}(x, t)$, $W^{(0)}(x, t)$ and $Q(x, t)$, $W(x, t)$ are two different solutions of the same matrix evolution Eq. (2.18), and therefore it follows that the matrix

$$D(x, t, k) = \psi(x, t, k) \left(\psi^{(0)}(x, t, k) \right)^{(-1)}, \tag{2.82}$$

satisfies the differential equations

$$D_{x} = XD - DX^{(0)}, \quad D_{t} = TD + DT^{(0)}, \tag{2.83}$$

together with the algebraic (reduction) equation

$$D^{\dagger}(k^{*}) \sum D(k) = \sum. \tag{2.84}$$

The proof of these propositions is straightforward.

Definition of Eq. (2.82) can be viewed as a transformation of $\psi^{(0)}$ into ψ

$$\psi(x, t, k) = D(x, t, k) \psi^{(0)}(x, t, k), \tag{2.85}$$

which consequently yields a transformation of $Q^{(0)}$ and $W^{(0)}$ into, Q and W, respectively. Therefore, the dressing approach requires in the first place an explicit knowledge of $Q^{(0)}(x, t)$,

$W^{(0)}(x,t)$ and $\psi^{(0)}(x,t,k)$. The next step is the construction of the transformation matrix $D(x,t,k)$ via the integration of the ODEs (2.83). This task is however not straightforward since the coefficients X and T of these differential equations depend on the unknown matrices Q and W (see (2.25)). The way of solving this problem goes through the priori assignment of the dependence of the transformation matrix $D(x,t,k)$ on the spectral variable k.

In what follows, one investigates the set of $k-$dependent matrices $D(k)$ which (i) have a rational dependence on the complex variable k and (ii) have nonvanishing $k \to \infty$ limit. Moreover, if we consider a rational dependence on k which can be factorized as product of simple-pole terms, we need to deal only with matrices $D(k)$ which take the following one-pole expression

$$D(x,t,k) = 1 + \frac{R(x,t)}{k - \alpha}, \tag{2.86}$$

where the matrix $R(x,t)$ is the residue at the pole $k = \alpha$ and the value of $D(k)$ in the $k \to \infty$ limit is taken to be the identity for the sake of simplicity. The transformation (2.85) characterized by the matrix (2.86) has received considerable attention in the literature [248, 307, 308]. We refer to it as Darboux-dressing transformation (DDT), and its existence in our setting is proved below by construction.

The way to obtain an explicit expression of the residue matrix $R(x,t)$ depends on whether the pole α is off the real axis, $\alpha \neq \alpha^*$, or on the real axis, $\alpha = \alpha^*$. Therefore, we treat these two cases separately.

2.6.2 Dressing-Darboux transformation: complex pole

Let consider the case where α is not real, $\alpha \neq \alpha^*$, while the other case, α real, is discussed in the next subsection. The starting point is the requirement that the matrix $D(x,t,k)$ (see (2.86)) satisfies the algebraic condition (2.84) and the differential equations (2.83). The algebraic condition entails the two (equivalent) equations

$$\sum R + \frac{R^\dagger \sum R}{\alpha - \alpha^*} = 0, \ R^\dagger \sum - \frac{R^\dagger \sum R}{\alpha - \alpha^*} = 0, \tag{2.87}$$

whose solution is

$$R(x,t) = (\alpha - \alpha^*) P(x,t), \tag{2.88}$$

where the matrix $P(x,t)$ is a projector with the "Hermitianity" condition

$$P^2 = P, \ P^\dagger = \sum P \sum. \tag{2.89}$$

As for the differential equations (2.83), replacing $D(x,t,k)$ with its expression (2.86) and (2.88) yields the algebraic relations

$$Q = Q^{(0)} - i(\alpha - \alpha^*)[\sigma, P],$$

$$W = W^{(0)} + i(\alpha - \alpha^*)[C^{(1)}, \{\sigma, P\}], \tag{2.90}$$

which give the "dressed" matrices Q and W in terms of the *bare* matrices $Q^{(0)}$, $W^{(0)}$ and the projector P, together with the two differential equations

$$P_x = X(\alpha)P - PX^{(0)}(\alpha), P_t = T(\alpha)P - PT^{(0)}(\alpha), \qquad (2.91)$$

whose integration goes as follows. Consider first the differential equation (2.91) with respect to the variable x and replace Q with its expression in Eq. (2.90). The resulting equation is then the following nonlinear equation

$$P_x = X^{(0)}(\alpha)P - PX^{(0)}(\alpha) - i\left(\alpha - \alpha^*\right)\left(\sigma P - P\sigma P\right). \qquad (2.92)$$

Let z be an eigenvector of P, and differentiate with respect to x the eigenvalue equation

$$Pz = z, \qquad (2.93)$$

By replacing then, P_x with the right-hand side of (2.92), one arrives at the equation

$$(1 - P)\left[z_x - X^{(0)}(\alpha^*)z\right] = 0, \qquad (2.94)$$

which implies that the vector $z_x - X^{(0)}(\alpha^*)z$ is in the subspace on which P projects. At this point, we may well assume that this subspace is one-dimensional. Indeed, it is easy to prove that, if P projects on a subspace of higher dimension $n > 1$, then, the corresponding matrix D is a product of as many matrices $D^{(j)}$ of the form (2.86) with (2.88)

$$D^{(j)}\left(x, t, k\right) = 1 + \frac{\left(\alpha - \alpha^*\right)p^{(j)}\left(x, t\right)}{k - \alpha}, \ \ j = 1, ..., n, \qquad (2.95)$$

as the dimension n of this subspace, all of course with the same pole in α, and all with $P^{(j)}$ projecting on a one-dimensional subspace. Therefore, with no loss of generality, we let P in the DDT matrix

$$D\left(x, t, k\right) = 1 + \frac{\left(\alpha - \alpha^*\right)p\left(x, t\right)}{k - \alpha}, \qquad (2.96)$$

project on the one-dimensional subspace of the vector z, with the implication (see (2.94)) that the vector $z_x - X^{(0)}(\alpha^*)z$ is proportional to z. On the other hand, since the vector z is defined here modulo a scalar factor function, one may choose this factor in such a way that z satisfies the differential equation

$$z_x = X^{(0)}(\alpha^*)z. \qquad (2.97)$$

The differential equation (2.91) with respect to the variable t can be treated in a similar way. The substitution of Q and W with their expressions (2.90) yields the nonlinear equation

$$P_t = T^{(0)}(\alpha)P - PT^{(0)}(\alpha) - 2\gamma\left(\alpha - \alpha^*\right)\left(Q^{(0)}P - PQ^{(0)}P\right)$$
$$-2i\gamma\left(\alpha^2 - \alpha^{*2}\right)\left(\sigma P - P\sigma P\right) - 2i\left(\alpha - \alpha^*\right)\left[C^{(1)}, P\right]P. \qquad (2.98)$$

By differentiating now the eigenvalue Eq. (2.93) with respect to t and using both Eqs. (2.93) and (2.98), one ends up with the equation

$$(1 - P)\left[z_t - T^{(0)}(\alpha^*)z\right] = 0, \qquad (2.99)$$

which, by the same arguments as above, implies that the vector $z(x, t)$ satisfies the differential equation

$$z_t - T^{(0)}(\alpha^*)z. \tag{2.100}$$

Once the two Eqs. (2.97) and Eq. (2.100) are solved, the DDT transformation matrix $D(x, t, k)$ is finally given by Eq. (2.96) with

$$P(x, t) = \frac{z(x, t) \, z^\dagger(x, t) \sum}{\langle z(x, t) \sum z(x, t) \rangle}. \tag{2.101}$$

This expression is implied by the algebraic conditions (2.89). At this point, we conclude that the method of construction of a novel solution $Q(x, t)$, $W(x, t)$ of the evolution Eqs. (2.18), starting from the knowledge of given (seed) solution $Q^{(0)}(x, t)$, $W^{(0)}(x, t)$, is explicitly given by Eqs. (2.90) with (2.101), where the vector $z(x, t)$ is

$$z(x, t) = \psi^{(0)}(x, t, \alpha^*) \, z_0. \tag{2.102}$$

Here, $\psi^{(0)}(x, t, \alpha^*)$ is the solution $\psi^{(0)}(x, t, k)$ of the differential Eqs. (2.80) (Lax pair corresponding to $Q^{(0)}(x, t)$, $W^{(0)}(x, t)$), for $k = \alpha^*$, and it is assumed to be known, while z_0 is an arbitrary constant $(N^{(+)} + N^{(-)})$-dimensional vector.

The construction of the novel solution $Q(x, t)$, $W(x, t)$ provides, via formulae (2.19) and reduction (2.30), the construction of the novel solution $U(x, t)$, $W^{(\pm)}(x, t)$ of the matrix evolution Eqs. (2.31) which is our main concern here. The relevant expressions are obtained by first writing the block structure of the $(N^{(+)} + N^{(-)}) \times (N^{(+)} + N^{(-)})$ projector matrix $P(x, t)$

$$P = \begin{pmatrix} B^{(+)} & S^{(+)} B S^{(-)} \\ B & B^{(-)} \end{pmatrix}, \tag{2.103}$$

which therefore entails, in self-evident notation and by using Eqs. (2.90), the relations yield

$$U = U^{(0)} + 2i(\alpha - \alpha^*) B,$$

$$W^{(+)} = W^{(0)(+)} + 2i(\alpha - \alpha^*) \left[C^{(1)(+)}, B^{(+)} \right], \tag{2.104}$$

$$W^{(-)} = W^{(0)(-)} - 2i(\alpha - \alpha^*) \left[C^{(1)(-)}, B^{(-)} \right].$$

In view of its use in computations, one gives to this formula a more explicit expression by using the form (2.101) of the projector P. To this aim, it is convenient to split the vector z in two block column vectors, namely

$$z = \begin{pmatrix} z^{(+)} \\ z^{(-)} \end{pmatrix}, \tag{2.105}$$

where the vectors $z^{(+)}$ and $z^{(-)}$ have dimensions $N^{(+)}$ and $N^{(-)}$, respectively. Then, by inserting this block form of z in the diadic expression of P, (2.101) (and recalling (2.78)), one arrives at

the final relations

$$U = U^{(0)} + 2i \left(\alpha - \alpha^* \right) \frac{z^{(-)} z^{(+)\dagger} S^{(+)}}{\left\langle z^{(+)}, S^{(+)} z^{(+)} \right\rangle - \left\langle z^{(-)}, S^{(-)} z^{(-)} \right\rangle},$$

$$W^{(+)} = W^{(0)(+)} + 2i \left(\alpha - \alpha^* \right) \frac{\left(C^{(1)(+)} z^{(+)} z^{(+)\dagger} S^{(+)} - z^{(+)} z^{(+)\dagger} S^{(+)} C^{(1)(+)} \right)}{\left\langle z^{(+)}, S^{(+)} z^{(+)} \right\rangle - \left\langle z^{(-)}, S^{(-)} z^{(-)} \right\rangle} \tag{2.106}$$

$$W^{(-)} = W^{(0)(-)} - 2i \left(\alpha - \alpha^* \right) \frac{\left(C^{(1)(-)} z^{(-)} z^{(-)\dagger} S^{(-)} - z^{(-)} z^{(-)\dagger} S^{(-)} C^{(1)(-)} \right)}{\left\langle z^{(+)}, S^{(+)} z^{(+)} \right\rangle - \left\langle z^{(-)}, S^{(-)} z^{(-)} \right\rangle}.$$

2.6.3 Dressing-Darboux transformation: real pole

Let now investigate the alternative case in which the pole of the Darboux-dressing matrix $D(x,t,k)$ (see (2.82)) is real, $\alpha = \alpha^*$. The way to treat this case is the same as that one we followed in the previous case, but the resulting equations to be solved are indeed different. Thus, we first ask that $D(x,t,k)$, as given by the general expression (2.86), satisfies both the algebraic condition (2.84) and the differential Eqs. (2.83). The algebraic condition implies two equations for the residue matrix R

$$\sum R + R^\dagger \sum = 0, \ \ R^\dagger \sum R = 0. \tag{2.107}$$

These entail the following form of R,

$$R(x,t) = i\rho(x,t) \hat{P}(x,t) \sum, \tag{2.108}$$

together with the conditions that the scalar function $\rho(x,t)$ is real, the projector matrix $\hat{P}$ is Hermitian

$$\rho = \rho^*, \ \ \hat{P}^2 = \hat{P}, \ \ \hat{P} = \hat{P}^\dagger, \tag{2.109}$$

and it satisfies the equation

$$\hat{P} \sum \hat{P} = 0. \tag{2.110}$$

Therefore, in the present case, the transformation matrix (2.86) reads

$$D(x,t) = 1 + i\rho(x,t) \frac{\hat{P}(x,t) \sum}{k - \alpha}. \tag{2.111}$$

By the same arguments, let consider as in the previous case, that $\hat{P}$ may be assumed, with no loss of generality, to project on a one-dimensional subspace, namely

$$\hat{P} = \frac{\hat{z}\hat{z}^\dagger}{\langle \hat{z}, \hat{z} \rangle}, \tag{2.112}$$

where the vector $\hat{z}(x,t)$, because of Eq. (2.110), is constrained by the orthogonality condition

$$\left\langle \hat{z}, \sum \hat{z} \right\rangle = 0. \tag{2.113}$$

Let Consider now the differential equations (2.83) and insert in expression (2.111). Since k is of course, an arbitrary complex variable, one obtains the relations

$$Q = Q^{(0)} + \rho \left[\sigma, \hat{P}\right] \textstyle\sum,$$

$$W = W^{(0)} + \rho \left[\{\sigma, P\} \textstyle\sum, C^{(1)}\right],$$

(2.114)

which give the novel solution $Q(x,t)$, $W(x,t)$ of (2.18) in terms of the supposedly known solution $Q^{(0)}(x,t)$, $W^{(0)}(x,t)$, the function $\rho(x,t)$ and the projector $\hat{P}(x,t)$. There, also follows the relation

$$T(\alpha) - T^{(0)}(\alpha) = 4\gamma\alpha\rho \left[\sigma, \hat{P}\right] \sum - 2i\gamma\rho \left[Q^{(0)}, \hat{P}\sum\right] + 2i\gamma\rho^2 \frac{g}{f} \hat{P} \sum + 2\rho\sigma \left[C^{(1)}, \sigma\hat{P}\sum\right],$$

(2.115)

which is not an independent relation but it is instrumental in deriving formula (2.117) displayed below. In addition, one obtains two following differential equations, one with respect to x

$$\left(\rho\hat{P}\right)_x = \rho \left(X^{(0)}(\alpha)\hat{P} + \hat{P}X^{(0)\dagger}(\alpha) - \rho\frac{g}{f}\hat{P}\right),$$

(2.116)

and the other with respect to t

$$\left(\rho\hat{P}\right)_t = \rho \left(T^{(0)}(\alpha)\hat{P} + \hat{P}T^{(0)\dagger}(\alpha) - 4\alpha\gamma\rho\frac{g}{f}\hat{P} + 2i\gamma\rho\frac{h}{f}\hat{P} - 2\rho\frac{m}{f}\hat{P}\right).$$

(2.117)

In these last three equations, one conveniently introduces the functions $f(x,t)$, $g(x,t)$, $h(x,t)$ and $m(x,t)$ according to the definitions

$$f = \langle \hat{z}, \hat{z}\rangle, \quad g = \langle \hat{z}, S\hat{z}\rangle, \quad h = \left\langle \hat{z}, \sum Q^{(0)}\hat{z}\right\rangle, \quad m = \left\langle \hat{z}, \sum C^{(1)}\hat{z}\right\rangle.$$

(2.118)

One obtains the right-hand side of the differential equation (2.117) by using relation (2.115). At this point, we differentiate the eigenvalue equation (see (2.112))

$$\hat{P}\hat{z} = \hat{z}.$$

(2.119)

When this is done, with respect to x, one obtains the equation

$$\hat{P}\left[\hat{z}_x + X^{(0)}(\alpha)^\dagger\hat{z}\right] = \hat{z}_x - X^{(0)}(\alpha)\hat{z} + \left(\frac{\rho_x}{\rho} + \rho\frac{g}{f}\right)\hat{z},$$

(2.120)

which implies that, its right-hand side is proportional to the vector $\hat{z}$

$$\hat{z}_x - X^{(0)}(\alpha)\hat{z} + \left(\frac{\rho_x}{\rho} + \rho\frac{g}{f}\right)\hat{z} = \mu\hat{z}.$$

(2.121)

One more, the vector $\hat{z}$, which has been introduced through the diadic expression (2.112), is defined only modulo a factor scalar function, and therefore, by taking advantage of this freedom, one can ask that

$$\mu = \frac{\rho_x}{\rho} + \rho\frac{g}{f},$$

(2.122)

with the implication that the vector $\hat{z}$ satisfies the differential equation

$$\hat{z}_x = X^{(0)}(\alpha)\hat{z}. \tag{2.123}$$

One observes that the function μ, via its own definition

$$\hat{P}\left[\hat{z}_x + X^{(0)}(\alpha)^\dagger \hat{z}\right] = \mu\hat{z}, \tag{2.124}$$

takes the following expression

$$\mu = \frac{1}{f}\left\langle \hat{z}, \hat{z}_x + X^{(0)}(\alpha)^\dagger \hat{z}\right\rangle = \frac{1}{f}\left(\langle \hat{z}, \hat{z}_x\rangle + \langle \hat{z}_x, \hat{z}\rangle\right) = \frac{f_x}{f}, \tag{2.125}$$

where we have taken into account Eq. (2.123) and the definition of f (2.118). It is now readily found that combining this equation with relation (2.122) entails that the function $\rho(x,t)$ satisfies the following differential equation

$$\left(\frac{f}{\rho}\right)_x = g. \tag{2.126}$$

Let differentiate the eigenvalue Eq. (2.119) with respect to t. Following the same strategy as before, one concludes that the vector $\hat{z}$ satisfies the differential equation

$$\hat{z}_t = T^{(0)}(\alpha)\hat{z}, \tag{2.127}$$

while the following relations hold true

$$\hat{P}\left[\hat{z}t + T^{(0)}(\alpha)^\dagger \hat{z}\right] = \nu\hat{z},$$
$$\nu = \frac{\rho_t}{\rho} + 2\frac{\rho}{f}\left(2\alpha\gamma g - i\gamma h + m\right). \tag{2.128}$$

Again, Eqs. (2.128) imply the expression

$$\nu = \frac{1}{f}\left\langle \hat{z}, \hat{z}_t + T^{(0)}(\alpha)^\dagger \hat{z}\right\rangle = \frac{1}{f}\left(\langle \hat{z}, \hat{z}_t\rangle + \langle \hat{z}_t, \hat{z}\rangle\right) = \frac{f_t}{f}, \tag{2.129}$$

and the differential equation

$$\left(\frac{f}{\rho}\right)_t = 2\left(2\alpha\gamma g - i\gamma h + m\right), \tag{2.130}$$

respectively, for the function $\rho(x,t)$ with respect to the variable t. Since the vector $\hat{z}(x,t)$ satisfies the two (compatible) differential Eqs. (2.123) and (2.127), its general expression is

$$\hat{z}(x,t) = \psi^{(0)}(x,t,\alpha)\hat{z}_0, \tag{2.131}$$

where $\hat{z}_0$ is an arbitrary constant $\left(N^{(+)} + N^{(-)}\right)$-dimensional vector. The two differential Eqs. (2.126) and (2.130), which are also compatible with each other (the proof is straightforward and it is not reported here), can be easily integrated since the functions f, g, h and m are known (see (2.118)). The expression of their general solution then reads

$$\rho(x,t) = \frac{f(x,t)}{\left\{\frac{f(x_0,t_0)}{\rho(x_0,t_0)} + 2\int\limits_{t_0}^{t} dt'\left[2\alpha\gamma g(x_0,t') - i\gamma h(x_0,t') + m(x_0,t')\right] + \int\limits_{x_0}^{x} dx'g(x',t)\right\}}, \tag{2.132}$$

where x_0, t_0 and $\rho(x_0, t_0)$ are arbitrary real constants.

One concludes that if $Q^{(0)}(x,t)$, $W^{(0)}(x,t)$ and $\psi^{(0)}(x,t,k)$ are known, the explicit expressions of $\rho(x,t)$ and $\hat{z}(x,t)$ given above yield, via (2.111) and (2.112), the DDT matrix and therefore the new solution $Q(x,t)$, $W(x,t)$ through (2.114). As in the previous case, the corresponding formulae which give the expression of the solutions $U(x,t)$, $W^{(\pm)}(x,t)$ of Eqs. (2.31) follow from the block structure of Q and W, of $\sum$, of the projector $\hat{P}$,

$$\hat{P} = \begin{pmatrix} \hat{B}^{(+)} & \hat{B}^{\dagger} \\ \hat{B} & \hat{B}^{(-)} \end{pmatrix}, \tag{2.133}$$

and of the vector $\hat{z}$

$$\hat{z} = \begin{pmatrix} \hat{z}^{(+)} \\ \hat{z}^{(-)} \end{pmatrix}. \tag{2.134}$$

The relevant relations then read

$$U = U^{(0)} - 2\rho\hat{B}S^{(+)},$$

$$W^{(+)} = W^{(0)(+)} - 2\rho\left[C^{(1)(+)}, B^{(+)}S^{(+)}\right], \tag{2.135}$$

$$W^{(-)} = W^{(0)(-)} - 2\rho\left[C^{(1)(-)}, B^{(-)}S^{(-)}\right],$$

or, equivalently (see (2.112), (2.133) and (2.134)) and more explicitly

$$U = U^{(0)} - 2\rho\frac{\hat{z}^{(-)}\hat{z}^{(+)\dagger}S^{(+)}}{\langle\hat{z}^{(+)},\hat{z}^{(+)}\rangle + \langle\hat{z}^{(-)},\hat{z}^{(-)}\rangle},$$

$$W^{(+)} = W^{(0)(+)} - 2\rho\frac{\left(C^{(1)(+)}\hat{z}^{(+)}\hat{z}^{(+)\dagger}S^{(+)} - \hat{z}^{(+)}\hat{z}^{(+)\dagger}S^{(+)}C^{(1)(+)}\right)}{\langle\hat{z}^{(+)},\hat{z}^{(+)}\rangle + \langle\hat{z}^{(-)},\hat{z}^{(-)}\rangle}, \tag{2.136}$$

$$W^{(-)} = W^{(0)(-)} - 2\rho\frac{\left(C^{(1)(-)}\hat{z}^{(-)}\hat{z}^{(-)\dagger}S^{(+)} - \hat{z}^{(-)}\hat{z}^{(-)\dagger}S^{(-)}C^{(1)(-)}\right)}{\langle\hat{z}^{(+)},\hat{z}^{(+)}\rangle + \langle\hat{z}^{(-)},\hat{z}^{(-)}\rangle},$$

where the expression of $\rho = \rho(x,t)$ is given by (2.132) with (see (2.118))

$$f(x,t) = \langle\hat{z}^{(+)}, \hat{z}^{(+)}\rangle + \langle\hat{z}^{(-)}, \hat{z}^{(-)}\rangle,$$

$$g(x,t) = \langle\hat{z}^{(+)}, S^{(+)}\hat{z}^{(+)}\rangle + \langle\hat{z}^{(-)}, S^{(-)}\hat{z}^{(-)}\rangle,$$

$$h(x,t) = \langle\hat{z}^{(+)}, U^{(0)\dagger}S^{(-)}\hat{z}^{(-)}\rangle - \langle\hat{z}^{(-)}, S^{(-)}U^{(0)}\hat{z}^{(+)}\rangle, \tag{2.137}$$

$$m(x,t) = \langle\hat{z}^{(+)}, S^{(+)}C^{(1)(+)}\hat{z}^{(+)}\rangle - \langle\hat{z}^{(-)}, S^{(-)}C^{(1)(-)}\hat{z}^{(-)}\rangle.$$

To end, this subsection notice that the explicit formulae derived here and in the complex pole are meant to serve as the main tools to construct soliton and rogue wave solutions, and by repeated application of DDTs, multisoliton and higher-order rogue wave solutions of the matrix Eqs. (2.31). However, these formulae have been obtained by algebra and local integration of differential equations. One trusts that, new equations can be derived, based on the same DDT technique to find explicit solutions for potential applications in optics.

2.7 Numerical computation methods

Numerical computations play an important role in the study of nonlinear waves. In recent years, great advances have been made on numerical methods for nonlinear wave equations, and many highly accurate and efficient numerical techniques have been developed. One can mentioned the Petviashvili method and the accelerated imaginary-time evolution method (AITEM) which generally converge to the ground states of a linear waves system and diverge for excited states. Moreover, some numerical algorithms such as squared-operator iteration methods (SOM) and Newton conjugate-gradient (Newton-CG) methods were derived to converge for both ground states and excited states. Thus, many numerical methods have been applied in the literature to confront the analytical and experimental results. Among them, one denotes those which are commonly employed in the modelling of nonlinear beam propagation, that are, the split-step methods (first-order and fourth-order split-step methods) [187] and the finite difference methods [187] which have been modified to be adequate to nonlinear wave propagation equation with higher-order effects. Hence, the derivation of the Modified split-step method [187] and the difference-differential equation method [187]. In addition, some convenient commercial software for scientific computing (such as MATLAB) have also become available, which greatly facilitated the coding and implementation of some numerical algorithms such as the pseudospectral method, split-step methods, integrating factor method [187] and so on. It has been shown that high overall accuracy can be achieved, in various spectral methods when coupling with high-order time-stepping schemes such as Runge-Kutta methods [187]. Due to the accuracy, numerical stability and convergence of one pseudospectral method namely, difference-differential equation method. This approach has been chosen to compute the NLS models for a purely matter of convenience.

2.7.1 Pseudospectral method

One of the first spectral methods derived for numerical computations of wave equations is the pseudospectral method. This method was first derived in 1971 by Orszag [309] and by Fornberg and Whitham in 1978 [310] for early applications, then by Gottlieb and Orszag in 1977 [311], Fornberg in 1998 [312], Trefethen in 2000 [313], and finally by Boyd in 2001 [314] for more explanations. To describe this method, let consider a standard NLS equation bellow

$$iu_t + u_{xx} + 2|u|^2 u = 0. \tag{2.138}$$

The basic of the pseudospectral method is to use the discrete Fourier transform to evaluate the spatial derivative $u_{n,xx}$ and use any appropriate time-stepping scheme such as Runge-Kutta to advance in time. So doing, the discretization of Eq. (2.138) in space becomes

$$u_{n,t} = i \left(u_{n,xx} + 2|u_n|^2 u_n \right), \tag{2.139}$$

where u_n is the solution on a grid point x_n. Then, the computation of the spatial derivative $u_{n,xx}$ yields

$$u_{n,xx} = F^{-1} \left[(ik)^2 F(u_n) \right], \tag{2.140}$$

where F and F^{-1} are the discrete Fourier and inverse Fourier transforms, respectively. k is the wave number. It has been shown in the literature [313, 314] that the discretization error is smaller than any power of spatial spacing Δx. Therefore, one can confirm that the accuracy of the computation of the spatial derivative is spectral for a smooth function $u(x, t)$. This is due to the fact that the discretized function has a finite spectral bandwidth of $[-\pi/\Delta x, \pi/\Delta x]$, while the continuous function has an infinite spectral. Moreover, energy in high wave numbers is smaller than any inverse power of the wave number, which can be proved by repeated use of integration by parts to the Fourier transform formula. In the case where the function $u(x)$ is extended to an analytical function in a horizontal strip of the complex x plane, then, this discretization error decays exponentially with Δx due to the Paley-Wiener theorem [313]. Having $u_{n,xx}$, the discretized Eq. (2.139) can be advanced in time by a time-stepping scheme of the fourth-order Runge-Kutta method for a fourth-order temporal accuracy.

2.7.2   Stability condition of the pseudospectral method

The pseudospectral method has a numerical stability restriction on the time-step size Δt. This method is stable if eigenvalues of the linearized spatial discretization operator, when multiplied by Δt, absolutely lie in the stability region of the time-stepping scheme [313]. For small various spacing Δx, the largest eigenvalues of the linearized spatial discretization operator of Eq. (2.139) yield $\pm i\pi^2/\Delta x$. Those eigenvalues are induced on the one hand, by the spatial derivative term $i\partial_{xx}$ of the NLS Eq. (2.139) and on the other hand by the highest wave numbers $\pm\pi/\Delta x$. As the stability region on the imaginary axis is bounded in interval $\pm 2\sqrt{2}i$, the stability condition of the pseudospectral method is given by

$$\frac{\Delta t}{\Delta x^2} \leq \frac{2\sqrt{2}}{\pi^2}. \tag{2.141}$$

Equation (2.141) is the necessary and sufficient stability condition of the pseudospectral method based on NLS Eq. (2.139). The fourth-order Runge-Kutta method associated to the pseudospectral algorithm should also obey to the same stability condition (2.141).

In summary, the pseudospectral method is highly accurate and easy to implement for any wave equation and in any dimension. Nevertheless, it should be noted that, for some extended nonlinear NLS equation as the nonparaxial NLS equation, this stability condition is not any more valid when violated by the time-step size Δt. Hence, the derivation of the difference-differential equation method [61].

2.7.3   Difference-differential equation method

The difference-differential equation method is a nonparaxial beam propagation method that overcomes spurious oscillations in the solution. To describe this method, let consider the nonparaxial NLS equation in a self-focusing Kerr medium

$$K\frac{\partial^2 u}{\partial \zeta^2} + i\frac{\partial u}{\partial \zeta^2} + \frac{1}{2}\frac{\partial^2 u}{\partial \xi^2} + |u|^2 u = 0, \tag{2.142}$$

79

where $u(\xi, \zeta)$ is the scalar envelope field of a continuous wave beam experiencing linear diffraction in one transverse dimension. ζ and ξ are longitudinal and transverse coordinates, respectively. This method requires the employ of finite difference formulae to approximate derivatives with respect to the propagation direction ζ in Eq. (2.142). Then, due to the difficulties resulting from the finite difference representation on transverse derivative $u_{\xi\xi}$ in Eq. (2.142), the diffraction operator is implemented in the spectral domain. Thus, the finite difference formulae of the nonparaxial and propagation terms are written as follows

$$\left[\frac{\partial^2 u(\xi, \zeta)}{\partial \zeta^2}\right]_{\zeta=n\Delta\zeta} = \frac{u_{n+1}(\xi) - 2u_n(\xi) + u_{n-1}(\xi)}{\Delta\zeta^2} + \mathrm{O}(\Delta\zeta^2)$$

$$\left[\frac{\partial u(\xi, \zeta)}{\partial \zeta}\right]_{\zeta=n\Delta\zeta} = \frac{u_{n+1}(\xi) - u_{n-1}(\xi)}{2\Delta\zeta} + \mathrm{O}(\Delta\zeta^2),$$

(2.143)

where $u_n(\xi) \equiv u(\xi, n\Delta\zeta)$. Therefore, the substitution on these formulae in Eq. (2.142) yields

$$u_{n+1}(\xi) = \frac{1}{(2K + i\Delta\zeta)}\left[\left(4K - \Delta\zeta^2\frac{\partial^2}{\partial\zeta^2} - 2\Delta\zeta^2|u_n(\xi)|^2\right)u_n(\xi) - (2K - i\Delta\zeta)u_{n-1}(\xi)\right].$$

(2.144)

Equation (2.144) is the difference-differential equation and defines the explicit algorithm in which the transverse differential operator $\partial^2/\partial\xi^2$ can be compute efficiently by using FFTs as shown in the description of the pseudospectral method. The accuracy and the convergence of the difference-differential equation method has been analyzed in the literature [61].

As output, the difference-differential equation method has more general applicability with high accuracy and employs an explicit finite difference scheme in longitudinal direction. The resulting solution can contain both forward-and backward waves which can be filtered out individually without affecting the integrity of the exact solution and the conservation of energy in the system. Moreover, it has the advantage of being explicit. Hence, the simple implementation and low computation load in the solution of nonparaxial NLS equation [61]. More importantly, the difference-differential approach is flexible in the modeling of extended nonparaxial NLS equation with higher-order effects and can be used with much greater confidence [61].

2.8 Conclusion

This chapter describes the analytical and numerical methods used in the study of generation and propagation of rogue waves in optical fibers and chiral media. Among analytical methods, the similarity transformation, the mDT and DDT methods have played an important role and are of special interest, in the study of optical rogue wave phenomena. The importance of similarity transformation has been shown for nonintegrable NLS models. Moreover, a complementarity between the similarity transformation, Lax Pair method and mDT or DDT methods has been revealed to be benefit on construction of rogue wave prototypes. This combination of methods has been revealed to be powerful in the finding of rogue wave solutions. This, due to their accuracy and simplicity. In addition to this, another complementarity has been shown for numerical computations. It concerns the pseudospectral method related to FFTs and Runge-Kutta method which were used to compute efficiently the diffractions in the spectral domain.

Moreover, the difference-difference method that has a wider applicability on nonparaxial beam propagation methods, has been adopted as the numerical computation key for nonparaxial NLS models.

Chapter 3

Results and Discussions

3.1   Introduction

In this chapter, a particular attention is focused on the effect of nonparaxiality on rogue wave propagation in optical Kerr media, to solve the problem of controllability in the nonparaxial approximation. Then, the derivation of the two-dimensional NLS equation in chiral optical fibers is presented. The symmetry reduction and the mDT are used to generate the analytical chiral optical rogue wave solutions in the presence and in the absence of management. Then, the influence of optical activity on optical rogue wave propagation is presented, showing their possible control in chiral media. The exact solutions of the chiral CNLS equations with coupled space-dependence coupling field are constructed. Then, the physical properties of vector rogue waves with mixed polarization in chiral optical fiber are given. Then, the nonparaxial chiral optical rogue waves with modulated coefficients are constructed with the mDT method. An investigation on the dynamical behavior and features of nonparaxial chiral optical rogue waves is made and the influence of combined effects of nonparaxiality, optical activity and walk-off on their propagation is revealed through the vector nonparaxial chiral NLS equations with constant and modulated coefficients. Lastly, an extended NLS model is introduced and the integrability constraints are presented. Then, the first-and second-order rogue wave solutions are investigated analytically by the mDT and numerically by the difference-differential equation method. Moreover, the contrast of optical activity through the rogue wave profiles is shown and the interplay of chiral materials is elucidated. The chapter ends with the summarize of the outcomes.

3.2   Nonparaxial rogue waves in optical Kerr media

The generation of solitons in optical fibers, predicted by Hasegawa and Tappert [77] through the balance between the pulse broadening due to self-phase modulation and compression due to negative group velocity dispersion (GVD), has enabled the generation of stable picosecond and subpicosecond pulses in the near infrared. In a weakly nonlinear, dispersive medium, the

dynamics of the pulse envelope is governed, in the paraxial approximation, by the cubic nonlinear Schrödinger (NLS) equation [77]. An important property of NLS equation solitons is that they emerge from particular initial profiles as long as a particular threshold condition is met. As a consequence, it is possible to experimentally observe solitons when neither the initial pulse amplitude nor the initial pulse shape corresponds to a pure soliton. Therefore, verification of many of the predicted soliton pulse characteristics was carried out in a series of experiments by Mollenauer and co-workers [78, 79, 80]. Temporal, spatial and spatiotemporal optical solitons can find applications, which range from all-optical routing, to transparent beam interconnects, to the massive integration of optical operations in a fully three-dimensional environment. In fact, light is self-guiding in bulk media, which have modes with numerical apertures that violate the paraxial approximation. We recall that the paraxial approximation is valid when the radius of the beam is sufficiently large compared to the wavelength. Nonparaxiality may arise in the miniaturization of devices and in other configurations, such as those involving multiplexed beams [87]. Analytical and numerical studies of nonparaxial bright and dark solitons in optical Kerr media have been reported in the literature [60, 62, 315]. The focusing NLS equation, which describes generic nonlinear phenomena, supports a whole hierarchy of recently discovered Peregrine soliton or rational solutions [14, 39], Ma soliton [199] and Akhmediev breathers [41, 316]. Although solitary by nature, these rational solutions or rogue waves are different from the usual solitons, in that they are rare, short lived, and unstable. They can emerge from a turbulent state of random fields, while ordinary solitons are stable waves with characteristic collision properties, commonly appearing in deterministic setting of nonlinear evolution partial differential equations. Rogue waves are giant single waves that may suddenly appear in oceans [15]. In recent years, the idea of rogue waves have been extended far beyond oceanic expanses. The concept has been applied to pulses emerging from optical fibres [15, 19, 21, 39, 110, 235, 317, 318, 319, 320], waves in Bose-Einstein condensates [23], in superfluids [317], in optical cavities [21], in the atmosphere [31] and even in finance [34]. In particular, rogue wave solutions emerging from optical fibers, have analytically been found for many types of generalized NLS models such as NLS models with constant coefficients [39, 63] and NLS models with varying coefficients [14, 64]. Recently, this interesting phenomenon of optical rogue waves has been experimentally verified [19, 321]. According to the controllability of rogue waves, which have been studied before [322, 323, 324, 325, 326, 327], the problem now is what waves, which are localized both in space and time and depict a unique event that appears from nowhere and disappears without a trace [12], can exist in the presence of the GVD and Kerr nonlinearity in the nonparaxial approximation.

3.2.1 Model

The complex envelope of the optical field $\psi(z,x)$ of a continuous-wave beam liable to a linear diffraction in one transverse dimension in isotropic Kerr media moves according to the nonparaxial NLS equation in the form [315]

$$d\psi_{zz} + i\psi_z + p\psi_{xx} + q|\psi|^2\psi = 0, \tag{3.1}$$

where z and x are the longitudinal and transverse coordinates, respectively,

$$x = \tilde{x}/r_0, \quad z = \tilde{z}/2L_{DF}, \quad \psi = \sqrt{2n_2/n_0} r_0 k_0 \tilde{A}, \tag{3.2}$$

where r_0 is the input beam radius with diffraction length $L_{DF} = k_0 r_0{}^2$, k_0 is the linear wave number, n_0 is the linear index of refraction, n_2 is the Kerr coefficient, $\tilde{A}(x, z)$ is unscaled field assumed to be slowly varying and $d = \frac{1}{(r_0 k_0)^2}$ is the nonparaxiality parameter. The parameters p and q are related to the GVD and Kerr nonlinearity, respectively. Equation (3.1) quantifies changes in the transverse profile of a light beam with respect to a forward-propagating reference frame and can be seen as the nonparaxial NLS equation. This equation has been used in the literature [60, 62, 328, 329] for fixed values of the dimensionless parameters p and q.

In the presence of management, the optical pulse propagation in Kerr media can be described by the nonparaxial NLS equation with variable coefficients, in the form (see Appendix (A18))

$$d(z)\psi_{zz} + i\psi_z + p(z)\psi_{xx} + q(z)|\psi|^2\psi = 0, \tag{3.3}$$

Here z is taken as time parameter. The variable coefficients $d(z)$, $p(z)$ and $q(z)$ which are functions of the propagation distance z, are related to the nonparaxiality, GVD and Kerr nonlinearity, respectively.

3.2.2 Similarity transformation

Inspired by the previous work of Yan and Dai [71], the envelope field is taken in the form

$$\psi(z, x) = \rho(z) V(Z(z), X(z, x)) \exp(i\varphi(z, x)), \tag{3.4}$$

to investigate the rational solutions related to nonparaxial rogue waves, where $\rho(z)$ is the amplitude, $Z(z)$ the effective propagation distance, $X(z, x)$ the similitude variable, $V[Z(z), X(z, x)]$ the complex field. The variable $\varphi(z, x)$ is the phase of the wave. This form of envelope field is also known as the similarity transformation or the symmetry reduction method. This method which is also based on the self-similarity of some specific partial differential equations, has been applied in NLS equations to search the exact and the asymptotic self-similar solutions [330, 331, 332]. Equation (3.3) is not integrable because of varying dispersion, non-linearity and nonparaxiality coefficients. This equation governs the nonlinear wave propagation in an inhomogeneous optical fiber system. To construct the exact analytical solutions of Eq. (3.3), one should transform and reduce it into an integrable differential equation: the standard NLS equation. In what follows, the symmetry transformation method is used to obtain the integrability conditions. This approach of exact analytical solution has more attractive properties than those of soliton because its reduces interaction and smaller peak power than that of the soliton [333] and allows a possible pedestal-free pulse compression [334]. Notice that the similarity and the modified Darboux transformation methods are analytical methods that enable to construct rational solutions related to rogue waves.

Substituting Eq. (3.4) into Eq. (3.3) gives a couple system of partial differential equations

with variable coefficients

$$
\begin{aligned}
&\rho_z V + 2p\rho X_x \varphi_x V_X + \rho Z_z V_Z + \rho X_z V_X + 2\rho d\varphi_z X_z V_X + p\rho \varphi_{xx} V \\
&+\rho dV \varphi_{zz} + 2d\rho_z V \varphi_z + 2\rho d\varphi_z Z_z V_Z = 0,
\end{aligned}
\tag{3.5}
$$

$$
\begin{aligned}
&d\rho_{zz} V + 2d\rho_z Z_z V_Z + 2d\rho_z X_z V_X + \rho d Z_z{}^2 V_{ZZ} + 2d\rho Z_z X_z V_{ZX} \\
&+\rho d Z_{zz} V_Z + \rho d X_z{}^2 V_{XX} + d\rho X_{zz} V_X - d\rho V \varphi_z{}^2 - \rho V \varphi_z + p\rho X_x{}^2 V_{XX} \\
&+p\rho X_{xx} V_x - p\rho V \varphi_x{}^2 + q|\rho|^2 |V|^2 \rho V = 0.
\end{aligned}
\tag{3.6}
$$

According to previous works [14, 64], one considers the above symmetry reduction or similarity transformation (3.4) that would reduce Eq. (3.3) to the standard NLS equation

$$
i\psi_z + \frac{1}{2}\psi_{xx} + |\psi|^2 \psi = 0.
\tag{3.7}
$$

By connecting the solutions of Eq. (3.3) with those of the above standard NLS equation, the complex field $V[Z(z), X(z,x)]$ should satisfy that equation in the form

$$
i\frac{\partial V}{\partial Z} + \frac{1}{2}\frac{\partial^2 V}{\partial X^2} + |V|^2 V = 0.
\tag{3.8}
$$

With $V[Z(z), X(z,x)]$ satisfying the relation (3.8), one deduces after the symmetry reduction of Eqs. (3.5) and (3.6)

$$
d(z)X_{zz} + p(z)X_{xx} = 0,
\tag{3.9}
$$

$$
q(z)\rho^2 + Z_z = 0,
\tag{3.10}
$$

$$
Z_z + d(z)\varphi_z Z_z = 0,
\tag{3.11}
$$

$$
\frac{1}{2}Z_z + p(z)X_x{}^2 + d(z)X_z{}^2 = 0,
\tag{3.12}
$$

$$
\varphi_z + d(z)\varphi_z{}^2 + p(z)\varphi_x{}^2 = 0,
\tag{3.13}
$$

$$
\rho_z + \rho\left(p(z)\varphi_{xx} + d(z)\varphi_{zz}\right) + 2d(z)\rho_z \varphi_z = 0,
\tag{3.14}
$$

$$
\rho_{zz} V + 2\rho_z Z_z V_Z + 2\rho_z X_z V_X + \rho Z_z{}^2 V_{ZZ} + 2\rho Z_z X_z V_{ZX} + \rho Z_{zz} V_Z = 0.
\tag{3.15}
$$

3.2.3 Rational solutions of the nonparaxial nonlinear Schrödinger equation with variable coefficients

The resolution of system $(3.9) - (3.15)$ starts by solving Eq. (3.9). To look for rational solutions, several conditions are imposed

$$
Z_z = -\tfrac{1}{2}p(z)X_x{}^2, \quad q(z) = \tfrac{1}{2}p(z)\rho(z)^{-2}X_x{}^2, \quad X_x = \alpha(z),
\tag{3.16}
$$

which verify Eq. (3.10). The above parameters can generate the constraints for the variable $Z(z)$ and the nonlinear Kerr coefficient $q(z)$. More specifically, it follows that

$$
X_x = \alpha(z), \quad X_{xx} = 0.
\tag{3.17}
$$

As $d(z) \neq 0$ and $p(z) \neq 0$, Eq. (3.9) leads to the condition $X_{zz} = 0$, which implies that $\alpha_{zz} = \delta_{zz} = 0$. So, from relations (3.17), one obtains

$$X(z,x) = \alpha(z)x + \delta(z), \tag{3.18}$$

where $\alpha(z)$ is the inverse of the wave width and $\delta(z)$ the position of its center of mass $(-\delta(z)/\alpha(z))$. Quantities $\alpha(z)$ and $\delta(z)$ are free functions of z. From condition (3.16), the effective dimensionless propagation distance yields

$$Z(z) = -\frac{1}{2} \int_0^z p(s)\alpha(s)^2 ds. \tag{3.19}$$

Substituting Eq. (3.16) into Eq. (3.12), leads to

$$X_z{}^2 = -\frac{3p(z)\alpha(z)^2}{4d(z)}. \tag{3.20}$$

The relation above is true for $d(z) < 0$ or $p(z) < 0$. In this work, one chooses $p(z) < 0$. For $Z_z \neq 0$, Eq. (3.11) becomes

$$\varphi_z = -\frac{1}{d(z)}. \tag{3.21}$$

Substituting Eq. (3.21) into Eq. (3.13) gives the phase expression

$$\varphi_x = 0, \quad \varphi_{xx} = 0, \quad \varphi(z,x) = -\int_0^z \frac{1}{d(s)} ds + \varphi_0(x), \tag{3.22}$$

where $\varphi_0(x)$ is a constant. From Eq. (3.14), one arrives at

$$\rho(z) = \rho_0 \exp\left\{ \int_0^z \gamma(s) ds \right\}, \tag{3.23}$$

which is the amplitude of the wave, assumed to be a real function, and where $\gamma(s)$, leads to

$$\gamma(s) = d(s)\varphi_{zz}. \tag{3.24}$$

Here, ρ_0 is a constant. Now let deduce the Kerr coefficient given by

$$q(z) = \frac{1}{2} \frac{p(s)\alpha(s)^2}{\rho_0{}^2 e^{2\int_0^z \gamma(s) ds}}. \tag{3.25}$$

For the defined values of $d(z)$, $p(z)$, $\alpha(z)$ and $\delta(z)$, the expressions of $X(z,x)$, $Z(z)$, $\rho(z)$, $\varphi(z,x)$ and $q(z)$ can be derived. The variable $V[Z(z), X(z,x)]$ is determined by the modified Darboux transformation [24, 63, 94, 335]. The first-order of the standard NLS equation given by Eq. (3.1) was found by Peregrine [39] and the second-order was proposed by Soto-Crespo et al. [11]. According to the modified Darboux transformation, one obtains the first-and the second-order of rational solutions.

If one set $V[Z(z), X(z, x)] = \Psi[Z(z), X(z, x)]$, the first-order presented in Ref. [14, 39] is given by

$$\Psi_1 = V_1 = \left[1 - \frac{G_1 + iZ(z)H_1}{1 + 2X^2 + 4Z^2}\right] \exp i\{Z(z)\}, \qquad (3.26)$$

where

$$G_1 = 4, \quad H_1 = 8, \quad D_1 = 1 + 2X^2 + 4Z^2. \qquad (3.27)$$

This solution is known as the Peregrine soliton [39] when the correspondence $Z = z$ and $X = x\sqrt{2}$ are considered. Then, collecting the partial solutions together, the construction of the first-order rational solution related to the exact nonparaxial rogue wave solution of Eq. (3.3) yields

$$\psi_1 = \rho_0 \exp\left\{\int_0^z \gamma(s)ds\right\} \left[1 - 4\frac{1+2iZ(z)}{1+2X(z,x)^2+4Z(z)^2}\right] \exp i\{Z(z) + \varphi(z, x)\}. \qquad (3.28)$$

The intensity of the first order non-paraxial rogue wave is given by

$$|\psi_1|^2 = \rho_0^2 \exp\left\{2\int_0^z \gamma(s)ds\right\} \left(\frac{\left(2X^2+4Z^2-3\right)^2+64Z^2}{(1+2X^2+4Z^2)^2}\right). \qquad (3.29)$$

This first-order rational solution is used to describe the dynamics of rogue wave in optical fibers. This solution is used to show the effect of the nonparaxiality on rogue wave propagation and then to present the different cases in which the choice of parameters of the original Eq. (3.3) leads to the control of rogue waves. The second-order rogue wave presented in Ref. [14] is given by

$$\Psi_2 = V_2 = \left[1 + \frac{G_2 + iZ(z)H_2}{D_2}\right] \exp i\{Z(z)\}, \qquad (3.30)$$

where G_2, H_2 and D_2 are given by the relations

$$\begin{array}{l} G_2 = \frac{3}{8} - \frac{3}{2}X^2 - \frac{1}{2}X^4 - 9Z^2 - 10Z^4 - 6X^2Z^2, \\ H_2 = \frac{15}{4} + 3X^2 - X^4 - 2Z^2 - 4Z^4 - 4X^2Z^2, \\ D_2 = \frac{3}{32} + \frac{9}{16}X^2 + \frac{1}{8}X^4 + \frac{1}{12}X^6 + \frac{33}{8}Z^2 + \frac{9}{2}Z^4 + \frac{2}{3}Z^6 - \frac{3}{2}X^2Z^2 + \frac{1}{2}X^4Z^2 + X^2Z^4. \end{array} \qquad (3.31)$$

According to the same correspondence of variables z and x as on the first-order, this solution is the one found by Soto-Crespo $et\ al.$ [11]. Collecting the partial solutions together, the final second-order rational solution related to the exact nonparaxial rogue wave solution of Eq. (3.3) is constructed

$$\psi_2 = \rho_0 \exp\left\{\int_0^z \gamma(s)ds\right\} \left[1 + \frac{G_2+iZ(z)H_2}{D_2}\right] \exp i\{Z(z) + \varphi(z, x)\}. \qquad (3.32)$$

The intensity of the second-order nonparaxial rogue wave solution is

$$|\psi_2|^2 = \rho_0^2 \exp\left\{2\int_0^z \gamma(s)ds\right\} \left(\frac{(D_2 + G_2)^2 + Z^2 H_2^2}{D_2^2}\right). \qquad (3.33)$$

This second-order rational solution is more precise than the first one. It describes the dynamics of two rogue waves propagating in optical fiber as well as collisions between them. This solution is used to illustrate the effect of the nonparaxiality on rogue wave collisions.

3.2.4 Effect of the nonparaxiality on the propagation of rogue waves in optical fiber

To illustrate the effect of the nonparaxiality on the propagation of rogue waves related to the first-and second-order rational solutions, let fix values of parameters $\rho_0 = 1$. Then follows the presentation of managed cases, in which the choice of parameter functions leads to the controlled of rogue waves.

A. Influence of polynomial function on nonparaxial rogue waves

The goal now is to choose appropriately, free functions $d(z)$, $P(z)$, $\alpha(z)$ and $\delta(z)$ to generate abundant structures of nonparaxial rogue waves. They are chosen as polynomial functions. Let keep in mind that parameters are chosen in order to be bounded in the intervals $-5 < z < 5$ and $-5 < x < 5$.

For the chosen coefficients and free functions

$$d(z) = \tfrac{z}{4}, \quad p(z) = -\tfrac{z^2}{4}, \quad \alpha(z) = 1, \quad \delta(z) = z. \tag{3.34}$$

The wave propagations is presented in Figs. 29, in three-dimension (3D) [Fig. 29(a)] and (2D) [Figs. 29(b) and 29(c)] representations showing the nonparaxial effects, respectively. For the given parameters

$$d(z) = \tfrac{1}{4}, \quad p(z) = -\tfrac{z^2}{4}, \quad \alpha(z) = 1, \quad \delta(z) = z. \tag{3.35}$$

Figure 30 depicts the dynamics of the first-order rational solution for the intensity $|\psi_1(x, z)|^2$ in 3D [Fig. 30(a)] and 2D [Figs. 30(b) and 30(c)] representations illustrating the nonparaxial effects on the propagation of rogue waves.

Here the intensity of the first-and second-order rational solutions is plotted with the help of MATLAB. One can see in Figs. 29 and 30 that the behavior of nonparaxial rogue waves is more surrounded in Fig. 29 than in Fig. 30. One observes that the space where the usual rogue waves reach their maximum moves from the center to the periphery on Fig. 29. So, the usual symmetry of Peregrine soliton is absent in Fig. 29 with nonparaxial parameter $d(z)$ taken as polynomial function and present in Fig. 30 with $d(z)$ taken as a constant. This means that the choice of nonparaxial parameter $d(z)$, given in relation (3.34) is appropriate to obtain particularities of non-paraxial effects. The intensity profile of Fig 29 increases rapidly than the ones of usual cases in paraxial approximation. It follows that the nonparaxiality increases the length and reduces the width of the wave peak simultaneously. It is also responsible for the unusual symmetry of Peregrine soliton (rogue waves) in Fig. 29.

B. Influence of Jacobian elliptic functions on nonparaxial rogue waves

One shows the influence of polynomial functions given to $d(z)$, $p(z)$, $\alpha(z)$ and $\delta(z)$ on the structure of nonparaxial rogue waves. In what follows, let choose them now as Jacobian elliptic
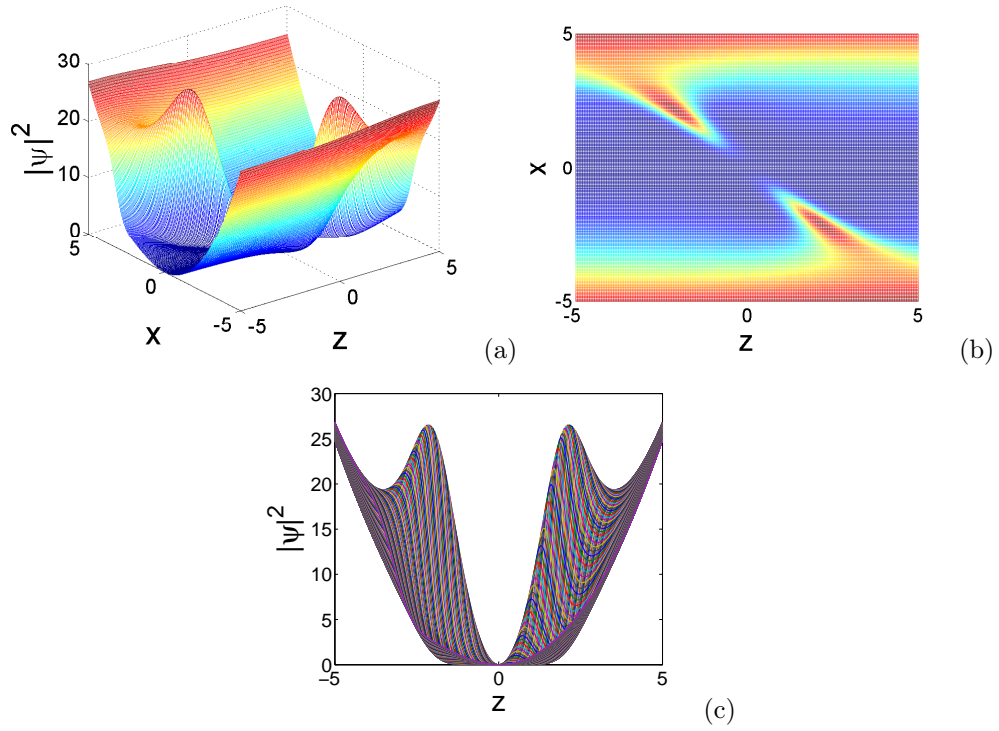
Figure 29: Wave propagation in 2D and 3D representation of the first order rational solution for the intensity $|\psi_1(x,z)|^2$ with $d(z) = \frac{z}{4}$; $p(z) = -\frac{z^2}{4}$; $\alpha(z) = 1$ and $\delta(z) = z$.
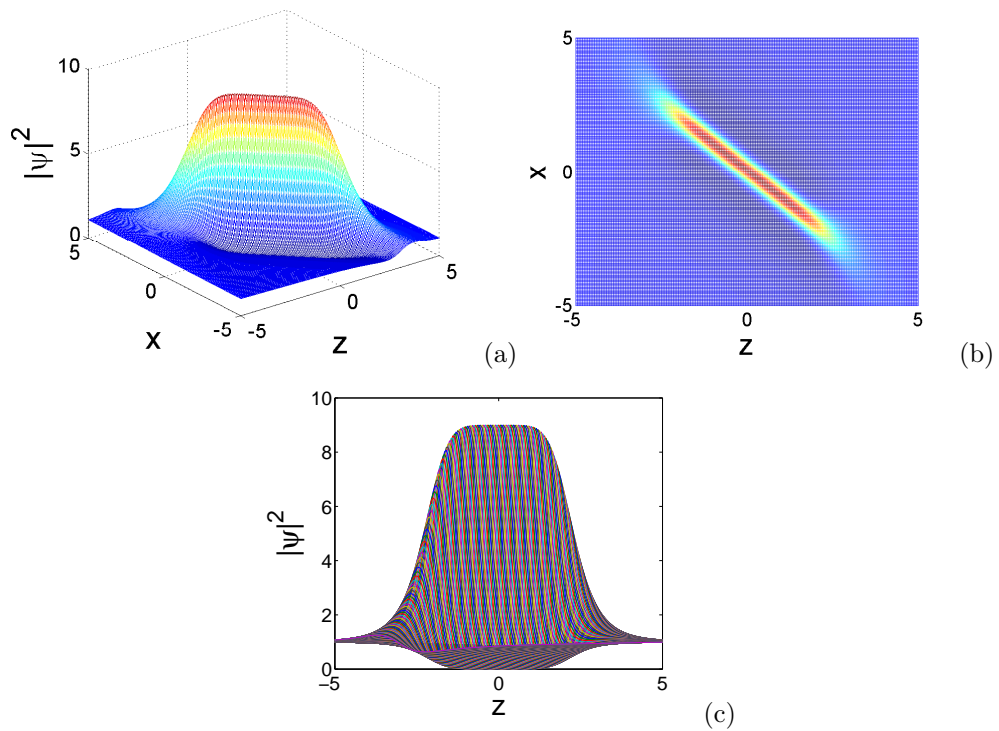
Figure 30: Wave propagation in 2D and 3D representation of the first order rational solution for the intensity $|\psi_1(x,z)|^2$ with $d(z) = \frac{1}{4}$; $p(z) = -\frac{z^2}{4}$; $\alpha(z) = 1$ and $\delta(z) = z$.

functions. When k is weaker than one, the approximative formulas of Jacobian elliptic functions [336] are given by

$$
\begin{aligned}
dn(z, k) &\approx 1 - \frac{k^2 \sin{(z)}^2}{2}, \\
cn(z, k) &\approx \cos(z) - k^2 \sin(z) \left(\frac{z - \sin(z)\cos(z)}{4} \right), \\
sn(z, k) &\approx \sin(z) - k^2 \cos(z) \left(\frac{z - \sin(z)\cos(z)}{4} \right).
\end{aligned}
\tag{3.36}
$$

Here, let choose $k = 0.6$. If one sets coefficients and free functions as

$$
d(z) = cn(z, k), \quad p(z) = -\tfrac{1}{2} sn\left(k, z\right), \quad \alpha(z) = z, \quad \delta(z) = z,
\tag{3.37}
$$

one can obtain the 3D and 2D representation profiles in Figs. 31(a) and 31(c), respectively, showing the nonparaxial effects on rogue waves.

(a)

(b)

(c)
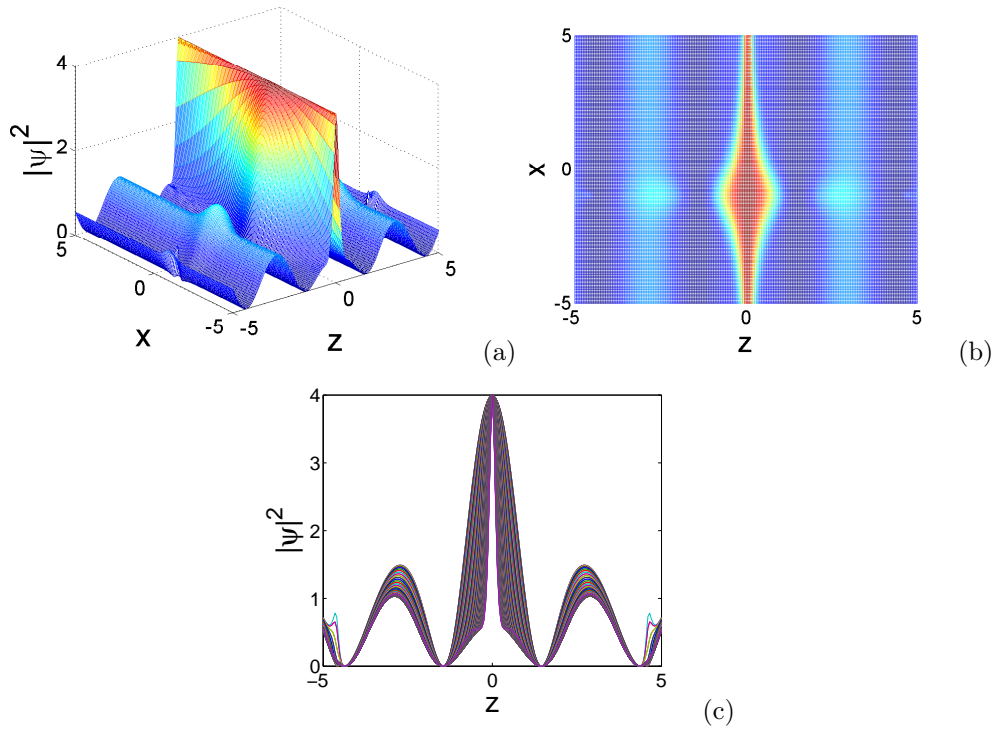
Figure 31: Wave propagation in 2D and 3D representation of the first order rational solution for the intensity $|\psi_1(x, z)|^2$ with $d(z) = cn(z, k)$; $p(z) = -\frac{1}{2} sn\left(k, z\right)$; $\alpha(z) = z$ and $\delta(z) = z$.

Figures $31(a) - 31(c)$ depict the behavior of nonparaxial rogue waves with $d(z)$ and $p(z)$ taken as Jacobian elliptic functions. The profiles show waves with usual symmetry along the z direction. The intensity profiles of the nonparaxial rogue waves given on Figs. $31(a)$ and $31(c)$ show how they are localized in z direction (with z taken as time parameter). These waves appear spontaneously and decrease rapidly as shown on previous works [14, 63, 337, 338].

Having completed with the first-order, let study the dynamic behavior of the nonparaxial effect on the propagation of nonparaxial rogue waves related to the second-order rational solutions. Here the parameters that were used to plot the first-order rational solutions are also used

to obtain the intensity profiles of the second-order. So from Eq. (3.34), the nonparaxial effects on rogue waves are shown in 3D [Fig. 32] and 2D [Figs. 32(b) and 32(c)] representations.

(a)

(b)

(c)
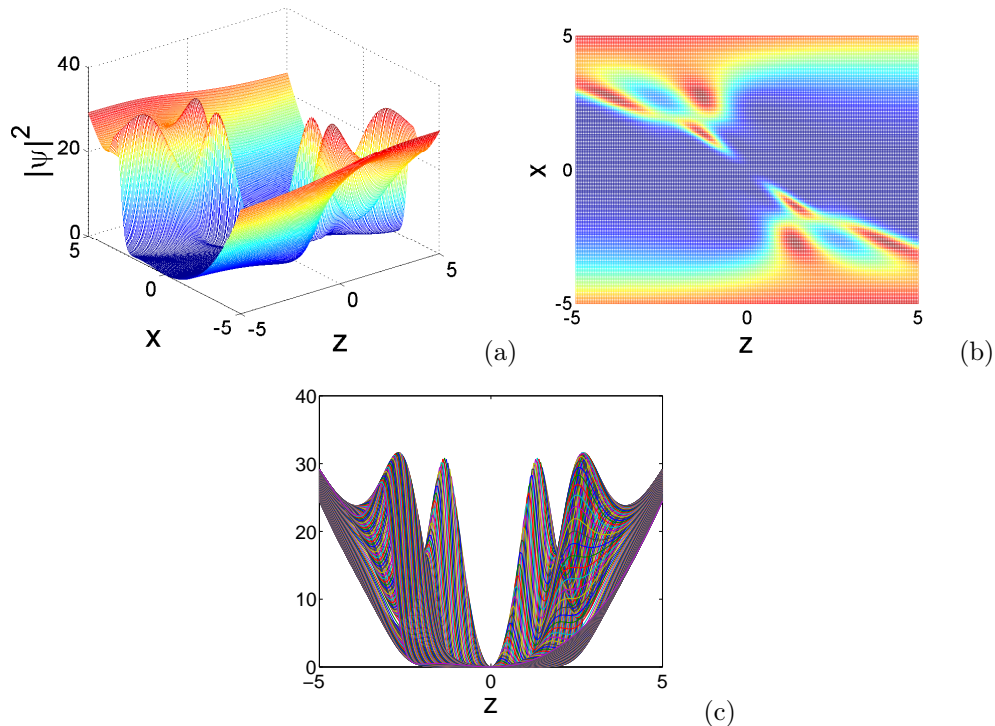
Figure 32: Wave propagation in 2D and 3D representation of the second order rational solution for the intensity $|\psi_2(x,z)|^2$ with $d(z) = \frac{z}{4}$; $p(z) = -\frac{z^2}{4}$; $\alpha(z) = 1$ and $\delta(z) = z$.

It follows from Eq. (3.35) that Fig. 33 reveals the nonparaxiality effect [Figs. 33(a) and 33(b)]. The intensity profiles of Figs. 32 and 33 are remarkably similar to Figs. 29 and 30. Nevertheless, one records a difference, particularly notable in the number of collisions and peaks near to the periphery of the center. In the same way, the Jacobian elliptic functions are used to plot the profiles of second-order. By using Eq. (3.37), one obtains Figs. 34(a) − 34(c), showing the influence of the nonparaxiality on rogue waves.

In Fig. 34 many collisions can be seen between waves. An unusual symmetry of nonparaxial rogue waves in Fig. 34(a) is observed. The wave peak of Fig. 34(c) splits into two and this split is due to the diffraction effect in lossy medium. It is noted that in the presence of the nonparaxiality, the collisions between waves are rare but significant when they appear [see Figs. 34(a) and 34(b)].

3.3   Influence of optical activity on rogue waves propagating in chiral optical fibers

Recently, propagation phenomena of solitons [77, 78, 79, 80, 339] and vector solitons [340, 341, 342] in nonlinear media with natural or induced linear optical activity [81, 82, 84, 85, 86]
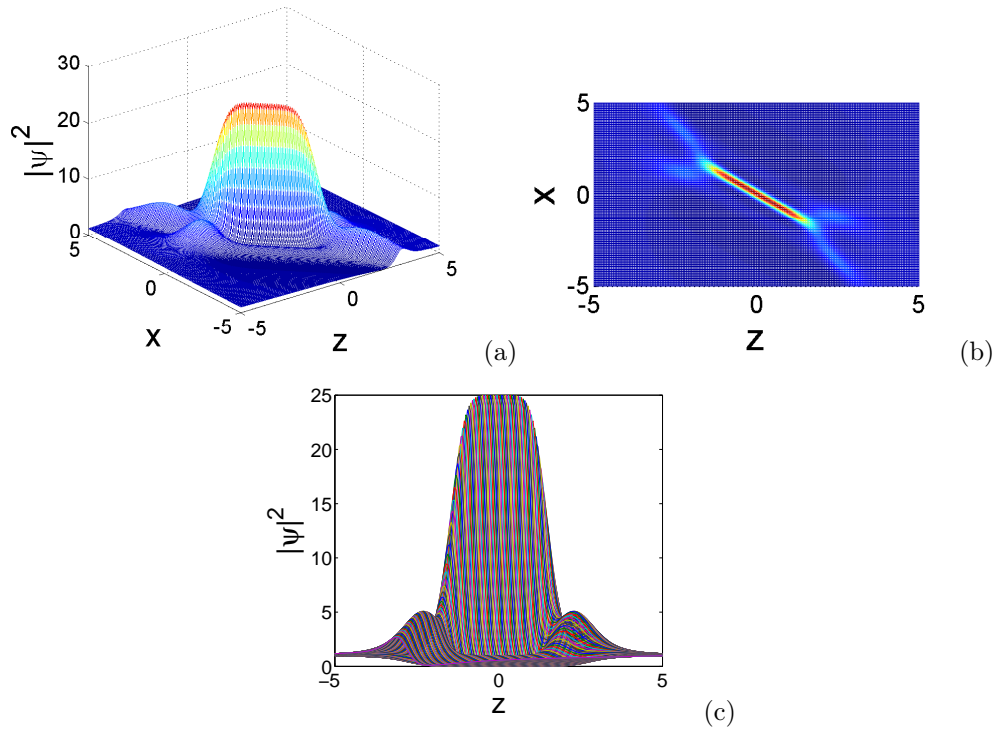
Figure 33: Wave propagation in 2D and 3D of the second order rational solution for the intensity $|\psi_2(x,z)|^2$ with $d(z) = \frac{1}{4}$; $p(z) = -\frac{z^2}{4}$; $\alpha(z) = 1$ and $\delta(z) = z$.
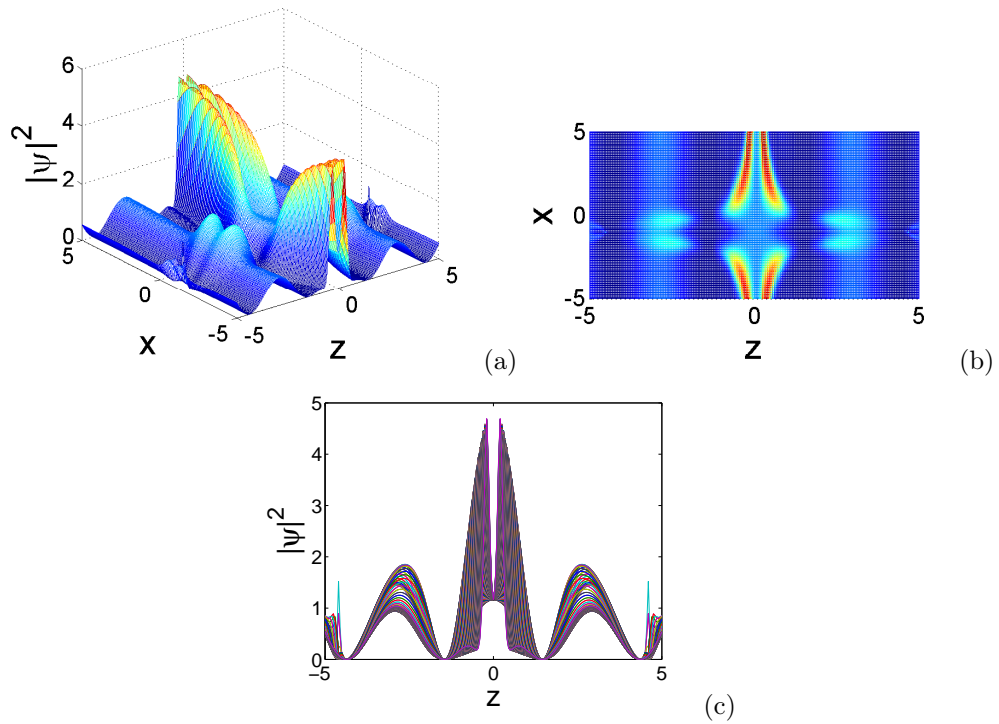
Figure 34: Wave propagation in 2D and 3D representation of the second order rational solution for the intensity $|\psi_2(x,z)|^2$ with $d(z) = cn(z,k)$; $p(z) = -\frac{1}{2}sn(k,z)$; $\alpha(z) = z$ and $\delta(z) = z$.

have attracted more attention and have lead to important advances from the fundamental and technological point of view. More recently in optics, the study of propagation [343, 344] in birefringent optical fibers allows to introduce the concept of shape-changing solitons that share energy among themselves during propagation. So, when two optical waves copropagate inside a birefringent single-mode fiber, their states of polarization change during propagation as a result of optically induced nonlinear birefringence. This polarization instability manifests itself as large changes in the output state of polarization, when the input power or the polarization state is changed slightly [345]. Those optical activities are the consequence of intrinsic linear birefringence [346] or circular birefringence [83] known as natural chirality or artificial chirality. The natural chirality is caused by the spatial dispersion of optical response either in chiral molecules or in chiral arrangements of molecules and the artificial chirality is induced by structural chirality, i.e., by artificially chiral structural features in subwavelength scale. This notion of chirality refers to the lack of bilateral symmetry of an object and can be considered as a purely geometric property of a medium. So, chirality is a geometrical concept that describes the inability of an object and its mirror image to be superimposed solely through translations and rotations. This asymmetry of chiral molecules gives rise to optical rotation, which is an example of circular birefringence with the material possessing a different refractive index for right-hand circularly polarized and left-hand circularly polarized light. This fact is expected to play an important role in the potential application of the chiral media in the microwave and optical regimes. In fact, several nonlinear phenomena in chiral media [81, 82, 83, 84, 85, 86, 347] have been studied over the last decade for many applications and the principle problem in working with a chiral medium is on the control of chirality level. After some investigations, it has been suggested that the use of chiral material in optical fibers may be studied with polymer optical fibers [348, 349]. But after some experimental studies, scientists show that, because of organic nature of most chiral materials, some of them are not indicated at the processing temperature of silica and soft glasses; they will simply be damaged. In order to solve this problem, some investigations on the controllability of spontaneous waves in optical fiber have been done [350]. Among various solutions of spontaneous waves, the PS [39], ABs [41], and KM solitons [351] are considered as theoretical prototypes to describe the interesting phenomenon of rogue waves.

3.3.1 Derivation of the nonlinear Schrödinger equation in chiral optical fibers

The phenomenological theory based on the Beltrami-Maxwell formalism extended to nonlinear chiral medium [82] has given rise to new effect of great significance in chiral applications. First observed in optical activity, chirality corresponds to the rotation of the polarization plane in a linear isotropic material. In an anisotropic cubic media, we add to the polarization P and/or to the magnetization M, an additional term T_c proportional to $\vec{\nabla} \times \vec{H}$ which measure per units length, the chirality. The spatial chirality effect in a medium is characterized through the Born-Fedorov formalism, based on the predicted Maxwell's equations. In chiral optical fibers, the Born-Fedorov equations are the most adequate for the study of optical activity. As they satisfy to the edge conditions [352], this allows the characterisation of the nonlinear chiral medium by the given equations [82, 84, 85]

$$\vec{D} = \varepsilon_n \vec{E} + \varepsilon_0 T_c \vec{\nabla} \times \vec{E},$$
$$\vec{B} = \mu_0 \left(\vec{H} + T_c \vec{\nabla} \times \vec{H} \right), \tag{3.38}$$

where the flux densities $\vec{D}$ and $\vec{B}$ arise in response to the electric and magnetic field $\vec{E}$ and $\vec{H}$ propagating in the chiral medium with $\varepsilon_n = \varepsilon_0 + \varepsilon_2 \left| \vec{E} \right|$. Here ε_0 and ε_2 are linear and nonlinear permittivity, respectively. μ_0 is the permeability and T_c the chiral parameter of the optical fiber. In our medium, the predicted Maxwell equations are

$$\vec{\nabla} \cdot \vec{D} = \rho_V, \quad \vec{\nabla} \cdot \vec{B} = 0,$$
$$\vec{\nabla} \times \vec{E} = -\frac{\partial \vec{B}}{\partial t}, \quad \vec{\nabla} \times \vec{H} = \vec{J} + \frac{\partial \vec{D}}{\partial t}, \tag{3.39}$$

where, the current density $\vec{J} = \sigma \vec{E}$ and the charge density ρ represents the sources for the electromagnetic field. The quantity σ is the electrical conductivity and V the volume. Substituting Eq. (3.38) into Eq. (3.39), gives the following wave equation

$$\vec{\nabla}^2 \vec{E} + \mu_0 \varepsilon_0 T_c{}^2 \frac{\partial^2 \vec{\nabla}^2 \vec{E}}{\partial t^2} = \mu_0 \varepsilon_0 \frac{\partial^2 \vec{E}}{\partial t^2} + \mu_0 \sigma \frac{\partial \vec{E}}{\partial t} + \mu_0 \varepsilon_2 \left| \vec{E} \right| \frac{\partial^2 \vec{E}}{\partial t^2} + 2 \mu_0 \varepsilon_0 T_c \vec{\nabla} \times \frac{\partial^2 \vec{E}}{\partial t^2}$$
$$+ \mu_0 \varepsilon_2 T_c \left| \vec{E} \right|^2 \vec{\nabla} \times \frac{\partial^2 \vec{E}}{\partial t^2} + \mu_0 \sigma T_c \vec{\nabla} \times \frac{\partial \vec{E}}{\partial t}. \tag{3.40}$$

The optical field $\vec{E}$ is represented by a right-(R) or left-hand (L) polarizations in the z direction as

$$\vec{E}(\vec{r}, t) = (\hat{x} \mp j\hat{y}) \vec{A}(\vec{r}, t) \exp\left[-j\left(K_\pm z - \omega_0 t\right)\right]$$
$$= \vec{\psi}_{R,L} \exp\left[-j\left(K_\pm z - \omega_0 t\right)\right], \tag{3.41}$$

where $\vec{\psi}_{R,L}$ is the complex envelope of the optical field in the nonlinear chiral medium, K the wave number and ω_0 the frequency.

After evaluation of different derivations of $\vec{E}$ in x, y and z directions in Eq. (3.40), one neglects the second-order terms and suppose that the wave is propagating in z direction. This implies that

$$K_x = K_y = 0, \quad E_z = 0. \tag{3.42}$$

Considering the slowly varying envelope of the amplitude, we can do the paraxial approximation bellow

$$\left| \frac{\partial^2 E_x}{\partial z^2} \right| << \left| 2jK_z \frac{\partial E_x}{\partial z} \right|, \quad \left| \frac{\partial^2 E_y}{\partial z^2} \right| << \left| 2jK_z \frac{\partial E_y}{\partial z} \right|. \tag{3.43}$$

The final result of Eq. (3.40), after approximations, stands for (see the Appendix (B18))

$$j\frac{\partial \phi}{\partial z'} + \frac{1}{2} K'' \frac{\partial^2 \phi}{\partial t'^2} - j\frac{1}{6} K''' \frac{\partial^3 \phi}{\partial t'^3} + j\frac{\omega \alpha}{2K_0} \left(1 \mp KT_c\right) \phi - \frac{\beta \omega^2}{2K_0} \left(1 \mp KT_c\right) |\phi|^2 \phi \mp K^2 T_c \phi + j\frac{\omega \beta}{K_0} |\phi|^2 \frac{\partial \phi}{\partial t'} = 0, \tag{3.44}$$

where $K' = \frac{\partial K}{\partial \omega} = \frac{1}{v_g}$ is the inverse of group-velocity, $K'' = \frac{\partial K'}{\partial \omega}$ is the group-velocity dispersion coefficient which takes the plus and minus signs ($\pm$), representing the anomalous and normal dispersion regimes, respectively. The parameter $K''' = \frac{\partial K''}{\partial \omega}$ is the TOD term. In the fourth term, the attenuation coefficient α is weighted towards the chiral parameter T_c. The factor to $|\phi|^2 \phi$ is the SPM and the term $K^2 T_c \phi$ occurs as an additional correction to the chirality of the

fiber. The last term has the physical sense of SS and is necessary to perform the description of spontaneous waves.

The new variables, namely

$$q = \frac{\omega_0^{2/3}\beta^{1/3}}{(2K_0)^{1/3}}\phi, \quad \xi = \frac{\omega_0^{2/3}\beta^{1/3}}{(2K_0)^{1/3}}z', \quad \tau = \frac{\omega_0^{1/3}\beta^{1/6}}{\sqrt{K''}(2K_0)^{1/6}}t', \quad \Gamma = \frac{\omega_0^{1/3}\alpha}{(2K_0)^{1/3}\beta^{1/3}},$$

$$\gamma = \frac{\beta^{1/6}K'''}{6K''}\frac{\omega_0^{1/3}}{\sqrt{(2K_0)^{1/3}K''}}, \quad C = 1 \mp T_c K, \quad D = \frac{K^2 T_c(2K_0)^{1/3}}{\beta^{1/3}\omega_0^{2/3}}, \quad \alpha_3 = \frac{(2K_0)^{5/6}\beta^{1/6}}{\sqrt{K''}\omega_0^{2/3}K_0}, \tag{3.45}$$

allow to express Eq. (3.44) in the form

$$j\frac{\partial q}{\partial \xi} + \frac{1}{2}\frac{\partial^2 q}{\partial \tau^2} - j\gamma\frac{\partial^3 q}{\partial \tau^3} + jC\Gamma q \mp Dq - C|q|^2 q + j\alpha_3|q|^2\frac{\partial q}{\partial \tau} = 0. \tag{3.46}$$

Equation (3.46) is the NLS equation for a chiral optical fiber. This generalized chiral NLS equation can be used to describe the propagation of right-hand(+) and left-hand(-) hand polarized rogue waves in a higher-order dispersive and nonlinear chiral optical fiber. For $\alpha_3 = 0$, one obtains another form of NLS equation for a chiral optical fiber without the SS term [82]. For $T_c = 0$, $C = 1$, $D = 0$, $\gamma = 0$ and $\Gamma = 0$, Eq. (3.46) stands for the standard NLS equation.

If one set $q(\xi, \tau) = \psi(\xi, \tau)$, $\varphi = \frac{1}{2}$ and $\mu = C\Gamma$, the model becomes

$$j\frac{\partial \psi}{\partial \xi} + \varphi\frac{\partial^2 \psi}{\partial \tau^2} - j\gamma\frac{\partial^3 \psi}{\partial \tau^3} + j\mu\psi \mp D\psi - C|\psi|^2\psi + j\alpha_3|\psi|^2\frac{\partial \psi}{\partial \tau} = 0. \tag{3.47}$$

One should keep in mind that the controllability condition should be verified in Eq. (3.47). With the aim of taking into account the missing condition of controllability (on higher-order NLS models) Yan *et al.* [71] showed that the sum of parameters related to the SS, that is, a_2 and to the SFS, that is, a_3 should be zero: $a_2 + a_3 = 0$. To achieve this aim, let write the sum of the SS (α_3) and the SFS (α_4) in the following form

$$j\left[\alpha_3(|\psi|^2\psi)_\tau + \alpha_4\psi(|\psi|^2)_\tau\right] = j\left[\alpha_3|\psi|^2\psi_\tau + (\alpha_3 + \alpha_4)\psi(|\psi|^2)_\tau\right], \tag{3.48}$$

and let $\alpha_3 + \alpha_4 = 0$; it will remain another term of SS given by $j\alpha_3|\psi|^2\psi_\tau$. Thus, the assumption of controllability is verified by the model given in Eq. (3.47). Our main aim now is to find the rational solutions of Eq. (3.47) with variable and constant coefficients which may be useful to control the propagation of chiral optical rogue waves.

3.3.2 Symmetry reduction of the chiral nonlinear Schrödinger equation with variable coefficients

In the presence of management in Eq. (3.47), the optical pulse propagation in chiral media can be described by the chiral NLS equation with variable coefficients, in the form

$$j\frac{\partial \psi}{\partial \xi} + \varphi(\xi)\frac{\partial^2 \psi}{\partial \tau^2} - j\gamma(\xi)\frac{\partial^3 \psi}{\partial \tau^3} + j\mu(\xi)\psi \mp D(\xi)\psi - C(\xi)|\psi|^2\psi + j\alpha_3(\xi)|\psi|^2\frac{\partial \psi}{\partial \tau} = 0, \tag{3.49}$$

where τ is taken as time parameter and ξ as spatial parameter. The variable coefficients $\varphi(\xi)$, $\gamma(\xi)$, $\mu(\xi)$, $D(\xi)$, $C(\xi)$ and $\alpha_3(\xi)$ are related to the GVD, TOD, the gain and loss term of the induced optical activity, linear birefringence, SPM and SS coefficients, respectively.

Since Eq. (3.49) has varying coefficients, it becomes not integrable and this strongly affects the wave propagation in chiral optical fiber. In order to solve this problem of non integrability of the model, one can either use the symmetry reduction method using third-order propagation vector field [275] or the envelope field in gauge form [276] to obtain the integrability conditions. This method has been applied in NLS models to look for exact analytical solutions and is the most adequate method for the construction of rogue wave solutions. From this preliminary method, varying coefficients are obtained but the complex field is deduced from the modified Darboux transformation or from the Lax pair method [277]. In what follows, the envelope field is used in the form [64, 71, 353]

$$\psi(\xi, \tau) = A(\xi) V [Z(\xi), T(\xi, \tau)] \exp \{i\rho(\xi, \tau)\}, \tag{3.50}$$

to construct the rational solutions related to chiral optical rogue waves, where $A(\xi)$ is the amplitude, $Z(\xi)$ the effective propagation distance, $T(\xi, \tau)$ the similitude variable, $V[Z(\xi), T(\xi, \tau)]$ the complex field. The variable $\rho(\xi, \tau)$ is the phase of the wave. This form of envelope field is also known as the similarity transformation or the reduction method. Substituting Eq. (3.50) into Eq. (3.49) gives a couple system of partial differential equations with variable coefficients

$$-\gamma A V_T T_{\tau\tau} + 3\gamma A V T_\tau \rho_\tau{}^2 + A V_T T_\xi + A V_T T_\tau \rho_\tau - \gamma A V_{TTT} T_\tau{}^3 + 3\gamma A V \rho_{\tau\tau} \rho_\tau$$
$$+ A_\xi V + \mu V + A V_Z Z_\xi + \varphi A V \rho_{\tau\tau} + \alpha_3 A^2 |V|^2 A V_T T_\tau - 3\gamma A V_{TT} T_\tau T_{\tau\tau} = 0, \tag{3.51}$$

$$-A V \rho_\xi + \varphi A V_{TT} T_\tau{}^2 + \varphi A V_T T_{\tau\tau} - \varphi A V \rho_\tau{}^2 + \gamma A V \rho_{\tau\tau\tau} + 3\gamma A V_T T_{\tau\tau} \rho_\tau + 3\gamma A V_T T_\tau \rho_{\tau\tau}$$
$$-\gamma A V \rho_\tau{}^3 + 3\gamma A V_{TT} T_\tau{}^2 \rho_\tau - \alpha_3 A^2 |V|^2 A V_T \rho_\tau \mp D A V - C A^2 |V|^2 A V = 0. \tag{3.52}$$

To simplify the script of differential equations above, let write $A(\xi) = A$, $Z(\xi) = Z$, $T(\xi, \tau) = T$, $\rho(\xi, \tau) = \rho$. According to previous works [64, 71], let use the symmetry transformation given by Eq. (3.50) that would reduce Eq. (3.49) to the integrable Hirota equation in the form [116]

$$i\frac{\partial V}{\partial Z} = -\frac{\partial^2 V}{\partial T^2} + G|V|^2 V + 2\sqrt{2}i\nu \left(\frac{\partial^3 V}{\partial T^3} + 3|V|^2\frac{\partial V}{\partial T}\right). \tag{3.53}$$

In the case of rogue waves finding, we take $G = -1$. The parameter ν is a real constant. With $V[Z(\xi), T(\xi, \tau)]$ satisfying the relation (3.53), the similarity reduction of Eqs. (3.51) and (3.52) leads to

$$\gamma(\xi) T_\tau T_{\tau\tau} = 0, \tag{3.54}$$

$$\varphi(\xi) T_{\tau\tau} + 3\gamma(\xi) (T_{\tau\tau} \rho_\tau + T_\tau \rho_{\tau\tau}) = 0, \tag{3.55}$$

$$\mp D(\xi) + \rho_\xi + \varphi(\xi) \rho_\tau{}^2 + \gamma(\xi) \left(\rho_\tau{}^3 - \rho_{\tau\tau\tau}\right) = 0, \tag{3.56}$$

$$A_\xi + A(\varphi(\xi) \rho_{\tau\tau} + 3\gamma(\xi) \rho_{\tau\tau} \rho_\tau + \mu(\xi)) = 0, \tag{3.57}$$

$$T_\xi + T_\tau \rho_\tau - \gamma(\xi)\left(T_{\tau\tau} - 3T_\tau \rho_\tau{}^2\right) = 0, \tag{3.58}$$

$$Z_\xi + T_\tau{}^2\left(\varphi(\xi) + 3\gamma(\xi)\rho_\tau\right) = 0, \tag{3.59}$$

$$\gamma(\xi)T_\tau{}^3 + 2\sqrt{2}\nu Z_\xi = 0, \tag{3.60}$$

$$A^2\left(C(\xi) + \alpha_3(\xi)\rho_\tau\right) + GZ_\xi = 0, \tag{3.61}$$

$$\alpha_3(\xi)A^2 T_\tau - 6\sqrt{2}\nu Z_\xi = 0. \tag{3.62}$$

Here, the subscripts ξ and τ, denote spatial and temporal derivatives, respectively.

3.3.3 First-and second-order of the chiral nonlinear Schrödinger equation with variable and constant coefficients

The resolution of the system $(3.54) - (3.62)$ yields for $\gamma(\xi) \neq 0$ and $T_\tau T_{\tau\tau} = 0$ to the similarity variable

$$T(\xi, \tau) = T_1(\xi)\tau + T_0(\xi), \tag{3.63}$$

where $T_{1_\xi}(\xi) = 0$. The substitution of Eq. (3.63) into Eq. (3.55) tends to $3\gamma(\xi)T_\tau \rho_{\tau\tau} = 0$. As $\gamma(\xi) \neq 0$, $T_1(\xi) \neq 0$ and $\rho_{\tau\tau} = 0$, the phase can be written as

$$\rho(\xi, \tau) = \rho_1(\xi)\tau + \rho_0(\xi), \tag{3.64}$$

where $\rho_{1_\xi}(\xi) = 0$.

From Eq. (3.60), the effective propagation distance $Z(\xi)$ will be

$$Z(\xi) = -\frac{\sqrt{2}}{4\nu}\int_0^\xi \gamma(s)T_1(s)^3 ds. \tag{3.65}$$

Equation (3.59) stands for

$$\varphi(\xi) = -\gamma(\xi)\left(3\rho_1(\xi) - \frac{T_1(\xi)}{2\sqrt{2}\nu}\right). \tag{3.66}$$

Through Eq. (3.58), one arrives at

$$\gamma(\xi) = -\left(\frac{T_{0_\xi}(\xi) + T_1(\xi)\rho_1(\xi)}{3T_1(\xi)\rho_1{}^2(\xi)}\right). \tag{3.67}$$

Relation (3.57) is transformed to

$$A(\xi) = A_0 \exp\left\{-\int_0^\xi \mu(s)ds\right\}, \tag{3.68}$$

where, A_0 is a constant. The result coming from Eq. (3.58), is out to be

$$\mp D(\xi) = -\left\{\gamma(\xi)\rho_1{}^2(\xi)\left(2\rho_1(\xi) - \frac{T_1(\xi)}{2\sqrt{2}\nu}\right) - \rho_{0_\xi}(\xi)\right\}, \tag{3.69}$$

with $D_-(\xi) = -D_+(\xi)$. Equation (3.62) gives the result

$$\alpha_3(\xi) = -3\gamma(\xi)T_1{}^2(\xi)A^{-2}(\xi). \tag{3.70}$$

Through relation (3.61), one finds that

$$C(\xi) = \gamma(\xi)T_1{}^2(\xi)\left(3\rho_1(\xi) + \frac{GT_1(\xi)}{2\sqrt{2}\nu}\right)A^{-2}(\xi). \tag{3.71}$$

The TOD parameter $\gamma(\xi)$ is used to control the effective propagation distance $Z(\xi)$, the GVD parameter $\varphi(\xi)$, the coefficient of linear birefringence $D(\xi)$, the SS coefficient $\alpha_3(\xi)$ and the SPM nonlinearity $C(\xi)$. The gain and loss term of the induce optical activity $\mu(\xi)$ can be used to manage the optical activity on the amplitude $A(\xi)$, on the SS coefficient $\alpha_3(\xi)$ and on the SPM nonlinearity $C(\xi)$. To determine the complex field $V[Z(\xi), T(\xi, \tau)]$, the modified Darboux transformation method [24, 63, 94, 335] is used. The first-and second-order rational solutions of the Hirota equation, namely by Eq. (3.53), was recently found by Ankiewicz *et al.* [116]. They showed how to construct the hierarchy of rational solutions of the Hirota equation. According to the modified Darboux transformation, the first-and second-order rational solutions are constructed in the following paragraph.

Considering the correspondence $Z(\xi) = x$, $\frac{1}{\sqrt{2}}T(\xi, \tau) = t$ and $\nu = \alpha_3$ in the Ref. [116], the first-order of the complex field $V[Z(\xi), T(\xi, \tau)]$ leads to

$$V_1[Z(\xi), T(\xi, \tau)] = \left[1 - \frac{G_1 + iH_1}{D_1}\right]\exp\{iZ(\xi)\}, \tag{3.72}$$

where

$$G_1 = 4, \quad H_1 = 8Z(\xi), \quad D_1 = 1 + \left[\sqrt{2}T(\xi, \tau) + 12\nu Z(\xi)\right]^2 + 4Z(\xi)^2. \tag{3.73}$$

Taking into account the above correspondence, solution (3.72) is known as the Peregrine soliton [39]. Then, collecting the partial solutions together, one constructs the first-order rational solution related to the exact chiral optical rogue wave solution of Eq. (3.49)

$$\psi_1 = A(\xi)\left[1 - \frac{G_1 + iH_1}{D_1}\right]\exp\{iZ(\xi) + i\rho(\xi, \tau)\}. \tag{3.74}$$

The intensity of the first-order chiral optical rogue wave is

$$|\psi_1|^2 = A_0{}^2 \exp\left\{-2\int_0^\xi \mu(s)ds\right\}\left[\frac{\left(\left[\sqrt{2}T + 12\nu Z\right]^2 + 4Z^2 - 3\right)^2 + 64Z^2}{\left(1 + \left[\sqrt{2}T + 12\nu Z\right]^2 + 4Z^2\right)^2}\right]. \tag{3.75}$$

This first-order rational solution is used to describe the propagation of rogue wave in chiral optical fibers. We use it to show the influence of optical activity on the propagation of rogue

waves and with a suitable choice of parameters of the original Eq. (3.49), we manage the controllability of chiral optical rogue wave.

Then the second-order rational solution of the complex field $V[Z(\xi), T(\xi, \tau)]$ presented by Ankiewicz *et al.* [116] stands for

$$V_2[Z(\xi), T(\xi, \tau)] = \left[1 + \frac{G_2 + iZ(\xi)H_2}{D_2}\right] \exp i\{Z(\xi)\}, \tag{3.76}$$

where G_2, H_2 and D_2 are given by the relations

$G_2 = -48T^4 - 1152\sqrt{2}\nu ZT^3 - 144T^2[4Z^2(36\nu^2 + 1) + 1] - 576\sqrt{2}\nu ZT[12Z^2(12\nu^2 + 1) + 7]$
$-192Z^4[216(6\nu^4 + \nu^2) + 5] - 864Z^2(44\nu^2 + 1) - 36,$
$H_2 = -96T^4 - 2304\sqrt{2}\nu ZT^3 - 96T^2[4Z^2(108\nu^2 + 1) - 3] - 1152\sqrt{2}\nu ZT[4Z^2(36\nu^2 + 1)]$
$-384Z^4(36\nu^2 + 1)^2 - 192Z^2(180\nu^2 + 1) + 360,$
$D_2 = 8T^6 + 288\sqrt{2}\nu ZT^5 - 432Z^4(624\nu^4 - 40\nu^2 - 1) + 36Z^2(556\nu^2 + 11) + 9 + 64Z^6(36\nu^2 + 1)^3$
$+96\sqrt{2}ZT^3[12Z^2(60\nu^2 + 1) - 1] + 12T^4[4Z^2(180\nu^2 + 1) + 1] + 6T^2[16Z^4[216\nu^2(30\nu^2 + 1) - 1]$
$-24Z^2(60\nu^2 + 1) + 9] + 72\sqrt{2}\nu ZT[16Z^4(36\nu^2 + 1) + 8Z^2(1 - 108\nu^2) + 17].$

$$\tag{3.77}$$

According to the same correspondence of variables as for first-order, we obtain the second-order solution found by Akhmediev *et al.* [301]. Collecting the partial solutions together, we construct the final second-order rational solution related to the exact solution of Eq. (3.49)

$$\psi_2 = A(\xi)\left[1 + \frac{G_2 + iZ(\xi)H_2}{D_2}\right] \exp\{iZ(\xi) + i\rho(\xi, \tau)\}. \tag{3.78}$$

The intensity of the second-order chiral optical rogue wave solution is

$$|\psi_2|^2 = A_0{}^2 \exp\left\{-2\int_0^\xi \mu(s)ds\right\}\left[\frac{(G_2 + D_2)^2 + Z(\xi)^2 H_2{}^2}{D_2{}^2}\right]. \tag{3.79}$$

This second-order rational solution is more precise than the first one. It describes the optical activity effect on two rogue waves propagating in a chiral optical fiber as well as collisions between them. This solution is used in the next section to investigate the features of chirality on rogue wave collisions.

Now, let turn the attention to the case of chiral NLS equation with constant coefficients. Thus, the new variables of the first-and second-order rational solutions become

$$T(\xi, \tau) = T_1(\xi)\tau + T_0(\xi), \quad \rho(\xi, \tau) = \rho_1(\xi)\tau + \rho_0(\xi), \quad Z(\xi) = -\frac{\sqrt{2}\gamma}{4\nu}\int_0^\xi T_1(s)^3 ds,$$
$$A(\xi) = A_0 \exp\{-\mu\xi\}, \tag{3.80}$$

where, $T_{1_\xi}(\xi) = 0$, $\rho_{1_\xi}(\xi) = 0$ and $\mu = b_3(1 \pm KT_c)$. By taking into account the new variables above, the first-and second-order rational solutions of the chiral NLS equation with constant coefficients are given by Eq. (3.74) and Eq. (3.78), respectively. With these exact solutions, one can appreciate the influence of optical activity on rogue wave in chiral NLS equation with constant coefficients.

After the construction of the above exact solutions, their parameters are chosen to investigate the dynamics behavior and the features of chiral optical rogue waves. So doing, let alternate the sign of values in both space and time, which is required to optimize the eventual stability of the solutions.

3.3.4   Optical activity effects on rogue wave propagation

To illustrate the effect of optical activity on the propagation of rogue waves related to the first-and second-order rational solutions, free functions $T_1(\xi)$, $T_0(\xi)$, $\mu(\xi)$ and $\gamma(\xi)$ are chosen appropriately to generate abundant structures of chiral optical rogue waves. One presents managed cases, in which the choice of chiral parameter leads to the control of chiral optical rogue waves. It is noted that parameters are chosen in order to be bounded in the intervals $-15 < \xi < 15$ and $-15 < \tau < 15$. In this work, curves are plotted with the help of Matlab. Through Jacobian elliptic functions, the intensities of the first-and second-order rational solutions are used to show the influence of optical activity on the structure of chiral optical rogue waves. Their approximative formulas are given in reference by [336]

$$
\begin{aligned}
dn(z,k) &\approx 1 - \frac{k^2 \sin(z)^2}{2}, \\
cn(z,k) &\approx \cos(z) - k^2 \sin(z) \left(\frac{z - \sin(z)\cos(z)}{4} \right), \\
sn(z,k) &\approx \sin(z) - k^2 \cos(z) \left(\frac{z - \sin(z)\cos(z)}{4} \right).
\end{aligned}
\tag{3.81}
$$

(a)   (b)
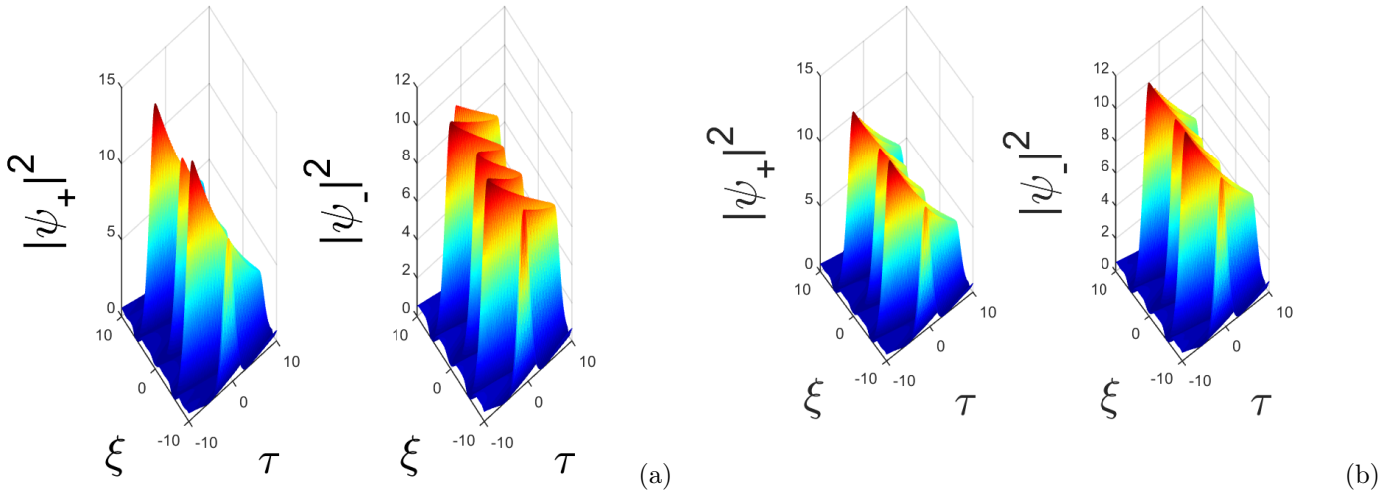
Figure 35: First-order chiral optical rogue waves on the left-and right-hand side with variable coefficients, where the parameters are (a) $T_c = 0.5$; (b) $T_c = 0.1$; with $b_1 = 0.2$, $K = 1$, $b_3 = 0.1$, $\nu = 0.6$, $k_3 = 0.6$, $k_4 = 0.9$, $T_1(\xi) = \sqrt{2}b_1$, $T_0(\xi) = cn(\xi, k_4)$, $\gamma(\xi) = k_3{}^2 sn(\xi, k_3) cn(\xi, k_3)$ in each case and $\mu(\xi) = b_3(1 - KT_c) sn(\xi, k_4) dn(\xi, k_4)$ for the left-hand intensity $|\psi_-|^2$ and $\mu(\xi) = b_3(1 + KT_c) sn(\xi, k_4) dn(\xi, k_4)$ for the right-hand intensity $|\psi_+|^2$.

To generate more stable chiral optical rogue wave, one uses the Jacobian elliptic functions which are responsible for the snaker form of waves as seen in Figs. 35, Figs. 36 and Figs. 37, where $|\psi_-|^2$ and $|\psi_+|^2$ are chiral optical rogue waves in the left-and right-hand side, respectively. It is observed through these figures that when the chiral parameter T_c is weak, the waves in both
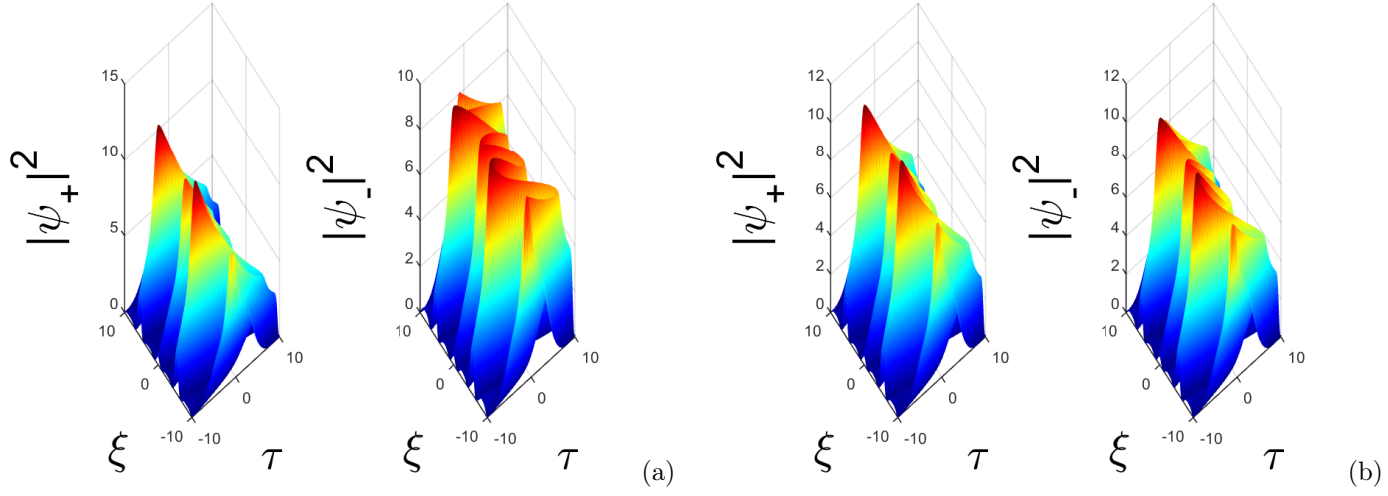
Figure 36: Second-order chiral optical rogue waves on the left-and right-hand side with variable coefficients, where the parameters are (a) $T_c = 0.5$; (b) $T_c = 0.1$; with $b_1 = 0.2$, $K = 1$, $b_3 = 0.1$, $\nu = 0.6$, $k_3 = 0.6$, $k_4 = 0.9$, $T_1(\xi) = \sqrt{2}b_1$, $T_0(\xi) = cn\,(\xi, k_4)$, $\gamma\,(\xi) = k_3{}^2 sn\,(\xi, k_3)\, cn\,(\xi, k_3)$ in each case and $\mu(\xi) = b_3\,(1 - KT_c)\, sn\,(\xi, k_4)\, dn\,(\xi, k_4)$ for the left-hand intensity $|\psi_-|^2$ and $\mu(\xi) = b_3\,(1 + KT_c)\, sn\,(\xi, k_4)\, dn\,(\xi, k_4)$ for the right-hand side intensity $|\psi_+|^2$.
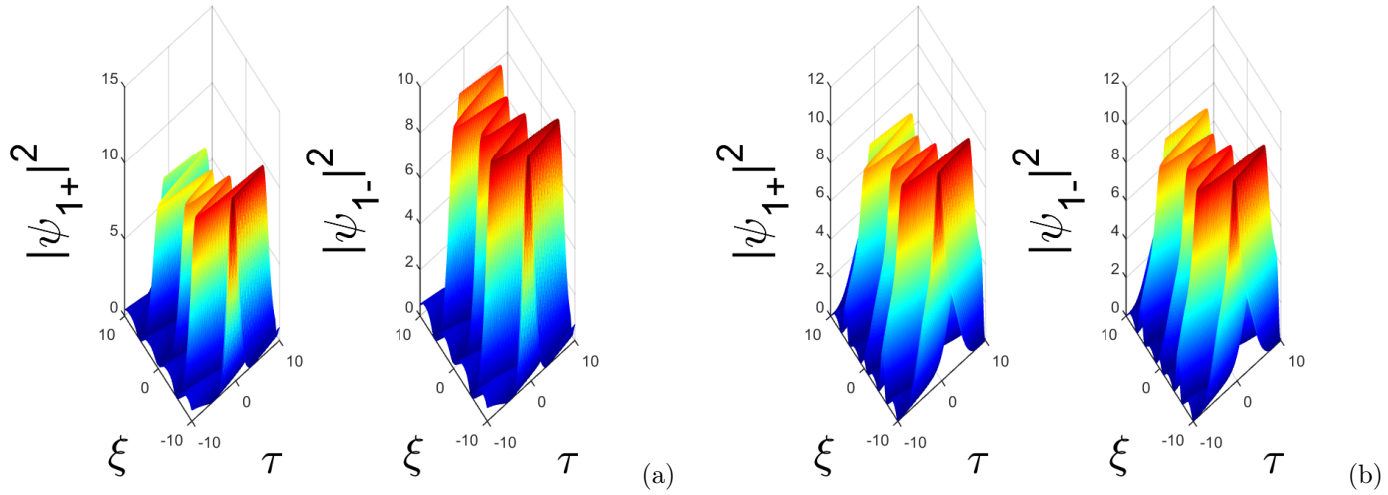
Figure 37: First(a)-and second (b)-order chiral optical rogue waves on the right-and left-hand side with constant coefficients, where parameters are (a) $T_c = 0.5$; (b) $T_c = 0.1$; with $b_1 = 0.2$, $K = 1$, $b_3 = 0.01$, $\nu = 0.6$, $\gamma = 0.03$, $k_4 = 0.9$, $T_1(\xi) = \sqrt{2}b_1$, $T_0(\xi) = cn\,(\xi, k_4)$ in each case and $\mu = b_3\,(1 - KT_c)$ for the left-hand intensity $|\psi_-|^2$ and $\mu = b_3\,(1 + KT_c)$ for the right-hand intensity $|\psi_+|^2$.

hands have the same form [Figs. 35(b) , Figs. 36(b) and Figs. 37(b)] and the same amplitude [Figs. 36(b) and Figs. 37(b)]. One notices that the increase of chiral parameter reveals a notable difference on the form of waves between the left-and right-hand intensities [see Figs. 35(a), Figs. 36(a) and Figs. 37(a)]. One denotes that the second-order solutions [Figs. 36 and Figs. 37(b)] with more curvatures than the first-order solutions [Figs. 35 and Figs. 37(a)] and this, in addition to the coefficients with management, yield a more accurate study of the influence of the optical activity on rogue waves. As conclusion the increase of the right-hand intensities and the decrease of the left-hand intensities are slightly due to the order of the solution and highly caused by the increase of the optical activity [see Figs. 36 and Figs. 37]. The exchange of energy observe here is also due to the two-wave mixing (TWM) effect. The main difference between parameters of Figs. 35-37 depends on the order of rational solutions through the parameters G_i, H_i and D_i (i=1, 2). The parameters G_1, H_1 and D_1 given in Eq. (3.73) have been used to construct the first-order rational solution (3.74) while G_2, H_2 and D_2 given in Eq. (3.77) have been used to construct the second-order rational solution (3.78) and where the parameters μ and γ depend on the variable ξ in Figs. 35 and Figs. 36. In contrast to Figs. 37, where the first-and second-order rational solutions are constructed with parameters μ and γ taken as constants. To perform this study, the chiral CNLS equations is used in what follows.

3.4 Chiral optical vector rogue waves in coupled nonlinear Schrödinger equation with coupled space-dependance coupling field

3.4.1 Model

From the model obtained in Eq. (3.46), the coupled system of NLS equation in chiral optical fibers with coupled space-dependence coupling field is given by

$$i\psi_{1\xi} + \varphi\psi_{1\tau\tau} - i\gamma\psi_{1\tau\tau\tau} + i\mu\psi_1 \mp D\psi_1 - \left(C_1|\psi_1|^2 + C|\psi_2|^2\right)\psi_1 + i\alpha_3|\psi_1|^2\psi_{1\tau} - \beta(\xi)\psi_2 = 0,$$
$$i\psi_{2\xi} + \varphi\psi_{2\tau\tau} - i\gamma\psi_{2\tau\tau\tau} + i\mu\psi_2 \mp D\psi_2 - \left(C|\psi_1|^2 + C_2|\psi_2|^2\right)\psi_2 + i\alpha_3|\psi_2|^2\psi_{2\tau} - \beta(\xi)\psi_1 = 0,$$
$$(3.82)$$

where the last term $\beta(\xi)$ describes the coupling between mixed polarizations. As we consider an isotropic medium with circular polarization and linear birefringence, the presence of FWM becomes implicit through the reference changing [see Appendix (A7)] whereas the SPM terms $(C_1|\psi_1|^2\psi_1; C_2|\psi_2|^2\psi_2)$ and XPM terms $(C|\psi_1|^2\psi_2; C|\psi_2|^2\psi_1)$ can be identified in the above model. In fact, C_1 and C_2 are SPM nonlinearities (interactions) and C is the XPM nonlinearity (interactions). The FWM in this coupled system of equations should be responsible for the exchange of energy between components.

The study is based on the theory of determinant of the nonlinear coefficients in the form [24]

$$\Delta = C_1C_2 - C^2,$$
$$(3.83)$$

which determines the thermodynamic instability of the system. To reduce the number of figures, one chooses only one value of the chiral parameter $T_c = 0.5$ and the case where the SPM interactions have the same signs of the scattering length, i.e. when $C_1C_2 > 0$ or the opposite

signs.

3.4.2 Chiral optical rogue waves in the case: $\Delta = 0$

A. First case: $\Delta = 0 \quad and \quad CC_{1,2} > 0$

In this case, the XPM and SPM interactions are either focusing or defocusing. For mixed polarizations of two different kinds, $\beta(\xi) \equiv 0$. To simplify the evaluation of this coupled system, one deduces the compact form from the Manakov system as follows [354]

$$iu_\xi + \varphi u_{\tau\tau} - i\gamma u_{\tau\tau\tau} + i\mu u \mp Du - Cu^+ uu + i\alpha_3 u^+ u_\tau = 0. \tag{3.84}$$

where $u = \begin{pmatrix} u_1 \\ u_2 \end{pmatrix}$ and $C_1 = C_2 = C$.

The SU(2) rotations are defined by two matrices as

$$R_0 = \begin{pmatrix} \cos\alpha & \sin\alpha \\ -\sin\alpha & \cos\alpha \end{pmatrix}, \quad R_1 = \begin{pmatrix} e^{iB(\xi)} & -e^{-iB(\xi)} \\ e^{iB(\xi)} & e^{-iB(\xi)} \end{pmatrix}, \tag{3.85}$$

where α is a constant and $B(\xi)$, the real function write down in the form $B(\xi) = -\int \beta(\xi)d\xi$. Let define $\psi = R_1 R_0 u$ and for the invariant norm i.e. $u^+ u = \psi^+ \psi$, the evolution equation yields

$$i\psi_\xi + \varphi\psi_{\tau\tau} - i\gamma\psi_{\tau\tau\tau} + i\mu\psi \mp D\psi - C\psi^+ \psi\psi + i\alpha_3 \psi^+ \psi_\tau - \beta(\xi)\sigma_1\psi = 0, \tag{3.86}$$

where $\sigma_j (j = 1, 2, 3)$ are the standard Pauli matrices. To construct the rational solution of Eq. (3.84), let choose it in the form of one component chiral optical rogue wave as

$$u = \Psi(\xi, \tau) \begin{pmatrix} 1 \\ 0 \end{pmatrix}, \quad where$$
$$\Psi(\xi, \tau) = \frac{A_0}{\sqrt{-C}} \left[1 - \frac{4 + i8Z(\xi)}{1 + \left[\sqrt{2}T(\xi,\tau) + 12\nu Z(\xi) \right]^2 + 4Z(\xi)^2} \right] \exp\{-\mu\xi\} \exp\{iZ(\xi) + i\rho(\xi, \tau)\}, \tag{3.87}$$

which is valid for $C < 0$, and where the variables are

$$T(\xi, \tau) = T_1(\xi)\tau + T_0(\xi), \quad \rho(\xi, \tau) = \rho_1(\xi)\tau + \rho_0(\xi), \quad Z(\xi) = -\frac{\sqrt{2}\gamma}{4\nu} \int_0^\xi T_1(s)^3 ds, \tag{3.88}$$

with $\mu = b_3 (1 \pm KT_c)$, $T_0(\xi) = cn(\xi, k_2)$, $T_1(\xi) = dn(\xi, k_1)$, $\rho_0(\xi) = sn(\xi, k_4)$ and $\rho_1(\xi) = cn(\xi, k_3)$. The above solution helps us to obtain a parametric family of chiral optical rogue wave solutions of Eq. (3.86) in the form

$$\psi = \frac{1}{\sqrt{-2C}} \Psi(\xi, \tau) \begin{pmatrix} \cos\alpha e^{iB(\xi)} + \sin\alpha e^{-iB(\xi)} \\ \cos\alpha e^{iB(\xi)} - \sin\alpha e^{-iB(\xi)} \end{pmatrix}. \tag{3.89}$$

The varying parameters $T_1(\xi)$ and $\rho_1(\xi)$ in this section, excite complex structures which may be useful to control the propagation of chiral optical vector rogue waves.

B. Second case: $\Delta = 0 \quad and \quad CC_{1,2} < 0$

Here, the scattering lengths of the XPM and SPM interactions have the same signs and this allows us to let $\beta(\xi) \equiv 0$. Therefore, Eqs. (3.82) are reduced to

$$
\begin{aligned}
iw_{1\xi} + \varphi w_{1\tau\tau} - i\gamma w_{1\tau\tau\tau} + i\mu w_1 \mp Dw_1 - C\left(|w_1|^2 - |w_2|^2\right)w_1 + i\alpha_3|w_1|^2 w_{1\tau} = 0, \\
iw_{2\xi} + \varphi w_{2\tau\tau} - i\gamma w_{2\tau\tau\tau} + i\mu w_2 \mp Dw_2 - C\left(|w_2|^2 - |w_1|^2\right)w_2 + i\alpha_3|w_2|^2 w_{2\tau} = 0,
\end{aligned}
\tag{3.90}
$$

where $w = \begin{pmatrix} w_1 \\ w_2 \end{pmatrix}$. The compact form of Eqs. (3.90) is given by

$$
iw_\xi + \varphi w_{\tau\tau} - i\gamma w_{\tau\tau\tau} + i\mu w \mp Dw - C\left(w^+\sigma_3 w\right)\sigma_3 w + i\alpha_3\left(w^+\sigma_3 w\right)\sigma_3 w_\tau = 0.
\tag{3.91}
$$

For the defined unitary matrices

$$
P_0 = \begin{pmatrix} \cosh\alpha & \sinh\alpha \\ -\sinh\alpha & \cosh\alpha \end{pmatrix}, \quad P_1 = \begin{pmatrix} \sinh\alpha & \cosh\alpha \\ \cosh\alpha & \sinh\alpha \end{pmatrix},
\tag{3.92}
$$

let generate the wave function $\psi = P_j w$ $(j = 0, 1)$ which will solve the system

$$
\begin{aligned}
i\psi_{1\xi} + \varphi\psi_{1\tau\tau} - i\gamma\psi_{1\tau\tau\tau} + i\mu\psi_1 \mp D\psi_1 - (-1)^j C\left(|\psi_1|^2 - |\psi_2|^2\right)\psi_1 + i\alpha_3|\psi_1|^2\psi_{1\tau} = 0, \\
i\psi_{2\xi} + \varphi\psi_{2\tau\tau} - i\gamma\psi_{2\tau\tau\tau} + i\mu\psi_2 \mp D\psi_2 - (-1)^j C\left(|\psi_1|^2 - |\psi_2|^2\right)\psi_2 + i\alpha_3|\psi_2|^2\psi_{2\tau} = 0.
\end{aligned}
\tag{3.93}
$$

The use of a given value for the constant α in the unitary matrixes can reduce the coupled systems (3.93) to (3.90) for $|w_1|^2 = |w_2|^2$. This imply that the system is purely linear and as consequence, this case can not support chiral optical vector rogue waves of the type $\psi_1 \approx \psi_2$.

3.4.3 Chiral optical vector rogue waves in the case: $\Delta \neq 0$

A. Modulation instability and condition of unstable background

Let start the study on the case $\Delta \neq 0$ with two polarized electromagnetic waves without linear coupling. One considers $\beta(\xi) \equiv 0$ in the coupled systems (3.82). As the solution of one component chiral optical rogue wave is known, one can deduce an analog form for two components as follows [24]

$$
\begin{aligned}
\psi_1(\xi, \tau) &= a_1 \Psi(\xi, \tau), \\
\psi_2(\xi, \tau) &= a_2 \Psi(\xi, \tau)\exp(i\delta),
\end{aligned}
\tag{3.94}
$$

where $\Psi(\xi, \tau)$ is given in relation (3.87), δ, the constant phase mismatch, a_1 and a_2 are the amplitudes which yield

$$
a_1{}^2 = \frac{C - C_2}{\Delta}, \quad a_2{}^2 = \frac{C - C_1}{\Delta}.
\tag{3.95}
$$

Here, we let

$$
C = \pm 1, \; C_1 = d_1 \pm KT_c, \; C_2 = d_2 \pm KT_c,
\tag{3.96}
$$

where C and $C_{1,2}$ are XPM and SPM nonlinearities and $d_{1,2}$ the arbitrary constants. Relation (3.95) is the condition for the existence of the synchronized vector rogue waves. The solution (3.94) obtained in two components, describes the propagation of vector rogue waves in chiral

optical fibers. It is well-known that a rogue wave is generated by an unstable background and in order to transform the background solution to become unstable, one sets $\left(\psi_1^{(0)}, \psi_2^{(0)}\right) = (a_1, a_2)$. By so doing, the solution of Eqs. (3.82) is chosen in the form of weakly modulated constant background [24, 44]

$$\psi_j\left(\xi, \tau\right) = [a_j + \alpha_j \exp(iK\xi - i\omega\tau) + \beta_j \exp\left(-iK\xi + i\omega\tau\right)] \exp[-i\left(C_j a_j{}^2 + C a_{3-j}{}^2\right)\tau], \tag{3.97}$$

where a_j is a constant background, α_j and β_j, the amplitudes of the two components, K is the wave number and ω the frequency. Here, we suppose that $\alpha_j, \beta_j << a_j (j = 1, 2)$.

B. Existence of vector rogue waves

The substitution of solution (3.97) into the coupled systems (3.82) gives after the linearizing with respect to α_j and β_j, the dispersion relation

$$\begin{aligned}
&\gamma^2\omega^6 - \gamma\left(\eta_1 + \eta_2\right)\omega^5 + [\eta_1\eta_2 - \gamma\left(\beta_1 + \beta_2\right)]\omega^4 + [\beta_1\eta_2 + \beta_2\eta_1 - \gamma\left(\alpha_1 + \alpha_2\right)]\omega^3 \\
&+(\beta_1\beta_2 + \eta_1\alpha_2 + \eta_2\alpha_1)\omega^2 + \left(\beta_1\alpha_2 + \beta_2\alpha_1\right)\omega + \alpha_1\alpha_2 - 4a_1{}^2 a_2{}^2 C^2 = 0,
\end{aligned} \tag{3.98}$$

where the parameters are

$$\begin{aligned}
\phi_{12} &= C_1 a_1{}^2 + C a_2{}^2, \quad \phi_{22} = C_2 a_2{}^2 + C a_1{}^2, \\
\eta_1 &= \varphi - 3\gamma\phi_{12}, \quad \eta_2 = \varphi - 3\gamma\phi_{22}, \\
\beta_1 &= \phi_{12} + 3i\gamma\phi_{12}{}^2 - \alpha a_1{}^2, \quad \beta_2 = \phi_{22} + 3i\gamma\phi_{22}{}^2 - \alpha a_2{}^2, \\
\alpha_1 &= K + \gamma\phi_{12}{}^3 - i\mu \mp D - i\varphi\phi_{12}{}^2 + 2C_1 a_1{}^2 - 3\alpha\phi_{12}a_1{}^2 + \phi_{12}, \\
\alpha_2 &= K + \gamma\phi_{22}{}^3 - i\mu \mp D - i\varphi\phi_{22}{}^2 + 2C_2 a_2{}^2 - 3\alpha\phi_{22}a_2{}^2 + \phi_{22}.
\end{aligned} \tag{3.99}$$

Between the roots of the polynomial given in Eq. (3.98), one should have at least one imaginary root ω to obtain an unstable background and this can be possible under the conditions $C_{1,2} < 0$ or $\Delta < 0$. Thus, Eq. (3.98) is the condition of modulational instability of the background.

3.4.4 Stable and unstable branches of chiral optical rogue waves

For some specific set of parameters given in Figs. 38-42 captions, let determine the stable and unstable branches of chiral optical rogue waves and indirectly, the existence of vector rogue waves through the dispersion relation given by Eq. (3.98). All the possible cases for the same and opposite signs of SPM and XPM nonlinearities are analyzed in table 2.

Table 2: Occurrence of modulation instability and chiral vector rogue waves for mixed cases of SPM and XPM interactions.

SPM interactions	XPM interactions	Unstable Branches	Stable Branches	Chiral vector rogue waves
$C_{1,2} < 0$	$-: C > C_{1,2}, \Delta > 0$ $+: C < C_{1,2}, \Delta < 0$	$-: 4$ $+: 4$	$-: 2$ $+: 2$	$-: exist$ $+: not$ $exist$
	$-: |C| < |C_{1,2}|, \Delta > 0$ $+: |C| < |C_{1,2}|, \Delta > 0$	$-: 4$ $+: 4$	$-: 2$ $+: 2$	$-: exist$ $+: exist$
	$-: C < |C_{1,2}|, \Delta > 0$ $+: C > |C_{1,2}|, \Delta < 0$	$-: 4$ $+: 4$	$-: 2$ $+: 2$	$-: not$ $exist$ $+: not$ $exist$
$C_{1,2} > 0$	$-: C > C_{1,2}, \Delta < 0$ $+: C < C_{1,2}, \Delta > 0$	$-: 4$ $+: 3$	$-: 2$ $+: 3$	$-: not$ $exist$ $+: not$ $exist$
	$-: |C| > C_{1,2}, \Delta < 0$ $+: |C| < C_{1,2}, \Delta > 0$	$-: 4$ $+: 4$	$-: 2$ $+: 2$	$-: exist$ $+: not$ $exist$
	$-: C < -C_{1,2}, \Delta < 0$ $+: C > -C_{1,2}, \Delta > 0$	$-: 3$ $+: 3$	$-: 3$ $+: 3$	$-: exist$ $+: not$ $exist$
$C_1 < 0, C_2 > 0$	$-: C < C_{1,2}, \Delta < 0$ $+: C < C_{1,2}, \Delta < 0$	$-: 5$ $+: 4$	$-: 1$ $+: 2$	$-: not$ $exist$ $+: exist$

3.5 Chiral vector rogue waves with mixed polarization in chiral optical fiber

3.5.1 Chiral optical rogue waves on mixed polarization without linear coupling

A. Case of focusing XPM and SPM interactions $(C, C_{1,2} < 0)$

We first consider the case where the focusing XPM and SPM interactions are focusing, i.e. C, $C_{1,2} < 0$. Under this consideration, the initial conditions given in the form of exact solution in relation (3.94), induce the excitation of chiral optical vector rogue waves in the left-and right-hand side [see Figs. 38(a) and 38(b)]. To show how sensitive is the evolution of chiral optical rogue wave, let choose another initial conditions with slightly difference on the amplitude. Therefore, one obtains chiral optical vector rogue waves in each hand, where one remarks a weak amplitude in the first components and significant one, in the second components [see Figs. 38(c) and 38(d)]. In this regard, vector rogue waves most exist in Figs. 38(a) and 38(b) whereas they do not exist in Figs. 38(c) and 38(d). This weak appearance of chiral optical rogue waves in the first components can be understood if we suppose that $|\psi_1|^2 << |\psi_2|^2$. In consequence, the function ψ_1 on each hand can be considered as a linear wave-function localizes around the minima of the trap potential $U = -|\psi_2|^2$, created by the second component ψ_2, localized around the maxima of the potential barrier. one can conclude that the second components have a self-focusing character that protect them from destructive action of the optical lattice (trapping potential) whereas the first components, exposed to the self-defocusing character of the potential barriers are trapped in the lattice. Fortunately, it would remained one component

in each side in the chiral optical fiber and the transport of information by two components can always takes place.
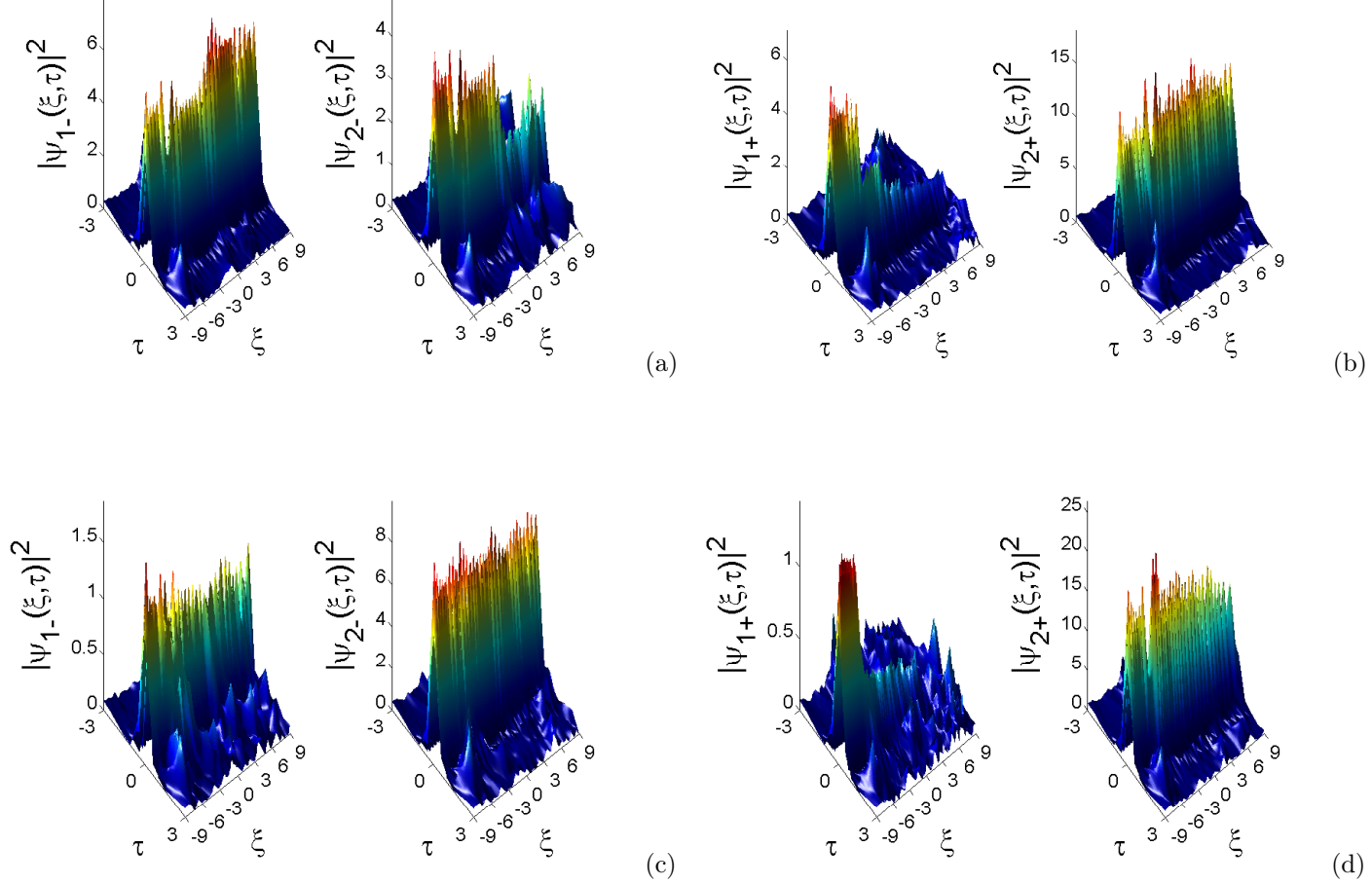
Figure 38: Chiral optical vector rogue waves of the right-and left-hand intensity $|\psi_{1,2}(\xi,\tau)|^2$ where the parameters are for (a) and (c) $C_1 = -1.6$, $C_2 = -1.8$, $\Delta > 0$, $\mu = b_3\left(1 - KT_c\right)$; for (b) and (d) $C_1 = -0.6$, $C_2 = -0.8$, $\Delta < 0$, $\mu = b_3\left(1 + KT_c\right)$; with $K = 1$, $T_c = 0.5$, $d_1 = -1.1$, $d_2 = -1.3$, $\alpha 3 = 0.2$, $\gamma = 0.02$, $D = 0.6$, $k_1 = 0.4$, $k_2 = k_4 = 0.6$, $k_3 = 0.5$, $b_3 = 0.01$ and $C = -1$ in each case. At $\xi = -9$, the initial condition takes the form of exact solutions (3.87) with $\delta = 0$ for (a) and (b) then $\psi_1 = \left(a_1{}^2 - 0.3\right)^{1/2}\Psi\left(\xi,\tau\right)$, $\psi_2 = \left(a_1{}^2 + 0.3\right)^{1/2}\Psi\left(\xi,\tau\right)$ for (c) and (d).

3.5.2 Case of focusing $(C < 0)$ and defocusing $(C > 0)$ nature of the cross-phase modulation with focusing self-phase modulation nonlinearity $(C_{1,2} < 0)$

Now, let consider the case depicted in Figs. 39 where a comparison is made between the focusing $(C < 0)$ and the defocusing $(C > 0)$ nature of the XPM nonlinearity with the focusing SPM nonlinearities $C_{1,2} < 0$. It is observed in the mixed case of the defocusing nature of the XPM and focusing SPM nonlinearities that the amplitudes are much higher [see Figs. 39(c) and 39(d)] than the ones observed in the unmixed case of defocusing XPM and SPM nonlinearities [see

Figs. 39(a) and 39(b)]. An interesting phenomenon occurs on the right-hand [Figs. 39(d)] and it can be seen that the components have the same amplitude and the second one is similar to the usual rogue waves which are localized both in space and time. This special aspect of chiral optical rogue waves, that is, to send two signals through a vector of rogue waves with the same frequency, can help in optic communication domain.
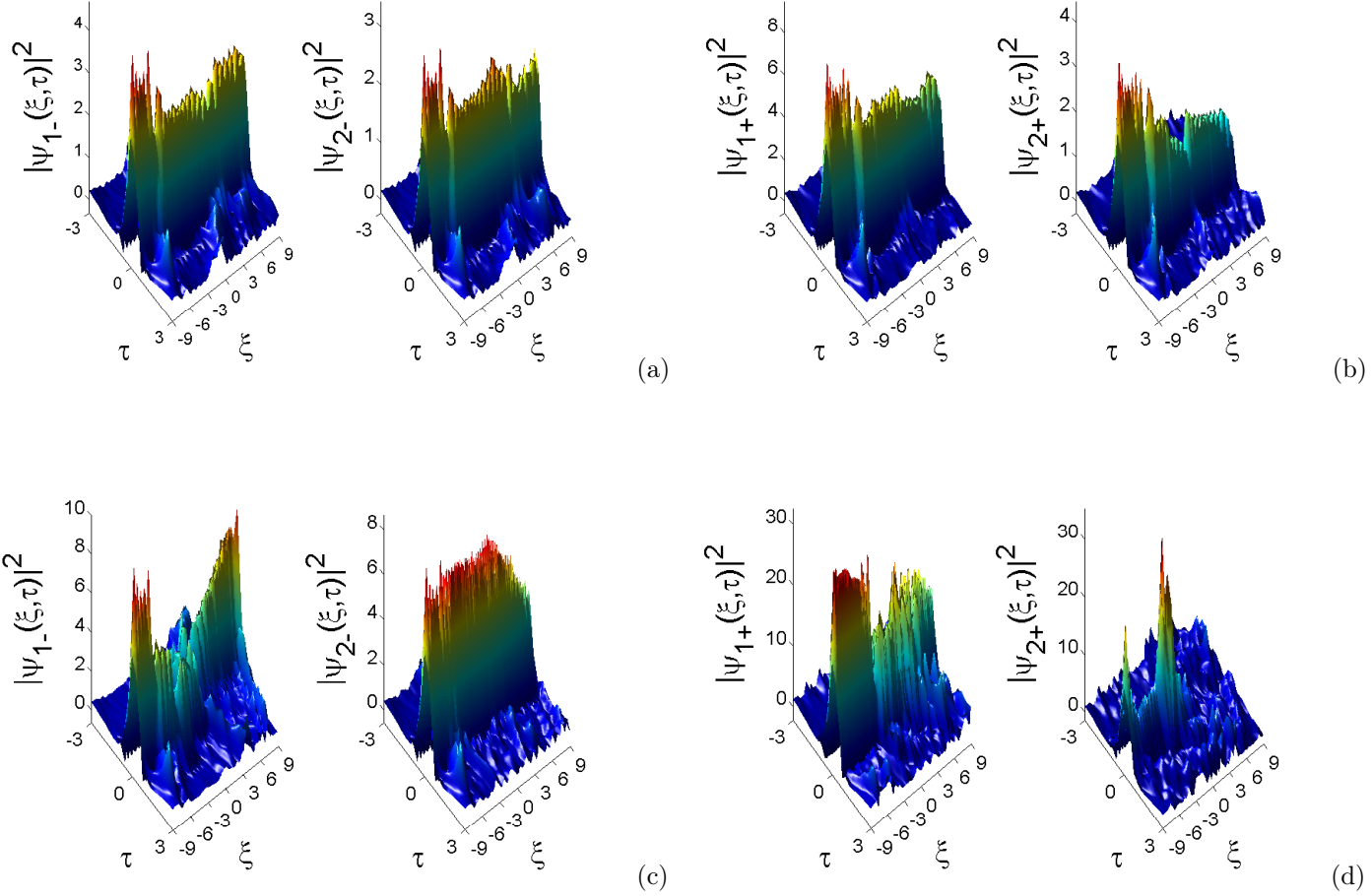
Figure 39: Chiral optical vector rogue waves of the right-and left-hand intensity $|\psi_{1,2}(\xi,\tau)|^2$ where the parameters are for (a) and (c) $C_1 = -2.5$, $C_2 = -3.0$, $\Delta > 0$, $\mu = b_3(1 - KT_c)$; for (b) and (d) $C_1 = -1.5$, $C_2 = -2.0$, $\Delta < 0$, $\mu = b_3(1 + KT_c)$; with $K = 1$, $T_c = 0.5$, $d_1 = -2$, $d_2 = -2.5$, $\alpha_3 = 0.2$, $\gamma = 0.02$, $D = 0.6$, $k_1 = 0.4$, $k_2 = k_4 = 0.6$, $k_3 = 0.5$ and $b_3 = 0.01$ in each case; $C = -1$ for (a) and (b); $C = 1$ for (c) and (d). At $\xi = -9$, the initial condition takes the form of exact solutions (3.87) with $\delta = 0$.

3.5.3 Focusing $(C_1 < 0)$ and defocusing $(C_2 > 0)$ self-phase modulation interactions with focusing cross-phase modulation $(C < 0)$

When one choose focusing $(C_1 < 0)$ and defocusing $(C_2 > 0)$ SPM interactions with focusing XPM interactions, the inverse situation observed in Figs. 38(c) and 38(d) occurs in Figs.

40 where the self-focusing character of the first component, ten time more higher than the amplitude of the linear wave function ψ_2, created a trap potential $U = -|\psi_1|^2$ that trap the second component in the lattice. Because of the nonexistence of the left-hand chiral optical rogue waves, this other aspect can help to guide waves in the right-hand side only.
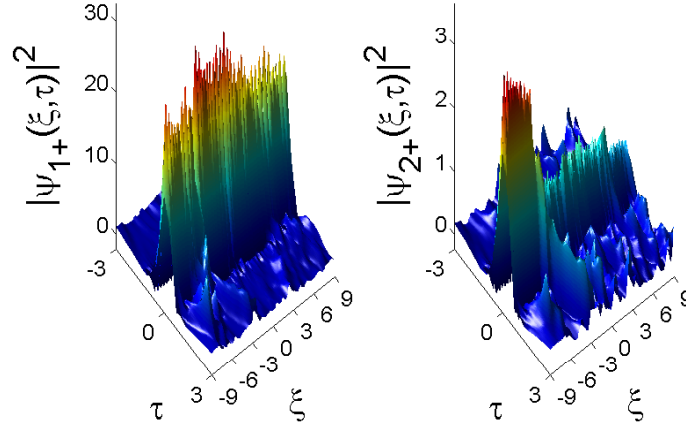
Figure 40: Non existence of chiral optical vector rogue waves of the left-hand and existence of the right-hand intensity $|\psi_{1,2}(\xi,\tau)|^2$ where the parameters are $C_1 = -0.6$, $C_2 = 1.5$, $\Delta < 0$ and $\mu = b_3(1 + KT_c)$ on the right-hand and $C_1 = -1.6$, $C_2 = 0.5$, $\Delta < 0$ and $\mu = b_3(1 - KT_c)$ on the left-hand; with $K = 1$, $T_c = 0.5$, $d_1 = -1.1$, $d_2 = 1$, $\alpha_3 = 0.2$, $\gamma = 0.02$, $D = 0.6$, $k_1 = 0.4$, $k_2 = k_4 = 0.6$, $k_3 = 0.5$, $C = -1$ and $b_3 = 0.01$ in each case. At $\xi = -9$, the initial condition takes the form of exact solutions (3.87) with $\delta = 0$.

3.5.4 Equal self-phase modulation nonlinearities $(C_1 = C_2)$ with defocusing cross-phase modulation $(C > 0)$

Now, one decides to generate chiral optical rogue wave in the form of one component with equal SPM interactions which are either defocusing $C_{1,2} > 0$ or focusing $C_{1,2} < 0$ with defocusing XPM interactions $C > 0$.With slightly excitation in the second component as depicted in Figs. 41, one remarks that the amplitudes of the second components are too weak in such a way that one can say, they do no exist and consequently that, there is not chiral optical vector rogue waves in both left-and right-hand side.Finally, we can confirm that the defocusing nature of the XPM is responsible for the generation of holes or chiral optical dark rogue waves in the second components and to the unperturbed rogue waves or bright chiral optical rogue waves in the first components. In summary, one can construct a bright-dark vector of rogue waves in chiral optical fiber.
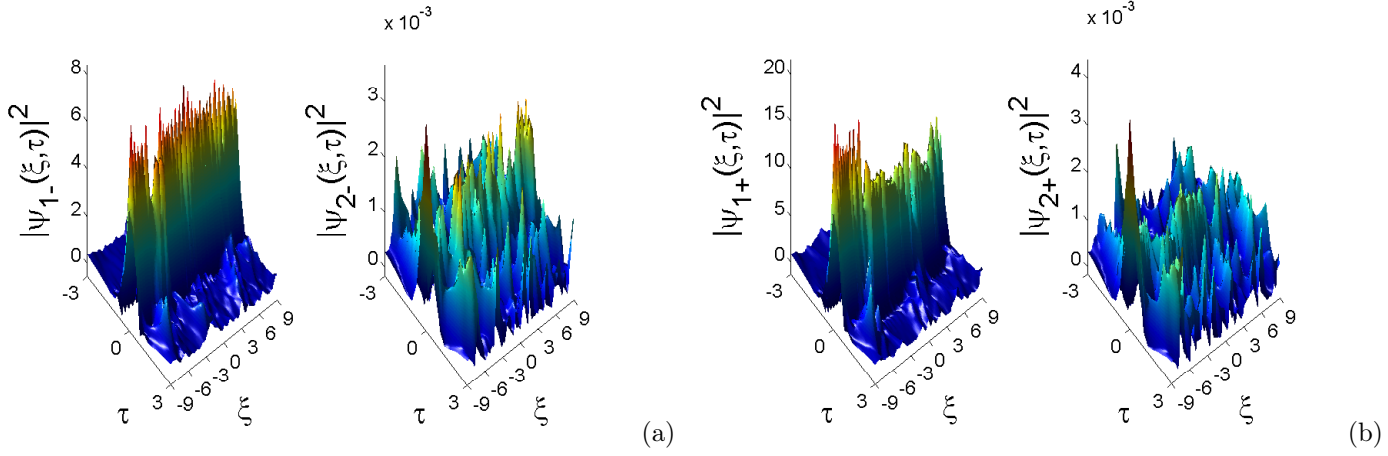
Figure 41: Chiral optical vector rogue waves of the right-and left-hand intensity $|\psi_{1,2}(\xi,\tau)|^2$ where the parameters are $C_1 = C_2 = 1.96$, and $\mu = b_3 (1 - KT_c)$ on the left-hand and $C_1 = C_2 = -0.96$ and $\mu = b_3 (1 + KT_c)$ on the right-hand; with $K = 1$, $T_c = 0.5$, $d_1 = d_2 = -1.46$ $\alpha_3 = 0.2$, $\gamma = 0.02$, $D = 0.6$, $k_1 = 0.4$, $k_2 = k_4 = 0.6$, $k_3 = 0.5$, $b_3 = 0.01$ and $C = 1$; then $\psi_1 = (-C_1)^{-1/2} \Psi(\xi,\tau)$ and $\psi_2 = 0.02\Psi(\xi,\tau)$ in each case at the origin space $\xi = -9$.

3.5.5 Case of defocusing interactions of self-phase modulation nonlinearities ($C_{1,2} > 0$) with focusing interaction of cross-phase modulation nonlinearity ($C < 0$)

Let consider now the case of defocusing interactions of the SPM nonlinearities ($C_{1,2} > 0$) with focusing interactions of XPM nonlinearity ($C < 0$) depicted in Figs. 42, where is observed the nonexistence of right-hand chiral optical rogue waves and the propagation of waves in the left-hand side only. Through Figs. 40, it can be seen that vector rogue waves can be guided only in the right-hand and through Figs. 42 that they can be guided only in the left-hand. In summary, one can control the propagation direction of vector rogue waves in chiral optical fiber. The presence of several peaks in some profiles in the text is caused by the strong instability of the background and also due to interactions and collisions between components. They are unusual rogue waves also known as ABs or KM solitons which are not localized in both space and time like usual rogue waves.

3.5.6 Chiral optical rogue waves on mixed polarization with linear coupling

Let take into account the last term of Eq. (3.82), $\beta(\xi)$ which is responsible for the exchange between the two wave components. One sets N_1 and N_2 as the power in the first and second components, relative to the total power in the system, respectively in the following form

$$\begin{aligned}
N_1 &= \frac{\int |\psi_1(\tau)|^2 d\tau}{\int |\Psi(\tau)|^2 d\tau} = \frac{-1}{2C}\left[1 + \sin(2\alpha)\cos(2B(\xi))\right], \\
N_2 &= \frac{\int |\psi_2(\tau)|^2 d\tau}{\int |\Psi(\tau)|^2 d\tau} = \frac{-1}{2C}\left[1 - \sin(2\alpha)\cos(2B(\xi))\right],
\end{aligned} \tag{3.100}$$
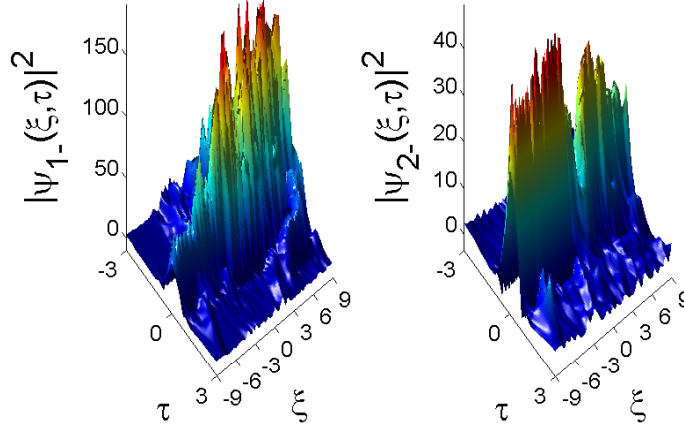
Figure 42: Existence of chiral vector rogue waves of the left-hand and non existence of the right-hand intensity $|\psi_{1,2}(\xi,\tau)|^2$ where the parameters are $C_1 = 0.6$, $C_2 = 0.8$, $\Delta < 0$ and $\mu = b_3(1 - KT_c)$ on the left-hand and $C_1 = 1.6$, $C_2 = 1.8$, $\Delta > 0$ and $\mu = b_3(1 + KT_c)$ on the right-hand; with $K = 1$, $T_c = 0.5$, $d_1 = 1.1$, $d_2 = 1.3$, $\alpha_3 = 0.03$, $\gamma = 0.02$, $D = 0.6$, $k_1 = 0.4$, $k_2 = k_4 = 0.6$, $k_3 = 0.5$, $b_3 = 0.01$ and C=-1 in each case. At $\xi = -9$, the initial condition takes the form of exact solutions (3.87) with $\delta = 0$.

where $\psi_{1,2}$ are deduced from Eq. (3.89), $C = -1$, $\alpha = \frac{\pi}{4} + \frac{n\pi}{2}$ with n being an integer. Now, let choose $B(\xi)$ in the form

$$B(\xi) = \frac{\pi}{4}\left[1 - b\frac{\xi - \xi_0}{\xi_0}\right], \tag{3.101}$$

and make a choice where the linear dependance of the phase $B(\xi)$ depends on ξ. Through analytical simulation, one obtains chiral optical vector rogue waves in the left-and right-hand depicted in Figs. 43. For $b = 1$, the first components in both side have the behavior of rogons which after their disappearance, reappear without major shape change in the amplitude [See Figs. 43(a) and 43(b)]. One remarks that, all particles are concentrated in the second components in the vicinity of $\xi = 0$. Thus, the fast oscillations of the background [see Figs. 43(c) and 43(d)] for $b = 15$ is exhibited. One denotes in an equal way, the increase of the amplitude in the left-hand and the decrease of the amplitude on the right-hand and in consequence, this process reveals the presence of FWM which is responsible for the exchange of energy between components in the system. Let show throughout Figs. 38(c) and 38(d) and then through Figs. 40 and Figs. 41(a) and 41(b), how strong XPM interaction can causes the nonexistence of synchronized chiral vector rogue waves. Nevertheless, it is observed in these cases that, such waves can exist but with weak amplitude in one component. Then, with the matrices $P_{0,1}$ defined in Eq. (3.92), one arrives to the equal relation $|\psi_1|^2 = |\psi_2|^2$ from system (3.93) which describes pure linear dispersive dynamics.
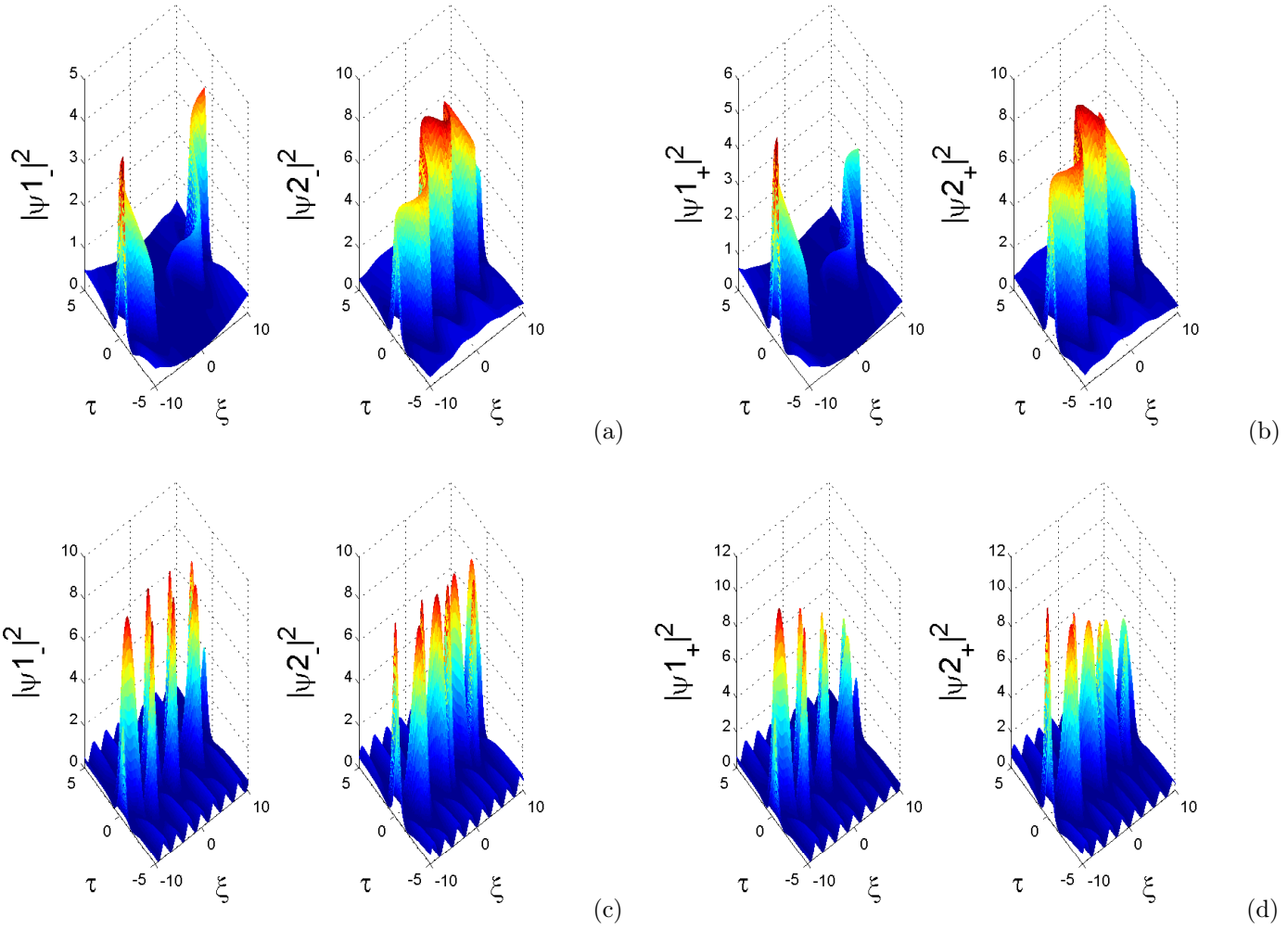
Figure 43: Chiral vector rogue waves of the right-and left-hand intensity $|\psi_{1,2}(\xi,\tau)|^2$ of Eq. (3.89), where the parameters are given in Eq. (3.87), Eq. (3.88) and Eq. (3.101) with $\mu = b_3\,(1 - KT_c)$ on the left-hand and $\mu = b_3\,(1 + KT_c)$ on the right-hand; $b = 1.0$ in (a) and (b) and then $b = 15$ in (c) and (d); with $K = 1$, $T_c = 0.7$, $C = -1$, $\alpha = \pi/4$, $b_3 = 0.01$, $\gamma = 0.03$, $k_1 = 0.4$, $k_2 = 0.6$, $\nu = 0.6$, $\xi_0 = -10$, $T_0(\xi) = cn\,(\xi, k_2)$ and $T_1(\xi) = dn\,(\xi, k_1)$ in each case.

3.6 Combined effects of nonparaxiality, optical activity and walk-off on rogue wave propagation in optical fibers filled with chiral materials

After the investigation of fundamental problems of electromagnetic wave interaction with chiral materials, the area of wave propagation in chiral media has renewed attention both from theoretical and experimental points of view [355]. The electromagnetic wave propagation through such medium displays two unequal characteristic wave numbers for the right-and left-circularly polarized eigenmodes, which results in both optical activity and circular dichrosim, as consequences of the circular birefringence [355, 89]. Significant advances have taken place on some aspects relating to the applications of chiral media. One can mention the wave-guiding structures filled with chiral materials,which show many interesting features through the integrated optic applications like directional couplers, which can be used as optical switches for energy transfer from one fiber to another adjacent one. In fact, chiral medium has many potentials and the development of integrated circuitry with chiral substrates and the multiplexing in chiral fibers are important progress with potential applications in optics [346, 356]. The concept of rogue waves which refers to rogons has been applied to pulses emerging from optical fibers, and both numerical simulations and experiments show that the probability of their generations increases with the increase of the initial noise level responsible for the modulation instability (MI) [51]. It is worth noting that the MI that leads to their generation evolves two distinct directions with opposite sense. On the one hand, it deals with the undesirable effects like the non-return-to-zero code in optical communication, the drastic enhancement of MI gain in the WDM (wavelength-division multiplexing) systems which sets the limitation of the bandwidth window of the communication system, MI lasers, and the new frequency generations of ultra-short pulses in optical systems. On the other hand, a suitable manipulation of MI has also found important applications in optical amplification of weak signal, dispersion management, optical switching, and the production of ultrashort pulses.Despite multiple observations in many other fields, the origin and the predictability of rogons remains uncertain [113], as does the kind of MI that leads to rogue wave generation [45, 46]. Important progress has been made very recently by Baronio *et al.* [55], who showed that the MI is a necessary but not a sufficient condition for the existence of rogue waves. scientists [55, 39] recognized that describing complex systems with the standard NLS equation is oversimplifying the nonlinear phenomena that can occur in those systems. Moreover, it was pointed out that the vector NLS equations describe rogue waves with higher accuracy than the scalar models [74, 75, 76]. Under this assumption, the existence of vector rogue waves in the defocusing regime was a crucial progress in the explanation of rogue waves in multicomponent systems [55]. Among different models that have been studied before, no report to the best of our knowledge is adequate to perform the description of the generation and the propagation of nonparaxial rogue waves in optical fibers filled with chiral materials. As the study is done under the assumption of high intensity and beam narrowness, one investigates both scalar and vector models, which can be used efficiently to describe simultaneous effects of nonparaxiality, optical activity, and walk-off on rogue waves propagating in optical fibers,

filled with chiral materials. As physical phenomena require modeling waves with two or more components to account for different modes, frequencies, or polarizations [74, 89, 90], it is also necessary to use the vector NLS equations, which allow energy transfer between components and which potentially yields rich and significant new families of vector rogue wave solutions.

3.6.1 Derivation of the homogeneous higher-order nonparaxial nonlinear Schrödinger equation in chiral optical fibers

To describe the optical rogue wave propagation in chiral media, one deduces from Eq. (C25) derived in the Appendix, the nonparaxial chiral NLS equation with modulated coefficients, in the form

$$
\begin{aligned}
&d(\xi)\frac{\partial^2\psi}{\partial\xi^2} + j\frac{\partial\psi}{\partial\xi} + P(\xi,\tau)\frac{\partial^2\psi}{\partial\tau^2} - j\gamma(\xi)\frac{\partial^3\psi}{\partial\tau^3} + j\mu(\xi,\tau)\psi \mp D(\xi,\tau)\psi - C(\xi,\tau)|\psi|^2\psi \\
&+ j\alpha_3(\xi)|\psi|^2\frac{\partial\psi}{\partial\tau} + \eta(\xi)\frac{\partial\psi}{\partial\tau} \pm j\sigma_3(\xi,\tau)\frac{\partial\psi}{\partial\tau} = 0,
\end{aligned}
\tag{3.102}
$$

where ξ is the propagation distance and τ, the retarded time. The subscripts ξ and τ stand for partial differentiation. The variable coefficients $P(\xi,\tau)$, $\mu(\xi,\tau)$, $D(\xi,\tau)$, $C(\xi,\tau)$ and $\sigma_3(\xi,\tau)$ are related to the space/time-modulated group-velocity dispersion (GVD), gain or loss term of the induced optical activity, linear birefringence, self-phase modulation (SPM) and linear group velocity or walk-off. Parameters $d(\xi)$, $\gamma(\xi)$, $\alpha_3(\xi)$ and $\eta(\xi)$ are related to the space-modulated nonparaxial parameter, TOD (third-order dispersion), SS (self-steepening) and the differential gain or loss term, respectively. Through Eq. (3.102), we can see the importance and the necessity to take into account those parameters which are responsible of nonparaxial, optical activity and walk-off effects. These additional terms will help to improve the description and the control of rogue wave propagation under the above assumptions. As the assumption of controllability [71] is verified by the above model, let find the rational solutions with variable coefficients which may be useful to control the propagation of the nonparaxial chiral optical rogue waves.

3.6.2 Similarity reduction of nonparaxial chiral nonlinear Schrödinger equation

Modulated coefficients in Eq. (3.102) can strongly affect the wave propagation in chiral optical fiber because of the non integrability of the model. To solve this problem, let use the symmetry reduction method [275, 276] to obtain the integrability conditions and reduce the generalized nonparaxial chiral NLS equation to the higher-order integrable Hirota equation. So doing, the envelope field is used in the form [64, 71, 353]

$$
\psi(\xi,\tau) = A(\xi)V[Z(\xi), T(\xi,\tau)]\exp\{i\rho(\xi,\tau)\},
\tag{3.103}
$$

to construct the rational solutions related to nonparaxial chiral optical rogue waves, where $A(\xi)$ is the amplitude, $Z(\xi)$ the effective propagation distance, $T(\xi,\tau)$ the similitude variable, $V[Z(\xi), T(\xi,\tau)]$ the complex field. The variable $\rho(\xi,\tau)$ is the phase of the wave. This form of envelope field is also known as the similarity transformation or the reduction method.

Substituting Eq. (3.103) into Eq. (3.102) gives a coupled system of partial differential equations with variable coefficients

$$d(\xi)(A_{\xi\xi}V + 2A_\xi Z_\xi V_Z + 2A_\xi T_\xi V_T + 2AZ_\xi T_\xi V_{ZT} + AZ_{\xi\xi}V_Z + AT_{\xi\xi}V_T + AZ_\xi{}^2 V_{ZZ} + AT_\xi{}^2 V_{TT}$$
$$-A\rho_\xi{}^2 V) - AV\rho_\xi + P(\xi,\tau)(AV_{TT}T_\tau{}^2 + AV_T T_{\tau\tau} - AV\rho_\tau{}^2) + \gamma(\xi)(3AV_T T_{\tau\tau}\rho_\tau + 3AV_T T_\tau \rho_{\tau\tau}$$
$$+3AV_{TT}T_\tau{}^2\rho_\tau + AV\rho_{\tau\tau\tau} - AV\rho_\tau{}^3) \mp D(\xi,\tau)AV - C(\xi,\tau)A^2|V|^2 AV - \alpha_3(\xi)A^2|V|^2 AV\rho_\tau$$
$$+\eta(\xi)AT_\tau V_T \mp \sigma(\xi,\tau)AV\rho_\tau = 0,$$

$$\text{(3.104)}$$

$$d(\xi)(AV\rho_{\xi\xi} + 2A_\xi\rho_\xi V + 2AZ_\xi\rho_\xi V_Z + 2A\rho_\xi T_\xi V_T) + A_\xi V + AV_Z Z_\xi + AV_T T_\xi + P(\xi,\tau)(AV\rho_{\tau\tau}$$
$$+2AV_T T_\tau\rho_\tau) - \gamma(\xi)(AV_T T_{\tau\tau\tau} + 3AV_{TT}T_\tau T_{\tau\tau} + AV_{TTT}T_\tau{}^3 - 3AV_T T_\tau\rho_\tau{}^2 - 3AV\rho_{\tau\tau}\rho_\tau)$$
$$+\mu(\xi,\tau)AV + \alpha_3(\xi)A^2|V|^2 AV_T T_\tau + \eta(\xi)AV\rho_\tau \pm \sigma(\xi,\tau)AT_\tau V_T = 0,$$

$$\text{(3.105)}$$

where the scripts of differential equations are simplified as $A(\xi) = A$, $Z(\xi) = Z$, $T(\xi,\tau) = T$, $\rho(\xi,\tau) = \rho$ and $V[Z(\xi), T(\xi,\tau)] = V$. According to previous works [64, 71], let use the symmetry reduction given by Eq. (3.103) that would reduce Eq. (3.102) to the higher-order integrable Hirota equation in the form [116]

$$i\frac{\partial V}{\partial Z} = -\frac{\partial^2 V}{\partial T^2} + G|V|^2 V + 2\sqrt{2}i\nu\left(\frac{\partial^3 V}{\partial T^3} + 3|V|^2\frac{\partial V}{\partial T}\right). \tag{3.106}$$

In the case of rogue waves finding, we take $G = -1$ to obtain rational solutions. The parameter ν is a real constant. With $V[Z(\xi), T(\xi,\tau)]$ satisfying the relation (3.106), the similarity reduction of Eqs. (3.104) and (3.105) yields

$$\gamma(\xi)T_\tau T_{\tau\tau} = 0, \tag{3.107}$$

$$T_\xi + 2d(\xi)T_\tau\rho_\tau + 2P(\xi,\tau)T_\tau\rho_\tau \pm \sigma(\xi,\tau)T_\tau - \gamma(\xi)\left(T_{\tau\tau\tau} - 3T_\tau\rho_\tau{}^2\right) = 0, \tag{3.108}$$

$$A_\xi + A(d(\xi)\rho_{\xi\xi} + \rho_{\tau\tau}P(\xi,\tau) + 3\gamma(\xi)\rho_{\tau\tau}\rho_\tau + \mu(\xi,\tau) + \eta(\xi)\rho_\tau) = 0, \tag{3.109}$$

$$\gamma(\xi)T_\tau{}^3 + 2\sqrt{2}\nu Z_\xi = 0, \tag{3.110}$$

$$A_\xi V + AZ_\xi V_Z + AT_\xi V_T = 0, \tag{3.111}$$

$$\alpha_3(\xi)A^2 T_\tau - 6\sqrt{2}\nu Z_\xi = 0, \tag{3.112}$$

$$d(\xi)T_{\xi\xi} + P(\xi,\tau)T_{\tau\tau} + 3\gamma(\xi)\left(T_{\tau\tau}\rho_\tau + T_\tau\rho_{\tau\tau}\right) + \eta(\xi)T_\tau = 0, \tag{3.113}$$

$$Z_\xi + d(\xi)T_\xi{}^2 + P(\xi,\tau)T_\tau{}^2 + 3\gamma(\xi)\rho_\tau T_\tau{}^2 = 0, \tag{3.114}$$

$$\rho_\xi + d(\xi)\rho_\xi{}^2 + P(\xi,\tau)\rho_\tau{}^2 + \gamma(\xi)\left(\rho_\tau{}^3 - \rho_{\tau\tau\tau}\right) \pm \sigma(\xi,\tau)\rho_\tau \pm D(\xi,\tau) = 0, \tag{3.115}$$

$$GZ_\xi + A^2\left(C(\xi,\tau) + \alpha_3(\xi)\rho_\tau\right) = 0, \tag{3.116}$$

$$A_{\xi\xi}V + 2A_\xi Z_\xi V_Z + 2A_\xi T_\xi V_T + 2AZ_\xi T_\xi V_{ZT} + AZ_{\xi\xi}V_Z + AZ_\xi{}^2 V_{ZZ} = 0. \tag{3.117}$$

Here, the subscripts ξ and τ, denote spatial and temporal derivatives, respectively. Through the above symmetry reduction method, the constraints or integrability conditions of the model given in Eq. (3.102) are derived from the differential equations of which the simplified forms stand from Eq. (3.107) to Eq. (3.117), respectively as follows $-3AV_{TT} \neq 0$, $AV_T \neq 0$, $V \neq 0$, $-AV_{TTT} \neq 0$, $2d\rho_\xi \neq 0$, $A|V|^2 V_T \neq 0$, $AV_T \neq 0$, $AV_{TT} \neq 0$, $-AV \neq 0$, $-A|V|^2 V \neq 0$ and $d \neq 0$.

Let keep in mind that each constraint plays an important role in the choice of arbitrary functions and parameters of the system.

3.6.3 First-and second-order nonparaxial chiral optical rogue waves with modulated coefficients

To have an aperture of dynamics behavior of parameters, the above equations should be solved to give the information on the form and order of each coefficient of the model and on variables related to the complex field. The resolution of Eq. (3.107) yields for $\gamma(\xi) \neq 0$ and for $T_\tau T_{\tau\tau} = 0$ to the similarity variable

$$T(\xi, \tau) = T_1(\xi)\tau + T_0(\xi), \tag{3.118}$$

where $T_1(\xi)$ and $T_0(\xi)$ are arbitrary functions. From Eq. (3.110), the effective propagation distance $Z(\xi)$ will be

$$Z(\xi) = -\frac{\sqrt{2}}{4\nu} \int_0^\xi \gamma(s)T_1(s)^3 ds. \tag{3.119}$$

Equation (3.112) gives the result

$$\alpha_3(\xi) = -3\gamma(\xi)T_1{}^2(\xi)A^{-2}(\xi). \tag{3.120}$$

$\alpha_3(\xi)$ has the physical sense of SS. The substitution of Eq. (3.118) into Eq. (3.113) tends to $d(\xi)T_{\xi\xi} + 3\gamma(\xi)T_\tau\rho_{\tau\tau} + \eta(\xi)T_\tau = 0$. As $\gamma(\xi) \neq 0$, $T_1(\xi) \neq 0$ and $T_{\xi\xi} = T_{1_{\xi\xi}}\tau + T_{0_{\xi\xi}}$, the phase of the envelope field can be written as

$$\rho(\xi, \tau) = \rho_3(\xi)\tau^3 + \rho_2(\xi)\tau^2 + \rho_1(\xi)\tau + \rho_0(\xi), \tag{3.121}$$

with

$$\rho_3(\xi) = -\frac{1}{18}\frac{d(\xi)T_1(\xi)_{\xi\xi}}{\gamma(\xi)T_1(\xi)}, \quad \rho_2(\xi) = -\frac{1}{6}\frac{d(\xi)T_0(\xi)_{\xi\xi} + \eta(\xi)T_1(\xi)}{\gamma(\xi)T_1(\xi)}, \tag{3.122}$$

where $\rho_1(\xi)$ and $\rho_0(\xi)$ are arbitrary functions. Through relation (3.116), one finds that

$$C(\xi, \tau) = C_2(\xi)\tau^2 + C_1(\xi)\tau + C_0(\xi), \tag{3.123}$$

with

$$C_2(\xi) = -\frac{1}{2}\frac{T_1(\xi)d(\xi)T_1(\xi)_{\xi\xi}}{A(\xi)^2}, \quad C_1(\xi) = -\frac{T_1(\xi)\left(d(\xi)T_0(\xi)_{\xi\xi} + T_1(\xi)^2\eta(\xi)\right)}{A(\xi)^2},$$
$$C_0(\xi) = \frac{\gamma(\xi)T_1(\xi)^2}{A(\xi)^2}\left(3\rho_1(\xi) + \frac{1}{4}\frac{\sqrt{2}GT_1(\xi)}{\nu}\right). \tag{3.124}$$

$C(\xi, \tau)$ is the space/time-modulated SPM. Equation (3.114) stands for

$$P(\xi, \tau) = P_2(\xi)\tau^2 + P_1(\xi)\tau + P_0(\xi), \tag{3.125}$$

with

$$P_2(\xi) = \frac{1}{2}\frac{d(\xi)T_1(\xi)_{\xi\xi}}{T_1(\xi)} - \frac{d(\xi)T_1(\xi)_\xi{}^2}{T_1(\xi)^2}, \quad P_1(\xi) = \eta(\xi) + \frac{d(\xi)T_0(\xi)_{\xi\xi}}{T_1(\xi)} - 2\frac{d(\xi)T_1(\xi)_\xi T_0(\xi)_\xi}{T_1(\xi)^2},$$
$$P_0(\xi) = \frac{1}{4}\frac{\gamma(\xi)T_1(\xi)\sqrt{2}}{\nu} - 3\gamma(\xi)\rho_1(\xi) - \frac{d(\xi)T_0(\xi)_\xi{}^2}{T_1(\xi)^2}. \tag{3.126}$$

$P(\xi, \tau)$ is the space/time modulated GVD. Through Eq. (3.108), one arrives at

$$\pm\sigma(\xi, \tau) = \sigma_4(\xi)\tau^4 + \sigma_3(\xi)\tau^3 + \sigma_2(\xi)\tau^2 + \sigma_1(\xi)\tau + \sigma_0(\xi), \tag{3.127}$$

where the parameters $\sigma_4(\xi)$, $\sigma_3(\xi)$, $\sigma_2(\xi)$, $\sigma_1(\xi)$ and $\sigma_0(\xi)$ are expressed in the Appendix (D). $\pm\sigma(\xi,\tau)$ is the left-and right-hand of the walk-off effect. Equation instead of relation (3.109) is transformed to

$$A(\xi) = A_0 \exp\left\{\int_0^\xi f(s)ds\right\}, \tag{3.128}$$

where, A_0 is a constant and with

$$\begin{aligned}
f &= \mu_3(\xi)\tau^3 + \mu_2(\xi)\tau^2 + \mu_1(\xi)\tau + \mu_0(\xi) - \mu(\xi,\tau), \\
\mu(\xi,\tau) &= \mu_3(\xi)\tau^3 + \mu_2(\xi)\tau^2 + \mu_1(\xi)\tau + 2\mu_0(\xi),
\end{aligned} \tag{3.129}$$

where the parameters of the gain or loss term $\mu(\xi,\tau)$ are given in the Appendix (E). $\mu(\xi,\tau)$ is the space/time modulated gain or loss term. It follows from the above equations that the amplitude of the envelope field becomes

$$A(\xi) = A_0 \exp\left\{\int_0^\xi -\mu_0(s)ds\right\}, \tag{3.130}$$

with

$$\begin{aligned}
\mu_0\left(\xi\right) &= -\frac{1}{3}\frac{d(\xi)T_0(\xi)_\xi{}^2\eta(\xi)}{\gamma(\xi)T_1(\xi)^2} - \frac{1}{3}\frac{d(\xi)^2T_0(\xi)_\xi{}^2T_0(\xi)_{\xi\xi}}{\gamma(\xi)T_1(\xi)^3} + \frac{1}{12}\frac{T_1(\xi)\sqrt{2}\eta(\xi)}{\nu} - \eta\left(\xi\right)\rho_1\left(\xi\right) \\
&+ \frac{1}{12}\frac{\sqrt{2}d(\xi)T_0(\xi)_{\xi\xi}}{\nu} - d\left(\xi\right)\rho_0\left(\xi\right)_{\xi\xi}.
\end{aligned} \tag{3.131}$$

The result coming from Eq. (3.115), is out to be

$$\pm D(\xi,\tau) = D_6(\xi)\tau^6 + D_5(\xi)\tau^5 + D_4(\xi)\tau^4 + D_3(\xi)\tau^3 + D_2(\xi)\tau^2 + D_1(\xi)\tau + D_0(\xi), \tag{3.132}$$

with $D_-\left(\xi\right) = -D_+\left(\xi\right)$ and where $D_6(\xi)$, $D_5(\xi)$, $D_4(\xi)$, $D_3(\xi)$, $D_2(\xi)$, $D_1(\xi)$ and $D_0(\xi)$ are given in the Appendix (F). $\pm D(\xi,\tau)$ is the left-and right-hand of the space/time modulated linear birefringence.

The resolution of the above differential equations reveals and confirms the assumption of the space/time modulated variable of the TOD, gain or loss term, linear birefringence, SPM and walk-off coefficients. More specifically, it reveals the optically active nature of the system through the left-and right-hand of mathematical expressions of the linear birefringence and walk-off term. In fact, the chirality, known as optical activity in optics, is the ability to rotate plane polarized light and this happens when the plane polarized light hits an optically active compound. The more compounds it hits, the more it rotates. Physically, when the polarized light leaves the chiral optical fiber which is optically active, one should rotate the analyzer to allow the plane of light to pass through. This angle of rotation, called observed rotation, can be directed to the right-hand side, that is a positive rotation or clockwise rotation, also called dextrorotatory. In the case of which the analyzer has to be rotated to the left-hand side for the polarized light to pass through, that is a negative rotation or counter-clockwise rotation, called levorotatory. Hence, the mathematical expressions of relations (3.127) and (3.132) with positive signs refer to the dextrorotatory components and the ones with negative signs to the

levorotatory components of the system. As we can see, they are equal in magnitude but opposite in sign.

One can observe through the above variable coefficients of the model that, $P(\xi, \tau)$, $\mu(\xi, \tau)$, $D(\xi, \tau)$, $C(\xi, \tau)$ and $\sigma_3(\xi, \tau)$ are polynomials in τ with coefficients being functions of ξ. Parameters $d(\xi)$, $\gamma(\xi)$, $\alpha_3(\xi)$ and $\eta(\xi)$ are arbitrary functions except the SS which depends on the TOD and amplitude. Since the nonparaxial parameter $d(\xi)$, the differential gain or loss term $\eta(\xi)$ and third-order dispersion $\gamma(\xi)$, are major functions of the base equation coefficients, it appears from analytical results that there are the main keys to control the amplitude, the SS, the GVD, the SPM, the walk-off term and linear birefringence in optical fibers. Therefore, they can be considered as specific control parameters of the system. The TOD coefficient, $\gamma(\xi)$ can also be used to control the effective propagation distance $Z(\xi)$. The gain or loss term of the induce optical activity $\mu(\xi, \tau)$ can be used to manage the optical activity on the amplitude $A(\xi)$, SS coefficient $\alpha_3(\xi)$ and on the SPM nonlinearity $C(\xi, \tau)$.

According to the MDT method [24, 94, 159, 335], which is well-known and clearly derived by many authors, the first-and second-order of the complex field $V\left[Z(\xi), T(\xi, \tau)\right]$ are expressed by Akhmediev *et al.* [116]. It's good to mention that the first-order of the complex field $V\left[Z(\xi), T(\xi, \tau)\right]$ was found by Peregrine [39] and the second-order by Akhmediev *et al.* [?]. later, Ankiewicz *et al.* [116] found the first-and second-order of the Hirota equation. By considering the correspondence $Z(\xi) = x$, $\frac{1}{\sqrt{2}}T(\xi, \tau) = t$ and $\nu = \alpha_3$, in this last reference, the first-order complex field $V\left[Z(\xi), T(\xi, \tau)\right]$ yields

$$V_1\left[Z(\xi), T(\xi, \tau)\right] = \left[1 - \frac{G_1 + iH_1}{D_1}\right]\exp\left\{iZ(\xi)\right\}, \tag{3.133}$$

where

$$G_1 = 4, \quad H_1 = 8Z(\xi), \quad D_1 = 1 + \left[\sqrt{2}T(\xi, \tau) + 12\nu Z(\xi)\right]^2 + 4Z(\xi)^2. \tag{3.134}$$

The partial solution (3.133), is known as the Peregrine soliton [39]. Then, collecting this solution together with the founded amplitude and phase of the wave, one constructs the first-order rational solution related to the nonparaxial chiral optical rogue wave given by

$$\psi_1 = A(\xi)\left[1 - \frac{G_1 + iH_1}{D_1}\right]\exp\left\{iZ(\xi) + i\rho(\xi, \tau)\right\}, \tag{3.135}$$

which result becomes

$$\psi_1 = A_0 \exp\left\{-\int_0^\xi \mu_0(s)ds\right\}\left[1 - \frac{G_1 + iH_1}{D_1}\right]\exp\left\{iZ(\xi) + i\rho(\xi, \tau)\right\}. \tag{3.136}$$

This first-order rational solution is used to describe the propagation of nonparaxial optical rogue wave in a fiber filled with chiral materials. For suitable choice of arbitrary parameters of the original Eq. (3.102), one can manage through a simultaneous controllability, the rogue wave structures with the specific control parameters. The second-order rational solution of the complex field $V\left[Z(\xi), T(\xi, \tau)\right]$ stands for

$$V_2\left[Z(\xi), T(\xi, \tau)\right] = \left[1 + \frac{G_2 + iZ(\xi)H_2}{D_2}\right]\exp i\left\{Z(\xi)\right\}. \tag{3.137}$$

where G_2, H_2 and D_2 are given by the relations

$$G_2 = -48T^4 - 1152\sqrt{2}\nu ZT^3 - 144T^2[4Z^2(36\nu^2 + 1) + 1] - 576\sqrt{2}\nu ZT[12Z^2(12\nu^2 + 1) + 7]$$
$$-192Z^4[216(6\nu^4 + \nu^2) + 5] - 864Z^2(44\nu^2 + 1) - 36,$$
$$H_2 = -96T^4 - 2304\sqrt{2}\nu ZT^3 - 96T^2[4Z^2(108\nu^2 + 1) - 3] - 1152\sqrt{2}\nu ZT[4Z^2(36\nu^2 + 1)]$$
$$-384Z^4(36\nu^2 + 1)^2 - 192Z^2(180\nu^2 + 1) + 360,$$
$$D_2 = 8T^6 + 288\sqrt{2}\nu ZT^5 - 432Z^4(624\nu^4 - 40\nu^2 - 1) + 36Z^2(556\nu^2 + 11) + 9 + 64Z^6(36\nu^2 + 1)^3$$
$$+96\sqrt{2}ZT^3[12Z^2(60\nu^2 + 1) - 1] + 12T^4[4Z^2(180\nu^2 + 1) + 1] + 6T^2[16Z^4[216\nu^2(30\nu^2 + 1) - 1]$$
$$-24Z^2(60\nu^2 + 1) + 9] + 72\sqrt{2}\nu ZT[16Z^4(36\nu^2 + 1) + 8Z^2(1 - 108\nu^2) + 17].$$

$$(3.138)$$

According to the same correspondence joined with the founded variables including the above solutions, the second-order rational solution, related to a particular solution of Eq. (3.102) was obtained

$$\psi_2 = A(\xi)\left[1 + \frac{G_2 + iZ(\xi)H_2}{D_2}\right]\exp\left\{iZ(\xi) + i\rho(\xi,\tau)\right\}. \qquad (3.139)$$

Then, the construction of the second-order nonparaxial chiral optical rogue wave yields

$$\psi_2 = A_0 \exp\left\{-\int_0^\xi \mu_0(s)ds\right\} \times \left[1 + \frac{G_2 + iZ(\xi)H_2}{D_2}\right]\exp\left\{iZ(\xi) + i\rho(\xi,\tau)\right\}. \qquad (3.140)$$

These second-order rational solutions arise due to the collision between two or more ultrashort pulses in the optical fiber. More specifically, they are nonparaxial chiral optical rogue waves which can propagate through a fiber filled with chiral materials. The particularity of these solutions is the simultaneous controllability of their amplitudes through the three specific control parameters, which can be used to manage the intensity and the shape of the waves. As the nonparaxiality, TOD and differential gain or loss terms depend on specific control parameterts, they can therefore provide a more convenient and controlled environment to experimentally study specific optical communication problems.

3.6.4 Dynamics behavior and features of combined effect on nonparaxial chiral optical rogue waves

After the construction of the above solutions, the parameters are chosen to investigate the dynamics behavior and the features of combined effects on nonparaxial chiral optical rogue waves. After wards, let plot the specific control parameters of the system, the GVD and the amplitudes of the envelope field in the left-and right-hand to have an aperture of their dynamic in the nonparaxial chiral optical fiber [see Figs. 44, 45 and 46]. Then, let alternate the sign of chiral parameters in both space and time in the first-and second-order of nonparaxial chiral optical rogue wave solutions to analyze their behavior and therefore to optimize the eventual stability of the solutions [see Figs. 47 and 48].

Figure 44 depicts the dynamical behavior of each specific parameter in the system. On the one hand, one can observe the influence of chiral nature of the differential gain or loss term through it weak peak in the left-hand side and high peak in the right-hand side. On the other hand, the amplitude and the width of each parameter depend on the value of their moduli
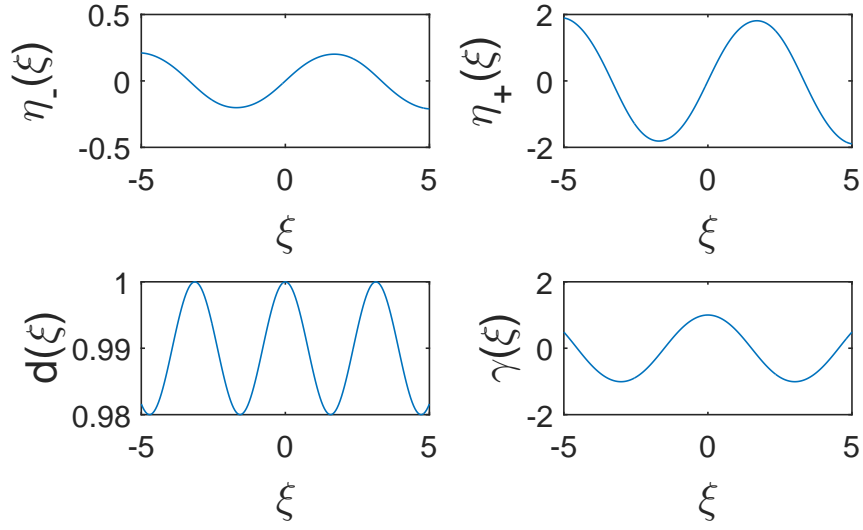
Figure 44: Specific control parameters: the left-and right-hand side of the gain or loss differential term $\eta(\xi)$, nonparaxial parameter $d(\xi)$, and TOD $\gamma(\xi)$, where $\eta(\xi) = C_T sn(\xi, k_7)$, $d(\xi) = dn(\xi, k_5)$, $\gamma(\xi) = cn(\xi, k_6)$ and $C_T = 1 \pm KT_c$ with $k_5 = 0.2$, $k_6 = 0.4$, $k_7 = 0.5$ and $KT_c = 0.8$.
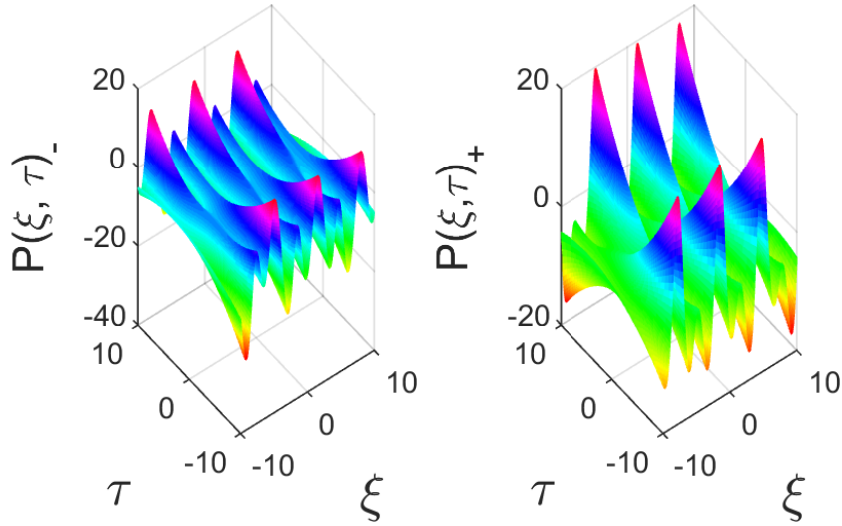
Figure 45: The space/time-modulated Group Velocity Dispersion $P(\xi, \tau)$ on the left-and right-hand side, respectively, expressed in relation (3.125) where, $\eta(\xi) = C_T sn(\xi, k_7)$, $d(\xi) = dn(\xi, k_5)$, $\gamma(\xi) = cn(\xi, k_6)$, $T_0(\xi) = sn(\xi, k_3)$, $T_1(\xi) = dn(\xi, k_3)$, $\rho_0(\xi) = dn(\xi, k_2)$, $\rho_1(\xi) = cn(\xi, k_1)$ with $C_T = 1 \pm KT_c$ and $k_1 = 0.3$, $k_2 = 0.5$, $k_3 = 0.6$, $k_4 = 0.4$, $k_5 = 0.2$, $k_6 = 0.4$, $k_7 = 0.5$, $\nu = 0.2$ and $KT_c = 0.8$.
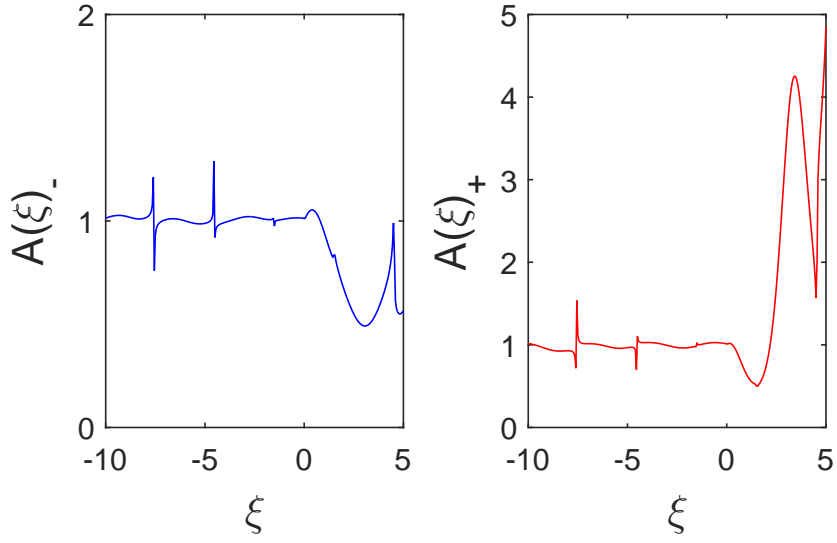
Figure 46: The left-and right-hand side amplitude $A(\xi)$, presented in relation (3.130) where, $\eta(\xi) = C_T sn\,(\xi, k_7)$, $d(\xi) = dn\,(\xi, k_5)$, $\gamma\,(\xi) = cn\,(\xi, k_6)$, $T_0(\xi) = sn\,(\xi, k_3)$, $T_1(\xi) = dn\,(\xi, k_3)$, $\rho_0(\xi) = dn\,(\xi, k_2)$, $\rho_1(\xi) = cn\,(\xi, k_1)$ and $C_T = 1 \pm KT_c$ with $k_1 = 0.3$, $k_2 = 0.5$, $k_3 = 0.6$, $k_4 = 0.4$, $k_5 = 0.2$, $k_6 = 0.4$, $k_7 = 0.5$ and $KT_c = 0.8$.
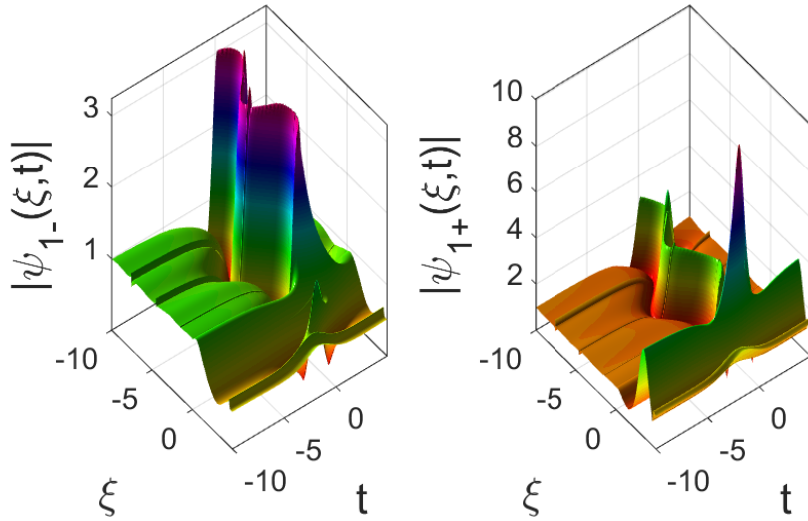
Figure 47: First-order nonparaxial chiral optical rogue waves on the left-and right-hand side of the rational solution given by Eq. (3.136) where $\eta(\xi) = C_T sn\,(\xi, k_7)$, $d(\xi) = dn\,(\xi, k_5)$, $\gamma\,(\xi) = cn\,(\xi, k_6)$, $T_0(\xi) = sn\,(\xi, k_3)$, $T_1(\xi) = dn\,(\xi, k_3)$, $\rho_0(\xi) = dn\,(\xi, k_2)$, $\rho_1(\xi) = cn\,(\xi, k_1)$ and $C_T = 1 \pm KT_c$ with $k_1 = 0.3$, $k_2 = 0.5$, $k_3 = 0.6$, $k_4 = 0.4$, $k_5 = 0.2$, $k_6 = 0.4$, $k_7 = 0.5$, $\nu = 0.2$ and $KT_c = 0.8$.
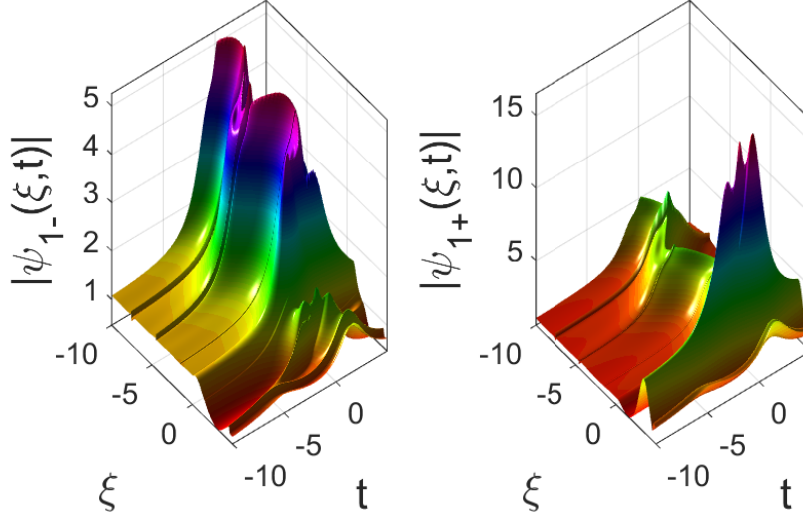
Figure 48: Second-order nonparaxial chiral optical rogue waves on the left-and right-hand side of the rational solution given by Eq. (3.140) where $\eta(\xi) = C_T\, sn\,(\xi, k_7)$, $d(\xi) = dn\,(\xi, k_5)$, $\gamma(\xi) = cn\,(\xi, k_6)$, $T_0(\xi) = sn\,(\xi, k_3)$, $T_1(\xi) = dn\,(\xi, k_3)$, $\rho_0(\xi) = dn\,(\xi, k_2)$, $\rho_1(\xi) = cn\,(\xi, k_1)$ and $C_T = 1 \pm KT_c$ with $k_1 = 0.3$, $k_2 = 0.5$, $k_3 = 0.6$, $k_4 = 0.4$, $k_5 = 0.2$, $k_6 = 0.4$, $k_7 = 0.5$, $\nu = 0.2$ and $KT_c = 0.8$.

$k_i (i = 5, 6, 7)$ and on the type of Jacobian elliptic function they carry (cn, dn, sn). The left-and right-hand of the space/time-modulated group-velocity dispersion $P(\xi, \tau)$, are illustrated in Fig. 45 and expressed by relation (3.125) with their arbitrary Jacobian elliptic functions and moduli given in the figure caption. It can be seen that the structure of GVD differs from one hand to the other. Figure 46 depicts the profiles of the amplitudes of the envelope field $A(\xi)$ on both hands. One remarks on the trace of each evolution, the presence of two dark-bright collisions in the right-hand and two bright-dark collisions in the left-hand. These collisions are better observed through analytical simulation of the first-and second-order nonparaxial chiral optical rogue waves which are illustrated in Figs. 47 and 48. Throughout these figures, we notice a main difference on the structure and on the amplitude of the first-and second-order in both hands. The energy transfer from the left-hand to right-hand on each solution is noticed.

More specifically in Fig. 46, it can be seen that the contrast of optical activity in the sense of oscillation of each component of the amplitude as it increase then decrease on the left-hand whereas it decrease then increase on the right-hand. Generally in optically active media, components are equal in magnitude but different in sign. However, in this case, the equality of magnitude is affected by the differential gain or loss term $\eta(\xi) = (1 \pm KT_c)sn\,(\xi, k_7)$ which is responsible for the observed difference on it both hands and consequently, on the both hands of the amplitude. It can be seen throughout Fig. 44 that the amplitude of the differential gain or loss term is four time more higher in the right-hand compare to the left-hand. Now, when having a look at the mathematical expression of the space/time modulated GVD, one denotes that it depends also on the differential gain or loss term, however GVD profiles are nearly equal in magnitude as shown in Fig. 45. This contrast is due to the fact that the differential gain or loss term plays a role of loss in the expression of the amplitude and the role of gain in the

expression of GVD. This is an advantage for the waves which become more stable as observed in Figs. 47 and 48. As the vector NLS equations describe extreme waves with higher accuracy than the scalar NLS equation models, let use the vector nonparaxial NLS equations to enrich the work.

3.7 The influence of combined effects on the numerical solutions of vector nonparaxial nonlinear Schrödinger equations with constant coefficients

3.7.1 Model

To illustrate the nonparaxiality, optical activity and walk-off effects on the propagation of nonparaxial chiral optical rogue waves, one derives from the model obtain in Eq. (C25), the vector nonparaxial NLS equations with constant and modulated coefficients which governs the propagation of rogons in optical fibers filled with chiral materials. So doing, the coupled system of the nonparaxial NLS equation with constant coefficients is given by

$$d\psi_{1\xi\xi} + i\psi_{1\xi} + P\psi_{1\tau\tau} - i\gamma\psi_{1\tau\tau\tau} + i\mu\psi_1 \mp D\psi_1 - C\left(|\psi_1|^2 + |\psi_2|^2\right)\psi_1 + i\alpha_3\left(|\psi_1|^2 + |\psi_2|^2\right)\psi_{1\tau}$$
$$+ (\eta \pm i\sigma)\psi_{1\tau} = 0,$$
$$d\psi_{2\xi\xi} + i\psi_{2\xi} + P\psi_{2\tau\tau} - i\gamma\psi_{2\tau\tau\tau} + i\mu\psi_2 \mp D\psi_2 - C\left(|\psi_1|^2 + |\psi_2|^2\right)\psi_2 + i\alpha_3\left(|\psi_1|^2 + |\psi_2|^2\right)\psi_{2\tau}$$
$$+ (\eta \pm i\sigma)\psi_{2\tau} = 0.$$

$$(3.141)$$

To simplify the expressions of waves functions, one sets $\psi_1(\xi, \tau) = u(\xi, \tau)$ and $\psi_2(\xi, \tau) = v(\xi, \tau)$. In this part of work, let focus the attention on the generation and propagation of bright and dark rogue wave solutions when the nonparaxial effect arises fundamentally from chiral optical fibers.

3.7.2 Explicit algorithm of the model: difference-differential equations

To study the influence of combined effects of the nonparaxiality, optical activity and walk-off on optical rogue wave propagation, one uses an algorithm scheme derived by Chamorro-Posada et al. [61], namely, difference-differential equation method that has a wider applicability on nonparaxial beam propagation methods. In this method, the finite difference formulae are used to approximate derivatives with respect to ξ coordinate and then, the fast Fourier transforms (FFTs) is used to compute efficiently the second-and third-order diffractions in the spectral domain.

The finite difference formulae for the derivatives are given in the Appendix (G). Substituting these formulae in the coupled nonparaxial NLS equations with constant coefficients, one obtains

the difference-differential equations below

$$
\begin{aligned}
u_{n+1}(\tau) &= \tfrac{1}{2d+i\Delta\xi}[(4d - 2P\Delta\xi^2 \tfrac{\partial^2}{\partial\tau^2} + 2i\gamma\Delta\xi^2 \tfrac{\partial^3}{\partial\tau^3} - 2i\mu\Delta\xi^2 \pm 2\Delta\xi^2 D + 2C\Delta\xi^2 \left(|u_n(\tau)|^2 + |v_n(\tau)|^2\right) \\
&\quad -2i\alpha_3\Delta\xi^2 \left(|u_n(\tau)|^2 + |v_n(\tau)|^2\right) \tfrac{\partial}{\partial\tau} - 2\Delta\xi^2 \left(\eta \pm i\sigma\right) \tfrac{\partial}{\partial\tau})u_n(\tau) - (2d - i\Delta\xi)\, u_{n-1}(\tau)], \\
v_{n+1}(\tau) &= \tfrac{1}{2d+i\Delta\xi}[(4d - 2P\Delta\xi^2 \tfrac{\partial^2}{\partial\tau^2} + 2i\gamma\Delta\xi^2 \tfrac{\partial^3}{\partial\tau^3} - 2i\mu\Delta\xi^2 \pm 2\Delta\xi^2 D + 2C\Delta\xi^2 \left(|u_n(\tau)|^2 + |v_n(\tau)|^2\right) \\
&\quad -2i\alpha_3\Delta\xi^2 \left(|u_n(\tau)|^2 + |v_n(\tau)|^2\right) \tfrac{\partial}{\partial\tau} - 2\Delta\xi^2 \left(\eta \pm i\sigma\right) \tfrac{\partial}{\partial\tau})v_n(\tau) - (2d - i\Delta\xi)\, v_{n-1}(\tau)].
\end{aligned}
\tag{3.142}
$$

These equations define the explicit algorithm in which the effects of the transverse differential operators $\frac{\partial^2}{\partial\tau^2}$ and $\frac{\partial^3}{\partial\tau^3}$ are computed efficiently and accurately by the FFTs. An implementation on the index n gives us the numerical solutions of each component. One uses as initial conditions, the rational solutions of the envelope fields [55], constructed by the DDT method where the correspondence $t \to \xi$ and $x \to \tau$ is considered

$$
\begin{aligned}
u(\xi,\tau) &= u_{01} \left(\frac{p^2\tau^2 + p^4\xi^2 + p\tau(\alpha_1+\beta\theta_1) - i\alpha_1 p^2\xi + \beta\theta_1}{p^2\tau^2 + p^4\xi^2 + \beta(p\tau+1)} \right) \\
v(\xi,\tau) &= v_{01} \left(\frac{p^2\tau^2 + p^4\xi^2 + p\tau(\alpha_2+\beta\theta_2) - i\alpha_2 p^2\xi + \beta\theta_2}{p^2\tau^2 + p^4\xi^2 + \beta(p\tau+1)} \right),
\end{aligned}
\tag{3.143}
$$

where the parameters are

$$
\begin{aligned}
u_{01} &= a_1 \exp\left(i\left(q_1\tau - v_1\xi\right)\right), \quad v_{01} = a_1 \exp\left(i\left(q_2\tau - v_2\xi\right)\right), \quad v_1 = q_1{}^2 + 2\left(a_1{}^2 + a_2{}^2\right), \\
v_2 &= q_2{}^2 + 2\left(a_1{}^2 + a_2{}^2\right) \alpha_1 = \tfrac{4p^2}{p^2+4q_1{}^2}, \quad \alpha_2 = \tfrac{4p^2}{p^2+4q_2{}^2}, \quad \theta_1 = \tfrac{2q_1+ip}{2q_1-ip}, \quad \theta_2 = \tfrac{2q_2+ip}{2q_2-ip},
\end{aligned}
\tag{3.144}
$$

with

$$
\begin{aligned}
p &= 2\mathrm{Im}(\lambda + k), \quad \chi = \mathrm{Im}(k), \quad q_1 + q_2 = 2\mathrm{Re}(\lambda + k), \\
q_1 - q_2 &= 2q, \quad \beta = \tfrac{p^3}{\chi(p^2+4q_1q_2)}, \quad k = 2.36954 + 1.1972i, \\
\lambda &= -1.69162 - 1.79721i.
\end{aligned}
\tag{3.145}
$$

3.7.3 Numerical representations

To plot the numerical solutions, one chooses appropriately, free functions $T_1(\xi)$, $T_0(\xi)$, $\mu(\xi)$ and $\gamma(\xi)$ and the Jacobian elliptic functions below [84]

$$
\begin{aligned}
dn(z,k) &= 1 - \tfrac{k^2 \sin(z)^2}{2}, \\
cn(z,k) &= \cos(z) - k^2 \sin(z) \left(\tfrac{z - \sin(z)\cos(z)}{4} \right), \\
sn(z,k) &= \sin(z) - k^2 \cos(z) \left(\tfrac{z - \sin(z)\cos(z)}{4} \right).
\end{aligned}
\tag{3.146}
$$

The parameters are chosen in order to be bounded in the intervals $-10 < \xi < 10$ and $-10 < \tau < 10$. Curves are plotted with the help of Matlab through a pseudospectral method. So doing, one obtains identical right-and left-hand of nonparaxial chiral optical vector rogue waves with constant coefficients [see Figs. 49, 50 and 51].

These representations show the rapid convergence of the pseudo spectral method based on the difference-differential equation method [61] when $\Delta\xi/d \to 0$. In the case of constant coefficients, it can be seen that the vector nonparaxial chiral optical rogue waves are localized in space and time as usual rogue waves and that the forward and backward of each component are similar. It is noticed that the mixture of bright and dark structures on each component
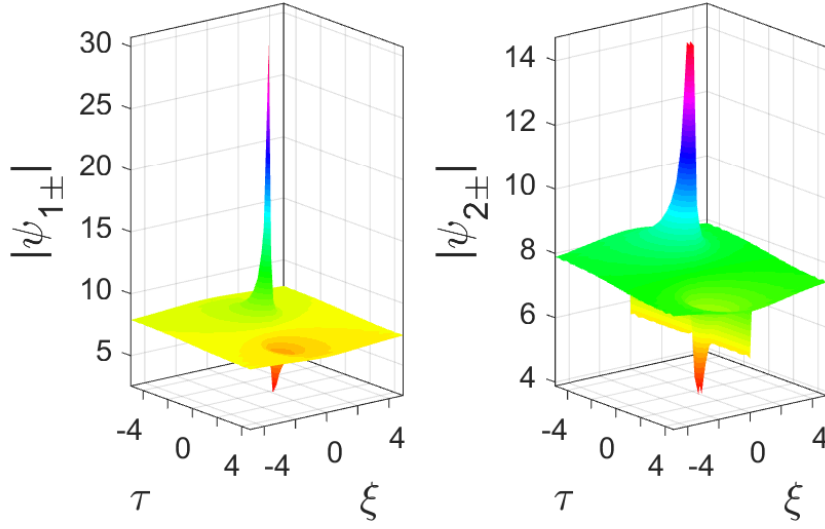
Figure 49: Nonparaxial chiral optical vector rogue waves with constant coefficients on the right-and left-hands $|\psi_{1,2}(\xi,\tau)|$ where the parameters are $a_1 = 3$, $a_2 = 3$, $d = 10$, $P = -0.5$, $\gamma = 0.4$, $\mu = 0.3$, $D = \pm 0.6$, $C = 2$, $\alpha 3 = 0.2$, $\eta = 0.5$, $\sigma = \pm 0.1$, $k_1 = 0.3$, $k_2 = 0.5$, $k_3 = 0.6$, $k_4 = 0.4$, $k_5 = 0.2$, $k_6 = 0.4$, and $k_7 = 0.5$. Here, the initial conditions take the form of exact solutions (3.143), (3.144) and (3.145).
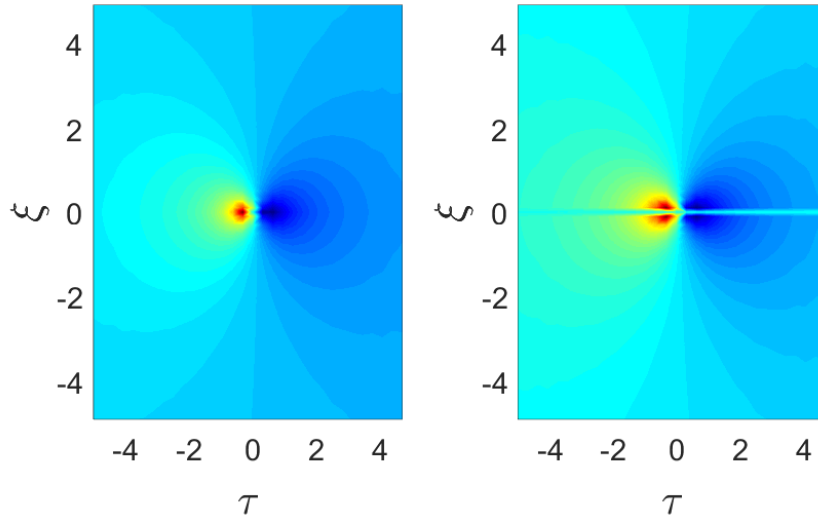
Figure 50: 2D representations of the nonparaxial chiral optical vector rogue waves with constant coefficients in both hands where the initial conditions take the form of exact solutions (3.143), (3.144) and (3.145) with the following parameters $a_1 = 1$, $a_2 = 1$, $d = 100$, $P = -0.5$, $\gamma = 0.4$, $\mu = 0.3$, $D = \pm 0.6$, $C = 2$, $\alpha 3 = 0.2$, $\eta = 0.5$, $\sigma = \pm 0.1$, $k_1 = 0.3$, $k_2 = 0.5$, $k_3 = 0.6$, $k_4 = 0.4$, $k_5 = 0.2$, $k_6 = 0.4$ and $k_7 = 0.5$.
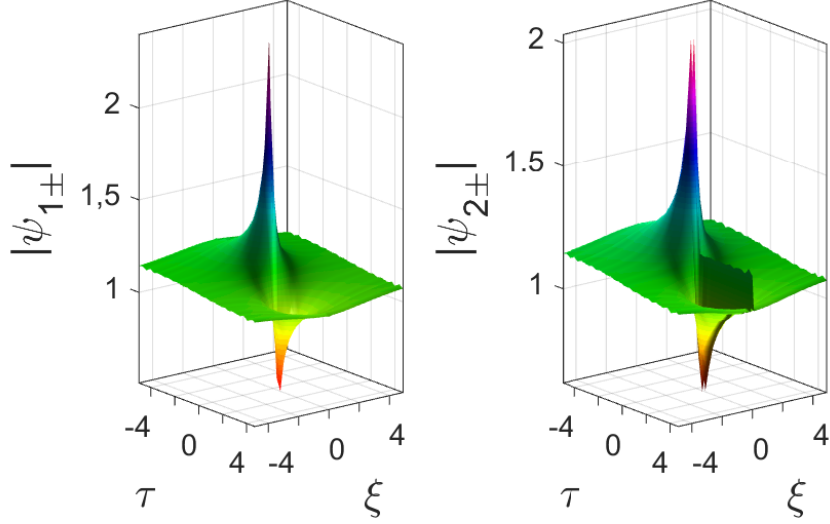
Figure 51: Nonparaxial chiral optical vector rogue waves with constant coefficients in both hands, where the initial conditions are expressed in the form of exact solutions (3.143), (3.144) and (3.145) with the parameters $a_1 = 1$, $a_2 = 1$, $d = 10$, $P = -0.5$, $\gamma = 0.4$, $\mu = 0.3$, $D = \pm 0.6$, $C = 2$, $\alpha 3 = 0.2$, $\eta = 10$, $\sigma = \pm 10$, $k_1 = 0.3$, $k_2 = 0.5$, $k_3 = 0.6$, $k_4 = 0.4$, $k_5 = 0.2$, $k_6 = 0.4$ and $k_7 = 0.5$.

are due to the coupling of vectorial model on the one hand, and to the interaction between waves as consequence of narrowness of the two components in the system, on the other hand. The 2D representations of Fig. 50 showed the limit of the extension of bright and dark spectral structures in the retarded time axis at $\tau = 0$. One can see how the intensity of each spectrum increases when $\tau \to 0$ and the attenuation when moving from each side of $\tau = 0$. It is noted that the weak values of the walk-off are responsible for the wave smoothing.

3.7.4 Influence of combined effects on the vector nonparaxial chiral nonlinear Schrödinger equations with modulated coefficients

3.7.5 Model and explicit algorithm

To improve the description of the waves, one uses the vector nonparaxial chiral NLS equations with modulated coefficients. From the model obtained in Eq. (C25), the coupled system of the nonparaxial NLS equations in chiral optical fibers with coupled space-dependence coupling field is expressed as

$$d(\xi)\psi_{1\xi\xi} + i\psi_{1\xi} + P(\xi,\tau)\psi_{1\tau\tau} - i\gamma(\xi)\psi_{1\tau\tau\tau} + i\mu(\xi,\tau)\psi_1 \mp D(\xi,\tau)\psi_1 - C(\xi,\tau)\left(|\psi_1|^2 + |\psi_2|^2\right)\psi_1$$
$$+i\alpha_3(\xi)\left(|\psi_1|^2 + |\psi_2|^2\right)\psi_{1\tau} + (\eta(\xi) \pm i\sigma(\xi,\tau))\psi_{1\tau} = 0,$$
$$d(\xi)\psi_{2\xi\xi} + i\psi_{2\xi} + P(\xi,\tau)\psi_{2\tau\tau} - i\gamma(\xi)\psi_{2\tau\tau\tau} + i\mu(\xi,\tau)\psi_2 \mp D(\xi,\tau)\psi_2 - C(\xi,\tau)\left(|\psi_1|^2 + |\psi_2|^2\right)\psi_2$$
$$+i\alpha_3(\xi)\left(|\psi_1|^2 + |\psi_2|^2\right)\psi_{2\tau} + (\eta(\xi) \pm i\sigma(\xi,\tau))\psi_{2\tau} = 0.$$

$$(3.147)$$

It can been seen from Eqs. (3.103) that the differential gain and loss term $\eta(\xi)$, the self-steepening $\alpha_3(\xi)$, the gain or loss term $\mu(\xi,\tau)$ and the self-phase modulation $C(\xi,\tau)$, depend on chiral parameter T_c through the relation $C_T = 1 \pm KT_c$ and the linear birefringence $D(\xi,\tau)$ and

walk-off term $\sigma(\xi, \tau)$ are functions of chiral parameter T_c. Considering the order of polynomials of each parameter of the number like Eq. (3.102) obtained from the analytical results, one can choose them as Jacobian elliptic functions for the good stability of the waves and their forms, arbitrarily

$$\alpha_3(\xi) = C_T \times cn(\xi, k), \ \ \eta(\xi) = C_T \times sn(\xi, k),$$
$$d(\xi) = dn(\xi, k), \ \ \gamma(\xi) = cn(\xi, k),$$
$$C(\xi, \tau) = (dn(\xi, k)\tau^2 + cn(\xi, k)\tau + sn(\xi, k)) \times C_T,$$
$$P(\xi, \tau) = -(dn(\xi, k)\tau^2 + cn(\xi, k)\tau + sn(\xi, k)),$$
$$\mu(\xi, \tau) = (dn(\xi, k)\tau^3 + cn(\xi, k)\tau^2 + sn(\xi, k)\tau + dn(\xi, k)) \times C_T,$$
$$\sigma(\xi, \tau) = (dn(\xi, k)\tau^4 + cn(\xi, k)\tau^3 + sn(\xi, k)\tau^2 + dn(\xi, k)\tau + cn(\xi, k)) \times KT_c,$$
$$D(\xi, \tau) = (dn(\xi, k)\tau^6 + cn(\xi, k)\tau^5 + sn(\xi, k)\tau^4 + dn(\xi, k)\tau^3 + cn(\xi, k)\tau^2 + sn(\xi, k)\tau$$
$$+dn(\xi, k)) \times KT_c.$$

$$(3.148)$$

One may also choose them as polynomial functions but our interest is motivated by functions which can generate stable waves. As the propagation variable ξ tends to $n\Delta\xi$ in the discretized domain, the Jacobian elliptic functions take the form

$$dn(\xi, k) \to dn(n\Delta\xi, k) = 1 - \frac{k^2 \sin(n\Delta\xi)^2}{2},$$
$$cn(\xi, k) \to cn(n\Delta\xi, k) = \cos(n\Delta\xi) - k^2 \sin(n\Delta\xi)\left(\frac{n\Delta\xi - \sin(n\Delta\xi \cos(n\Delta\xi))}{4}\right),$$
$$sn(\xi, k) \to sn(n\Delta\xi, k) = \sin(n\Delta\xi) - k^2 \cos(n\Delta\xi)\left(\frac{n\Delta\xi - \sin(n\Delta\xi \cos(n\Delta\xi))}{4}\right).$$

$$(3.149)$$

It can be seen that, by splitting Eqs. (3.147) in the right-and left-hands, four coupled non-paraxial NLS equations which differ by the signs of linear birefringence and walk-off term are obtained. The substitution of the finite difference formulae in Eqs. (3.147) yields

$$u_{n+1}(\tau) = \frac{1}{2d + i\Delta\xi}[(4d - 2P\Delta\xi^2 \frac{\partial^2}{\partial\tau^2} + 2i\gamma\Delta\xi^2 \frac{\partial^3}{\partial\tau^3} - 2i\mu\Delta\xi^2 \pm 2\Delta\xi^2 D$$
$$+2C\Delta\xi^2 \left(|u_n(\tau)|^2 + |v_n(\tau)|^2\right) - 2i\alpha_3\Delta\xi^2 \left(|u_n(\tau)|^2 + |v_n(\tau)|^2\right) \frac{\partial}{\partial\tau}$$
$$-2\Delta\xi^2 \left(\eta \pm i\sigma\right) \frac{\partial}{\partial\tau})u_n(\tau) - (2d - i\Delta\xi) u_{n-1}(\tau)],$$
$$v_{n+1}(\tau) = \frac{1}{2d + i\Delta\xi}[(4d - 2P\Delta\xi^2 \frac{\partial^2}{\partial\tau^2} + 2i\gamma\Delta\xi^2 \frac{\partial^3}{\partial\tau^3} - 2i\mu\Delta\xi^2 \pm 2\Delta\xi^2 D$$
$$+2C\Delta\xi^2 \left(|u_n(\tau)|^2 + |v_n(\tau)|^2\right) - 2i\alpha_3\Delta\xi^2 \left(|u_n(\tau)|^2 + |v_n(\tau)|^2\right) \frac{\partial}{\partial\tau}$$
$$-2\Delta\xi^2 \left(\eta \pm i\sigma\right) \frac{\partial}{\partial\tau})v_n(\tau) - (2d - i\Delta\xi) v_{n-1}(\tau)].$$

$$(3.150)$$

3.7.6 Numerical simulations

By using the difference-differential equation method and fast Fourier transforms (FFTs), let plot the numerical solutions of the coupled nonparaxial chiral NLS equations of each beam (ψ_1 and ψ_2) in both hands, left(-) and right(+) [see Figs. 52, 53 and 54].

Throughout these figures, one remarks that the structure of each component is similar from one hand to the other but a notable difference is observed in the amplitude as observed in Fig. 52. The 2D representations depict in Fig. 53(a), the symmetries of the bright and dark maxima through the retarded time axis τ and the dark-dark symmetries through the propagation distance axis ξ in both side. In Fig. 53(b), a significant decrease of the envelope fields is
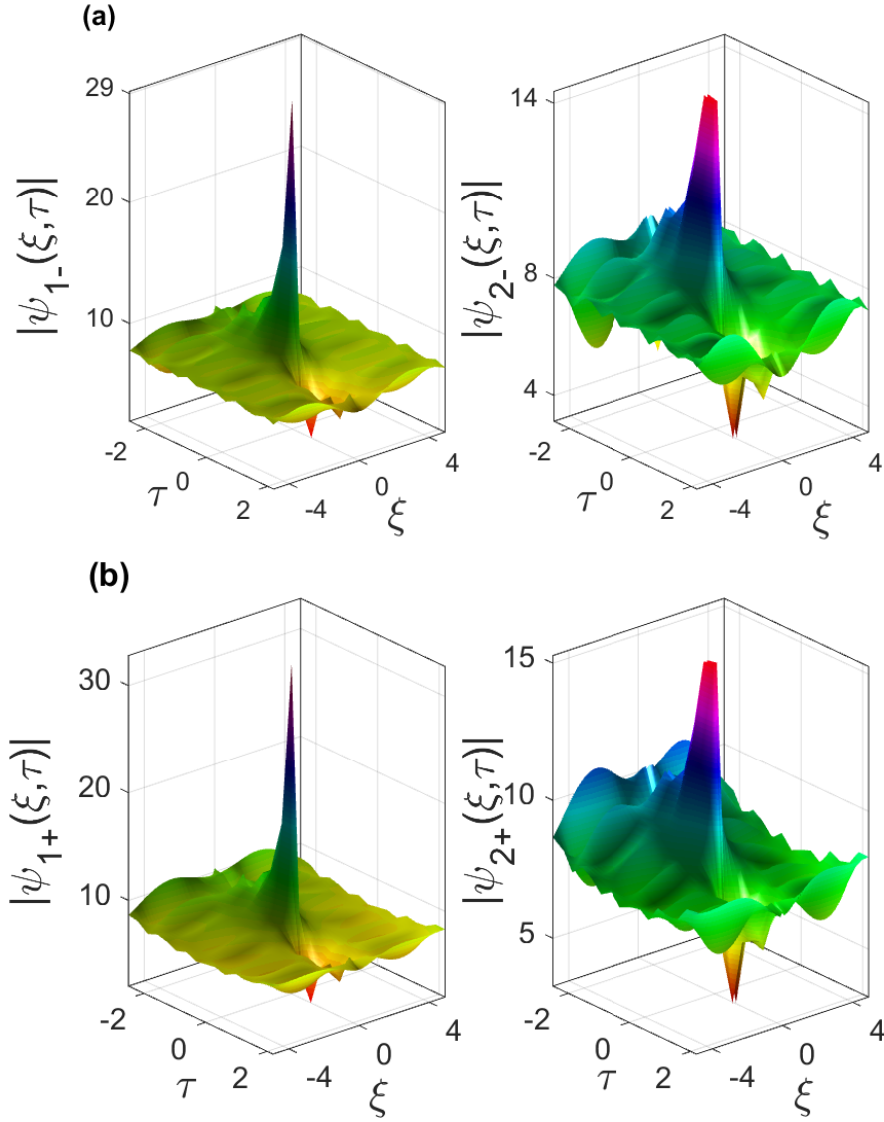
Figure 52: The nonparaxial chiral optical rogue waves with management are derived from Eqs. (3.150), where the parameters of the base equations are given in relations (3.148) and (3.147) and the initial conditions take the form of exact solutions given in relations (3.143), (3.144) and (3.145) with the following arbitrary constant $a_1 = 3$, $a_2 = 3$, $k_5 = 0.2$, $k_6 = 0.4$, $k_7 = 0.5$, $P(\xi, \tau) = dn(\xi, k)\tau^2 + cn(\xi, k)\tau + sn(\xi, k)$, $KT_c = 0.8$ and $C_T = 1 \pm KT_c$.
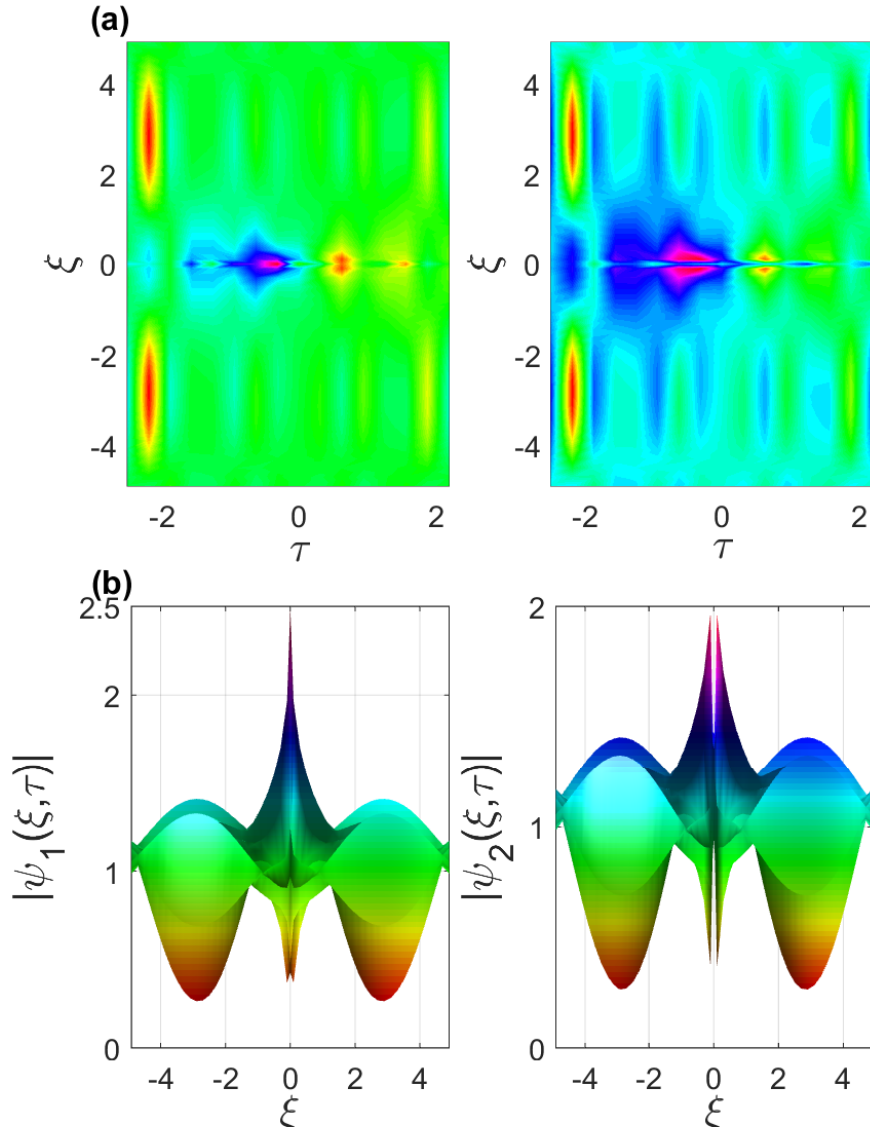
Figure 53: The 2D representation of the nonparaxial chiral optical vector rogue waves where variable coefficients are derived from Eqs. (3.150), and the parameters of the base equations are given in relations (3.148) and (3.147) and the initial conditions take the form of exact solutions given in relations (3.143), (3.144) and (3.145) with the following arbitrary constant $a_1 = 1$, $a_2 = 1$, $k_5 = 0.2$, $k_6 = 0.4$, $k_7 = 0.5$, $P(\xi, \tau) = dn(\xi, k)\tau^2 + cn(\xi, k)\tau + sn(\xi, k)$, $KT_c = 0.8$ and $C_T = 1 \pm KT_c$.
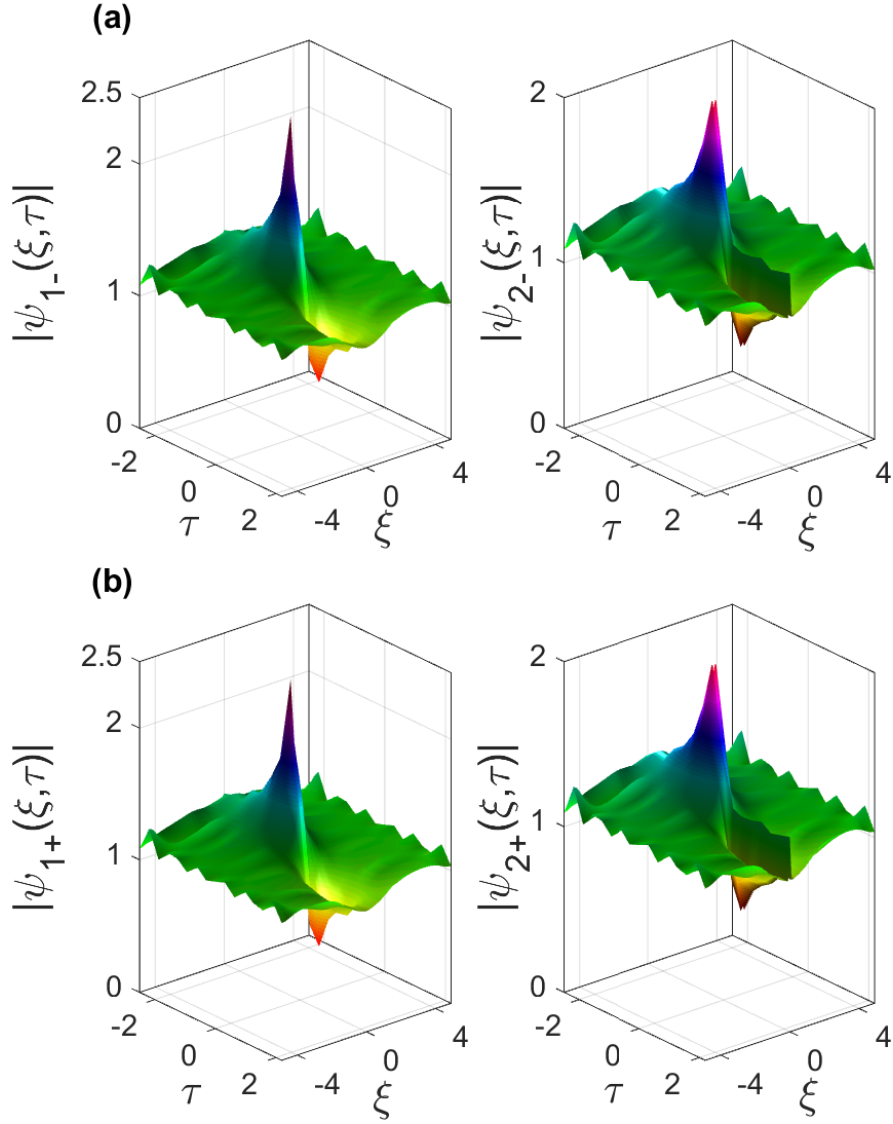
Figure 54: Nonparaxial chiral optical vector rogue waves with modulated coefficients are derived from Eqs. (3.150), where the parameters of the base equations are given in relations (3.148) and (3.147) and where the initial conditions take the form of exact solutions given in relations (3.143), (3.144) and (3.145) with the following arbitrary constant $a_1 = 1$, $a_2 = 1$ and $k_5 = k_6 = k_7 = 1$, $d(\xi) = 10 \times dn(\xi, k)$, $P(\xi, \tau) = -(dn(\xi, k)\tau^2 + cn(\xi, k)\tau + sn(\xi, k))$, $KT_c = 0.8$ and $C_T = 1 \pm KT_c$.

observed when the amplitudes of the solutions are reduced. One also denotes a similitude on the structure and amplitude in Figs. 54. The appearance of curvatures in the four components are due to the unity value of their moduli as expressed in Fig. 54.

3.8 Contrast of optical activity and rogue wave propagation in chiral materials

The term chirality [95] is a well-known concept of great interest in chemistry, biology, pharmacology and optical fields [357, 358]. In the context of chemistry, chirality refers to molecules that lack mirror symmetry. One of the most universally known example is the human hands. In fact, no matter how the two hands are oriented, it is impossible for the both hands to be coincide through translations and rotations. In the context of optics, chirality refers to optical activity which is the ability to rotate plane polarized light. The observe rotation of this plane polarized light can be directed to the right-hand, that is a clockwise rotation, called dextrorotatory or to the left-hand, that is a counter clockwise rotation, called levorotatory. As consequence, enantiomers or optical isomers are designated in the literature as right-and left-handed [203]. Therefore, chirality can be defined as fundamental property of molecules and materials that leads to optical activity effects [204]. Among chiral materials, chiral optical fibers are materials of crucial importance. They give rise to optical activity effects such as optical rotation and circular dichroism which are optical characterization techniques of molecules [357]. In fact, these effects are used to investigate the structures of molecules and to elucidate the secondary structure of biomolecules. Optical activity has attracted and inspired great effort in the developing of active photonic chiral metamaterials [205]. These materials are designated to deliver an unusual electromagnetic response, in spite of the fact that optical activity is a linear effect. Optical activity effects have been found in both linear and nonlinear optics. In nonlinear optical fields, others characterization techniques like the second-harmonic generation circular dichroism (SHG - CD) and the second-harmonic generation optical rotatory dispersion (SHG - ORD) were undertaken by T. Verbiest *et al.* [206]. Later, A. Bruyere *et al.* [207] have studied the formation of chiral supramolecular aggregates at an air-water interface with the SHG technique. Futhermore, Huttunen *et al.* [208] have shown that the third-harmonic generation circular dichroism (THG - CD) effects could occur in biological materials. Briefly, many works have been done in chiral metamaterials [209], nanomaterials [210, 211] and in photonic crystals [212]. In view of great scientific importance of chiral molecules in life science and pharmaceutical industries [92], One mainly focuses the interest on the impact of chiral materials like chiral optical fibers in optical communication. Several nonlinear phenomena have been studied in chiral media [84, 85, 86] with the objectives to control the chiral level and protect organic chiral materials from damage during the processing temperature of silica. Therefore, controllability of spontaneous waves has been performed in both theoretical and experimental approaches to investigate the interesting phenomena of rogue waves in optical fibers. One focuses the attention on the contrast of optical activity to elucidate the interplay of chiral optical fiber on rogue wave propagation. This investigation is based on an extended integrable Hirota equation with

linear and nonlinear effects, namely, nonparaxial chiral NLS equation.

3.8.1 Model and integrability constraints

To reveal the contrast of optical activity and elucidate the interplay of chiral optical fibers on rogue wave propagation, one considers an extended NLS equation with linear and nonlinear effects [91]

$$d\psi_{\xi\xi} + i\psi_\xi + P\psi_{\tau\tau} - i\gamma\psi_{\tau\tau\tau} + r_1\left(i\mu \mp D\right)\psi - C|\psi|^2\psi + i\alpha_3|\psi|^2\psi_\tau + r_2\left(\eta \pm i\sigma_3\right)\psi_\tau = 0, \tag{3.151}$$

where ξ and τ (z and t) are the scaled (unscaled) coordinates in the propagation direction and temporal dimension, respectively. $\psi\left(\xi, \tau\right)$ is the envelope field of the forward and backward components of the waves. In regard of the derivation of the above model (Eq. (3.151)) in reference [91], the parameters r_1 and r_2 are equal to unity. Nevertheless, these parameters can be different in these cases. In the absence of either the linear gain/loss (μ) or linear birefringence (D), on the one hand, and in the absence of either the differential gain/loss (η) or linear group velocity (σ_3), on the other hand, the parameters r_1 and r_2, respectively, can be different to the unity depending now to the term in factor to them. Moreover, these parameters depend in major cases, to the physical system. Thus, for $r_1 = r_2 = 1$, the relations between the scaled and unscaled variables stand for

$$\tau = \frac{\omega_0^{1/3}\beta^{1/6}}{\sqrt{K''}(2K_0)^{1/6}}t', \ \xi = \frac{\omega_0^{2/3}\beta^{1/3}}{(2K_0)^{1/3}}z' = \frac{z}{L_D},$$

$$L_D = \frac{(2K_0)^{1/3}\left(1 - K_0^2T_c^2\right)}{\beta^{1/3}\omega_0^{2/3}} = \frac{-\left(1 - K_0^2T_c^2\right)}{2K_0d},$$

$$\psi\left(\xi, \tau\right) = \frac{\omega_0^{2/3}\beta^{1/3}}{(2K_0)^{1/3}}\phi = -2K_0d\phi,$$

$$\phi = \Psi_{R,L} = E_x \pm iE_y, \begin{cases} E_x = E_x\left(z, t\right) \\ \\ E_y = E_y\left(z, t\right) \end{cases}, \tag{3.152}$$

$$\begin{cases} t' = t - \frac{1}{v_g}z^* \\ \\ z' = z^* \end{cases}, \ z^* = \frac{z}{\left(1 - K_0^2T_c^2\right)},$$

132

where, $\Psi_{R,L}$ are the right(R)-and left(L)-handed of wave components. Then, the parameters of the Eq. (3.151) are

$$d = -\frac{\beta^{1/3}\omega_0^{2/3}}{(2k_0)^{4/3}}, \quad \eta = \frac{\alpha C}{\sqrt{K''}\omega_0^{1/3}\beta^{1/6}(2k_0)^{5/6}},$$

$$\gamma = \frac{K'''}{6}\frac{\beta^{1/6}\omega_0^{1/3}}{(2K_0)^{1/6}\left(K''\right)^{3/2}}, \quad C = 1 \pm K_0 T_c,$$

$$\mu = C\Gamma, \quad \Gamma = \frac{\omega_0^{1/3}\alpha}{(2K_0)^{1/3}\beta^{1/3}}, \tag{3.153}$$

$$P = \tfrac{1}{2}\left(1 - \frac{k'^2}{K''k_0}\right), \quad \sigma_3 = \frac{k_0 T_c(2k_0)^{7/6}}{\sqrt{K''}\omega_0^{4/3}\beta^{1/6}},$$

$$D = \frac{K_0^2 T_c(2K_0)^{1/3}}{\beta^{1/3}\omega_0^{2/3}}, \quad \alpha_3 = \frac{C(2K_0)^{5/6}\beta^{1/6}}{\sqrt{K''}\omega_0^{2/3}K_0},$$

with

$$\begin{cases} K' = \frac{\partial K}{\partial \omega} = \frac{1}{v_g} \\ \\ K'' = \frac{\partial K'}{\partial \omega} \to GVD \quad , \\ \\ K''' = \frac{\partial K''}{\partial \omega} \to TOD \end{cases} \begin{cases} K_0 = \frac{\omega_0}{v} \\ \\ v^2 = \frac{1}{\mu_0 \varepsilon_0} \\ \\ \beta = \mu_0 \varepsilon_2 \\ \\ \alpha = \mu_0 \sigma \end{cases}, \tag{3.154}$$

in which, L_D is the diffraction length of the beam, α, the attenuation coefficient, σ, the electrical conductivity, ε_0, the linear permittivity, ε_2, the nonlinear permittivity, μ_0, the permeability, T_c, chiral parameter of the optical fiber, ω_0, the frequency of the wave, K_0, the wave number, v, the light velocity and ϕ, the complex envelope of the optical field in the chiral fiber. Then, coefficients d, P, γ, μ, D, C, α_3, η and σ_3 are nonparaxial, group-velocity dispersion (GVD), third-order dispersion (TOD), linear gain or loss term, linear birefringence, self-phase modulation (SPM), self-steepening (SS), differential gain or loss and linear group-velocity, respectively.

The envelope field $\psi(\xi, \tau)$ contains both forward and backward propagating components in such a way that the change from the unscaled to scaled longitudinal coordinate of the oscillation of the field is given by

$$\exp\{-iK_\pm z\} = \exp\left\{i\frac{\xi}{2d}\left(1 - K_0^2 T_c^2\right)\right\}, \tag{3.155}$$

where $K_\pm = K = K_0$. It can be seen from this relation (3.155) that apart from the wave number K_0, the scaled longitudinal coordinate is related to two important parameters. That are the nonparaxial (d) and chiral parameter (T_c) which will improve the description of waves propagating in chiral medium. Equation (3.151) contains other cases of NLS equation. If one sets $d = 0$, $P = \frac{1}{2}$, $\gamma = 0$, $\mu = 0$, $D = 0$, $\alpha_3 = 0$, $\eta = 0$ and $\sigma_3 = 0$, Eq. (3.151)becomes the standard NLS equation in the focusing regime for $C = -1$ and defocusing regime for $C = 1$. If in addition to these conditions, $d \neq 0$, Eq. (3.151) stands for the nonparaxial NLS equation. The integrable Hirota equation is also obtained for $d = 0$, $P = 1$, $\gamma = 2\sqrt{2}$, $\mu = 0$, $D = 0$,

$\alpha_3 = -6\sqrt{2}$, $\eta = 0$, $\sigma_3 = 0$ and $C = -1$. Equation (3.151) has been found as a nonparaxial chiral NLS equation in our previous work [91]. This study is based now on the scalar form with constant coefficients. In this case, instead of Jacobian elliptic functions, parameters of the system will be taken as polynomial functions.

A higher-order NLS equation is eminently suitable to describe realistic problems when it satisfies the integrability and controllability conditions. Throughout the term in factor to the SS coefficient α_3, it can be seen that Eq. (3.151) verifies the condition of controllability of higher-order NLS equations [71]. The integrability of the model is satisfied for $\gamma = \frac{\alpha_3}{6C}$, $P = \frac{1}{2}$, $r_1 = r_2 = \frac{\alpha_3}{2C}$ and $d = \frac{5\alpha_3}{3C}$. If $\alpha_3 = 0$, then, Eq. (3.151) is reduced to the standard NLS equation. In the case where $r_1 = r_2 = 1$, let find the integrability constraints of the model by means of similarity reduction method. Thus, let use the envelope filed in the form [71]

$$\psi(\xi, \tau) = A(\xi)V\left[Z(\xi), T(\xi, \tau)\right]\exp\left\{i\rho(\xi, \tau)\right\}, \tag{3.156}$$

to find the integrability conditions of the parameters related to the envelope field in which $A(\xi)$ is the amplitude, $Z(\xi)$ the effective propagation distance, $T(\xi, \tau)$ the similitude variable and $V\left[Z(\xi), T(\xi, \tau)\right]$ the complex field. The variable $\rho(\xi, \tau)$ is the phase of the wave. The substitution of Eq. (3.156) into Eq. (3.151) gives a coupled system of partial differential equations with constant coefficients

$$
\begin{aligned}
&d(A_{\xi\xi}V + 2A_\xi Z_\xi V_Z + 2A_\xi T_\xi V_T + 2AZ_\xi T_\xi V_{ZT} + AZ_{\xi\xi}V_Z + AT_{\xi\xi}V_T \\
&+AZ_\xi{}^2 V_{ZZ} + AT_\xi{}^2 V_{TT} - A\rho_\xi{}^2 V) - AV\rho_\xi + P(AV_{TT}T_\tau{}^2 + AV_T T_{\tau\tau} - AV\rho_\tau{}^2) \\
&+\gamma(3AV_T T_{\tau\tau}\rho_\tau + 3AV_T T_\tau\rho_{\tau\tau} + 3AV_{TT}T_\tau{}^2\rho_\tau + AV\rho_{\tau\tau\tau} - AV\rho_\tau{}^3) \\
&\mp DAV - CA^2|V|^2AV - \alpha_3 A^2|V|^2 AV\rho_\tau + \eta AT_\tau V_T \mp \sigma_3 AV\rho_\tau = 0,
\end{aligned}
\tag{3.157}
$$

$$
\begin{aligned}
&d(AV\rho_{\xi\xi} + 2A_\xi\rho_\xi V + 2AZ_\xi\rho_\xi V_Z + 2A\rho_\xi T_\xi V_T) + A_\xi V + AV_Z Z_\xi + AV_T T_\xi \\
&+P(AV\rho_{\tau\tau} + 2AV_T T_\tau\rho_\tau) - \gamma(AV_T T_{\tau\tau\tau} + 3AV_{TT}T_\tau T_{\tau\tau} + AV_{TTT}T_\tau{}^3 \\
&-3AV_T T_\tau\rho_\tau{}^2 - 3AV\rho_{\tau\tau}\rho_\tau) + \mu AV + \alpha_3 A^2|V|^2 AV_T T_\tau + \eta AV\rho_\tau \pm \sigma_3 AT_\tau V_T = 0,
\end{aligned}
\tag{3.158}
$$

where the scripts of differential equations are simplified as $A(\xi) = A$, $Z(\xi) = Z$, $T(\xi, \tau) = T$, $\rho(\xi, \tau) = \rho$ and $V\left[Z(\xi), T(\xi, \tau)\right] = V$. It is of crucial interest to reduce Eq. (3.151) into the integrable Hirota equation which has a well-known integrability conditions [116], satisfying the complex filed of the ansatz $V\left[Z(\xi), T(\xi, \tau)\right]$

$$i\frac{\partial V}{\partial Z} = -\frac{\partial^2 V}{\partial T^2} + G|V|^2 V + 2\sqrt{2}i\nu\left(\frac{\partial^3 V}{\partial T^3} + 3|V|^2\frac{\partial V}{\partial T}\right). \tag{3.159}$$

Thus, the coupled system can be reduced as follows

$$\gamma T_\tau T_{\tau\tau} = 0, \tag{3.160}$$

$$T_\xi + 2dT_\tau\rho_\tau + 2PT_\tau\rho_\tau \pm \sigma_3 T_\tau - \gamma\left(T_{\tau\tau\tau} - 3T_\tau\rho_\tau{}^2\right) = 0, \tag{3.161}$$

$$A_\xi + A(d\rho_{\xi\xi} + \rho_{\tau\tau}P + 3\gamma\rho_{\tau\tau}\rho_\tau + \mu + \eta\rho_\tau) = 0, \tag{3.162}$$

$$\gamma T_\tau{}^3 + 2\sqrt{2}\nu Z_\xi = 0, \tag{3.163}$$

$$A_\xi V + A Z_\xi V_Z + A T_\xi V_T = 0, \tag{3.164}$$

$$\alpha_3 A^2 T_\tau - 6\sqrt{2}\nu Z_\xi = 0, \tag{3.165}$$

$$dT_{\xi\xi} + PT_{\tau\tau} + 3\gamma\left(T_{\tau\tau}\rho_\tau + T_\tau\rho_{\tau\tau}\right) + \eta T_\tau = 0, \tag{3.166}$$

$$Z_\xi + dT_\xi{}^2 + PT_\tau{}^2 + 3\gamma\rho_\tau T_\tau{}^2 = 0, \tag{3.167}$$

$$\rho_\xi + d\rho_\xi{}^2 + P\rho_\tau{}^2 + \gamma\left(\rho_\tau{}^3 - \rho_{\tau\tau\tau}\right) \pm \sigma_3\rho_\tau \pm D = 0, \tag{3.168}$$

$$GZ_\xi + A^2\left(C + \alpha_3\rho_\tau\right) = 0, \tag{3.169}$$

$$A_{\xi\xi}V + 2A_\xi Z_\xi V_Z + 2A_\xi T_\xi V_T + 2AZ_\xi T_\xi V_{ZT} + AZ_{\xi\xi}V_Z + AZ_\xi{}^2 V_{ZZ} = 0. \tag{3.170}$$

From this preliminary method of rogue wave finding, the constraints are deduced from the differential equations of which the simplified forms stand from Eq. (3.160) to Eq. (3.170), respectively, as follows: $-3AV_{TT} \neq 0$, $AV_T \neq 0$, $V \neq 0$, $-AV_{TTT} \neq 0$, $2d\rho_\xi \neq 0$, $A|V|^2V_T \neq 0$, $AV_T \neq 0$, $AV_{TT} \neq 0$, $-AV \neq 0$, $-A|V|^2V \neq 0$ and $d \neq 0$. These conditions play an important role in the sense that they are necessary to find the integrability constants of parameters related to the envelope field.

3.8.2 Analytical and numerical rogue wave solutions

To construct the analytical rogue wave solutions, one firstly finds the parameters of the envelope field by solving the above differential equations. The integration is made from the simplest differential equation to the highly complex one. In doing so, Eq. (3.160) yields for $\gamma(\xi) \neq 0$ and $T_\tau T_{\tau\tau} = 0$ to the similarity variable

$$T\left(\xi, \tau\right) = T_1(\xi)\tau + T_0(\xi), \tag{3.171}$$

where the arbitrary functions $T_1(\xi)$ and $T_0(\xi)$ should be defined. One notices that $T_{\tau\tau} = 0$ is the second derivative condition of the similarity variable in the temporal dimension. Equation (3.163) gives the effective propagation distance

$$Z(\xi) = -\frac{\sqrt{2}\gamma}{4\nu}\int_0^\xi T_1(s)^3 ds. \tag{3.172}$$

The substitution of expressions (3.171) and (3.172) into Eq. (3.165) tends to

$$A(\xi) = \sqrt{\frac{-3\gamma T_1(\xi)^2}{\alpha_3}}, \tag{3.173}$$

with $\alpha_3 < 0$ and $\gamma > 0$. Then, the substitution of expressions (3.172) and (3.173) into Eq. (3.169) gives the phase of the envelope field which can be written as

$$\rho(\xi, \tau) = -\left(\frac{GT_1(\xi)}{6\sqrt{2}\nu} + \frac{C}{\alpha_3}\right)\tau + \rho_0(\xi), \tag{3.174}$$

where $\rho_0(\xi)$ should be defined by taking into account, the second derivative condition in the temporal dimension of the phase, that is, $\rho_{\tau\tau} = 0$. Through relations (3.171) and (3.174) one finds from Eq. (3.166), the second derivative condition in the propagation direction of the similarity variable

$$T_{\xi\xi} = \frac{-\eta T_1(\xi)}{d}. \tag{3.175}$$

The substitution of relations (3.171) and (3.174) in Eqs. (3.161) and (3.167) shows that the first derivative of the similarity variable is independent of the temporal variable τ. This means that $T_{1\xi} = 0$ and $T_{0\xi} = T_\xi \neq 0$. Therefore, $T_1(\xi)$ must be a constant. Thus, the arbitrary function $T_0(\xi)$ deduced from Eq. (3.175) becomes

$$T_0(\xi) = \frac{-\eta T_1(\xi)}{2d}\xi^2. \tag{3.176}$$

The substitution of relations (3.171), (3.174) and (3.173) in Eqs. (3.162) and (3.168) shows that the first derivative of the phase is independent of the temporal variable τ. This means that $\rho_{1\xi} = 0$ and $\rho_{0\xi} = \rho_\xi \neq 0$. This implies that $\rho_1(\xi) = -\left(\frac{GT_1(\xi)}{6\sqrt{2}\nu} + \frac{C}{\alpha_3}\right)$ is a constant. This affirmation is true as it has been shown that $T_1(\xi)$ is a constant. Therefore, the second derivative condition of the phase in the propagation direction yields

$$\rho_{\xi\xi} = \frac{1}{d}\left[\eta\left(\frac{GT_1(\xi)}{6\sqrt{2}\nu} + \frac{C}{\alpha_3}\right) - \mu\right]. \tag{3.177}$$

From this second derivative condition, one deduces the arbitrary function of the phase

$$\rho_0(\xi) = \frac{1}{2d}\left[\eta\left(\frac{GT_1(\xi)}{6\sqrt{2}\nu} + \frac{C}{\alpha_3}\right) - \mu\right]\xi^2. \tag{3.178}$$

By choosing the arbitrary constant $T_1(\xi) = 2$, the parameters are summarized as follows

$$\begin{cases} T(\xi, \tau) = 2\tau - \frac{\eta}{d}\xi^2, \\[2mm] Z(\xi) = \frac{-2\sqrt{2}\gamma}{\nu}\xi, \\[2mm] A(\xi) = \left(\frac{-12\gamma}{\alpha_3}\right)^{\frac{1}{2}}, \begin{cases} \gamma > 0, \\ \alpha_3 < 0, \end{cases} \\[4mm] \rho(\xi, \tau) = -\left(\frac{\sqrt{2}G}{6\nu} + \frac{C}{\alpha_3}\right)\tau + \frac{1}{2d}\left[\eta\left(\frac{\sqrt{2}G}{6\nu} + \frac{C}{\alpha_3}\right) - \mu\right]\xi^2. \end{cases} \tag{3.179}$$

In view of great success of the Peregrine soliton in the modelling of realistic rogue wave, one constructs the rogue wave solutions through the modified Darboux transformation method.

From the well-known rogue wave solutions of the integrable Hirota equation [116], one deduces the first-and second-order of the complex field $V\left[Z(\xi), T(\xi, \tau)\right]$ which is valid for $G = -1$ for rogue wave finding. Therefore, the different expressions of the complex field yield

$$V_1\left[Z(\xi), T\left(\xi, \tau\right)\right] = \left[1 - \frac{G_1 + iH_1}{D_1}\right]\exp\left\{iZ(\xi)\right\}, \tag{3.180}$$

where

$$G_1 = 4, \quad H_1 = 8Z(\xi),$$

$$D_1 = 1 + \left[\sqrt{2}T\left(\xi, \tau\right) + 12\nu Z(\xi)\right]^2 + 4Z(\xi)^2. \tag{3.181}$$

and

$$V_2\left[Z(\xi), T\left(\xi, \tau\right)\right] = \left[1 + \frac{G_2 + iZ(\xi)H_2}{D_2}\right]\exp i\left\{Z(\xi)\right\}. \tag{3.182}$$

where G_2, H_2 and D_2 are given by the relations

$$G_2 = -48T^4 - 1152\sqrt{2}\nu Z T^3 - 144T^2[4Z^2\left(36\nu^2 + 1\right) + 1] - 576\sqrt{2}\nu Z T \times$$
$$[12Z^2\left(12\nu^2 + 1\right) + 7] - 192Z^4\left[216\left(6\nu^4 + \nu^2\right) + 5\right] - 864Z^2\left(44\nu^2 + 1\right) - 36,$$

$$H_2 = -96T^4 - 2304\sqrt{2}\nu Z T^3 - 96T^2[4Z^2\left(108\nu^2 + 1\right) - 3] - 1152\sqrt{2}\nu Z T \times$$
$$[4Z^2\left(36\nu^2 + 1\right)] - 384Z^4(36\nu^2 + 1)^2 - 192Z^2\left(180\nu^2 + 1\right) + 360, \tag{3.183}$$

$$D_2 = 8T^6 + 288\sqrt{2}\nu Z T^5 - 432Z^4\left(624\nu^4 - 40\nu^2 - 1\right) + 36Z^2\left(556\nu^2 + 11\right) + 9$$
$$+ 64Z^6(36\nu^2 + 1)^3 + 96\sqrt{2}Z T^3\left[12Z^2\left(60\nu^2 + 1\right) - 1\right]$$
$$+ 12T^4[4Z^2\left(180\nu^2 + 1\right) + 1] + 6T^2[16Z^4\left[216\nu^2\left(30\nu^2 + 1\right) - 1\right]$$
$$- 24Z^2\left(60\nu^2 + 1\right) + 9] + 72\sqrt{2}\nu Z T[16Z^4\left(36\nu^2 + 1\right) + 8Z^2\left(1 - 108\nu^2\right) + 17].$$

Then, collecting the founded variables with the above solutions of complex field together, one obtains the first-and second-order rational solutions, related to a particular solution of Eq. (3.151), respectively, in the form

$$\psi_1 = A(\xi)\left[1 - \frac{G_1 + iH_1}{D_1}\right]\exp\left\{iZ(\xi) + i\rho\left(\xi, \tau\right)\right\}, \tag{3.184}$$

$$\psi_2 = A(\xi)\left[1 + \frac{G_2 + iZ(\xi)H_2}{D_2}\right]\exp\left\{iZ(\xi) + i\rho\left(\xi, \tau\right)\right\}, \tag{3.185}$$

where parameters are given in relations (3.179), (3.180), (3.181), (3.182) and (3.183). These first-and second-order rational solutions are used to describe the propagation of nonparaxial optical rogue waves in chiral materials. The second-order rational solution is due to the collision between ultrashort pulses in the optical fiber. The particularity of these solutions is the simultaneous controllability of their amplitudes through the parameters, which can be used to manage their amplitudes and shapes. As the nonparaxiality, TOD, SS, SPM and differential gain or loss terms step in the system, they can therefore provide a more convenient and controlled environment for further applications in optical communication.

The methodology of the numerical integration is based on a pseudo-spectral method namely, difference-differential equation method. The basic of the pseudo-spectral method is to use the discrete Fourier transform to evaluate the spatial derivative of the model. Nevertheless, within the context of optical fiber, these derivatives depend on coordinates of the propagation direction; those are $\psi_{\xi\xi}$ and ψ_{ξ} which stand for the nonparaxial and propagation terms, respectively. The using of their finite difference formulae with errors of second-order gives the difference-differential equation below related to the model (Eq. (3.151)) for $\psi(\xi, \tau) = u(\xi, \tau)$

$$u_{n+1}(\tau) = \frac{1}{2d+i\Delta\xi}[(4d - 2P\Delta\xi^2\frac{\partial^2}{\partial\tau^2} + 2i\gamma\Delta\xi^2\frac{\partial^3}{\partial\tau^3} - 2i\mu\Delta\xi^2 \pm 2\Delta\xi^2 D + 2C\Delta\xi^2|u_n(\tau)|^2$$
$$-2i\alpha_3\Delta\xi^2|u_n(\tau)|^2\frac{\partial}{\partial\tau} - 2\Delta\xi^2(\eta \pm i\sigma)\frac{\partial}{\partial\tau})u_n(\tau) - (2d - i\Delta\xi)u_{n-1}(\tau),$$

(3.186)

with

$$\begin{cases} u_n(\tau) \equiv u(n\Delta\xi, \tau) \\ u_{n-1}(\tau) \equiv u((n-1)\Delta\xi, \tau) \\ u_{n+1}(\tau) \equiv f(u_n(\tau), u_{n-1}(\tau)) \end{cases}.$$

(3.187)

Equation (3.186) defines the explicit algorithm in the discretized domain in which the propagation variable ξ tends to $n\Delta\xi$. Then, the transverse differential operators $\partial^2/\partial\tau^2$, $\partial^3/\partial\tau^3$ and $\partial/\partial\tau$ are computed efficiently and accurately by the fast Fourier transforms (FFTs). The accuracy and convergence of this method has been demonstrated in the literature [61]. This method has the advantage of being explicit, means, simple implementation and low computation of the model and then its flexibility in the modeling of nonparaxial NLS equation with higher-order nonlinear effects. In this work, the first-and second-order analytical solutions are used as initial conditions for the numerical simulation. Therefore, the implementation of the index n in Eq. (3.186), in view of relation (3.187), gives the numerical solutions of optical rogue wave propagating in chiral materials.

3.8.3 Contrast of optical activity and interplay of chiral materials

The representation of analytical and numerical solutions of optical rogue waves constructed in previous section is of special interest, in the sense that their profiles will reveal the contrast of optical activity. It can be seen from relation (3.153) that, among coefficients which are functions of chiral parameter (T_c), η, C and μ are two components chiral parameters, whereas D and σ_3 are one component chiral parameters. Therefore, they can be chosen as follows

$$\begin{cases} \alpha_3 = -\alpha_0(1 \pm K_0 T_c) \\ \alpha_0 = 4, \begin{cases} \alpha_{3+} = -6 \\ \alpha_{3-} = -2 \end{cases} \end{cases}, \quad \begin{cases} \eta = \eta_0(1 \pm K_0 T_c) \\ \eta_0 = \frac{2}{3}, \begin{cases} \eta_+ = 1 \\ \eta_- = \frac{1}{3} \end{cases} \end{cases},$$

(3.188)

$$\begin{cases} C = C_0(1 \pm K_0 T_c) \\ C_0 = -\frac{2}{3}, \begin{cases} C_+ = -1 \\ C_- = -\frac{1}{3} \end{cases} \end{cases}, \quad \begin{cases} \mu = \mu_0(1 \pm K_0 T_c) \\ \mu_0 = 0.2, \begin{cases} \mu_+ = 0.3 \\ \mu_- = 0.1 \end{cases} \end{cases},$$

where $K_0 T_c = 0.5$ and with $\gamma = 0.2$, $G = -1$, $P = 0.5$, $D = 0.06$ and $\sigma_3 = 0.1$. To plot the first-and second-order analytical rogue wave solutions, one uses a MATLAB program in

which the coordinates ξ, τ are bounded in the interval $[-10, 10]$. Thus, the first-order rogue wave solutions depicted in Figs. 55, 56 and 57 are computed from Eqs. (3.179), (3.181), (3.184) and (3.188). Then, the second-order rogue wave solutions represented in Figs. 58, 59 and 60 are computed from Eq. (3.179), (3.183), (3.185) and (3.188). Each figure is obtained for a different value of parameters d and ν as shown in figure captions. The guideline techniques given above are of special interest for the numerical simulation in Figs. 61 and 62. The differential operators are expressed in the spectral domain through the FFTs in which the spectral parameter k is defined for $N = 128$ iterations with the given length $L = 40$. Therefore, the implementation of n in Eq. (3.186) is done for 102 iterations in the propagation direction ξ and where $\Delta\xi = 0.05$. According to the above parameters, the analytical and numerical representations are illustrated.
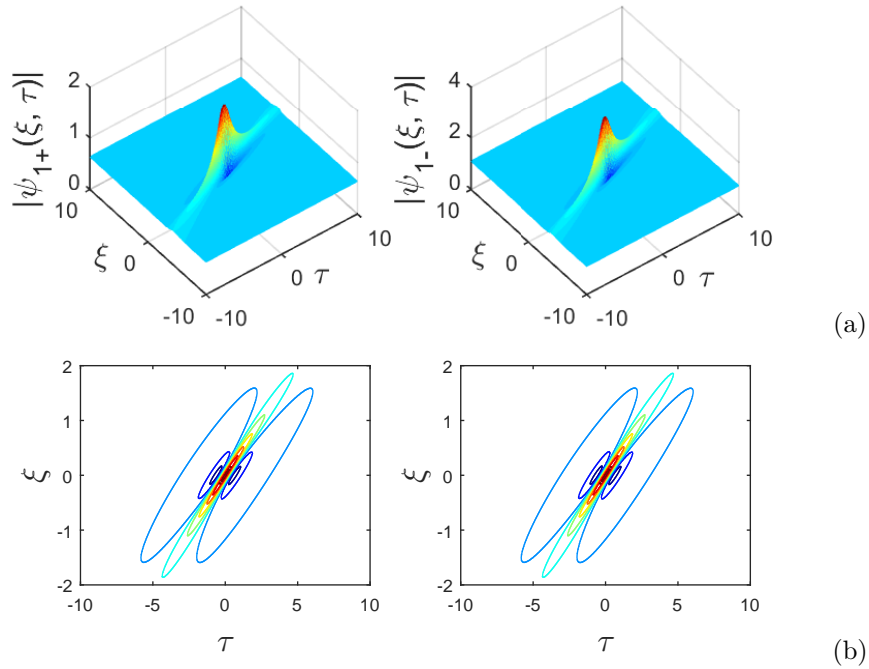
Figure 55: Plot (a) and contour plot (b) of the first-order rogue wave solution: Eq. (3.184), with $d = 10$ and $\nu = 0.6$.

Due to the electromagnetic nature of chiral medium, there are two coupled characteristic waves in chiral optical fibers. This property of chiral medium is therefore observed in analytical and numerical representations throughout the LCP and RCP components. The structure of the waves are in accordance with rogue waves features. The short lifetime of rogue wave profiles is well observed throughout the point of their appearance and disappearance [see Figs. 55, 56, 58, 59, 60 and 61]. Figures 58, 59, 60, 61 and 62 exhibit the collision of rogue waves, but it can be seen that their amplitudes are almost the same when one compares the maximum peak in Figs. 55 and 58 and then, 56 and 59. It means that after collision, the waves keep their amplitude. This is a property of solitary waves, but as these waves are also localized in both space (τ) and time (ξ), they are usual rogue waves. Nevertheless, a difference is observed when comparing the high peak in Figs. 57 and 60. This difference is due to the weak value of the nonparaxial
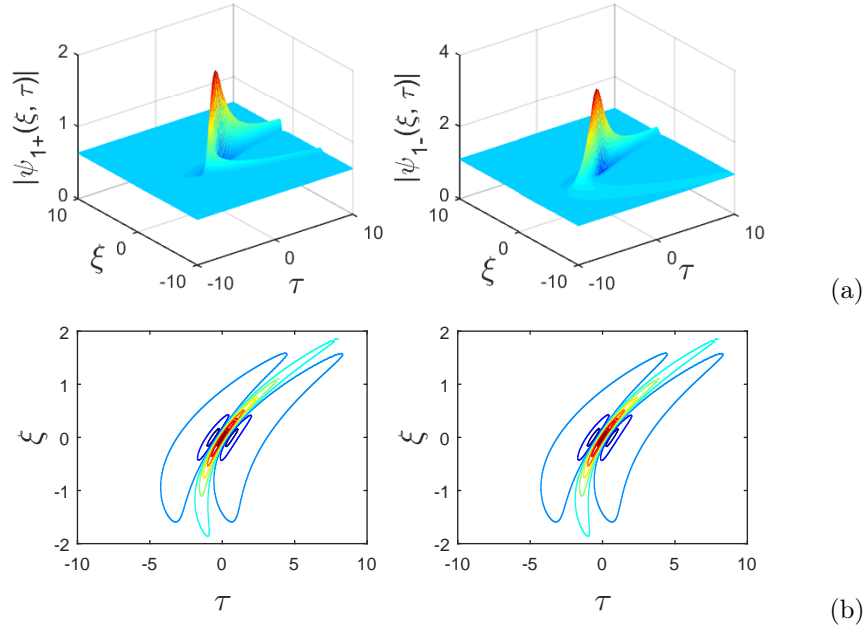
Figure 56: 3D representation (a) and contour plot (b) of the first-order analytical rogue wave amplitude of Eq. (3.184), for $d = 0.5$ and $\nu = 0.6$.
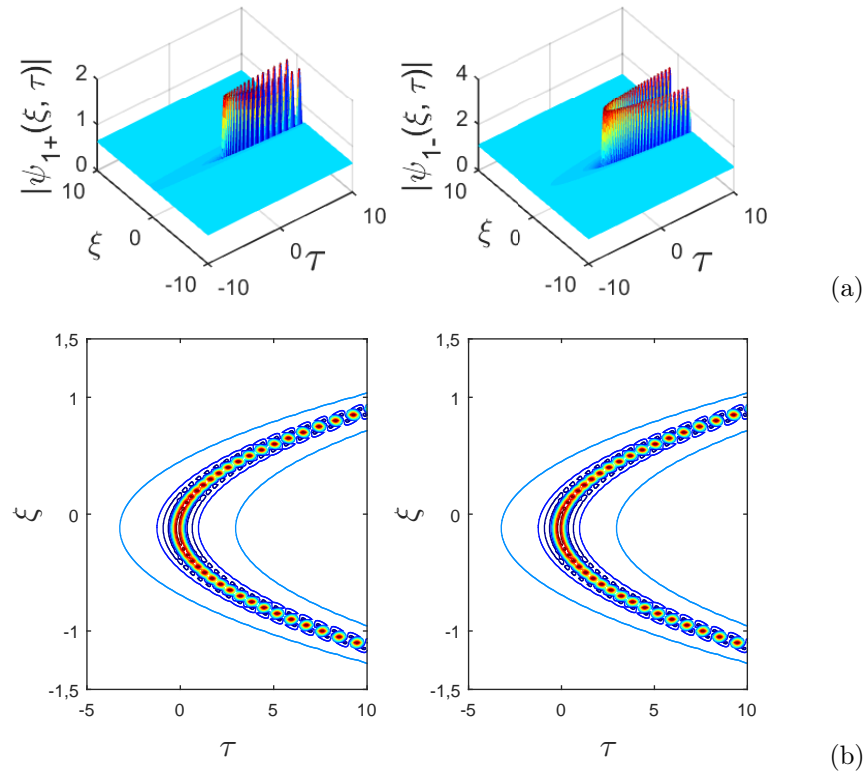
Figure 57: First-order amplitude of nonparaxial chiral optical rogue waves of Eq. (3.184), with $d = 0.05$ and $\nu = 6$.
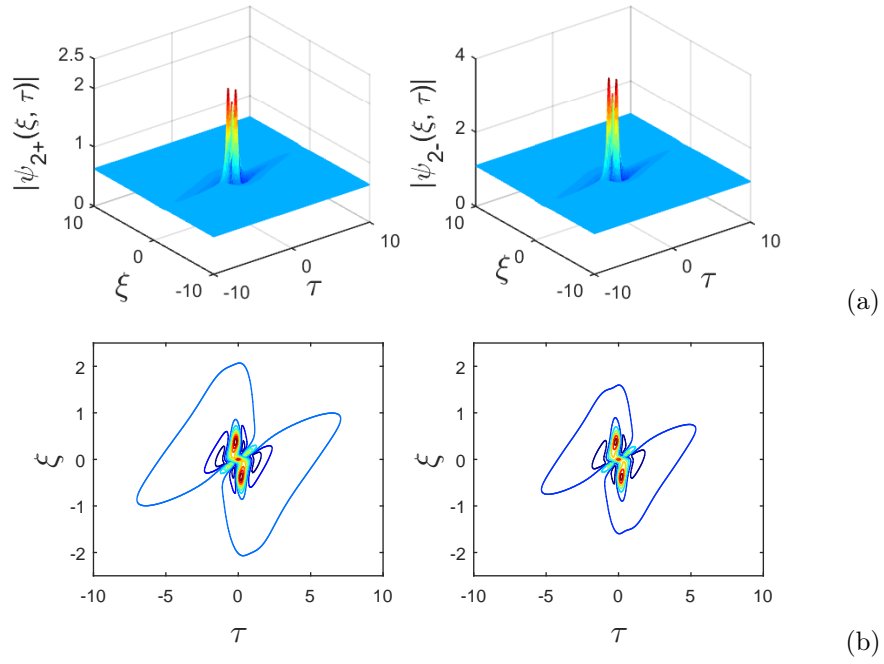
Figure 58: Second-order amplitude of nonparaxial chiral optical rogue waves of Eq. (3.185), with $d = 10$ and $\nu = 0.6$.
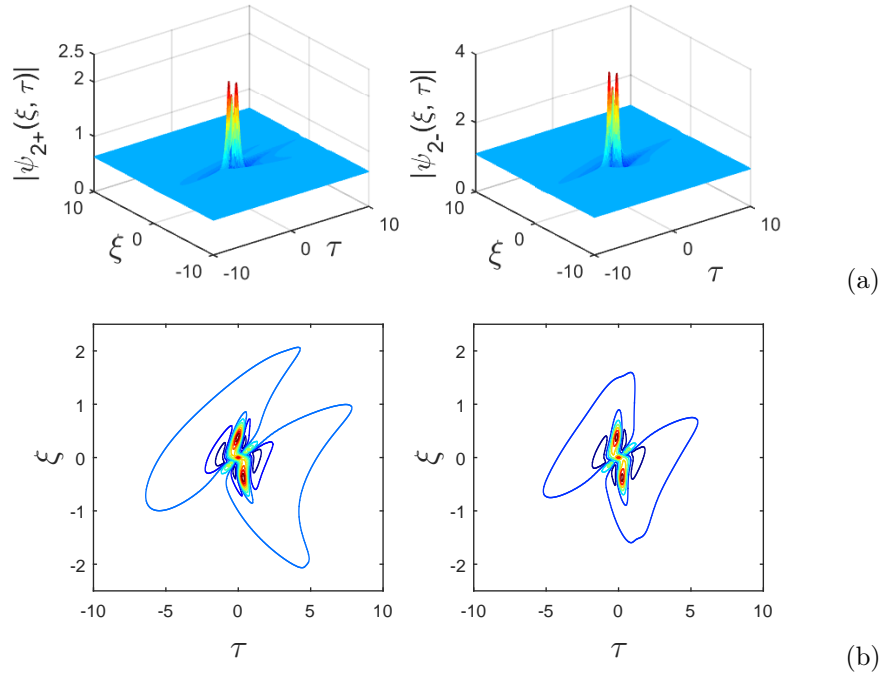
Figure 59: Plot (a) and contour plot (b) of the second-order rogue wave solution: Eq. (3.185), with $d = 0.5$ and $\nu = 0.6$.
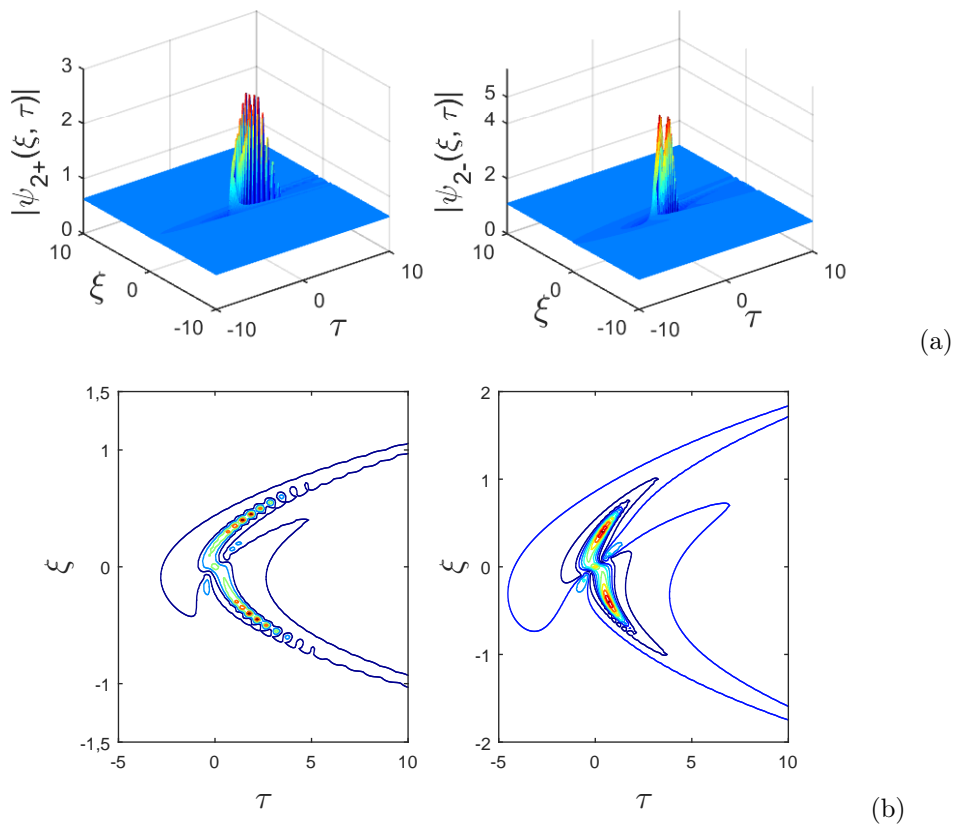
Figure 60: 3D representation (a) and contour plot (b) of the second-order analytical rogue wave amplitude of Eq. (3.185), for $d = 0.05$ and $\nu = 6$.
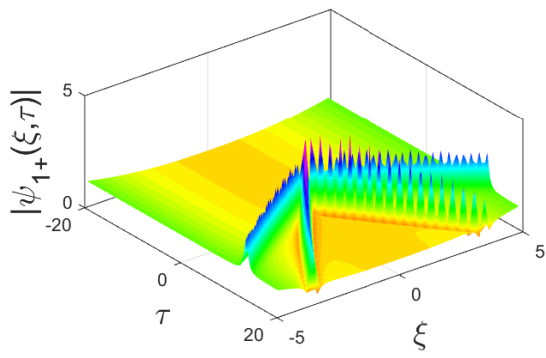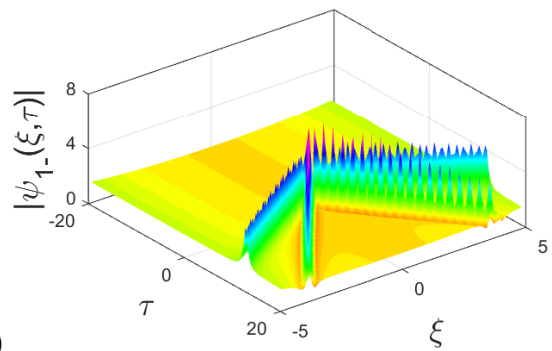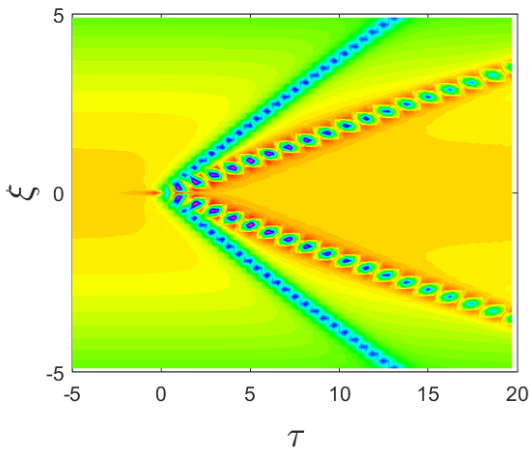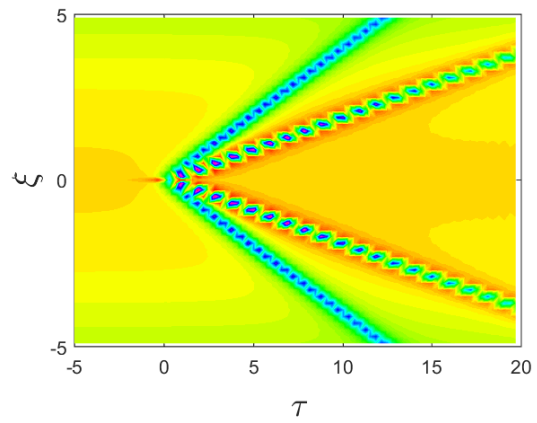
Figure 61: 3D (a) and 2D (b) representations of the first-order numerical rogue wave amplitude of Eq. (3.151), for $d = 10$ and $\nu = 6$.

143
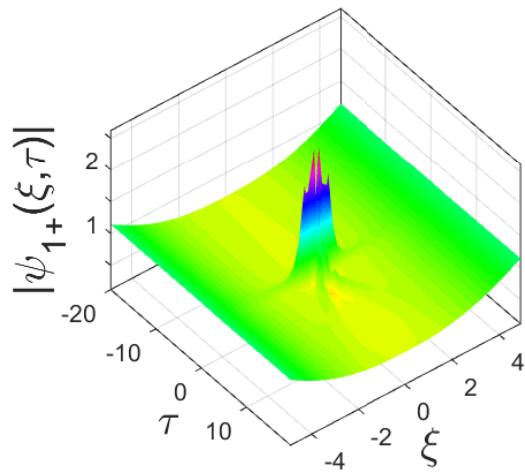
(a)
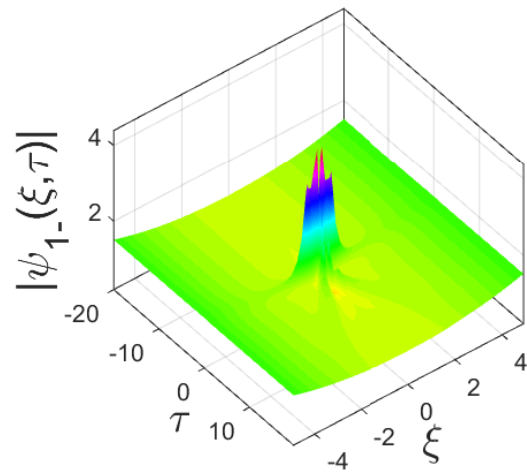
(b)
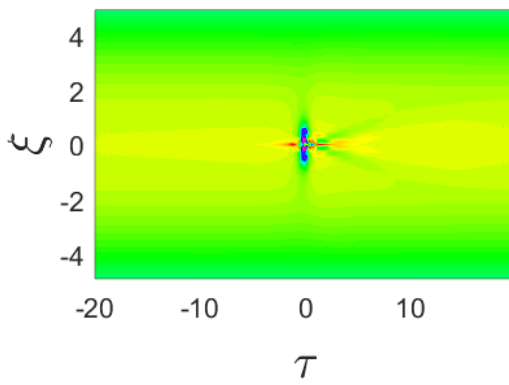
(c)
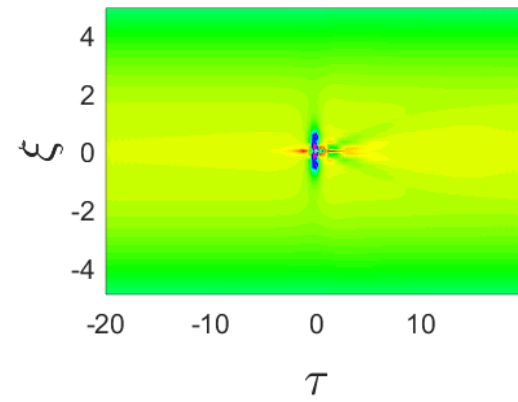
(d)

Figure 62: 3D (a) and 2D (b) representations of the second-order numerical rogue wave amplitude of Eq. (3.151), for $d = 10$ and $\nu = 6$.

144

parameter d which perturbs, on the one hand, the both localization to coordinates and, on the other hand, the short propagation of rogue waves. This can be an advantage in the case where, one needs to extend the lifetime of rogue waves in physical systems. Moreover, this depicts the behavior of waves in systems where the paraxial approximation is violated. A similar behavior is also observed in Figs. 61, but this time with a high value of the parameter d. It can be seen that the property of central character of the maximum peak of rogue wave is verified, but the property of localization of rogue wave prototypes is not anymore valid. In contrary to Fig. 61 which depicts the first-order solution, Fig. 62 (second-order solution) presents a different behavior, in the sense that the both localization and central character properties remain valid. This confirms the evidence of second-order rogue wave solutions of being more interesting in view of their precisions in realistic problems in optics.

One can added that Figs. 55, 56, 58 , 59, and 62 depict the PS behavior throughout their both localization to coordinates, whereas Figs. 57, 60, and 61 depict a behavior near to the ABs. In the above figures, the diversity of shape is also observed. One denotes structures with one peak and two holes [see Figs. 55 and 56] and then structures with triple peaks and two holes [see Figs. 58 and 59]. More specifically, one founds a rogue wave structure with a multiplicity of peaks surrounding by holes which become linear to the vicinity of coordinates. This phenomenon is due to the degeneration of the rogue wave structure which start by the break up of joined holes then by the degeneration of holes which loss their lobes so far to become linear structures. As a consequence, a weak value of nonparaxiality can be benefit to reduce the amplitude of waves in physical systems when the MI increases drastically. This framework can be used to improve the stability of ultrashort pulses during their propagation in chiral optical fibers. In contrast to second-order analytical rogue waves which has butterfly structures, numerical rogue wave solutions have a rectilinear structures in both hands on the first-order [see Fig. 61] and one peak issue from the collision of waves at the center of coordinates, more visible in second-order numerical solutions [see Fig. 62]. Moreover, Figs. 55, 58 and 61 exhibit a linear motions, whereas Figs. 56, 57, 59, 60 and 62 reveal a rotational motions. The slight rotation of the shape observed in Figs. 56 and 59 is amplified on Figs. 61 and 60, respectively. The amplification of rotation motion is due to the weak value of nonparaxial parameter d. This behavior of motion conversion is a property of chiral materials [359]. A concordance is observed on the motion conversion property as shown in Fig. 57 (first-order rogue wave analytical solutions) and in Figs. 61 (c) and (d) (first-order rogue wave numerical solutions), on the one hand. On the other hand, a concordance can be observed on the shape of the maximum peak, central character of their localization and on the amplitude as shown in Figs. 58 (a) and 59 (a) (for the second-order rogue wave analytical solutions) and in Figs. 62 (a),(b) (for the second-order rogue wave numerical solutions). Moreover, the contours plot of the LCP ($|\psi_{2-}(\xi, \tau)|$) in Fig. 60 (a) (second-order rogue wave analytical solution) reveals as shown in Fig. 62, the rotational conversion property of chiral materials. Moreover, the conversion is also due to the chiral parameter related to coefficients of the original equation. Those coefficients are related to the effective propagation distance, similarity variable, amplitude and phase of the wave. These are the main parameters responsible of rotational conversion on the LCP and RCP components. However, the prompt

action of rotational conversion is observed for a high value of parameter ν related to TOD and weak value of nonparaxial parameter d. The inverse process is also observed for a weak of parameter ν and high value of parameter d.

3.9 Conclusion

In this chapter, derivation of extended NLS models and construction of rational solutions related to rogue wave prototypes have been done to study the generation and propagation as well as the controllability of rogue waves in optical fibers and chiral media.

First-and the second-order rational analytical solutions related to rogue wave have been presented through the nonparaxial NLS equation. The similarity and Darboux transformations method have been used to construct the rational solutions of the model. Due to the richness of this method which can also be applied to the higher orders, the effect of nonparaxiality on rogue wave propagation as been revealed. It has been shown that for height values of nonparaxial parameter, the rogue wave intensities were increasing rapidly through the simultaneous process on the increase of the length and decrease of the width peak. The rapidity of nonparaxial optical rogue waves was observed and recognized higher compare to the ones obtained from the standard NLS equation. The effects of polynomial and Jacobian elliptic functions on rogue waves have been examined. It has been recorded that the nonparaxiality moves the higher peak of rogue waves from the center to the periphery. It has been concluded that the displacement of the wave peak from the center to the periphery is due to height velocity of nonparaxial rogue waves.

Then, the derivation of the NLS equation in chiral optical fiber with right-and left-hand nonlinear polarization has been done. This model has been used to describe the propagation of optical rogue waves in chiral fiber. Through the symmetry reduction and the mDT methods, first-and second-order chiral optical rogue waves have been constructed from the chiral NLS equation with variable and constant coefficients, respectively. To show the influence of optical activity on rogue wave propagation, Jacobian elliptic functions have been chosen for good stability of the waves. One recordes from analytical results two components, left-and right-hand intensities in the chiral optical fiber. It has been observed that the shape and amplitude of chiral optical rogue waves change with the increase of the chiral parameter. This behavior allows to conclude that the slightly change of the amplitude is due to the optical activity and TWM effects. The study has been improved by using chiral CNLS equations and FWM effect has been revealed through the exchange of energy between the four components of chiral optical vector rogue waves. The influence of optical activity on unusual rogue waves like ABs or KM soliton has been shown in focusing and defocusing XPM interaction cases. One notices that the destruction of one component contributes to the perturbations that lead to modulation instability and that the defocusing nature of XPM generates chiral optical dark rogue waves. It has been shown that positive and negative scattering lengths can generate a potential barrier for one component in the left-or right-hand side. Thus, one may confirm that the control and guide of the propagation direction of chiral optical vector rogue waves either in the left-hand or in the right-hand is made possible.

Moreover, the derivation of both scalar and vector nonparaxial NLS equations with constant and modulated coefficients is made to improve the description of rogue waves propagation in optical fibers filled with chiral materials. Under the assumption of controllability and the presence of nonparaxiality, optical activity and walk-off effects, first-and second-order nonparaxial chiral optical rogue waves were investigated by the MDT method. The nonparaxiality, TOD and differential gain or loss terms have been revealed as the main keys to control the amplitude of the envelope fields, SS, GVD, SPM, walk-off effect, linear birefringence and the effective propagation distance. Such models derived in this thesis can improve the description of rogue waves and their control in chiral optical fibers with higher-order nonlinear effects. Then, the algorithm scheme namely, difference-differential equation method, was used to compute efficiently the diffractions in the spectral domain. As outcomes, the increase or decrease of the three specific control parameters can affect the wave shape and the amplitude of each component. It has also been shown that, among those specific control parameters, the nonparaxial coefficient has the most influential effect whereas the two others that are differential gain or loss and walk-off terms, are physically inactives and equivalent in the absence of nonparaxial parameter. One may conclude that the vector rogue wave solutions based on the vector nonparaxial NLS equations which modeled the coupling of two nonlinear waves under the assumptions of nonparaxiality, optical activity and walk-off, contributed to better control rogue wave phenomena in optical fibers filled with chiral materials and in a variety of complex dynamics.

Finally, one fucuses attention on the higher-order nonparaxial chiral NLS equation, to understand the physical nature of the optical activity and to elucidate the chiral material properties on rogue wave propagation in chiral optical fiber. One founds that optical fibers filled with chiral material have a plurality of physical behaviors. Optical fibers with chiral core allow the propagation of two modes with different vectors. The LCP component refers to the counter clock-wise rotation, namely, levorotatory, and the RCP component refers to clock-wise rotation, namely, dextrorotatory. Their structures in some cases are well localized in coordinates and for others similar to the ABs behavior. This localization is degenerated for weak value of nonparaxial parameter which governs both the central character of peak and rogue wave localization to coordinates. Moreover, this weak value is also responsible to the violation of paraxial approximation. Therefore, one may control the paraxial approximation, in multiplexed systems and in nanostructures in which this violation can occur. In addition, second-order rogue wave solutions was claimed to be more interesting in the study of waves propagation in realistic problems in optics. The remarkable rotational property of chiral optical fibers is observed throughout the degeneration of lobes of butterfly structures which are converted from linear to rotational motion. This conversion is well-observed on contour plots of analytical and numerical simulations. As additional property of chiral materials, chiral optical refractive index has the peculiarity of being slightly higher compare to the refractive index of the cladding. This slight difference play an undeniable role in optical propagation, in the sense that it is responsible to the total reflection of the light through the chiral core of optical fibers. Hence, the great importance of chiral materials. Moreover, helical structures, with given chirality have an excellent mechanical behavior due to their remarkable rotational property. They provide the direct way to convert

147

linear motion to rotational motion and vice versa. In consequence, in addition to the simultaneous controllability of the degeneration of waves and chiral level of materials, this thesis provides a theoretical framework to improve, the controllable conversion of LCP and RCP waves, from linear to rotational motion and vice versa, as well as further experimental investigation of rogue waves propagation in chiral optical fibers. These aspects are additional features and can find application in optics, notably in telecommunications and in many other physical systems.

General Conclusion

Summary and Contributions

In this thesis, one has improved extended NLS models to study the generation and propagation of rogue waves in optical fibers and chiral media. More attention has been focused on understanding rogue wave phenomena to improve their controllability in Kerr and chiral media. Investigation on rogue wave behaviors has revealed their properties in optical fibers and potential applications in life-science and industry.

First, the historical context of rogue waves in ocean is revealed, starting from hydrodynamic to optics, as well as advanced technology in optical communication and chiral media. Experimental generation of rogue waves in optical fibers has been described and the characteristic properties of the equipments underlined. A concordance between the analytical, numerical and experimental rogue wave generation methods has been presented. Significant advances of rogue wave origins and predictability, likewise description and controllability have been summarized. The important progress of rogue wave field and their potential applications have been elucidated.

Second, the integrability method names symmetry reduction method has been developed for non integrable NLS models. The modulation instability method has been applied to determine the stable and unstable branches and by the way the existence and non existence of rogue wave components in chiral media. Then, the Lax pair, the mDT and DDT methods have been presented as the key to construct the prototypes of rogue wave solutions. Forth-order Runge-Kutta method, difference-differential equation method and fast Fourier transforms (FFTs) have been presented as efficient numerical methods to generate usual and unusual rogue waves.

The main results of the thesis are summarized in the third chapter as follows.

Firstly, the first-and the second-order rational solutions related to rogue wave have been presented. Direct methods such as similarity reduction and Darboux transformation have been used to construct the rational solutions of nonparaxial NLS equation. The richness of these methods is based on the fact that they can also be applied to higher orders (third, fourth, etc.). Through the 2D and 3D representations, the effect of nonparaxiality on rogue wave propagation has been revealed. It has been shown that the nonparaxiality increases rapidly the intensity of rogue waves by increasing the length and reducing the width peak simultaneously. One denotes that the nonparaxial rogue waves are faster than the ones obtained from the standard NLS equation. It has been recorded that the nonparaxiality moves the higher peak of rogue waves from the center to the periphery. The effects of the polynomial and Jacobian elliptic functions on

rogue waves have been examined. It has been concluded that the displacement of the wave peak from the center to the periphery is due to height velocity of the nonparaxial rogue waves. As the nonparaxial effect increases the velocity of waves, it also penalizes the interactions between them. These aspects are additional features and can find application in optics and in many other physical systems.

Secondly, the derivation of the NLS-type equation in chiral optical fiber with right-and left-hand nonlinear polarization has been done. This model has been used to describe the propagation of optical rogue waves in chiral fiber. The symmetry reduction and the mDT have been used to generate the rational solutions. So doing, first-and second-order chiral optical rogue waves have been constructed through the chiral NLS equation with variable and constant coefficients, respectively. To show the influence of optical activity on rogue wave propagation, Jacobian elliptic functions have been chosen for good stability of the waves. One recordes from analytical results two components, left-and right-hand intensities in chiral optical fiber. It has been observed that the shape and the amplitude of chiral optical rogue waves change with the increase of the chiral parameter. This behavior allows to conclude that the slightly change of the amplitude is due to the optical activity and TWM effects. The study has been improved by using chiral CNLS equations and the obtention of chiral optical vector rogue waves with four components has revealed through the exchange of energy, the FWM effect. In the case of focusing and defocusing XPM interactions, one obtains unusual rogue waves like ABs or KM soliton. Then, the influence of optical activity on different profiles has been shown. One notices that the destruction of one component contributes to the perturbations that lead to modulation instability and that the defocusing nature of XPM generates chiral optical dark rogue waves. It has been shown that positive and negative scattering lengths can generate a potential barrier for one component in the left-or right-hand side. From this result, one may confirm that the control and guiding of chiral optical vector rogue waves are possible, either in the left-hand or in the right-hand side, for some specific set of parameters likewise chiral parameter.

Thirdly, the derivation of both scalar and vector nonparaxial NLS equations with constant and modulated coefficients is made to improve the description of rogue waves propagation in optical fibers filled with chiral materials. The models in particular, verified the assumption of controllability on the one hand, and takes into account the parameters responsible of non-paraxiality, optical activity and walk-off effect, on the other hand. The first-and second-order nonparaxial chiral optical rogue waves were investigated by the MDT method. As the non-paraxiality, TOD and differential gain or loss terms depend on the system control parameters, it appeared that they are the main keys to control the amplitude of the envelope fields, SS, GVD, SPM, walk-off effect, linear birefringence and the effective propagation distance. Therefore, one may conclude that among previous models that have been studied before, the models derived in this thesis can improve the description of rogue waves and their control in chiral optical fibers with higher-order nonlinear effects. In these models, one denotes the influences of TOD and differential gain or loss term. The algorithm scheme derived here, namely, difference-differential equation method, is known in the literature as an efficient method to compute the diffractions in the spectral domain. A plurality of numerical simulation has shown that the increase or

decrease of the three specific control parameters can affect the wave shape and the amplitude of each component. Among the specific control parameters, the nonparaxial coefficient has been considered as the most influential effect whereas the two others, that are, differential gain or loss and walk-off terms, are physically inactives. One founds that in the absence of nonparaxial parameter, the influence of the two others are effective and equivalent. It has been noticed that in the absence of two specific control parameters, the last one becomes the powerful influential effect in the system. One improves reader understanding, through models under consideration of combined effects on rogue wave propagation in optical fibers filled with chiral materials. The necessity to take into account the parameters responsible of the simultaneous controllability of different effects in the system has been shown. Those parameters revealed the control key and the novel properties of nonparaxial chiral optical rogue wave solutions. For some specific set of parameter, usual rogue waves, such as the vector Peregrine were obtained, showing the collisions between bright and dark rogue waves. The study of combined effects has allowed to determine the powerful influence among the effects and the nonparaxial effect was claimed to be the most influential one. The vector rogue waves obtained from the vectorial nonparaxial NLS equations are of special interest in the modeling of coupled nonlinear waves. Most importantly, they are useful under the assumptions of nonparaxiality, optical activity and walk-off and have contributed to improve the control of rogue wave phenomena in optical fibers filled with chiral materials.

Fourthly, this thesis work was also based on the higher-order nonparaxial chiral NLS equation, to understand the physical nature of the optical activity and to elucidate the chiral material properties and their interplay on the rogue wave propagation. One founds that optical fibers filled with chiral material have a plurality of physical behaviors. Chiral core allows the propagation of two modes with different vectors. One denotes, the LCP component which refers to the counter clock-wise rotation names, levorotatory and RCP component which refers to clock-wise rotation names, dextrorotatory. Hence, the given components $|\psi_{j-}(\xi, \tau)|$ and $|\psi_{j+}(\xi, \tau)|$ for $j = 1, 2$ as LCP and RCP chiral optical rogue waves, respectively. The structures of the LCP and RCP waves are well localized in coordinates for weak values of the parameter ν related to the TOD. This localization is degenerated for high values of ν. Therefore, one can confirm that the TOD governs both the central character of peak to coordinates and localization of Peregrine soliton. As property of chiral materials, chiral optical refractive index has the peculiarity of being slightly higher compare to the refractive index of the cladding. This slight difference play an undeniable role in optical propagation in the sense that it is responsible to the total reflection of the light through the chiral core of optical fibers. Hence, the great importance of chiral materials. Moreover, helical structures, with given chirality have an excellent mechanical behavior due to their remarkable rotational property. They provide the direct way to convert linear motion to rotational motion and vice versa. This behavior is observed throughout the degeneration of lobes of butterfly structures which are converted from linear to rotational ones. This conversion is well observed in this work on contour plots of analytical and numerical simulations. In consequence, in addition to the simultaneous controllability of the degeneration of waves and chiral level of materials, this work provides a theoretical framework to improve, the

controllable conversion of LCP and RCP waves, from linear to rotational and vice versa as well as further experimental investigation of rogue waves propagation in chiral optical fibers.

Open problems and future directions

Although the interesting results obtained in this thesis, some aspects need to be reconsidered due to the novelty of the optical rogue waves field. From the origins to the generation of optical rogue waves, as well as their propagation and control in Kerr and chiral materials. Many questions remain unsolved and are now scientists preoccupations and investigations.

- Despite the evidence progress in optical rogue wave fields, the problem of controllability of nonlinear effects on their propagation is not fully understand and need to be reconsidered.
- In view of great scientific importance of chiral molecules in life-science and pharmaceutical industries, one may focus on chiral properties in chiral fibers to point up the impact of chiral materials in optical communication, in medical science and biology.
- One should improve the design and fabrication of SC-PBG fibers to reduce the transmission losses.
- Made possible the control of rogue waves-bullet in chiral optical fibers.

APPENDICES

It should be noted that in the whole thesis, the so-called management, known here as the variation of parameters in both scalar and vector models is taken into account, according to the effective non homogeneity of nonlinear Kerr and chiral media. This management plays a fundamental role according to different nonlinear stabilization mechanism that may arise in those media. One denotes the nonlinear absorption, saturation of the nonlinearity, ionization changes of the type of nonlinearization and splitting of the beam into filaments, that arrest the catastrophic beam collapse. As the prediction of the collapse is a general statement for all media with Kerr nonlinearity, which is present in all the models of this study, one should mention that close to the point of nonlinear focusing, the radiation beam width approaches the wavelength of light. Then, the so-called paraxial approximation, known as the slowly varying envelope approximation (SVEA) in the propagation direction of light beams in Kerr media is not valid anymore and may produce a catastrophic collapse of a self-focusing beam, means the exponential increase of the amplitude to infinity. Hence, the importance of the nonparaxiality that replaces the catastrophic focusing with a sequence of focusing and defocusing cycles. Therefore, the attention is focused on the nonparaxiality and other nonlinear effects as well, in the study of rogue wave propagation in optical Kerr and chiral media through the nonparaxial NLS models of which, the nonparaxial term is the factor which arrest the collapse. The scalar nonparaxial NLS model reduces the beam narrowing whereas the spatial variation of nonlinear polarization is quite well more pronounced in vector nonparaxial NLS models.

APPENDIX A: DERIVATION OF THE STANDARD NONPARAXIAL NLS EQUATION IN OPTICAL FIBER

In this appendix, one presents de derivation of Eq. (3.1).

A nonlinear Kerr medium is characterized by the relations

$$\vec{D} = \varepsilon_n \vec{E}, \quad (A1)$$
$$\vec{B} = \mu_0 \vec{H}$$

where the flux densities $\vec{D}$ and $\vec{B}$ arise in response to the electric and magnetic field $\vec{E}$ and $\vec{H}$ propagating in the chiral medium with $\varepsilon_n = \varepsilon_0 + \varepsilon_2 \left| \vec{E} \right|$. Here ε_0 and ε_2 are linear and nonlinear permittivity, respectively. μ_0 is the permeability. In absence of the current density $\vec{J} = 0$ and

the charge density $\rho = 0$, the Maxwell equations are

$$\vec{\nabla} \cdot \vec{D} = 0, \quad \vec{\nabla} \cdot \vec{B} = 0,$$
$$\vec{\nabla} \times \vec{E} = -\frac{\partial \vec{B}}{\partial t}, \quad \vec{\nabla} \times \vec{H} = \frac{\partial \vec{D}}{\partial t}, \quad (A2)$$

Substituting Eq. (A1) into Eq. (A2), one obtains the following wave equation

$$\vec{\nabla}^2 \vec{E} = \mu_0 \varepsilon_0 \frac{\partial^2 \vec{E}}{\partial t^2} + \mu_0 \varepsilon_2 \left| \vec{E} \right| \frac{\partial^2 \vec{E}}{\partial t^2}. (A3)$$

The optical field $\vec{E}$ in the z direction as the form

$$\vec{E}(\vec{r}, t) = \vec{\psi}_{x,z} \exp\left(-j(Kz - \omega_0 x)\right), (A4)$$

where $\vec{\psi}_{z,x}$ is the complex envelope of the optical field in the nonlinear Kerr medium, K the wave number and ω_0 the frequency.

After evaluation of different derivations of $\vec{E}$ in x and z directions in Eq. (A3)), one neglects the second-order terms and suppose that the wave is propagating in z direction. This implies that

$$K_x = 0, \quad E_z = 0. \ (A5)$$

The paraxial approximation given by Eq. (A6) is not any more valid.

$$\left| \frac{\partial^2 E_x}{\partial z^2} \right| << \left| 2jk_z \frac{\partial E_x}{\partial z} \right| (A6)$$

Considering the nonparaxial approximation $\frac{\partial^2 E_x}{\partial z^2} \neq 0$ the result of Eq. (3.1), after approximations, stands for

$$\frac{\partial^2 E_x}{\partial z^2} - 2jk_z \frac{\partial E_x}{\partial z} - k_z{}^2 E_x = \left(\mu_0 \varepsilon_0 + \mu_0 \varepsilon_2 |E_x|^2\right) \left[2j\omega \frac{\partial E_x}{\partial t} - \omega^2 E_x \right] (A7)$$

By neglecting the SS and dividing Eq. (A7) by $-2k_z$ one obtains for the following set of parameters

$$v^2 = \frac{1}{\mu_0 \varepsilon_0}, \quad \beta = \mu_0 \varepsilon_2, \quad K_0 = \frac{\omega}{v}, \quad z^* = z, \quad K_z = K_0, \ (A8)$$

the simplified form of Eq. (A7) as follows

$$-\frac{1}{2k_0} \frac{\partial^2 E_x}{\partial z^2} + j \frac{\partial E_x}{\partial z} + j \frac{1}{v} \frac{\partial E_x}{\partial t} - \frac{\beta \omega^2}{2k_0} |E_x|^2 E_x = 0. \quad (A9)$$

If one sets

$$E_x = \phi, \ |E_x|^2 = |\phi|^2, \quad (A10)$$

Eq. (A9) yields

$$-\frac{1}{2k_0} \frac{\partial^2 \phi}{\partial z^2} + j \frac{\partial \phi}{\partial z} + j \frac{1}{v} \frac{\partial \phi}{\partial t} - \frac{\beta \omega^2}{2k_0} |\phi|^2 \phi = 0. \quad (A11)$$

The Taylor series of the wave number $K(\omega)$ at the second-order and the Fourier transform of $\Delta\omega$ and ΔK help to express in an approximate form, the second term of Eq. (A11) as

$$j \frac{1}{v} \frac{\partial \phi}{\partial t} = j \frac{1}{v_g} \frac{\partial \phi}{\partial t} + \frac{1}{2} K'' \frac{\partial^2 \phi}{\partial t^2}, \quad (A12)$$

where

$$K'' = \frac{\partial^2 K}{\partial \omega^2}, K' = \frac{1}{v_g} = \frac{\partial K}{\partial \omega}. \quad (A13)$$

Then, for the following change of variable

$$\begin{aligned} t' = t - \frac{1}{v_g}z \\ z' = z \end{aligned} \Rightarrow \begin{aligned} \frac{\partial}{\partial t} \to \frac{\partial}{\partial t'} \\ \frac{\partial}{\partial z} \to \frac{\partial}{\partial z'} - \frac{1}{v_g}\frac{\partial}{\partial t'} \end{aligned}, \quad (A14)$$

Eq. (A11) stands for

$$-\frac{1}{2k_0}\frac{\partial^2 \phi}{\partial z^2} + j\frac{\partial \phi}{\partial z} + \frac{1}{2}\left(K'' - \frac{K'^2}{K}\right)\frac{\partial^2 \phi}{\partial t'^2} - \frac{\beta \omega^2}{2k_0}|\phi|^2\phi = 0. \quad (A15)$$

where $K' = \frac{\partial K}{\partial \omega} = \frac{1}{v_g}$ is the inverse of group-velocity, $K'' = \frac{\partial K'}{\partial \omega}$ is the group-velocity dispersion coefficient which takes the plus and minus signs ($\pm$), representing the anomalous and normal dispersion regimes, respectively. The factor to $|\phi|^2\phi$ is the SPM.

The new variables, namely

$$\begin{aligned} q = \frac{\omega_0^{2/3}\beta^{1/3}}{(2K_0)^{1/3}}\phi, \quad \xi = \frac{\omega_0^{2/3}\beta^{1/3}}{(2K_0)^{1/3}}z', \quad d = -\frac{\beta^{1/3}\omega_0^{2/3}}{(2k_0)^{4/3}}, \\ \tau = \frac{\omega_0^{1/3}\beta^{1/6}}{\sqrt{K''}(2K_0)^{1/6}}t', \quad C = 1, \quad P = \frac{1}{2}\left(1 - \frac{k'^2}{K''k_0}\right), \end{aligned} \quad (A16)$$

allow us to express for $q(\xi,\tau) = \psi(z,x)$, Eq. (A15) in the form

$$d\psi_{zz} + j\psi_z + P\psi_{xx} - C|\psi|^2\psi = 0. \quad (A17)$$

For $q = -C$, Eq. (A17) gives in presence of management

$$d(z)\psi_{zz} + j\psi_z + P(z)\psi_{xx} + q(z)|\psi|^2\psi = 0. \quad (A18)$$

APPENDIX B: DERIVATION OF THE NLS EQUATION IN CHIRAL OPTICAL FIBERS

In this appendix, one presents de derivation of Eq. (3.40).

Equation (3.40) is reduced in x, y and z directions, respectively, as follows

$$-2jK_z\frac{\partial E_x}{\partial z} - K_z^2 E_x + \mu_0\varepsilon_0 T_c^2\left(\omega^2 K_z^2 E_x + 2jK_z\omega^2\frac{\partial E_x}{\partial z} - 2jK_z^2\omega\frac{\partial E_x}{\partial t}\right)$$
$$= (\mu_0\varepsilon_0 + \mu_0\varepsilon_2|\vec{E}|)\left(2j\omega\frac{\partial E_x}{\partial t} - \omega^2 E_x\right) + \mu_0\sigma\left(\frac{\partial E_x}{\partial t} + j\omega E_x\right) + \left(2\mu_0\varepsilon_0 T_c + \mu_0\varepsilon_2 T_c|\vec{E}|^2\right) \quad (B1)$$
$$\times\left[\omega^2\frac{\partial E_y}{\partial z} + jK_z\left(2j\omega\frac{\partial E_x}{\partial t} - \omega^2 E_y\right)\right] + \mu_0\sigma T_c\left[-j\omega\frac{\partial E_y}{\partial z} + jK_z\left(\frac{\partial E_y}{\partial t} + j\omega E_y\right)\right],$$

$$-2jK_z\frac{\partial E_y}{\partial z} - K_z^2 E_y + \mu_0\varepsilon_0 T_c^2\left(\omega^2 K_z^2 E_y + 2jK_z\omega^2\frac{\partial E_y}{\partial z} - 2jK_z^2\omega\frac{\partial E_y}{\partial t}\right)$$
$$= (\mu_0\varepsilon_0 + \mu_0\varepsilon_2|\vec{E}|)\left(2j\omega\frac{\partial E_y}{\partial t} - \omega^2 E_y\right) + \mu_0\sigma\left(\frac{\partial E_y}{\partial t} + j\omega E_y\right) + (2\mu_0\varepsilon_0 T_c + \mu_0\varepsilon_2 T_c|\vec{E}|^2) \quad (B2)$$
$$\times\left[-\omega^2\frac{\partial E_x}{\partial z} - jK_z\left(2j\omega\frac{\partial E_x}{\partial t} - \omega^2 E_x\right)\right] + \mu_0\sigma T_c\left[j\omega\frac{\partial E_x}{\partial z} - jK_z\left(\frac{\partial E_x}{\partial t} + j\omega E_x\right)\right],$$

$$\left[-\omega^2\left(2\mu_0\varepsilon_0 T_c + \mu_0\varepsilon_2 T_c|\vec{E}|^2\right) + j\omega\mu_0\sigma T_c\right]\left(\frac{\partial E_y}{\partial x} - \frac{\partial E_x}{\partial y}\right) = 0. \quad (B3)$$

Equation (B3) leads to

$$\frac{\partial E_y}{\partial x} = \frac{\partial E_x}{\partial y} = cst, \quad E_y = E_y(z,t), \quad E_x = E_x(z,t). \quad (B4)$$

Having multiply Eq. (B2) by $\pm j$, follows the addition of Eqs. (B1) and (B2) where one considers the paraxial approximation

$$\left|\frac{\partial E_x}{\partial t}\right| << |2j\omega E_x|, \quad \left|\frac{\partial^2 E_y}{\partial z^2}\right| << |2j\omega E_y|. \quad (B5)$$

Therefore, the novel form of wave equation can be written as

$$
\begin{aligned}
&\left[\pm j\left[\left(2\mu_0\varepsilon_0 T_c + \mu_0\varepsilon_2 T_c\left|\vec{E}\right|^2\right)\omega^2 - j\omega\mu_0\sigma T_c\right] - 2jK_z + 2jK_z\omega^2\mu_0\varepsilon_0 T_c^2\right]\frac{\partial\psi_{R,L}}{\partial z} \\
&+\left[-K_z^2 + \mu_0\varepsilon_0 T_c^2\omega^2 K_z^2 + \omega^2\left(\mu_0\varepsilon_0 + \mu_0\varepsilon_2\left|\vec{E}\right|^2\right) - j\omega\mu_0\sigma\right. \\
&\pm j\left(-jK_z\omega^2\left(2\mu_0\varepsilon_0 T_c + \mu_0\varepsilon_2 T_c\left|\vec{E}\right|^2\right) - K_z\omega\mu_0\sigma T_c\right)\right]\psi_{R,L} \\
&+\left[-2jK_z^2\omega\mu_0\varepsilon_0 T_c^2 - 2j\omega\left(\mu_0\varepsilon_0 + \mu_0\varepsilon_2\left|\vec{E}\right|^2\right)\right]\frac{\partial\psi_{R,L}}{\partial t} = 0,
\end{aligned}
\quad (B6)
$$

where $\psi_{R,L} = E_x \pm jE_y$. Then, the reference changing is

$$
\begin{aligned}
\psi_R &= E_x + jE_y \quad \psi_L = E_x - jE_y, \\
E_x &= \frac{\psi_R + \psi_L}{2} \quad E_y = \frac{\psi_R - \psi_L}{2}.
\end{aligned}
\quad (B7)
$$

The division of Eq. (B6) by $-2K_z$ yields

$$
\begin{aligned}
&j\left(1 - K_0^2 T_c^2\right)\frac{\partial\psi_{R,L}}{\partial z} \mp j\frac{K_0^2 T_c}{K_z}\frac{\partial\psi_{R,L}}{\partial z} + j\frac{\omega\mu_0\varepsilon_2}{K_z}|\psi_{R,L}|^2\frac{\partial\psi_{R,L}}{\partial t} \mp j\frac{\mu_0\varepsilon_2\omega^2 T_c}{2K_z}|\psi_{R,L}|^2\frac{\partial\psi_{R,L}}{\partial z} \\
&+j\frac{K_0}{K_z c}\left(1 + K_z^2 T_c^2\right)\frac{\partial\psi_{R,L}}{\partial t} \mp \frac{j\omega\mu_0\sigma T_c}{2}\psi_{R,L} + \frac{1}{2}\left(K_z - K_z K_0^2 T_c^2 - \frac{K_0^2}{K_z}\right)\psi_{R,L} - \frac{\mu_0\varepsilon_2\omega^2}{2K_z} \\
&\times|\psi_{R,L}|^2\psi_{R,L} \mp \frac{\omega^2}{2}\left(\mu_0\varepsilon_2 T_c|\psi_{R,L}|^2\right)\psi_{R,L} + j\frac{\omega\mu_0\sigma}{2K_z}\psi_{R,L} \mp K_0^2 T_c\psi_{R,L} \mp \frac{\omega\mu_0\sigma T_c}{2K_z}\frac{\partial\psi_{R,L}}{\partial z} = 0,
\end{aligned}
\quad (B8)
$$

where

$$K_0 = \frac{\omega}{c}, \quad \mu_0\varepsilon_0 c^2 = 1. \quad (B9)$$

The dispersion relation is given by

$$K_z = \frac{K_0}{1 \pm K_0 T_c}. \quad (B10)$$

For $K_0^2 T_c^2 << 1$, one gets $K_z = K_0$. By neglecting the nonlinear diffraction, the second and the last terms of Eq. (B8), and for the following set of parameters

$$v^2 = \frac{1}{\mu_0\varepsilon_0}, \quad \alpha = \mu_0\sigma, \quad \beta = \mu_0\varepsilon_2, \quad K_0 = \frac{\omega}{v}, \quad z^* = \frac{z}{1 - K_0^2 T_c^2}, \quad (B11)$$

Eq. (B8) takes the form

$$
\begin{aligned}
&j\frac{\partial\psi_{R,L}}{\partial z^*} + j\frac{1}{v}\frac{\partial\psi_{R,L}}{\partial t} + j\frac{\omega\alpha}{2K_0}\psi_{R,L} \mp K_0^2 T_c\psi_{R,L} - \frac{\beta\omega^2}{2K_0}|\psi_{R,L}|^2\psi_{R,L} \mp \frac{j\omega\alpha T_c}{2}\psi_{R,L} \\
&\mp\frac{\omega^2\beta T_c}{2}|\psi_{R,L}|^2\psi_{R,L} + \frac{j\omega\beta}{K_0}|\psi_{R,L}|^2\frac{\partial\psi_{R,L}}{\partial t} = 0.
\end{aligned}
\quad (B12)
$$

156

If one sets

$$\psi_{R,L} = \phi, \quad K = K_0 = K_z, \quad (A13)$$

Equation (B11) yields

$$j\frac{\partial \phi}{\partial z^*} + j\frac{1}{v}\frac{\partial \phi}{\partial t} + j\frac{\omega\alpha}{2K_0}\left(1 \mp KT_c\right)\phi - \frac{\beta\omega^2}{2K_0}\left(1 \mp KT_c\right)|\phi|^2\phi \mp K^2T_c\phi + j\frac{\omega\beta}{K_0}|\phi|^2\frac{\partial \phi}{\partial t} = 0. \quad (B14)$$

The Taylor series of the wave number $K(\omega)$ at the third-order and the Fourier transform of $\Delta\omega$ and ΔK help to express in an approximate form, the second term of Eq. (B13) as

$$j\frac{1}{v}\frac{\partial \phi}{\partial t} = j\frac{1}{v_g}\frac{\partial \phi}{\partial t} + \frac{1}{2}K''\frac{\partial^2 \phi}{\partial t^2} - j\frac{1}{6}K'''\frac{\partial^3 \phi}{\partial t^3}, \quad (B15)$$

where

$$K'' = \frac{\partial^2 K}{\partial \omega^2}, K''' = \frac{\partial^3 K}{\partial \omega^3}, K' = \frac{1}{v_g} = \frac{\partial K}{\partial \omega}. \quad (B16)$$

Then, for the following change of variable

$$\begin{aligned}t' = t - \frac{1}{v_g}z^* \\ z' = z^*\end{aligned} \quad \Rightarrow \quad \begin{aligned}\frac{\partial}{\partial t} \to \frac{\partial}{\partial t'} \\ \frac{\partial}{\partial z^*} \to \frac{\partial}{\partial z'} - \frac{1}{v_g}\frac{\partial}{\partial t'}\end{aligned}, \quad (B17)$$

Eq. (B14) stands for

$$\begin{aligned}j\frac{\partial \phi}{\partial z'} + \frac{1}{2}K''\frac{\partial^2 \phi}{\partial t'^2} - j\frac{1}{6}K'''\frac{\partial^3 \phi}{\partial t'^3} + j\frac{\omega\alpha}{2K_0}\left(1 \mp KT_c\right)\phi - \frac{\beta\omega^2}{2K_0}\left(1 \mp KT_c\right)|\phi|^2\phi \\ \mp K^2T_c\phi + j\frac{\omega\beta}{K_0}|\phi|^2\frac{\partial \phi}{\partial t'} = 0.\end{aligned} \quad (B18)$$

APPENDIX C: THE DERIVATION OF THE HOMOGENEOUS HIGHER-ORDER NONPARAXIAL NLS IN CHIRAL OPTICAL FIBERS

One consider a model which satisfies both, the breakdown of the paraxial approximation as well as the requirements of time-reversal symmetry and reciprocity through the Drude-Born-Federov formalism. Under this formalism, the adequate constitutive relations for the study of propagation of waves in chiral medium are expressed as [64, 71, 353]

$$\vec{D} = \varepsilon_n\vec{E} + \varepsilon_0 T_c\vec{\nabla} \times \vec{E}, \quad \vec{B} = \mu_0\left(\vec{H} + T_c\vec{\nabla} \times \vec{H}\right), \quad (C1)$$

where the flux densities $\vec{D}$ and $\vec{B}$ arise in response to the electric and magnetic field $\vec{E}$ and $\vec{H}$ propagating in the chiral medium with $\varepsilon_n = \varepsilon_0 + \varepsilon_2\left|\vec{E}\right|^2$. Here ε_0 and ε_2 are linear and nonlinear permittivity, respectively. μ_0 is the permeability and T_c the chiral parameter of the optical fiber. In the chiral optical medium, the predicted Maxwell equations can be written as

$$\begin{aligned}\vec{\nabla} \cdot \vec{D} = \rho_v, \quad \vec{\nabla} \cdot \vec{B} = 0, \\ \vec{\nabla} \times \vec{E} = -\frac{\partial \vec{B}}{\partial t}, \quad \vec{\nabla} \times \vec{H} = \vec{J} + \frac{\partial \vec{D}}{\partial t},\end{aligned} \quad (C2)$$

where the current density $\vec{J} = \sigma\vec{E}$ and the charge density ρ represents the sources for the electromagnetic field. The quantity σ is the electrical conductivity and v the volume. Substituting

Eq. (C1) into Eq. (C2), one obtains the following wave equation

$$\nabla^2\vec{E} + \mu_0\varepsilon T^2\frac{\partial^2\vec{\nabla}^2\vec{E}}{\partial t^2} = \mu_0\varepsilon_0\frac{\partial^2\vec{E}}{\partial t^2} + \mu_0\sigma\frac{\partial\vec{E}}{\partial t} + \mu_0\varepsilon_2\left|\vec{E}\right|^2\frac{\partial^2\vec{E}}{\partial t^2}$$
$$+2\mu_0\varepsilon_0 T\vec{\nabla}\times\frac{\partial^2\vec{E}}{\partial t^2} + \mu_0\varepsilon_2 T\left|\vec{E}\right|^2\vec{\nabla}\times\frac{\partial^2\vec{E}}{\partial t^2} + \mu_0\sigma T\vec{\nabla}\times\frac{\partial\vec{E}}{\partial t}. \tag{C3}$$

The optical field $\vec{E}$ is represented by a right-(R) or left-hand(L) polarizations in the z direction as

$$\vec{E}(\vec{r},t) = (\hat{x}\mp j\hat{y})A(\vec{r},t)\exp\left[-j(k_\pm z - \omega_0 t)\right]$$
$$= \vec{\psi}_{R,L}\exp\left[-j(k_\pm z - \omega_0 t)\right], \tag{C4}$$

where $\vec{\psi}_{R,L}$ is the complex envelope of the optical field in the nonlinear chiral medium, K the wave number and ω_0 the frequency.

After evaluation of different derivations of $\vec{E}$ in x, y and z directions in Eq. (C3), one neglects all the second-order terms, except the nonparaxial one. Considering that the wave is propagating in z direction implies

$$K_x = K_y = 0, \quad E_z = 0. \tag{C5}$$

Therefore, Eq. (C3) is reduced in x, y and z directions, respectively as follows

$$\left(1 - \mu_0\varepsilon_0 T_c^2\omega^2\right)\left[\frac{\partial^2 E_x}{\partial x^2} + \frac{\partial^2 E_x}{\partial y^2} + \frac{\partial^2 E_x}{\partial z^2}\right] - 2jK_z\frac{\partial E_x}{\partial z} - K_z^2 E_x + \mu_0\varepsilon T_c^2(\omega^2 K_z^2 E_x + 2jK_z\omega^2\frac{\partial E_x}{\partial z}$$
$$-2jK_z^2\omega\frac{\partial E_x}{\partial t} - K_z^2\frac{\partial^2 E_x}{\partial t^2}) = \left(\mu_0\varepsilon_0 + \mu_0\varepsilon_2\left|\vec{E}\right|^2\right)\left[\frac{\partial^2 E_x}{\partial t^2} + 2j\omega\frac{\partial E_x}{\partial t} - \omega^2 E_x\right] + \mu_0\sigma\left(\frac{\partial E_x}{\partial t} + j\omega E_x\right)$$
$$+\left(2\mu_0\varepsilon_0 T_c + \mu_0\varepsilon_2 T_c\left|\vec{E}\right|^2\right)\left[\omega^2\frac{\partial E_y}{\partial z} + jK_z\left(\frac{\partial^2 E_y}{\partial t^2} + 2j\omega\frac{\partial E_y}{\partial t} - \omega^2 E_y\right)\right] + \mu_0\sigma T_c(-j\omega\frac{\partial E_y}{\partial z} + jK_z\frac{\partial E_y}{\partial t}$$
$$-\omega K_z E_y), \tag{C6}$$

$$\left(1 - \mu_0\varepsilon_0 T_c^2\omega^2\right)\left[\frac{\partial^2 E_y}{\partial x^2} + \frac{\partial^2 E_y}{\partial y^2} + \frac{\partial^2 E_y}{\partial z^2}\right] - 2jK_z\frac{\partial E_y}{\partial z} - K_z^2 E_y + \mu_0\varepsilon T_c^2(\omega^2 K_z^2 E_y + 2jK_z\omega^2\frac{\partial E_y}{\partial z}$$
$$-2jK_z^2\omega\frac{\partial E_y}{\partial t} - K_z^2\frac{\partial^2 E_y}{\partial t^2}) = \left(\mu_0\varepsilon_0 + \mu_0\varepsilon_2\left|\vec{E}\right|^2\right)\left[\frac{\partial^2 E_y}{\partial t^2} + 2j\omega\frac{\partial E_y}{\partial t} - \omega^2 E_y\right] + \mu_0\sigma\left(\frac{\partial E_y}{\partial t} + j\omega E_y\right)$$
$$+\left(2\mu_0\varepsilon_0 T + \mu_0\varepsilon_2 T\left|\vec{E}\right|^2\right)(-\omega^2\frac{\partial E_x}{\partial z} - jK_z(\frac{\partial^2 E_x}{\partial t^2} + 2j\omega\frac{\partial E_x}{\partial t} - \omega^2 E_x)) + \mu_0\sigma T(j\omega\frac{\partial E_x}{\partial z} - jK_z\frac{\partial E_x}{\partial t}$$
$$+\omega K_z E_x), \tag{C7}$$

$$\left[-\left(2\mu_0\varepsilon_0 T_c + \mu_0\varepsilon_2 T_c\left|\vec{E}\right|^2\right)\omega^2 + j\omega\mu_0\sigma T_c\right]\left[\frac{\partial E_y}{\partial x} - \frac{\partial E_x}{\partial y}\right] = 0. \tag{C8}$$

Eq. (C8) leads to

$$\frac{\partial E_y}{\partial x} = \frac{\partial E_x}{\partial y} = cst, \quad E_y = E_y(z,t), \quad E_x = E_x(z,t). \tag{C9}$$

Having multiply Eq. (C7) by $\pm j$, follows the addition of Eqs. (C6) and (C7), where one considers the conditions given in relation (C9) and the following approximations

$$\left|\frac{\partial E_x}{\partial t}\right| << |2j\omega E_x|, \quad \left|\frac{\partial^2 E_y}{\partial z^2}\right| << |2j\omega E_y|. \tag{C10}$$

Therefore, the novel form of wave equation can be written as

$$(1 - \mu_0\varepsilon_0 T_c{}^2\omega^2)\frac{\partial^2\psi_{R,L}}{\partial z^2} + (-2jK_z + 2jK_z\omega^2\mu_0\varepsilon T_c{}^2 \pm j((2\mu_0\varepsilon_0 T_c + \mu_0\varepsilon_2 T_c\left|\vec{E}\right|^2)\omega^2 - j\omega\mu_0\sigma T_c))\frac{\partial\psi_{R,L}}{\partial z}$$

$$+(-K_z{}^2 + \mu_0\varepsilon_0 T_c{}^2\omega^2 K_z{}^2 + \omega^2(\mu_0\varepsilon_0 + \mu_0\varepsilon_2\left|\vec{E}\right|^2) - j\omega\mu_0\sigma \pm j(-jK_z\omega^2(2\mu_0\varepsilon_0 T_c + \mu_0\varepsilon_2 T_c\left|\vec{E}\right|^2)$$

$$-K_z\omega\mu_0\sigma T_c))\psi_{R,L} + (-2jK_z{}^2\omega\mu_0\varepsilon_0 T_c{}^2 - \mu_0\sigma - 2j\omega(\mu_0\varepsilon_0 + \mu_0\varepsilon_2\left|\vec{E}\right|^2) \pm j(-2\omega K_z(2\mu_0\varepsilon_0 T_c$$

$$+\mu_0\varepsilon_2 T_c\left|\vec{E}\right|^2) + jK_z\mu_0\sigma T_c))\frac{\partial\psi_{R,L}}{\partial t} = 0, \tag{C11}$$

where $\psi_{R,L} = E_x \pm jE_y$. Then, the reference changing is

$$\psi_R = E_x + jE_y \quad \psi_L = E_x - jE_y,$$
$$E_x = \frac{\psi_R+\psi_L}{2} \quad E_y = \frac{\psi_R-\psi_L}{2}. \tag{C12}$$

The division of Eq. (C6) by $-2K_z$ yields

$$-\frac{(1-\mu_0\varepsilon_0 T_c{}^2\omega^2)}{2K_z}\frac{\partial^2\psi_{R,L}}{\partial z^2} + j\left(1 - K_0{}^2 T_c{}^2\right)\frac{\partial\psi_{R,L}}{\partial z} \mp j\frac{K_0{}^2 T_c}{K_z}\frac{\partial\psi_{R,L}}{\partial z} + j\frac{\omega\mu_0\varepsilon_2}{K_z}|\psi_{R,L}|^2\frac{\partial\psi_{R,L}}{\partial t} \mp j\frac{\mu_0\varepsilon_2\omega^2 T_c}{2K_z}$$

$$\times|\psi_{R,L}|^2\frac{\partial\psi_{R,L}}{\partial z} + j\frac{K_0}{K_z c}\left(1 + K_z{}^2 T_c{}^2\right)\frac{\partial\psi_{R,L}}{\partial t} \pm \frac{j\omega\mu_0\sigma T_c}{2}\psi_{R,L} + \frac{1}{2}\left(K_z - K_z K_0{}^2 T_c{}^2 - \frac{K_0{}^2}{K_z}\right)\psi_{R,L} \tag{C13}$$

$$-\frac{\mu_0\varepsilon_2\omega^2}{2K_z}|\psi_{R,L}|^2\psi_{R,L} \mp \frac{\omega^2}{2}\left(\mu_0\varepsilon_2 T_c|\psi_{R,L}|^2\right)\psi_{R,L} + j\frac{\omega\mu_0\sigma}{2K_z}\psi_{R,L} \mp K_0{}^2 T_c\psi_{R,L} \mp \frac{\omega\mu_0\sigma T}{2K_z}\frac{\partial\psi_{R,L}}{\partial z}$$

$$\pm\frac{\mu_0\sigma T_c}{2}\frac{\partial\psi_{R,L}}{\partial t} \pm j\frac{2K_0 T_c}{C}\frac{\partial\psi_{R,L}}{\partial t} + \frac{\mu_0\sigma}{2K_z}\frac{\partial\psi_{R,L}}{\partial t} \pm j\omega\mu_0\varepsilon_2 T_c|\psi_{R,L}|^2\frac{\partial\psi_{R,L}}{\partial t} = 0,$$

where

$$K_0 = \frac{\omega}{c}, \quad \mu_0\varepsilon_0 c^2 = 1. \tag{C14}$$

The dispersion relation is given by

$$K_z = \frac{K_0}{1 \pm K_0 T_c}. \tag{C15}$$

For $K_0{}^2 T_c{}^2 << 1$, we get $K_z = K_0$. By neglecting the nonlinear diffraction, the second and the last terms of Eq. (C13), and for the following set of parameters

$$v^2 = \frac{1}{\mu_0\varepsilon_0}, \quad \alpha = \mu_0\sigma, \quad \beta = \mu_0\varepsilon_2, \quad K_0 = \frac{\omega}{v}, \quad z^* = \frac{z}{1-K_0{}^2 T_c{}^2}. \tag{C16}$$

Equation (C13) takes the form

$$-\frac{1}{2K_0}\frac{\partial^2\psi_{R,L}}{\partial z^{*2}} + j\frac{\partial\psi_{R,L}}{\partial z^*} + j\frac{1}{v}\frac{\partial\psi_{R,L}}{\partial t} + j\frac{\omega\alpha}{2K_0}(1 \pm K_0 T_c)\psi_{R,L} \mp K_0{}^2 T_c\psi_{R,L} - \frac{\beta\omega^2}{2K_0}(1 \pm K_0 T_c)$$

$$\times|\psi_{R,L}|^2\psi_{R,L} + \frac{\alpha}{2K_0}(1 \pm K_0 T_c)\frac{\partial\psi_{R,L}}{\partial t} \pm \frac{j2K_0{}^2 T_c}{\omega}\frac{\partial\psi_{R,L}}{\partial t} + \frac{j\omega\beta}{K_0}(1 \pm K_0 T_c)|\psi_{R,L}|^2\frac{\partial\psi_{R,L}}{\partial t} = 0. \tag{C17}$$

If one sets

$$\psi_{R,L} = \phi, \quad K = K_0 = K_z. \tag{C18}$$

Equation (C16) yields

$$-\frac{1}{2K}\frac{\partial^2\phi}{\partial z^{*2}} + j\frac{\partial\phi}{\partial z^*} + j\frac{1}{v}\frac{\partial\phi}{\partial t} + j\frac{\omega\alpha}{2K}\left(1 \mp KT_c\right)\phi - \frac{\beta\omega^2}{2K}\left(1 \mp KT_c\right)|\phi|^2\phi \mp K^2 T_c\phi$$

$$+\frac{\alpha}{2K}(1 \pm KT_c)\frac{\partial\phi}{\partial t} \pm j\frac{2K^2 T_c}{\omega}\frac{\partial\psi_{R,L}}{\partial t} + j\frac{\omega\beta}{K_0}(1 \pm KT_c)|\phi|^2\frac{\partial\phi}{\partial t} = 0. \tag{C19}$$

The Taylor series of the wave number $K(\omega)$ at the third-order and the Fourier transform of $\Delta\omega$ and ΔK help to express in an approximate form, the second term of Eq. (C18) as

$$j\frac{1}{v}\frac{\partial\phi}{\partial t} = j\frac{1}{v_g}\frac{\partial\phi}{\partial t} + \frac{1}{2}K''\frac{\partial^2\phi}{\partial t^2} - j\frac{1}{6}K'''\frac{\partial^3\phi}{\partial t^3}, \tag{C20}$$

where

$$K'' = \frac{\partial^2 K}{\partial \omega^2}, K''' = \frac{\partial^3 K}{\partial \omega^3}, K' = \frac{1}{v_g} = \frac{\partial K}{\partial \omega}. \quad (C21)$$

Then, for the following change of variable

$$\begin{array}{l} t' = t - \frac{1}{v_g} z^* \\ z' = z^*, \end{array} \quad \Rightarrow \quad \begin{array}{l} \frac{\partial}{\partial t} \rightarrow \frac{\partial}{\partial t'} \\ \frac{\partial}{\partial z^*} \rightarrow \frac{\partial}{\partial z'} - \frac{1}{v_g} \frac{\partial}{\partial t'}, \end{array} \quad (C22)$$

Eq. (C19) stands for

$$-\frac{1}{2K} \frac{\partial^2 \phi}{\partial z'^2} + j \frac{\partial \phi}{\partial z'} + \frac{1}{2} \left(K'' - \frac{K'^2}{K} \right) \frac{\partial^2 \phi}{\partial t'^2} - j \frac{1}{6} K''' \frac{\partial^3 \phi}{\partial t'^3} + j \frac{\omega \alpha}{2K} \left(1 \pm K T_c \right) \phi - \frac{\beta \omega^2}{2K} \left(1 \mp K T_c \right) |\phi|^2 \phi$$
$$\mp K^2 T \phi + \frac{\alpha}{2K} \left(1 \pm K T_c \right) \frac{\partial \phi}{\partial t'} \pm j \frac{2K^2 T_c}{\omega} \frac{\partial \phi}{\partial t'} + j \frac{\omega \beta}{K} |\phi|^2 \left(1 \pm K T_c \right) \frac{\partial \phi}{\partial t'} = 0, \quad (C23)$$

where $K' = \frac{\partial K}{\partial \omega} = \frac{1}{v_g}$ is the inverse of group-velocity, $K'' = \frac{\partial K'}{\partial \omega}$ is the group-velocity dispersion (GVD) coefficient which can take the plus and minus signs ($\pm$), representing the anomalous and normal dispersion regimes, respectively. The parameter $K''' = \frac{\partial K''}{\partial \omega}$ is the third-order dispersion (TOD) term. In the fourth term, the attenuation coefficient α is weighted towards the chiral parameter T_c. The factor to $|\phi|^2 \phi$ is the self-phase modulation (SPM) and the term $K^2 T_c \phi$ occurs as an additional correction to the chirality of the fiber. The expressions at the eighth and ninth positions are the differential gain or loss term and the walk-off effect. The last term has the physical sense of self-steepening (SS) and is necessary to perform the description of spontaneous waves.

The new variables, namely

$$\begin{array}{llll} q = \frac{\omega_0^{2/3} \beta^{1/3}}{(2K_0)^{1/3}} \phi, & \xi = \frac{\omega_0^{2/3} \beta^{1/3}}{(2K_0)^{1/3}} z', & d = -\frac{\beta^{1/3} \omega_0^{2/3}}{(2k_0)^{4/3}}, & \eta = \frac{\alpha C_T}{\sqrt{K''} \omega_0^{1/3} \beta^{1/6} (2k_0)^{5/6}}, \\ \tau = \frac{\omega_0^{1/3} \beta^{1/6}}{\sqrt{K''} (2K_0)^{1/6}} t', & \gamma = \frac{K'''}{6} \frac{\beta^{1/6} \omega_0^{1/3}}{(2K_0)^{1/6} (K'')^{3/2}}, & C_T = 1 \mp T_c K, & \Gamma = \frac{\omega_0^{1/3} \alpha}{(2K_0)^{1/3} \beta^{1/3}}, \\ \mu = C_T \Gamma, & P = \frac{1}{2} \left(1 - \frac{k'^2}{K'' k_0} \right), & \sigma_3 = \frac{k_0 T_c (2k_0)^{7/6}}{\sqrt{K''} \omega_0^{4/3} \beta^{1/6}}, & D = \frac{K^2 T_c (2K_0)^{1/3}}{\beta^{1/3} \omega_0^{2/3}}, \\ \alpha_3 = \frac{C_T (2K_0)^{5/6} \beta^{1/6}}{\sqrt{K''} \omega_0^{2/3} K_0}, & & & \end{array} \quad (C24)$$

allow us to express for $q(\xi, \tau) = \psi(\xi, \tau)$, Eq. (C23) in the form

$$d \frac{\partial^2 \psi}{\partial \xi^2} + j \frac{\partial \psi}{\partial \xi} + P \frac{\partial^2 \psi}{\partial \tau^2} - j \gamma \frac{\partial^3 \psi}{\partial \tau^3} + j \mu \psi \mp D \psi - C_T |\psi|^2 \psi + j \alpha_3 |\psi|^2 \frac{\partial \psi}{\partial \tau} + \eta \frac{\partial \psi}{\partial \tau} \pm j \sigma_3 \frac{\partial \psi}{\partial \tau} = 0. \quad (C25)$$

Equation (C25) is the higher-order nonparaxial chiral NLSE and can be used to describe the propagation of the right(+) and left(-) hand polarized rogue waves in a higher-order dispersive and nonlinear chiral optical fiber. For $d = 0$, $P = \frac{1}{2}$, $T_c = 0$, $C_T = 1$, $D = 0$, $\gamma = 0$, $\mu = 0$, $\eta = 0$ and $\sigma_3 = 0$, Eq. (C25) stands for the standard NLS equation.

APPENDIX D: THE PARAMETERS OF THE WALK-OFF EFFECT $\sigma(\xi, \tau)$

$$\sigma_4(\xi) = -\frac{1}{3} \frac{d(\xi)^2 T_1(\xi)_\xi^2 T_1(\xi)_{\xi\xi}}{T_1(\xi)^3 \gamma(\xi)} + \frac{1}{12} \frac{d(\xi)^2 T_1(\xi)_{\xi\xi}^2}{T_1(\xi)^2 \gamma(\xi)} - \frac{1}{9} \frac{d(\xi) T_1(\xi)_\xi (\frac{d(\xi) T_1(\xi)_{\xi\xi}}{\gamma(\xi) T_1(\xi)})_\xi}{T_1(\xi)}, \quad (D1)$$

$$\sigma_3\left(\xi\right) = -\frac{2}{3}\frac{d(\xi)^2 T_1(\xi)_\xi{}^2 T_0(\xi)_{\xi\xi}}{T_1(\xi)^3\gamma(\xi)} - \frac{2}{3}\frac{d(\xi)^2 T_1(\xi)_\xi T_0(\xi)_\xi T_1(\xi)_{\xi\xi}}{T_1(\xi)^3\gamma(\xi)} - \frac{2}{3}\frac{d(\xi)\,T1_z{}^2\eta(\xi)}{T_1(\xi)^2\gamma(\xi)}$$

$$+\frac{1}{3}\frac{d(\xi)T_1(\xi)_\xi\left(\frac{d(\xi)T_0(\xi)_{\xi\xi}+\eta(\xi)T_1(\xi)}{\gamma(\xi)T_1(\xi)}\right)_\xi}{T_1(\xi)} + \frac{1}{3}\frac{d\xi\,T_1(\xi)_{\xi\xi}\eta(\xi)}{\gamma(\xi)T_1(\xi)} + \frac{1}{3}\frac{d(\xi)^2 T_1(\xi)_{\xi\xi}T_0(\xi)_{\xi\xi}}{T_1(\xi)^2\gamma(\xi)} \quad (D2)$$

$$+\frac{1}{9}\frac{d(\xi)T_0(\xi)_\xi\left(\frac{d\xi\,T_1(\xi)_{\xi\xi}}{\gamma(\xi)T_1(\xi)}\right)_\xi}{T_1(\xi)},$$

$$\sigma_2\left(\xi\right) = 2\frac{d(\xi)\,T1(\xi)_\xi{}^2\rho_1(\xi)}{T_1(\xi)^2} - 2\frac{d(\xi)T_1(\xi)_\xi\rho_1(\xi)_\xi}{T_1(\xi)} - \frac{d(\xi)T_1(\xi)_{\xi\xi}\rho_1(\xi)}{T_1(\xi)} + \frac{2}{3}\frac{d(\xi)T_0(\xi)_{\xi\xi}\eta(\xi)}{\gamma(\xi)T_1(\xi)}$$

$$-\frac{4}{3}\frac{d(\xi)\,T_1(\xi)_\xi{}^2\eta(\xi)}{T_1(\xi)^2\gamma(\xi)} + \frac{1}{3}\frac{\eta(\xi)^2}{\gamma(\xi)} + \frac{1}{3}\frac{d(\xi)T_0(\xi)_\xi\left(\frac{d(\xi)\,T_0(\xi)_{\xi\xi}+\eta(\xi)T_1(\xi)}{\gamma(\xi)T_1(\xi)}\right)_\xi}{T_1(\xi)} + \frac{1}{3}\frac{d(\xi)^2 T_0(\xi)_{\xi\xi}{}^2}{\gamma(\xi)T_1(\xi)^2} \quad (D3)$$

$$+\frac{1}{12}\frac{\sqrt{2}d(\xi)T_1(\xi)_{\xi\xi}}{\nu} - \frac{4}{3}\frac{d(\xi)^2 T_1(\xi)_\xi T_0(\xi)_\xi T_0(\xi)_{\xi\xi}}{T_1(\xi)^3\gamma(\xi)} - \frac{1}{3}\frac{d(\xi)^2 T_0(\xi)_\xi{}^2 T_1(\xi)_{\xi\xi}}{T_1(\xi)^3\gamma(\xi)},$$

$$\sigma_1\left(\xi\right) = -2\,\eta\left(\xi\right)\rho_1\left(\xi\right) - 2\frac{d(\xi)T_1(\xi)_\xi\rho_0(\xi)_\xi}{T_1(\xi)} - 2\frac{d(\xi)\,T_0(\xi)_{\xi\xi}\rho_1(\xi)}{T_1(\xi)} + \frac{1}{6}\frac{\sqrt{2}T_1(\xi)\eta(\xi)}{\nu}$$

$$-2\frac{d(\xi)T_0(\xi)_\xi\rho_1(\xi)_\xi}{T_1(\xi)} + 4\frac{d(\xi)\,T_1(\xi)_\xi T_0(\xi)_\xi\rho_1(\xi)}{T_1(\xi)^2} - \frac{2}{3}\frac{d(\xi)T_0(\xi)_\xi{}^2\eta(\xi)}{T_1(\xi)^2\gamma(\xi)} + \frac{1}{6}\frac{\sqrt{2}d(\xi)T_0(\xi)_{\xi\xi}}{\nu} \quad (D4)$$

$$-\frac{2}{3}\frac{d(\xi)^2 T_0(\xi)_\xi{}^2 T_0(\xi)_{\xi\xi}}{T_1(\xi)^3\gamma(\xi)} - \frac{T_1(\xi)_\xi}{T_1(\xi)},$$

$$\sigma_0\left(\xi\right) = -12\frac{\sqrt{2}\gamma(\xi)T_1(\xi)\rho_1(\xi)}{\nu} - \frac{T_0(\xi)_\xi}{T_1(\xi)} + 3\,\gamma\left(\xi\right)\rho_1\left(\xi\right)^2 + 2\frac{d(\xi)\,T_0(\xi)_\xi{}^2\rho_1(\xi)}{T_1(\xi)^2} - 2\frac{d(\xi)T_0(\xi)_\xi\rho_0(\xi)_\xi}{T_1(\xi)}. \quad (D5)$$

APPENDIX E: THE PARAMETERS OF THE GAIN OR LOSS TERM $\mu(\xi,\tau)$

$$\mu_3\left(\xi\right) = -\frac{1}{3}\frac{d(\xi)^2 T_1(\xi)_\xi{}^2 T_1(\xi)_{\xi\xi}}{T_1(\xi)^3\gamma(\xi)} + \frac{1}{18}d\left(\xi\right)\left(\frac{d(\xi)T_1(\xi)_{\xi\xi}}{\gamma(\xi)T_1(\xi)}\right)_{\xi\xi}, \quad (E1)$$

$$\mu_2\left(\xi\right) = \frac{1}{6}\frac{\eta(\xi)d(\xi)T_1(\xi)_{\xi\xi}}{\gamma(\xi)T_1(\xi)} - \frac{1}{3}\frac{d(\xi)T_1(\xi)_\xi{}^2\eta(\xi)}{T_1(\xi)^2\gamma(\xi)} - \frac{2}{3}\frac{d(\xi)^2 T_1(\xi)_\xi T_0(\xi)_\xi T_1(\xi)_{\xi\xi}}{T_1(\xi)^3\gamma(\xi)} - \frac{1}{3}\frac{d(\xi)^2 T_1(\xi)_\xi{}^2 T_0(\xi)_{\xi\xi}}{T_1(\xi)^3\gamma(\xi)}$$

$$+\frac{1}{6}d\left(\xi\right)\left(\frac{d(\xi)T_0(\xi)_{\xi\xi}+\eta(\xi)T_1(\xi)}{\gamma(\xi)T_1(\xi)}\right)_{\xi\xi}, \quad (E2)$$

$$\mu_1\left(\xi\right) = -\frac{2}{3}\frac{d(\xi)T_1(\xi)_\xi T_0(\xi)_\xi\eta(\xi)}{T_1(\xi)^2\gamma(\xi)} + \frac{1}{3}\frac{\eta(\xi)d(\xi)T_0(\xi)_{\xi\xi}}{\gamma(\xi)T_1(\xi)} + \frac{1}{3}\frac{\eta(\xi)^2}{\gamma(\xi)} - \frac{2}{3}\frac{d(\xi)^2 T_1(\xi)_\xi T_0(\xi)_\xi T_0(\xi)_{\xi\xi}}{T_1(\xi)^3\gamma(\xi)}$$

$$-\frac{1}{3}\frac{d(\xi)^2 T_0(\xi)_\xi{}^2 T_1(\xi)_{\xi\xi}}{T_1(\xi)^3\gamma(\xi)} + \frac{1}{12}\frac{\sqrt{2}d(\xi)T_1(\xi)_{\xi\xi}}{\nu} - d\left(\xi\right)\rho_1\left(\xi\right)_{\xi\xi}, \quad (E3)$$

$$\mu_0\left(\xi\right) = -\frac{1}{3}\frac{d(\xi)T_0(\xi)_\xi{}^2\eta(\xi)}{\gamma(\xi)T_1(\xi)^2} - \frac{1}{3}\frac{d(\xi)^2 T_0(\xi)_\xi{}^2 T_0(\xi)_{\xi\xi}}{\gamma(\xi)T_1(\xi)^3}$$

$$+\frac{1}{12}\frac{T_1(\xi)\sqrt{2}\eta(\xi)}{\nu} - \eta\left(\xi\right)\rho_1\left(\xi\right) + \frac{1}{12}\frac{\sqrt{2}d(\xi)T_0(\xi)_{\xi\xi}}{\nu} - d\left(\xi\right)\rho_0\left(\xi\right)_{\xi\xi}. \quad (E4)$$

APPENDIX F: THE PARAMETERS OF THE LINEAR BIREFRINGENCE $D(\xi,\tau)$

$$D_6\left(\xi\right) = -\frac{d(\xi)^2 T_1(\xi)_\xi T_1(\xi)_{\xi\xi}\frac{d(\xi)T_1(\xi)_{\xi\xi}}{\gamma(\xi)T_1(\xi)}{}_\xi}{54\,\gamma(\xi)T_1(\xi)^2} - \frac{d(\xi)^3 T_1(\xi)_{\xi\xi}{}^3}{216\,\gamma(\xi)^2 T_1(\xi)^3} + \frac{1}{36}\frac{d(\xi)^3 T_1(\xi)_\xi{}^2 T_1(\xi)_{\xi\xi}{}^2}{T_1(\xi)^4\gamma(\xi)^2}, \quad (F1)$$

$$D_5\left(\xi\right) = \frac{1}{9}\frac{d(\xi)^2 T_1(\xi)_\xi{}^2 T_1(\xi)_{\xi\xi}\eta(\xi)}{T_1(\xi)^3\gamma(\xi)^2} - \frac{d(\xi)^2 T_0(\xi)_\xi T_1(\xi)_{\xi\xi}(\frac{d(\xi)T_1(\xi)_{\xi\xi}}{\gamma(\xi)T_1(\xi)})_\xi}{54\,\gamma(\xi)T_1(\xi)^2}$$

$$-\frac{1}{18}\frac{d(\xi)^2 T_1(\xi)_\xi T_1(\xi)_{\xi\xi}(\frac{d(\xi)T_0(\xi)_{\xi\xi}+\eta(\xi)T_1(\xi)}{\gamma(\xi)T_1(\xi)})_\xi}{\gamma(\xi)T_1(\xi)^2} - \frac{d(\xi)^2 T_1(\xi)_\xi T_0(\xi)_{\xi\xi}(\frac{d(\xi)T_1(\xi)_{\xi\xi}}{\gamma(\xi)T_1(\xi)})_\xi}{54\,\gamma(\xi)T_1(\xi)^2}$$

$$+\frac{1}{18}\frac{d(\xi)^3 T_1(\xi)_\xi T_0(\xi)_\xi T_1(\xi)_{\xi\xi}{}^2}{T_1(\xi)^4\gamma(\xi)^2} + \frac{1}{9}\frac{d(\xi)^3 T_1(\xi)_\xi{}^2 T_1(\xi)_{\xi\xi}T_0(\xi)_{\xi\xi}}{T_1(\xi)^4\gamma(\xi)^2} - \frac{1}{36}\frac{d(\xi)^2 T_1(\xi)_{\xi\xi}{}^2\eta(\xi)}{\gamma(\xi)^2 T_1(\xi)^2}$$

$$-\frac{1}{27}\frac{d(\xi)T_1(\xi)_\xi\eta(\xi)(\frac{d(\xi)T_1(\xi)_{\xi\xi}}{\gamma(\xi)T_1(\xi)})_\xi}{\gamma(\xi)T_1(\xi)} - \frac{1}{36}\frac{d(\xi)^3 T_1(\xi)_{\xi\xi}{}^2 T_0(\xi)_{\xi\xi}}{T_1(\xi)^3\gamma(\xi)^2}, \tag{F2}$$

$$D_4\left(\xi\right) = -\frac{1}{3}\frac{d(\xi)^2 T_1(\xi)_\xi{}^2 T_1(\xi)_{\xi\xi}\rho_1(\xi)}{T_1(\xi)^3\gamma(\xi)} + \frac{2}{9}\frac{d(\xi)^2 T_1(\xi)_\xi{}^2 T_0(\xi)_{\xi\xi}\eta(\xi)}{T_1(\xi)^3\gamma(\xi)^2}$$

$$-\frac{1}{18}\frac{d(\xi)^2 T_0(\xi)_\xi T_1(\xi)_{\xi\xi}(\frac{d(\xi)T_0(\xi)_{\xi\xi}+\eta(\xi)T_1(\xi)}{\gamma(\xi)T_1(\xi)})_\xi}{\gamma(\xi)T_1(\xi)^2} + \frac{1}{3}\frac{d(\xi)^2 T_1(\xi)_\xi T_1(\xi)_{\xi\xi}\rho_1(\xi)_\xi}{\gamma(\xi)T_1(\xi)^2}$$

$$-\frac{1}{9}\frac{d(\xi)^2 T_1(\xi)_\xi T_0(\xi)_{\xi\xi}(\frac{d(\xi)T_0(\xi)_{\xi\xi}+\eta(\xi)T_1(\xi)}{\gamma(\xi)T_1(\xi)})_\xi}{\gamma(\xi)T_1(\xi)^2} + \frac{1}{36}\frac{d(\xi)^3 T_0(\xi)_\xi{}^2 T_1(\xi)_{\xi\xi}{}^2}{T_1(\xi)^4\gamma(\xi)^2} - \frac{1}{9}\frac{d(\xi)^2 T_1(\xi)_{\xi\xi}T_0(\xi)_{\xi\xi}\eta(\xi)}{\gamma(\xi)^2 T_1(\xi)^2}$$

$$+\frac{1}{9}\frac{d(\xi)T_1(\xi)_\xi\rho_1(\xi)(\frac{d(\xi)T_1(\xi)_{\xi\xi}}{\gamma(\xi)T_1(\xi)})_\xi}{T_1(\xi)} + \frac{1}{9}\frac{d(\xi)T_1(\xi)_\xi{}^2\eta(\xi)^2}{\gamma(\xi)^2 T_1(\xi)^2} - \frac{\sqrt{2}d(\xi)^2 T_1(\xi)_{\xi\xi}{}^2}{144\,\nu\,\gamma(\xi)T_1(\xi)}$$

$$+\frac{2}{9}\frac{d(\xi)^3 T_1(\xi)_\xi T_0(\xi)_\xi T_1(\xi)_{\xi\xi}T_0(\xi)_{\xi\xi}}{T_1(\xi)^4\gamma(\xi)^2} + \frac{2}{9}\frac{d(\xi)^2 T_1(\xi)_\xi T_0(\xi)_\xi T_1(\xi)_{\xi\xi}\eta(\xi)}{T_1(\xi)^3\gamma(\xi)^2} \tag{F3}$$

$$+\frac{1}{9}\frac{d(\xi)^3 T_1(\xi)_\xi{}^2 T_0(\xi)_{\xi\xi}{}^2}{T_1(\xi)^4\gamma(\xi)^2} + \frac{1}{12}\frac{d(\xi)^2 T_1(\xi)_{\xi\xi}{}^2\rho_1(\xi)}{\gamma(\xi)T_1(\xi)^2} - \frac{1}{18}\frac{d(\xi)^3 T_1(\xi)_{\xi\xi}T_0(\xi)_{\xi\xi}{}^2}{T_1(\xi)^3\gamma(\xi)^2} - \frac{1}{18}\frac{d(\xi)T_1(\xi)_{\xi\xi}\eta(\xi)^2}{\gamma(\xi)^2 T_1(\xi)}$$

$$-\frac{1}{9}\frac{d(\xi)T_1(\xi)_\xi\eta(\xi)(\frac{d(\xi)T_0(\xi)_{\xi\xi}+\eta(\xi)T_1(\xi)}{\gamma(\xi)T_1(\xi)})_\xi}{\gamma(\xi)T_1(\xi)} - \frac{1}{27}\frac{d(\xi)\eta(\xi)T_0(\xi)_\xi(\frac{d(\xi)T_1(\xi)_{\xi\xi}}{\gamma(\xi)T_1(\xi)})_\xi}{\gamma(\xi)T_1(\xi)},$$

$$D_3\left(\xi\right) = \frac{2}{9}\frac{d(\xi)^3 T_1(\xi)_\xi T_0(\xi)_\xi T_0(\xi)_{\xi\xi}{}^2}{T_1(\xi)^4\gamma(\xi)^2} - \frac{1}{9}\frac{d(\xi)T_0(\xi)_\xi\eta(\xi)(\frac{d(\xi)T_0(\xi)_{\xi\xi}+\eta(\xi)T_1(\xi)}{\gamma(\xi)T_1(\xi)})_\xi}{\gamma(\xi)T_1(\xi)}$$

$$+\frac{2}{9}\frac{d(\xi)T_1(\xi)_\xi T_0(\xi)_\xi\eta(\xi)^2}{T_1(\xi)^2\gamma(\xi)^2} + \frac{1}{9}\frac{d(\xi)T_0(\xi)_\xi\rho_1(\xi)\frac{d(\xi)T_1(\xi)_{\xi\xi}}{\gamma(\xi)T_1(\xi)}_\xi}{T_1(\xi)} - \frac{1}{9}\frac{d(\xi)^2 T_0(\xi)_{\xi\xi}{}^2\eta(\xi)}{T_1(\xi)^2\gamma(\xi)^2} + \frac{1}{6}\frac{T_1(\xi)_\xi d(\xi)T_1(\xi)_{\xi\xi}}{\gamma(\xi)T_1(\xi)^2}$$

$$-\frac{d(\xi)T_1(\xi)_{\xi\xi}}{\gamma(\xi)T_1(\xi)}_\xi - \frac{1}{9}\frac{d(\xi)T_0(\xi)_{\xi\xi}\eta(\xi)^2}{\gamma(\xi)^2 T_1(\xi)} - \frac{1}{27}\frac{\eta(\xi)^3}{\gamma(\xi)^2} + \frac{1}{3}\frac{d(\xi)^2 T_0(\xi)_\xi T_1(\xi)_{\xi\xi}\rho_1(\xi)_\xi}{\gamma(\xi)T_1(\xi)^2} + \frac{1}{3}\frac{d(\xi)^2 T_1(\xi)_\xi T_1(\xi)_{\xi\xi}\rho_0(\xi)_\xi}{\gamma(\xi)T_1(\xi)^2}$$

$$+\frac{2}{3}\frac{d(\xi)^2 T_1(\xi)_\xi T_0(\xi)_{\xi\xi}\rho_1(\xi)_\xi}{\gamma(\xi)T_1(\xi)^2} - \frac{\sqrt{2}d(\xi)T_1(\xi)_{\xi\xi}\eta(\xi)}{648\,\gamma(\xi)\nu} - \frac{2}{3}\frac{d(\xi)T_1(\xi)_\xi{}^2\eta(\xi)\rho_1(\xi)}{\gamma(\xi)T_1(\xi)^2} + \frac{4}{9}\frac{d(\xi)^2 T_1(\xi)_\xi T_0(\xi)_\xi T_0(\xi)_{\xi\xi}\eta(\xi)}{T_1(\xi)^3\gamma(\xi)^2} \tag{F4}$$

$$-\frac{2}{3}\frac{d(\xi)^2 T_1(\xi)_\xi T_0(\xi)_\xi T_1(\xi)_{\xi\xi}\rho_1(\xi)}{T_1(\xi)^3\gamma(\xi)} - \frac{1}{36}\frac{\sqrt{2}d(\xi)^2 T_1(\xi)_{\xi\xi}T_0(\xi)_{\xi\xi}}{\gamma(\xi)T_1(\xi)\nu} + \frac{1}{3}\frac{T_1(\xi)_\xi d(\xi)\rho_1(\xi)(\frac{d(\xi)T_0(\xi)_{\xi\xi}+\eta(\xi)T_1(\xi)}{\gamma(\xi)T_1(\xi)})_\xi}{T_1(\xi)}$$

$$-\frac{2}{3}\frac{d(\xi)^2 T_1(\xi)_\xi{}^2 T_0(\xi)_{\xi\xi}\rho_1(\xi)}{T_1(\xi)^3\gamma(\xi)} + \frac{1}{9}\frac{d(\xi)^2 T_0(\xi)_\xi{}^2 T_1(\xi)_{\xi\xi}\eta(\xi)}{T_1(\xi)^3\gamma(\xi)^2} + \frac{1}{3}\frac{d(\xi)^2 T_1(\xi)_{\xi\xi}T_0(\xi)_{\xi\xi}\rho_1(\xi)}{\gamma(\xi)T_1(\xi)^2}$$

$$+\frac{1}{3}\frac{d(\xi)T_1(\xi)_{\xi\xi}\eta(\xi)\rho_1(\xi)}{\gamma(\xi)T_1(\xi)} + \frac{1}{9}\frac{d(\xi)^3 T_0(\xi)_\xi{}^2 T_1(\xi)_{\xi\xi}T_0(\xi)_{\xi\xi}}{T_1(\xi)^4\gamma(\xi)^2} + \frac{2}{3}\frac{T_1(\xi)_\xi d(\xi)\eta(\xi)\rho_1(\xi)_\xi}{\gamma(\xi)T_1(\xi)}$$

$$-\frac{1}{9}\frac{d(\xi)^2 T_0(\xi)_\xi T_0(\xi)_{\xi\xi}(\frac{d(\xi)T_0(\xi)_{\xi\xi}+\eta(\xi)T_1(\xi)}{\gamma(\xi)T_1(\xi)})_\xi}{\gamma(\xi)T_1(\xi)^2} - \frac{1}{27}\frac{d(\xi)^3 T_0(\xi)_{\xi\xi}{}^3}{T_1(\xi)^3\gamma(\xi)^2} - \frac{1}{18}\frac{d(\xi)T_1(\xi)_{\xi\xi}}{\gamma(\xi)T_1(\xi)},$$

$$D_2\left(\xi\right) = \frac{1}{3}\frac{\eta(\xi)^2\rho_1(\xi)}{\gamma(\xi)} + \frac{1}{3}\frac{d(\xi)T_0(\xi)_\xi\rho_1(\xi)(\frac{d(\xi)T_0(\xi)_{\xi\xi}+\eta(\xi)T_1(\xi)}{\gamma(\xi)T_1(\xi)})_\xi}{T_1(\xi)}$$
$$+\frac{2}{3}\frac{d(\xi)T_0(\xi)_{\xi\xi}\eta(\xi)\rho_1(\xi)}{\gamma(\xi)T_1(\xi)} - \frac{1}{3}\frac{d(\xi)^2T_0(\xi)_\xi{}^2T_1(\xi)_{\xi\xi}\rho_1(\xi)}{T_1(\xi)^3\gamma(\xi)} + \frac{2}{9}\frac{d(\xi)^2T_0(\xi)_\xi{}^2T_0(\xi)_{\xi\xi}\eta(\xi)}{T_1(\xi)^3\gamma(\xi)^2}$$
$$-\frac{1}{6}\frac{d(\xi)T_0(\xi)_{\xi\xi}+\eta(\xi)T_1(\xi)}{\gamma(\xi)T_1(\xi)} - \frac{1}{36}\frac{T_1(\xi)\sqrt{2}\eta(\xi)^2}{\nu\,\gamma(\xi)} + \frac{1}{12}\frac{\sqrt{2}d(\xi)T_1(\xi)_{\xi\xi}\rho_1(\xi)}{\nu} + \frac{1}{6}\frac{T_0(\xi)_\xi d(\xi)T_1(\xi)_{\xi\xi}}{\gamma(\xi)T_1(\xi)^2}$$
$$+\frac{1}{3}\frac{T_1(\xi)_\xi d(\xi)T_0(\xi)_{\xi\xi}}{\gamma(\xi)T_1(\xi)^2} - \frac{1}{6}\frac{d(\xi)T_0(\xi)_{\xi\xi}+\eta(\xi)T_1(\xi)}{\gamma(\xi)T_1(\xi)_\xi} + \frac{2}{3}\frac{d(\xi)T_1(\xi)_\xi\eta(\xi)\rho_0(\xi)_\xi}{\gamma(\xi)T_1(\xi)} + \frac{2}{3}\frac{d(\xi)T_0(\xi)_\xi\eta(\xi)\rho_1(\xi)_\xi}{\gamma(\xi)T_1(\xi)}$$
$$+\frac{2}{3}\frac{d(\xi)^2T_1(\xi)_\xi T_0(\xi)_{\xi\xi}\rho_0(\xi)_\xi}{\gamma(\xi)T_1(\xi)^2} - \frac{1}{36}\frac{\sqrt{2}d(\xi)^2T_0(\xi)_{\xi\xi}{}^2}{\nu\,\gamma(\xi)T_1(\xi)} - \frac{1}{18}\frac{\sqrt{2}d(\xi)T_0(\xi)_{\xi\xi}\eta(\xi)}{\nu\,\gamma(\xi)}$$
$$+\frac{1}{3}\frac{d(\xi)^2T_0(\xi)_\xi T_1(\xi)_{\xi\xi}\rho_0(\xi)_\xi}{\gamma(\xi)T_1(\xi)^2} + \frac{2}{3}\frac{d(\xi)^2T_0(\xi)_\xi T_0(\xi)_{\xi\xi}\rho_1(\xi)_\xi}{\gamma(\xi)T_1(\xi)^2} + \frac{1}{3}\frac{d(\xi)^2T_0(\xi)_{\xi\xi}{}^2\rho_1(\xi)}{\gamma(\xi)T_1(\xi)^2} - \frac{1}{2}\frac{d(\xi)T_1(\xi)_{\xi\xi}\rho_1(\xi)^2}{T_1(\xi)}$$
$$+\frac{d(\xi)T_1(\xi)_\xi{}^2\rho_1(\xi)^2}{T_1(\xi)^2} + \frac{1}{3}\frac{T_1(\xi)_\xi\eta(\xi)}{\gamma(\xi)T_1(\xi)} - \frac{4}{3}\frac{d(\xi)^2T_1(\xi)_\xi T_0(\xi)_\xi T_0(\xi)_{\xi\xi}\rho_1(\xi)}{T_1(\xi)^3\gamma(\xi)}$$
$$-\frac{4}{3}\frac{d(\xi)T_1(\xi)_\xi T_0(\xi)_\xi\eta(\xi)\rho_1(\xi)}{\gamma(\xi)T_1(\xi)^2} + \frac{1}{9}\frac{d(\xi)T_0(\xi)_\xi{}^2\eta(\xi)^2}{T_1(\xi)^2\gamma(\xi)^2} - 2\frac{d(\xi)T_1(\xi)_\xi\rho_1(\xi)\rho_1(\xi)_\xi}{T_1(\xi)} + \frac{1}{9}\frac{d(\xi)^3T_0(\xi)_\xi{}^2T_0(\xi)_{\xi\xi}{}^2}{T_1(\xi)^4\gamma(\xi)^2},\qquad (F5)$$

$$D_1\left(\xi\right) = \frac{1}{6}\frac{\sqrt{2}d(\xi)T_0(\xi)_{\xi\xi}\rho_1(\xi)}{\nu} - 2\frac{d(\xi)T_0(\xi)_\xi\rho_1(\xi)\rho_1(\xi)_\xi}{T_1(\xi)} + \frac{2}{3}\frac{d(\xi)^2T_0(\xi)_\xi T_0(\xi)_{\xi\xi}\rho_0(\xi)_\xi}{\gamma(\xi)T_1(\xi)^2} - \frac{2}{3}\frac{d(\xi)^2T_0(\xi)_\xi{}^2T_0(\xi)_{\xi\xi}\rho_1(\xi)}{T_1(\xi)^3\gamma(\xi)}$$
$$+\frac{1}{6}\frac{T_1(\xi)\sqrt{2}\eta(\xi)\rho_1(\xi)}{\nu} - 2\frac{d(\xi)T_1(\xi)_\xi\rho_1(\xi)\rho_0(\xi)_\xi}{T_1(\xi)} + 2\frac{d(\xi)T_1(\xi)_\xi T_0(\xi)_\xi\rho_1(\xi)^2}{T_1(\xi)^2} - \frac{T_1(\xi)_\xi\rho_1(\xi)}{T_1(\xi)} + \rho_1\left(\xi\right)_\xi$$
$$+\frac{1}{3}\frac{T_0(\xi)_\xi\eta(\xi)}{\gamma(\xi)T_1(\xi)} + \rho_1\left(\xi\right) - \eta\left(\xi\right)\rho_1\left(\xi\right)^2 - \frac{d(\xi)T_0(\xi)_{\xi\xi}\rho_1(\xi)^2}{T_1(\xi)} + \frac{1}{3}\frac{d(\xi)T_0(\xi)_\xi T_0(\xi)_{\xi\xi}}{\gamma(\xi)T_1(\xi)^2}$$
$$+\frac{2}{3}\frac{d(\xi)T_0(\xi)_\xi\eta(\xi)\rho_0(\xi)_\xi}{\gamma(\xi)T_1(\xi)} - \frac{2}{3}\frac{d(\xi)T_0(\xi)_\xi{}^2\eta(\xi)\rho_1(\xi)}{\gamma(\xi)T_1(\xi)^2},\qquad (F6)$$

$$D_0\left(\xi\right) = -2\frac{d(\xi)T_0(\xi)_\xi\rho_1(\xi)\rho_0(\xi)_\xi}{T_1(\xi)} - \frac{1}{4}\frac{\sqrt{2}\gamma(\xi)T_1(\xi)\rho_1(\xi)^2}{\nu} + \frac{1}{3}\frac{d(\xi)T_1(\xi)_{\xi\xi}}{T_1(\xi)}$$
$$+\frac{d(\xi)T_0(\xi)_\xi{}^2\rho_1(\xi)^2}{T_1(\xi)^2} - \frac{T_0(\xi)_\xi\rho_1(\xi)}{T_1(\xi)} + \gamma\left(\xi\right)\rho_1\left(\xi\right)^3.\qquad (F7)$$

APPENDIX G: THE FINITE DIFFERENCE FORMULAE FOR THE DERIVATIVES

$$\left[\frac{\partial^2 u(\xi,\tau)}{\partial\xi^2}\right]_{\xi=n\Delta\xi} = \frac{u_{n+1}(\tau)-2u_n(\tau)+u_{n-1}(\tau)}{\Delta\xi^2} + 0(\Delta\xi^2),$$
$$\left[\frac{\partial u(\xi,\tau)}{\partial\xi}\right]_{\xi=n\Delta\xi} = \frac{u_{n+1}(\tau)-u_{n-1}(\tau)}{2\Delta\xi} + 0(\Delta\xi^2),\qquad (G1)$$

$$\left[\frac{\partial^2 v(\xi,\tau)}{\partial\xi^2}\right]_{\xi=n\Delta\xi} = \frac{v_{n+1}(\tau)-2v_n(\tau)+v_{n-1}(\tau)}{\Delta\xi^2} + 0(\Delta\xi^2),$$
$$\left[\frac{\partial v(\xi,\tau)}{\partial\xi}\right]_{\xi=n\Delta\xi} = \frac{v_{n+1}(\tau)-v_{n-1}(\tau)}{2\Delta\xi} + 0(\Delta\xi^2),\qquad (G2)$$

where

$$u_n(\tau) \equiv u\left(n\Delta\xi,\tau\right)$$
$$u_{n-1}(\tau) \equiv u\left((n-1)\Delta\xi,\tau\right) \qquad , \quad (G3)$$
$$u_{n+1}(\tau) \equiv f\left(u_n(\tau), u_{n-1}(\tau), v_n(\tau)\right)$$

$$v_n(\tau) \equiv v\left(n\Delta\xi,\tau\right)$$
$$v_{n-1}(\tau) \equiv v\left((n-1)\Delta\xi,\tau\right) \qquad . \quad (G4)$$
$$v_{n+1}(\tau) \equiv f\left(v_n(\tau), v_{n-1}(\tau), u_n(\tau)\right)$$

163

Bibliography

[1] J. Verny, C. Grigentin, International Journal of Production Economics **122**, 107 (2009).

[2] S. Haver, and D. Karunakaran, *Probabilistic description of crest heights of ocean waves*, (in: Proc. 5th Interna- tional Workshop of Wave Hindcasting and Forecasting, Melbourne, FL 1998).

[3] S. Haver, *A possible freak wave event measured at the Draupner Jacket January 1 1995*, (in: Proc. of Rogue Waves, M. Olagnon and M. Prevosto (eds.), Brest, France 2004).

[4] M. Onorato, A. R. Osborne, M. Serio, and S. Bertone, Phys. Rev. Lett. **86**, 5831 (2001).

[5] C. Kharif, and E. Pelinovsky, Eur. J. Mech. B, Fluids, **22**, 603 (2003).

[6] C. Kharif, E. Pelinovsky, and A. Slunyaev, *Rogue Waves in the Ocean, Observation, Theories and Modeling*, (Springer, New York, 2009).

[7] C. Kharif, E. Pelinovsky, and A. Slunyaev, *Rogue waves in the ocean*, (Springer, Heidelberg, 2009).

[8] A. R. Osborne, M. Onorato, and M. Serio, Phys. Lett. A **275**, 386 (2000).

[9] A. R. Osborne, *Nonlinear Ocean Waves*, (Academic Press, New York, 2009).

[10] P. A. E. M. Janssen, J. Physical Oceanography **33**, 863 (2003).

[11] J. M. Soto-Crespo, Ph. Grelu, and N. Akhmediev Phys. Rev. E **84**, 016604 (2011).

[12] N. Akhmediev, A. Ankiewicz, and M. Taki, Phys. Lett. A **373**, 675 (2009).

[13] N. Akhmediev, J. M. Soto-Crespo, and A. Ankiewicz, Phys. Lett. A **373**, 2137 (2009).

[14] Z. Yan, Phys. Lett. A **374**, 672 (2010).

[15] J. M. Dudley, G. Genty, F. Dias, B. Kibler, and N. Akhmediev, Opt. Express **17**, 21497 (2009).

[16] N. Akhmediev, and E. Pelinovsky, Eur. Phys. J. Special Topics **185**, 1 (2010).

[17] J. M. Dudley, F.Dias, M. Erkintalo, and G. Genty, Nat. Photonics **8**, 755 (2014).

[18] B. Frisquet *et al.*, Sci. Rep. **6**, 20785 (2016).

[19] D. R. Solli, C. Ropers, P.Koonath, and B. Jalali, Nature (London) **450**, 1054 (2007).

[20] D. Buccoliero, H. Steffensen, H. Ebendorff-Heidepriem, T. M. Monro, and O. Bang, Opt. Express **19**, 17973 (2011).

[21] P. Müller, C. Garrett, and A. Osborne, Oceanography **18**, 66 (2005).

[22] Y. V. Bludov, V. V. Konotop, and N. Akhmediev, Opt. Lett. **34**, 3015 (2009).

[23] Y. V. Bludov, V. V. Konotop, and N. Akhmediev, Phys. Rev. A **80**, 033610 (2009).

[24] Y. V. Bludov, V. V. Konotop, and N. Akhmediev, Eur. Phys. J. ST **185**, 169 (2010).

[25] S. Loomba, H. Kaur, R. Gupta, C. N. Kumar, and T. S. Raju, Phys. Rev. E **89**, 052915 (2014).

[26] E. Wamba, K. Porsezian, A. Mohamadou, and T. C. Kofane, Phys. Lett. A **377**, 262 (2013).

[27] M. Shats, H. Punzmann, and H. Xia, Phys. Rev. Lett. **104**, 104503 (2010).

[28] A. N. W. Hone, J. Phys. A: Math. Gen. **30**, 7473 (1997).

[29] H. Bailung, S. K. Sharma, and Y. Nakamura, Phys. Rev. Lett. **107**, 255005 (2011).

[30] Y. V. Bludov, R. Driben, V. V. Konotop, and B. A. Malomed, J. Opt. **15**, 064010 (2013).

[31] L. Stenflo, and M. Marklund, J. Plasma Phys. **76**, 293 (2010).

[32] J. C. Wyngaard, *Turbulence in the Atmosphere*, (Academic Press, New York, 2010).

[33] L. Wen, L. Li, Z. D. Li, S. W. Song, X. F. Zhang, and W. M. Liu, Eur. Phys. J. D **64**, 473 (2011).

[34] Z. Yan, Commun. Theor. Phys. **54**, 947 (2010).

[35] Z. Yan, Phys. Lett. A **375**, 4274 (2011).

[36] C. Lecaplain, Ph. Grelu, J. M. Soto-Crespo, and N. Akhmediev, Phys. Rev. Lett. **108**, 233901 (2012).

[37] S. Birkholz, E. T. J. Nibbering, C. Bree, S. Skupin, A. Demircan, G. Genty, and G. Steinmeyer, Phys. Rev. Lett. **111**, 243903 (2013).

[38] D. Pierangelie, F. Di Mei, C. Conti, A. J. Agranat, and E. DelRe, Phys. Rev. Lett. **115**, 093901 (2015)

[39] D. H. Peregrine, J. Aust. Math. Soc. Ser. B: Appl. Math. **25**, 16 (1983).

[40] B. Kibler, J. Fatome, C. Finot, G. Millot, G. Genty, b. Wetzel, N. Akhmediev, F. Dias, and J M Dudly, Sci. Rep. **2**, 463 (2012).

[41] N. Akhmediev, V. I. Korneev, Theor. Math. Phys. **69**, 1089 (1986).

[42] S. Chen, F. Baronio, J. M. Soto-Crespo, Ph. Grelu, and D. Mihalache, J. Phys. A: Math. Theor. **50** 1 (2017).

[43] T. B. Benjamin and J. E. Fier, J. Fluid Mech. **27**, 417 (1967).

[44] N. A. Kostov, V. Z. Enolskii, V. S. Gerdjikov, V. V. Konotop, and M. Salerno, Phys. Rev. E **70**, 056617 (2004).

[45] A. Slunyaev, Eur. Phys. J. Spec. Top. **185**, 67 (2010).

[46] C. Kharif, and J. Touboul, Eur. Phys. J. Spec. Top. **185**, 159 (2010).

[47] V. E. Zakharov, and A. A. Gelash, Phys. Rev. Lett. **111**, 054101 (2013).

[48] A. Iafrati, A. Babanin, and M. Onorato, Phys. Rev. Lett. **110**, 184504 (2013).

[49] D. Solli, G. Herink, B. Jalali, and C. Ropers, Nat. Photon. **6**, 463 (2012).

[50] B. Kibler, A. Chabchoub, A. Gelash, N. Akhmediev, and, V. E. Zakharov, Phys. Rev. X **5**, 041026 (2015).

[51] J. M. Soto-Crespo, N. Devine, and N. Akhmediev, Phys. Rev. Lett. **116**, 103901 (2016).

[52] G. P. Agrawal,*Nonlinear Fiber Optics*, 2nd ed. (Acdemic Press, New York, 1995).

[53] *Optical Fiber Communications III*, edited by I. P. Kaminow and T. L. Koch (Academic Press, New York, 1997).

[54] L. J. Richardson, W. Forysiak, and N. J. Doran, IEEE Photonics Technol. Lett. **13**, 209 (2001).

[55] F. Baronio, M. Conforti, A. Degasperis, S. Lombardo, M. Onorato, and S. Wabnitz, Phys. Rev. Lett. **113**, 034101 (2014).

[56] A. R. Osborne, *Nonlinear Ocean Waves*, (Academic Press, 2010).

[57] A. Chabchoub, N. P. Hoffmann, and N. Akhmediev, Phys. Rev. Lett. **106**, 204502 (2011).

[58] A. R. Osborne, *Nonlinear ocean waves and the inverse scattering transform*, (Elsevier, 2010).

[59] A. Chabchoub *et al.*, Ann. Phys. **361**, 490 (2015).

[60] P. Chamorro-Posada, G. S. McDonald, and G. H. C. New, J. Mod. Opt. **45**, 1111 (1998).

[61] P. Chamorro-Posada, G. S. McDonald, and G. H. C. New, Opt. Commun. **192**, 1 (2001).

[62] G. Baruch, G. Fibich, and S. Tsynkov, Opt. Express **16**, 13323 (2008).

[63] N. Akhmediev, A. Ankiewicz, and J. M. Soto-Crespo, Phys. Rev. E **80**, 026601 (2009).

[64] W.-P. Zhong, M. R. Belic, and T. Huang, Phys. Rev. E **87**, 065201 (2013).

[65] D. D. Estelle Temgoua, and T. C. Kofane, Phys. Rev. E **91**, 063201 (2015).

[66] Y. Kodama, and A. Hasegawa, IEEE J. Quantum Electron. **23**, 510 (1987).

[67] N. Sasa, and J. Satsuma, J. Phys. Soc. Japan **60**, 409 (1991).

[68] G. P. Agrawal, *Nonlinear Fiber Optics*, (4th ed) (San Diego:Academic, 2007).

[69] R. Hirota, J. Math. Phys. **14**, 805 (1973).

[70] M. Taki, A. Mussot, A. Kudlinski, E. Louvergneaux, M. I. Kolobov, and M. Douay, Phys. Lett. A **374**, 691 (2010).

[71] Z. Yan, and C. Dai, J. Opt. **15**, 064012 (2013).

[72] D. D. Estelle Temgoua, and T. C. Kofane, Phys. Rev. E **93**, 062223 (2016).

[73] V. E. Zakharov, and A. B. Shabat, J. Exp. Theor. Phys. **34**, 62 (1972).

[74] F. Baronio, A. Degasperis, M. Conforti, and S. Wabnitz, Phys. Rev. Lett. **109**, 044102 (2012).

[75] F. Baronio, M. Conforti, A. Degasperis, and S. Lombardo, Phys. Rev. Lett. **111**, 114101 (2013).

[76] S. Chen, J. M. Soto-Crespo, and Ph. Grelu, Phys. Rev. E **90**, 033203 (2014).

[77] A. Hasegawa, and F. Tappert, Appl. Phys. Lett. **23**, 142 (1973).

[78] L. F. Mollenauer, R. H. Stolen, and J. P. Gordon, Phys. Rev. Lett. **45**, 1095 (1980).

[79] L. F.Mollenauer, R. H. Stolen, J. P.Gordon, and W. J. Tomlinson, Opt. Lett. **8**, 289 (1983).

[80] R. H. Stolen, L. F. Mollenauer, and W. J. Tomlison, Opt. Lett. **8**, 186 (1983).

[81] H. Torres-Silva, C. Villarroel, P. H. Sakanaka, and N. Reggiani, Pramana J. Phys. **49**, 431 (1997).

[82] H. Torres-Silva, and M. Zamorano, Math. Comput. Sim. **62**, 149 (2003).

[83] A. Argyros, J. Pla, F. Ladouceur, and L. Poladian, Opt. Express **17**, 15983 (2009)

[84] B. Bai, Y. Svirko, J. Turunen, and T. Vallius, Phys. Rev. A **76**, 023811 (2007).

[85] B. Bai, J. Laukkanen, A. Lehmuskero, and J. Turunen, Phys. Rev. B **81**, 115424 (2010).

[86] L. Poladian, M. Straton, A. Doccherty, and A. Argyros, Opt. Express **19**, 968 (2011).

[87] P. D. Miller, and N. Akhmediev, Phys. Rev. E **53**, 4098 (1996).

[88] S. I. Fewo, H. Moussambi, and T. C. Kofane, Phys. Scr. **84**, 035002 (2011).

[89] E. Yomba, and G.-A. Zakeri, Chaos **26**, 083115 (2016).

[90] L. C. Zhao, and J. Liu, Phys. Rev. E **87**, 013201 (2013).

[91] D. D. Estelle Temgoua, M. B. Tchoula Tchokonte, and T. C. Kofane, Phys. Rev. E **97**, 042205 (2018).

[92] T. Verbiest, M. Kauranen, A. Persoons, M. Ikonen, J. Kurkela, and H. Lemmetyinen, J. Am. Chem. Soc. **116**, 9203 (1994).

[93] J. Li, T. Xu, X.-H. Meng, Y.-X. Zang, H.-Q. Zhanga, and B. Tiang, J. Math. Anal. Appl. **336**, 1443 (2007).

[94] A. T. Avelar, D. Bazeia, and W. B. Cardoso, Phys. Rev. E **79**, 025602 (2009).

[95] A. Degasperis, and S. Lombardo, J. Phys. A **40**, 961 (2007).

[96] A. Degasperis, and S. Lombardo, J. Pyhs. A **42**, 385206 (2009).

[97] A. Degasperis, and S. Lombardo, Phys. Rev. E **88**, 052914 (2013).

[98] F. Baronio, S. Chen, P.Grelu, S.Wabnitz, and M. Conforti, Phys. Rev. A **91**, 033804 (2015).

[99] S. Chen, J. M. Soto-Crespo, F. Baronio, P. Grelu, and D. Mihalache, Opt. Express **24**, 15251 (2016).

[100] M. Onorato, S. Resitori, and F. Baronio, *Rogue and Shock Waves in Nonlinear Dispersive Media*, (ed) (Switzerland: Springer 2016).

[101] E. Pelinovsky, and C. Kharif *Extreme Ocean Waves*, (ed) (Netherlands: Springer 2008).

[102] K. Dysthe, H. E. Krogstad, and P. Müller, Annu. Rev. Fluid Mech. **40**, 287 (2008).

[103] N. Akhmediev *et al.*, J. Opt. **18** 063001 (2016).

[104] A. Zaviyalov, O. Egorov, R. Iliew, and F. Lederer, Phys. Rev. A **85**, 013828 (2012).

[105] M. G. Kovalsky, A. A. Hnilo, and J. R. Tredicce, Opt. Lett. **36**, 4449 (2011).

[106] Lecaplain, Ph. Grelu, J. M. Soto-Crespo, and N. Akhmediev, J. Opt. **15**, 064005 (2013).

[107] S. A. Kolpakov, H. Kbashi, and S. V. Sergeyev, Optica **3**, 870 (2016).

[108] M. Tlidi, K. Panajotov, M. l. Ferre, and M. G. Clerc, Chaos **27**, 114312 (2017).

[109] S. Residori, Bortolozzo, A. Montina, F. Lenzini, and F. T. Arecchi, Fluctuat. Noise Lett. **11**, 1240014 (2012).

[110] A. Montina, U. Bortolozzo, S. Residori, and F. T. Arecchi, Phys. Rev. Lett. **103**, 173901 (2009).

[111] P.-H. Hanzard, M. Talbi, D. Mallek, A. Kellou, H. Leblond, F. Sanchez, T. Godin, and A. Hideur, Sci. Rep. **78**, 45868 (2017).

[112] A. F. J. Runge, C. Aguergaray, N. G. R. Broderick, and M. Erkintalo, Opt. Lett. **39**, 319 (2014).

[113] M. Onorato, S. Residori, U. Bortolozzo, A. Montina, and F. Arecchi, Phys. Rep. **528**, 47 (2013).

[114] W. Chang, J. M. Soto-Crespo, P. Vouzas, and N. Akhmediev, Phys. Rev. E **92**, 022926 (2015).

[115] W. Chang, J. M. Soto-Crespo, P. Vouzas, and N. Akhmediev, Opt. Lett. **40**, 2949 (2015).

[116] A. Ankiewicz, J. M. Soto-Crespo, and N. Akhmediev, Phys. Rev. E **81**, 046602 (2010).

[117] Y. Ohta, and J. Yang, Phys. Rev. E **86**, 036604 (2012).

[118] J. G. Rao, Y. B. Liu, C. Qian, and J. S. He, Z. Fr. Naturforschung A **72**, 026601 (2017).

[119] N. Akhmediev, J. M. Soto-Crespo, N. Devine, and N. P. Hoffmann, Physica D **294**, 37 (2015).

[120] J. He, S. Xu, and K. Porsezian J. Phys. Soc. Jpn. **81**, 4007 (2012).

[121] C. F. O. Graeff, M. Stutzmann, and M. S. Brandt, Phys. Rev. E **88**, 022918 (2013).

[122] S. Chen, and L.-Y. Song, Phys. Rev. E **87**, 83 (2013).

[123] X. Wang, C. Liu, and L.-Y. Wang, J. Math. Anal. Appl. **449**, 1534 (2017).

[124] D. W. Zuo, Y.-T. Gao, Y.-J. Feng, and L. Xue, Nonlinear Dyn. **78**, 2309 (2014).

[125] J. Chen, Y. Chen, B. F. Feng, and K. Maruno, Physics **40**, 737 (2014).

[126] Zh. Yang, W.-P. Zhong, M. Belic, and Y. Zhang, Opt. Express **26**, 7587 (2018).

[127] B. Kibler, J. Fatome, C. Finot, G. Millot, F. Dias, G. Genty, N. Akhmediev, and J. M. Dudley, Nat. Phys. **6**, 790 (2010).

[128] K. Hammani, B. Wetzel, B. Kibler, J. Fatome, C. Finot, G. Millot, N. Akhmediev, and J. M. Dudley, Opt. Lett. **36**, 2140 (2011).

[129] A. Toffoli, D. Proment, H. Salman, J. Monbaliu, F. Frascoli, M. Dafilis, E. Stramignoni, R. Forza, M. Manfrin, and M. Onorato, Phys. Rev. Lett. **118**, 144503 (2017).

[130] A. Kundu, A. Mukherjee, and T. Naskar, Proc R. Soc. A **470**, 2164 (2014).

[131] G. Lawton, New Scientist. **170**, 28 (2001).

[132] I. Lavrenov, Natural Hazards **17**, 117 (1998).

[133] D. M. Graham, *NOAA vessel swamped by rogue wave*, (No. 284) (Oceanspace, 2000).

[134] M. Olagnon, http://www.ifremer.fr/webcom/molagnon/jpo2000/

[135] G. A. Chase, http://bell.mma.edu/ achase/NS-221-Big-Wave.html

[136] S. Haver, Proc. of Rogue waves **2004**, 1 (2004).

[137] K. A. Magnusson, and M. A. Donelan, Journal of Offshore Mechanics and Arctic Engineering **135**, 031108 (2013).

[138] E. M. Bitner-Gregersen, L. Fernandez, J. M. Lefèvre, J. Monbaliu, and A. Toffoli, Natural Hazards and Earth System Science **14**, 1407 (2014).

[139] F. Dias, J. Brennan, S. Ponce de Leon, C. Clancy, and J. Dudley, In ASME 2015 34th International Conference on Ocean, Offshore and Arctic Engineering, OMAE2015-41458 (American Society of Mechanical Engineers, 2015).

[140] M. A. Tayfun, Journal of Physical Oceanography **38**, 2784 (2008).

[141] M. A. Tayfun, Journal of Geophysical Research: Oceans **85**, 1548 (1980).

[142] F. Fedele, Physica D **237**, 2127 (2008).

[143] F. Fedele, and M. A. Tayfun, J. Fluid Mech **620**, 221 (2009).

[144] M. A. Tayfun, and F. Fedele, Ocean Engineering **34**, 1631 (2007).

[145] M. Christou, and K. Ewans, Journal of Physical Oceanography **44**, 2317 (2014).

[146] J. Flanagan, *et al.* In The Proceedings of the 26th (2016) International Offshore and Polar Engineering, Rhodes, Greece, June 26 - July 2, 2016 (International Society of Offshore and Polar Engineers, 2016).

[147] F. Fedele, J. Brennan, Sonia Ponce de Leon, J. Dudley, and F. Dias, Sci. Rep. **6**, 1 (2016).

[148] S. Haver, In Rogue Waves, 129 (2001).

[149] V. Ruban *et al.* Eur. Phys. J. Topics **185**, 5 (2010).

[150] S. Toenger *et al.* Sci. Rep. **5**, 10380 (2015).

[151] P. Walczak, S. Randoux, and P. Suret, Phys. Rev. Lett. **144**, 143903 (2015).

[152] V. E. Zakharov, Stud. Appl. Math. **122**, 219 (2009).

[153] D. Agafontsev, and V. E. Zakharov, Nonlinearity **28**, 2791 (2015).

[154] S. Randoux, P. Suret, and G. El, Sci. Rep. 6, doi:10.1038/srep29238 (2016).

[155] A. Mathis *et al.* Sci. Rep. **5**, 12822 (2015).

[156] S. Coles, *An Introduction to Statistical Modeling of Extreme Values*, (Springer-Verlag, London, 2001).

[157] G. Genty *et al.* Phys. Lett. A **374**, 989 (2010).

[158] K. Hammani, C. Finot, J. M. Dudley, and G. Millot, Opt. Express **16**, 16467 (2008).

[159] N. Akhmediev, J. M. Soto-Crespo, and A. Ankiewicz, Phys. Rev. A **80**, 043818 (2009).

[160] K. L. Henderson, K. L. Peregrine, and J. W. Dold, Wave Motion **29**, 341 (1999).

[161] M. Onorato, A. R. Osborne, and M. Serio, Phys. Rev. Lett. **96**, 014503 (2006).

[162] P. K. Shukla, I. Kourakis, B. Eliasson, M. Marklund, and L. Stenflo, Phys. Rev. Lett. **97**, 094501 (2006).

[163] B. S. White, and B. Fornberg, J. Fluid Mech. **355**, 113 (1998).

[164] K. Dysthe, H. Socquet-Juglard, K. Trulsen, H. E. Krogstad, and J. Liu, "Freak" waves and large-scale simulations of surface gravity waves. Rogue Waves, Proc. 14th "Aha Huliko"a Hawaiian Winter Workshop 91-99 (Univ. Hawaii, Honolulu, 2005).

[165] P. C. Liu, and K. R. MacHutchon, Are there different kinds of rogue waves? Proc. OMAE2006, 25th Int. Conf. Offshore Mechanics and Arctic Engineering, Paper No. 92619, 1-6 (American Society of Mechanical Engineers, New York, 2006).

[166] H. Segur *et al.* J. Fluid Mech. **539**, 229 (2005).

[167] P. Suret *et al.* , Nat. commun. **7**, 13136 (2016).

[168] B. Frisquet, B. kibler, and G. Millot, Phys. Rev. X **3**, 041032 (2013).

[169] Y. Bromberg, U. Lahini, E. Small, and Y. Silberberg, Nat. Photon. **4**, 721 (2010).

[170] M. Erkintalo, G. Genty, and J. M. Dudley, Opt. Lett. **34**, 2468 (2009).

[171] A. Mussot *et al.* Opt. Express **17**, 17010 (2009).

[172] B. H. Kolner, and M. Nazarathy, Opt. lett. **14**, 630 (1989).

[173] C. Bennett, and B. Kolner, Opt. lett. **24**, 783 (1999).

[174] M. A. Foster, *et al.*, Nature **456**, 81 (2008).

[175] G. Keiser, Optical fiber communications, (3rd ed) (McGraw-Hill, Boston, 2000).

[176] P. Diament, *Wave Transmission and Fiber Optics* (Macmillan, New York, 1990).

[177] Y. R. Shen, *Principles of Nonlinear Optics*, (Wiley, New York, 1984).

[178] G. P. Agrawal, *Applications of Nonlinear Fiber Optics*, (second ed.) (Academic Press, Burlington, 2008).

[179] G. Origlio, "Properties and Radiation Response of Optical Fibers: Role of Dopants".

[180] D. L. Griscom, "The Nature of point defects in amorphous silicon dioxyde, " in Defects in SiO2 and Related Dielectrics: Science and Technology, G. Pacchioni, L. Skuja, and D. L. Griscom, eds., p. 117 (2000).

[181] K. Nagayama, M. Kakui, M. M. I. Saitoh, and Y. Chigusa, "Ultra-low-loss (0.1484 dB/km) pure silica core fibre and extension of transmission distance," Electron. Lett. **38**, 1168 (2002).

[182] F. Xu, Z.-X. Wu, and Y.-Q. Lu, Progress in Quantum Electronics **55**, 35 (2017).

[183] K. Okamoto, *Fundamentals of Optical Waveguides*, (second ed.) (Elsevier, Amsterdam , Boston, 2006).

[184] S. Saint-Jalm, *Soliton-based fiber light sources for nonlinear spectroscopy and microscopy*, Ph.D. Thesis, Aix Marseille University (2014).

[185] J. M. Dudley, *Supercontinuum Generation in Optical Fibers. Applications of Nonlinear Fiber Optics*, (second ed.) (Cambridge University Press, 2008).

[186] M. Oberthaler, and R. A. Höpfel, Appl. Phys. Lett. **63**, 1017 (1993).

[187] J. Yang, *Nonlinear waves in integrable and nonintegrable systems*, (SIAM, Philadelphia 2010).

[188] G. P. Agrawal, Nonlinear Fiber Optics, (4th ed.) (Academic Press, Boston 2007).

[189] M. Miyagi and S. Nishida, Appl. Opt. **18**, 678 (1979).

[190] G. P. Agrawal, Applications of Nonlinear Fiber Optics, (AcademicPress, San Diego, 2001).

[191] J. P. Gordon, Opt. Lett. **11**, 662 (1986).

[192] S. A. Akhmanov, R. V. Khokhlov, and A. P. Sukhorukov, *in Laser Handbook*, Vol. 2, F. T. Arecchi and E. O. Schulz-Dubois, (Eds.) (North-Holland, Amsterdam, 1972).

[193] G. P. Agrawal, Lightwave Technology: Teleommunication Systems (Wiley, Hoboken, NJ, 2005).

[194] G. P. Agrawal, P. L. Baldeck, and R. R. Alfano, Opt. Lett. 14, 137 (1989).

[195] P. M. Ramos and C. R. Pavia, IEEE J. Sel. Topics Quantum Electron. 3, 1224 (1997).

[196] N. Akhmediev, and A. Ankiewicz, *Solitons: Non-linear pulses and beams*, (Chapman and Hall, 1997).

[197] G. P. Agrawal, *Nonlinear Fiber Optics*, (5th Ed.), (Academic Press, 2013).

[198] Kuznetsov, Sov. Phys. Dokl. **22**, 507 (1977).

[199] Y. C. Ma, Stud. Appl. Math. **60**, 43 (1979).

[200] K. Tai, A. Tomita, J. L. Jewell, and A. Hasegawa, Appl. Phys. Lett. **49**, 236 (1986).

[201] E. J. Greer, D. M. Patrick, P. G. J. Wigley, and J. R. Taylor, Electron. Lett. **25**, 1246 (1989).

[202] L. D. Barron, *Molecular Light Scattering and Optical Activity*, (Cambridge University Press, 1982).

[203] S. B. Singham, J. Chem. Phys. **87**, 1873 (1987).

[204] T. Verbiest, G. Koeckelberghs, and B. Champagne, Opt. Mater. Express **4**, 264 (2014).

[205] M. lapine, I. Shadrivov, D. Powell, and Y. Kivshar, Scientific Reports **138**, 1 (2011).

[206] T. Verbiest, K. clays, and V. Rodriguez, *Nonlinear optical charaterization techniques: An introduction* (CRC press, 2009).

[207] A. Buyere, E. Benichou, L. Guy, A. Bensalah-Ledoux, S. Guy, and P.-F. Brevet, Opt. Mater. Express **4** 2516 (2014).

[208] M. J. Huttunen, M. Partanen, G. Bautista, S.-W. Chu, and M. Kauranen, Opt. Mater. Express **5** 11 (2015).

[209] V. K. Valev, J. J. Baumberg, C. Sibila, and T. Verbiest, Adv. Mater. **25**, 2517 (2013).

[210] N. Potravkin, E. Cherpetskaya, I. Perezhogin, and V. Makarov, Opt. Mater. Express **4**, 2090 (2014).

[211] A. Chadha, D Zhao, and W. Zhou, Opt. Mater. Exress **4**, 2460 (2014).

[212] K. Lee, J. Wu, and K. Kim, Opt. Mater. Express **4**, 2542 (2014).

[213] P. St. J. Russell, Science **299**, 358 (2003).

[214] J. E. Sharping, M. Fiorentino, P. Kumar, and R. S. Windeler, Opt. Lett. **27**, 1675 (2002).

[215] J. Hansryd, P. Andrekson, M. Westlund, J. Li, and P. Hedekvist, IEEE J. Sel. Top. Quant. **8**, 506 (2002).

[216] T. G. Philbin, C. Kuklewicz, S. Robertson, S. Hill, F. König, and U. Leonhardt, Science **319**, 1367 (2008).

[217] J. K. Ranka, R. S. Windeler, and A. J. Stentz, Opt. Lett. **25**, 25 (2000).

[218] J. M. Dudley, G. Genty, and S. Coen, Reviews of Modern Physics **78**, 1135 (2006).

[219] H. Kano, and H. Hamaguchi, Opt. Express **14**, 2798 (2006).

[220] R. Holzwarth, T. Udem, T. W. Hänsch, J. C. Knight, W. J. Wadsworth, and P. St. J. Russell, Phys. Rev. Lett. **85**, 2264 (2000).

[221] B. Povazay, K. Bizheva, A. Unterhuber, B. Hermann, H. Sattmann, A. F. Fercher, W. Drexler, A. Apolonski, W. J. Wadsworth, J. C. Knight, P. St. J. Russell, M. Vetterlein, and E. Scherzer, Opt. Lett. **27**, 1800 (2002).

[222] T. A. Birks, J. C. Knight, and P. St. J. Russell, Opt. Lett. **22**, 961 (1997).

[223] J. C. Knight, J. Broeng, T. A. Birks, and P. St. J. Russell, Science **282**, 1476 (1998).

[224] T. Birks, P. Roberts, P. St. J. Russell, D. M. Atkin, and T. Shepherd, Electron. Lett. **31**, 1941 (1995).

[225] G. Bouwmans, F. Luan, J. Knight, P. St. J. Russell, L. Farr, B. Mangan, and H. Sabert, Opt. Express **11**, 1613 (2003).

[226] F. Benabid, Philos. T. Roy. Soc. B **364**, 3439 (2006).

[227] P. J. Roberts, F. Couny, H. Sabert, B. J. Mangan, D. P. Williams, L. Farr, M. W. Mason, A. Tomlinson, T. A. Birks, J. C. Knight, and P. St. J. Russell, Opt. Express **13**, 236 (2005).

[228] F. Benabid, J. C. Knight, G. Antonopoulos, and P. St. J. Russell, Science **298**, 399 (2002).

[229] F. Couny, F. Benabid, and P. S. Light, Opt. Lett. **31**, 3574 (2006).

[230] F. Luan, A. K. George, T. D. Hedley, G. J. Pearce, D. M. Bird, J. C. Knight, and P. St. J. Russell, Opt. Lett. **29**, 2369 (2004).

[231] A. Isomäki, and O. G. Okhotnikov, Opt. Express **14**, 9238 (2006).

[232] K. Saitoh, T. Murao, L. Rosa, and M. Koshiba, Opt. Fib. Technol. **16**, 409 (2010).

[233] A. Shirakawa, H. Maruyama, K. Ueda, C. B. Olausson, J. K. Lyngsø, and J. Broeng, Opt. Express **17**, 447 (2009).

[234] A. Bétourné, A. Kudlinski, G. Bouwmans, O. Vanvincq, A. Mussot, and Y. Quiquempois, Opt. Lett. **34**, 3083 (2009).

[235] A. N. Ganshin, V. B. Efimov, G. V. Kolmakov, L. P. Mezhov-Deglin, and P. V. E. McClintock, Phys. Rev. Lett. **101**, 065303 (2008).

[236] R. Höhmann, U. Kuhl, H.-J. Stöckmann, L. Kaplan, and E. J. Heller, Phys. Rev. Lett. **104**, 093901 (2010).

[237] V. B. Efimov, A. N. Ganshin, G. V. Kolmakov, P. V. E. Mcclintock, and L. P. Mezhov-Deglin, European Physical Journal - Special Topics **185**, 181 (2010).

[238] E. J. Heller, L. Kaplan, and A. Dahlen, Journal of Geophysical Research **113**, C09023 (2008).

[239] F. T. Arecchi, U. Bortolozzo, A. Montina, and S. Residori, Phys. Rev. Lett. **106**, 153901 (2011).

[240] M. Faraday, Philosophical Transactions of the Royal Society of London **121**, 319 (1831).

[241] G. Nicolis, and C. Nicolis, *Foundations of Complex Systems: Nonlinear Dynamics, Statistical Physics, Information and Prediction*, (World Scientific, 2007).

[242] W. M. Moslem, R. Sabry, S. K. El-Labany, and P.K. Shukla, Phys. Rev. E **84**, 066402 (2011).

[243] D. Laveder, T. T. Passot, P. Sulem, and G. Sánchez-Arriaga, Phys. Lett. A **375**, 3997 (2011).

[244] D. J. Benney, and A. C. Newell, Studies in Applied Mathematics **46**, 133 (1967).

[245] V. E. Zakharov, Journal of Applied Mechanics and Technical Physics, **2**, 190 (1968).

[246] G. P. Agrawal, Modulation instability induced by cross-phase modulation, Phys. Rev. Lett. **59**, 880 (1987).

[247] C. R. Menyuk, IEEE J. Quantum Electron. **23**, 174 (1987).

[248] V. B. Matveev, and M. A. Salle, J. Neurochem, **42**, 1667 (1991).

[249] S. Xu, J. He, L. wang, and J. Phys. A Math. Theor. **44**, 6629 (2011).

[250] M. J. Ablowitz, and P. A. Clarkson, *Nonlinear Evolution Equations and Inverse Scattering*, (Cambridge University Press, Cambridge 2000).

[251] M. J. Ablowitz , P. A. Clarkson . *Solitons, Nonlinear Evolution Equations and Inverse Scattering*, (Cambridge University Press, Cambridge, UK, 1991).

[252] G. Tanolu, Int. J. Nonlinear Sci. **1**, 1479 (2006).

[253] S. Kakei, N. Sasa, and J. Satsuma, J. Phys. Soc. Jpn. **64**, 1519 (2012).

[254] A.-M. Wazwaz, Applied Mathematics and Computation **200**, 160 (2008).

[255] J. Hietarinta, Physics AUC **15**, 31 (2015).

[256] J.-H. He, International Journal of Nonlinear Sciences and Numerical Simulation **6**, 207 (2005).

[257] J.-H. He, Chaos, Solitons and Fractals **26**, 695 (2005).

[258] M. Wadati, I. Journal of the Physical Society of Japan, **38**, 673 (1975).

[259] H. Lui, J. Li, and Q Zhang, Journal of Computational and Applied Mathematics **228**, 1 (2009).

[260] K. U. Rehman, A. A. Malik, M. Y. Malik, and T. Hayat, Results in Physics **7**, 3537 (2017).

[261] M. Shakeel, and S. T. Mohyud-Din, Journal of the Association of Arab Universities for Basic and Applied Sciences **18**, 66 (2015).

[262] H. Naher, and F. AiniAbdullah, Journal of the Egyptian Mathematical Society **22**, 390 (2014).

[263] A. Ebaid, and E. H. Aly, Wave Motion **49**, 296 (2012).

[264] A. Filiz, M. Ekici, and A. Sonmezoglu, Scientific World Journal **2014**, 534063 (2014).

[265] Md. S. Islam, K. Khan, and M. A. Akbar, Journal of the Egyptian Mathematical Society (2016).

[266] S. Liu, Z. Fu, S. Liu, and Q. Zhao, Physics Letters A **289**, 69 (2001).

[267] G.-T. Liu , and T.-Y. Fan, Physics Letters A **345**, 161 (2005).

[268] J. Weiss, M. Tabor, and G. Carnevale, Journal of Mathematical Physics **24**, 522 (1982).

[269] J.-H. He, and X.-H. Wu, Chaos, Solitons and Fractals **30**, 700 (2006).

[270] A. Ebaid, Physics Letters A. **365**, 213 (2007).

[271] A. Ebaid, Journal of Computational and Applied Mathematics **223**, 278 (2009).

[272] E. Fan, Physics Letters A **277**, 212 (2000).

[273] Z. Yan, and H. Zhang, Physics Letters A **285**, 355 (2001).

[274] L. Gagnon, and P. Winternitz, Phys. Rev. A **39**, 296 (1989).

[275] G. W. Bluman, and S. Kumei, *Symmetries and Differential Equations*, (Springer, New York, 1989).

[276] G. W. Bluman, and Z. Y. Yan, Eur. J. Appl. Math. **16**, 239 (2005).

[277] B. Guo, L. Ling, and Q. P. Liu, Phys. Rev. E **85**, 026607 (2012).

[278] S. Lie, *Vorlesungen über Differentialgleichungen mit Bekannten Inftnitesimalen Transformationen*, (Teubner, Leipzig, 1891).

[279] P. J. Olver, *Applications of Lie Groups to Differential Equations*, (Springer, New York, 1986).

[280] G. W. Bluman, and J. D. Cole, *Similarity Method for Differential Equations*, (Springer, New York, 1974).

[281] L. V. Ovsiannikov, *Group Analysis of Differential Equations* (Academic, New York, 1982).

[282] P. Winternitz, *in Nonlinear Phenomena, Vol. 189 of Lecture Notes in Physics, edited by J. Ehlers, K. Hepp, R. Kippenhahn, H. A. Weidenmüller, and J. Ziffartz*, (Springer, New York, 1983), p. 263.

[283] L. Gagnon, and P. Winternitz, J. Phys. A **21**, 1493 (1988).

[284] G. W. Griffiths, https://www.researchgate.net/publication/270581873 Lax Pairs (2012).

[285] P. Lax, Comm. Pure Applied Math., 21, 467 (1968).

[286] M. J. Ablowitz, *Nonlinear Dispersive Waves: Asymptonic Analysis and Solitons*, (Cambridge University Press, Cambridge 2011).

[287] P. G. Drazin, and R. S. Johnson, *Solitons: an introduction*, (Cambridge University Press, Cambridge 1992).

[288] C. S. Gardener, J. Greene, M. Kruskal, and R. M. Miura, Phys. Rev. Lett. **19**, 1095 (1967).

[289] M. J. Ablowitz, D. J. Kaup, A. C. Newell, and H. Segur, Stud. Appl. Math. **53**, 249 (1974).

[290] F. Calogero, and A. Degasperis, Appl. Math. **113**, 91 (2004).

[291] F. Calogero, and A. Degasperis, J. Phys. A: Math. Gen. **39**, 8349 (2006).

[292] F. Calogero, and A. Degasperis, Physica D **200**, 244 (2005).

[293] A. Degasperis, M. Conforti, F. Baronio, and S. Wabnitz, Phys. Rev. Lett. **97**, 1 (2006).

[294] V. B. Matveev, and M. A. Salle, *Darboux Transformation and Solitons* (Springer-Verlag, Berlin, 1991).

[295] J. L. Ceislinski, J. Phys. A **42**, 404003 (2009).

[296] E. V. Doktorov, and S. B. Leble, *A Dressing Method in Mathematical Physics*, (Springer-Verlag, Berlin, 2007).

[297] M. Adler, and J. Moser, Commun. Math. Phys. **61**, 1 (1978).

[298] G. Neugebauer, and R. Meinel, Phys. Lett. A **100**, 467 (1984).

[299] Y. Li, X. Gu, and M. Zou, Acta Math. Sinica 3, **143** (1987).

[300] C. L. Terng, and K. Uhlenbeck, Commun. Pure Appl. Math. **53**, 1 (2000).

[301] N. N. Akhmediev, V. M. Eleonskii, and N. E. Kulagin, Sov. Phys. JETP **89**, 1542 (1985).

[302] A. Ankiewicz, D. J. Kedziora, and N. Akhmediev, Phys. Lett. A **375**, 2782 (2011).

[303] F. Calogero, and A. Degasperis, *Spectral Transform and Solitons*, (Amsterdam, North-Holland, 1982).

[304] F. Calogero, *Why are certain nonlinear PDEs both widely applicable and integrable? What is Integrability? ed V E Zakharov*, (Berlin, Springer 1991).

[305] A. Degasperis, S. V. Manakov, and P. M. Santini, Physica D **100**, 187 (1997).

[306] V. E. Zakharov, and A. B. Shabat, Sov. Phys. JEPT **37**, 823 (1973).

[307] C. Rogers, and W. K. Schief *Bäcklund and Darboux Transformations*, (Cambridge University Press, Cambridge, 2002).

[308] A. Degasperis, and S. Lombardo, Physica D **214**, 157 (2006).

[309] S. A. Orszag, J. Fluid Mech. **50**, 689 (1971).

[310] B. Fornberg, and G. B. Whitham, Philos. Trans. Roy. Soc. London Ser. A **289**, 373 (1978).

[311] D. Gottlieb, and S. A. Orszag, *Numerical Analysis of Spectral Methods: Theory and Applications*, (SIAM, Philadelphia 1977).

[312] B. Fornberg, *A Practical Guide to Pseudospectral Methods*, (Cambridge University Press, Cambridge, UK 1998).

[313] L. N. Trefethen, *Spectral Method in MATLAB*, (SIAM, Philadelphia 2000).

[314] J. P. Boyd, *Chebyshev and Fourier Spectral Methods*, (2nd edition) (Dover, Mineola, NY 2001).

[315] S. I. Fewo, H. Moussambi, and T. C. Kofane, Phys. Scr. **84**, 035002 (2011).

[316] N. Akhmediev, V. M. Eleonskii, and N. E. Kulagin, Theor. Math. Phys. **72**, 809 (1987).

[317] A. N. W. Hone, J. Phys. A: Math. Gen. **30**, 7473 (1997).

[318] A. Nakamura, and R. Hirota, J. Phys. Soc. Japan **54**, 491 (1985).

[319] M. Noumi, and Y. Yamada, Nagoya Math. J. **153**, 53 (1999).

[320] M. Ballav, and A. R. Chowdhury, Chaos **17**, 013102 (2007).

[321] D. R. Solli, C. Ropers, and B. Jalali, Phys. Rev. Lett. **101**, 233902 (2008).

[322] R. Y. Hao, L. Li, Z. H. Li, and G. S. Zhou, Phys. Rev. E **70**, 066603 (2004).

[323] J. F. Zhang, Q. Yang, and C. Q. Dai, Opt. Commun. **248**, 257 (2005).

[324] J. F. Wang *et al.*, Opt. Commun. **263**, 328 (2006).

[325] J. Li *et al.*, J. Phys. A: Math. Gen. **40**, 13299 (2007).

[326] K. Porsezian *et al.*, Phys. Lett. A **361**, 504 (2007).

[327] C. Q. Dai, G. Q. Zhou, and J. F. Zhang, Phys. Rev. E **85**, 016603 (2012).

[328] H. Wang, and W. She, Opt. Commun **245**, 145 (2005).

[329] F. Biancalana, and C. Creatore, Opt. Express **16**, 14882 (2008).

[330] S. Chen, L. Yi, D.-S. Guo, and P. Lu, Phys. Rev. E **72**,016622 (2005).

[331] V. M. Pérez-García, P. J. Torres, and V. V. Konotop, Physica D **221**, 31 (2006).

[332] S. A. Ponomarenko and G. P. Agrawal, Phys. Rev. Lett. **97**, 013901 (2006).

[333] S. Kumar, and A. Hasegawa, Opt. Lett. **6**, 372 (1997).

[334] Y. Ozeki and T. Inoue, Opt. Lett. **31**, 1606 (2006).

[335] E. N. Tsoy, A. Ankiewicz, and N. Akhmediev Phys. Rev. E **73**, 036621 (2006).

[336] P. F. Byrd, and M. D. Friedman, *Handbook of Elliptic Integrals for Engineers and Scientists*, 2nd ed. (Springer, Berlin, 1971).

[337] P. Gaillard (unpublished).

[338] X.-L. Wang, W.-G. Zhang, B.-G. Zhai, and H.-Q. Zhang, Commun. Theor. Phys. **58**, 531 (2012).

[339] N. N. Akmediev, and E. A. Ostrovskaya, Opt. Commun. **132**, 190 (1996).

[340] M. V. Tratnik, and J. E. Sipe, Phys. Rev. A **38**, 2011 (1988).

[341] N. N. Akhmediev, V. M. Eleonskii, N. E. Kulagin, and L. P. Shil'nikov, Pis'ma Zh. Sov. Tech. Phys. Lett. **15**, 587 (1989).

[342] M. Haelterman, and A. Sheppard, Phys. Rev. E **49**, 3376 (1994).

[343] Y. Chen, and J. Atai, J. Opt. Soc. Am. B **14**, 2365 (1997).

[344] H. Torres-Silva, and M. Zamorano Lucero, Pramana-J. Phys. **62**, 37 (2004).

[345] P. D. Maker, R.W. Terhune, and C. M. Savage, Phys. Rev. Lett. **12**, 507 (1964).

[346] P. K. Choudhury, and T. Yoshino, Optik **113**, 89 (2002).

[347] Kh. S. Singh, P. Khastgir, S. P. Ojha, and P. K. Choudhury, J. Phys. Soc. Jpn. **62**, 1978 (1993).

[348] N. S. Pujari, M. R. Kulkarni, M. C. J. Large, I. M. Bassett, and S. Ponrathnam, J. Appl. Polym. Sci. **98**, 58 (2005).

[349] A. Argyros, M. Straton, A. Docherty, E. H. Min, Z. Ge, K. H. Wong, F. Ladouceur, and L. Poladin, Frontiers Optoelectron. China **3**, 67 (2010).

[350] C. Dai, Y. Wang, and X. Zang, Opt. Express **22**, 29862 (2014).

[351] E. A. Kuznetsov, and Dokl. Akad. Nauk SSSR **236**, 575 (1977).

[352] A. Laktakia, and V. K. Varadan, *Time-harmonic electromagnetic fields in chiral media*, Lecture Notes in Physics, vol. 335 (Springer, Berlin,1985).

[353] Z. Yan, V. V. Konotop, and N. Akhmediev, Phys. Rev. E **82**, 033610 (2010).

[354] S. V. Manokov, and Zh. Eksp. Teor. Fiz. **67**, 543 (1974).

[355] V. Prelog, Science **193**, 17 (1976).

[356] C. Rizza, A. D. DiFalco, M. Scalora, and A. Ciattoni, Phys. Rev. Lett. **115**, 057401 (2015).

[357] L. D. Barron, *Molecular Light Scattering and Optical Activity* (Cambridge University Press, 1982).

[358] F. Egidi, I. Carnimeo, and C. Cappeli, Opt. Mater. Express **5**, 196 (2005).

[359] L. Dai, K.-D. Zhu, W. Shen, X. Huang, L. Zhang, and A. Goriely, Nanoscale **10**, 6343 (2018).

Related works of the thesis

1. **D. D. Estelle Temgoua**, and T. C. Kofane, "*Nonparaxial rogue waves in optical Kerr media*", Phys. Rev. E **91**, 063201 (2015).

2. **D. D. Estelle Temgoua**, and T. C. Kofane, "*Influence of optical activity on rogue waves propagating in chiral optical fibers*", Phys. Rev. E **93**, 062223 (2016).

3. **D. D. Estelle Temgoua**, M. B. Tchoula Tchokonte, and T. C. Kofane, "*Combined effects of nonparaxiality, optical activity, and walk-off on rogue wave propagation in optical fibers filled with chiral materials*", Phys. Rev. E **97**, 042205 (2018).

4. **D. D. Estelle Temgoua**, M. B. Tchoula Tchokonte, M. Maaza and T. C. Kofane, "*Contrast of optical activity and rogue wave propagation in chiral materials*", Nonlinear Dyn **95**, 2691 (2019). https://doi.org/10.1007/s11071-018-4716-x

Nonparaxial rogue waves in optical Kerr media

D. D. Estelle Temgoua[1,*] and T. C. Kofane[1,2,†]

[1]*Laboratory of Mechanics, Department of Physics, Faculty of Science, University of Yaounde I, P.O. Box 812, Yaounde, Cameroon*

[2]*Centre d'Excellence Africain en Technologies de l'Information et de la Communication, University of Yaounde I, P.O. Box 812,*

Yaounde, Cameroon

We consider the inhomogeneous nonparaxial nonlinear Schrödinger (NLS) equation with varying dispersion, nonlinearity, and nonparaxiality coefficients, which governs the nonlinear wave propagation in an inhomogeneous optical fiber system. We present the similarity and Darboux transformations and for the chosen specific set of parameters and free functions, the first- and second-order rational solutions of the nonparaxial NLS equation are generated. In particular, the features of rogue waves throughout polynomial and Jacobian elliptic functions are analyzed, showing the nonparaxial effects. It is shown that the nonparaxiality increases the intensity of rogue waves by increasing the length and reducing the width simultaneously, by the way it increases their speed and penalizes interactions between them. These properties and the characteristic controllability of the nonparaxial rogue waves may give another opportunity to perform experimental realizations and potential applications in optical fibers.

PACS number(s): 05.45.−a, 42.65.−k, 42.25.Bs, 42.70.−a

I. INTRODUCTION

The generation of solitons in optical fibers, predicted by Hasegawa and Tappert [1] through the balance between the pulse broadening due to self-phase modulation and compression due to negative group-velocity dispersion (GVD), has enabled the generation of stable picosecond and subpicosecond pulses in the near infrared. In a weakly nonlinear dispersive medium, the dynamics of the pulse envelope is governed in the paraxial approximation by the cubic nonlinear Schrödinger (NLS) equation [1].

An important property of NLS equation solitons is that they emerge from particular initial profiles as long as a particular threshold condition is met. As a consequence, it is possible to experimentally observe solitons when neither the initial pulse amplitude nor the initial pulse shape corresponds to a pure soliton. Therefore, verification of many of the predicted soliton pulse characteristics was carried out in a series of experiments by Mollenauer and co-workers [2–4].

Temporal, spatial, and spatiotemporal optical solitons can find applications including all-optical routing, transparent beam interconnections, and the massive integration of optical operations in a fully three-dimensional environment. In fact, light is self-guiding in bulk media, which have modes with numerical apertures that violate the paraxial approximation. We recall that the paraxial approximation is valid when the radius of the beam is sufficiently large compared to the wavelength. Nonparaxiality may arise in the miniaturization of devices and in other configurations, such as those involving multiplexed beams [5]. Analytical and numerical studies of nonparaxial bright and dark solitons in optical Kerr media have been reported [6]. In particular, Barruch *et al.* [6] solved numerically the (2+1)-dimensional nonlinear Helmholtz equation for input beams that collapse in the simpler model. They used a Kerr-

slab material of finite length and solved the (1+1)-dimensional nonlinear Helmholtz equation for an incoming soliton profile.

It is found that the solution inside the Kerr-slab propagates virtually unchanged and solitonlike solutions still exist even for such a narrow beam for which the nonparaxiality is still moderate. Chamorra-Posada *et al.* [7] have investigated and shown that the nonlinear Helmholtz equation, which can also be taken as the NLS equation, has an exact nonparaxial soliton solution from which the paraxial soliton is recovered in the appropriate limit. Based on the general particlelike nature of solitons, Fewo *et al.* [8] have described some physical parameters for the pulses such as the amplitude, the chirp, the frequency, and the pulse width. They derived the generalization of the matrix equation using a collective variable approach, leading to a set of second-order differential equations of motion of the nonparaxial spatial optical solitons.

The focusing NLS equation, which describes generic nonlinear phenomena, supports a whole hierarchy of recently discovered Peregrine soliton or rational solutions [9,10], Ma solitons [11], and Akhmediev breathers [12,13]. Although solitary by nature, these rational solutions or rogue waves are different from the usual solitons in that they are rare, short lived, and unstable. They can emerge from a turbulent state of random fields, while ordinary solitons are stable waves with characteristic collision properties, commonly appearing in a deterministic setting of nonlinear evolution partial differential equations. Rogue waves are giant single waves that may suddenly appear in oceans [14]. In recent years, the idea of rogue waves has been extended far beyond oceanic expanses. The concept has been applied to pulses emerging from optical fibers [10,14–22] and waves in Bose-Einstein condensates [23], in superfluids [16], in optical cavities [18], in the atmosphere [24], and even in finance [25].

In particular, rogue wave solutions emerging from optical fibers have been found analytically for many types of generalized NLS models such as NLS models with constant coefficients [10,26–29] and NLS models with varying coefficients [9,30,31]. Recently, this interesting phenomenon of optical rogue waves has been verified experimentally [21,32].

---

*Corresponding author: estelletemgoua@yahoo.fr

†tckofane@yahoo.com

According to the controllability of rogue waves, which has been studied before [33–38], the problem now is what waves, which are localized in both space and time and depict a unique event that appears from nowhere and disappears without a trace [39], can exist in the presence of the GVD and Kerr nonlinearity in the nonparaxial approximation.

The present paper is organized as follows. In Sec. II we use the similarity transformation and the modified Darboux transformation to investigate the analytical nonparaxial rogue wave solutions. In Sec. III we focus our attention on the effect of the nonparaxiality on the propagation of rogue waves to solve the problem of controllability of rogue waves in the nonparaxial approximation by selecting parameters of the original equation. In Sec. IV a summary is given.

II. SIMILARITY TRANSFORMATION AND RATIONAL SOLUTIONS OF THE NONPARAXIAL NONLINEAR SCHRÖDINGER EQUATION WITH VARIABLE COEFFICIENTS

The complex envelope of the optical field $\psi(z,x)$ of a continuous-wave beam liable to a linear diffraction in one transverse dimension in isotropic Kerr media moves according to the nonparaxial NLS equation in the form [8]

$$d\psi_{zz} + i\psi_z + p\psi_{xx} + q|\psi|^2\psi = 0, \qquad (1)$$

where z and x are the longitudinal and transverse coordinates, respectively,

$$x = \tilde{x}/r_0, \quad z = \tilde{z}/2L_{DF}, \quad \psi = \sqrt{2n_2/n_0}r_0k_0\tilde{A}, \qquad (2)$$

where r_0 is the input beam radius with diffraction length $L_{DF} = k_0 r_0^2$, k_0 is the linear wave number, n_0 is the linear index of refraction, n_2 is the Kerr coefficient, $\tilde{A}(x,z)$ is unscaled field assumed to be slowly varying, and $d = \frac{1}{(r_0 k_0)^2}$ is the nonparaxiality parameter. The parameters p and q are related to the GVD and Kerr nonlinearity, respectively. Equation (1) quantifies changes in the transverse profile of a light beam with respect to a forward-propagating reference frame and can be seen as the nonparaxial NLS equation. This equation has been used in the literature [6,7,40,41] for fixed values of the dimensionless parameters p and q.

In the presence of management, the optical pulse propagation in Kerr media can be described by the nonparaxial NLS equation with variable coefficients in the form

$$d(z)\psi_{zz} + i\psi_z + p(z)\psi_{xx} + q(z)|\psi|^2\psi = 0. \qquad (3)$$

Here z is taken as the time parameter. The variable coefficients $d(z)$, $p(z)$, and $q(z)$, which are functions of the propagation distance z, are related to the nonparaxiality, GVD, and Kerr nonlinearity, respectively. Inspired by the previous work of Yan and Dai [42], we use the envelope field in the form

$$\psi(z,x) = \rho(z)V[Z(z),X(z,x)]\exp[i\varphi(z,x)] \qquad (4)$$

to investigate the rational solutions related to nonparaxial rogue waves, where $\rho(z)$ is the amplitude, $Z(z)$ the effective propagation distance, $X(z,x)$ the similitude variable, and $V[Z(z),X(z,x)]$ the complex field. The variable $\varphi(z,x)$ is the phase of the wave. This form of the envelope field is also known as the similarity transformation or the symmetry reduction method. This method, which is also based on the self-similarity

of specific partial differential equations, has been applied in NLS equations to search for the exact and the asymptotic self-similar solutions [43–45]. Equation (3) is not integrable because of varying dispersion, nonlinearity, and nonparaxiality coefficients, which govern the nonlinear wave propagation in an inhomogeneous optical fiber system. In order to construct exact analytical solutions of Eq. (3) we should reduce it to some integrable differential equation: the standard NLS equation. So in what follows we use the symmetry transformation method to obtain integrability conditions. This kind of exact analytical solution has more attractive properties than those of the soliton because of its reduced interaction and smaller peak power than that of the soliton [46] and allows a possible pedestal-free pulse compression [47]. Notice that the similarity and the modified Darboux transformation methods are analytical methods that enable us to construct rational solutions related to rogue waves.

Substituting Eq. (4) into Eq. (3) gives a couple system of partial differential equations with variable coefficients

$$\rho_z V + 2p\rho X_x\varphi_x V_X + \rho Z_z V_Z + \rho X_z V_X + 2\rho d\varphi_z X_z V_X$$
$$+ p\rho\varphi_{xx}V + \rho dV\varphi_{zz} + 2d\rho_z V\varphi_z + 2\rho d\varphi_z Z_z V_Z = 0, \quad (5)$$

$$d\rho_{zz}V + 2d\rho_z Z_z V_Z + 2d\rho_z X_z V_X + \rho dZ_z^2 V_{ZZ}$$
$$+ 2d\rho Z_z X_z V_{ZX} + \rho dZ_{zz}V_Z + \rho dX_z^2 V_{XX} + d\rho X_{zz}V_X$$
$$- d\rho V\varphi_z^2 - \rho V\varphi_z + p\rho X_x^2 V_{XX} + p\rho X_{xx}V_x$$
$$- p\rho V\varphi_x^2 + q|\rho|^2|V|^2\rho V = 0. \qquad (6)$$

According to previous works [9,30], we consider the above symmetry (reduction) transformation or similarity transformation (4) that would reduce Eq. (3) to the standard NLS equation

$$i\psi_z + \tfrac{1}{2}\psi_{xx} + |\psi|^2\psi = 0. \qquad (7)$$

By connecting the solutions of Eq. (3) with those of the above standard NLS equation, the complex field $V[Z(z),X(z,x)]$ should satisfy that equation in the form

$$i\frac{\partial V}{\partial Z} + \frac{1}{2}\frac{\partial^2 V}{\partial X^2} + |V|^2 V = 0. \qquad (8)$$

With $V[Z(z),X(z,x)]$ satisfying the relation (8), we have after the similarity reduction of Eqs. (5) and (6)

$$d(z)X_{zz} + p(z)X_{xx} = 0, \qquad (9)$$

$$q(z)\rho^2 + Z_z = 0, \qquad (10)$$

$$Z_z + d(z)\varphi_z Z_z = 0, \qquad (11)$$

$$\tfrac{1}{2}Z_z + p(z)X_x^2 + d(z)X_z^2 = 0, \qquad (12)$$

$$\varphi_z + d(z)\varphi_z^2 + p(z)\varphi_x^2 = 0, \qquad (13)$$

$$\rho_z + \rho(p(z)\varphi_{xx} + d(z)\varphi_{zz}) + 2d(z)\rho_z\varphi_z = 0, \qquad (14)$$

$$\rho_{zz}V + 2\rho_z Z_z V_Z + 2\rho_z X_z V_X + \rho Z_z^2 V_{ZZ}$$
$$+ 2\rho Z_z X_z V_{ZX} + \rho Z_{zz}V_Z = 0. \qquad (15)$$

We start the resolution of the system (9)–(15) by solving Eq. (9).

In order to look for rational solutions, several conditions are imposed,

$$Z_z = -\tfrac{1}{2}p(z)X_x^2, \quad q(z) = \tfrac{1}{2}p(z)\rho(z)^{-2}X_x^2, \quad X_x = \alpha(z), \qquad (16)$$

which verify Eq. (10). The above parameters can generate the constraints for the variable $Z(z)$ and the nonlinear Kerr coefficient $q(z)$. More specifically, it follows that

$$X_x = \alpha(z), \quad X_{xx} = 0. \quad (17)$$

As $d(z) \neq 0$ and $p(z) \neq 0$, Eq. (9) leads to the condition $X_{zz} = 0$, which implies that $\alpha_{zz} = \delta_{zz} = 0$. So from relations (17) we obtain

$$X(z,x) = \alpha(z)x + \delta(z), \quad (18)$$

where $\alpha(z)$ is the inverse of the wave width and $\delta(z)$ the position of its center of mass $-\delta(z)/\alpha(z)$. Quantities $\alpha(z)$ and $\delta(z)$ are free functions of z.

From condition (16) we obtain the effective dimensionless propagation distance

$$Z(z) = -\frac{1}{2}\int_0^z p(s)\alpha(s)^2 ds. \quad (19)$$

Substituting Eq. (16) into Eq. (12) leads to

$$X_z^2 = -\frac{3p(z)\alpha(z)^2}{4d(z)}. \quad (20)$$

The relation above is true for $d(z) < 0$ or $p(z) < 0$. In this work we choose $p(z) < 0$. For $Z_z \neq 0$, Eq. (11) becomes

$$\varphi_z = -\frac{1}{d(z)}. \quad (21)$$

Substituting Eq. (21) into Eq. (13), we obtain the phase expression

$$\varphi_x = 0, \quad \varphi_{xx} = 0, \quad \varphi(z,x) = -\int_0^z \frac{1}{d(s)}ds + \varphi_0(x), \quad (22)$$

where $\varphi_0(x)$ is a constant.

From Eq. (14) we have

$$\rho(z) = \rho_0 \exp\left(\int_0^z \gamma(s)ds\right), \quad (23)$$

which is the amplitude of the wave, assumed to be a real function, and where $\gamma(s)$ leads to

$$\gamma(s) = d(s)\varphi_{zz}. \quad (24)$$

Here ρ_0 is a constant. Now we can deduce the Kerr coefficient given by

$$q(z) = \frac{1}{2}\frac{p(s)\alpha(s)^2}{\rho_0^2 \exp\left(2\int_0^z \gamma(s)ds\right)}. \quad (25)$$

For the defined values of $d(z)$, $p(z)$, $\alpha(z)$, and $\delta(z)$, we can give the expressions of $X(z,x)$, $Z(z)$, $\rho(z)$, $\varphi(z,x)$, and $q(z)$.

To determine the variable $V[Z(z),X(z,x)]$, we use a dressing method of the modified Darboux transformation [26,48–50]. The first order of the standard NLS equation given by Eq. (1) was found by Peregrine [10] and the second order was proposed by Soto-Crespo *et al.* [51].

According to the modified Darboux transformation, we obtain the first and the second order of rational solutions. If we let $V[Z(z),X(z,x)] = \Psi[Z(z),X(z,x)]$, the first order presented in Refs. [9,10] is given by

$$\Psi_1 = V_1 = \left[1 - \frac{G_1 + iZ(z)H_1}{1 + 2X^2 + 4Z^2}\right]\exp i\{Z(z)\}, \quad (26)$$

where

$$G_1 = 4, \quad H_1 = 8, \quad D_1 = 1 + 2X^2 + 4Z^2. \quad (27)$$

This solution is known as the Peregrine soliton [10] when we consider the correspondence $Z = z$ and $X = x\sqrt{2}$. Then, collecting the partial solutions together, we construct the first-order rational solution related to the exact nonparaxial rogue wave solution of Eq. (3)

$$\psi_1 = \rho_0 \exp\left\{\int_0^z \gamma(s)ds\right\}\left[1 - 4\frac{1 + 2iZ(z)}{1 + 2X(z,x)^2 + 4Z(z)^2}\right]$$
$$\times \exp i\{Z(z) + \varphi(z,x)\}. \quad (28)$$

The intensity of the first-order nonparaxial rogue wave is given by

$$|\psi_1|^2 = \rho_0^2 \exp\left\{2\int_0^z \gamma(s)ds\right\}\left(\frac{(2X^2 + 4Z^2 - 3)^2 + 64Z^2}{(1 + 2X^2 + 4Z^2)^2}\right). \quad (29)$$

This first-order rational solution is used to describe the dynamics of rogue waves in optical fibers. We use it to show the effect of the nonparaxiality on the propagation of rogue waves and present the different cases in which the choice of parameters of the original equation (3) lead to the control of rogue waves. The second-order rogue wave presented in Ref. [9] is given by

$$\Psi_2 = V_2 = \left[1 + \frac{G_2 + iZ(z)H_2}{D_2}\right]\exp i\{Z(z)\}, \quad (30)$$

where G_2, H_2, and D_2 are given by the relations

$$G_2 = \frac{3}{8} - \frac{3}{2}X^2 - \frac{1}{2}X^4 - 9Z^2 - 10Z^4 - 6X^2Z^2,$$
$$H_2 = \frac{15}{4} + 3X^2 - X^4 - 2Z^2 - 4Z^4 - 4X^2Z^2,$$
$$D_2 = \frac{3}{32} + \frac{9}{16}X^2 + \frac{1}{8}X^4 + \frac{1}{12}X^6 + \frac{33}{8}Z^2$$
$$+ \frac{9}{2}Z^4 + \frac{2}{3}Z^6 - \frac{3}{2}X^2Z^2 + \frac{1}{2}X^4Z^2 + X^2Z^4. \quad (31)$$

According to the same correspondence of variables z and x as for first order, this solution is the one found by Soto-Crespo *et al.* [51]. Collecting the partial solutions together, we construct the final second-order rational solution related to the exact nonparaxial rogue wave solution of Eq. (3)

$$\psi_2 = \rho_0 \exp\left\{\int_0^z \gamma(s)ds\right\}\left[1 + \frac{G_2 + iZ(z)H_2}{D_2}\right]$$
$$\times \exp i\{Z(z) + \varphi(z,x)\}. \quad (32)$$

The intensity of the second-order nonparaxial rogue wave solution is

$$|\psi_2|^2 = \rho_0^2 \exp\left\{2\int_0^z \gamma(s)ds\right\}\left(\frac{(D_2 + G_2)^2 + Z^2H_2^2}{D_2^2}\right). \quad (33)$$

This second-order rational solution is more precise than the first one. It describes the dynamics of two rogue waves propagating in an optical fiber as well as collisions between them. We will use it to illustrate the effect of the nonparaxiality on rogue wave collisions.

FIG. 1. (Color online) Wave propagation in 2D and 3D representations of the first-order rational solution for the intensity $|\psi_1(x,z)|^2$ with $d(z) = \frac{z}{4}$, $p(z) = -\frac{z^2}{4}$, $\alpha(z) = 1$, and $\delta(z) = z$.

III. EFFECT OF THE NONPARAXIALITY ON THE PROPAGATION OF ROGUE WAVES IN OPTICAL FIBER

To illustrate the effect of the nonparaxiality on the propagation of rogue waves related to the first- and second-order rational solutions, we fix values of parameters $\rho_0 = 1$. We present managed cases, in which the choice of parameter functions leads to the control of rogue waves.

Our goal now is to choose appropriately free functions $d(z)$, $P(z)$, $\alpha(z)$, and $\delta(z)$ so that we can generate abundant structures of nonparaxial rogue waves. We choose them as polynomial functions. We noted that parameters are chosen in order to be bounded in the intervals $-5 < z < 5$ and $-5 < x < 5$.

For the chosen coefficients and free functions

$$d(z) = \frac{z}{4}, \quad p(z) = -\frac{z^2}{4}, \quad \alpha(z) = 1, \quad \delta(z) = z. \quad (34)$$

The wave propagations is presented in Fig. 1 in three-dimensional (3D) [Fig. 1(a)] and 2D [Figs. 1(b) and 1(c)] representations showing the nonparaxial effects. For the given parameters

$$d(z) = \frac{1}{4}, \quad p(z) = -\frac{z^2}{4}, \quad \alpha(z) = 1, \quad \delta(z) = z. \quad (35)$$

Figure 2 depicts the dynamics of the first-order rational solution for the intensity $|\psi_1(x,z)|^2$ in 3D [Fig. 2(a)] and 2D [Figs. 2(b) and 2(c)] representations illustrating the nonparaxial effects on the propagation of rogue waves.

In this paper we plot the intensity of the first- and second-order rational solutions with the help of MATLAB. We can see in Figs. 1 and 2 that the behavior of the nonparaxial rogue waves is more surrounded in Fig. 1 than in Fig. 2. We observe that

the space where the usual rogue waves reach their maximum moves from the center to the periphery in Fig. 1. So the usual symmetry of the Peregrine soliton is absent in Fig. 1 with the nonparaxial parameter $d(z)$ taken as the polynomial function and present in Fig. 2 with $d(z)$ taken as a constant. This means that the choice of nonparaxial parameter $d(z)$, given in relation (34), is appropriate to obtain particularities of nonparaxial effects. The intensity profile of Fig. 1 increases more rapidly than the ones of the usual cases in the paraxial approximation. It follows that the nonparaxiality increases the length and reduces the width of the wave peak simultaneously. It is also responsible for the unusual symmetry of the Peregrine soliton (rogue waves) in Fig. 1.

We first show the influence of polynomial functions $d(z)$, $p(z)$, $\alpha(z)$ and $\delta(z)$ on the structure of nonparaxial rogue waves. Second, we choose some of them now as Jacobian elliptic functions. When k is weaker than one, the approximative formulas of Jacobian elliptic functions [52] are given by

$$dn(z,k) \approx 1 - \frac{k^2 \sin(z)^2}{2},$$

$$cn(z,k) \approx \cos(z) - k^2 \sin(z) \left(\frac{z - \sin(z)\cos(z)}{4} \right), \quad (36)$$

$$sn(z,k) \approx \sin(z) - k^2 \cos(z) \left(\frac{z - \sin(z)\cos(z)}{4} \right).$$

Here we choose $k = 0.6$. If we set coefficients and free functions as

$$d(z) = cn(z,k), \quad p(z) = -\tfrac{1}{2}sn(k,z) \quad \alpha(z) = z, \quad \delta(z) = z, \quad (37)$$
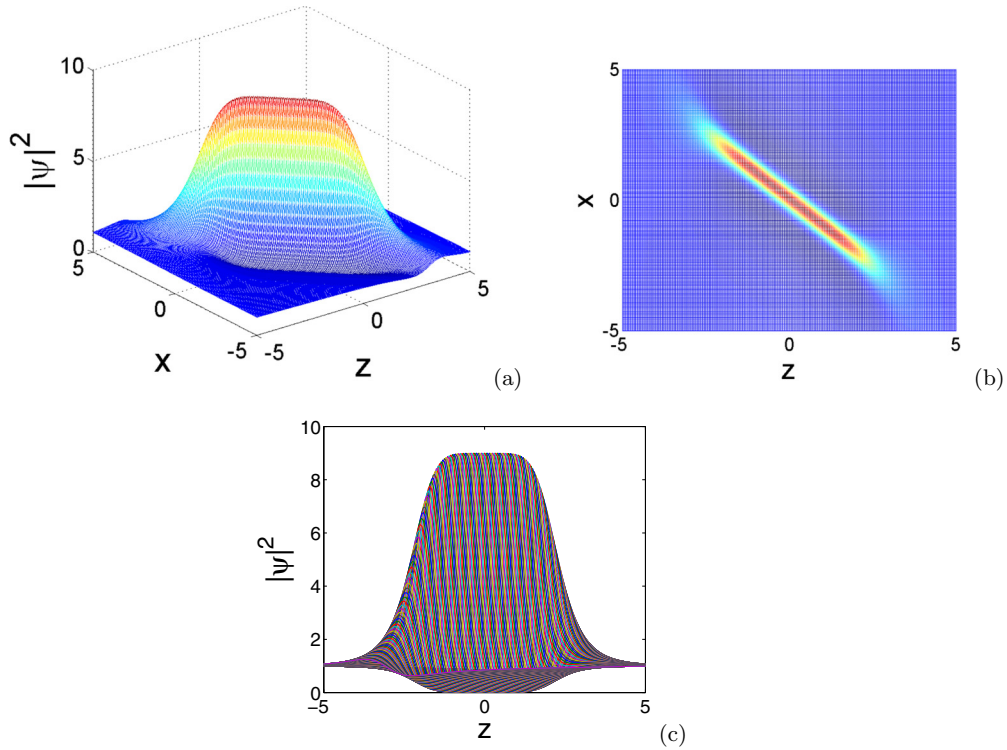
FIG. 2. (Color online) Wave propagation in 2D and 3D representations of the first-order rational solution for the intensity $|\psi_1(x,z)|^2$ with $d(z) = \frac{1}{4}$, $p(z) = -\frac{z^2}{4}$, $\alpha(z) = 1$, and $\delta(z) = z$.

we can obtain the 3D and 2D representation profiles in Figs. 3(a) and 3(c), respectively, showing the nonparaxial effects on rogue waves.

Figures 3(a)–3(c) depict the behavior of nonparaxial rogue waves with $d(z)$ and $p(z)$ taken as Jacobian elliptic functions. The profiles show waves with usual symmetry along the
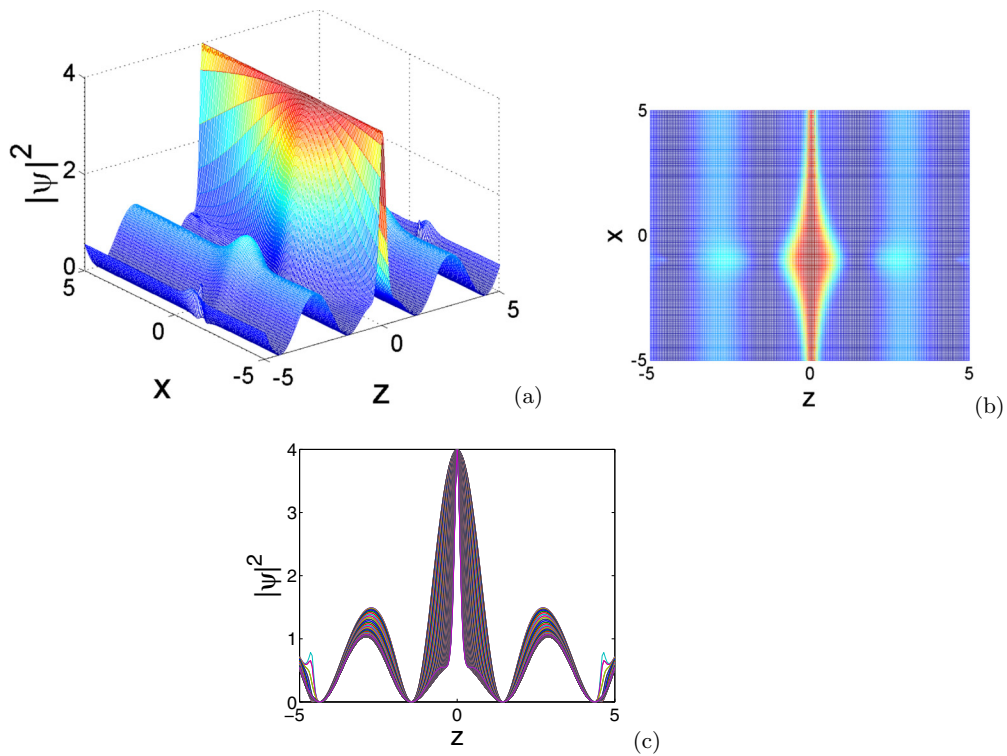
FIG. 3. (Color online) Wave propagation in 2D and 3D representations of the first-order rational solution for the intensity $|\psi_1(x,z)|^2$ with $d(z) = \text{cn}(z,k)$, $p(z) = -\frac{1}{2}\text{sn}(k,z)$, $\alpha(z) = z$, and $\delta(z) = z$.
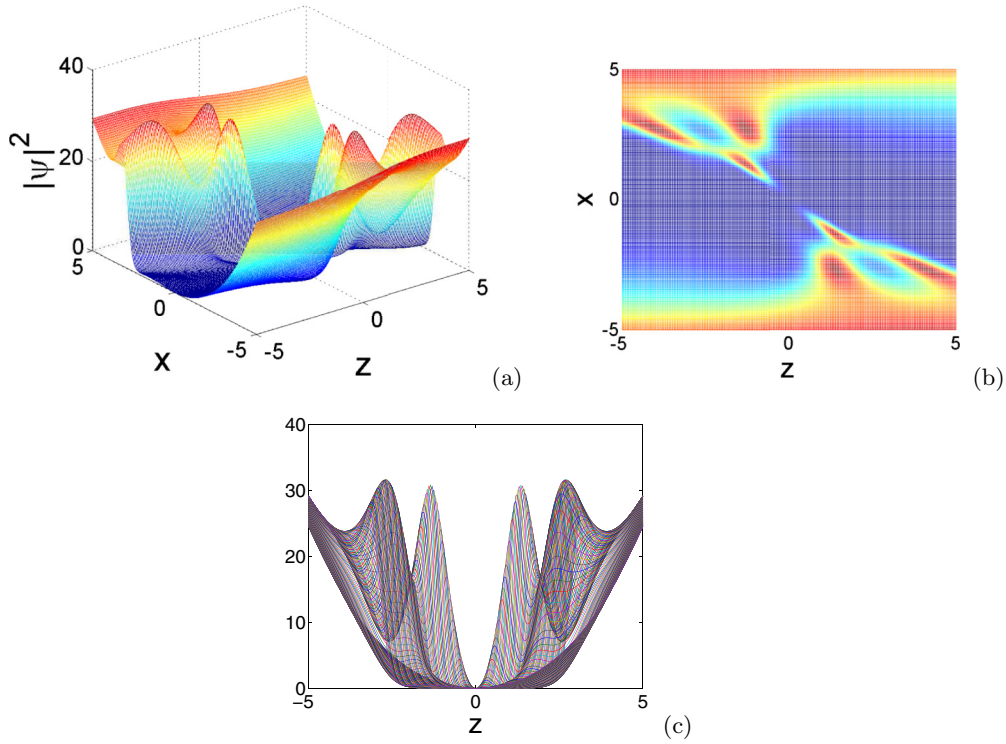
FIG. 4. (Color online) Wave propagation in 2D and 3D representations of the second-order rational solution for the intensity $|\psi_2(x,z)|^2$ with $d(z) = \frac{z}{4}$, $p(z) = -\frac{z^2}{4}$, $\alpha(z) = 1$, and $\delta(z) = z$.
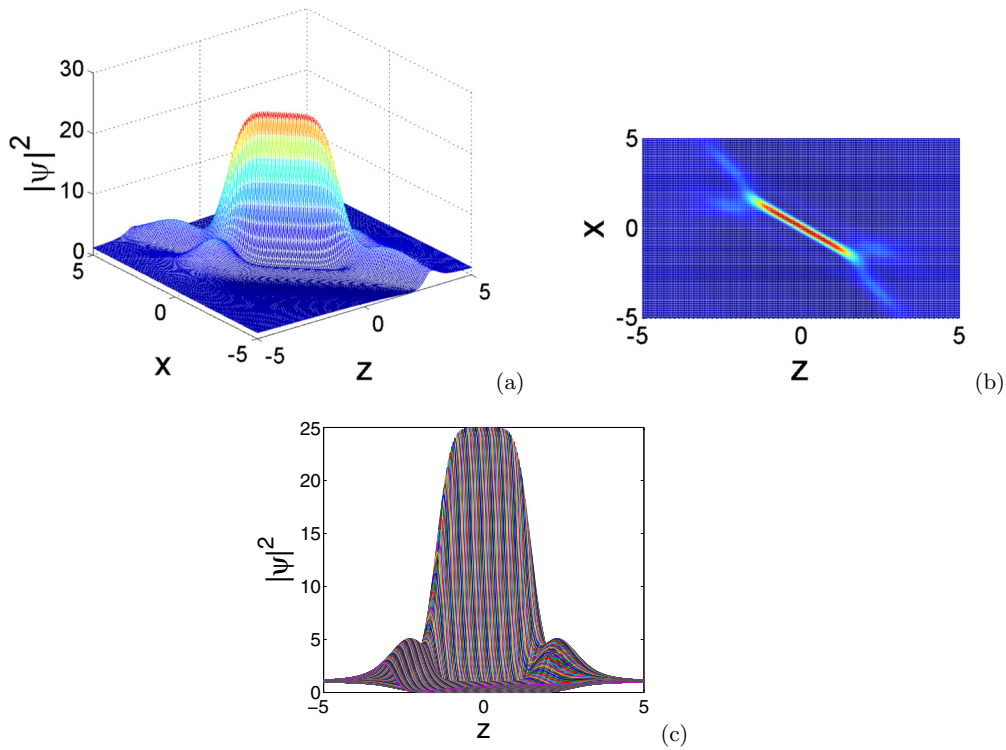
FIG. 5. (Color online) Wave propagation in 2D and 3D representations of the second-order rational solution for the intensity $|\psi_2(x,z)|^2$ with $d(z) = \frac{1}{4}$, $p(z) = -\frac{z^2}{4}$, $\alpha(z) = 1$, and $\delta(z) = z$.
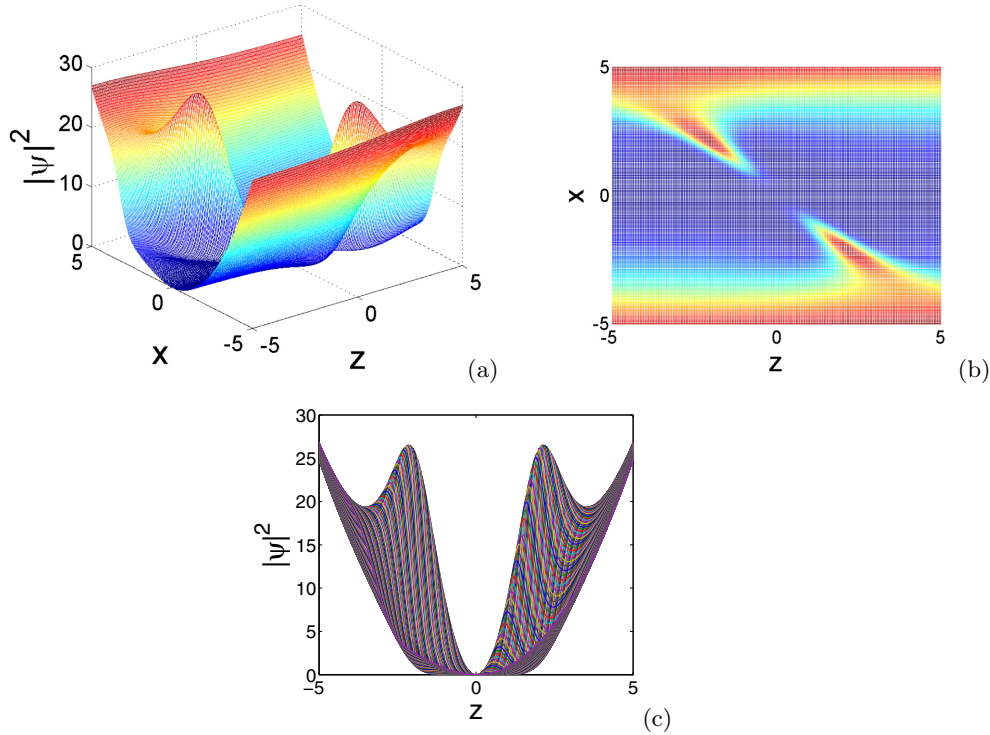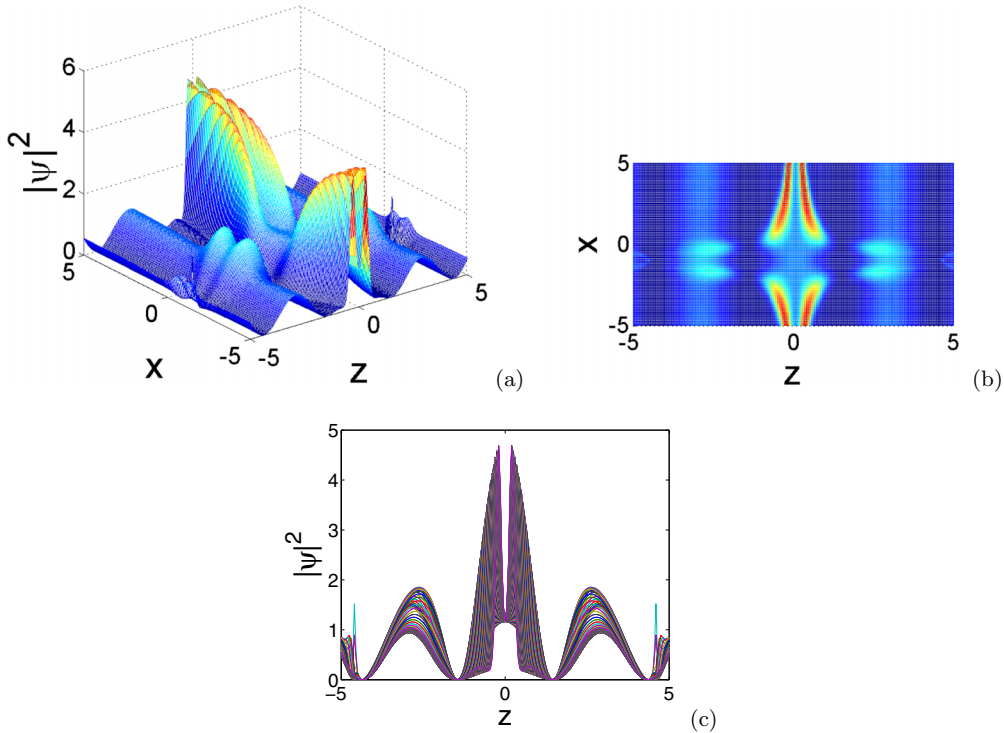
FIG. 6. (Color online) Wave propagation in 2D and 3D representations of the second-order rational solution for the intensity $|\psi_2(x,z)|^2$ with $d(z) = \text{cn}(z,k)$, $p(z) = -\frac{1}{2}\text{sn}(k,z)$, $\alpha(z) = z$, and $\delta(z) = z$.

z direction. The intensity profiles of the nonparaxial rogue waves given in Figs. 3(a) and 3(c) show how they are localized in the z direction (with z taken as the time parameter). These waves appear spontaneously and decrease rapidly as shown in previous works [9,26,53,54].

Having completed the first order, we now study the dynamic behavior of the nonparaxial effect on the propagation of nonparaxial rogue waves related to the second-order rational solutions. Here the parameters that were used to plot the first-order rational solutions are also used to obtain the intensity profiles of second order. So from Eq. (34) the nonparaxial effects on rogue waves are shown in 3D [Fig. 4(a)] and 2D [Figs. 4(b) and 4(c)] representations.

It follows from Eq. (35) that Fig. 5 reveals the nonparaxiality effect [Figs. 5(a) and 5(b)]. The intensity profiles of Figs. 4 and 5 are remarkably similar to Figs. 1 and 2. Nevertheless, we record a difference, particularly notable in the number of collisions and peaks near the periphery of the center.

In the same way, we use the Jacobian elliptic functions to plot the profiles of second order. By using Eq. (37) we obtain Figs. 6(a)–6(c), which show the influence of the nonparaxiality on rogue waves.

In Fig. 6 we observe many collisions between waves. We record again an unusual symmetry of the nonparaxial rogue waves in Fig. 6(a). The wave peak of Fig. 6(c) splits into two and this split is due to the diffraction effect in a lossy medium. We note that in the presence of the nonparaxiality,

the collisions between waves are rare but significant when they appear [see Figs. 6(a) and 6(b)].

IV. CONCLUSION

In this work we have presented the first- and the second-order rational solutions related to the analytical rogue wave solutions. By using one direct method known as the similarity transformation and Darboux transformation, we have constructed the final rational solutions of the nonparaxial NLS equation by collecting partial solutions obtained from the standard NLS equation and the ones from the similarity reduction. This method can also be applied to the higher orders (third, fourth, etc.). Through the 2D and 3D representations we showed the effect of the nonparaxiality on the propagation of rogue waves: It follows that the nonparaxiality increases rapidly the intensity of rogue waves by increasing the length and reducing the width peak simultaneously. We noted that the nonparaxial rogue waves are faster than the ones obtained from the standard NLS equation. We have recorded that the nonparaxiality moves the higher peak of rogue waves from the center to the periphery. We also showed the effect of the polynomial and Jacobian elliptic functions on rogue waves. We concluded that the displacement of the wave peak from the center to the periphery is due to height velocity of the nonparaxial rogue waves. As the nonparaxial effect increases the velocity of waves, it also penalizes the interactions between them. These aspects are additional features and can find application in optics, notably in telecommunications, and in many other physical systems.

[1] A. Hasegawa and F. Tappert, Appl. Phys. Lett. **23**, 142 (1973).

[2] L. F. Mollenauer, R. H. Stolen, and J. P. Gordon, Phys. Rev. Lett. **45**, 1095 (1980).

[3] R. H. Stolen, L. F. Mollenauer, and W. J. Tomlison, Opt. Lett. **8**, 186 (1983).

[4] L. F. Mollenauer, R. H. Stolen, J. P. Gordon, and W. J. Tomlinson, Opt. Lett. **8**, 289 (1983).

[5] P. D. Miller and N. N. Akhmediev, Phys. Rev. E **53**, 4098 (1996).

[6] G. Baruch, G. Fibich, and S. Tsynkov, Opt. Express **16**, 13323 (2008).

[7] P. Chamorro-Posada, G. S. McDonald, and G. H. C. New, J. Mod. Opt. **45**, 1111 (1998).

[8] S. I. Fewo, H. Moussambi, and T. C. Kofane, Phys. Scr. **84**, 035002 (2011).

[9] Z. Yan, Phys. Lett. A **374**, 672 (2010).

[10] D. H. Peregrine, J. Aust. Math. Soc. Ser. B **25**, 16 (1983).

[11] Y. C. Ma, Stud. Appl. Math. **60**, 43 (1979).

[12] N. Akhmediev and V. I. Korneev, Theor. Math. Phys. **69**, 1089 (1986).

[13] N. Akhmediev, V. M. Eleonskii, and N. E. Kulagin, Theor. Math. Phys. **72**, 809 (1987).

[14] J. M. Dudley, G. Genty, F. Dias, B. Kibler, and N. Akhmediev, Opt. Express **17**, 21497 (2009).

[15] A. N. Ganshin, V. B. Efimov, G. V. Kolmakov, L. P. Mezhov-Deglin, and P. V. E. McClintock, Phys. Rev. Lett. **101**, 065303 (2008).

[16] A. N. W. Hone, J. Phys. A: Math. Gen. **30**, 7473 (1997).

[17] A. Montina, U. Bortolozzo, S. Residori, and F. T. Arecchi, Phys. Rev. Lett. **103**, 173901 (2009).

[18] P. Müller, C. Garrett, and A. Osborne, Oceanography **18**, 66 (2005).

[19] A. Nakamura and R. Hirota, J. Phys. Soc. Jpn. **54**, 491 (1985).

[20] M. Noumi and Y. Yamada, Nagoya Math. J. **153**, 53 (1999).

[21] D. R. Solli, C. Ropers, P. Koonath, and B. Jalali, Nature (London) **450**, 1054 (2007).

[22] M. Ballav and A. R. Chowdhury, Chaos **17**, 013102 (2007).

[23] Y. V. Bludov, V. V. Konotop, and N. Akhmediev, Phys. Rev. A **80**, 033610 (2009).

[24] L. Stenflo and M. Marklund, J. Plasma Phys. **76**, 293 (2010).

[25] Z. Yan, Commun. Theor. Phys. **54**, 947 (2010).

[26] N. Akhmediev, A. Ankiewicz, and J. M. Soto-Crespo, Phys. Rev. E **80**, 026601 (2009).

[27] J. Atangana, B. G. O. Essama, F. Biya-Motto, B. Mokhtari, N. C. Eddeqaqi, and T. C. Kofane, J. Mod. Opt. **62**, 392 (2015).

[28] B. G. O. Essama, J. Atangana, F. Biya-Motto, B. Mokhtari, N. C. Eddeqaqi, and T. C. Kofane, J. Mod. Opt. **61**, 1002 (2014).

[29] B. G. O. Essama, J. Atangana, B. M. Frederick, B. Mokhtari, N. C. Eddeqaqi, and T. C. Kofane, Phys. Rev. E **90**, 032911 (2014).

[30] W.-P. Zhong, M. R. Belic, and T. Huang, Phys. Rev. E **87**, 065201 (2013).

[31] B. G. O. Essama, J. Atangana, F. Biya-Motto, B. Mokhtari, N. C. Eddeqaqi, and T. C. Kofane, Opt. Commun. **331**, 334 (2014).

[32] D. R. Solli, C. Ropers, and B. Jalali, Phys. Rev. Lett. **101**, 233902 (2008).

[33] R. Y. Hao, L. Li, Z. H. Li, and G. S. Zhou, Phys. Rev. E **70**, 066603 (2004).

[34] J. F. Zhang, Q. Yang, and C. Q. Dai, Opt. Commun. **248**, 257 (2005).

[35] J. F. Wang *et al.*, Opt. Commun. **263**, 328 (2006).

[36] J. Li *et al.*, J. Phys. A: Math. Gen. **40**, 13299 (2007).

[37] K. Porsezian *et al.*, Phys. Lett. A **361**, 504 (2007).

[38] C. Q. Dai, G. Q. Zhou, and J. F. Zhang, Phys. Rev. E **85**, 016603 (2012).

[39] N. Akhmediev, A. Ankiewicz, and M. Taki, Phys. Lett. A **373**, 675 (2009).

[40] H. Wang and W. She, Opt. Commun. **245**, 145 (2005).

[41] F. Biancalana and C. Creatore, Opt. Express **16**, 14882 (2008).

[42] Z. Yan and C. Dai, J. Opt. **15**, 064012 (2013).

[43] S. Chen, L. Yi, D.-S. Guo, and P. Lu, Phys. Rev. E **72**, 016622 (2005).

[44] V. M. Pérez-García, P. J. Torres, and V. V. Konotop, Physica D **221**, 31 (2006).

[45] S. A. Ponomarenko and G. P. Agrawal, Phys. Rev. Lett. **97**, 013901 (2006).

[46] S. Kumar and A. Hasegawa, Opt. Lett. **22**, 372 (1997).

[47] Y. Ozeki and T. Inoue, Opt. Lett. **31**, 1606 (2006).

[48] E. N. Tsoy, A. Ankiewicz, and N. Akhmediev, Phys. Rev. E **73**, 036621 (2006).

[49] Yu. V. Bludov, V. V. Konotop, and N. Akhmediev, Eur. Phys. J. ST **185**, 169 (2010).

[50] A. T. Avelar, D. Bazeia, and W. B. Cardoso, Phys. Rev. E **79**, 025602 (2009).

[51] J. M. Soto-Crespo, Ph. Grelu, and N. Akhmediev, Phys. Rev. E **84**, 016604 (2011).

[52] P. F. Byrd and M. D. Friedman, *Handbook of Elliptic Integrals for Engineers and Scientists*, 2nd ed. (Springer, Berlin, 1971).

[53] P. Gaillard (unpublished).

[54] X.-L. Wang, W.-G. Zhang, B.-G. Zhai, and H.-Q. Zhang, Commun. Theor. Phys. **58**, 531 (2012).

Influence of optical activity on rogue waves propagating in chiral optical fibers

D. D. Estelle Temgoua[1,2,3,*] and T. C. Kofane[1,2,†]

[1]*Laboratory of Mechanics, Materials and Structures, Post Graduate School in Sciences, Technology and Geosciences, Doctoral Research Unit in Physics and Applications, University of Yaounde I, P.O. Box 812, Yaounde, Cameroon*
[2]*Centre d'Excellence Africain en Technologies de l'Information et de la Communication, University of Yaounde I, P.O. Box 812, Yaounde, Cameroon*
[3]*Organization for Women in Science for the Developing World, ICTP Campus, Strada Costiera 11, 34151 Trieste, Italy*

We derive the nonlinear Schrödinger (NLS) equation in chiral optical fiber with right- and left-hand nonlinear polarization. We use the similarity transformation to reduce the generalized chiral NLS equation to the higher-order integrable Hirota equation. We present the first- and second-order rational solutions of the chiral NLS equation with variable and constant coefficients, based on the modified Darboux transformation method. For some specific set of parameters, the features of chiral optical rogue waves are analyzed from analytical results, showing the influence of optical activity on waves. We also generate the exact solutions of the two-component coupled nonlinear Schrödinger equations, which describe optical activity effects on the propagation of rogue waves, and their properties in linear and nonlinear coupling cases are investigated. The condition of modulation instability of the background reveals the existence of vector rogue waves and the number of stable and unstable branches. Controllability of chiral optical rogue waves is examined by numerical simulations and may bring potential applications in optical fibers and in many other physical systems.

I. INTRODUCTION

Recently, propagation phenomena of solitons [1–5] and vector solitons [6–8] in nonlinear media with natural or induced linear optical activity [9–13] have attracted more attention and have lead to important advances from the fundamental and technological point of view. More recently in optics, the study of propagation [14,15] in birefringent optical fibers allows to introduce the concept of shape-changing solitons that share energy among themselves during propagation. So, when two optical waves copropagate inside a birefringent single-mode fiber, their states of polarization change during propagation as a result of optically induced nonlinear birefringence. This polarization instability manifests itself as large changes in the output state of polarization, when the input power or the polarization state is changed slightly [16]. Those optical activities are the consequence of intrinsic linear birefringence [17] or circular birefringence [18] known as natural chirality or artificial chirality. The natural chirality is caused by the spatial dispersion of optical response either in chiral molecules or in chiral arrangements of molecules and the artificial chirality is induced by structural chirality, i.e., by artificially chiral structural features in subwavelength scale.

This notion of chirality refers to the lack of bilateral symmetry of an object and can be considered as a purely geometric property of a medium. So, chirality is a geometrical concept that describes the inability of an object and its mirror image to be superimposed solely through translations and rotations. This asymmetry of chiral molecules gives rise to optical rotation, which is an example of circular birefringence with the material possessing a different refractive index for right-hand circularly polarized and left-hand circularly polarized light. This fact is expected to play an important role in the potential application of the chiral media in the microwave and optical regimes.

In fact, several nonlinear phenomena in chiral media [9–13,18,19] have been studied over the last decade for many applications and the principle problem in working with a chiral medium is on the control of chirality level. After some investigations, it has been suggested that the use of chiral material in optical fibers may be studied with polymer optical fibers [20,21]. But after some experimental studies, scientists show that, because of organic nature of most chiral materials, some of them are not indicated at the processing temperature of silica and soft glasses; they will simply be damaged. In order to solve this problem, some investigations on the controllability of spontaneous waves in optical fiber have been done [22]. Among various solutions of spontaneous waves, the Peregrine soliton [23], Akhmediev breather [24], and Kuznetsov-Ma soliton [25] are considered as theoretical prototypes to describe the interesting phenomenon of rogue waves.

As pointed out by many scientists, rogue waves are freak waves, giant waves, monster waves, and killer waves, first observed and measured scientifically at the Draupner oil platform in the North Sea [26]. They are nonlinear single oceanic waves of extremely large amplitude, much higher than the average waves and are localized both in space and time [27–29]. They appear from nowhere and disappear without a trace and their reappearance without major shape changes gives rise to a novel appellation of rogue waves, namely rogons. Because of their more complicated way to be studied in oceans, researchers extended this strange phenomenon in optical fibers [23,30–38] for better understanding and the cause of their enormous growth became a subject of scientific research. The investigation on rogue waves dynamics argue that they arise due to modulational instability [39,40] and their occurrence has been later observed in physical systems as optical wave guides [41], capillary waves [42], Bose-Einstein

---

*Corresponding author: estelletemgoua@yahoo.fr
†tckofane@yahoo.com

condensates [43–46], laser-plasma interactions [47], and in econophysics [48].

As it is necessary to transmit pulses of the order of sub-picosecond and femtosecond frequencies, the most adequate models to describe rogue wave phenomenon are higher-order nonlinear Schrödinger (NLS) equations, which take into account group-velocity dispersion (GVD), third-order dispersion (TOD), and nonlinear effects such as self-phase modulation (SPM), cross-phase modulation (XPM), self-steepening (SS), self-frequency shift (SFS), and four-wave mixing (FWM). Thus, many works have been carried out based on higher-order NLS equations with constant coefficients [15,49] and with varying coefficients [50]. Furthermore, rogue wave solutions have been analytically found from coupled nonlinear Schrödinger (CNLS) equations describing two-dimensional waves [43]. Apart from exact solitary waves obtained from CNLS equations in chiral optical fibers, no work has been done in chiral optical fiber for the generation of optical rogue waves. Motivate by the idea to generate the chiral optical rogue waves and to control their evolution without any chiral fiber destruction, we focus our attention on the chiral parameter to underline the properties of chiral optical fiber and indirectly to show the influence of optical activity on rogue waves.

The present paper is organized as follows. In Sec. II we show how to derive two-dimensional NLS equation in chiral optical fibers starting from Born-Fedorov equations. In Sec. III we use the symmetry reduction and the modified Darboux transformation to generate the analytical chiral optical rogue wave solutions in the presence and in the absence of management. In Sec. IV we present the influence of optical activity on the propagation of optical rogue waves, for their possible control in chiral media. In Sec. V we present the exact solutions of the chiral CNLS equations with coupled space-dependence coupling field. In Sec. VI physical properties of vector rogue waves with mixed polarization in chiral optical fiber are given. In Sec. VII we summarize the outcomes.

II. DERIVATION OF THE NONLINEAR SCHRÖDINGER EQUATION IN CHIRAL OPTICAL FIBERS

The phenomenological theory based on the Beltrami-Maxwell formalism extended to nonlinear chiral medium [10] has given rise to new effects of great significance in chiral applications. First observed in optical activity, chirality corresponds to the rotation of the polarization plane in a linear isotropic material. In an anisotropic cubic media, we add to the polarization P and/or to the magnetization M, an additional term T_c proportional to $\vec{\nabla} \times \vec{H}$, which measure per units length, the chirality. The spatial chirality effect in a medium is characterized through the Born-Fedorov formalism, based on the predicted Maxwell's equations. In chiral optical fibers, the Born-Fedorov equations are the most adequate for the study of optical activity. As they satisfy to the edge conditions [51], this allows us to characterize the nonlinear chiral medium by the given equations [9,10,12]

$$
\begin{aligned}
\vec{D} &= \varepsilon_n \vec{E} + \varepsilon_0 T_c \vec{\nabla} \times \vec{E}, \\
\vec{B} &= \mu_0 (\vec{H} + T_c \vec{\nabla} \times \vec{H}),
\end{aligned}
\tag{1}
$$

where the flux densities $\vec{D}$ and $\vec{B}$ arise in response to the electric and magnetic field $\vec{E}$ and $\vec{H}$ propagating in the chiral medium with $\varepsilon_n = \varepsilon_0 + \varepsilon_2 |\vec{E}|$. Here ε_0 and ε_2 are linear and nonlinear permittivity, respectively. μ_0 is the permeability and T_c the chiral parameter of the optical fiber. In our medium, the predicted Maxwell equations are

$$
\vec{\nabla} \cdot \vec{D} = \rho_V, \quad \vec{\nabla} \cdot \vec{B} = 0,
$$

$$
\vec{\nabla} \times \vec{E} = -\frac{\partial \vec{B}}{\partial t}, \quad \vec{\nabla} \times \vec{H} = \vec{J} + \frac{\partial \vec{D}}{\partial t},
\tag{2}
$$

where the current density $\vec{J} = \sigma \vec{E}$ and the charge density ρ represents the sources for the electromagnetic field. The quantity σ is the electrical conductivity and V the volume. Substituting Eq. (1) into Eq. (2), we obtain the following wave equation

$$
\begin{aligned}
\nabla^2 &\vec{E} + \mu_0 \varepsilon_0 T_c{}^2 \frac{\partial^2 \nabla^2 \vec{E}}{\partial t^2} \\
&= \mu_0 \varepsilon_0 \frac{\partial^2 \vec{E}}{\partial t^2} + \mu_0 \sigma \frac{\partial \vec{E}}{\partial t} + \mu_0 \varepsilon_2 |\vec{E}| \frac{\partial^2 \vec{E}}{\partial t^2} \\
&\quad + 2\mu_0 \varepsilon_0 T_c \vec{\nabla} \times \frac{\partial^2 \vec{E}}{\partial t^2} + \mu_0 \varepsilon_2 T_c |\vec{E}|^2 \vec{\nabla} \times \frac{\partial^2 \vec{E}}{\partial t^2} \\
&\quad + \mu_0 \sigma T_c \vec{\nabla} \times \frac{\partial \vec{E}}{\partial t}.
\end{aligned}
\tag{3}
$$

The optical field $\vec{E}$ is represented by a right- (R) or left-hand (L) polarization in the z direction as

$$
\begin{aligned}
\vec{E}(\vec{r}, t) &= (\hat{x} \mp j\hat{y}) \vec{A}(\vec{r}, t) \exp[-j(K_{\pm} z - \omega_0 t)] \\
&= \vec{\psi}_{R,L} \exp[-j(K_{\pm} z - \omega_0 t)],
\end{aligned}
\tag{4}
$$

where $\vec{\psi}_{R,L}$ is the complex envelope of the optical field in the nonlinear chiral medium, K the wave number, and ω_0 the frequency.

After evaluation of different derivations of $\vec{E}$ in x, y, and z directions in Eq. (3), we neglect the second-order terms and suppose that the wave is propagating in the z direction. This imply that

$$
K_x = K_y = 0, \quad E_z = 0.
\tag{5}
$$

Considering the slowly varying envelope of the amplitude, we can do the paraxial approximation bellow

$$
\begin{aligned}
\left| \frac{\partial^2 E_x}{\partial z^2} \right| &\ll \left| 2j K_z \frac{\partial E_x}{\partial z} \right|, \\
\left| \frac{\partial^2 E_y}{\partial z^2} \right| &\ll \left| 2j K_z \frac{\partial E_y}{\partial z} \right|.
\end{aligned}
\tag{6}
$$

The final result of Eq. (3), after approximations, stands for (see the Appendix)

$$
\begin{aligned}
&j \frac{\partial \phi}{\partial z'} + \frac{1}{2} K'' \frac{\partial^2 \phi}{\partial t'^2} - j \frac{1}{6} K''' \frac{\partial^3 \phi}{\partial t'^3} + j \frac{\omega \alpha}{2 K_0} (1 \mp K T_c) \phi \\
&- \frac{\beta \omega^2}{2 K_0} (1 \mp K T_c) |\phi|^2 \phi \mp K^2 T_c \phi + j \frac{\omega \beta}{K_0} |\phi|^2 \frac{\partial \phi}{\partial t'} = 0,
\end{aligned}
\tag{7}
$$

where $K' = \frac{\partial K}{\partial \omega} = \frac{1}{v_g}$ is the inverse of group velocity $K'' = \frac{\partial K'}{\partial \omega}$ is the group-velocity dispersion coefficient, which takes the plus and minus signs ($\pm$), representing the anomalous and normal dispersion regimes, respectively. The parameter $K''' = \frac{\partial K''}{\partial \omega}$ is the TOD term. In the fourth term, the attenuation coefficient α is weighted towards the chiral parameter T_c. The factor to $|\phi|^2\phi$ is the SPM and the term $K^2 T_c \phi$ occurs as an additional correction to the chirality of the fiber. The last term has the physical sense of SS and is necessary to perform the description of spontaneous waves.

The new variables, namely

$$q = \frac{\omega_0^{2/3}\beta^{1/3}}{(2K_0)^{1/3}}\phi, \quad \xi = \frac{\omega_0^{2/3}\beta^{1/3}}{(2K_0)^{1/3}}z',$$

$$\tau = \frac{\omega_0^{1/3}\beta^{1/16}}{\sqrt{K''}(2K_0)^{1/6}}t', \quad \Gamma = \frac{\omega_0^{1/3}\alpha}{(2K_0)^{1/3}\beta^{1/3}}$$

$$\gamma = \frac{\beta^{1/6}K'''}{6K''}\frac{\omega_0^{1/3}}{\sqrt{(2K_0)^{1/3}K''}}, \quad C = 1 \mp T_c K$$

$$D = \frac{K^2 T_c (2K_0)^{1/3}}{\beta^{1/3}\omega_0^{2/3}}, \quad \alpha_3 = \frac{(2K_0)^{5/6}\beta^{1/6}}{\sqrt{K''}\omega_0^{2/3}K_0} \quad (8)$$

allow us to express Eq. (7) in the form

$$j\frac{\partial q}{\partial \xi} + \frac{1}{2}\frac{\partial^2 q}{\partial \tau^2} - j\gamma\frac{\partial^3 q}{\partial \tau^3} + jC\Gamma q \mp Dq - C|q|^2 q$$

$$+ j\alpha_3|q|^2\frac{\partial q}{\partial \tau} = 0. \quad (9)$$

Equation (9) is the NLS equation for a chiral optical fiber. This generalized chiral NLS equation can be used to describe the propagation of right-hand ($+$) and left-hand ($-$) polarized rogue waves in a higher-order dispersive and nonlinear chiral optical fiber. If we let $\alpha_3 = 0$, we obtain another form of NLS equation for a chiral optical fiber without the SS term [10]. For $T_c = 0$, $C = 1$, $D = 0$, $\gamma = 0$, and $\Gamma = 0$, Eq. (9) stands for the standard NLS equation.

If we let $q(\xi,\tau) = \psi(\xi,\tau)$, $\varphi = \frac{1}{2}$, and $\mu = C\Gamma$, the model becomes

$$j\frac{\partial \psi}{\partial \xi} + \varphi\frac{\partial^2 \psi}{\partial \tau^2} - j\gamma\frac{\partial^3 \psi}{\partial \tau^3} + j\mu\psi \mp D\psi - C|\psi|^2\psi$$

$$+ j\alpha_3|\psi|^2\frac{\partial \psi}{\partial \tau} = 0. \quad (10)$$

We should keep in mind that the controllability condition should be verified in Eq. (10). With the aim of taking into account the missing condition of controllability (on higher-order NLS models) Yan et al. [52] showed that the sum of parameters related to the SS, that is, a_2 and to the SFS, that is, a_3 should be zero: $a_2 + a_3 = 0$. In order to achieve this aim, let us write the sum of the SS (α_3) and the SFS (α_4) in the following form

$$j[\alpha_3(|\psi|^2\psi)_\tau + \alpha_4\psi(|\psi|^2)_\tau]$$

$$= j[\alpha_3|\psi|^2\psi_\tau + (\alpha_3 + \alpha_4)\psi(|\psi|^2)_\tau] \quad (11)$$

and let $\alpha_3 + \alpha_4 = 0$; it will remain another term of SS given by $j\alpha_3|\psi|^2\psi_\tau$. Thus, the assumption of controllability is verified by the model given in Eq. (10). Our main aim now is to find

the rational solutions of Eq. (10) with variable and constant coefficients, which may be useful to control the propagation of chiral optical rogue waves.

III. SYMMETRY REDUCTION, FIRST- AND SECOND-ORDER RATIONAL SOLUTIONS OF THE CHIRAL NONLINEAR SCHRÖDINGER EQUATION WITH VARIABLE AND CONSTANT COEFFICIENTS

In the presence of management in Eq. (10), the optical pulse propagation in chiral media can be described by the chiral NLS equation with variable coefficients, in the form

$$j\frac{\partial \psi}{\partial \xi} + \varphi(\xi)\frac{\partial^2 \psi}{\partial \tau^2} - j\gamma(\xi)\frac{\partial^3 \psi}{\partial \tau^3} + j\mu(\xi)\psi$$

$$\mp D(\xi)\psi - C(\xi)|\psi|^2\psi + j\alpha_3(\xi)|\psi|^2\frac{\partial \psi}{\partial \tau} = 0, \quad (12)$$

where τ is taken as time parameter and ξ as spatial parameter. The variable coefficients $\varphi(\xi)$, $\gamma(\xi)$, $\mu(\xi)$, $D(\xi)$, $C(\xi)$, and $\alpha_3(\xi)$ are related to the GVD, TOD, the gain and loss term of the induced optical activity, linear birefringence, SPM, and SS coefficients, respectively.

Since Eq. (12) has varying coefficients, it becomes not integrable and this strongly affects the wave propagation in chiral optical fiber. In order to solve this problem of nonintegrability of the model, we can either use the symmetry reduction method using third-order propagation vector field [53] or the envelope field in gauge form [54] to obtain some integrability conditions. This method has been applied in NLS models to look for exact analytical solutions and is the most adequate method for the construction of rogue wave solutions. From this preliminary method, varying coefficients are obtained but the complex field is deduced from the modified Darboux transformation or from the Lax pair method [55]. In what follows, we use the envelope field in the form [52,56,57]

$$\psi(\xi,\tau) = A(\xi)V[Z(\xi),T(\xi,\tau)]\exp\{i\rho(\xi,\tau)\} \quad (13)$$

to construct the rational solutions related to chiral optical rogue waves, where $A(\xi)$ is the amplitude, $Z(\xi)$ the effective propagation distance, $T(\xi,\tau)$ the similitude variable, and $V[Z(\xi),T(\xi,\tau)]$ the complex field. The variable $\rho(\xi,\tau)$ is the phase of the wave. This form of envelope field is also known as the similarity transformation or the reduction method.

Substituting Eq. (8) into Eq. (13) gives a couple system of partial differential equations with variable coefficients

$$-\gamma AV_T T_{\tau\tau} + 3\gamma AV T_\tau \rho_\tau^2 + AV_T T_\xi$$
$$+ AV_T T_\tau \rho_\tau - \gamma AV_{TTT}T_\tau^3 + 3\gamma AV\rho_{\tau\tau}\rho_\tau$$
$$+ A_\xi V + \mu V + AV_Z Z_\xi + \varphi AV\rho_{\tau\tau}$$
$$+ \alpha_3 A^2|V|^2 AV_T T_\tau - 3\gamma AV_{TT}T_\tau T_{\tau\tau} = 0, \quad (14)$$

$$-AV\rho_\xi + \varphi AV_{TT}T_\tau^2 + \varphi AV_T T_{\tau\tau} - \varphi AV\rho_\tau^2$$
$$+ \gamma AV\rho_{\tau\tau\tau} + 3\gamma AV_T T_{\tau\tau}\rho_\tau + 3\gamma AV_T T_\tau \rho_{\tau\tau}$$
$$- \gamma AV\rho_\tau^3 + 3\gamma AV_{TT}T_\tau^2 \rho_\tau - \alpha_3 A^2|V|^2 AV_T \rho_\tau$$
$$\mp DAV - CA^2|V|^2 AV = 0. \quad (15)$$

In order to simplify the script of differential equations above, we write $A(\xi) = A$, $Z(\xi) = Z$, $T(\xi,\tau) = T$, $\rho(\xi,\tau) = \rho$. According to the previous works [52,57], we use the symmetry transformation given by Eq. (13) that would reduce Eq. (12) to the integrable Hirota equation in the form [58]

$$i\frac{\partial V}{\partial Z} = -\frac{\partial^2 V}{\partial T^2} + G|V|^2 V + 2\sqrt{2}i\nu\left(\frac{\partial^3 V}{\partial T^3} + 3|V|^2\frac{\partial V}{\partial T}\right). \tag{16}$$

In the case of rogue waves finding, we take $G = -1$. The parameter ν is a real constant. With $V[Z(\xi),T(\xi,\tau)]$ satisfying the relation (16), the similarity reduction of Eqs. (14) and (15) leads to

$$\gamma(\xi)T_\tau T_{\tau\tau} = 0, \tag{17}$$

$$\varphi(\xi)T_{\tau\tau} + 3\gamma(\xi)(T_{\tau\tau}\rho_\tau + T_\tau\rho_{\tau\tau}) = 0, \tag{18}$$

$$\mp D(\xi) + \rho_\xi + \varphi(\xi)\rho_\tau^2 + \gamma(\xi)(\rho_\tau^3 - \rho_{\tau\tau\tau}) = 0, \tag{19}$$

$$A_\xi + A[\varphi(\xi)\rho_{\tau\tau} + 3\gamma(\xi)\rho_{\tau\tau}\rho_\tau + \mu(\xi)] = 0, \tag{20}$$

$$T_\xi + T_\tau\rho_\tau - \gamma(\xi)\left(T_{\tau\tau\tau} - 3T_\tau\rho_\tau^2\right) = 0, \tag{21}$$

$$Z_\xi + T_\tau^2[\varphi(\xi) + 3\gamma(\xi)\rho_\tau] = 0, \tag{22}$$

$$\gamma(\xi)T_\tau^3 + 2\sqrt{2}\nu Z_\xi = 0, \tag{23}$$

$$A^2[C(\xi) + \alpha_3(\xi)\rho_\tau] + GZ_\xi = 0, \tag{24}$$

$$\alpha_3(\xi)A^2 T_\tau - 6\sqrt{2}\nu Z_\xi = 0. \tag{25}$$

Here, the subscripts ξ and τ denote spatial and temporal derivatives, respectively. The resolution of the system (17)–(25) yields for $\gamma(\xi) \neq 0$ and $T_\tau T_{\tau\tau} = 0$ to the similarity variable

$$T(\xi,\tau) = T_1(\xi)\tau + T_0(\xi), \tag{26}$$

where $T_{1_\xi}(\xi) = 0$. The substitution of Eq. (26) into Eq. (18) tends to $3\gamma(\xi)T_\tau\rho_{\tau\tau} = 0$. As $\gamma(\xi) \neq 0$, $T_1(\xi) \neq 0$, and $\rho_{\tau\tau} = 0$, the phase can be written as

$$\rho(\xi,\tau) = \rho_1(\xi)\tau + \rho_0(\xi), \tag{27}$$

where $\rho_{1_\xi}(\xi) = 0$.

From Eq. (23), the effective propagation distance $Z(\xi)$ will be

$$Z(\xi) = -\frac{\sqrt{2}}{4\nu}\int_0^\xi \gamma(s)T_1(s)^3 ds. \tag{28}$$

Equation (22) stands for

$$\varphi(\xi) = -\gamma(\xi)\left(3\rho_1(\xi) - \frac{T_1(\xi)}{2\sqrt{2}\nu}\right). \tag{29}$$

Through Eq. (21), we arrive at

$$\gamma(\xi) = -\left(\frac{T_{0_\xi}(\xi) + T_1(\xi)\rho_1(\xi)}{3T_1(\xi)\rho_1^2(\xi)}\right). \tag{30}$$

Relation (20) is transformed to

$$A(\xi) = A_0 \exp\left\{-\int_0^\xi \mu(s)ds\right\}, \tag{31}$$

where, A_0 is a constant. The result coming from Eq. (21), is out to be

$$\mp D(\xi) = -\left\{\gamma(\xi)\rho_1^2(\xi)\left(2\rho_1(\xi) - \frac{T_1(\xi)}{2\sqrt{2}\nu}\right) - \rho_{0_\xi}(\xi)\right\}, \tag{32}$$

with $D_-(\xi) = -D_+(\xi)$. Equation (25) gives the result

$$\alpha_3(\xi) = -3\gamma(\xi)T_1^2(\xi)A^{-2}(\xi). \tag{33}$$

Through relation (24), one finds that

$$C(\xi) = \gamma(\xi)T_1^2(\xi)\left(3\rho_1(\xi) + \frac{GT_1(\xi)}{2\sqrt{2}\nu}\right)A^{-2}(\xi). \tag{34}$$

The TOD parameter $\gamma(\xi)$ is used to control the effective propagation distance $Z(\xi)$, the GVD parameter $\varphi(\xi)$, the coefficient of linear birefringence $D(\xi)$, the SS coefficient $\alpha_3(\xi)$, and the SPM nonlinearity $C(\xi)$. The gain and loss term of the induce optical activity $\mu(\xi)$ can be used to manage the optical activity on the amplitude $A(\xi)$, on the SS coefficient $\alpha_3(\xi)$, and on the SPM nonlinearity $C(\xi)$. To determine the complex field $V[Z(\xi),T(\xi,\tau)]$, we use the modified Darboux transformation method [43,59–61]. The first- and second-order rational solutions of the Hirota equation, namely by Eq. (16), were recently found by Ankiewicz *et al.* [58]. They showed how to construct the hierarchy of rational solutions of the Hirota equation. According to the modified Darboux transformation, the first- and second-order rational solutions are constructed in the following paragraph.

Considering the correspondence $Z(\xi) = x$, $\frac{1}{\sqrt{2}}T(\xi,\tau) = t$, and $\nu = \alpha_3$ in Ref. [58], the first-order of the complex field $V[Z(\xi),T(\xi,\tau)]$ leads to

$$V_1[Z(\xi),T(\xi,\tau)] = \left[1 - \frac{G_1 + iH_1}{D_1}\right]\exp\{iZ(\xi)\}, \tag{35}$$

where

$$G_1 = 4, \quad H_1 = 8Z(\xi),$$
$$D_1 = 1 + [\sqrt{2}T(\xi,\tau) + 12\nu Z(\xi)]^2 + 4Z(\xi)^2. \tag{36}$$

Taking into account the above correspondence, solution (35) is known as the Peregrine soliton [23]. Then, collecting the partial solutions together, we construct the first-order rational solution related to the exact chiral optical rogue wave solution of Eq. (12)

$$\psi_1 = A(\xi)\left[1 - \frac{G_1 + iH_1}{D_1}\right]\exp\{iZ(\xi) + i\rho(\xi,\tau)\}. \tag{37}$$

The intensity of the first-order chiral optical rogue wave is

$$|\psi_1|^2 = A_0^2 \exp\left\{-2\int_0^\xi \mu(s)ds\right\}$$
$$\times\left[\frac{\left([\sqrt{2}T + 12\nu Z]^2 + 4Z^2 - 3\right)^2 + 64Z^2}{(1 + [\sqrt{2}T + 12\nu Z]^2 + 4Z^2)^2}\right]. \tag{38}$$

This first-order rational solution is used to describe the propagation of rogue wave in chiral optical fibers. We use it to show the influence of optical activity on the propagation of rogue waves and with a suitable choice of parameters of the original Eq. (12), we manage the controllability of chiral optical rogue wave.

Then the second-order rational solution of the complex field $V[Z(\xi),T(\xi,\tau)]$ presented by Ankiewicz *et al.* [58] stands for

$$V_2[Z(\xi),T(\xi,\tau)] = \left[1 + \frac{G_2 + i\,Z(\xi)H_2}{D_2}\right] \exp i\{Z(\xi)\},$$
(39)

where G_2, H_2 and D_2 are given by the relations

$$
\begin{aligned}
G_2 =\ & -48T^4 - 1152\sqrt{2}\nu ZT^3 - 144T^2[4Z^2(36\nu^2+1)+1] - 576\sqrt{2}\nu ZT[12Z^2(12\nu^2+1)+7] \\
& - 192Z^4[216(6\nu^4+\nu^2)+5] - 864Z^2(44\nu^2+1) - 36, \\
H_2 =\ & -96T^4 - 2304\sqrt{2}\nu ZT^3 - 96T^2[4Z^2(108\nu^2+1)-3] - 1152\sqrt{2}\nu ZT[4Z^2(36\nu^2+1)] - 384Z^4(36\nu^2+1)^2 \\
& - 192Z^2(180\nu^2+1) + 360, \\
D_2 =\ & 8T^6 + 288\sqrt{2}\nu ZT^5 - 432Z^4(624\nu^4 - 40\nu^2 - 1) + 36Z^2(556\nu^2+11) + 9 + 64Z^6(36\nu^2+1)^3 \\
& + 96\sqrt{2}ZT^3[12Z^2(60\nu^2+1)-1] + 12T^4[4Z^2(180\nu^2+1)+1] + 6T^2[16Z^4[216\nu^2(30\nu^2+1)-1] \\
& - 24Z^2(60\nu^2+1)+9] + 72\sqrt{2}\nu ZT[16Z^4(36\nu^2+1)+8Z^2(1-108\nu^2)+17].
\end{aligned}
$$
(40)

According to the same correspondence of variables as for first-order, we obtain the second-order solution found by Akhmediev *et al.* [62]. Collecting the partial solutions together, we construct the final second-order rational solution related to the exact solution of Eq. (12)

$$\psi_2 = A(\xi)\left[1 + \frac{G_2 + i\,Z(\xi)H_2}{D_2}\right] \exp\{i\,Z(\xi) + i\rho(\xi,\tau)\}.$$
(41)

The intensity of the second-order chiral optical rogue wave solution is

$$
\begin{aligned}
|\psi_2|^2 = A_0{}^2 \exp\left\{-2\int_0^\xi \mu(s)ds\right\} \\
\times \left[\frac{(G_2+D_2)^2 + Z(\xi)^2 H_2{}^2}{D_2{}^2}\right].
\end{aligned}
$$
(42)

This second-order rational solution is more precise than the first one. It describes the optical activity effect on two rogue waves propagating in a chiral optical fiber as well as collisions between them. We use it in the next section to investigate the features of chirality on rogue wave collisions.

Now, we turn our attention to the case of chiral NLS equation with constant coefficients. Then, the new variables of the first- and second-order rational solutions become

$$
\begin{aligned}
T(\xi,\tau) &= T_1(\xi)\tau + T_0(\xi), \\
\rho(\xi,\tau) &= \rho_1(\xi)\tau + \rho_0(\xi), \\
Z(\xi) &= -\frac{\sqrt{2}\gamma}{4\nu}\int_0^\xi T_1(s)^3 ds, \\
A(\xi) &= A_0 \exp\{-\mu\xi\},
\end{aligned}
$$
(43)

where, $T_{1_\xi}(\xi) = 0$, $\rho_{1_\xi}(\xi) = 0$, and $\mu = b_3(1 \pm KT_c)$. By taking into account the new variables above, the first- and second-order rational solutions of the chiral NLS equation with constant coefficients are given by Eq. (37) and Eq. (41), respectively. With these exact solutions, we can appreciate the influence of optical activity on rogue wave in chiral NLS equation with constant coefficients.

After the construction of the above exact solutions, we can choose their parameters to investigate the dynamics behavior and the features of chiral optical rogue waves. So doing, we alternate the sign of values in both space and time, which is required to optimize the eventual stability of the solutions.

IV. OPTICAL ACTIVITY EFFECTS ON THE PROPAGATION OF ROGUE WAVES

To illustrate the effect of optical activity on the propagation of rogue waves related to the first- and second-order rational solutions, we choose, appropriately, free functions $T_1(\xi)$, $T_0(\xi)$, $\mu(\xi)$, and $\gamma(\xi)$ to generate abundant structures of chiral optical rogue waves. We present managed cases, in which the choice of chiral parameter leads to the control of chiral optical rogue waves. We note that parameters are chosen in order to be bounded in the intervals $-15 < \xi < 15$ and $-15 < \tau < 15$. In this work, curves are plotted with the help of MATLAB. Through Jacobian elliptic functions, the intensities of the first- and second-order rational solutions are used to show the influence of optical activity on the structure of chiral optical rogue waves. Their approximative formulas are given in reference by [63]

$$
\begin{aligned}
dn(z,k) &\approx 1 - \frac{k^2 \sin(z)^2}{2}, \\
cn(z,k) &\approx \cos(z) - k^2 \sin(z)\left(\frac{z - \sin(z)\cos(z)}{4}\right), \\
sn(z,k) &\approx \sin(z) - k^2 \cos(z)\left(\frac{z - \sin(z)\cos(z)}{4}\right).
\end{aligned}
$$
(44)

In order to generate more stable chiral optical rogue waves, we use the Jacobian elliptic functions, which are responsible for the snaker form of waves as seen in Figs. 1, 2, and 3, where $|\psi_-|^2$ and $|\psi_+|^2$ are chiral optical rogue waves in the left- and right-hand side, respectively. We observe through these figures that when the chiral parameter T_c is weak, the waves in both hands have the same form [Figs. 1(b), 2(b), and 3(b)] and the same amplitude [Figs. 2(b) and 3(b)]. We notice that the increase of chiral parameter reveals a notable difference on the
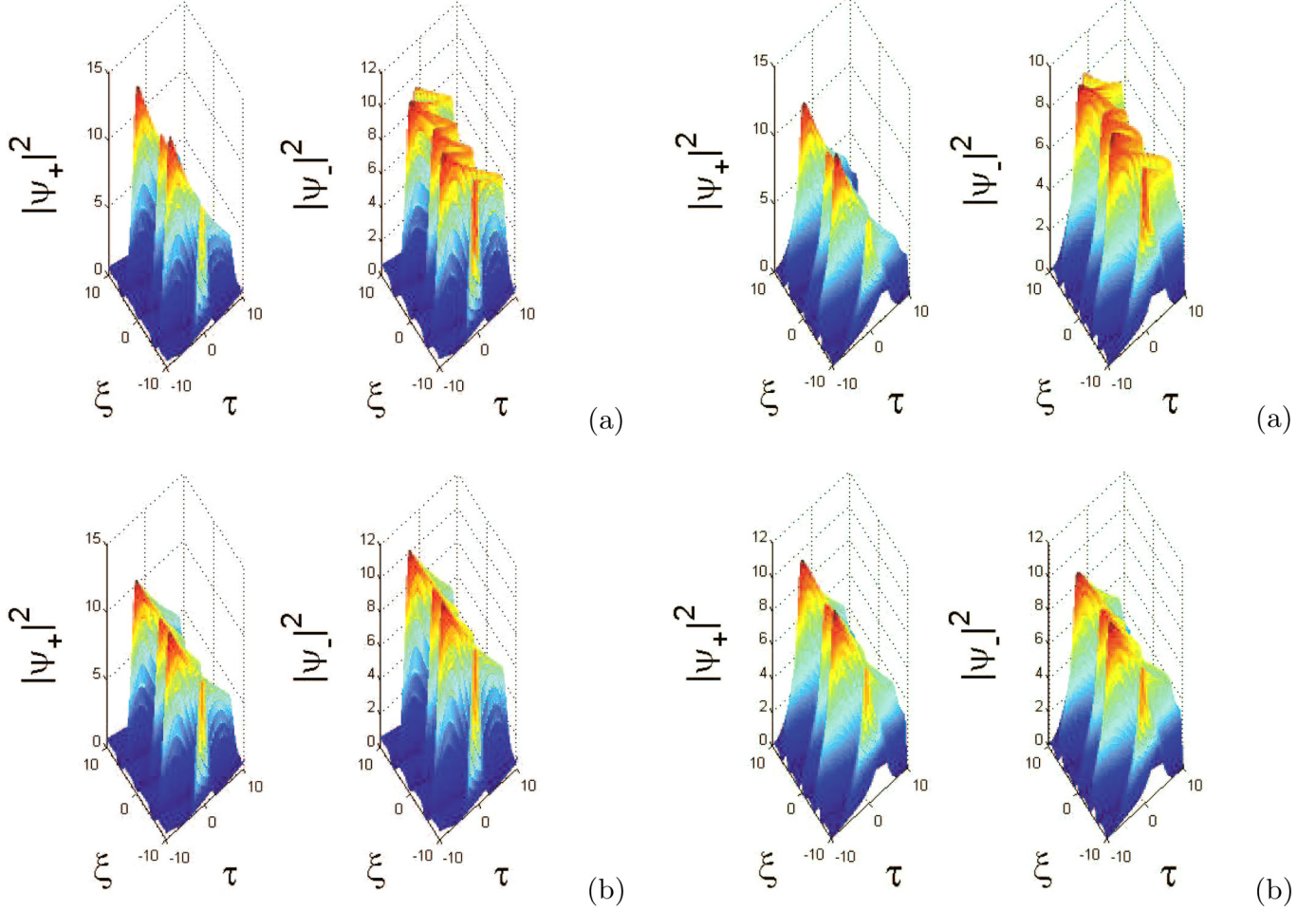
FIG. 1. First-order chiral optical rogue waves on the left- and right-hand side with variable coefficients, where the parameters are (a) $T_c = 0.5$; (b) $T_c = 0.1$; with $b_1 = 0.2$, $K = 1$, $b_3 = 0.1$, $\nu = 0.6$, $k_3 = 0.6$, $k_4 = 0.9$, $T_1(\xi) = \sqrt{2}b_1$, $T_0(\xi) = cn(\xi,k_4)$, $\gamma(\xi) = k_3{}^2 sn(\xi,k_3)cn(\xi,k_3)$ in each case and $\mu(\xi) = b_3(1 - KT_c)sn(\xi,k_4)dn(\xi,k_4)$ for the left-hand intensity $|\psi_-|^2$ and $\mu(\xi) = b_3(1 + KT_c)sn(\xi,k_4)dn(\xi,k_4)$ for the right-hand intensity $|\psi_+|^2$.

form of waves between the left- and right-hand intensities [see Figs. 1(a), 2(a), and 3(a)]. We denote that the second-order solutions [Figs. 2 and 3(b)] with more curvatures than the first-order solutions [Figs. 1 and 3(a)] and this, in addition to the coefficients with management, yields a more accurate study of the influence of the optical activity on rogue waves. We can conclude that the increase of the right-hand intensities and the decrease of the left-hand intensities are slightly due to the order of the solution and highly caused by the increase of the optical activity [see Figs. 2 and 3]. The exchange of energy observed here is also due to the two-wave mixing (TWM) effect. The main difference between parameters of Figs. 1–3 depends on the order of rational solutions through the parameters G_i, H_i, and D_i ($i = 1,2$). The parameters G_1, H_1, and D_1 given in Eq. (36) have been used to construct the first-order rational solution (37) while G_2, H_2, and D_2 given in Eq. (40) have been used to construct the second-order rational solution (41) and where the parameters μ and γ depend on the variable ξ in Figs. 1 and 2. In contrast, in Fig. 3, where we have also

FIG. 2. Second-order chiral optical rogue waves on the left- and right-hand side with variable coefficients, where the parameters are (a) $T_c = 0.5$; (b) $T_c = 0.1$; with $b_1 = 0.2$, $K = 1$, $b_3 = 0.1$, $\nu = 0.6$, $k_3 = 0.6$, $k_4 = 0.9$, $T_1(\xi) = \sqrt{2}b_1$, $T_0(\xi) = cn(\xi,k_4)$, $\gamma(\xi) = k_3{}^2 sn(\xi,k_3)cn(\xi,k_3)$ in each case and $\mu(\xi) = b_3(1 - KT_c)sn(\xi,k_4)dn(\xi,k_4)$ for the left-hand intensity $|\psi_-|^2$ and $\mu(\xi) = b_3(1 + KT_c)sn(\xi,k_4)dn(\xi,k_4)$ for the right-hand side intensity $|\psi_+|^2$.

constructed the first- and second-order rational solutions, the parameters μ and γ are constants. In order to perform this study, we use the chiral CNLS equations in what follows.

V. CHIRAL OPTICAL VECTOR ROGUE WAVES IN COUPLED NLS EQUATIONS WITH COUPLED SPACE-DEPENDENCE COUPLING FIELD

From the model obtain in Eq. (9), the coupled system of NLS equation in chiral optical fibers with coupled space-dependence coupling field is given by

$$i\psi_{1\xi} + \varphi\psi_{1\tau\tau} - i\gamma\psi_{1\tau\tau\tau} + i\mu\psi_1 \mp D\psi_1 - (C_1|\psi_1|^2$$
$$+ C|\psi_2|^2)\psi_1 + i\alpha_3|\psi_1|^2\psi_{1\tau} - \beta(\xi)\psi_2 = 0,$$
$$i\psi_{2\xi} + \varphi\psi_{2\tau\tau} - i\gamma\psi_{2\tau\tau\tau} + i\mu\psi_2 \mp D\psi_2 - (C|\psi_1|^2$$
$$+ C_2|\psi_2|^2)\psi_2 + i\alpha_3|\psi_2|^2\psi_{2\tau} - \beta(\xi)\psi_1 = 0,$$

$$(45)$$
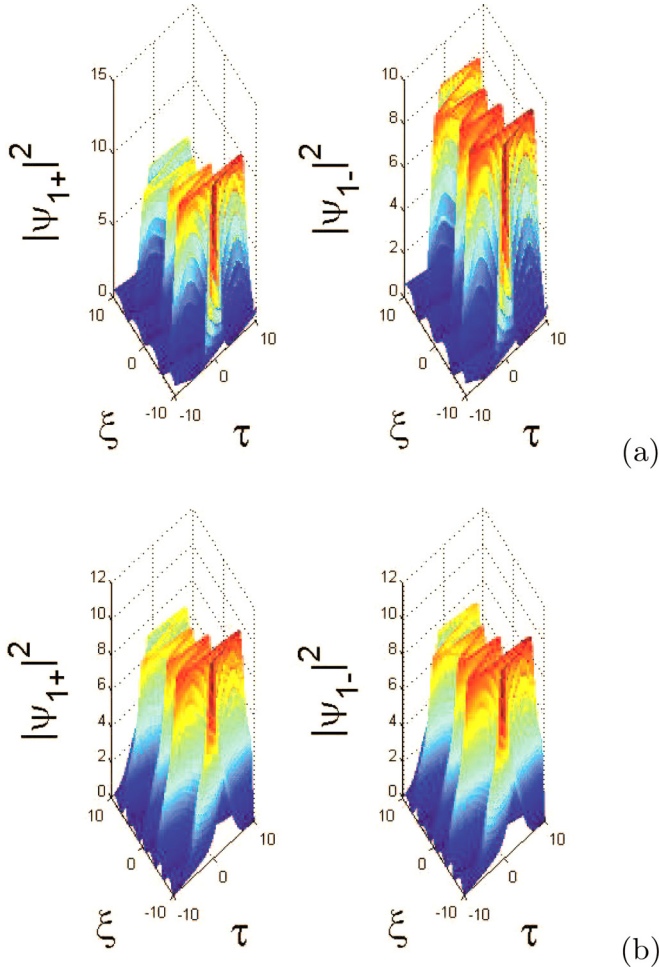
FIG. 3. (a) First- and (b) second-order chiral optical rogue waves on the right- and left-hand side with constant coefficients, where parameters are (a) $T_c = 0.5$; (b) $T_c = 0.1$; with $b_1 = 0.2$, $K = 1$, $b_3 = 0.01$, $\nu = 0.6$, $\gamma = 0.03$, $k_4 = 0.9$, $T_1(\xi) = \sqrt{2}b_1$, $T_0(\xi) = cn(\xi, k_4)$ in each case and $\mu = b_3(1 - KT_c)$ for the left-hand intensity $|\psi_-|^2$ and $\mu = b_3(1 + KT_c)$ for the right-hand intensity $|\psi_+|^2$.

where the last term $\beta(\xi)$ describes the coupling between mixed polarizations. As we consider an isotropic medium with circular polarization and linear birefringence, the presence of FWM becomes implicit through the reference changing [see Appendix (A7)] whereas the SPM terms $(C_1|\psi_1|^2\psi_1; C_2 |\psi_2|^2\psi_2)$ and XPM terms $(C|\psi_1|^2\psi_2; C|\psi_2|^2\psi_1)$ can be identified in the above model. In fact, C_1 and C_2 are SPM nonlinearities (interactions) and C is the XPM nonlinearity (interactions). The FWM in our system will be responsible for the exchanging of energy between components.

Our study is based on the theory of determinant of the nonlinear coefficients in the form [43]

$$\Delta = C_1 C_2 - C^2, \qquad (46)$$

which determines the thermodynamic instability of the system. In order to reduce the number of figures, we choose only one value of the chiral parameter $T_c = 0.5$ and the case where the SPM interactions have the same signs of the scattering length, i.e., when $C_1 C_2 > 0$ or the opposite signs.

A. Chiral optical rogue waves in the case: $\Delta = 0$

1. First case: $\Delta = 0$ and $CC_{1,2} > 0$

In this case, the XPM and SPM interactions are either focusing or defocusing. For mixed polarizations of two different kinds, $\beta(\xi) \equiv 0$. To simplify the evaluation of this coupled system, we deduce the compact form from the Manakov system as follows [64]

$$
\begin{aligned}
&i u_\xi + \varphi u_{\tau\tau} - i\gamma u_{\tau\tau\tau} \\
&+ i\mu u \mp Du - Cu^+ uu + i\alpha_3 u^+ u_\tau = 0.
\end{aligned}
\qquad (47)
$$

where $u = \binom{u_1}{u_2}$ and $C_1 = C_2 = C$.

The SU(2) rotations are defined by two matrices as

$$
\begin{aligned}
R_0 &= \begin{pmatrix} \cos\alpha & \sin\alpha \\ -\sin\alpha & \cos\alpha \end{pmatrix}, \\
R_1 &= \begin{pmatrix} e^{iB(\xi)} & -e^{-iB(\xi)} \\ e^{iB(\xi)} & e^{-iB(\xi)} \end{pmatrix},
\end{aligned}
\qquad (48)
$$

where α is a constant and $B(\xi)$ is the real function written down in the form $B(\xi) = -\int \beta(\xi)d\xi$. We defined $\psi = R_1 R_0 u$ and for the invariant norm, i.e., $u^+ u = \psi^+ \psi$, we obtain the evolution equation

$$
\begin{aligned}
&i\psi_\xi + \varphi\psi_{\tau\tau} - i\gamma\psi_{\tau\tau\tau} + i\mu\psi \mp D\psi - C\psi^+\psi\psi \\
&+ i\alpha_3\psi^+\psi_\tau - \beta(\xi)\sigma_1\psi = 0,
\end{aligned}
\qquad (49)
$$

where $\sigma_j(j = 1,2,3)$ are the standard Pauli matrices. As we construct the rational solution of Eq. (47), we choose it in the form of one component chiral optical rogue wave as

$$u = \Psi(\xi, \tau)\binom{1}{0}, \quad \text{where}$$

$$\Psi(\xi, \tau) = \frac{A_0}{\sqrt{-C}}\left[1 - \frac{4 + i8Z(\xi)}{1 + [\sqrt{2}T(\xi, \tau) + 12\nu Z(\xi)]^2 + 4Z(\xi)^2}\right]$$
$$\times \exp\{-\mu\xi\}\exp\{iZ(\xi) + i\rho(\xi, \tau)\}, \qquad (50)$$

which is valid for $C < 0$, and where the variables are

$$
\begin{aligned}
T(\xi, \tau) &= T_1(\xi)\tau + T_0(\xi), \\
\rho(\xi, \tau) &= \rho_1(\xi)\tau + \rho_0(\xi), \\
Z(\xi) &= -\frac{\sqrt{2}\gamma}{4\nu}\int_0^\xi T_1(s)^3 ds
\end{aligned}
\qquad (51)
$$

with $\mu = b_3(1 \pm KT_c)$, $T_0(\xi) = cn(\xi, k_2)$, $T_1(\xi) = dn(\xi, k_1)$, $\rho_0(\xi) = sn(\xi, k_4)$, and $\rho_1(\xi) = cn(\xi, k_3)$. The above solution helps us to obtain a parametric family of chiral optical rogue wave solutions of Eq. (49) in the form

$$\psi = \frac{1}{\sqrt{-2C}}\Psi(\xi, \tau)\begin{pmatrix} \cos\alpha e^{iB(\xi)} + \sin\alpha e^{-iB(\xi)} \\ \cos\alpha e^{iB(\xi)} - \sin\alpha e^{-iB(\xi)} \end{pmatrix}. \qquad (52)$$

The varying parameters $T_1(\xi)$ and $\rho_1(\xi)$ in this section, excite complex structures which may be useful to control the propagation of chiral optical vector rogue waves.

2. Second case: $\Delta = 0$ and $CC_{1,2} < 0$

Here, the scattering lengths of the XPM and SPM interactions have the same signs and this allows us to let $\beta(\xi) \equiv 0$.

Therefore, Eqs. (45) are reduced to

$$
\begin{aligned}
&iw_{1\xi} + \varphi w_{1\tau\tau} - i\gamma w_{1\tau\tau\tau} + i\mu w_1 \mp D w_1 \\
&\quad - C(|w_1|^2 - |w_2|^2)w_1 + i\alpha_3|w_1|^2 w_{1\tau} = 0, \\
&iw_{2\xi} + \varphi w_{2\tau\tau} - i\gamma w_{2\tau\tau\tau} + i\mu w_2 \mp D w_2 \\
&\quad - C(|w_2|^2 - |w_1|^2)w_2 + i\alpha_3|w_2|^2 w_{2\tau} = 0,
\end{aligned}
\tag{53}
$$

where $w = \binom{w_1}{w_2}$. The compact form of Eqs. (53) is given by

$$
\begin{aligned}
&iw_\xi + \varphi w_{\tau\tau} - i\gamma w_{\tau\tau\tau} + i\mu w \mp D w \\
&\quad - C(w^+\sigma_3 w)\sigma_3 w + i\alpha_3(w^+\sigma_3 w)\sigma_3 w_\tau = 0.
\end{aligned}
\tag{54}
$$

For the defined unitary matrices

$$
\begin{aligned}
P_0 &= \begin{pmatrix} \cosh\alpha & \sinh\alpha \\ -\sinh\alpha & \cosh\alpha \end{pmatrix}, \\
P_1 &= \begin{pmatrix} \sinh\alpha & \cosh\alpha \\ \cosh\alpha & \sinh\alpha \end{pmatrix},
\end{aligned}
\tag{55}
$$

we generate the wave function $\psi = P_j w$ $(j = 0,1)$, which solves the system

$$
\begin{aligned}
&i\psi_{1\xi} + \varphi\psi_{1\tau\tau} - i\gamma\psi_{1\tau\tau\tau} + i\mu\psi_1 \mp D\psi_1 \\
&\quad - (-1)^j C(|\psi_1|^2 - |\psi_2|^2)\psi_1 + i\alpha_3|\psi_1|^2\psi_{1\tau} = 0, \\
&i\psi_{2\xi} + \varphi\psi_{2\tau\tau} - i\gamma\psi_{2\tau\tau\tau} + i\mu\psi_2 \mp D\psi_2 \\
&\quad - (-1)^j C(|\psi_1|^2 - |\psi_2|^2)\psi_2 + i\alpha_3|\psi_2|^2\psi_{2\tau} = 0.
\end{aligned}
\tag{56}
$$

The use of a given value for the constant α in the unitary matrixes can reduce the coupled systems (56) to (53) for $|w_1|^2 = |w_2|^2$. This imply that the system is purely linear and as consequence, this case can not support chiral optical vector rogue waves of the type $\psi_1 \approx \psi_2$.

B. Chiral optical vector rogue waves in the case: $\Delta \neq 0$

We start the study on the case $\Delta \neq 0$ with two polarized electromagnetic waves without linear coupling. We consider $\beta(\xi) \equiv 0$ in the coupled systems (45). As we know the solution of one component chiral optical rogue wave, we can deduce an analog form for two components as follows [43]:

$$
\begin{aligned}
\psi_1(\xi,\tau) &= a_1 \Psi(\xi,\tau), \\
\psi_2(\xi,\tau) &= a_2 \Psi(\xi,\tau)\exp(i\delta),
\end{aligned}
\tag{57}
$$

where $\Psi(\xi,\tau)$ is given in relation (50), δ, the constant phase mismatch, a_1 and a_2 are the amplitudes, which yield

$$
a_1{}^2 = \frac{C - C_2}{\Delta}, \quad a_2{}^2 = \frac{C - C_1}{\Delta}.
\tag{58}
$$

Here, we let

$$
C = \pm 1, \quad C_1 = d_1 \pm KT_c, \quad C_2 = d_2 \pm KT_c,
\tag{59}
$$

where C and $C_{1,2}$ are XPM and SPM nonlinearities and $d_{1,2}$ the arbitrary constants. Relation (58) is the condition for the existence of the synchronized vector rogue waves. The solution (57) obtained in two components describes the propagation of vector rogue waves in chiral optical fibers. We know that a rogue wave is generated by an unstable background and in order to transform our background solution

to become unstable, we let $(\psi_1{}^{(0)}, \psi_2{}^{(0)}) = (a_1, a_2)$. By so doing, we choose the solution of Eqs. (45) in the form of a weakly modulated constant background [40,43]

$$
\begin{aligned}
\psi_j(\xi,\tau) = {}&[a_j + \alpha_j \exp(iK\xi - i\omega\tau) \\
&+ \beta_j \exp(-iK\xi + i\omega\tau)] \\
&\times \exp[-i(C_j a_j{}^2 + C a_{3-j}{}^2)\tau],
\end{aligned}
\tag{60}
$$

where a_j is a constant background, α_j and β_j, the amplitudes of the two components, K is the wave number and ω the frequency. Here, we suppose that $\alpha_j, \beta_j \ll a_j (j = 1,2)$. The substitution of solution (60) into the coupled systems (45) gives after the linearizing with respect to α_j and β_j, the dispersion relation

$$
\begin{aligned}
&\gamma^2\omega^6 - \gamma(\eta_1 + \eta_2)\omega^5 + [\eta_1\eta_2 - \gamma(\beta_1 + \beta_2)]\omega^4 \\
&\quad + [\beta_1\eta_2 + \beta_2\eta_1 - \gamma(\alpha_1 + \alpha_2)]\omega^3 \\
&\quad + (\beta_1\beta_2 + \eta_1\alpha_2 + \eta_2\alpha_1)\omega^2 + (\beta_1\alpha_2 + \beta_2\alpha_1)\omega \\
&\quad + \alpha_1\alpha_2 - 4a_1{}^2 a_2{}^2 C^2 = 0,
\end{aligned}
\tag{61}
$$

where the parameters are

$$
\begin{aligned}
&\phi_{12} = C_1 a_1{}^2 + C a_2{}^2, \quad \phi_{22} = C_2 a_2{}^2 + C a_1{}^2, \\
&\eta_1 = \varphi - 3\gamma\phi_{12}, \quad \eta_2 = \varphi - 3\gamma\phi_{22}, \\
&\beta_1 = \phi_{12} + 3i\gamma\phi_{12}{}^2 - \alpha a_1{}^2, \quad \beta_2 = \phi_{22} + 3i\gamma\phi_{22}{}^2 - \alpha a_2{}^2, \\
&\alpha_1 = K + \gamma\phi_{12}{}^3 - i\mu \mp D - i\varphi\phi_{12}{}^2 + 2C_1 a_1{}^2 \\
&\qquad - 3\alpha\phi_{12}a_1{}^2 + \phi_{12}, \\
&\alpha_2 = K + \gamma\phi_{22}{}^3 - i\mu \mp D - i\varphi\phi_{22}{}^2 + 2C_2 a_2{}^2 \\
&\qquad - 3\alpha\phi_{22}a_2{}^2 + \phi_{22}.
\end{aligned}
\tag{62}
$$

Between the roots of the polynomial given in Eq. (61), we should have at least one imaginary root ω to obtain an unstable background and this can be possible under the conditions $C_{1,2} < 0$ or $\Delta < 0$. Thus, Eq. (61) is the condition of modulational instability of the background. For some specific set of parameters given in Figs. 4–8 captions, we determine the stable and unstable branches of chiral optical rogue waves and indirectly, the existence of vector rogue waves through the dispersion relation given by Eq. (61). We analyze all possible cases for the same and opposite signs of SPM and XPM nonlinearities in the Table I presented in the Appendix.

VI. CHIRAL VECTOR ROGUE WAVES WITH MIXED POLARIZATION IN CHIRAL OPTICAL FIBER

A. Chiral optical rogue waves on mixed polarization without linear coupling

We first consider the case where the XPM and SPM interactions are focusing, i.e., C, $C_{1,2} < 0$. Under this consideration, the initial conditions given in the form of exact solution in relation (57), induce the excitation of chiral optical vector rogue waves in the left- and right-hand side [see Figs. 4(a) and 4(b)]. In order to show how sensitive is the evolution of chiral optical rogue wave, we choose another initial conditions with slightly difference on the amplitude. Therefore, we obtain chiral optical vector rogue waves in each hand, where we remark a weak amplitude in the first

FIG. 4. Chiral optical vector rogue waves of the right- and left-hand intensity $|\psi_{1,2}(\xi,\tau)|^2$ where the parameters are for (a) and (c) $C_1 = -1.6$, $C_2 = -1.8$, $\Delta > 0$, $\mu = b_3(1 - KT_c)$; for (b) and (d) $C_1 = -0.6$, $C_2 = -0.8$, $\Delta < 0$, $\mu = b_3(1 + KT_c)$; with $K = 1$, $T_c = 0.5$, $d_1 = -1.1$, $d_2 = -1.3$, $\alpha_3 = 0.2$, $\gamma = 0.02$, $D = 0.6$, $k_1 = 0.4$, $k_2 = k_4 = 0.6$, $k_3 = 0.5$, $b_3 = 0.01$, and $C = -1$ in each case. At $\xi = -9$, the initial condition takes the form of exact solutions (50) with $\delta = 0$ for (a) and (b) then $\psi_1 = (a_1{}^2 - 0.3)^{1/2}\Psi(\xi,\tau)$, $\psi_2 = (a_1{}^2 + 0.3)^{1/2}\Psi(\xi,\tau)$ for (c) and (d).

FIG. 5. Chiral optical vector rogue waves of the right- and left-hand intensity $|\psi_{1,2}(\xi,\tau)|^2$ where the parameters are for (a) and (c) $C_1 = -2.5$, $C_2 = -3.0$, $\Delta > 0$, $\mu = b_3(1 - KT_c)$; for (b) and (d) $C_1 = -1.5$, $C_2 = -2.0$, $\Delta < 0$, $\mu = b_3(1 + KT_c)$; with $K = 1$, $T_c = 0.5$, $d_1 = -2$, $d_2 = -2.5$, $\alpha_3 = 0.2$, $\gamma = 0.02$, $D = 0.6$, $k_1 = 0.4$, $k_2 = k_4 = 0.6$, $k_3 = 0.5$, and $b_3 = 0.01$ in each case; $C = -1$ for (a) and (b); $C = 1$ for (c) and (d). At $\xi = -9$, the initial condition takes the form of exact solutions (50) with $\delta = 0$.

components and a significant one in the second components [see Figs. 4(c) and 4(d)]. In this regard, vector rogue waves most exist in Figs. 4(a) and 4(b) whereas they do not exist in Figs. 4(c) and 4(d). This weak appearance of chiral optical rogue waves in the first components can be understood if we suppose that $|\psi_1|^2 \ll |\psi_2|^2$. In consequence, the function ψ_1

on each hand can be considered as a linear wave function localizes around the minima of the trap potential $U = -|\psi_2|^2$, created by the second component ψ_2, localized around the maxima of the potential barrier. We can conclude that the second components have a self-focusing character that protect them from destructive action of the optical lattice (trapping

FIG. 6. Nonexistence of chiral optical vector rogue waves of the left-hand and existence of the right-hand intensity $|\psi_{1,2}(\xi,\tau)|^2$ where the parameters are $C_1 = -0.6$, $C_2 = 1.5$, $\Delta < 0$, and $\mu = b_3(1 + KT_c)$ on the right-hand side and $C_1 = -1.6$, $C_2 = 0.5$, $\Delta < 0$ and $\mu = b_3(1 - KT_c)$ on the left-hand side; with $K = 1$, $T_c = 0.5$, $d_1 = -1.1$, $d_2 = 1$, $\alpha_3 = 0.2$, $\gamma = 0.02$, $D = 0.6$, $k_1 = 0.4$, $k_2 = 0.6$, $k_4 = 0.6$, $k_3 = 0.5$, $C = -1$, and $b_3 = 0.01$ in each case. At $\xi = -9$, the initial condition takes the form of exact solutions (50) with $\delta = 0$.
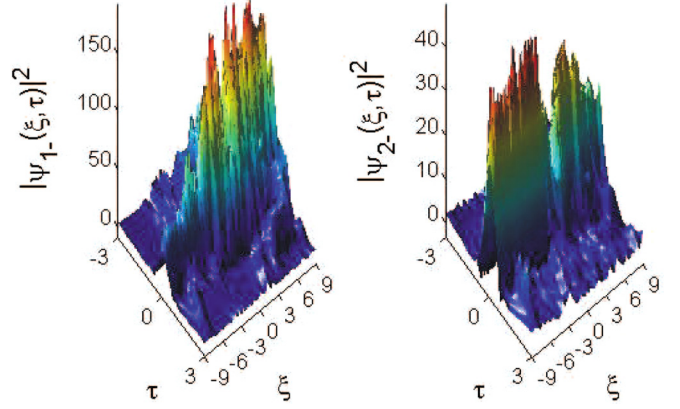
FIG. 8. Existence of chiral vector rogue waves of the left-hand and nonexistence of the right-hand intensity $|\psi_{1,2}(\xi,\tau)|^2$ where the parameters are $C_1 = 0.6$, $C_2 = 0.8$, $\Delta < 0$, and $\mu = b_3(1 - KT_c)$ on the left-hand side and $C_1 = 1.6$, $C_2 = 1.8$, $\Delta > 0$ and $\mu = b_3(1 + KT_c)$ on the right-hand side; with $K = 1$, $T_c = 0.5$, $d_1 = 1.1$, $d_2 = 1.3$, $\alpha_3 = 0.03$, $\gamma = 0.02$, $D = 0.6$, $k_1 = 0.4$, $k_2 = k_4 = 0.6$, $k_3 = 0.5$, $b_3 = 0.01$, and $C = -1$ in each case. At $\xi = -9$, the initial condition takes the form of exact solutions (50) with $\delta = 0$.

(a)

(b)
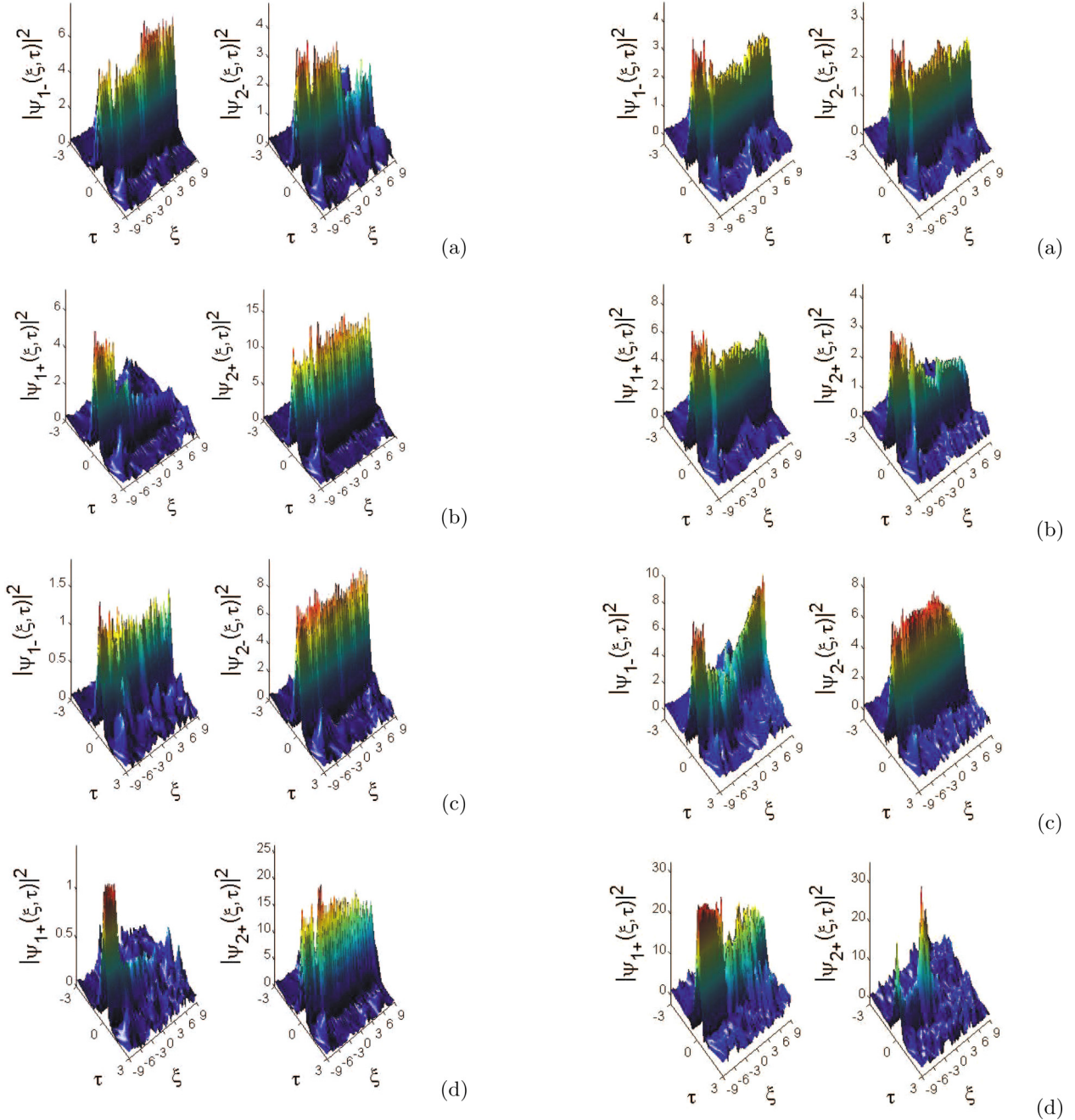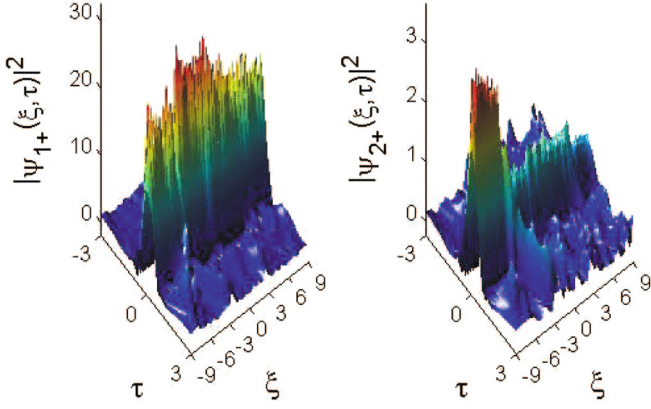
FIG. 7. Chiral optical vector rogue waves of the right- and left-hand intensity $|\psi_{1,2}(\xi,\tau)|^2$ where the parameters are $C_1 = C_2 = 1.96$, and $\mu = b_3(1 - KT_c)$ on the left-hand side and $C_1 = C_2 = -0.96$ and $\mu = b_3(1 + KT_c)$ on the right-hand side; with $K = 1$, $T_c = 0.5$, $d_1 = d_2 = -1.46$ $\alpha_3 = 0.2$, $\gamma = 0.02$, $D = 0.6$, $k_1 = 0.4$, $k_2 = k_4 = 0.6$, $k_3 = 0.5$, $b_3 = 0.01$, and $C = 1$; then $\psi_1 = (-C_1)^{-1/2}\Psi(\xi,\tau)$ and $\psi_2 = 0.02\Psi(\xi,\tau)$ in each case at the origin space $\xi = -9$.

potential) whereas the first components, exposed to the self-defocusing character of the potential barriers are trapped in the lattice. Fortunately, there would remain one component in each side in the chiral optical fiber and the transport of information by two components can always take place.

Now, we consider the case depicted in Fig. 5 where we compare the focusing ($C < 0$) and the defocusing ($C > 0$) nature of the XPM nonlinearity with the focusing SPM nonlinearities $C_{1,2} < 0$. We observe in the mixed case of the defocusing nature of the XPM and focusing SPM nonlinearities that the amplitudes are much higher [see Figs. 5(c) and 5(d)] than the ones observed in the unmixed case of defocusing XPM and SPM nonlinearities [see Figs. 5(a) and 5(b)]. An interesting phenomenon occurs on the right-hand side Fig. 5(d) and it can be seen that the components have the same amplitude and the second one is similar to the usual rogue waves, which are localized both in space and time. This special aspect of chiral optical rogue waves, that is, to send two signals through a vector of rogue waves with the same frequency, can help in optic communication domain.

When we choose focusing ($C_1 < 0$) and defocusing ($C_2 > 0$) SPM interactions with focusing XPM interactions, the inverse situation observed in Figs. 4(c) and 4(d) occurs in Figs. 6 where the self-focusing character of the first component, ten times higher than the amplitude of the linear wave function ψ_2, created a trap potential $U = -|\psi_1|^2$ that trap the second component in the lattice. Because of the nonexistence of the left-hand chiral optical rogue waves, this other aspect can help to guide waves in the right-hand side only.

Now, we decide to generate a chiral optical rogue wave in the form of one component with equal SPM interactions, which are either defocusing $C_{1,2} > 0$ or focusing $C_{1,2} < 0$ with defocusing XPM interactions $C > 0$. With slight excitation in the second component as depicted in Fig. 7, we remark that the amplitudes of the second components are too weak in such

a way that we can say, they do no exist and consequently that there is not chiral optical vector rogue waves in both left- and right-hand side. Finally, we can confirm that the defocusing nature of the XPM is responsible for the generation of holes or chiral optical dark rogue waves in the second components and to the unperturbed rogue waves or bright chiral optical rogue waves in the first components. In summary, we can construct a bright-dark vector of rogue waves in chiral optical fiber.

We consider now the case of defocusing interactions of the SPM nonlinearities ($C_{1,2} > 0$) with focusing interactions of XPM nonlinearity ($C < 0$) depicted in Fig. 8, where we can also observe the nonexistence of right-hand chiral optical rogue waves and the propagation of waves in the left-hand side only. Through Fig. 6, we show that vector rogue waves can be guided only in the right-hand side and through Fig. 8 that they can be guided only in the left-hand side. In summary, we can control the propagation direction of vector rogue waves in chiral optical fiber. The presence of several peaks in some profiles in the text is caused by the strong instability of the background and also due to interactions and collisions between components. They are unusual rogue waves also known as Akhmediev breathers or Kuznetsov-Ma soliton, which are not localized in both space and time like usual rogue waves.

B. Chiral optical rogue waves on mixed polarization with linear coupling

We take into account the last term of Eq. (45), $\beta(\xi)$, which is responsible for the exchange between the two wave components. We let N_1 and N_2 as the power in the first and second components, relative to the total power in the system, respectively, in the following form

$$N_1 = \frac{\int |\psi_1(\tau)|^2 d\tau}{\int |\Psi(\tau)|^2 d\tau} = \frac{-1}{2C}\{1 + \sin(2\alpha)\cos[2B(\xi)]\},$$

$$N_2 = \frac{\int |\psi_2(\tau)|^2 d\tau}{\int |\Psi(\tau)|^2 d\tau} = \frac{-1}{2C}\{1 - \sin(2\alpha)\cos[2B(\xi)]\},$$

(63)

where $\psi_{1,2}$ are deduced from Eq. (52), $C = -1$, $\alpha = \frac{\pi}{4} + \frac{n\pi}{2}$ with n being an integer. Now, we choose $B(\xi)$ in the form

$$B(\xi) = \frac{\pi}{4}\left[1 - b\frac{\xi - \xi_0}{\xi_0}\right].$$

(64)

We make a choice where the linear dependance of the phase $B(\xi)$ depends on ξ. Through analytical simulation, we obtain chiral optical vector rogue waves in the left- and right-hand side depicted in Fig. 9. For $b = 1$, the first components in both sides have the behavior of rogons, which after their disappearance, reappear without major shape change in the amplitude [see Figs. 9(a) and 9(b)]. We also remark that all particles are concentrated in the second components in the vicinity of $\xi = 0$. We can see fast oscillations of the background [see Figs. 9(c) and 9(d)] for $b = 15$. We denote in an equal way, the increase of the amplitude in the left-hand and the decrease of the amplitude on the right-hand side and in consequence, this process reveals the presence of FWM, which is responsible for the exchange of energy between components in the system. We show throughout Figs. 4(c) and 4(d) and then through Fig. 6 and Figs. 7(a) and 7(b), how strong XPM interaction can cause the nonexistence of synchronized chiral

(a)

(b)

(c)

(d)

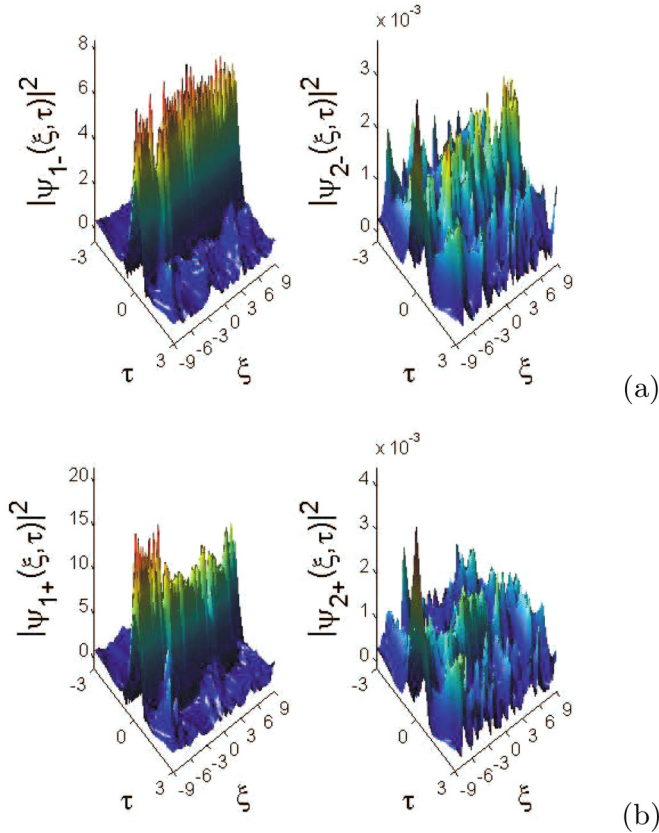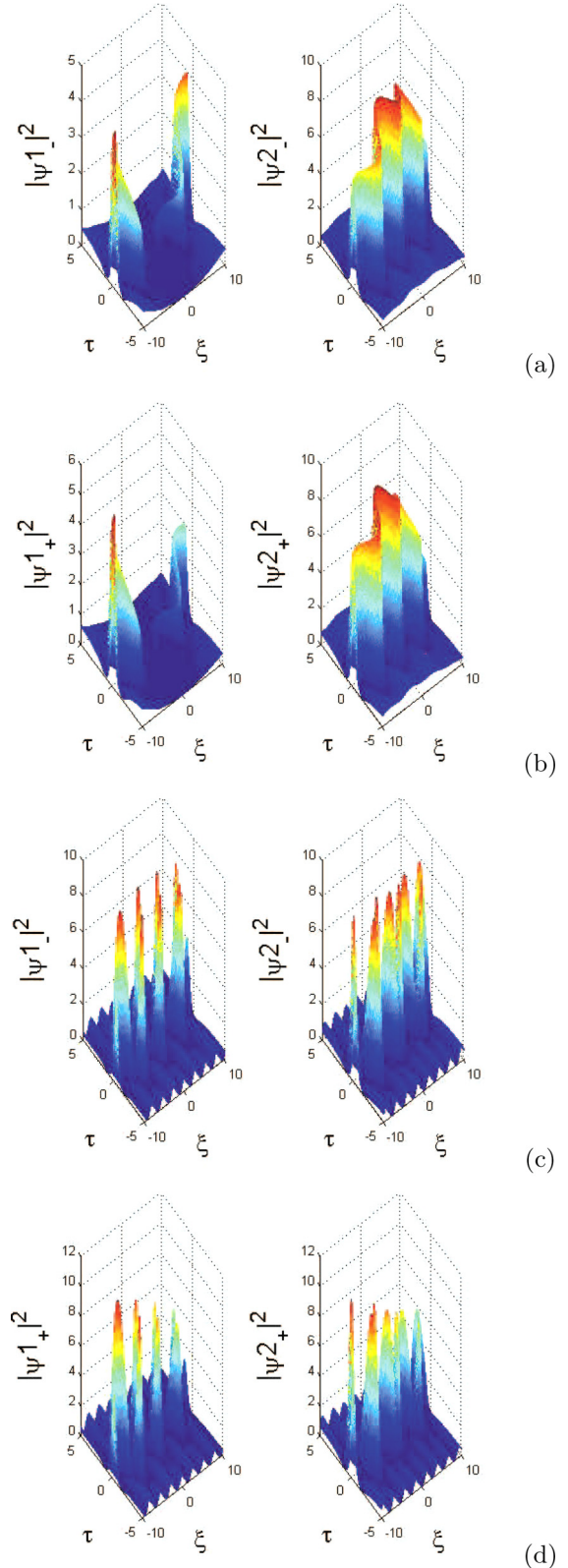FIG. 9. Chiral vector rogue waves of the right- and left-hand intensity $|\psi_{1,2}(\xi,\tau)|^2$ of Eq. (52) where the parameters are given in Eq. (50), Eq. (51), and Eq. (64) with $\mu = b_3(1 - KT_c)$ on the left-hand side and $\mu = b_3(1 + KT_c)$ on the right-hand side; $b = 1.0$ in (a) and (b) and then $b = 15$ in (c) and (d); with $K = 1$, $T_c = 0.7$, $C = -1$, $\alpha = \pi/4$, $b_3 = 0.01$, $\gamma = 0.03$, $k_1 = 0.4$, $k_2 = 0.6$, $\nu = 0.6$, $\xi_0 = -10$, $T_0(\xi) = cn(\xi, k_2)$, and $T_1(\xi) = dn(\xi, k_1)$ in each case.

vector rogue waves. Nevertheless, we observe that in these cases such waves can exist but with weak amplitude in one component. Then, with the matrices $P_{0,1}$ defined in Eq. (55), we arrive to the equal relation $|\psi_1|^2 = |\psi_2|^2$ from system (56), which describes pure linear dispersive dynamics.

VII. CONCLUSION

In this work, we have derived the NLS-type equation in chiral optical fiber with right- and left-hand nonlinear polarization. The model is used to describe the propagation of optical rogue waves in chiral fiber. We have used the symmetry reduction and the modified Darboux transformation to generate the rational solutions. In so doing, we have constructed the first- and second-order chiral optical rogue waves from the chiral NLS equation with variable and constant coefficients, respectively. In order to show the influence of optical activity on the propagation of rogue waves, we have chosen Jacobian elliptic functions for good stability of the waves. We have recorded from analytical results that in chiral optical fiber we obtained two components, left- and right-hand intensities. We have observed that the shape and the amplitude of chiral optical rogue waves change with the increase of the chiral parameter. This allows us to conclude that the slight change of the amplitude is due to the optical activity and TWM

effects. We have performed our study by using chiral CNLS equations and with the help of MATLAB, we have generated the chiral optical vector rogue waves with four components showing, through the exchange of energy, the FWM effect. In the case of focusing and defocusing XPM interactions, we have found unusual rogue waves such as Akhmediev breathers or the Kuznetsov-Ma soliton. Then, we have shown the influence of optical activity on different profiles. We have noticed that the destruction of one component contributes to the perturbations that lead to modulation instability and that the defocusing nature of XPM generates chiral optical dark rogue waves. We have also shown that positive and negative scattering lengths can generate a potential barrier for one component in the left- or right-hand side. Finally, we can control and guide the propagation direction of chiral optical vector rogue waves either in the left-hand or in the right-hand side for some specific set of parameters, including chiral parameter. This aspect can find applications in telecommunication and in many other physical systems.

APPENDIX

In this Appendix, we present the derivation of Eq. (3).

Equation (3) is reduced in x, y, and z directions, respectively, as follows

$$-2jK_z\frac{\partial E_x}{\partial z} - K_z^2 E_x + \mu_0\varepsilon_0 T_c^2\left(\omega^2 K_z^2 E_x + 2jK_z\omega^2\frac{\partial E_x}{\partial z} - 2jK_z^2\omega\frac{\partial E_x}{\partial t}\right)$$

$$= (\mu_0\varepsilon_0 + \mu_0\varepsilon_2|\vec{E}|)\left(2j\omega\frac{\partial E_x}{\partial t} - \omega^2 E_x\right) + \mu_0\sigma\left(\frac{\partial E_x}{\partial t} + j\omega E_x\right) + (2\mu_0\varepsilon_0 T_c + \mu_0\varepsilon_2 T_c|\vec{E}|^2)$$

$$\times\left(\omega^2\frac{\partial E_y}{\partial z} + jK_z\left(2j\omega\frac{\partial E_x}{\partial t} - \omega^2 E_y\right)\right) + \mu_0\sigma T_c\left[-j\omega\frac{\partial E_y}{\partial z} + jK_z\left(\frac{\partial E_y}{\partial t} + j\omega E_y\right)\right] \quad \text{(A1)}$$

$$-2jK_z\frac{\partial E_y}{\partial z} - K_z^2 E_y + \mu_0\varepsilon_0 T_c^2\left(\omega^2 K_z^2 E_y + 2jK_z\omega^2\frac{\partial E_y}{\partial z} - 2jK_z^2\omega\frac{\partial E_y}{\partial t}\right)$$

$$= (\mu_0\varepsilon_0 + \mu_0\varepsilon_2|\vec{E}|)\left(2j\omega\frac{\partial E_y}{\partial t} - \omega^2 E_y\right) + \mu_0\sigma\left(\frac{\partial E_y}{\partial t} + j\omega E_y\right) + (2\mu_0\varepsilon_0 T_c + \mu_0\varepsilon_2 T_c|\vec{E}|^2)$$

$$\times\left[-\omega^2\frac{\partial E_x}{\partial z} - jK_z\left(2j\omega\frac{\partial E_x}{\partial t} - \omega^2 E_x\right)\right] + \mu_0\sigma T_c\left[j\omega\frac{\partial E_x}{\partial z} - jK_z\left(\frac{\partial E_x}{\partial t} + j\omega E_x\right)\right] \quad \text{(A2)}$$

$$[-\omega^2(2\mu_0\varepsilon_0 T_c + \mu_0\varepsilon_2 T_c|\vec{E}|^2) + j\omega\mu_0\sigma T_c]\left(\frac{\partial E_y}{\partial x} - \frac{\partial E_x}{\partial y}\right) = 0. \quad \text{(A3)}$$

Equation (A3) leads to

$$\frac{\partial E_y}{\partial x} = \frac{\partial E_x}{\partial y} = cst, \quad E_y = E_y(z,t), \quad E_x = E_x(z,t). \quad \text{(A4)}$$

Having multiplied Eq. (A2) by $\pm j$, we do the addition of Eqs. (A1) and (A2) where we also consider the paraxial approximation

$$\left|\frac{\partial E_x}{\partial t}\right| \ll |2j\omega E_x|, \quad \left|\frac{\partial^2 E_y}{\partial z^2}\right| \ll |2j\omega E_y|. \quad \text{(A5)}$$

Therefore, the novel form of wave equation can be written as

$$\Big[\pm j[(2\mu_0\varepsilon_0 T_c + \mu_0\varepsilon_2 T_c|\vec{E}|^2)\omega^2 - j\omega\mu_0\sigma T_c] - 2jK_z + 2jK_z\omega^2\mu_0\varepsilon_0 T_c^2\Big]\frac{\partial\psi_{R,L}}{\partial z} + \Big[-K_z^2 + \mu_0\varepsilon_0 T_c^2\omega^2 K_z^2$$

$$+ \omega^2(\mu_0\varepsilon_0 + \mu_0\varepsilon_2|\vec{E}|^2) - j\omega\mu_0\sigma \pm j(-jK_z\omega^2(2\mu_0\varepsilon_0 T_c + \mu_0\varepsilon_2 T_c|\vec{E}|^2) - K_z\omega\mu_0\sigma T_c)\Big]\psi_{R,L}$$

$$+ \Big[-2j\times K_z^2\omega\mu_0\varepsilon_0 T_c^2 - 2j\omega(\mu_0\varepsilon_0 + \mu_0\varepsilon_2|\vec{E}|^2)\Big]\frac{\partial\psi_{R,L}}{\partial t} = 0, \quad \text{(A6)}$$

TABLE I. Occurrence of modulation instability and chiral vector rogue waves for mixed cases of SPM and XPM interactions.

SPM interactions	XPM interactions	Unstable Branches	Stable Branches	Chiral vector rogue waves
$C_{1,2} < 0$	$- : C > C_{1,2}, \Delta > 0$ $+ : C < C_{1,2}, \Delta < 0$	$- : 4$ $+ : 4$	$- : 2$ $+ : 2$	$- : exist$ $+ : not$ $exist$
	$- : |C| < |C_{1,2}|, \Delta > 0$ $+ : |C| < |C_{1,2}|, \Delta > 0$	$- : 4$ $+ : 4$	$- : 2$ $+ : 2$	$- : exist$ $+ : exist$
	$- : C < |C_{1,2}|, \Delta > 0$ $+ : C > |C_{1,2}|, \Delta < 0$	$- : 4$ $+ : 4$	$- : 2$ $+ : 2$	$- : not$ $exist$ $+ : not$ $exist$
$C_{1,2} > 0$	$- : C > C_{1,2}, \Delta < 0$ $+ : C < C_{1,2}, \Delta > 0$	$- : 4$ $+ : 3$	$- : 2$ $+ : 3$	$- : not$ $exist$ $+ : not$ $exist$
	$- : |C| > C_{1,2}, \Delta < 0$ $+ : |C| < C_{1,2}, \Delta > 0$	$- : 4$ $+ : 4$	$- : 2$ $+ : 2$	$- : exist$ $+ : not$ $exist$
	$- : C < -C_{1,2}, \Delta < 0$ $+ : C > -C_{1,2}, \Delta > 0$	$- : 3$ $+ : 3$	$- : 3$ $+ : 3$	$- : exist$ $+ : not$ $exist$
$C_1 < 0, C_2 > 0$	$- : C < C_{1,2}, \Delta < 0$ $+ : C < C_{1,2}, \Delta < 0$	$- : 5$ $+ : 4$	$- : 1$ $+ : 2$	$- : not$ $exist$ $+ : exist$

where $\psi_{R,L} = E_x \pm jE_y$. Then the reference changes is out to be

$$\begin{cases} \psi_R = E_x + jE_y \\ \psi_L = E_x - jE_y \end{cases} \quad \begin{cases} E_x = \frac{\psi_R + \psi_L}{2} \\ E_y = \frac{\psi_R - \psi_L}{2}. \end{cases} \tag{A7}$$

The division of Eq. (A6) by $-2K_z$ yields

$$j\left(1 - K_0{}^2 T_c{}^2\right)\frac{\partial \psi_{R,L}}{\partial z} \mp j\frac{K_0{}^2 T_c}{K_z}\frac{\partial \psi_{R,L}}{\partial z} + j\frac{\omega \mu_0 \varepsilon_2}{K_z}|\psi_{R,L}|^2\frac{\partial \psi_{R,L}}{\partial t} \mp j\frac{\mu_0 \varepsilon_2 \omega^2 T_c}{2K_z}|\psi_{R,L}|^2\frac{\partial \psi_{R,L}}{\partial z}$$

$$+ j\frac{K_0}{K_z c}\left(1 + K_z{}^2 T_c{}^2\right)\frac{\partial \psi_{R,L}}{\partial t} \mp \frac{j\omega \mu_0 \sigma T_c}{2}\psi_{R,L} + \frac{1}{2}\left(K_z - K_z K_0{}^2 T_c{}^2 - \frac{K_0{}^2}{K_z}\right)\psi_{R,L} - \frac{\mu_0 \varepsilon_2 \omega^2}{2K_z}$$

$$\times |\psi_{R,L}|^2 \psi_{R,L} \mp \frac{\omega^2}{2}(\mu_0 \varepsilon_2 T_c|\psi_{R,L}|^2)\psi_{R,L} + j\frac{\omega \mu_0 \sigma}{2K_z}\psi_{R,L} \mp K_0{}^2 T_c \psi_{R,L} \mp \frac{\omega \mu_0 \sigma T_c}{2K_z}\frac{\partial \psi_{R,L}}{\partial z} = 0, \tag{A8}$$

where

$$K_0 = \frac{\omega}{c}, \quad \mu_0 \varepsilon_0 c^2 = 1. \tag{A9}$$

The dispersion relation is given by

$$K_z = \frac{K_0}{1 \pm K_0 T_c}. \tag{A10}$$

For $K_0{}^2 T_c{}^2 \ll 1$, we get $K_z = K_0$. By neglecting the nonlinear diffraction, the second and the last terms of Eq. (A8), and for the following set of parameters

$$v^2 = \frac{1}{\mu_0 \varepsilon_0}, \quad \alpha = \mu_0 \sigma, \quad \beta = \mu_0 \varepsilon_2$$

$$K_0 = \frac{\omega}{v}, \quad z^* = \frac{z}{1 - K_0{}^2 T_c{}^2}, \tag{A11}$$

Eq. (A8) takes the form

$$j\frac{\partial \psi_{R,L}}{\partial z^*} + j\frac{1}{v}\frac{\partial \psi_{R,L}}{\partial t} + j\frac{\omega \alpha}{2K_0}\psi_{R,L} \mp K_0{}^2 T_c \psi_{R,L}$$

$$- \frac{\beta \omega^2}{2K_0}|\psi_{R,L}|^2 \psi_{R,L} \mp \frac{j\omega \alpha T_c}{2}\psi_{R,L} \mp \frac{\omega^2 \beta T_c}{2}$$

$$\times |\psi_{R,L}|^2 \psi_{R,L} + \frac{j\omega \beta}{K_0}|\psi_{R,L}|^2\frac{\partial \psi_{R,L}}{\partial t} = 0. \tag{A12}$$

If we let

$$\psi_{R,L} = \phi, \quad K = K_0 = K_z, \tag{A13}$$

Eq. (A11) yields

$$j\frac{\partial\phi}{\partial z^*} + j\frac{1}{v}\frac{\partial\phi}{\partial t} + j\frac{\omega\alpha}{2K_0}(1\mp KT_c)\phi$$
$$-\frac{\beta\omega^2}{2K_0}(1\mp KT_c)|\phi|^2\phi \mp K^2 T_c\phi + j\frac{\omega\beta}{K_0}|\phi|^2\frac{\partial\phi}{\partial t} = 0.$$
$$\text{(A14)}$$

The Taylor series of the wave number $K(\omega)$ at the third order and the Fourier transform of $\Delta\omega$ and ΔK help to express in an approximate form, the second term of Eq. (A13) as

$$j\frac{1}{v}\frac{\partial\phi}{\partial t} = j\frac{1}{v_g}\frac{\partial\phi}{\partial t} + \frac{1}{2}K''\frac{\partial^2\phi}{\partial t^2} - j\frac{1}{6}K'''\frac{\partial^3\phi}{\partial t^3}, \qquad \text{(A15)}$$

where

$$K'' = \frac{\partial^2 K}{\partial\omega^2}, \quad K''' = \frac{\partial^3 K}{\partial\omega^3}, \quad K' = \frac{1}{v_g} = \frac{\partial K}{\partial\omega}. \quad \text{(A16)}$$

Then, for the following change of variable

$$\begin{cases} t' = t - \frac{1}{v_g}z^* \\ z' = z^* \end{cases} \Rightarrow \begin{cases} \frac{\partial}{\partial t} \to \frac{\partial}{\partial t'} \\ \frac{\partial}{\partial z^*} \to \frac{\partial}{\partial z'} - \frac{1}{v_g}\frac{\partial}{\partial t'} \end{cases}, \qquad \text{(A17)}$$

Eq. (A14) stands for

$$j\frac{\partial\phi}{\partial z'} + \frac{1}{2}K''\frac{\partial^2\phi}{\partial t'^2} - j\frac{1}{6}K'''\frac{\partial^3\phi}{\partial t'^3} + j\frac{\omega\alpha}{2K_0}(1\mp KT_c)\phi$$
$$-\frac{\beta\omega^2}{2K_0}(1\mp KT_c)|\phi|^2\phi \mp K^2 T_c\phi + j\frac{\omega\beta}{K_0}|\phi|^2\frac{\partial\phi}{\partial t'} = 0.$$
$$\text{(A18)}$$

In the table below, we analyze the specific cases of SPM and XPM interactions when they have the same and opposite signs.

[1] A. Hasegawa and F. Tappert, Appl. Phys. Lett. **23**, 142 (1973).

[2] L. F. Mollenauer, R. H. Stolen, and J. P. Gordon, Phys. Rev. Lett. **45**, 1095 (1980).

[3] R. H. Stolen, L. F. Mollenauer, and W. J. Tomlison, Opt. Lett. **8**, 186 (1983).

[4] L. F. Mollenauer, R. H. Stolen, J. P. Gordon, and W. J. Tomlinson, Opt. Lett. **8**, 289 (1983).

[5] N. N. Akmediev and E. A. Ostrovskaya, Opt. Commun. **132**, 190 (1996).

[6] M. V. Tratnik and J. E. Sipe, Phys. Rev. A **38**, 2011 (1988).

[7] N. N. Akhmediev, V. M. Eleonskii, N. E. Kulagin, and L. P. Shil'nikov, Pis'ma Zh. Sov. Tech. Phys. Lett. **15**, 587 (1989).

[8] M. Haelterman and A. Sheppard, Phys. Rev. E **49**, 3376 (1994).

[9] B. Bai, Y. Svirko, J. Turunen, and T. Vallius, Phys. Rev. A **76**, 023811 (2007).

[10] H. Torres-Silva and M. Zamorano, Math. Comput. Sim. **62**, 149 (2003).

[11] L. Poladian, M. Straton, A. Doccherty, and A. Argyros, Opt. Express **19**, 968 (2011).

[12] B. Bai, J. Laukkanen, A. Lehmuskero, and J. Turunen, Phys. Rev. B **81**, 115424 (2010).

[13] H. Torres-Silva, C. Villarroel, P. H. Sakanaka, and N. Reggiani, Pramana–J. Phys. **49**, 431 (1997).

[14] Y. Chen and J. Atai, J. Opt. Soc. Am. B **14**, 2365 (1997).

[15] H. Torres-Silva and M. Zamorano Lucero, Pramana–J. Phys. **62**, 37 (2004).

[16] P. D. Maker, R. W. Terhune, and C. M. Savage, Phys. Rev. Lett. **12**, 507 (1964).

[17] P. K. Choudhury and T. Yoshino, Optik **113**, 89 (2002).

[18] A. Argyros, J. Pla, F. Ladouceur, and L. Poladian, Opt. Express **17**, 15983 (2009).

[19] Kh. S. Singh, P. Khastgir, S. P. Ojha, and P. K. Choudhury, J. Phys. Soc. Jpn. **62**, 1978 (1993).

[20] N. S. Pujari, M. R. Kulkarni, M. C. J. Large, I. M. Bassett, and S. Ponrathnam, J. Appl. Polym. Sci. **98**, 58 (2005).

[21] A. Argyros, M. Straton, A. Docherty, E. H. Min, Z. Ge, K. H. Wong, F. Ladouceur, and L. Poladin, Frontiers Optoelectron. China **3**, 67 (2010).

[22] C. Dai, Y. Wang, and X. Zang, Opt. Express **22**, 29862 (2014).

[23] D. H. Peregrine, J. Aust. Math. Soc. Series B, Appl. Math. **25**, 16 (1983).

[24] N. Akhmediev and V. I. Korneev, Theor. Math. Phys. **69**, 1089 (1986).

[25] E. A. Kuznetsov, Dokl. Akad. Nauk SSSR **236**, 575 (1977).

[26] Z. Y. Yan, Phys. Lett. A **374**, 672 (2010).

[27] N. Akhmediev, A. Ankiewicz, and M. Taki, Phys. Lett. A **373**, 675 (2009).

[28] N. Akhmediev, J. M. Soto-Crespo, and A. Ankiewicz, Phys. Lett. A **373**, 2137 (2009).

[29] D. D. Estelle Temgoua and T. C. Kofane, Phys. Rev. E **91**, 063201 (2015).

[30] J. M. Dudley, G. Genty, F. Dias, B. Kibler, and N. Akhmediev, Opt. Express **17**, 21497 (2009).

[31] A. N. Ganshin, V. B. Efimov, G. V. Kolmakov, L. P. Mezhov-Deglin, and P. V. E. McClintock, Phys. Rev. Lett. **101**, 065303 (2008).

[32] A. N. W. Hone, J. Phys. A: Math. Gen. **30**, 7473 (1997).

[33] A. Montina, U. Bortolozzo, S. Residori, and F. T. Arecchi, Phys. Rev. Lett. **103**, 173901 (2009).

[34] P. Müller, C. Garrett, and A. Osborne, Oceanography **18**, 66 (2005).

[35] A. Nakamura and R. Hirota, J. Phys. Soc. Jpn. **54**, 491 (1985).

[36] M. Noumi and Y. Yamada, Nagoya Math. J. **153**, 53 (1999).

[37] D. R. Solli, C. Ropers, P. Koonath, and B. Jalali, Nature (London) **450**, 1054 (2007).

[38] M. Ballav and A. R. Chowdhury, Chaos **17**, 013102 (2007).

[39] T. B. Benjamin and J. E. Fier, J. Fluid Mech. **27**, 417 (1967).

[40] N. A. Kostov, V. Z. Enolskii, V. S. Gerdjikov, V. V. Konotop, and M. Salerno, Phys. Rev. E **70**, 056617 (2004).

[41] Y. V. Bludov, V. V. Konotop, and N. Akhmediev, Opt. Lett. **34**, 3015 (2009).

[42] M. Shats, H. Punzmann, and H. Xia, Phys. Rev. Lett. **104**, 104503 (2010).

[43] Y. V. Bludov, V. V. Konotop, and N. Akhmediev, Eur. Phys. J. ST **185**, 169 (2010).

[44] Y. V. Bludov, V. V. Konotop, and N. Akhmediev, Phys. Rev. A **80**, 033610 (2009).

[45] S. Loomba, H. Kaur, R. Gupta, C. N. Kumar, and T. S. Raju, Phys. Rev. E **89**, 052915 (2014).

[46] E. Wamba, K. Porsezian, A. Mohamadou, and T. C. Kofane, Phys. Lett. A **377**, 262 (2013).

[47] Y. V. Bludov, R. Driben, V. V. Konotop, and B. A. Malomed, J. Opt. **15**, 064010 (2013).

[48] L. Wen, L. Li, Z. D. Li, S. W. Song, X. F. Zhang, and W. M. Liu, Eur. Phys. J. D **64**, 473 (2011).

[49] J. Atangana, B. G. O. Essama, F. Biya-Motto, B. Mokhtari, N. C. Eddeqaqi, and T. C. Kofane, J. Mod. Opt. **62**, 392 (2015).

[50] B. G. O. Essama, J. Atangana, F. Biya-Motto, B. Mokhtari, N. C. Eddeqaqi, and T. C. Kofane, Opt. Commun. **331**, 334 (2014).

[51] A. Laktakia and V. K. Varadan, *Time-Harmonic Electromagnetic Fields in Chiral Media*, Lecture Notes in Physics, Vol. 335 (Springer, Berlin, 1985).

[52] Z. Yan and C. Dai, J. Opt. **15**, 064012 (2013).

[53] G. W. Bluman and S. Kumei, *Symmetries and Differential Equations* (Springer, New York, 1989).

[54] G. W. Bluman and Z. Y. Yan, Eur. J. Appl. Math. **16**, 239 (2005).

[55] B. Guo, L. Ling, and Q. P. Liu, Phys. Rev. E **85**, 026607 (2012).

[56] Zhenya Yan, V. V. Konotop, and N. Akhmediev, Phys. Rev. E **82**, 036610 (2010).

[57] W.-P. Zhong, M. R. Belic, and T. Huang, Phys. Rev. E **87**, 065201 (2013).

[58] A. Ankiewicz, J. M. Soto-Crespo, and N. Akhmediev, Phys. Rev. E **81**, 046602 (2010).

[59] N. Akhmediev, A. Ankiewicz, and J. M. Soto-Crespo, Phys. Rev. E **80**, 026601 (2009).

[60] E. N. Tsoy, A. Ankiewicz, and N. Akhmediev, Phys. Rev. E **73**, 036621 (2006).

[61] A. T. Avelar, D. Bazeia, and W. B. Cardoso, Phys. Rev. E **79**, 025602 (2009).

[62] N. Akhmediev, V. M. Eleonskii, and N. E. Kulagin, Sov. Phys. JETP **89**, 1542 (1985).

[63] P. F. Byrd and M. D. Friedman, *Handbook of Elliptic Integrals for Engineers and Scientists*, 2nd ed. (Springer, Berlin, 1971).

[64] S. V. Manakov, Zh. Eksp. Teor. Fiz. **67**, 543 (1974).

Combined effects of nonparaxiality, optical activity, and walk-off on rogue wave propagation in optical fibers filled with chiral materials

D. D. Estelle Temgoua,[1,2,3,*] M. B. Tchoula Tchokonte,[3,†] and T. C. Kofane[1,4,‡]

[1]*Laboratory of Mechanics, Materials and Structures, Post Graduate School in Sciences, Technology and Geosciences, Doctoral Research, Unit in Physics and Applications, University of Yaounde I, P.O. Box 812, Yaounde, Cameroon*

[2]*Organization for Women in Science for the Developing World, ICTP Campus, Strada Costiera 11, 34151 Trieste, Italy*

[3]*Department of Physics and Astronomy, University of the Western Cape, Private Bag X17, Bellville, 7535 South Africa*

[4]*Centre d'Excellence Africain en Technologies de l'Information et de la Communication, University of Yaounde I, P.O. Box 812, Yaounde, Cameroon*

The generalized nonparaxial nonlinear Schrödinger (NLS) equation in optical fibers filled with chiral materials is reduced to the higher-order integrable Hirota equation. Based on the modified Darboux transformation method, the nonparaxial chiral optical rogue waves are constructed from the scalar model with modulated coefficients. We show that the parameters of nonparaxiality, third-order dispersion, and differential gain or loss term are the main keys to control the amplitude, linear, and nonlinear effects in the model. Moreover, the influence of nonparaxiality, optical activity, and walk-off effect are also evidenced under the defocusing and focusing regimes of the vector nonparaxial NLS equations with constant and modulated coefficients. Through an algorithm scheme of wider applicability on nonparaxial beam propagation methods, the most influential effect and the simultaneous controllability of combined effects are underlined, showing their properties and their potential applications in optical fibers and in a variety of complex dynamical systems.

I. INTRODUCTION

After the investigation of fundamental problems of electromagnetic wave interaction with chiral materials, the area of wave propagation in chiral media has renewed attention both from theoretical and experimental points of view [1]. Chirality, which refers to the handedness of an object or a medium, has to play an important role in a variety of fields, including chemistry [2], optics [3], particle physics [4,5], and mathematics [6]. The electromagnetic wave propagation through such medium displays two unequal characteristic wave numbers for the right-and left-circularly polarized eigenmodes, which results in both optical activity and circular dichrosim, as consequences of the circular birefringence [1,7]. Significant advances have taken place on some aspects relating to the applications of chiral media. One can mention the wave-guiding structures filled with chiral materials, which show many interesting features through the integrated optic applications like directional couplers, which can be used as optical switches for energy transfer from one fiber to another adjacent one. In fact, chiral medium has many potentials and the development of integrated circuitry with chiral substrates and the multiplexing in chiral fibers are important progress with potential applications in optics [8,9].

In recent times, much attention has been focused on understanding of rogue wave propagation in optical fibers filled with chiral materials. The nature of rogue waves has been discussed in hydrodynamics [10–12] and initiated in nonlinear optics, by the pioneering measurement of Solli *et al.* [13] through the analysis of the supercontinuum generation in optical fibers, and later in a photonic crystal fiber [14]. Their occurrences have been later observed in optical cavities [15], optical wave guides [16], Bose-Einstein condensates [17–19], laser-plasma interactions [20], econophysics [21], and even in finance [22].

The concept of rogue waves which refers to rogons has been applied to pulses emerging from optical fibers, and both numerical simulations and experiments show that the probability of their generations increases with the increase of the initial noise level responsible for the modulation instability (MI) [23]. It is worth noting that the MI that leads to their generation evolves two distinct directions with opposite sense. On the one hand, it deals with the undesirable effects like the non-return-to-zero code in optical communication, the drastic enhancement of MI gain in the WDM (wavelength-division multiplexing) systems which sets the limitation of the bandwidth window of the communication system, MI lasers, and the new frequency generations of ultrashort pulses in optical systems. On the other hand, a suitable manipulation of MI has also found important applications in optical amplification of weak signal, dispersion management, optical switching, and the production of ultrashort pulses.

Despite multiple observations in many other fields, the origin and the predictability of rogons remains uncertain [24], as does the kind of MI that leads to rogue wave generation [25,26]. In fact, in optical communication systems [27–29], many works have been done with the objective of reducing the disastrous effects caused by MI. Important progress has been made very recently by Baronio *et al.* [30], who showed

*Corresponding author: estelletemgoua@yahoo.fr
†mtchokonte@uwc.ac.za
‡tckofane@yahoo.com

that the MI is a necessary but not a sufficient condition for the existence of rogue waves. Through their results, they confirmed that rogue waves can exist if and only if the MI gain band also contains the zero-frequency perturbation as a limiting case known as baseband MI.

In the context of adequate model, the focusing nonlinear Schrödinger (NLS) equation has played an important role of universal model for rogue waves description in both optics [31] and hydrodynamics [32] and, later on, in many physical systems [33,34]. Therefore, the nonparaxial NLS equation model was used in the literature by Baruch *et al.* [35] and Chamoro-Posada *et al.* [36]. Moreover, the development and testing of two alternative nonparaxial beam propagation methods investigated by Chamoro-Posada *et al.* [37] have provided the foundations upon which further investigations as the modeling of numerous higher-order effects and different physical geometries can now be undertaken with much greater confidence. Therefore, the difference-differential approach that is used in this work is flexible in the accommodation of additional effects. Furthermore, the same model has been used in the literature by many authors [38,39].

Then after many years, scientists [30,40] recognized that describing complex systems with the standard NLS equation is oversimplifying the nonlinear phenomena that can occur in those systems. As a consequence, this problem pushes researchers [41,42] to turn to higher-order NLS equations. Moreover, it was pointed out that the vector NLS equations describe rogue waves with higher accuracy than the scalar models [43–45]. Under this assumption, the existence of vector rogue waves in the defocusing regime was a crucial progress in the explanation of rogue waves in multicomponent systems [30].

Among different models that have been studied before, no report to the best of our knowledge is adequate to perform the description of the generation and the propagation of nonparaxial rogue waves in optical fibers filled with chiral materials. As we are working under the assumption of high intensity and beam narrowness, we investigated both scalar and vector models, which can be used efficiently to describe simultaneous effects of nonparaxiality, optical activity, and walk-off on rogue waves propagating in optical fibers, filled with chiral materials. As physical phenomena require modeling waves with two or more components to account for different modes, frequencies, or polarizations [7,43,46], it is also necessary to use the vector NLS equations, which allow energy transfer between components and which potentially yields rich and significant new families of vector rogue wave solutions.

As methodology of resolution of the higher-order nonparaxial chiral NLS equations derived in Appendix A, we use both similitude reduction and modified Darboux transformation (MDT) methods [47–49] to find the analytical solutions of the scalar model, and both difference-differential equation method and Darboux dressing transformation (DDT) methods [44,50–54] to find the numerical solutions of the vector model. Indeed, the properties of simultaneous controllability of nonparaxiality, optical activity, and walk-off effects on rogue waves are underlined.

The paper is organized as follows: In Sec. II we find under the boundedness condition the nonparaxial chiral optical rogue waves with modulated coefficients via the MDT method. In Sec. III we investigate the dynamical behavior and features of

nonparaxial chiral optical rogue waves through their specific control parameters. In Sec. IV we analyze the influence of nonparaxiality, optical activity, and walk-off on the vector nonparaxial chiral NLS equations with constant coefficients. In Sec. V we present the influence of combined effects through the vector nonparaxial chiral NLS equations with modulated coefficients. In Sec. VI we summarize the outcomes.

II. SIMILARITY REDUCTION, FIRST- AND SECOND-ORDER NONPARAXIAL CHIRAL OPTICAL ROGUE WAVES WITH MODULATED COEFFICIENTS

To describe the optical rogue wave propagation in chiral media, we deduce from Eq. (A25), derived in Appendix A, the nonparaxial chiral NLS equation with modulated coefficients, in the form

$$d(\xi)\frac{\partial^2 \psi}{\partial \xi^2} + j\frac{\partial \psi}{\partial \xi} + P(\xi,\tau)\frac{\partial^2 \psi}{\partial \tau^2} - j\gamma(\xi)\frac{\partial^3 \psi}{\partial \tau^3} + j\mu(\xi,\tau)\psi$$
$$\mp D(\xi,\tau)\psi - C(\xi,\tau)|\psi|^2\psi + j\alpha_3(\xi)|\psi|^2\frac{\partial \psi}{\partial \tau} + \eta(\xi)\frac{\partial \psi}{\partial \tau}$$
$$\pm j\sigma_3(\xi,\tau)\frac{\partial \psi}{\partial \tau} = 0, \tag{1}$$

where ξ is the propagation distance, and τ is the retarded time. The subscripts ξ and τ stand for partial differentiation. The variable coefficients $P(\xi,\tau)$, $\mu(\xi,\tau)$, $D(\xi,\tau)$, $C(\xi,\tau)$, and $\sigma_3(\xi,\tau)$ are related to the space- and time-modulated group-velocity dispersion (GVD), gain or loss term of the induced optical activity, linear birefringence, self-phase modulation (SPM), and linear group velocity or walk-off. Parameters $d(\xi)$, $\gamma(\xi)$, $\alpha_3(\xi)$, and $\eta(\xi)$ are related to the space-modulated nonparaxial parameter, TOD (third-order dispersion), SS (self-steepening), and the differential gain or loss term, respectively. Through Eq. (1), we can see the importance and the necessity to take into account those parameters which are responsible of nonparaxial, optical activity, and walk-off effects. These additional terms will help to improve the description and the control of rogue wave propagation under the above assumptions. As the assumption of controllability [55] is verified by the above model, we are going to find the rational solutions with variable coefficients which may be useful to control the propagation of the nonparaxial chiral optical rogue waves.

Modulated coefficients in Eq. (1) can strongly affect the wave propagation in chiral optical fiber because of the non-integrability of the model. To solve this problem, we use the symmetry reduction method [56,57] to obtain some integrability conditions and to reduce the generalized nonparaxial chiral NLS equation to the higher-order integrable Hirota equation. So doing, we use the envelope field in the form [55,58,59]

$$\psi(\xi,\tau) = A(\xi)V[Z(\xi),T(\xi,\tau)]\exp\{i\rho(\xi,\tau)\}, \tag{2}$$

to construct the rational solutions related to nonparaxial chiral optical rogue waves, where $A(\xi)$ is the amplitude, $Z(\xi)$ the effective propagation distance, $T(\xi,\tau)$ the similitude variable, and $V[Z(\xi),T(\xi,\tau)]$ the complex field. The variable $\rho(\xi,\tau)$ is the phase of the wave. This form of envelope field is also known as the similarity transformation or the reduction method.

Substituting Eq. (2) into Eq. (1) gives a coupled system of partial differential equations with variable coefficients:

$$d(\xi)\left(A_{\xi\xi}V + 2A_\xi Z_\xi V_Z + 2A_\xi T_\xi V_T + 2AZ_\xi T_\xi V_{ZT} + AZ_{\xi\xi}V_Z + AT_{\xi\xi}V_T + AZ_\xi^2 V_{ZZ} + AT_\xi^2 V_{TT} - A\rho_\xi^2 V\right)$$
$$- AV\rho_\xi + P(\xi,\tau)\left(AV_{TT}T_\tau^2 + AV_T T_{\tau\tau} - AV\rho_\tau^2\right) + \gamma(\xi)\left(3AV_T T_{\tau\tau}\rho_\tau + 3AV_T T_\tau \rho_{\tau\tau} + 3AV_{TT}T_\tau^2 \rho_\tau\right.$$
$$\left. + AV\rho_{\tau\tau\tau} - AV\rho_\tau^3\right) \mp D(\xi,\tau)AV - C(\xi,\tau)A^2|V|^2 AV - \alpha_3(\xi)A^2|V|^2 AV\rho_\tau + \eta(\xi)AT_\tau V_T \mp \sigma(\xi,\tau)AV\rho_\tau = 0, \quad (3)$$

$$d(\xi)(AV\rho_{\xi\xi} + 2A_\xi \rho_\xi V + 2AZ_\xi \rho_\xi V_Z + 2A\rho_\xi T_\xi V_T) + A_\xi V + AV_Z Z_\xi + AV_T T_\xi + P(\xi,\tau)(AV\rho_{\tau\tau} + 2AV_T T_\tau \rho_\tau)$$
$$- \gamma(\xi)(AV_T T_{\tau\tau\tau} + 3AV_{TT}T_\tau T_{\tau\tau} + AV_{TTT}T_\tau^3 - 3AV_T T_\tau \rho_\tau^2 - 3AV\rho_{\tau\tau}\rho_\tau) + \mu(\xi,\tau)AV$$
$$+ \alpha_3(\xi)A^2|V|^2 AV_T T_\tau + \eta(\xi)AV\rho_\tau \pm \sigma(\xi,\tau)AT_\tau V_T = 0, \quad (4)$$

where the scripts of differential equations are simplified as $A(\xi) = A$, $Z(\xi) = Z$, $T(\xi,\tau) = T$, $\rho(\xi,\tau) = \rho$, and $V[Z(\xi), T(\xi,\tau)] = V$. According to the previous works [55,59], we use the symmetry reduction given by Eq. (2) that would reduce Eq. (1) to the higher-order integrable Hirota equation in the form [60]

$$i\frac{\partial V}{\partial Z} = -\frac{\partial^2 V}{\partial T^2} + G|V|^2 V$$
$$+ 2\sqrt{2}i\nu\left(\frac{\partial^3 V}{\partial T^3} + 3|V|^2 \frac{\partial V}{\partial T}\right). \quad (5)$$

In the case of rogue waves finding, we take $G = -1$ to obtain rational solutions. The parameter ν is a real constant. With $V[Z(\xi), T(\xi,\tau)]$ satisfying the relation Eq. (5), the similarity reduction of Eqs. (3) and (4) yields

$$\gamma(\xi)T_\tau T_{\tau\tau} = 0, \quad (6)$$

$$T_\xi + 2d(\xi)T_\tau \rho_\tau + 2P(\xi,\tau)T_\tau \rho_\tau \pm \sigma(\xi,\tau)T_\tau$$
$$- \gamma(\xi)(T_{\tau\tau\tau} - 3T_\tau \rho_\tau^2) = 0, \quad (7)$$

$$A_\xi + A[d(\xi)\rho_{\xi\xi} + \rho_{\tau\tau}P(\xi,\tau) + 3\gamma(\xi)\rho_{\tau\tau}\rho_\tau + \mu(\xi,\tau)$$
$$+ \eta(\xi)\rho_\tau] = 0, \quad (8)$$

$$\gamma(\xi)T_\tau^3 + 2\sqrt{2}\nu Z_\xi = 0, \quad (9)$$

$$A_\xi V + AZ_\xi V_Z + AT_\xi V_T = 0, \quad (10)$$

$$\alpha_3(\xi)A^2 T_\tau - 6\sqrt{2}\nu Z_\xi = 0, \quad (11)$$

$$d(\xi)T_{\xi\xi} + P(\xi,\tau)T_{\tau\tau} + 3\gamma(\xi)(T_{\tau\tau}\rho_\tau + T_\tau \rho_{\tau\tau})$$
$$+ \eta(\xi)T_\tau = 0, \quad (12)$$

$$Z_\xi + d(\xi)T_\xi^2 + P(\xi,\tau)T_\tau^2 + 3\gamma(\xi)\rho_\tau T_\tau^2 = 0, \quad (13)$$

$$\rho_\xi + d(\xi)\rho_\xi^2 + P(\xi,\tau)\rho_\tau^2 + \gamma(\xi)(\rho_\tau^3 - \rho_{\tau\tau})$$
$$\pm \sigma(\xi,\tau)\rho_\tau \pm D(\xi,\tau) = 0, \quad (14)$$

$$GZ_\xi + A^2(C(\xi,\tau) + \alpha_3(\xi)\rho_\tau) = 0, \quad (15)$$

$$A_{\xi\xi}V + 2A_\xi Z_\xi V_Z + 2A_\xi T_\xi V_T + 2AZ_\xi T_\xi V_{ZT}$$
$$+ AZ_{\xi\xi}V_Z + AZ_\xi^2 V_{ZZ} = 0. \quad (16)$$

Here, the subscripts ξ and τ denote spatial and temporal derivatives, respectively. Through the above symmetry reduction method, the constraints or integrability conditions of the model given in Eq. (1) are derived from the differential equations of which the simplified forms stand from Eq. (6) to Eq. (16), respectively, as follows $-3AV_{TT} \neq 0$, $AV_T \neq 0$, $V \neq 0$, $-AV_{TTT} \neq 0$, $2d\rho_\xi \neq 0$, $A|V|^2 V_T \neq 0$, $AV_T \neq 0$, $AV_{TT} \neq 0$, $-AV \neq 0$, $-A|V|^2 V \neq 0$, and $d \neq 0$.

We should keep in mind that each constraint plays an important role in the choice of arbitrary functions and parameters of the system. To have an aperture of dynamics behavior of parameters, the above equations should be solved to give the information on the form and order of each coefficient of the model and on variables related to the complex field. The resolution of Eq. (6) yields for $\gamma(\xi) \neq 0$ and for $T_\tau T_{\tau\tau} = 0$ to the similarity variable

$$T(\xi,\tau) = T_1(\xi)\tau + T_0(\xi), \quad (17)$$

where $T_1(\xi)$ and $T_0(\xi)$ are arbitrary functions. From Eq. (9), the effective propagation distance $Z(\xi)$ will be

$$Z(\xi) = -\frac{\sqrt{2}}{4\nu}\int_0^\xi \gamma(s)T_1(s)^3 ds. \quad (18)$$

Equation (11) gives the result

$$\alpha_3(\xi) = -3\gamma(\xi)T_1^2(\xi)A^{-2}(\xi). \quad (19)$$

$\alpha_3(\xi)$ has the physical sense of SS. The substitution of Eq. (17) into Eq. (12) tends to $d(\xi)T_{\xi\xi} + 3\gamma(\xi)T_\tau \rho_{\tau\tau} + \eta(\xi)T_\tau = 0$. As $\gamma(\xi) \neq 0$, $T_1(\xi) \neq 0$, and $T_{\xi\xi} = T_{1_{\xi\xi}}\tau + T_{0_{\xi\xi}}$, the phase of the envelope field can be written as

$$\rho(\xi,\tau) = \rho_3(\xi)\tau^3 + \rho_2(\xi)\tau^2 + \rho_1(\xi)\tau + \rho_0(\xi), \quad (20)$$

with

$$\rho_3(\xi) = -\frac{1}{18}\frac{d(\xi)T_1(\xi)_{\xi\xi}}{\gamma(\xi)T_1(\xi)},$$
$$\rho_2(\xi) = -\frac{1}{6}\frac{d(\xi)T_0(\xi)_{\xi\xi} + \eta(\xi)T_1(\xi)}{\gamma(\xi)T_1(\xi)}, \quad (21)$$

where $\rho_1(\xi)$ and $\rho_0(\xi)$ are arbitrary functions. Through relation Eq. (15), one finds that

$$C(\xi,\tau) = C_2(\xi)\tau^2 + C_1(\xi)\tau + C_0(\xi), \quad (22)$$

with

$$C_2(\xi) = -\frac{1}{2} \frac{T_1(\xi) d(\xi) T_1(\xi)_{\xi\xi}}{A(\xi)^2},$$

$$C_1(\xi) = -\frac{T_1(\xi)[d(\xi) T_0(\xi)_{\xi\xi} + T_1(\xi)^2 \eta(\xi)]}{A(\xi)^2}, \qquad (23)$$

$$C_0(\xi) = \frac{\gamma(\xi) T_1(\xi)^2}{A(\xi)^2} \left[3\rho_1(\xi) + \frac{1}{4} \frac{\sqrt{2} G T_1(\xi)}{\nu} \right].$$

$C(\xi,\tau)$ is the space- and time-modulated SPM. Equation (13) stands for

$$P(\xi,\tau) = P_2(\xi)\tau^2 + P_1(\xi)\tau + P_0(\xi), \qquad (24)$$

with

$$P_2(\xi) = \frac{1}{2} \frac{d(\xi) T_1(\xi)_{\xi\xi}}{T_1(\xi)} - \frac{d(\xi) T_1(\xi)_\xi{}^2}{T_1(\xi)^2},$$

$$P_1(\xi) = \eta(\xi) + \frac{d(\xi) T_0(\xi)_{\xi\xi}}{T_1(\xi)} - 2 \frac{d(\xi) T_1(\xi)_\xi T_0(\xi)_\xi}{T_1(\xi)^2},$$

$$P_0(\xi) = \frac{1}{4} \frac{\gamma(\xi) T_1(\xi)\sqrt{2}}{\nu} - 3\gamma(\xi)\rho_1(\xi) - \frac{d(\xi) T_0(\xi)_\xi{}^2}{T_1(\xi)^2}. \qquad (25)$$

$P(\xi,\tau)$ is the space- and time-modulated GVD. Through Eq. (7), we arrive at

$$\pm\sigma(\xi,\tau) = \sigma_4(\xi)\tau^4 + \sigma_3(\xi)\tau^3 + \sigma_2(\xi)\tau^2 + \sigma_1(\xi)\tau + \sigma_0(\xi), \qquad (26)$$

where the parameters $\sigma_4(\xi)$, $\sigma_3(\xi)$, $\sigma_2(\xi)$, $\sigma_1(\xi)$, and $\sigma_0(\xi)$ are expressed in Appendix B. $\pm\sigma(\xi,\tau)$ is the left- and right-hand side of the walk-off effect. Equation instead of relation Eq. (8) is transformed to

$$A(\xi) = A_0 \exp\left\{ \int_0^\xi f(s)ds \right\}, \qquad (27)$$

where A_0 is a constant and with

$$f = \mu_3(\xi)\tau^3 + \mu_2(\xi)\tau^2 + \mu_1(\xi)\tau + \mu_0(\xi) - \mu(\xi,\tau),$$

$$\mu(\xi,\tau) = \mu_3(\xi)\tau^3 + \mu_2(\xi)\tau^2 + \mu_1(\xi)\tau + 2\mu_0(\xi), \qquad (28)$$

where the parameters of the gain or loss term $\mu(\xi,\tau)$ are given in Appendix C. $\mu(\xi,\tau)$ is the space- and time-modulated gain or loss term. It follows from the above equations that the amplitude of the envelope field becomes

$$A(\xi) = A_0 \exp\left\{ \int_0^\xi -\mu_0(s)ds \right\}, \qquad (29)$$

with

$$\mu_0(\xi) = -\frac{1}{3} \frac{d(\xi) T_0(\xi)_\xi{}^2 \eta(\xi)}{\gamma(\xi) T_1(\xi)^2} - \frac{1}{3} \frac{d(\xi)^2 T_0(\xi)_\xi{}^2 T_0(\xi)_{\xi\xi}}{\gamma(\xi) T_1(\xi)^3}$$

$$+ \frac{1}{12} \frac{T_1(\xi)\sqrt{2}\eta(\xi)}{\nu} - \eta(\xi)\rho_1(\xi)$$

$$+ \frac{1}{12} \frac{\sqrt{2} d(\xi) T_0(\xi)_{\xi\xi}}{\nu} - d(\xi)\rho_0(\xi)_{\xi\xi}. \qquad (30)$$

The result coming from Eq. (14) is

$$\pm D(\xi,\tau) = D_6(\xi)\tau^6 + D_5(\xi)\tau^5 + D_4(\xi)\tau^4 + D_3(\xi)\tau^3 + D_2(\xi)\tau^2 + D_1(\xi)\tau + D_0(\xi), \qquad (31)$$

with $D_-(\xi) = -D_+(\xi)$ and where $D_6(\xi)$, $D_5(\xi)$, $D_4(\xi)$, $D_3(\xi)$, $D_2(\xi)$, $D_1(\xi)$, and $D_0(\xi)$ are given in Appendix D. $\pm D(\xi,\tau)$ is the left- and right-hand side of the space- and time-modulated linear birefringence.

The resolution of the above differential equations reveals and confirms the assumption of the space- and time-modulated variable of the TOD, gain or loss term, linear birefringence, SPM, and walk-off coefficients. More specifically, it reveals the optically active nature of the system through the left- and right-hand sides of mathematical expressions of the linear birefringence and walk-off term. In fact, the chirality, known as optical activity in optics, is the ability to rotate plane polarized light and this happens when the plane polarized light hits an optically active compound. The more compounds it hits, the more it rotates. Physically, when the polarized light leaves the chiral optical fiber which is optically active, we have to rotate the analyzer to allow the plane of light to pass through. This angle of rotation, called observed rotation, can be directed to the right-hand side, that is a positive rotation or clockwise rotation, also called dextrorotatory. In the case of which the analyzer has to be rotated to the left-hand side for the polarized light to pass through, that is a negative rotation or counterclockwise rotation, called levorotatory. Hence, the mathematical expressions of relation Eqs. (26) and (31) with positive signs refer to the dextrorotatory components and the ones with negative signs to the levorotatory components of the system. As we can see, they are equal in magnitude but opposite in sign.

We can observe through the above variable coefficients of the model that $P(\xi,\tau)$, $\mu(\xi,\tau)$, $D(\xi,\tau)$, $C(\xi,\tau)$, and $\sigma_3(\xi,\tau)$ are polynomials in τ with coefficients being functions of ξ. Parameters $d(\xi)$, $\gamma(\xi)$, $\alpha_3(\xi)$, and $\eta(\xi)$ are arbitrary functions, except the SS, which depends on the TOD and amplitude. Since the nonparaxial parameter $d(\xi)$, the differential gain or loss term $\eta(\xi)$, and third-order dispersion $\gamma(\xi)$ are major functions of the base equation coefficients, it appears from analytical results that they are are the main keys to control the amplitude, the SS, the GVD, the SPM, the walk-off term, and linear birefringence in optical fibers. Therefore, they can be considered as specific control parameters of the system. The TOD coefficient $\gamma(\xi)$ can also be used to control the effective propagation distance $Z(\xi)$. The gain or loss term of the induce optical activity $\mu(\xi,\tau)$ can be used to manage the optical activity on the amplitude $A(\xi)$, SS coefficient $\alpha_3(\xi)$, and on the SPM nonlinearity $C(\xi,\tau)$.

According to the MDT method [47–49,61], which is well-known and clearly derived by many authors, the first- and second-order of the complex field $V[Z(\xi), T(\xi,\tau)]$ are expressed by Akhmediev et al. [60]. It is good to mention that the first-order of the complex field $V[Z(\xi), T(\xi,\tau)]$ was found by Peregrine [40] and the second-order by Akhmediev et al. [62]. Later, Ankiewicz et al. [60] found the first- and second-order of the Hirota equation. By considering the correspondence $Z(\xi) = x$, $\frac{1}{\sqrt{2}} T(\xi,\tau) = t$, and $\nu = \alpha_3$, in this last reference,

the first-order complex field $V[Z(\xi), T(\xi, \tau)]$ yields

$$V_1[Z(\xi), T(\xi, \tau)] = \left[1 - \frac{G_1 + iH_1}{D_1}\right] \exp\{iZ(\xi)\}, \quad (32)$$

where

$$
\begin{aligned}
G_1 &= 4, \quad H_1 = 8Z(\xi), \\
D_1 &= 1 + [\sqrt{2}T(\xi, \tau) + 12\nu Z(\xi)]^2 + 4Z(\xi)^2.
\end{aligned}
\quad (33)
$$

The partial solution Eq. (32), is known as the Peregrine soliton [40]. Then, collecting this solution together with the founded amplitude and phase of the wave, we construct the first-order rational solution related to the nonparaxial chiral optical rogue wave given by

$$\psi_1 = A(\xi)\left[1 - \frac{G_1 + iH_1}{D_1}\right] \exp\{iZ(\xi) + i\rho(\xi, \tau)\}, \quad (34)$$

which result becomes

$$
\begin{aligned}
\psi_1 = A_0 \exp&\left\{-\int_0^\xi \mu_0(s)ds\right\} \\
&\times \left[1 - \frac{G_1 + iH_1}{D_1}\right] \exp\{iZ(\xi) + i\rho(\xi, \tau)\}. \quad (35)
\end{aligned}
$$

This first-order rational solution is used to describe the propagation of nonparaxial optical rogue wave in a fiber filled with chiral materials. For suitable choice of arbitrary parameters of the original Eq. (1), we can manage through a simultaneous controllability, the rogue wave structures with the specific control parameters. The second-order rational solution of the complex field $V[Z(\xi), T(\xi, \tau)]$ stands for

$$V_2[Z(\xi), T(\xi, \tau)] = \left[1 + \frac{G_2 + iZ(\xi)H_2}{D_2}\right] \exp i\{Z(\xi)\}, \quad (36)$$

where G_2, H_2, and D_2 are given by the relations

$$
\begin{aligned}
G_2 = &-48T^4 - 1152\sqrt{2}\nu ZT^3 - 144T^2[4Z^2(36\nu^2 + 1) + 1] \\
&- 576\sqrt{2}\nu ZT[12Z^2(12\nu^2 + 1) + 7] - 192Z^4 \\
&\times [216(6\nu^4 + \nu^2) + 5] - 864Z^2(44\nu^2 + 1) - 36,
\end{aligned}
$$

$$
\begin{aligned}
H_2 = &-96T^4 - 2304\sqrt{2}\nu ZT^3 - 96T^2[4Z^2(108\nu^2 + 1) - 3] \\
&- 1152\sqrt{2}\nu ZT[4Z^2(36\nu^2 + 1)] - 384Z^4(36\nu^2 + 1)^2 \\
&- 192Z^2(180\nu^2 + 1) + 360,
\end{aligned}
$$

$$
\begin{aligned}
D_2 = &8T^6 + 288\sqrt{2}\nu ZT^5 - 432Z^4(624\nu^4 - 40\nu^2 - 1) \\
&+ 36Z^2(556\nu^2 + 11) + 9 + 64Z^6(36\nu^2 + 1)^3 + 96\sqrt{2} \\
&\times ZT^3[12Z^2(60\nu^2 + 1) - 1] \\
&+ 12T^4[4Z^2(180\nu^2 + 1) + 1] \\
&+ 6T^2[16Z^4[216\nu^2(30\nu^2 + 1) - 1] \\
&- 24Z^2(60\nu^2 + 1) + 9] + 72\sqrt{2}\nu ZT[16Z^4(36\nu^2 + 1) \\
&+ 8Z^2(1 - 108\nu^2) + 17].
\end{aligned}
\quad (37)
$$

According to the same correspondence joined with the founded variables including the above solutions, the second-order rational solution, related to a particular solution of Eq. (1),

was obtained:

$$\psi_2 = A(\xi)\left[1 + \frac{G_2 + iZ(\xi)H_2}{D_2}\right] \exp\{iZ(\xi) + i\rho(\xi, \tau)\}. \quad (38)$$

Then, the construction of the second-order nonparaxial chiral optical rogue wave yields

$$
\begin{aligned}
\psi_2 = A_0 \exp&\left\{-\int_0^\xi \mu_0(s)ds\right\} \\
&\times \left[1 + \frac{G_2 + iZ(\xi)H_2}{D_2}\right] \exp\{iZ(\xi) + i\rho(\xi, \tau)\}. \quad (39)
\end{aligned}
$$

These second-order rational solutions arise due to the collision between two or more ultrashort pulses in the optical fiber. More specifically, they are nonparaxial chiral optical rogue waves which can propagate through a fiber filled with chiral materials. The particularity of these solutions is the simultaneous controllability of their amplitudes through the three specific control parameters, which can be used to manage the intensity and the shape of the waves. As the nonparaxiality, TOD, and differential gain or loss terms depend on specific control parameterts, they can therefore provide a more convenient and controlled environment to experimentally study specific optical communication problems.

III. DYNAMICS BEHAVIOR AND FEATURES OF COMBINED EFFECT ON NONPARAXIAL CHIRAL OPTICAL ROGUE WAVES

After the construction of the above solutions, the parameters are chosen to investigate the dynamics behavior and the features of combined effects on nonparaxial chiral optical rogue waves. Afterwards, we plot the specific control parameters of the system, the GVD, and the amplitudes of the envelope field in the left- and right-hand sides to have an aperture of their dynamic in the nonparaxial chiral optical fiber (see Figs. 1, 2, and 3).

Then, we alternate the sign of chiral parameters in both space and time in the first and second order of nonparaxial
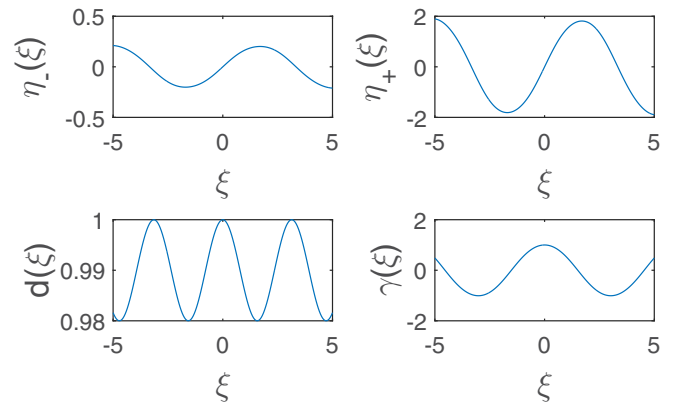

FIG. 1. Specific control parameters: the left- and right-hand side of the gain or loss differential term $\eta(\xi)$, nonparaxial parameter $d(\xi)$, and TOD $\gamma(\xi)$, where $\eta(\xi) = C_T sn(\xi, k_7)$, $d(\xi) = dn(\xi, k_5)$, $\gamma(\xi) = cn(\xi, k_6)$, and $C_T = 1 \pm KT_c$, with $k_5 = 0.2$, $k_6 = 0.4$, $k_7 = 0.5$, and $KT_c = 0.8$.
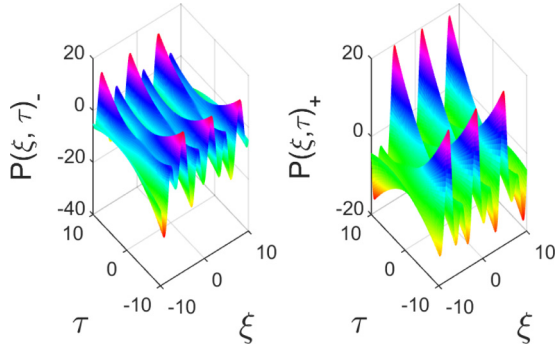
FIG. 2. The space- and time-modulated group velocity dispersion $P(\xi,\tau)$ on the left- and right-hand side, respectively, expressed in relation Eq. (24), where $\eta(\xi) = C_T sn(\xi,k_7)$, $d(\xi) = dn(\xi,k_5)$, $\gamma(\xi) = cn(\xi,k_6)$, $T_0(\xi) = sn(\xi,k_3)$, $T_1(\xi) = dn(\xi,k_3)$, $\rho_0(\xi) = dn(\xi,k_2)$, $\rho_1(\xi) = cn(\xi,k_1)$, and $C_T = 1 \pm KT_c$, with $k_1 = 0.3$, $k_2 = 0.5$, $k_3 = 0.6$, $k_4 = 0.4$, $k_5 = 0.2$, $k_6 = 0.4$, $k_7 = 0.5$, $\nu = 0.2$, and $KT_c = 0.8$.

FIG. 4. First-order nonparaxial chiral optical rogue waves on the left- and right-hand side of the rational solution given by Eq. (35), where $\eta(\xi) = C_T sn(\xi,k_7)$, $d(\xi) = dn(\xi,k_5)$, $\gamma(\xi) = cn(\xi,k_6)$, $T_0(\xi) = sn(\xi,k_3)$, $T_1(\xi) = dn(\xi,k_3)$, $\rho_0(\xi) = dn(\xi,k_2)$, $\rho_1(\xi) = cn(\xi,k_1)$, and $C_T = 1 \pm KT_c$, with $k_1 = 0.3$, $k_2 = 0.5$, $k_3 = 0.6$, $k_4 = 0.4$, $k_5 = 0.2$, $k_6 = 0.4$, $k_7 = 0.5$, $\nu = 0.2$, and $KT_c = 0.8$.

chiral optical rogue wave solutions to analyze their behavior and therefore to optimize the eventual stability of the solutions (see Figs. 4 and 5).

Figure 1 depicts the dynamical behavior of each specific parameter in the system. On the one hand, we can observe the influence of chiral nature of the differential gain or loss term through its weak peak in the left-hand side and high peak in the right-hand side. On the other hand, the amplitude and the width of each parameter depend on the value of their moduli $k_i (i = 5,6,7)$ and on the type of Jacobian elliptic function they carry (cn,dn,sn). The left- and right-hand sides of the space- and time-modulated group-velocity dispersion $P(\xi,\tau)$ are illustrated in Fig. 2 and expressed by relation Eq. (24) with their arbitrary Jacobian elliptic functions and moduli given in the figure caption. It can be seen that the structure of GVD differs from one side to the other. Figure 3 depicts the profiles of the amplitudes of the envelope field $A(\xi)$ on both sides. We remark on the trace of each evolution, the presence of two dark-bright collisions in the right-hand side and two bright-dark collisions in the left-hand side. These collisions are better observed through analytical simulation of the first- and second-order nonparaxial chiral optical rogue waves which
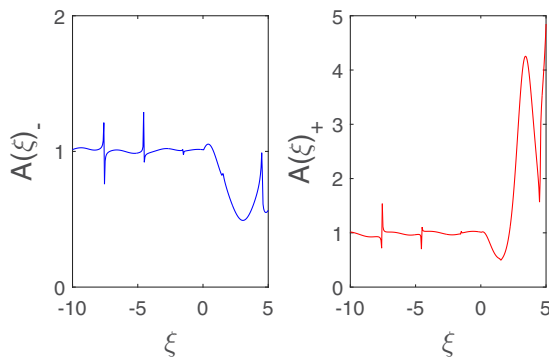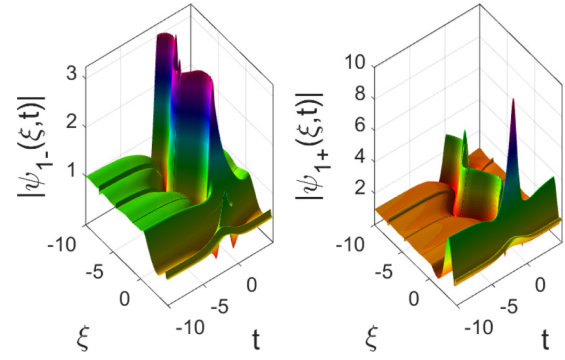
are illustrated in Figs. 4 and 5. Throughout these figures, we notice a main difference on the structure and on the amplitude of the first- and second-order in both sides. We also remark an energy transfer from the left-hand to right-hand side on each solution.

More specifically, in Fig. 3 we can see the contrast of optical activity in the sense of oscillation of each component of the amplitude as it increase then decrease on the left-hand side, whereas it decreases then increases on the right-hand side. Generally, in optically active media, components are equal in magnitude but different in sign. However, in this case, the equality of magnitude is affected by the differential gain or loss term $\eta(\xi) = (1 \pm KT_c)sn(\xi,k_7)$, which is responsible for the observed difference on both sides and, consequently, on both sides of the amplitude. It can be seen throughout Fig. 1 that the amplitude of the differential gain or loss term is four times higher in the right-hand side compare to the left-hand side. Now, when we look at the mathematical expression of the space- and time-modulated GVD, we denote that it depends also on the differential gain or loss term; however, GVD profiles are nearly equal in magnitude, as shown in Fig. 2. This

FIG. 3. The left- and right-hand side amplitude $A(\xi)$, presented in relation Eq. (29), where $\eta(\xi) = C_T sn(\xi,k_7)$, $d(\xi) = dn(\xi,k_5)$, $\gamma(\xi) = cn(\xi,k_6)$, $T_0(\xi) = sn(\xi,k_3)$, $T_1(\xi) = dn(\xi,k_3)$, $\rho_0(\xi) = dn(\xi,k_2)$, $\rho_1(\xi) = cn(\xi,k_1)$, and $C_T = 1 \pm KT_c$, with $k_1 = 0.3$, $k_2 = 0.5$, $k_3 = 0.6$, $k_4 = 0.4$, $k_5 = 0.2$, $k_6 = 0.4$, $k_7 = 0.5$, and $KT_c = 0.8$.
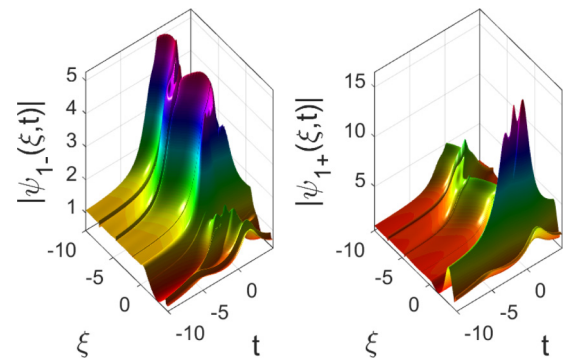
FIG. 5. Second-order nonparaxial chiral optical rogue waves on the left- and right-hand side of the rational solution given by Eq. (39), where $\eta(\xi) = C_T sn(\xi,k_7)$, $d(\xi) = dn(\xi,k_5)$, $\gamma(\xi) = cn(\xi,k_6)$, $T_0(\xi) = sn(\xi,k_3)$, $T_1(\xi) = dn(\xi,k_3)$, $\rho_0(\xi) = dn(\xi,k_2)$, $\rho_1(\xi) = cn(\xi,k_1)$, and $C_T = 1 \pm KT_c$, with $k_1 = 0.3$, $k_2 = 0.5$, $k_3 = 0.6$, $k_4 = 0.4$, $k_5 = 0.2$, $k_6 = 0.4$, $k_7 = 0.5$, $\nu = 0.2$, and $KT_c = 0.8$.

contrast is due to the fact that the differential gain or loss term plays a role of loss in the expression of the amplitude and the role of gain in the expression of GVD. This is an advantage for the waves, which become more stable as we can see in Figs. 4

and 5. As the vector NLS equations describe extreme waves with higher accuracy than the scalar NLS equation models, we are going to use the vector nonparaxial NLS equations to enrich the work.

IV. THE INFLUENCE OF COMBINED EFFECTS ON THE NUMERICAL SOLUTIONS OF VECTOR NONPARAXIAL NLS EQUATIONS WITH CONSTANT COEFFICIENTS

To illustrate the nonparaxiality, optical activity, and walk-off effects on the propagation of nonparaxial chiral optical rogue waves, we derive from the model obtained in Eq. (A25) the vector nonparaxial NLS equations with constant and modulated coefficients which governs the propagation of rogons in optical fibers filled with chiral materials. So doing, the coupled system of the nonparaxial NLS equation with constant coefficients is given by

$$d\psi_{1\xi\xi} + i\psi_{1\xi} + P\psi_{1\tau\tau} - i\gamma\psi_{1\tau\tau\tau} + i\mu\psi_1 \mp D\psi_1 - C(|\psi_1|^2 + |\psi_2|^2)\psi_1 + i\alpha_3(|\psi_1|^2 + |\psi_2|^2)\psi_{1\tau} + (\eta \pm i\sigma)\psi_{1\tau} = 0,$$

$$d\psi_{2\xi\xi} + i\psi_{2\xi} + P\psi_{2\tau\tau} - i\gamma\psi_{2\tau\tau\tau} + i\mu\psi_2 \mp D\psi_2 - C(|\psi_1|^2 + |\psi_2|^2)\psi_2 + i\alpha_3(|\psi_1|^2 + |\psi_2|^2)\psi_{2\tau} + (\eta \pm i\sigma)\psi_{2\tau} = 0.$$

$$(40)$$

To simplify the expressions of waves functions, we let $\psi_1(\xi,\tau) = u(\xi,\tau)$ and $\psi_2(\xi,\tau) = v(\xi,\tau)$. In this part of the work, we focus our attention on the generation and propagation of bright and dark rogue wave solutions when the nonparaxial effect arises fundamentally from chiral optical fibers. To study the influence of combined effects of the nonparaxiality, optical activity, and walk-off on optical rogue wave propagation, we used an algorithm scheme derived by Chamorro-Posada *et al.* [37], namely, difference-differential equation method that has a wider applicability on nonparaxial beam propagation methods. In this method, we used the finite difference formulas to approximate derivatives with respect to ξ coordinate, and then the fast Fourier transforms (FFTs) are used to compute efficiently the second- and third-order diffractions in the spectral domain.

The finite difference formulas for the derivatives are given in Appendix E. Substituting these formulas in the coupled nonparaxial NLS equations with constant coefficients, we obtained the difference-differential equations below:

$$u_{n+1}(\tau) = \frac{1}{2d + i\Delta\xi}\left[\left(4d - 2P\Delta\xi^2\frac{\partial^2}{\partial\tau^2} + 2i\gamma\Delta\xi^2\frac{\partial^3}{\partial\tau^3} - 2i\mu\Delta\xi^2 \pm 2\Delta\xi^2 D + 2C\Delta\xi^2(|u_n(\tau)|^2 + |v_n(\tau)|^2)\right.\right.$$

$$\left.\left. - 2i\alpha_3\Delta\xi^2(|u_n(\tau)|^2 + |v_n(\tau)|^2)\frac{\partial}{\partial\tau} - 2\Delta\xi^2(\eta \pm i\sigma)\frac{\partial}{\partial\tau}\right)u_n(\tau) - (2d - i\Delta\xi)u_{n-1}(\tau)\right],$$

$$v_{n+1}(\tau) = \frac{1}{2d + i\Delta\xi}\left[\left(4d - 2P\Delta\xi^2\frac{\partial^2}{\partial\tau^2} + 2i\gamma\Delta\xi^2\frac{\partial^3}{\partial\tau^3} - 2i\mu\Delta\xi^2 \pm 2\Delta\xi^2 D + 2C\Delta\xi^2(|u_n(\tau)|^2 + |v_n(\tau)|^2)\right.\right.$$

$$\left.\left. - 2i\alpha_3\Delta\xi^2(|u_n(\tau)|^2 + |v_n(\tau)|^2)\frac{\partial}{\partial\tau} - 2\Delta\xi^2(\eta \pm i\sigma)\frac{\partial}{\partial\tau}\right)v_n(\tau) - (2d - i\Delta\xi)v_{n-1}(\tau)\right]. \quad (41)$$

These equations define the explicit algorithm in which the effects of the transverse differential operators $\frac{\partial^2}{\partial\tau^2}$ and $\frac{\partial^3}{\partial\tau^3}$ are computed efficiently and accurately by the FFTs. An implementation on the index n gives us the numerical solutions of each component. We used as initial conditions, the rational solutions of the envelope fields [30], constructed by the DDT method, where we consider the correspondence $t \to \xi$ and $x \to \tau$:

$$u(\xi,\tau) = u_{01}\left(\frac{p^2\tau^2 + p^4\xi^2 + p\tau(\alpha_1 + \beta\theta_1) - i\alpha_1 p^2\xi + \beta\theta_1}{p^2\tau^2 + p^4\xi^2 + \beta(p\tau + 1)}\right)$$

$$v(\xi,\tau) = v_{01}\left(\frac{p^2\tau^2 + p^4\xi^2 + p\tau(\alpha_2 + \beta\theta_2) - i\alpha_2 p^2\xi + \beta\theta_2}{p^2\tau^2 + p^4\xi^2 + \beta(p\tau + 1)}\right), \quad (42)$$

where the parameters are

$$u_{01} = a_1\exp[i(q_1\tau - v_1\xi)] \quad v_{01} = a_1\exp[i(q_2\tau - v_2\xi)],$$

$$v_1 = q_1^2 + 2(a_1^2 + a_2^2) \quad v_2 = q_2^2 + 2(a_1^2 + a_2^2),$$

$$\alpha_1 = \frac{4p^2}{p^2 + 4q_1^2} \quad \alpha_2 = \frac{4p^2}{p^2 + 4q_2^2},$$

$$\theta_1 = \frac{2q_1 + ip}{2q_1 - ip} \quad \theta_2 = \frac{2q_2 + ip}{2q_2 - ip}, \quad (43)$$

with

$$p = 2\mathrm{Im}(\lambda + k), \quad \chi = \mathrm{Im}(k), \quad q_1 + q_2 = 2\mathrm{Re}(\lambda + k),$$

$$q_1 - q_2 = 2q, \quad \beta = \frac{p^3}{\chi(p^2 + 4q_1q_2)},$$

$$k = 2.36954 + 1.1972i,$$

$$\lambda = -1.69162 - 1.79721i. \quad (44)$$

To plot the numerical solutions, we choose appropriately, free functions $T_1(\xi)$, $T_0(\xi)$, $\mu(\xi)$, and $\gamma(\xi)$ and the Jacobian elliptic
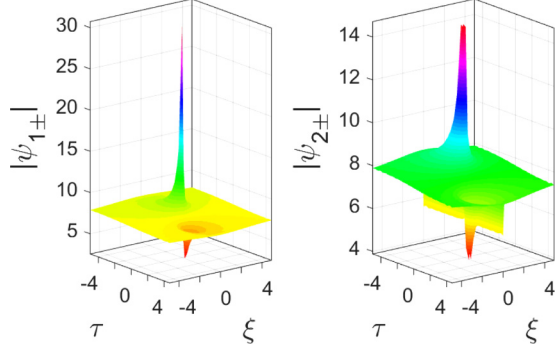
FIG. 6. Nonparaxial chiral optical vector rogue waves with constant coefficients on the right- and left-hand side $|\psi_{1,2}(\xi,\tau)|$, where the parameters are $a_1 = 3, a_2 = 3, d = 10, P = -0.5, \gamma = 0.4, \mu = 0.3, D = \pm 0.6, C = 2, \alpha3 = 0.2, \eta = 0.5, \sigma = \pm 0.1, k_1 = 0.3, k_2 = 0.5, k_3 = 0.6, k_4 = 0.4, k_5 = 0.2, k_6 = 0.4,$ and $k_7 = 0.5$. Here, the initial conditions take the form of exact solution Eqs. (42), (43), and (44).

functions below [64]:

$$dn(z,k) = 1 - \frac{k^2 \sin(z)^2}{2},$$

$$cn(z,k) = \cos(z) - k^2 \sin(z) \left[\frac{z - \sin(z)\cos(z)}{4} \right], \quad (45)$$

$$sn(z,k) = \sin(z) - k^2 \cos(z) \left[\frac{z - \sin(z)\cos(z)}{4} \right].$$

The parameters are chosen to be bounded in the intervals $-10 < \xi < 10$ and $-10 < \tau < 10$. Curves are plotted with the help of Matlab through a pseudospectral method. So doing, we obtained identical right- and left-hand sides of nonparaxial chiral optical vector rogue waves with constant coefficients (see Figs. 6, 7, and 8).

These representations showed us the rapid convergence of the pseudospectral method based on the difference-differential equation method [37] when $\Delta \xi / d \to 0$. In the case of constant coefficients, it can be seen that the vector nonparaxial
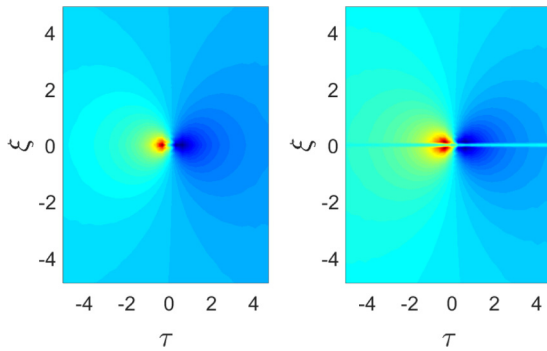
FIG. 7. Two-dimensional representations of the nonparaxial chiral optical vector rogue waves with constant coefficients in both sides, where the initial conditions take the form of exact solution Eqs. (42), (43), and (44) with the following parameters: $a_1 = 1, a_2 = 1, d = 100, P = -0.5, \gamma = 0.4, \mu = 0.3, D = \pm 0.6, C = 2, \alpha3 = 0.2, \eta = 0.5, \sigma = \pm 0.1, k_1 = 0.3, k_2 = 0.5, k_3 = 0.6, k_4 = 0.4, k_5 = 0.2, k_6 = 0.4,$ and $k_7 = 0.5$.
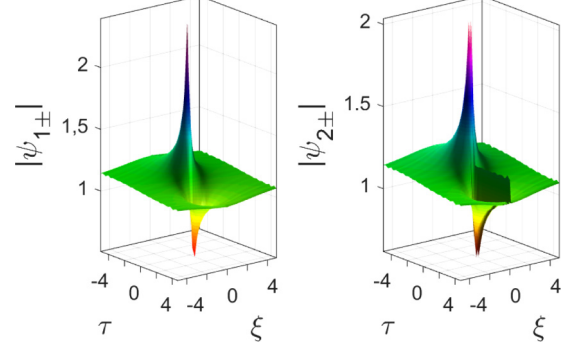
FIG. 8. Nonparaxial chiral optical vector rogue waves with constant coefficients in both sides, where the initial conditions are expressed in the form of exact solutions Eqs. (42), (43), and (44) with the parameters $a_1 = 1, a_2 = 1, d = 10, P = -0.5, \gamma = 0.4, \mu = 0.3, D = \pm 0.6, C = 2, \alpha3 = 0.2, \eta = 10, \sigma = \pm 10, k_1 = 0.3, k_2 = 0.5, k_3 = 0.6, k_4 = 0.4, k_5 = 0.2, k_6 = 0.4,$ and $k_7 = 0.5$.

chiral optical rogue waves are localized in space and time as usual rogue waves and that the forward and backward of each component are similar. We notice that the mixture of bright and dark structures on each component are due to

FIG. 9. The nonparaxial chiral optical rogue waves with management are derived from Eqs. (49), where the parameters of the base equations are given in relation Eqs. (47) and (46) and the initial conditions take the form of exact solutions given in relation Eqs. 42, 43, and 44, with the following arbitrary constants: $a_1 = 3, a_2 = 3, k_5 = 0.2, k_6 = 0.4, k_7 = 0.5, P(\xi,\tau) = dn(\xi,k)\tau^2 + cn(\xi,k)\tau + sn(\xi,k), KT_c = 0.8,$ and $C_T = 1 \pm KT_c$.

the coupling of vectorial model on the one hand, and to the interaction between waves as consequence of narrowness of the two components in the system on the other hand. The two-dimensional representations of Fig. 7 showed the limit of the extension of bright and dark spectral structures in the retarded time axis at $\tau = 0$. We can see how the intensity of each spectrum increases when $\tau \to 0$ and the attenuation when we are moving from each side of $\tau = 0$. We noted that the weak values of the walk-off are responsible for the wave smoothing.

V. INFLUENCE OF COMBINED EFFECTS ON THE VECTOR NONPARAXIAL CHIRAL NLS EQUATIONS WITH MODULATED COEFFICIENTS

To improve the description of the waves, we use the vector nonparaxial chiral NLS equations with modulated coefficients. From the model obtained in Eq. (A25), the coupled system of the nonparaxial NLS equations in chiral optical fibers with coupled space-dependence coupling field is expressed

as

$$d(\xi)\psi_{1\xi\xi} + i\psi_{1\xi} + P(\xi,\tau)\psi_{1\tau\tau} - i\gamma(\xi)\psi_{1\tau\tau\tau} + i\mu(\xi,\tau)\psi_1$$
$$\mp D(\xi,\tau)\psi_1 - C(\xi,\tau)(|\psi_1|^2 + |\psi_2|^2)\psi_1 + i\alpha_3(\xi)$$
$$\times (|\psi_1|^2 + |\psi_2|^2)\psi_{1\tau} + [\eta(\xi) \pm i\sigma(\xi,\tau)]\psi_{1\tau} = 0,$$
$$d(\xi)\psi_{2\xi\xi} + i\psi_{2\xi} + P(\xi,\tau)\psi_{2\tau\tau} - i\gamma(\xi)\psi_{2\tau\tau\tau} + i\mu(\xi,\tau)\psi_2$$
$$\mp D(\xi,\tau)\psi_2 - C(\xi,\tau)(|\psi_1|^2 + |\psi_2|^2)\psi_2 + i\alpha_3(\xi)$$
$$\times (|\psi_1|^2 + |\psi_2|^2)\psi_{2\tau} + [\eta(\xi) \pm i\sigma(\xi,\tau)]\psi_{2\tau} = 0. \quad (46)$$

It can been seen from Eqs. (2) that the differential gain and loss term $\eta(\xi)$, the self-steepening $\alpha_3(\xi)$, the gain or loss term $\mu(\xi,\tau)$, and the self-phase modulation $C(\xi,\tau)$ depend on chiral parameter T_c through the relation $C_T = 1 \pm K T_c$ and the linear birefringence $D(\xi,\tau)$ and walk-off term $\sigma(\xi,\tau)$ are functions of chiral parameter T_c. Considering the order of polynomials of each parameter of the number like Eq. (1) obtained from the analytical results, we can choose them as Jacobian elliptic functions for the good stability of the waves and their forms, arbitrarily

$$\alpha_3(\xi) = C_T \times cn(\xi,k), \; \eta(\xi) = C_T \times sn(\xi,k),$$
$$d(\xi) = dn(\xi,k), \; \gamma(\xi) = cn(\xi,k),$$
$$C(\xi,\tau) = [dn(\xi,k)\tau^2 + cn(\xi,k)\tau + sn(\xi,k)] \times C_T,$$
$$P(\xi,\tau) = -[dn(\xi,k)\tau^2 + cn(\xi,k)\tau + sn(\xi,k)],$$
$$\mu(\xi,\tau) = [dn(\xi,k)\tau^3 + cn(\xi,k)\tau^2 + sn(\xi,k)\tau + dn(\xi,k)] \times C_T,$$
$$\sigma(\xi,\tau) = [dn(\xi,k)\tau^4 + cn(\xi,k)\tau^3 + sn(\xi,k)\tau^2 + dn(\xi,k)\tau + cn(\xi,k)] \times KT_c,$$
$$D(\xi,\tau) = [dn(\xi,k)\tau^6 + cn(\xi,k)\tau^5 + sn(\xi,k)\tau^4 + dn(\xi,k)\tau^3 + cn(\xi,k)\tau^2 + sn(\xi,k)\tau + dn(\xi,k)]KT_c. \quad (47)$$

One may also choose them as polynomial functions but our interest is motivated by functions that can generate stable waves. As the propagation variable ξ tends to $n\Delta\xi$ in the discretized domain, the Jacobian elliptic functions take the form

$$dn(\xi,k) \to dn(n\Delta\xi,k) = 1 - \frac{k^2 \sin(n\Delta\xi)^2}{2},$$
$$cn(\xi,k) \to cn(n\Delta\xi,k) = \cos(n\Delta\xi) - k^2 \sin(n\Delta\xi)\left\{\frac{n\Delta\xi - \sin[n\Delta\xi\cos(n\Delta\xi)]}{4}\right\}, \quad (48)$$
$$sn(\xi,k) \to sn(n\Delta\xi,k) = \sin(n\Delta\xi) - k^2 \cos(n\Delta\xi)\left\{\frac{n\Delta\xi - \sin[n\Delta\xi\cos(n\Delta\xi)]}{4}\right\}.$$

It can be seen that, by splitting Eqs. (46) in the right- and left-hand sides, we obtained four coupled nonparaxial NLS equations which differ by the signs of linear birefringence and walk-off term. The substitution of the finite difference formulas in Eqs. (46) yields

$$u_{n+1}(\tau) = \frac{1}{2d(n\Delta\xi) + i\Delta\xi}\left[\left(4d(n\Delta\xi) - 2P(n\Delta\xi,\tau)\Delta\xi^2\frac{\partial^2}{\partial\tau^2} + 2i\gamma(n\Delta\xi)\Delta\xi^2\frac{\partial^3}{\partial\tau^3} - 2i\mu(n\Delta\xi,\tau)\Delta\xi^2 \pm 2\Delta\xi^2 D(n\Delta\xi,\tau)\right.\right.$$
$$+ 2C(n\Delta\xi,\tau)\Delta\xi^2(|u_n(\tau)|^2 + |v_n(\tau)|^2) - 2i\alpha_3(n\Delta\xi)\Delta\xi^2(|u_n(\tau)|^2 + |v_n(\tau)|^2)\frac{\partial}{\partial\tau}$$
$$\left.\left. - 2\Delta\xi^2(\eta(n\Delta\xi) \pm i\sigma(n\Delta\xi,\tau))\frac{\partial}{\partial\tau}\right)u_n(\tau) - (2d(n\Delta\xi,\tau) - i\Delta\xi u_{n-1}(\tau)\right],$$

$$v_{n+1}(\tau) = \frac{1}{2d(n\Delta\xi) + i\Delta\xi}\left[\left(4d(n\Delta\xi) - 2P(n\Delta\xi,\tau)\Delta\xi^2\frac{\partial^2}{\partial\tau^2} + 2i\gamma(n\Delta\xi)\Delta\xi^2\frac{\partial^3}{\partial\tau^3} - 2i\mu(n\Delta\xi,\tau)\Delta\xi^2 \pm 2\Delta\xi^2 D(n\Delta\xi,\tau)\right.\right.$$
$$+ 2C(n\Delta\xi,\tau)\Delta\xi^2(|u_n(\tau)|^2 + |v_n(\tau)|^2) - 2i\alpha_3(n\Delta\xi)\Delta\xi^2(|u_n(\tau)|^2 + |v_n(\tau)|^2)\frac{\partial}{\partial\tau}$$
$$\left.\left. - 2\Delta\xi^2(\eta(n\Delta\xi) \pm i\sigma(n\Delta\xi,\tau))\frac{\partial}{\partial\tau}\right)v_n(\tau) - (2d(n\Delta\xi,\tau) - i\Delta\xi v_{n-1}(\tau)\right]. \quad (49)$$

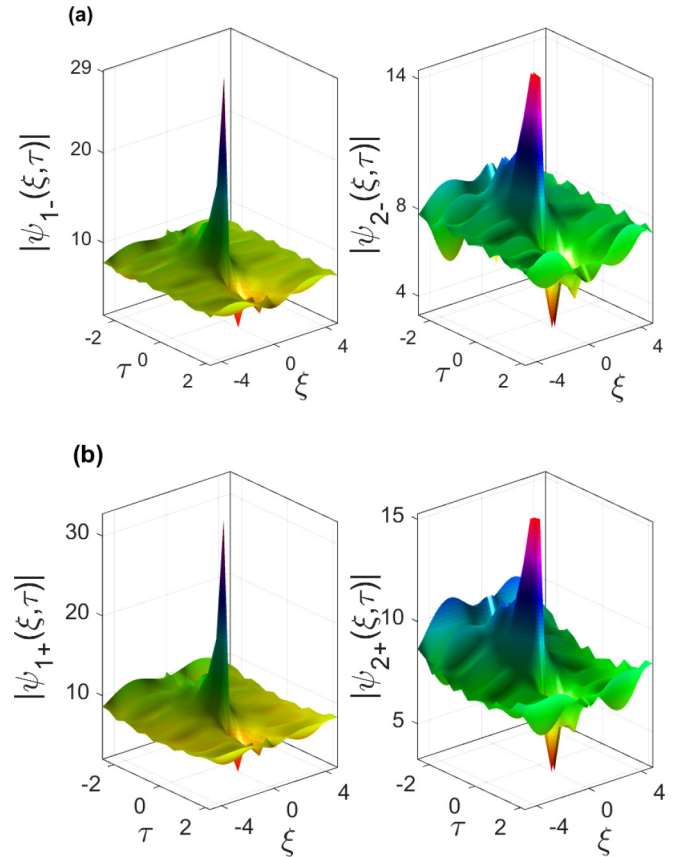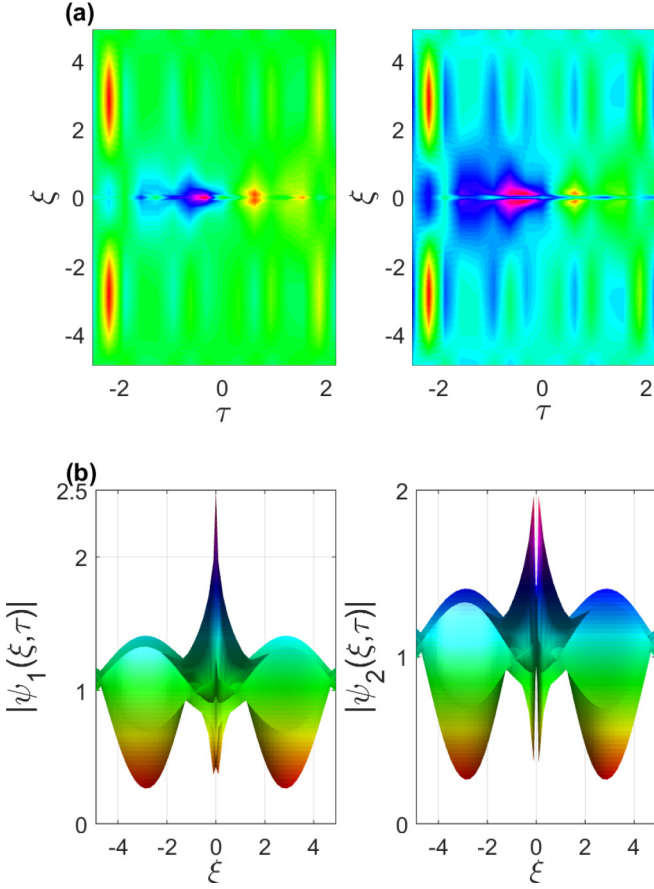FIG. 10. The two-dimensional representation of the nonparaxial chiral optical vector rogue waves with variable coefficients are derived from Eqs. (49), where the parameters of the base equations are given in relation Eqs. (47) and (46) and the initial conditions take the form of exact solutions given in relation Eqs. (42), (43) and (44), with the following arbitrary constants: $a_1 = 1, a_2 = 1, k_5 = 0.2, k_6 = 0.4, k_7 = 0.5, P(\xi,\tau) = dn(\xi,k)\tau^2 + cn(\xi,k)\tau + sn(\xi,k), KT_c = 0.8$, and $C_T = 1 \pm KT_c$.

By using the difference-differential equation method and fast Fourier transforms (FFTs), we plot the numerical solutions of the coupled nonparaxial chiral NLS equations of each beam (ψ_1 and ψ_2) in both sides, left (−) and right (+) (see Figs. 9–11).

Throughout these figures, we remark that the structure of each component is similar from one hand to the other but a notable difference is observed in the amplitude as we can see in Fig. 9. The two-dimensional representations depict in Fig. 10(a), the symmetries of the bright and dark maxima through the retarded time axis τ and the dark-dark symmetries through the propagation distance axis ξ in both side. On Fig. 10(b), we can observe a significant decrease of the envelope fields when we reduce the amplitudes of the seeding solutions. We also denote a similitude on the structure and amplitude in Figs. 11. The appearance of curvatures in the four components are due to the unity value of their moduli as expressed in Fig. 11.

VI. CONCLUSION

We derived both scalar and vector nonparaxial NLS equations with constant and modulated coefficients to improve
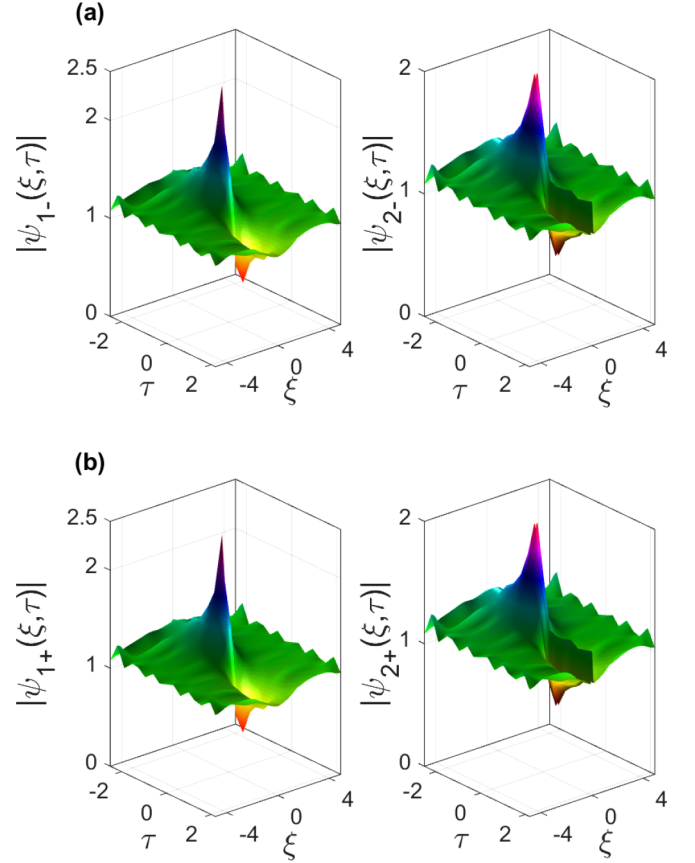
FIG. 11. Nonparaxial chiral optical vector rogue waves with modulated coefficients are derived from Eqs. (49) where the parameters of the base equations are given in relations Eqs. (47) and (46) and where the initial conditions take the form of exact solutions given in relations Eqs. (42), (43), and (44), with the following arbitrary constants: $a_1 = 1, a_2 = 1$ and $k_5 = k_6 = k_7 = 1, d(\xi) = 10 \times dn(\xi,k), P(\xi,\tau) = -(dn(\xi,k)\tau^2 + cn(\xi,k)\tau + sn(\xi,k)), KT_c = 0.8$, and $C_T = 1 \pm KT_c$.

the description of rogue waves propagation in optical fibers filled with chiral materials. Our models, in particular, verified the assumption of controllability on the one hand, and takes into account the parameters responsible for the nonparaxiality, optical activity, and walk-off effect, on the other hand. The first- and second-order nonparaxial chiral optical rogue waves were investigated by the MDT method. As the nonparaxiality, TOD, and differential gain or loss terms depend on specific control parameters $d(\xi)$, $\gamma(\xi)$, and $\eta(\xi)$, it appeared that they are the main keys to control the amplitude of the envelope fields, SS, GVD, SPM, walk-off effect, linear birefringence, and the effective propagation distance. Therefore, we have concluded that among previous models that have been studied before, the models derived in this work allowed us to improve the description of rogue waves and their control in chiral optical fibers with higher-order nonlinear effects. In these models, we also denoted the influences of TOD and differential gain or loss term. Then, the algorithm scheme derived for the nonparaxial beam propagation methods, namely, difference-differential equation method, was used to compute efficiently the diffractions in the spectral domain. After many numerical

simulation tests, we remarked that the increase or decrease of the three specific control parameters can affect the wave shape and the amplitude of each component. We have also shown that, among those specific control parameters, the nonparaxial coefficient has the most influential effect, whereas the two others that are differential gain or loss and walk-off terms are physically inactive. We found that in the absence of nonparaxial parameter, the influence of the two others are effective and equivalent. We also noticed that in the absence of two specific control parameters, the last one becomes the powerful influential effect in the system.

We improved our understanding through models under consideration of combined effects on rogue wave propagation in optical fibers filled with chiral materials. We have shown the necessity to take into account the parameters responsible of the simultaneous controllability of different effects in the system. Those parameters revealed the control key and the novel properties of nonparaxial chiral optical rogue wave solutions. For specific parameter values, usual rogue waves, such as the vector Peregrine, were obtained, showing the collisions between bright and dark rogue waves. The study of combined effects has allowed us to determine the powerful influence among the effects, and the nonparaxial effect was claimed to be the most influential one. The vector rogue wave solutions based on the vector nonparaxial NLS equations, which modeled the coupling of two nonlinear waves under the assumptions of nonparaxiality, optical activity, and walk-off, contributed to better control rogue wave phenomena in optical fibers filled with chiral materials and in a variety of complex dynamics.

APPENDIX A: THE DERIVATION OF THE HOMOGENEOUS HIGHER-ORDER NONPARAXIAL NLS IN CHIRAL OPTICAL FIBERS

We consider a model that satisfies both the breakdown of the paraxial approximation as well as the requirements of time-reversal symmetry and reciprocity through the Drude-Born-Federov formalism. Under this formalism, the adequate constitutive relations for the study of propagation of waves in chiral medium are expressed as [63–65]

$$\vec{D} = \varepsilon_n \vec{E} + \varepsilon_0 T_c \vec{\nabla} \times \vec{E}, \quad \vec{B} = \mu_0(\vec{H} + T_c \vec{\nabla} \times \vec{H}), \quad \text{(A1)}$$

where the flux densities $\vec{D}$ and $\vec{B}$ arise in response to the electric and magnetic field $\vec{E}$ and $\vec{H}$ propagating in the chiral medium with $\varepsilon_n = \varepsilon_0 + \varepsilon_2 |\vec{E}|^2$. Here, ε_0 and ε_2 are linear and nonlinear permittivity, respectively. μ_0 is the permeability and T_c the chiral parameter of the optical fiber. In the chiral optical medium, the predicted Maxwell equations can be written as

$$\vec{\nabla} \cdot \vec{D} = \rho_v, \quad \vec{\nabla} \cdot \vec{B} = 0,$$
$$\vec{\nabla} \times \vec{E} = -\frac{\partial \vec{B}}{\partial t}, \quad \vec{\nabla} \times \vec{H} = \vec{J} + \frac{\partial \vec{D}}{\partial t}, \quad \text{(A2)}$$

where the current density $\vec{J} = \sigma \vec{E}$ and the charge density ρ represents the sources for the electromagnetic field. The quantity σ is the electrical conductivity and v is the volume. Substituting Eq. (A1) into Eq. (A2), we obtain the following wave equation:

$$\nabla^2 \vec{E} + \mu_0 \varepsilon T^2 \frac{\partial^2 \vec{\nabla}^2 \vec{E}}{\partial t^2}$$
$$= \mu_0 \varepsilon_0 \frac{\partial^2 \vec{E}}{\partial t^2} + \mu_0 \sigma \frac{\partial \vec{E}}{\partial t} + \mu_0 \varepsilon_2 |\vec{E}|^2 \frac{\partial^2 \vec{E}}{\partial t^2}$$
$$+ 2\mu_0 \varepsilon_0 T \vec{\nabla} \times \frac{\partial^2 \vec{E}}{\partial t^2} + \mu_0 \varepsilon_2 T |\vec{E}|^2 \vec{\nabla} \times \frac{\partial^2 \vec{E}}{\partial t^2}$$
$$+ \mu_0 \sigma T \vec{\nabla} \times \frac{\partial \vec{E}}{\partial t}. \quad \text{(A3)}$$

The optical field $\vec{E}$ is represented by right-hand (R) or left-hand (L) polarizations in the z direction as

$$\vec{E}(\vec{r},t) = (\hat{x} \mp j\hat{y})A(\vec{r},t) \exp[-j(k_\pm z - \omega_0 t)]$$
$$= \vec{\psi}_{R,L} \exp[-j(k_\pm z - \omega_0 t)], \quad \text{(A4)}$$

where $\vec{\psi}_{R,L}$ is the complex envelope of the optical field in the nonlinear chiral medium, K is the wave number, and ω_0 is the frequency.

After evaluation of different derivations of $\vec{E}$ in x, y, and z directions in Eq. (A3), we neglect all the second-order terms, except the nonparaxial one. Considering that the wave is propagating in the z direction implies

$$K_x = K_y = 0, \quad E_z = 0. \quad \text{(A5)}$$

Therefore, Eq. (A3) is reduced in x, y, and z directions, respectively, as follows:

$$\left(1 - \mu_0 \varepsilon_0 T_c^2 \omega^2\right)\left[\frac{\partial^2 E_x}{\partial x^2} + \frac{\partial^2 E_x}{\partial y^2} + \frac{\partial^2 E_x}{\partial z^2}\right] - 2jK_z \frac{\partial E_x}{\partial z} - K_z^2 E_x$$
$$+ \mu_0 \varepsilon T_c^2 \left(\omega^2 K_z^2 E_x + 2jK_z\omega^2 \frac{\partial E_x}{\partial z} - 2jK_z^2 \omega \frac{\partial E_x}{\partial t} - K_z^2 \frac{\partial^2 E_x}{\partial t^2}\right)$$
$$= (\mu_0 \varepsilon_0 + \mu_0 \varepsilon_2 |\vec{E}|^2)\left[\frac{\partial^2 E_x}{\partial t^2} + 2j\omega \frac{\partial E_x}{\partial t} - \omega^2 E_x\right] + \mu_0 \sigma \left(\frac{\partial E_x}{\partial t} + j\omega E_x\right)$$
$$+ (2\mu_0 \varepsilon_0 T_c + \mu_0 \varepsilon_2 T_c |\vec{E}|^2)\left[\omega^2 \frac{\partial E_y}{\partial z} + jK_z\left(\frac{\partial^2 E_y}{\partial t^2} + 2j\omega \frac{\partial E_y}{\partial t} - \omega^2 E_y\right)\right] + \mu_0 \sigma T_c\left(-j\omega \frac{\partial E_y}{\partial z} + jK_z \frac{\partial E_y}{\partial t} - \omega K_z E_y\right),$$
$$\text{(A6)}$$

$$\left(1 - \mu_0\varepsilon_0 T_c^2\omega^2\right)\left[\frac{\partial^2 E_y}{\partial x^2} + \frac{\partial^2 E_y}{\partial y^2} + \frac{\partial^2 E_y}{\partial z^2}\right] - 2jK_z\frac{\partial E_y}{\partial z} - K_z^2 E_y$$

$$+\mu_0\varepsilon T_c^2\left(\omega^2 K_z^2 E_y + 2jK_z\omega^2\frac{\partial E_y}{\partial z} - 2jK_z^2\omega\frac{\partial E_y}{\partial t} - K_z^2\frac{\partial^2 E_y}{\partial t^2}\right)$$

$$= (\mu_0\varepsilon_0 + \mu_0\varepsilon_2|\vec{E}|^2)\left[\frac{\partial^2 E_y}{\partial t^2} + 2j\omega\frac{\partial E_y}{\partial t} - \omega^2 E_y\right] + \mu_0\sigma\left(\frac{\partial E_y}{\partial t} + j\omega E_y\right) + (2\mu_0\varepsilon_0 T + \mu_0\varepsilon_2 T|\vec{E}|^2)$$

$$\times\left[-\omega^2\frac{\partial E_x}{\partial z} - jK_z\left(\frac{\partial^2 E_x}{\partial t^2} + 2j\omega\frac{\partial E_x}{\partial t} - \omega^2 E_x\right)\right] + \mu_0\sigma T(j\omega\frac{\partial E_x}{\partial z} - jK_z\frac{\partial E_x}{\partial t} + \omega K_z E_x), \tag{A7}$$

$$[-(2\mu_0\varepsilon_0 T_c + \mu_0\varepsilon_2 T_c|\vec{E}|^2)\omega^2 + j\omega\mu_0\sigma T_c]\left[\frac{\partial E_y}{\partial x} - \frac{\partial E_x}{\partial y}\right] = 0. \tag{A8}$$

Equation (A8) leads to

$$\frac{\partial E_y}{\partial x} = \frac{\partial E_x}{\partial y} = cst, \quad E_y = E_y(z,t), \quad E_x = E_x(z,t). \tag{A9}$$

We multiply Eq. (A7) by $\pm j$, and we do the addition of Eqs. (A6) and (A7), where we consider the conditions given in relation Eq. (A9) and the following approximations:

$$\left|\frac{\partial E_x}{\partial t}\right| \ll |2j\omega E_x|, \quad \left|\frac{\partial^2 E_y}{\partial z^2}\right| \ll |2j\omega E_y|. \tag{A10}$$

Therefore, the alternative form of the wave equation can be written as

$$\left(1 - \mu_0\varepsilon_0 T_c^2\omega^2\right)\frac{\partial^2\psi_{R,L}}{\partial z^2} + \{-2jK_z + 2jK_z\omega^2\mu_0\varepsilon T_c^2 \pm j[(2\mu_0\varepsilon_0 T_c + \mu_0\varepsilon_2 T_c|\vec{E}|^2)\omega^2 - j\omega\mu_0\sigma T_c]\}\frac{\partial\psi_{R,L}}{\partial z}$$

$$+\{-K_z^2 + \mu_0\varepsilon_0 T_c^2\omega^2 K_z^2 + \omega^2(\mu_0\varepsilon_0 + \mu_0\varepsilon_2|\vec{E}|^2) - j\omega\mu_0\sigma \pm j[-jK_z\omega^2(2\mu_0\varepsilon_0 T_c + \mu_0\varepsilon_2 T_c|\vec{E}|^2)$$

$$-K_z\omega\mu_0\sigma T_c]\}\psi_{R,L} + \{-2jK_z^2\omega\mu_0\varepsilon_0 T_c^2 - \mu_0\sigma - 2j\omega(\mu_0\varepsilon_0 + \mu_0\varepsilon_2|\vec{E}|^2) \pm j[-2\omega K_z(2\mu_0\varepsilon_0 T_c$$

$$+\mu_0\varepsilon_2 T_c|\vec{E}|^2) + jK_z\mu_0\sigma T_c]\}\frac{\partial\psi_{R,L}}{\partial t} = 0, \tag{A11}$$

where $\psi_{R,L} = E_x \pm jE_y$. Then, the reference changing is

$$\psi_R = E_x + jE_y \quad \psi_L = E_x - jE_y,$$

$$E_x = \frac{\psi_R + \psi_L}{2} \quad E_y = \frac{\psi_R - \psi_L}{2}. \tag{A12}$$

The division of Eq. (A6) by $-2K_z$ yields

$$-\frac{\left(1 - \mu_0\varepsilon_0 T_c^2\omega^2\right)}{2K_z}\frac{\partial^2\psi_{R,L}}{\partial z^2} + j\left(1 - K_0^2 T_c^2\right)\frac{\partial\psi_{R,L}}{\partial z} \mp j\frac{K_0^2 T_c}{K_z}\frac{\partial\psi_{R,L}}{\partial z} + j\frac{\omega\mu_0\varepsilon_2}{K_z}|\psi_{R,L}|^2\frac{\partial\psi_{R,L}}{\partial t} \mp j\frac{\mu_0\varepsilon_2\omega^2 T_c}{2K_z}$$

$$\times|\psi_{R,L}|^2\frac{\partial\psi_{R,L}}{\partial z} + j\frac{K_0}{K_z c}\left(1 + K_z^2 T_c^2\right)\frac{\partial\psi_{R,L}}{\partial t} \pm \frac{j\omega\mu_0\sigma T_c}{2}\psi_{R,L} + \frac{1}{2}\left(K_z - K_z K_0^2 T_c^2 - \frac{K_0^2}{K_z}\right)\psi_{R,L}$$

$$-\frac{\mu_0\varepsilon_2\omega^2}{2K_z}|\psi_{R,L}|^2\psi_{R,L} \mp \frac{\omega^2}{2}\left(\mu_0\varepsilon_2 T_c|\psi_{R,L}|^2\right)\psi_{R,L} + j\frac{\omega\mu_0\sigma}{2K_z}\psi_{R,L} \mp K_0^2 T_c\psi_{R,L} \mp \frac{\omega\mu_0\sigma T}{2K_z}\frac{\partial\psi_{R,L}}{\partial z}$$

$$\pm\frac{\mu_0\sigma T_c}{2}\frac{\partial\psi_{R,L}}{\partial t} \pm j\frac{2K_0 T_c}{C}\frac{\partial\psi_{R,L}}{\partial t} + \frac{\mu_0\sigma}{2K_z}\frac{\partial\psi_{R,L}}{\partial t} \pm j\omega\mu_0\varepsilon_2 T_c|\psi_{R,L}|^2\frac{\partial\psi_{R,L}}{\partial t} = 0, \tag{A13}$$

where

$$K_0 = \frac{\omega}{c}, \quad \mu_0\varepsilon_0 c^2 = 1. \tag{A14}$$

The dispersion relation is given by

$$K_z = \frac{K_0}{1 \pm K_0 T_c}. \tag{A15}$$

For $K_0^2 T_c^2 \ll 1$, we get $K_z = K_0$. By neglecting the nonlinear diffraction, the second and the last terms of Eq. (A13), and for the following set of parameters become

$$v^2 = \frac{1}{\mu_0 \varepsilon_0}, \quad \alpha = \mu_0 \sigma, \quad \beta = \mu_0 \varepsilon_2, \quad K_0 = \frac{\omega}{v}, \quad z^* = \frac{z}{1 - K_0^2 T_c^2}. \tag{A16}$$

Equation (A13) takes the form

$$-\frac{1}{2K_0} \frac{\partial^2 \psi_{R,L}}{\partial z^{*2}} + j \frac{\partial \psi_{R,L}}{\partial z^*} + j \frac{1}{v} \frac{\partial \psi_{R,L}}{\partial t} + j \frac{\omega \alpha}{2K_0} (1 \pm K_0 T_c) \psi_{R,L} \mp K_0^2 T_c \psi_{R,L} - \frac{\beta \omega^2}{2K_0} (1 \pm K_0 T_c)$$

$$\times |\psi_{R,L}|^2 \psi_{R,L} + \frac{\alpha}{2K_0} (1 \pm K_0 T_c) \frac{\partial \psi_{R,L}}{\partial t} \pm \frac{j 2 K_0^2 T_c}{\omega} \frac{\partial \psi_{R,L}}{\partial t} + \frac{j \omega \beta}{K_0} (1 \pm K_0 T_c) |\psi_{R,L}|^2 \frac{\partial \psi_{R,L}}{\partial t} = 0. \tag{A17}$$

If we let

$$\psi_{R,L} = \phi, \text{ then } K = K_0 = K_z. \tag{A18}$$

Equation (A16) yields

$$-\frac{1}{2K} \frac{\partial^2 \phi}{\partial z^{*2}} + j \frac{\partial \phi}{\partial z^*} + j \frac{1}{v} \frac{\partial \phi}{\partial t} + j \frac{\omega \alpha}{2K} (1 \mp K T_c) \phi - \frac{\beta \omega^2}{2K} (1 \mp K T_c) |\phi|^2 \phi \mp K^2 T_c \phi$$

$$+ \frac{\alpha}{2K} (1 \pm K T_c) \frac{\partial \phi}{\partial t} \pm j \frac{2 K^2 T_c}{\omega} \frac{\partial \psi_{R,L}}{\partial t} + j \frac{\omega \beta}{K_0} (1 \pm K T_c) |\phi|^2 \frac{\partial \phi}{\partial t} = 0. \tag{A19}$$

The Taylor series of the wave number $K(\omega)$ at the third-order and the Fourier transform of $\Delta \omega$ and ΔK help to express in an approximate form, the second term of Eq. (A18) as

$$j \frac{1}{v} \frac{\partial \phi}{\partial t} = j \frac{1}{v_g} \frac{\partial \phi}{\partial t} + \frac{1}{2} K'' \frac{\partial^2 \phi}{\partial t^2} - j \frac{1}{6} K''' \frac{\partial^3 \phi}{\partial t^3}, \tag{A20}$$

where

$$K'' = \frac{\partial^2 K}{\partial \omega^2}, K''' = \frac{\partial^3 K}{\partial \omega^3}, K' = \frac{1}{v_g} = \frac{\partial K}{\partial \omega}. \tag{A21}$$

Then, for the following change of variable:

$$
\begin{aligned}
t' &= t - \frac{1}{v_g} z^* \\
z' &= z^*,
\end{aligned}
\Rightarrow
\begin{aligned}
\frac{\partial}{\partial t} &\rightarrow \frac{\partial}{\partial t'} \\
\frac{\partial}{\partial z^*} &\rightarrow \frac{\partial}{\partial z'} - \frac{1}{v_g} \frac{\partial}{\partial t'},
\end{aligned}
\tag{A22}
$$

Eq. (A19) stands for

$$-\frac{1}{2K} \frac{\partial^2 \phi}{\partial z'^2} + j \frac{\partial \phi}{\partial z'} + \frac{1}{2} \left(K'' - \frac{K'^2}{K} \right) \frac{\partial^2 \phi}{\partial t'^2} - j \frac{1}{6} K''' \frac{\partial^3 \phi}{\partial t'^3} + j \frac{\omega \alpha}{2K} (1 \pm K T_c) \phi - \frac{\beta \omega^2}{2K} (1 \mp K T_c) |\phi|^2 \phi \mp K^2 T \phi$$

$$+ \frac{\alpha}{2K} (1 \pm K T_c) \frac{\partial \phi}{\partial t'} \pm j \frac{2 K^2 T_c}{\omega} \frac{\partial \phi}{\partial t'} + j \frac{\omega \beta}{K} |\phi|^2 (1 \pm K T_c) \frac{\partial \phi}{\partial t'} = 0, \tag{A23}$$

where $K' = \frac{\partial K}{\partial \omega} = \frac{1}{v_g}$ is the inverse of group-velocity, $K'' = \frac{\partial K'}{\partial \omega}$ is the group-velocity dispersion (GVD) coefficient, which can take the plus and minus signs ($\pm$), representing the anomalous and normal dispersion regimes, respectively. The parameter $K''' = \frac{\partial K''}{\partial \omega}$ is the third-order dispersion (TOD) term. In the fourth term, the attenuation coefficient α is weighted toward the chiral parameter T_c. The factor to $|\phi|^2 \phi$ is the self-phase modulation (SPM) and the term $K^2 T_c \phi$ occurs as an additional correction to the chirality of the fiber. The expressions at the eighth and ninth positions are the differential gain or loss term and the walk-off effect. The last term has the physical sense of self-steepening (SS) and is necessary to perform the description of spontaneous waves.

The new variables, namely,

$$q = \frac{\omega_0^{2/3} \beta^{1/3}}{(2K_0)^{1/3}} \phi, \quad \xi = \frac{\omega_0^{2/3} \beta^{1/3}}{(2K_0)^{1/3}} z', \quad d = -\frac{\beta^{1/3} \omega_0^{2/3}}{(2k_0)^{4/3}},$$

$$\eta = \frac{\alpha C_T}{\sqrt{K''} \omega_0^{1/3} \beta^{1/6} (2k_0)^{5/6}}, \quad \tau = \frac{\omega_0^{1/3} \beta^{1/16}}{\sqrt{K''} (2K_0)^{1/6}} t',$$

$$\gamma = \frac{K'''}{6} \frac{\beta^{1/6} \omega_0^{1/3}}{(2K_0)^{1/6} (K'')^{3/2}}, \quad C_T = 1 \mp T_c K,$$

$$
\Gamma = \frac{\omega_0^{1/3}\alpha}{(2K_0)^{1/3}\beta^{1/3}}, \quad \mu = C_T\Gamma, \quad P = \frac{1}{2}\left(1 - \frac{k'^2}{K''k_0}\right),
$$

$$
\sigma_3 = \frac{k_0 T_c (2k_0)^{7/6}}{\sqrt{K''}\,\omega_0^{4/3}\beta^{1/6}}, \quad D = \frac{K^2 T_c (2K_0)^{1/3}}{\beta^{1/3}\omega_0^{2/3}},
$$

$$
\alpha_3 = \frac{C_T (2K_0)^{5/6}\beta^{1/6}}{\sqrt{K''}\,\omega_0^{2/3}K_0}, \tag{A24}
$$

allow us to express for $q(\xi,\tau) = \psi(\xi,\tau)$, and Eq. (A23) in the form

$$
d\frac{\partial^2\psi}{\partial\xi^2} + j\frac{\partial\psi}{\partial\xi} + P\frac{\partial^2\psi}{\partial\tau^2} - j\gamma\frac{\partial^3\psi}{\partial\tau^3} + j\mu\psi \mp D\psi - C_T|\psi|^2\psi + j\alpha_3|\psi|^2\frac{\partial\psi}{\partial\tau} + \eta\frac{\partial\psi}{\partial\tau} \pm j\sigma_3\frac{\partial\psi}{\partial\tau} = 0. \tag{A25}
$$

Equation (A25) is the higher-order nonparaxial chiral NLSE and can be used to describe the propagation of the right-hand ($+$) and left-hand ($-$) polarized rogue waves in a higher-order dispersive and nonlinear chiral optical fiber. For $d = 0$, $P = \frac{1}{2}$, $T_c = 0$, $C_T = 1$, $D = 0$, $\gamma = 0$, $\mu = 0$, $\eta = 0$, and $\sigma_3 = 0$, Eq. (A25) stands for the standard NLS equation.

APPENDIX B: THE PARAMETERS OF THE WALK-OFF EFFECT $\sigma(\xi,\tau)$

$$
\sigma_4(\xi) = -\frac{1}{3}\frac{d(\xi)^2 T_1(\xi)_\xi^2 T_1(\xi)_{\xi\xi}}{T_1(\xi)^3\gamma(\xi)} + \frac{1}{12}\frac{d(\xi)^2 T_1(\xi)_{\xi\xi}^2}{T_1(\xi)^2\gamma(\xi)} - \frac{1}{9}\frac{d(\xi)T_1(\xi)_\xi\left(\frac{d(\xi)T_1(\xi)_{\xi\xi}}{\gamma(\xi)T_1(\xi)}\right)_\xi}{T_1(\xi)}, \tag{B1}
$$

$$
\sigma_3(\xi) = -\frac{2}{3}\frac{d(\xi)^2 T_1(\xi)_\xi^2 T_0(\xi)_{\xi\xi}}{T_1(\xi)^3\gamma(\xi)} - \frac{2}{3}\frac{d(\xi)^2 T_1(\xi)_\xi T_0(\xi)_\xi T_1(\xi)_{\xi\xi}}{T_1(\xi)^3\gamma(\xi)} - \frac{2}{3}\frac{d(\xi)T1_z^2\eta(\xi)}{T_1(\xi)^2\gamma(\xi)} + \frac{1}{3}\frac{d(\xi)T_1(\xi)_\xi\left(\frac{d(\xi)T_0(\xi)_{\xi\xi}+\eta(\xi)T_1(\xi)}{\gamma(\xi)T_1(\xi)}\right)_\xi}{T_1(\xi)}
$$

$$
+\frac{1}{3}\frac{d\xi\, T_1(\xi)_{\xi\xi}\eta(\xi)}{\gamma(\xi)T_1(\xi)} + \frac{1}{3}\frac{d(\xi)^2 T_1(\xi)_{\xi\xi}T_0(\xi)_{\xi\xi}}{T_1(\xi)^2\gamma(\xi)} + \frac{1}{9}\frac{d(\xi)T_0(\xi)_\xi\left(\frac{d\xi\, T_1(\xi)_{\xi\xi}}{\gamma(\xi)T_1(\xi)}\right)_\xi}{T_1(\xi)}, \tag{B2}
$$

$$
\sigma_2(\xi) = 2\frac{d(\xi)T1(\xi)_\xi^2\rho_1(\xi)}{T_1(\xi)^2} - 2\frac{d(\xi)T_1(\xi)_\xi\rho_1(\xi)_\xi}{T_1(\xi)} - \frac{d(\xi)T_1(\xi)_{\xi\xi}\rho_1(\xi)}{T_1(\xi)} + \frac{2}{3}\frac{d(\xi)T_0(\xi)_{\xi\xi}\eta(\xi)}{\gamma(\xi)T_1(\xi)} - \frac{4}{3}\frac{d(\xi)T_1(\xi)_\xi^2\eta(\xi)}{T_1(\xi)^2\gamma(\xi)}
$$

$$
+\frac{1}{3}\frac{\eta(\xi)^2}{\gamma(\xi)} + \frac{1}{3}\frac{d(\xi)T_0(\xi)_\xi\left(\frac{d(\xi)T_0(\xi)_{\xi\xi}+\eta(\xi)T_1(\xi)}{\gamma(\xi)T_1(\xi)}\right)_\xi}{T_1(\xi)} + \frac{1}{3}\frac{d(\xi)^2 T_0(\xi)_{\xi\xi}^2}{\gamma(\xi)T_1(\xi)^2} + \frac{1}{12}\frac{\sqrt{2}d(\xi)T_1(\xi)_{\xi\xi}}{\nu}
$$

$$
-\frac{4}{3}\frac{d(\xi)^2 T_1(\xi)_\xi T_0(\xi)_\xi T_0(\xi)_{\xi\xi}}{T_1(\xi)^3\gamma(\xi)} - \frac{1}{3}\frac{d(\xi)^2 T_0(\xi)_\xi^2 T_1(\xi)_{\xi\xi}}{T_1(\xi)^3\gamma(\xi)}, \tag{B3}
$$

$$
\sigma_1(\xi) = -2\,\eta(\xi)\rho_1(\xi) - 2\frac{d(\xi)T_1(\xi)_\xi\rho_0(\xi)_\xi}{T_1(\xi)} - 2\frac{d(\xi)T_0(\xi)_{\xi\xi}\rho_1(\xi)}{T_1(\xi)} + \frac{1}{6}\frac{\sqrt{2}T_1(\xi)\eta(\xi)}{\nu} - 2\frac{d(\xi)T_0(\xi)_\xi\rho_1(\xi)_\xi}{T_1(\xi)}
$$

$$
+4\frac{d(\xi)\,T_1(\xi)_\xi T_0(\xi)_\xi\rho_1(\xi)}{T_1(\xi)^2} - \frac{2}{3}\frac{d(\xi)T_0(\xi)_\xi^2\eta(\xi)}{T_1(\xi)^2\gamma(\xi)} + \frac{1}{6}\frac{\sqrt{2}d(\xi)T_0(\xi)_{\xi\xi}}{\nu} - \frac{2}{3}\frac{d(\xi)^2 T_0(\xi)_\xi^2 T_0(\xi)_{\xi\xi}}{T_1(\xi)^3\gamma(\xi)} - \frac{T_1(\xi)_\xi}{T_1(\xi)}, \tag{B4}
$$

$$
\sigma_0(\xi) = -12\frac{\sqrt{2}\gamma(\xi)T_1(\xi)\rho_1(\xi)}{\nu} - \frac{T_0(\xi)_\xi}{T_1(\xi)} + 3\gamma(\xi)\rho_1(\xi)^2 + 2\frac{d(\xi)\,T_0(\xi)_\xi^2\rho_1(\xi)}{T_1(\xi)^2} - 2\frac{d(\xi)T_0(\xi)_\xi\rho_0(\xi)_\xi}{T_1(\xi)}. \tag{B5}
$$

APPENDIX C: THE PARAMETERS OF THE GAIN OR LOSS TERM $\mu(\xi,\tau)$

$$
\mu_3(\xi) = -\frac{1}{3}\frac{d(\xi)^2 T_1(\xi)_\xi^2 T_1(\xi)_{\xi\xi}}{T_1(\xi)^3\gamma(\xi)} + \frac{1}{18}d(\xi)\left(\frac{d(\xi)T_1(\xi)_{\xi\xi}}{\gamma(\xi)T_1(\xi)}\right)_{\xi\xi}, \tag{C1}
$$

$$
\mu_2(\xi) = \frac{1}{6}\frac{\eta(\xi)d(\xi)T_1(\xi)_{\xi\xi}}{\gamma(\xi)T_1(\xi)} - \frac{1}{3}\frac{d(\xi)T_1(\xi)_\xi^2\eta(\xi)}{T_1(\xi)^2\gamma(\xi)} - \frac{2}{3}\frac{d(\xi)^2 T_1(\xi)_\xi T_0(\xi)_\xi T_1(\xi)_{\xi\xi}}{T_1(\xi)^3\gamma(\xi)} - \frac{1}{3}\frac{d(\xi)^2 T_1(\xi)_\xi^2 T_0(\xi)_{\xi\xi}}{T_1(\xi)^3\gamma(\xi)}
$$

$$
+\frac{1}{6}d(\xi)\left(\frac{d(\xi)T_0(\xi)_{\xi\xi}+\eta(\xi)T_1(\xi)}{\gamma(\xi)T_1(\xi)}\right)_{\xi\xi}, \tag{C2}
$$

$$
\mu_1(\xi) = -\frac{2}{3}\frac{d(\xi)T_1(\xi)_\xi T_0(\xi)_\xi\eta(\xi)}{T_1(\xi)^2\gamma(\xi)} + \frac{1}{3}\frac{\eta(\xi)d(\xi)T_0(\xi)_{\xi\xi}}{\gamma(\xi)T_1(\xi)} + \frac{1}{3}\frac{\eta(\xi)^2}{\gamma(\xi)} - \frac{2}{3}\frac{d(\xi)^2 T_1(\xi)_\xi T_0(\xi)_\xi T_0(\xi)_{\xi\xi}}{T_1(\xi)^3\gamma(\xi)}
$$

$$
-\frac{1}{3}\frac{d(\xi)^2 T_0(\xi)_\xi^2 T_1(\xi)_{\xi\xi}}{T_1(\xi)^3\gamma(\xi)} + \frac{1}{12}\frac{\sqrt{2}d(\xi)T_1(\xi)_{\xi\xi}}{\nu} - d(\xi)\rho_1(\xi)_{\xi\xi}, \tag{C3}
$$

$$\mu_0(\xi) = -\frac{1}{3}\frac{d(\xi)T_0(\xi)_\xi^2\eta(\xi)}{\gamma(\xi)T_1(\xi)^2} - \frac{1}{3}\frac{d(\xi)^2 T_0(\xi)_\xi^2 T_0(\xi)_{\xi\xi}}{\gamma(\xi)T_1(\xi)^3}$$

$$+\frac{1}{12}\frac{T_1(\xi)\sqrt{2}\eta(\xi)}{\nu} - \eta(\xi)\rho_1(\xi) + \frac{1}{12}\frac{\sqrt{2}d(\xi)T_0(\xi)_{\xi\xi}}{\nu} - d(\xi)\rho_0(\xi)_{\xi\xi}. \tag{C4}$$

APPENDIX D: THE PARAMETERS OF THE LINEAR BIREFRINGENCE $D(\xi,\tau)$

$$D_6(\xi) = -\frac{d(\xi)^2 T_1(\xi)_\xi T_1(\xi)_{\xi\xi}\frac{d(\xi)T_1(\xi)_{\xi\xi}}{\gamma(\xi)T_1(\xi)}_\xi}{54\,\gamma(\xi)T_1(\xi)^2} - \frac{d(\xi)^3 T_1(\xi)_{\xi\xi}^3}{216\,\gamma(\xi)^2 T_1(\xi)^3} + \frac{1}{36}\frac{d(\xi)^3 T_1(\xi)_\xi^2 T_1(\xi)_{\xi\xi}^2}{T_1(\xi)^4\gamma(\xi)^2}, \tag{D1}$$

$$D_5(\xi) = \frac{1}{9}\frac{d(\xi)^2 T_1(\xi)_\xi^2 T_1(\xi)_{\xi\xi}\eta(\xi)}{T_1(\xi)^3\gamma(\xi)^2} - \frac{d(\xi)^2 T_0(\xi)_\xi T_1(\xi)_{\xi\xi}\left(\frac{d(\xi)T_1(\xi)_{\xi\xi}}{\gamma(\xi)T_1(\xi)}\right)_\xi}{54\,\gamma(\xi)T_1(\xi)^2}$$

$$-\frac{1}{18}\frac{d(\xi)^2 T_1(\xi)_\xi T_1(\xi)_{\xi\xi}\left(\frac{d(\xi)T_0(\xi)_{\xi\xi}+\eta(\xi)T_1(\xi)}{\gamma(\xi)T_1(\xi)}\right)_\xi}{\gamma(\xi)T_1(\xi)^2} - \frac{d(\xi)^2 T_1(\xi)_\xi T_0(\xi)_{\xi\xi}\left(\frac{d(\xi)T_1(\xi)_{\xi\xi}}{\gamma(\xi)T_1(\xi)}\right)_\xi}{54\,\gamma(\xi)T_1(\xi)^2}$$

$$+\frac{1}{18}\frac{d(\xi)^3 T_1(\xi)_\xi T_0(\xi)_\xi T_1(\xi)_{\xi\xi}^2}{T_1(\xi)^4\gamma(\xi)^2} + \frac{1}{9}\frac{d(\xi)^3 T_1(\xi)_\xi^2 T_1(\xi)_{\xi\xi}T_0(\xi)_{\xi\xi}}{T_1(\xi)^4\gamma(\xi)^2} - \frac{1}{36}\frac{d(\xi)^2 T_1(\xi)_{\xi\xi}^2\eta(\xi)}{\gamma(\xi)^2 T_1(\xi)^2}$$

$$-\frac{1}{27}\frac{d(\xi)T_1(\xi)_\xi\eta(\xi)\left(\frac{d(\xi)T_1(\xi)_{\xi\xi}}{\gamma(\xi)T_1(\xi)}\right)_\xi}{\gamma(\xi)T_1(\xi)} - \frac{1}{36}\frac{d(\xi)^3 T_1(\xi)_{\xi\xi}^2 T_0(\xi)_{\xi\xi}}{T_1(\xi)^3\gamma(\xi)^2}, \tag{D2}$$

$$D_4(\xi) = -\frac{1}{3}\frac{d(\xi)^2 T_1(\xi)_\xi^2 T_1(\xi)_{\xi\xi}\rho_1(\xi)}{T_1(\xi)^3\gamma(\xi)} + \frac{2}{9}\frac{d(\xi)^2 T_1(\xi)_\xi^2 T_0(\xi)_{\xi\xi}\eta(\xi)}{T_1(\xi)^3\gamma(\xi)^2}$$

$$-\frac{1}{18}\frac{d(\xi)^2 T_0(\xi)_\xi T_1(\xi)_{\xi\xi}\left(\frac{d(\xi)T_0(\xi)_{\xi\xi}+\eta(\xi)T_1(\xi)}{\gamma(\xi)T_1(\xi)}\right)_\xi}{\gamma(\xi)T_1(\xi)^2} + \frac{1}{3}\frac{d(\xi)^2 T_1(\xi)_\xi T_1(\xi)_{\xi\xi}\rho_1(\xi)_\xi}{\gamma(\xi)T_1(\xi)^2}$$

$$-\frac{1}{9}\frac{d(\xi)^2 T_1(\xi)_\xi T_0(\xi)_{\xi\xi}\left(\frac{d(\xi)T_0(\xi)_{\xi\xi}+\eta(\xi)T_1(\xi)}{\gamma(\xi)T_1(\xi)}\right)_\xi}{\gamma(\xi)T_1(\xi)^2} + \frac{1}{36}\frac{d(\xi)^3 T_0(\xi)_\xi^2 T_1(\xi)_{\xi\xi}^2}{T_1(\xi)^4\gamma(\xi)^2} - \frac{1}{9}\frac{d(\xi)^2 T_1(\xi)_{\xi\xi}T_0(\xi)_{\xi\xi}\eta(\xi)}{\gamma(\xi)^2 T_1(\xi)^2}$$

$$+\frac{1}{9}\frac{d(\xi)T_1(\xi)_\xi\rho_1(\xi)\left(\frac{d(\xi)T_1(\xi)_{\xi\xi}}{\gamma(\xi)T_1(\xi)}\right)_\xi}{T_1(\xi)} + \frac{1}{9}\frac{d(\xi)T_1(\xi)_\xi^2\eta(\xi)^2}{\gamma(\xi)^2 T_1(\xi)^2} - \frac{\sqrt{2}d(\xi)^2 T_1(\xi)_{\xi\xi}^2}{144\,\nu\,\gamma(\xi)T_1(\xi)}$$

$$+\frac{2}{9}\frac{d(\xi)^3 T_1(\xi)_\xi T_0(\xi)_\xi T_1(\xi)_{\xi\xi}T_0(\xi)_{\xi\xi}}{T_1(\xi)^4\gamma(\xi)^2} + \frac{2}{9}\frac{d(\xi)^2 T_1(\xi)_\xi T_0(\xi)_\xi T_1(\xi)_{\xi\xi}\eta(\xi)}{T_1(\xi)^3\gamma(\xi)^2}$$

$$+\frac{1}{9}\frac{d(\xi)^3 T_1(\xi)_\xi^2 T_0(\xi)_{\xi\xi}^2}{T_1(\xi)^4\gamma(\xi)^2} + \frac{1}{12}\frac{d(\xi)^2 T_1(\xi)_{\xi\xi}^2\rho_1(\xi)}{\gamma(\xi)T_1(\xi)^2} - \frac{1}{18}\frac{d(\xi)^3 T_1(\xi)_{\xi\xi}T_0(\xi)_{\xi\xi}^2}{T_1(\xi)^3\gamma(\xi)^2} - \frac{1}{18}\frac{d(\xi)T_1(\xi)_{\xi\xi}\eta(\xi)^2}{\gamma(\xi)^2 T_1(\xi)}$$

$$-\frac{1}{9}\frac{d(\xi)T_1(\xi)_\xi\eta(\xi)\left(\frac{d(\xi)T_0(\xi)_{\xi\xi}+\eta(\xi)T_1(\xi)}{\gamma(\xi)T_1(\xi)}\right)_\xi}{\gamma(\xi)T_1(\xi)} - \frac{1}{27}\frac{d(\xi)\eta(\xi)T_0(\xi)_\xi\left(\frac{d(\xi)T_1(\xi)_{\xi\xi}}{\gamma(\xi)T_1(\xi)}\right)_\xi}{\gamma(\xi)T_1(\xi)}, \tag{D3}$$

$$D_3(\xi) = \frac{2}{9}\frac{d(\xi)^3 T_1(\xi)_\xi T_0(\xi)_\xi T_0(\xi)_{\xi\xi}^2}{T_1(\xi)^4\gamma(\xi)^2} - \frac{1}{9}\frac{d(\xi)T_0(\xi)_\xi\eta(\xi)\left(\frac{d(\xi)T_0(\xi)_{\xi\xi}+\eta(\xi)T_1(\xi)}{\gamma(\xi)T_1(\xi)}\right)_\xi}{\gamma(\xi)T_1(\xi)}$$

$$+\frac{2}{9}\frac{d(\xi)T_1(\xi)_\xi T_0(\xi)_\xi\eta(\xi)^2}{T_1(\xi)^2\gamma(\xi)^2} + \frac{1}{9}\frac{d(\xi)T_0(\xi)_\xi\rho_1(\xi)\frac{d(\xi)T_1(\xi)_{\xi\xi}}{\gamma(\xi)T_1(\xi)}_\xi}{T_1(\xi)} - \frac{1}{9}\frac{d(\xi)^2 T_0(\xi)_{\xi\xi}^2\eta(\xi)}{T_1(\xi)^2\gamma(\xi)^2} + \frac{1}{6}\frac{T_1(\xi)_\xi d(\xi)T_1(\xi)_{\xi\xi}}{\gamma(\xi)T_1(\xi)^2}$$

$$-\frac{d(\xi)T_1(\xi)_{\xi\xi}}{\gamma(\xi)T_1(\xi)}_\xi - \frac{1}{9}\frac{d(\xi)T_0(\xi)_{\xi\xi}\eta(\xi)^2}{\gamma(\xi)^2 T_1(\xi)} - \frac{1}{27}\frac{\eta(\xi)^3}{\gamma(\xi)^2} + \frac{1}{3}\frac{d(\xi)^2 T_0(\xi)_\xi T_1(\xi)_{\xi\xi}\rho_1(\xi)_\xi}{\gamma(\xi)T_1(\xi)^2} + \frac{1}{3}\frac{d(\xi)^2 T_1(\xi)_\xi T_1(\xi)_{\xi\xi}\rho_0(\xi)_\xi}{\gamma(\xi)T_1(\xi)^2}$$

$$+\frac{2}{3}\frac{d(\xi)^2 T_1(\xi)_\xi T_0(\xi)_{\xi\xi}\rho_1(\xi)_\xi}{\gamma(\xi)T_1(\xi)^2} - \frac{\sqrt{2}d(\xi)T_1(\xi)_{\xi\xi}\eta(\xi)}{648\,\gamma(\xi)\nu} - \frac{2}{3}\frac{d(\xi)T_1(\xi)_\xi^2\eta(\xi)\rho_1(\xi)}{\gamma(\xi)T_1(\xi)^2} + \frac{4}{9}\frac{d(\xi)^2 T_1(\xi)_\xi T_0(\xi)_\xi T_0(\xi)_{\xi\xi}\eta(\xi)}{T_1(\xi)^3\gamma(\xi)^2}$$

$$-\frac{2}{3}\frac{d(\xi)^2 T_1(\xi)_\xi T_0(\xi)_\xi T_1(\xi)_{\xi\xi}\rho_1(\xi)}{T_1(\xi)^3\gamma(\xi)} - \frac{1}{36}\frac{\sqrt{2}d(\xi)^2 T_1(\xi)_{\xi\xi}T_0(\xi)_{\xi\xi}}{\gamma(\xi)T_1(\xi)\nu} + \frac{1}{3}\frac{T_1(\xi)_\xi d(\xi)\rho_1(\xi)\left(\frac{d(\xi)T_0(\xi)_{\xi\xi}+\eta(\xi)T_1(\xi)}{\gamma(\xi)T_1(\xi)}\right)_\xi}{T_1(\xi)}$$

$$-\frac{2}{3}\frac{d(\xi)^2 T_1(\xi)_\xi^2 T_0(\xi)_{\xi\xi}\rho_1(\xi)}{T_1(\xi)^3\gamma(\xi)}+\frac{1}{9}\frac{d(\xi)^2 T_0(\xi)_\xi^2 T_1(\xi)_{\xi\xi}\eta(\xi)}{T_1(\xi)^3\gamma(\xi)^2}+\frac{1}{3}\frac{d(\xi)^2 T_1(\xi)_{\xi\xi} T_0(\xi)_{\xi\xi}\rho_1(\xi)}{\gamma(\xi)T_1(\xi)^2}$$

$$+\frac{1}{3}\frac{d(\xi)T_1(\xi)_{\xi\xi}\eta(\xi)\rho_1(\xi)}{\gamma(\xi)T_1(\xi)}+\frac{1}{9}\frac{d(\xi)^3 T_0(\xi)_\xi^2 T_1(\xi)_{\xi\xi} T_0(\xi)_{\xi\xi}}{T_1(\xi)^4\gamma(\xi)^2}+\frac{2}{3}\frac{T_1(\xi)_\xi d(\xi)\eta(\xi)\rho_1(\xi)_\xi}{\gamma(\xi)T_1(\xi)}$$

$$-\frac{1}{9}\frac{d(\xi)^2 T_0(\xi)_\xi T_0(\xi)_{\xi\xi}\left(\frac{d(\xi)T_0(\xi)_{\xi\xi}+\eta(\xi)T_1(\xi)}{\gamma(\xi)T_1(\xi)}\right)_\xi}{\gamma(\xi)T_1(\xi)^2}-\frac{1}{27}\frac{d(\xi)^3 T_0(\xi)_\xi^3}{T_1(\xi)^3\gamma(\xi)^2}-\frac{1}{18}\frac{d(\xi)T_1(\xi)_{\xi\xi}}{\gamma(\xi)T_1(\xi)},\tag{D4}$$

$$D_2(\xi)=\frac{1}{3}\frac{\eta(\xi)^2\rho_1(\xi)}{\gamma(\xi)}+\frac{1}{3}\frac{d(\xi)T_0(\xi)_\xi\rho_1(\xi)\left(\frac{d(\xi)T_0(\xi)_{\xi\xi}+\eta(\xi)T_1(\xi)}{\gamma(\xi)T_1(\xi)}\right)_\xi}{T_1(\xi)}$$

$$+\frac{2}{3}\frac{d(\xi)T_0(\xi)_{\xi\xi}\eta(\xi)\rho_1(\xi)}{\gamma(\xi)T_1(\xi)}-\frac{1}{3}\frac{d(\xi)^2 T_0(\xi)_\xi^2 T_1(\xi)_{\xi\xi}\rho_1(\xi)}{T_1(\xi)^3\gamma(\xi)}+\frac{2}{9}\frac{d(\xi)^2 T_0(\xi)_\xi^2 T_0(\xi)_{\xi\xi}\eta(\xi)}{T_1(\xi)^3\gamma(\xi)^2}$$

$$-\frac{1}{6}\frac{d(\xi)T_0(\xi)_{\xi\xi}+\eta(\xi)T_1(\xi)}{\gamma(\xi)T_1(\xi)}-\frac{1}{36}\frac{T_1(\xi)\sqrt{2}\eta(\xi)^2}{\nu\,\gamma(\xi)}+\frac{1}{12}\frac{\sqrt{2}d(\xi)T_1(\xi)_{\xi\xi}\rho_1(\xi)}{\nu}+\frac{1}{6}\frac{T_0(\xi)_\xi d(\xi)T_1(\xi)_{\xi\xi}}{\gamma(\xi)T_1(\xi)^2}$$

$$+\frac{1}{3}\frac{T_1(\xi)_\xi d(\xi)T_0(\xi)_{\xi\xi}}{\gamma(\xi)T_1(\xi)^2}-\frac{1}{6}\frac{d(\xi)T_0(\xi)_{\xi\xi}+\eta(\xi)T_1(\xi)}{\gamma(\xi)T_1(\xi)_\xi}+\frac{2}{3}\frac{d(\xi)T_1(\xi)_\xi\eta(\xi)\rho_0(\xi)_\xi}{\gamma(\xi)T_1(\xi)}+\frac{2}{3}\frac{d(\xi)T_0(\xi)_\xi\eta(\xi)\rho_1(\xi)_\xi}{\gamma(\xi)T_1(\xi)}$$

$$+\frac{2}{3}\frac{d(\xi)^2 T_1(\xi)_\xi T_0(\xi)_{\xi\xi}\rho_0(\xi)_\xi}{\gamma(\xi)T_1(\xi)^2}-\frac{1}{36}\frac{\sqrt{2}d(\xi)^2 T_0(\xi)_{\xi\xi}^2}{\nu\,\gamma(\xi)T_1(\xi)}-\frac{1}{18}\frac{\sqrt{2}d(\xi)T_0(\xi)_{\xi\xi}\eta(\xi)}{\nu\,\gamma(\xi)}$$

$$+\frac{1}{3}\frac{d(\xi)^2 T_0(\xi)_\xi T_1(\xi)_{\xi\xi}\rho_0(\xi)_\xi}{\gamma(\xi)T_1(\xi)^2}+\frac{2}{3}\frac{d(\xi)^2 T_0(\xi)_\xi T_0(\xi)_{\xi\xi}\rho_1(\xi)_\xi}{\gamma(\xi)T_1(\xi)^2}+\frac{1}{3}\frac{d(\xi)^2 T_0(\xi)_{\xi\xi}^2\rho_1(\xi)}{\gamma(\xi)T_1(\xi)^2}-\frac{1}{2}\frac{d(\xi)T_1(\xi)_{\xi\xi}\rho_1(\xi)^2}{T_1(\xi)}$$

$$+\frac{d(\xi)T_1(\xi)_\xi^2\rho_1(\xi)^2}{T_1(\xi)^2}+\frac{1}{3}\frac{T_1(\xi)_\xi\eta(\xi)}{\gamma(\xi)T_1(\xi)}-\frac{4}{3}\frac{d(\xi)^2 T_1(\xi)_\xi T_0(\xi)_\xi T_0(\xi)_{\xi\xi}\rho_1(\xi)}{T_1(\xi)^3\gamma(\xi)}$$

$$-\frac{4}{3}\frac{d(\xi)T_1(\xi)_\xi T_0(\xi)_\xi\eta(\xi)\rho_1(\xi)}{\gamma(\xi)T_1(\xi)^2}+\frac{1}{9}\frac{d(\xi)T_0(\xi)_\xi^2\eta(\xi)^2}{T_1(\xi)^2\gamma(\xi)^2}-2\frac{d(\xi)T_1(\xi)_\xi\rho_1(\xi)\rho_1(\xi)_\xi}{T_1(\xi)}+\frac{1}{9}\frac{d(\xi)^3 T_0(\xi)_\xi^2 T_0(\xi)_{\xi\xi}^2}{T_1(\xi)^4\gamma(\xi)^2},\tag{D5}$$

$$D_1(\xi)=\frac{1}{6}\frac{\sqrt{2}d(\xi)T_0(\xi)_{\xi\xi}\rho_1(\xi)}{\nu}-2\frac{d(\xi)T_0(\xi)_\xi\rho_1(\xi)\rho_1(\xi)_\xi}{T_1(\xi)}+\frac{2}{3}\frac{d(\xi)^2 T_0(\xi)_\xi T_0(\xi)_{\xi\xi}\rho_0(\xi)_\xi}{\gamma(\xi)T_1(\xi)^2}-\frac{2}{3}\frac{d(\xi)^2 T_0(\xi)_\xi^2 T_0(\xi)_{\xi\xi}\rho_1(\xi)}{T_1(\xi)^3\gamma(\xi)}$$

$$+\frac{1}{6}\frac{T_1(\xi)\sqrt{2}\eta(\xi)\rho_1(\xi)}{\nu}-2\frac{d(\xi)T_1(\xi)_\xi\rho_1(\xi)\rho_0(\xi)_\xi}{T_1(\xi)}+2\frac{d(\xi)T_1(\xi)_\xi T_0(\xi)_\xi\rho_1(\xi)^2}{T_1(\xi)^2}-\frac{T_1(\xi)_\xi\rho_1(\xi)}{T_1(\xi)}+\rho_1(\xi)_\xi$$

$$+\frac{1}{3}\frac{T_0(\xi)_\xi\eta(\xi)}{\gamma(\xi)T_1(\xi)}+\rho_1(\xi)-\eta(\xi)\rho_1(\xi)^2-\frac{d(\xi)T_0(\xi)_{\xi\xi}\rho_1(\xi)^2}{T_1(\xi)}+\frac{1}{3}\frac{d(\xi)T_0(\xi)_\xi T_0(\xi)_{\xi\xi}}{\gamma(\xi)T_1(\xi)^2}$$

$$+\frac{2}{3}\frac{d(\xi)T_0(\xi)_\xi\eta(\xi)\rho_0(\xi)_\xi}{\gamma(\xi)T_1(\xi)}-\frac{2}{3}\frac{d(\xi)T_0(\xi)_\xi^2\eta(\xi)\rho_1(\xi)}{\gamma(\xi)T_1(\xi)^2},\tag{D6}$$

$$D_0(\xi)=-2\frac{d(\xi)T_0(\xi)_\xi\rho_1(\xi)\rho_0(\xi)_\xi}{T_1(\xi)}-\frac{1}{4}\frac{\sqrt{2}\gamma(\xi)T_1(\xi)\rho_1(\xi)^2}{\nu}+\frac{1}{3}\frac{d(\xi)T_1(\xi)_{\xi\xi}}{T_1(\xi)}$$

$$+\frac{d(\xi)T_0(\xi)_\xi^2\rho_1(\xi)^2}{T_1(\xi)^2}-\frac{T_0(\xi)_\xi\rho_1(\xi)}{T_1(\xi)}+\gamma(\xi)\rho_1(\xi)^3.\tag{D7}$$

APPENDIX E: THE FINITE DIFFERENCE FORMULAE FOR THE DERIVATIVES

$$\left[\frac{\partial^2 u(\xi,\tau)}{\partial\xi^2}\right]_{\xi=n\Delta\xi}=\frac{u_{n+1}(\tau)-2u_n(\tau)+u_{n-1}(\tau)}{\Delta\xi^2}+0(\Delta\xi^2),$$

$$\left[\frac{\partial u(\xi,\tau)}{\partial\xi}\right]_{\xi=n\Delta\xi}=\frac{u_{n+1}(\tau)-u_{n-1}(\tau)}{2\Delta\xi}+0(\Delta\xi^2),\tag{E1}$$

$$\left[\frac{\partial^2 v(\xi,\tau)}{\partial\xi^2}\right]_{\xi=n\Delta\xi}=\frac{v_{n+1}(\tau)-2v_n(\tau)+v_{n-1}(\tau)}{\Delta\xi^2}+0(\Delta\xi^2),$$

$$\left[\frac{\partial v(\xi,\tau)}{\partial\xi}\right]_{\xi=n\Delta\xi}=\frac{v_{n+1}(\tau)-v_{n-1}(\tau)}{2\Delta\xi}+0(\Delta\xi^2),\tag{E2}$$

where

$$u_n(\tau) \equiv u(n\Delta\xi, \tau)$$
$$u_{n-1}(\tau) \equiv u((n-1)\Delta\xi, \tau) \qquad \text{(E3)}$$
$$u_{n+1}(\tau) \equiv f(u_n(\tau), u_{n-1}(\tau), v_n(\tau))$$

$$v_n(\tau) \equiv v(n\Delta\xi, \tau)$$
$$v_{n-1}(\tau) \equiv v((n-1)\Delta\xi, \tau) \qquad \text{(E4)}$$
$$v_{n+1}(\tau) \equiv f(v_n(\tau), v_{n-1}(\tau), u_n(\tau))$$

[1] N. Engheta and M. W. Kowarz, J. Appl. Phys. **67**, 639 (1990).

[2] V. Prelog, Science **193**, 17 (1976).

[3] T. Verbit, G. Koeckelberghs, and B. Champagne, Opt. Mater. Express **4**, 2663 (2014).

[4] S. B. Singham, J. Chem. Phys. **87**, 1873 (1987).

[5] R. T. Co, K. Harigaya, and Y. Nomura, Phys. Rev. Lett. **118**, 101801 (2017).

[6] P. L. Guennec, J. Math. Phys. **41**, 5954 (2000).

[7] E. Yomba and G.-A. Zakeri, Chaos **26**, 083115 (2016).

[8] P. K. Choudhury and T. Yoshino, Optik **113**, 89 (2002).

[9] C. Rizza, A. D. DiFalco, M. Scalora, and A. Ciattoni, Phys. Rev. Lett. **115**, 057401 (2015).

[10] N. Akhmediev and E. Pelinovsky, Eur. Phys. J. Special Topics **185**, 1 (2010).

[11] B. Frisquet *et al.*, Sci. Rep. **6**, 20785 (2016).

[12] J. M. Dudley, F. Dias, M. Erkintalo, and G. Genty, Nat. Photonics **8**, 755 (2014).

[13] D. R. Solli, C. Ropers, P. Koonath, and B. Jalali, Nature (London) **450**, 1054 (2007).

[14] D. Buccoliero, H. Steffensen, H. Ebendorff-Heidepriem, T. M. Monro, and O. Bang, Opt. Express **19**, 17973 (2011).

[15] P. Muller, C. Garrett, and A. Osborne, Oceanography **18**, 66 (2005).

[16] Y. V. Bludov, V. V. Konotop, and N. Akhmediev, Opt. Lett. **34**, 3015 (2009).

[17] Y. V. Bludov, V. V. Konotop, and N. Akhmediev, Eur. Phys. J.: Spec. Top. **185**, 169 (2010).

[18] Y. V. Bludov, V. V. Konotop, and N. Akhmediev, Phys. Rev. A **80**, 033610 (2009).

[19] S. Loomba, H. Kaur, R. Gupta, C. N. Kumar, and T. S. Raju, Phys. Rev. E **89**, 052915 (2014).

[20] Y. V. Bludov, R. Driben, V. V. Konotop, and B. A. Malomed, J. Opt. **15**, 064010 (2013).

[21] L. Wen, L. Li, Z. D. Li, S. W. Song, X. F. Zhang, and W. M. Liu, Eur. Phys. J. D **64**, 473 (2011).

[22] Z. Yan, Commun. Theor. Phys. **54**, 947 (2010).

[23] J. M. Soto-Crespo, N. Devine, and N. Akhmediev, Phys. Rev. Lett. **116**, 103901 (2016).

[24] M. Onorato, S. Residori, U. Bortolozzo, A. Montina, and F. T. Arecchi, Phys. Rep. **528**, 47 (2013).

[25] A. Slunyaev, Eur. Phys. J. Spec. Top. **185**, 67 (2010).

[26] C. Kharif and J. Touboul, Eur. Phys. J. Spec. Top. **185**, 159 (2010).

[27] G. P. Agrawal, *Nonlinear Fiber Optics*, 2nd ed. (Acdemic Press, New York, 1995).

[28] *Optical Fiber Communications III*, edited by I. P. Kaminow and T. L. Koch (Academic Press, New York, 1997).

[29] L. J. Richardson, W. Forysiak, and N. J. Doran, IEEE Photonics Technol. Lett. **13**, 209 (2001).

[30] F. Baronio, M. Conforti, A. Degasperis, S. Lombardo, M. Onorato, and S. Wabnitz, Phys. Rev. Lett. **113**, 034101 (2014).

[31] C. Bonatto, M. Feyereisen, S. Barland, M. Giudici, C. Masoller, J. R. R. Leite, and J. R. Tredicce, Phys. Rev. lett. **107**, 053901 (2011).

[32] A. Chabchoub, N. P. Hoffmann, and N. Akhmediev, Phys. Rev. Lett. **106**, 204502 (2011).

[33] H. Bailung, S. K. Sharma, and Y. Nakamura, Phys. Rev. Lett. **107**, 255005 (2011).

[34] C. Lecaplain, Ph. Grelu, J. M. Soto-Crespo, and N. Akhmediev, Phys. Rev. Lett. **108**, 233901 (2012).

[35] G. Baruch, G. Fibich, and S. Tsynkov, Opt. Express **16**, 13323 (2008).

[36] P. Chamorro-Posada, G. S. McDonald, and G. H. C. New, J. Mod. Opt. **45**, 1111 (1998).

[37] P. Chamorro-Posada, G. S. McDonald, and G. H. C. New, Opt. Commun. **192**, 1 (2001).

[38] S. I. Fewo, H. Moussambi, and T. C. Kofane, Phys. Scr. **84**, 035002 (2011).

[39] F. Biancalana and C. Creatore, Opt. Express **16**, 14882 (2008).

[40] D. H. Peregrine, J. Aust. Math. Soc. Series B, Appl. Math. **25**, 16 (1983).

[41] S. Chen, J. M. Soto-Crespo, and Ph. Grelu, Opt. Express **23**, 349 (2015).

[42] J. He, L. Wang, L. Li, K. Porsezian, and R. Erdélyi, Phys. Rev. E **89**, 062917 (2014).

[43] F. Baronio, A. Degasperis, M. Conforti, and S. Wabnitz, Phys. Rev. Lett. **109**, 044102 (2012).

[44] F. Baronio, M. Conforti, A. Degasperis, and S. Lombardo, Phys. Rev. Lett. **111**, 114101 (2013).

[45] S. Chen, J. M. Soto-Crespo, and Ph. Grelu, Phys. Rev. E **90**, 033203 (2014).

[46] L. C. Zhao and J. Liu, Phys. Rev. E **87**, 013201 (2013).

[47] A. T. Avelar, D. Bazeia, and W. B. Cardoso, Phys. Rev. E **79**, 025602 (2009).

[48] N. Akhmediev, A. Ankiewicz, and J. M. Soto-Crespo, Phys. Rev. E **80**, 026601 (2009).

[49] J. Li, T. Xu, X.-H. Meng, Y.-X. Zang, H.-Q. Zhanga, and B. Tiang, J. Math. Anal. Appl. **336**, 1443 (2007).

[50] A. Degasperis and S. Lombardo, J. Phys. A **40**, 961 (2007).

[51] A. Degasperis and S. Lombardo, J. Pyhs. A **42**, 385206 (2009).

[52] A. Degasperis and S. Lombardo, Phys. Rev. E **88**, 052914 (2013).

[53] F. Baronio, S. Chen, P. Grelu, S. Wabnitz, and M. Conforti, Phys. Rev. A **91**, 033804 (2015).

[54] S. Chen, J. M. Soto-Crespo, F. Baronio, P. Grelu, and D. Mihalache, Opt. Express **24**, 15251 (2016).

[55] Z. Yan and C. Dai, J. Opt. **15**, 064012 (2013).

[56] G. W. Bluman and S. Kumei, *Symmetries and Differential Equations* (Springer, New York, 1989).

[57] G. W. Bluman and Z. Y. Yan, Eur. J. Appl. Math. **16**, 239 (2005).

[58] Z. Yan, V. V. Konotop, and N. Akhmediev, Phys. Rev. E **82**, 036610 (2010).

[59] W.-P. Zhong, M. R. Belic, and T. Huang, Phys. Rev. E **87**, 065201 (2013).

[60] A. Ankiewicz, J. M. Soto-Crespo, and N. Akhmediev, Phys. Rev. E **81**, 046602 (2010).

[61] E. N. Tsoy, A. Ankiewicz, and N. Akhmediev, Phys. Rev. E **73**, 036621 (2006).

[62] N. Akhmediev, V. M. Eleonskii, and N. E. Kulagin, Sov. Phys. JETP **89**, 1542 (1985).

[63] H. Torres-Silva and M. Zamorano, Math. Comput. Sim. **62**, 149 (2003).

[64] B. Bai, Y. Svirko, J. Turunen, and T. Vallius, Phys. Rev. A **76**, 023811 (2007).

[65] B. Bai, J. Laukkanen, A. Lehmuskero, and J. Turunen, Phys. Rev. B **81**, 115424 (2010).

CrossMark

REVIEW

Contrast of optical activity and rogue wave propagation in chiral materials

D. D. Estelle Temgoua (iD) · **M. B. Tchoula Tchokonte** · **M. Maaza** · **T. C. Kofane**

Abstract We report the contrast of optical activity and properties of nonparaxial optical rogue waves for the higher-order nonparaxial chiral nonlinear Schrödinger (NLS) equation. The latter describes the propagation of ultrashort optical pulses in chiral optical fibers. Both first- and second-order rogue wave solutions are investigated analytically by the modified Darboux transformation (MDT) and numerically by one pseudo-spectral method. The interplay of chiral materials on rogue wave propagation is elucidated, and the results can be applied on optical communication and in others physical systems.

Keywords Rogue wave propagation · Chirality and optical activity · Chiral materials · Chiral optical fibers

D. D. E. Temgoua (✉) · M. B. Tchoula Tchokonte
Department of Physics and Astronomy, University of the Western Cape, Private Bag X17, Bellville 7535, South Africa
e-mail: d.d.estelletemgoua@gmail.com

M. B. Tchoula Tchokonte
e-mail: mtchokonte@uwc.ac.za

D. D. E. Temgoua
Organization for Women in Science for the Developing World, ICTP Campus, Strada Costiera 11, 34151 Trieste, Italy

M. Maaza
I-Themba LABS, National Research Foundation, P. O. Box 722, Somerset West 7129, South Africa
e-mail: maaza@tlabs.ac.za

D. D. E. Temgoua · T. C. Kofane
University of Yaounde I, P. O. Box 812, Yaounde, Cameroon

T. C. Kofane
Centre d'Excellence Africain en Technologies de l'Information et de la Communication, University of Yaounde I, P. O. Box 812, Yaounde, Cameroon
e-mail: tckofane@yahoo.com

1 Introduction

The term chirality [1] is a well-known concept of great interest in chemistry, biology, pharmacology and optical fields [2,3]. In the context of chemistry, chirality refers to molecules that lack mirror symmetry. One of the most universally known examples is the human hands. In fact, no matter how the two hands are oriented, it is impossible for the both hands to be coincide through translations and rotations. In the context of optics, chirality refers to optical activity which is the ability to rotate plane polarized light. The observe rotation of this plane polarized light can be directed to the right hand that is a clockwise rotation, called dextrorotatory, or to the left hand that is a counterclockwise rotation, called levorotatory. As a consequence, enantiomers or optical isomers are designated in the literature as right- and left-handed [4]. Therefore, chirality can be defined as fundamental property of molecules and materials that leads to optical activity effects [5].

Among chiral materials, chiral optical fibers are materials of crucial importance. They give rise to optical activity effects such as optical rotation and circular dichroism which are optical characterization tech-

niques of molecules [2]. In fact, these effects are used to investigate the structures of molecules and to elucidate the secondary structure of biomolecules. Optical activity has attracted and inspired great effort in the developing of active photonic chiral metamaterials [6]. These materials are designated to deliver an unusual electromagnetic response, in spite of the fact that optical activity is a linear effect.

Optical activity effects have been found in both linear and nonlinear optics [7,8]. In nonlinear optical fields, other characterization techniques like the second-harmonic generation circular dichroism (SHG-CD) and the second-harmonic generation optical rotatory dispersion (SHG-ORD) were undertaken by T. Verbiest *et al.* [9]. Later, A. Bruyere *et al.* [10] have studied the formation of chiral supramolecular aggregates at an air–water interface with the SHG technique. Furthermore, Huttunen *et al.* [11] have shown that the third-harmonic generation circular dichroism (THG-CD) effects could occur in biological materials. Briefly, many works have been done in chiral metamaterials [12], nanomaterials [13,14] and photonic crystals [15].

In view of great scientific importance of chiral molecules in life science and pharmaceutical industries [16], we mainly focus our interest on the impact of chiral materials like chiral optical fibers in optical communication. Several nonlinear phenomena have been studied in chiral media [17–20] with the objectives to control the chiral level and protect organic chiral materials from damage during the processing temperature of silica. Therefore, controllability of spontaneous waves has been performed in both theoretical and experimental approaches to investigate the interesting phenomena of rogue waves in optical fibers [21].

Rogue wave phenomena can be described in both physical and mathematical aspects. In its physical aspect, three main features have been set to qualify a rogue wave phenomenon. First, the wave events should be twice more higher than the wave amplitude of the significant wave height (SWH) with extremely large amplitude. Secondly, they should appear and disappear unpredictably. This qualifier is equivalent to their unexpectedly reappearance and disappearance. Lastly, rogue wave events should arise more frequently and their probability distribution function (PDF) should display an L-shaped distribution of amplitude [22–24].

In its mathematical aspect, rogue wave is an exact rational solution obtained from the integrable scalar nonlinear Schrödinger (NLS) equation with finite back-

ground, called Peregrine soliton [25]. The Peregrine soliton (PS) is the mathematical rogue wave prototype in self-focusing regime due to its localization in both space and time, hence its denomination usual rogue wave. In the same aspect, other rogue wave solutions with finite backgrounds called unusual rogue waves were obtained from the focusing standard NLS equation. On the one hand, we have the Kuznetsov–Ma (K–M) solitons [26] which have the peculiarity of being localized in temporal dimension with periodicity along the propagation direction. On the other hand, we have the Akhmediev Breathers (ABs) [27] which have the peculiarity of being localized along the propagation direction with periodicity in temporal dimension [28].

The standard NLS equation is known as the universal model to describe rogue wave phenomenon in oceans [29], optical fibers [30–34], Bose–Einstein condensation [35,36], in laser–plasma interaction [37] and in econophysics [38]. In practice, the NLS equation is poetical to some realistic problems like the transmission of ultrashort pulses of the order of subpicosecond and femtosecond frequencies in highly dispersive optical fibers. Therefore, the NLS equation has been extended to take into account the third-order dispersion (TOD) and self-steepening (SS) nonlinearity [39]. Thus, the integrable Hirota equation [40] has been derived, even extended to take into account other nonlinear effects [41–44]. One of these effects is the nonparaxiality which arises in the miniaturization of devices involving multiplexed beams [45].

In this work, one focuses the attention on the contrast of optical activity to elucidate the interplay of chiral optical fiber on rogue wave propagation. This investigation is based on an extended integrable Hirota equation with linear and nonlinear effects, namely, nonparaxial chiral NLS equation. The ingenious analytical technique of Darboux transformation [46–49] is used to derive the rogue wave solutions, and a pseudo-spectral technique [50] is also used to highlighting the importance of this study on wave propagation in chiral materials.

The paper is organized as follows. In Sec. 2, the model is presented with its integrability conditions and the integrability constraints are derived through a direct ansatz. In Sec. 3, the first- and second-order rogue wave solutions are investigated analytically by the modified Darboux transformation (MDT) and numerically by one pseudo-spectral method, namely, difference-differential equation method. In Sec. 4, the

contrast of optical activity is revealed throughout the profiles of rogue waves and the interplay of chiral materials is elucidated. In Sec. 5, the outcomes are summarized.

2 Model and integrability constraints

To reveal the contrast of optical activity and elucidate the interplay of chiral optical fibers on rogue wave propagation, one considers an extended NLS equation with linear and nonlinear effects [51]

$$d\psi_{\xi\xi} + i\psi_\xi + P\psi_{\tau\tau} - i\gamma\psi_{\tau\tau\tau} + r_1 (i\mu \mp D) \psi$$
$$- C|\psi|^2\psi + i\alpha_3|\psi|^2\psi_\tau + r_2 (\eta \pm i\sigma_3) \psi_\tau = 0, \tag{1}$$

where ξ and τ (z and t) are the scaled (unscaled) coordinates in the propagation direction and temporal dimension, respectively. $\psi(\xi, \tau)$ is the envelope field of the forward and backward components of the waves. In regard of the derivation of the above model (Eq. (1)) in reference [51], the parameters r_1 and r_2 are equal to unity. Nevertheless, these parameters can be different in these cases. In the absence of either the linear gain/loss (μ) or linear birefringence (D), on the one hand, and in the absence of either the differential gain/loss (η) or linear group velocity (σ_3), on the other hand, the parameters r_1 and r_2, respectively, can be different to the unity depending now to the term in factor to them. Moreover, these parameters depend in major cases, to the physical system. Thus, for $r_1 = r_2 = 1$, the relations between the scaled and unscaled variables stand for

$$\tau = \frac{\omega_0^{1/3}\beta^{1/6}}{\sqrt{K''}(2K_0)^{1/6}}t', \quad \xi = \frac{\omega_0^{2/3}\beta^{1/3}}{(2K_0)^{1/3}}z' = \frac{z}{L_D},$$

$$L_D = \frac{(2K_0)^{1/3}(1 - K_0^2 T_c^2)}{\beta^{1/3}\omega_0^{2/3}} = \frac{-(1 - K_0^2 T_c^2)}{2K_0 d},$$

$$\psi(\xi, \tau) = \frac{\omega_0^{2/3}\beta^{1/3}}{(2K_0)^{1/3}}\phi = -2K_0 d\phi,$$

$$\phi = \Psi_{R,L} = E_x \pm iE_y, \quad \begin{cases} E_x = E_x(z, t) \\ \\ E_y = E_y(z, t) \end{cases}, \tag{2}$$

$$\begin{cases} t' = t - \frac{1}{v_g}z^* \\ \\ z' = z^* \end{cases}, \quad z^* = \frac{z}{(1 - K_0^2 T_c^2)},$$

where $\Psi_{R,L}$ are the right(R)- and left(L)-handed of wave components. Then, the parameters of Eq. (1) are

$$d = -\frac{\beta^{1/3}\omega_0^{2/3}}{(2k_0)^{4/3}}, \quad \eta = \frac{\alpha C}{\sqrt{K''}\omega_0^{1/3}\beta^{1/6}(2k_0)^{5/6}},$$

$$\gamma = \frac{K'''}{6}\frac{\beta^{1/6}\omega_0^{1/3}}{(2K_0)^{1/6}(K'')^{3/2}}, \quad C = 1 \pm K_0 T_c$$

$$\mu = C\Gamma, \quad \Gamma = \frac{\omega_0^{1/3}\alpha}{(2K_0)^{1/3}\beta^{1/3}}, \tag{3}$$

$$P = \frac{1}{2}\left(1 - \frac{k'^2}{K''k_0}\right), \quad \sigma_3 = \frac{k_0 T_c (2k_0)^{7/6}}{\sqrt{K''}\omega_0^{4/3}\beta^{1/6}},$$

$$D = \frac{K_0^2 T_c (2K_0)^{1/3}}{\beta^{1/3}\omega_0^{2/3}}, \quad \alpha_3 = \frac{C(2K_0)^{5/6}\beta^{1/6}}{\sqrt{K''}\omega_0^{2/3}K_0},$$

with

$$\begin{cases} K' = \frac{\partial K}{\partial\omega} = \frac{1}{v_g} \\ \\ K'' = \frac{\partial K'}{\partial\omega} \to GVD \\ \\ K''' = \frac{\partial K''}{\partial\omega} \to TOD \end{cases}, \quad \begin{cases} K_0 = \frac{\omega_0}{v} \\ \\ v^2 = \frac{1}{\mu_0\varepsilon_0} \\ \\ \beta = \mu_0\varepsilon_2 \\ \\ \alpha = \mu_0\sigma \end{cases}, \tag{4}$$

in which L_D is the diffraction length of the beam, α, the attenuation coefficient, σ, the electrical conductivity, ε_0, the linear permittivity, ε_2, the nonlinear permittivity, μ_0, the permeability, T_c, chiral parameter of the optical fiber, ω_0, the frequency of the wave, K_0, the wave number, v, the light velocity, and ϕ, the complex envelope of the optical field in the chiral fiber. Then, coefficients d, P, γ, μ, D, C, α_3, η and σ_3 are nonparaxial, group velocity dispersion (GVD), third-order dispersion (TOD), linear gain or loss term, linear birefringence, self-phase modulation (SPM), self-steepening (SS), differential gain or loss and linear group velocity, respectively.

The envelope field $\psi(\xi, \tau)$ contains both forward and backward propagating components in such a way that the change from the unscaled to scaled longitudinal coordinate of the oscillation of the field is given by

$$\exp\{-iK_\pm z\} = \exp\left\{i\frac{\xi}{2d}\left(1 - K_0^2 T_c^2\right)\right\}, \tag{5}$$

where $K_\pm = K = K_0$. It can be seen from relation (5) that apart from the wave number K_0, the scaled longitudinal coordinate is related to two important parameters. That are the nonparaxiality coefficient (d) and the chiral parameter (T_c) which will improve the description of waves propagating in chiral meduim. Equation (1)

contains other cases of NLS equation. If one sets $d = 0$, $P = \frac{1}{2}$, $\gamma = 0$, $\mu = 0$, $D = 0$, $\alpha_3 = 0$, $\eta = 0$ and $\sigma_3 = 0$, Eq. (1) becomes the standard NLS equation in the focusing regime for $C = -1$ and defocusing regime for $C = 1$. If in addition to these conditions, $d \neq 0$, Eq. (1) stands for the nonparaxial NLS equation. The integrable Hirota equation is also obtained for $d = 0$, $P = 1$, $\gamma = 2\sqrt{2}$, $\mu = 0$, $D = 0$, $\alpha_3 = -6\sqrt{2}$, $\eta = 0$, $\sigma_3 = 0$ and $C = -1$. Equation (1) has been found as a nonparaxial chiral NLS equation in our previous work [51]. This study is based now on the scalar form with constant coefficients. In this case, instead of Jacobian elliptic functions, parameters of the system will be taken as polynomial functions.

A higher-order NLS equation is eminently suitable to describe realistic problems when it satisfies the integrability and controllability conditions. Throughout the term in factor to the SS coefficient α_3, it can be seen that Eq. (1) verifies the condition of controllability of higher-order NLS equations [52]. The integrability of the model is satisfied for $\gamma = \frac{\alpha_3}{6C}$, $P = \frac{1}{2}$, $r_1 = r_2 = \frac{\alpha_3}{2C}$ and $d = \frac{5\alpha_3}{3C}$. If $\alpha_3 = 0$, then Eq. (1) is reduced to the standard NLS equation. In the case where $r_1 = r_2 = 1$, let us find the integrability constraints of the model by means of similarity reduction method. Thus, we use the envelope filed in the form [52]

$$\psi(\xi, \tau) = A(\xi) V[Z(\xi), T(\xi, \tau)] \exp\{i\rho(\xi, \tau)\}, \quad (6)$$

to find the integrability conditions of the parameters related to the envelope field in which $A(\xi)$ is the amplitude, $Z(\xi)$, the effective propagation distance, $T(\xi, \tau)$, the similitude variable and $V[Z(\xi), T(\xi, \tau)]$, the complex field. The variable $\rho(\xi, \tau)$ is the phase of the wave. The substitution of Eq. (6) into Eq. (1) gives a coupled system of partial differential equations with constant coefficients

$$d(A_{\xi\xi}V + 2A_\xi Z_\xi V_Z + 2A_\xi T_\xi V_T + 2AZ_\xi T_\xi V_{ZT}$$
$$+ AZ_{\xi\xi}V_Z + AT_{\xi\xi}V_T + AZ_\xi^2 V_{ZZ}$$
$$+ AT_\xi^2 V_{TT} - A\rho_\xi^2 V)$$
$$- AV\rho_\xi + P(AV_{TT}T_\tau^2 + AV_T T_{\tau\tau} - AV\rho_\tau^2)$$
$$+ \gamma(3AV_T T_{\tau\tau}\rho_\tau + 3AV_T T_\tau\rho_{\tau\tau} + 3AV_{TT}T_\tau^2\rho_\tau$$
$$+ AV\rho_{\tau\tau\tau} - AV\rho_\tau^3) \mp DAV - CA^2|V|^2 AV$$
$$- \alpha_3 A^2|V|^2 AV\rho_\tau + \eta AT_\tau V_T \mp \sigma_3 AV\rho_\tau = 0, \quad (7)$$

$$d(AV\rho_{\xi\xi} + 2A_\xi\rho_\xi V + 2AZ_\xi\rho_\xi V_Z$$
$$+ 2A\rho_\xi T_\xi V_T) + A_\xi V$$
$$+ AV_Z Z_\xi + AV_T T_\xi + P(AV\rho_{\tau\tau} + 2AV_T T_\tau\rho_\tau)$$

$$- \gamma(AV_T T_{\tau\tau\tau} + 3AV_{TT}T_\tau T_{\tau\tau} + AV_{TTT}T_\tau^3$$
$$- 3AV_T T_\tau\rho_\tau^2 - 3AV\rho_{\tau\tau}\rho_\tau) + \mu AV$$
$$+ \alpha_3 A^2|V|^2 AV_T T_\tau + \eta AV\rho_\tau \pm \sigma_3 AT_\tau V_T = 0, \quad (8)$$

where the scripts of differential equations are simplified as $A(\xi) = A$, $Z(\xi) = Z$, $T(\xi, \tau) = T$, $\rho(\xi, \tau) = \rho$ and $V[Z(\xi), T(\xi, \tau)] = V$. It is of crucial interest to reduce Eq. (1) into the integrable Hirota equation which has a well-known integrability conditions [53], satisfying the complex field of the ansatz $V[Z(\xi), T(\xi, \tau)]$

$$i\frac{\partial V}{\partial Z} = -\frac{\partial^2 V}{\partial T^2} + G|V|^2 V$$
$$+ 2\sqrt{2}i\nu\left(\frac{\partial^3 V}{\partial T^3} + 3|V|^2\frac{\partial V}{\partial T}\right). \quad (9)$$

Thus, the coupled system can be reduced as follows

$$\gamma T_\tau T_{\tau\tau} = 0, \quad (10)$$
$$T_\xi + 2dT_\tau\rho_\tau + 2PT_\tau\rho_\tau \pm \sigma_3 T_\tau$$
$$- \gamma\left(T_{\tau\tau\tau} - 3T_\tau\rho_\tau^2\right) = 0, \quad (11)$$
$$A_\xi + A(d\rho_{\xi\xi} + \rho_{\tau\tau}P + 3\gamma\rho_{\tau\tau}\rho_\tau + \mu + \eta\rho_\tau)$$
$$= 0, \quad (12)$$
$$\gamma T_\tau^3 + 2\sqrt{2}\nu Z_\xi = 0, \quad (13)$$
$$A_\xi V + AZ_\xi V_Z + AT_\xi V_T = 0, \quad (14)$$
$$\alpha_3 A^2 T_\tau - 6\sqrt{2}\nu Z_\xi = 0, \quad (15)$$
$$dT_{\xi\xi} + PT_{\tau\tau} + 3\gamma\left(T_{\tau\tau}\rho_\tau + T_\tau\rho_{\tau\tau}\right) + \eta T_\tau = 0, \quad (16)$$
$$Z_\xi + dT_\xi^2 + PT_\tau^2 + 3\gamma\rho_\tau T_\tau^2 = 0, \quad (17)$$
$$\rho_\xi + d\rho_\xi^2 + P\rho_\tau^2$$
$$+ \gamma\left(\rho_\tau^3 - \rho_{\tau\tau\tau}\right) \pm \sigma_3\rho_\tau \pm D = 0, \quad (18)$$
$$GZ_\xi + A^2(C + \alpha_3\rho_\tau) = 0, \quad (19)$$
$$A_{\xi\xi}V + 2A_\xi Z_\xi V_Z + 2A_\xi T_\xi V_T + 2AZ_\xi T_\xi V_{ZT}$$
$$+ AZ_{\xi\xi}V_Z + AZ_\xi^2 V_{ZZ} = 0. \quad (20)$$

From this preliminary method of rogue wave finding, the constraints are deduced from the differential equations of which the simplified forms stand from Eq. (10) to Eq. (20), respectively, as follows: $-3AV_{TT} \neq 0$, $AV_T \neq 0$, $V \neq 0$, $-AV_{TTT} \neq 0$, $2d\rho_\xi \neq 0$, $A|V|^2 V_T \neq 0$, $AV_T \neq 0$, $AV_{TT} \neq 0$, $-AV \neq 0$, $-A|V|^2 V \neq 0$ and $d \neq 0$. These conditions play an important role in the sense that they are necessary to find the integrability constants of parameters related to the envelope field.

3 Analytical and numerical rogue wave solutions

To construct the analytical rogue wave solutions, one firstly finds the parameters of the envelope field by solving the above differential equations. The integration is made from the simplest differential equation to the highly complex one. In doing so, Eq. (10) yields for $\gamma(\xi) \neq 0$ and $T_\tau T_{\tau\tau} = 0$ to the similarity variable

$$T(\xi, \tau) = T_1(\xi)\tau + T_0(\xi), \tag{21}$$

where the arbitrary functions $T_1(\xi)$ and $T_0(\xi)$ should be defined. One notices that $T_{\tau\tau} = 0$ is the second derivative condition of the similarity variable in the temporal dimension. Equation (13) gives the effective propagation distance

$$Z(\xi) = -\frac{\sqrt{2}\gamma}{4\nu} \int_0^\xi T_1(s)^3 ds. \tag{22}$$

The substitution of expressions (21) and (22) into Eq. (15) tends to

$$A(\xi) = \sqrt{\frac{-3\gamma T_1(\xi)^2}{\alpha_3}}, \tag{23}$$

with $\alpha_3 < 0$ and $\gamma > 0$. Then, the substitution of expressions (22) and (23) into Eq. (19) gives the phase of the envelope field which can be written as

$$\rho(\xi, \tau) = -\left(\frac{GT_1(\xi)}{6\sqrt{2}\nu} + \frac{C}{\alpha_3}\right)\tau + \rho_0(\xi), \tag{24}$$

where $\rho_0(\xi)$ should be defined by taking into account, the second derivative condition in the temporal dimension of the phase, that is, $\rho_{\tau\tau} = 0$. Through relations (21) and (24), we find from Eq. (16) the second derivative condition in the propagation direction of the similarity variable

$$T_{\xi\xi} = \frac{-\eta T_1(\xi)}{d}. \tag{25}$$

The substitution of relations (21) and (24) in Eqs. (11) and (17) shows that the first derivative of the similarity variable is independent of the temporal variable τ. This means that $T_{1\xi} = 0$ and $T_{0\xi} = T_\xi \neq 0$. Therefore, $T_1(\xi)$ must be a constant. Thus, the arbitrary function $T_0(\xi)$ deduced from Eq. (25) becomes

$$T_0(\xi) = \frac{-\eta T_1(\xi)}{2d}\xi^2. \tag{26}$$

The substitution of relations (21), (24) and (23) in Eqs. (12) and (18) shows that the first derivative of the phase is independent of the temporal variable τ. This also means that $\rho_{1\xi} = 0$ and $\rho_{0\xi} = \rho_\xi \neq 0$. This implies that $\rho_1(\xi) = -\left(\frac{GT_1(\xi)}{6\sqrt{2}\nu} + \frac{C}{\alpha_3}\right)$ is a constant. This affirmation is true as we have shown that $T_1(\xi)$ is a constant. Therefore, the second derivative condition of the phase in the propagation direction yields

$$\rho_{\xi\xi} = \frac{1}{d}\left[\eta\left(\frac{GT_1(\xi)}{6\sqrt{2}\nu} + \frac{C}{\alpha_3}\right) - \mu\right]. \tag{27}$$

From this second derivative condition, we deduce the arbitrary function of the phase

$$\rho_0(\xi) = \frac{1}{2d}\left[\eta\left(\frac{GT_1(\xi)}{6\sqrt{2}\nu} + \frac{C}{\alpha_3}\right) - \mu\right]\xi^2. \tag{28}$$

By choosing the arbitrary constant $T_1(\xi) = 2$, the parameters are summarized as follows

$$\begin{cases} T(\xi, \tau) = 2\tau - \frac{\eta}{d}\xi^2, \\[2mm] Z(\xi) = \frac{-2\sqrt{2}\gamma}{\nu}\xi, \\[2mm] A(\xi) = \left(\frac{-12\gamma}{\alpha_3}\right)^{\frac{1}{2}}, \quad \begin{cases} \gamma > 0, \\ \alpha_3 < 0, \end{cases} \\[4mm] \rho(\xi, \tau) = -\left(\frac{\sqrt{2}G}{6\nu} + \frac{C}{\alpha_3}\right)\tau + \frac{1}{2d}\left[\eta\left(\frac{\sqrt{2}G}{6\nu} + \frac{C}{\alpha_3}\right) - \mu\right]\xi^2. \end{cases} \tag{29}$$

In view of great success of the Peregrine soliton in the modeling of realistic rogue wave, we construct the rogue wave solutions through the modified Darboux transformation method [53]. From the well-known rogue wave solutions of the integrable Hirota equation [53], we deduce the first- and second order of the complex field $V[Z(\xi), T(\xi, \tau)]$ which is valid for $G = -1$ for rogue wave finding. Therefore, the different expressions of the complex field yield

$$\begin{aligned} V_1 & [Z(\xi), T(\xi, \tau)] \\ & = \left[1 - \frac{G_1 + iH_1}{D_1}\right]\exp\{iZ(\xi)\}, \end{aligned} \tag{30}$$

where

$$G_1 = 4, \quad H_1 = 8Z(\xi),$$

$$D_1 = 1 + \left[\sqrt{2}T(\xi, \tau) + 12\nu Z(\xi)\right]^2 + 4Z(\xi)^2. \tag{31}$$

and

$$\begin{aligned} V_2 & [Z(\xi), T(\xi, \tau)] \\ & = \left[1 + \frac{G_2 + iZ(\xi)H_2}{D_2}\right]\exp i\{Z(\xi)\}. \end{aligned} \tag{32}$$

where G_2, H_2 and D_2 are given by the relations

$$G_2 = -48T^4 - 1152\sqrt{2}\nu ZT^3$$
$$- 44T^2[4Z^2\left(36\nu^2 + 1\right) + 1]$$
$$- 576\sqrt{2}\nu ZT\left[12Z^2\left(12\nu^2 + 1\right) + 7\right] - 192Z^4$$
$$\times\left[216\left(6\nu^4 + \nu^2\right) + 5\right] - 864Z^2\left(44\nu^2 + 1\right) - 36,$$
$$H_2 = -96T^4 - 2304\sqrt{2}\nu ZT^3$$
$$- 96T^2[4Z^2\left(108\nu^2 + 1\right)$$
$$- 3] - 1152\sqrt{2}\nu ZT\left[4Z^2\left(36\nu^2 + 1\right)\right]$$
$$- 384Z^4\left(36\nu^2 + 1\right)^2$$
$$- 192Z^2\left(180\nu^2 + 1\right) + 360,$$
$$D_2 = 8T^6 + 288\sqrt{2}\nu ZT^5$$
$$- 432Z^4\left(624\nu^4 - 40\nu^2 - 1\right)$$
$$+ 36Z^2\left(556\nu^2 + 11\right) + 9$$
$$+ 64Z^6\left(36\nu^2 + 1\right)^3 + 96\sqrt{2}$$
$$\times ZT^3\left[12Z^2\left(60\nu^2 + 1\right) - 1\right]$$
$$+ 12T^4[4Z^2\left(180\nu^2 + 1\right) + 1]$$
$$+ 6T^2[16Z^4\left[216\nu^2\left(30\nu^2 + 1\right) - 1\right]$$
$$- 24Z^2\left(60\nu^2 + 1\right) + 9]$$
$$+ 72\sqrt{2}\nu ZT[16Z^4\left(36\nu^2 + 1\right)$$
$$+ 8Z^2\left(1 - 108\nu^2\right) + 17].$$
$$(33)$$

Then, collecting the founded variables with the above solutions of complex field together, one obtains the first- and second-order rational solutions, related to a particular solution of Eq. (1), respectively, in the form

$$\psi_1 = A(\xi)\left[1 - \frac{G_1 + iH_1}{D_1}\right]\exp\{iZ(\xi)$$
$$+ i\rho\left(\xi, \tau\right)\}, \qquad (34)$$
$$\psi_2 = A(\xi)\left[1 + \frac{G_2 + iZ(\xi)H_2}{D_2}\right]\exp\{iZ(\xi)$$
$$+ i\rho\left(\xi, \tau\right)\}. \qquad (35)$$

where parameters are given in relations (29), (30), (31), (32) and (33). These first- and second-order rational solutions are used to describe the propagation of nonparaxial optical rogue waves in chiral materials. The second-order rational solution is due to the collision between ultrashort pulses in the optical fiber. The particularity of these solutions is the simultaneous controllability of their amplitudes through the above parameters, which can be used to manage their amplitudes

and shapes. As the nonparaxiality, TOD, SS, SPM and differential gain or loss terms step in the system, they can therefore provide a more convenient and controlled environment for further applications in optical communication.

The methodology of the numerical integration is based on a pseudo-spectral method, namely, difference-differential equation method. The basic of the pseudo-spectral method is to use the discrete Fourier transform to evaluate the spatial derivative of the model. Nevertheless, within the context of optical fiber, these derivatives depend on coordinates of the propagation direction; those are $\psi_{\xi\xi}$ and ψ_{ξ} which stand for the nonparaxial and propagation terms, respectively. The using of their finite difference formulae with errors of second order gives the difference-differential equation below related to the model (Eq. (1)) for $\psi\left(\xi, \tau\right) = u\left(\xi, \tau\right)$

$$u_{n+1}(\tau) = \frac{1}{2d + i\Delta\xi}[(4d - 2P\Delta\xi^2\frac{\partial^2}{\partial\tau^2}$$
$$+ 2i\gamma\Delta\xi^2\frac{\partial^3}{\partial\tau^3}$$
$$- 2i\mu\Delta\xi^2 \pm 2\Delta\xi^2 D + 2C\Delta\xi^2|u_n(\tau)|^2$$
$$- 2i\alpha_3\Delta\xi^2|u_n(\tau)|^2\frac{\partial}{\partial\tau}$$
$$- 2\Delta\xi^2\left(\eta \pm i\sigma\right)\frac{\partial}{\partial\tau})u_n(\tau)$$
$$- \left(2d - i\Delta\xi\right)u_{n-1}(\tau)], \qquad (36)$$

with

$$\begin{cases} u_n(\tau) \equiv u\left(n\Delta\xi, \tau\right) \\ u_{n-1}(\tau) \equiv u\left((n-1)\Delta\xi, \tau\right) \\ u_{n+1}(\tau) \equiv f\left(u_n(\tau), u_{n-1}(\tau)\right). \end{cases} \qquad (37)$$

Equation (36) defines the explicit algorithm in the discretized domain in which the propagation variable ξ tends to $n\Delta\xi$. Then, the transverse differential operators $\partial^2/\partial\tau^2$, $\partial^3/\partial\tau^3$ and $\partial/\partial\tau$ are computed efficiently and accurately by the fast Fourier transforms (FFTs). The accuracy and convergence of this method have been demonstrated in the literature [50]. This method has the advantage of being explicit, means, simple implementation and low computation of the model and then its flexibility in the modeling of nonparaxial NLS equation with higher-order nonlinear effects. In this work, the first- and second-order analytical solutions are used as the initial conditions for the numerical simulation. Therefore, the implementation of the index n in Eq. (36), in view of relation (37), gives the numerical

solutions of optical rogue wave propagating in chiral materials.

## 4 Contrast of optical activity and interplay of chiral materials

The representation of analytical and numerical solutions of optical rogue waves constructed in previous section is of special interest, in the sense that their profiles will reveal the contrast of optical activity. It can be seen from relation (3) that, among coefficients which are functions of chiral parameter (T_c), η, C and μ are two component chiral parameters, whereas D and σ_3 are one component chiral parameters. Therefore, they can be chosen as follows

$$
\begin{cases}
\alpha_3 = -\alpha_0 \left(1 \pm K_0 T_c\right) \\
\alpha_0 = 4, \begin{cases} \alpha_{3+} = -6 \\ \alpha_{3-} = -2 \end{cases}
\end{cases}, \quad
\begin{cases}
\eta = \eta_0 \left(1 \pm K_0 T_c\right) \\
\eta_0 = \frac{2}{3}, \begin{cases} \eta_+ = 1, \\ \eta_- = \frac{1}{3} \end{cases}
\end{cases}
$$

$$
\begin{cases}
C = C_0 \left(1 \pm K_0 T_c\right) \\
C_0 = -\frac{2}{3}, \begin{cases} C_+ = -1 \\ C_- = -\frac{1}{3} \end{cases}
\end{cases}, \quad
\begin{cases}
\mu = \mu_0 \left(1 \pm K_0 T_c\right) \\
\mu_0 = 0.2, \begin{cases} \mu_+ = 0.3, \\ \mu_- = 0.1 \end{cases}
\end{cases}
$$

(38)

where $K_0 T_c = 0.5$ and with $\gamma = 0.2$, $G = -1$, $P = 0.5$, $D = 0.06$ and $\sigma_3 = 0.1$. To plot the first- and second-order analytical rogue wave solutions, one uses a MATLAB program in which the coordinates ξ and τ are bounded in the interval $[-10, 10]$. Thus, the first-order rogue wave solutions depicted in Figs. 1, 2 and 3 are computed from Eqs. (29), (31), (34) and (38). Then, the second-order rogue wave solutions represented in Figs. 4, 5 and 6 are computed from Eq. (29), (33), (35) and (38). Each figure is obtained for a different value of parameters d and v as shown in figure captions. The guideline techniques given above are of special interest for the numerical simulation in Figs. 7 and 8. The differential operators are expressed in the spectral domain through the FFTs in which the spectral parameter k is defined for $N = 128$ iterations with the given length $L = 40$. Therefore, the implementation of n in Eq. (36) is done for 102 iterations in the propagation direction ξ and where $\Delta \xi = 0.05$. According to the above parameters, the analytical and numerical representations are illustrated.

Due to the electromagnetic nature of chiral medium, there are two coupled characteristic waves in chiral optical fibers. This property of chiral medium is therefore observed in analytical and numerical representations throughout the LCP and RCP components. The
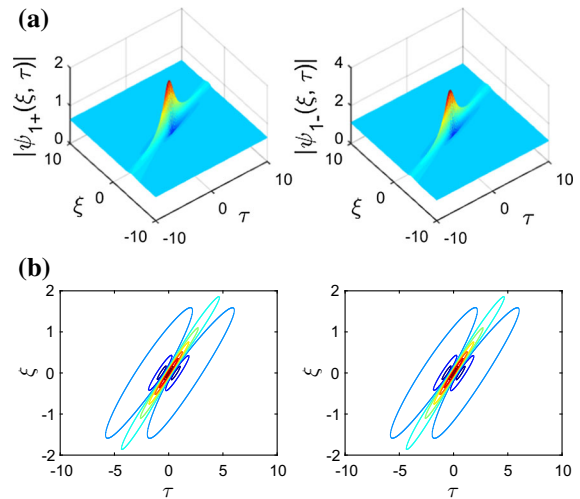

Fig. 1 Plot (**a**) and contour plot (**b**) of the first-order rogue wave solution: Eq. (34), with $d = 10$ and $v = 0.6$
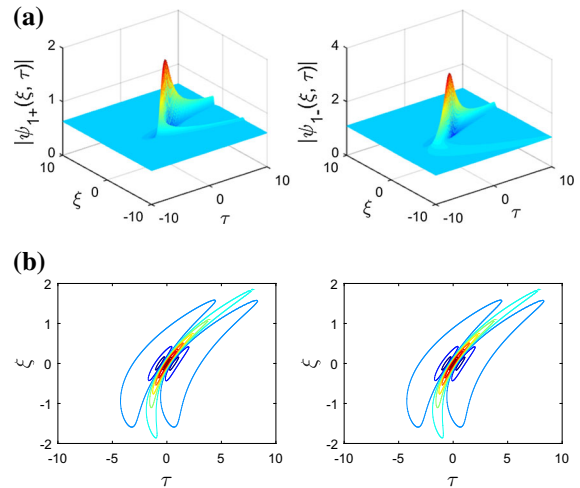

Fig. 2 3D representation (**a**) and contour plot (**b**) of the first-order analytical rogue wave amplitude of Eq. (34), for $d = 0.5$ and $v = 0.6$

structure of the waves is in accordance with rogue wave features. The short lifetime of rogue wave profiles is well observed throughout the point of their appearance and disappearance [see Figs. 1, 2, 4, 5, 6, 7]. Figures 4, 5, 6, 7 and 8 exhibit the collision of rogue waves, but it can be seen that their amplitudes are almost the same when one compares the maximum peak in Figs. 1 and 4 and then 2 and 5. It means that after collision, the waves keep their amplitude. This is a property of solitary waves, but as these waves are also localized in both space (τ) and time
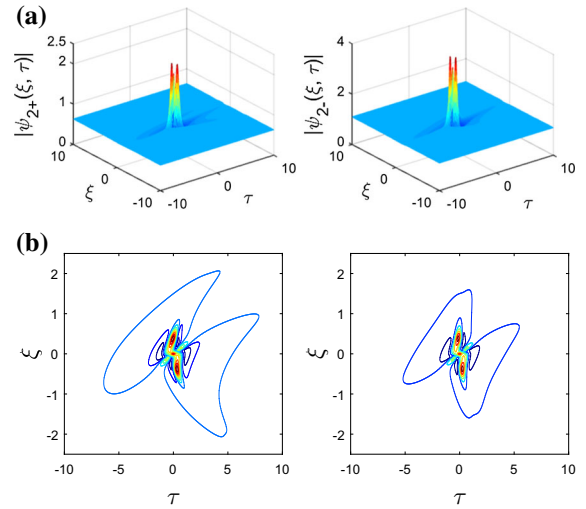
(a)

(b)
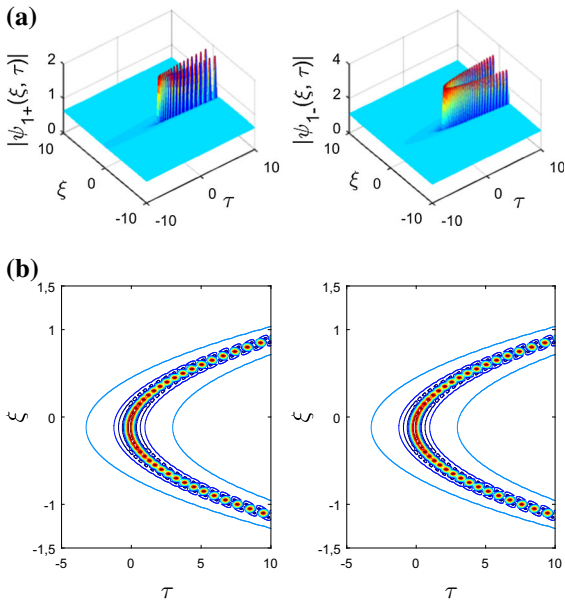
Fig. 3 First-order amplitude of nonparaxial chiral optical rogue waves of Eq. (34), with $d = 0.05$ and $\nu = 6$
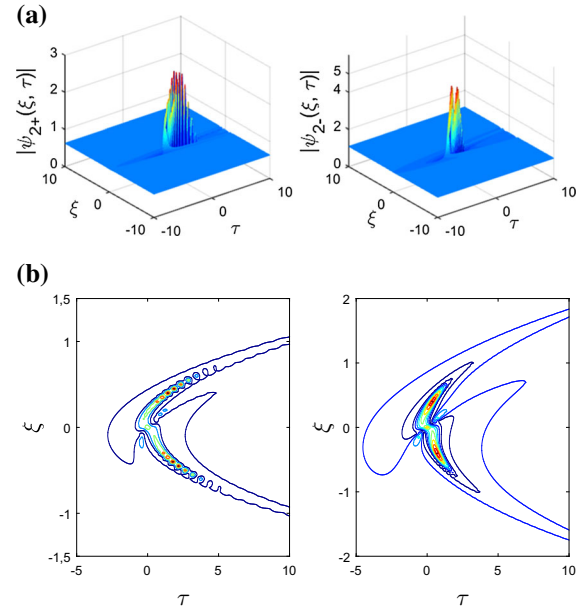
(a)

(b)
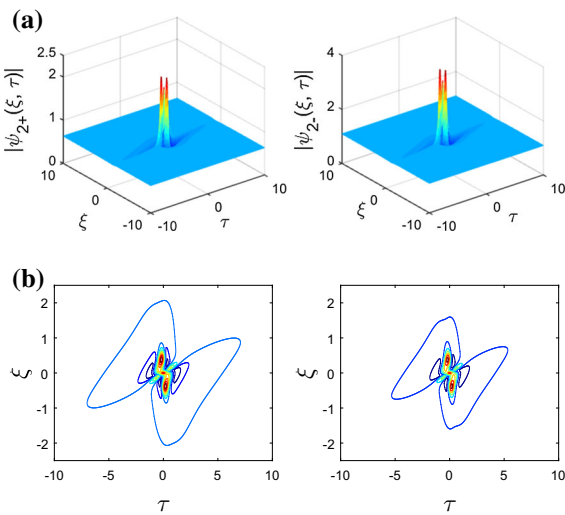
Fig. 4 Second-order amplitude of nonparaxial chiral optical rogue waves of Eq. (35), with $d = 10$ and $\nu = 0.6$

(a)

(b)

Fig. 5 Plot (**a**) and contour plot (**b**) of the second-order rogue wave solution: Eq. (35), with $d = 0.5$ and $\nu = 0.6$

(a)

(b)

Fig. 6 3D representation (**a**) and contour plot (**b**) of the second-order analytical rogue wave amplitude of Eq. (35), for $d = 0.05$ and $\nu = 6$

(ξ), they are usual rogue waves. Nevertheless, a difference is observed when comparing the high peak in Figs. 3 and 6. This difference is due to the weak value of the nonparaxial parameter d which perturbs, on the one hand, the both localization to coordinates and, on the other hand, the short propagation of rogue waves. This can be an advantage in the case where one needs to extend the lifetime of rogue waves in
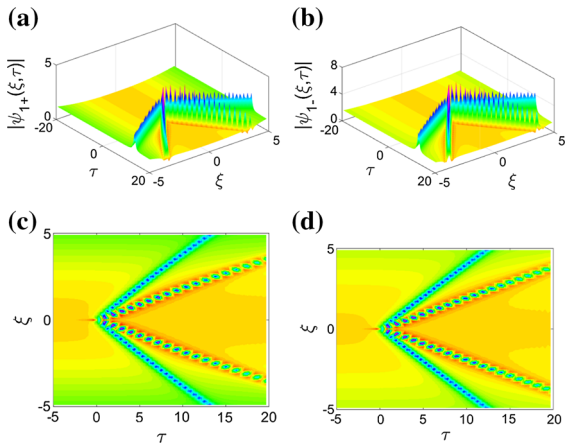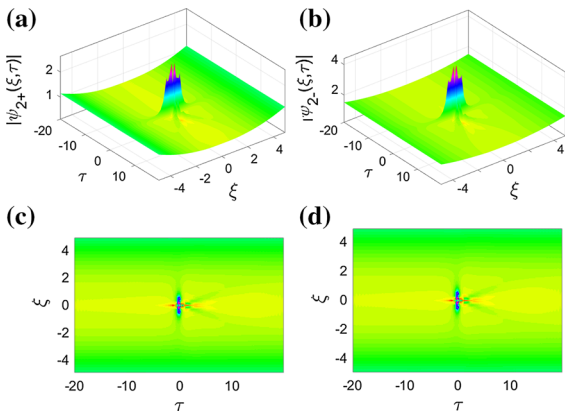
physical systems. Moreover, this depicts the behavior of waves in systems where the paraxial approximation is violated. A similar behavior is also observed in Fig. 7, but this time with a high value of the parameter d. It can be seen that the property of central character of the maximum peak of rogue wave is verified, but the property of localization of rogue wave proto-

Fig. 7 3D (**a**) and 2D (**b**) representations of the first-order numerical rogue wave amplitude of Eq. (1), for $d = 10$ and $\nu = 6$

Fig. 8 3D (**a**) and 2D (**b**) representations of the second-order numerical rogue wave amplitude of Eq. (1), for $d = 10$ and $\nu = 6$

with a multiplicity of peaks surrounding by holes which become linear to the vicinity of coordinates. This phenomenon is due to the degeneration of the rogue wave structure which starts by the break up of joined holes and then by the degeneration of holes which loss their lobes so far to become linear structures. As a consequence, a weak value of nonparaxiality can be benefit to reduce the amplitude of waves in physical systems when the MI increases drastically. This framework can be used to improve the stability of ultrashort pulses during their propagation in chiral optical fibers. In contrast to second-order analytical rogue wave solutions which have butterfly structures, numerical rogue wave solutions have rectilinear structures in both hands on the first order [see Fig. 7] and one peak issue from the collision of waves at the center of coordinates, more visible in second-order numerical solutions [see Fig. 8]. Moreover, Figs. 1, 4 and 7 exhibit a linear motions, whereas Figs. 2, 3, 5, 6 and 8 reveal a rotational motions. The slight rotation of the shape observed in Figs. 2 and 5 is amplified in Figs. 6 and 7, respectively. This amplification of rotation motion is due to the weak value of nonparaxial parameter d. This behavior of motion conversion is a property of chiral materials [20]. A concordance is observed on the motion conversion property as shown in Fig. 3 (first-order rogue wave analytical solutions) and in Fig. 7c, d (first-order rogue wave numerical solutions), on the one hand. On the other hand, a concordance can be observed on the shape of the maximum peak central character of their localization and on the amplitude as shown in Figs. 4a and 5a (for the second-order rogue wave analytical solutions) and in Fig. 8a, b (for the second-order rogue wave numerical solutions). Moreover, the contour plot of the LCP ($|\psi_{2-}(\xi, \tau)|$) in Fig. 6a (second-order rogue wave analytical solution) reveals as shown in Fig. 8 the rotational conversion property of chiral materials. Moreover, the conversion is also due to the chiral parameter related to coefficients of the original equation. Those coefficients are related to the effective propagation distance, similarity variable, amplitude and phase of the wave. These are the main parameters responsible of rotational conversion on the LCP and RCP components. However, the prompt action of rotational conversion is observed for a high value of parameter ν related to TOD and weak value of nonparaxial parameter d. The inverse process is also observed for a weak of parameter ν and high value of parameter d.

types is not anymore valid. Contrary to Fig. 7 which depicts the first-order solution, Fig. 8 (second-order solution) presents a different behavior, in the sense that the both localization and central character properties remain valid. This confirms the evidence of second-order rogue wave solutions of being more interesting in view of their precisions in realistic problems in optics.

One can add that Figs. 1, 2, 4, 5 and 8 depict the PS behavior throughout their both localization to coordinates, whereas Figs. 3, 6 and 7 depict a behavior near to the ABs. In the above figures, the diversity of shape is also observed. One denotes structures with one peak and two holes [see Figs. 1, 2] and then structures with triple peaks and two holes [see Figs. 4, 5]. More specifically, one founds a rogue wave structure

5 Conclusion

To understand the physical nature of the optical activity and to elucidate the chiral material properties on rogue wave propagation in chiral optical fiber, one focuses the attention on a higher-order nonparaxial chiral NLS equation. One founds that optical fibers filled with chiral material have a plurality of physical behaviors. Optical fibers with chiral core allow the propagation of two modes with different vectors. The LCP component refers to the counterclockwise rotation, namely, levorotatory, and the RCP component refers to the clockwise rotation, namely, dextrorotatory. Their structures in some cases are well localized in coordinates and for others similar to the ABs behavior. This localization is degenerated for weak value of nonparaxial parameter which governs both the central character of peak and rogue wave localization to coordinates. Moreover, this weak value is also responsible to the violation of paraxial approximation. Therefore, one may control the paraxial approximation, in multiplexed systems and in nanostructures in which this violation can occur. In addition, second-order rogue wave solutions were claimed to be more interesting in the study of wave propagation in realistic problems in optics.

The remarkable rotational property of chiral optical fibers is observed throughout the degeneration of lobes of butterfly structures which are converted from linear to rotational motion. This conversion is well observed in this work on contour plots of analytical and numerical simulations. As additional property of chiral materials, chiral optical refractive index has the peculiarity of being slightly higher compared to the refractive index of the cladding. This slight difference plays an undeniable role in optical propagation, in the sense that it is responsible to the total reflection of the light through the chiral core of optical fibers. Hence, there is the great importance of chiral materials. Moreover, helical structures with given chirality have an excellent mechanical behavior due to their remarkable rotational property. They provide the direct way to convert linear motion to rotational motion and vice versa. In consequence, in addition to the simultaneous controllability of the degeneration of waves and chiral level of materials, this work provides a theoretical framework to improve the controllable conversion of LCP and RCP waves, from linear to rotational motion and vice versa, as well as further experimental investigation of rogue wave propagation in chiral optical fibers.

Compliance with ethical standards

Conflict of interest The authors declare that they have no conflict of interest concerning the publication of this manuscript.

References

1. Degasperis, A., Lombardo, S.: Multicomponent integrable wave equations: I. Darboux-dressing transformation. J. Phys. A Math. Theor. **40**(5), 961–977 (2007)
2. Barron, L.D.: Molecular Light Scattering and Optical Activity. Cambridge University Press, Cambridge (1982)
3. Egidi, F., Carnimeo, I., Cappeli, C.: The optical rotatory dispersion of methyloxirane in aqueous solution: assessing the performance of density functional theory in combination with a fully polarization QM/MM/PCM approach. Opt. Mater. Express **5**(1), 196–201 (2005)
4. Singham, S.B.: Form and intrinsic optical activity in light scattering by chiral particles. J. Chem. Phys. **87**(3), 1873–1881 (1987)
5. Verbiest, T., Koeckelberghs, G., Champagne, B.: Feature issue introduction: chirality in optics. Opt. Mater. Express **4**(12), 264–265 (2014)
6. lapine, M., Shadrivov, I., Powell, D., Kivshar, Y.: Metamaterials with conformational nonlinearity, Scientific Reports, vol. 138, pp. 1–4 (2011)
7. Veretenov, N.A., Fedorov, S.V., Rosanov, N.N.: Topological vortex and knotted dissipative optical 3D solitons generated by 2D vortex solitons. PRL **119**(26), 263901 (2017)
8. Co, R.T., Harigaya, K., Nomura, Y.: Chiral dark sector. PRL **118**(10), 101801 (2017)
9. Verbiest, T., clays, K., Rodriguez, V.: Nonlinear Optical Charaterization Techniques: An Introduction. CRC press, Boca Raton (2009)
10. Buyere, A., Benichou, E., Guy, L., Bensalah-Ledoux, A., Guy, S., Brevet, P.-F.: Reversibility of the supramolecular chirality of bridged binaphtol derivatives at the air-water interface. Opt. Mater. Express **4**(12), 2516 (2014)
11. Huttunen, M.J., Partanen, M., Bautista, G., Chu, S.-W., Kauranen, M.: Nonlinear optical activity effects in complex anisotropic three-dimension media. Opt. Mater. Express **5**(1), 11–21 (2015)

12. Valev, V.K., Baumberg, J.J., Sibila, C., Verbiest, T.: Chirality and chiroptical effects in plasmonic nanostructures: fundamentals, recent progress, and outlook. Adv. Mater. **25**(18), 2517–2534 (2013)

13. Potravkin, N., Cherpetskaya, E., Perezhogin, I., Makarov, V.: Ultrashort elliptical polarized laser pulse interaction with helical photonic metamaterial. Opt. Mater. Express **4**(10), 2090–2101 (2014)

14. Chadha, A., Zhao, D., Zhou, W.: Comparative study of metallic and dielectric helix photonic metamaterial. Opt. Mater. Express **4**(12), 2460–2467 (2014)

15. Lee, K., Wu, J., Kim, K.: Defect modes in one-dimensional photonic crystal with a chiral defect layer. Opt. Mater. Express **4**(12), 2542–2550 (2014)

16. Verbiest, T., Kauranen, M., Persoons, A., Ikonen, M., Kurkela, J., Lemmetyinen, H.: Nonlinear optical activity and biomolecular chirality. J. Am. Chem. Soc. **116**(20), 9203–9205 (1994)

17. Bai, B., Svivko, Y., Turunen, J., Vallius, T.: Optical activity in planar chiral metamaterials: Theoretical study. Phys. Rev. A **76**(2), 023811–12 (2007)

18. Bai, B., Laukkanen, J., Lehmuskero, A., Turunen, J.: Simultaneously enhanced transmission and artificial optical activity in gold film perforated with chiral hole array. Phys. Rev. B **81**(11), 115424 (2010)

19. Poladian, L., Straton, M., Docherty, A., Argyros, A.: Pure chiral optical fibres. Opt. Express **19**(2), 968–80 (2011)

20. Dai, L., Zhu, K.-D., Shen, W., Huang, X., Zhang, L., Goriely, A.: Controllable rotational inversion in nanostructures with dual chirality. Nanoscale **10**(14), 6343–6348 (2018)

21. Akhmediev, N., et al.: Roadmap on optical rogue waves and extreme events. J. opt. **18**, 063001 (2016)

22. Solli, D.R., Ropers, C., Koonanth, P., Jalali, B.: Optical rogue waves. Nature **450**, 1054–7 (2007)

23. Lecaplain, C., Grelu, Ph, Soto-Crespo, J.M., Akhmediev, N.: Dissipative rogue waves generated by chaotic pulse bunching in a mode-locked laser. Phys. Rev. Lett. **108**(23), 233901–5 (2012)

24. Birkholz, S., Nibbering, E.T.J., Bree, C., Skupin, S., Demircan, A., Genty, G., Steinmeyer, G.: Spatiotemporal rogue events in optical multiple filamentation. Phys. Rev. Lett. **111**(24), 243903–5 (2013)

25. Peregrine, D.H.: Water waves, nonlinear schrödinger equation and their solutions. J. Aust. Math. Soc. Ser. B Appl. Math. **25**, 16–43 (1983)

26. Kibler, B., Fatome, J., Finot, C., Millot, G., Genty, G., Wetzel, b, Akhmediev, N., Dias, F., Dudly, J.M.: Observation of Kunetsov-Ma soliton dynamics in optical fiber. Sci. Rep. **2**(463), 1–5 (2012)

27. Akhmediev, N., Korneev, V.I.: Modulation instability and periodic solutions of the nonlinear schrödinger equation. Theor. Math. Phys. **69**(2), 1089–93 (1986)

28. Chen, S., Baronio, F., Soto-Crespo, J.M., Grelu, Ph, Mihalache, D.: Versatile rogue waves in scalar, vector and multidimensional nonlinear systems. J. Phys. A Math. Theor. **50**(463001), 1–78 (2017)

29. Onorato, M., Proment, D., Clauss, G., Klein, M.: Rogue waves: From nonlinear Schrödinger breather solutions to seer-keeping test. PLoS One **8**(2), e54629 (2013)

30. Agrawal, G.P.: Nonlinear Fiber Optics, 4th edn. Academic, San Diego (2007)

31. Walczak, P., Randoux, S., Suret, P.: Optical rogue waves in integrable turbulence. Phys. Rev. Lett. **114**(14), 143903–5 (2015)

32. Baronio, F., Conforti, M., Degasperis, A., Wabnitz, S.: Three-wave trapponinc solitons for tunable high-repetition rate pulse train generation. IEEE J. Quantum Electron **44**, 542–6 (2008)

33. Liu, W., Pang, L., Yan, H., Lei, M.: Optical soliton shaping in dispersion decreasing fibers. Nonlinear Dyn. **84**, 2205–2209 (2016)

34. Suret, P., Koussafi, R.E., Tikan, A., evain, C., randoux, s, szwaj, c, bielawski, s: Single-short observation of optical rogue waves in integrable turbulence using time microscopy. Nat. Commun. **13136**(7), 1–8 (2016)

35. Pitaevkii, L., Stringari, S.: Bose–Einstein Condensation. Oxford niversity Press, Oxford (2003)

36. Bagnato, V.S., Frantzeskakis, D.J., Kevrekidis, P.G., Malomed, B.A., Mihalache, D.: Bose-Einstein condensation: twenty years after. Rom. Rep. Phys. **67**(1), 5–50 (2015)

37. Malkin, V.M., shvets, G., Fisch, N.J.: Fast compression of laser beams to highly overcritical powers. Phys. Rev. Lett. **82**(22), 4448–51 (1999)

38. Wen, L., Li, L., Li, Z.D., Song, S.W., Zhong, X.F., Lui, W.M.: Matter rogue wave in Bose-Einstein condensates with attractive atomic interaction. Eur. Phys. J. D **64**, 473 (2011)

39. Kodama, Y., HAsegawa, A.: Nonlinear pulse propagation in a monomode dielectric guide. IEEE J. Quantum Electron **QE–23**(5), 510–524 (1987)

40. Hirota, R.: Exact envelope-soliton solutions of a nonlinear wave equation. J. Math. Phys. **14**, 805–9 (1973)

41. Chen, S., Song, L.-Y.: Peregrine solitons and algebraic soliton pairs in Kerr media considering space-time correction. Phys. Lett. A **378**, 1228–1232 (2014)

42. Chowdury, A., Krolikowski, W.: Breather solitons of a fourth-order nonlinear Schrödinger equation in the degenerate, soliton, and rogue wave limits. Phys. Rev. E **96**(4), 042209–13 (2017)

43. Ankiewicz, A., Akhmediev, N.: Rogue wave solutions for the infinite integrable nonlinear Schrödinger equation hierarchy. Phys. Rev. E **96**(1), 012219–8 (2017)

44. Wen, X.-Y., Yan, Zh, Malomed, B.A.: Higher-order vector dicrete rogue-wave states in the coupled Ablowitz-Ladik equations: exactsolutions and stability. Chaos **26**, 123110–1 (2016)

45. Miller, P.D., Akhmediev, N.N.: Transfer matrices for multiport devices made from solitons. Phys. Rev. E **53**(4), 4098–4108 (1996)

46. Matveev, V.B., Salle, M.A.: Darboux Transformation and Solitons. Springer, Berlin (1991)

47. Degasperis, A., Lombardo, S.: Multicomponent integrable wave equations: I. Darboux-dressing transformation. J. Phys. A Math. Theor. **40**, 961–977 (2007)

48. Degasperis, A., Lombardo, S.: Multicomponent integrable wave equations: II. Soliton solutions. J. Phys. A Math. Theor. **42**, 385206–22 (2009)

49. Mukam, S.P.T., Souleymanou, A., Kuetche, V.K., Bouetou, T.B.: Generalized Darboux transformation and parameter-dependent rogue wave solutions to a nonlinear shrodinger system. Nonlinear Dyn. **93**(2), 373–383 (2018)

50. Chamorro-Posada, P., McDonald, G.S., New, G.H.C.: Nonparaxial beam propagation methods. Opt. Commun. **192**, 1–12 (2001)

51. Temgoua, D.D.E., Tchoula, T.M.B., Kofane, T.C.: Combined effects of nonparaxiality, optical activity and walk-off on rogue wave propagation in optical fibers filled with chiral materials. Phys. Rev. E **97**(4), 042205–18 (2018)

52. Yan, Z., Dai, C.: Optical rogue waves in the generalized inhomogeneous higher-order nonlinear Schrödinger equation with modulating coefficients. J. Opt. **15**, 064012 (2013)

53. Ankiewicz, A., Soto-Crespo, J.M., Akhmediev, N.: Rogue waves and rational solutions of the Hirota equation. Phys. Rev. E **81**(4), 046602–8 (2010)